Proceedings of

First Conference for Engineering Sciences and Technology

Vol. 2

Editor

M. A. Elalem

AIJR Publisher

Series: AIJR Proceedings
More information about this series at
https://books.aijr.org/index.php/press/catalog/series/proceedings

First Volume of this Proceedings is Published in "AIJR Proceedings" Series 2, 2018

at

https://doi.org/10.21467/proceedings.2

M. A. Elalem

(Editor)

Proceedings of

First Conference for Engineering Sciences and Technology

CEST-2018 (25-27th September 2018)

Volume 2

Organized by

Garaboulli and Al-khoms Engineering Faculties,

Elmergib University (Libya)

Published by

AIJR Publisher, 73, Dhaurahra, Balrampur, India 271604

Proceedings of First Conference for Engineering Sciences and Technology (CEST-2018) 25-27th September 2018, Volume 2

Editor
Mohamed A. Elalem
Assistant Professor
Department: Electrical and Computer Engineering
Elmergib University, Libya

Conference Organizer
Garaboulli and Al-khoms Engineering Faculties, Elmergib University (Libya)

ISBN: 978-81-936820-6-7 (eBook)

Series
AIJR Proceedings
Series Volume: 4
DOI: 10.21467/proceedings.4
Series Editor
Dr. Adam A. Bahishti

Published
30 November 2018

Imprint
AIJR Books

Published by
AIJR Publisher, 73, Dhaurahra, Balrampur, India 271604

Table of Contents

Track 4

Track 5

Track 6

About CEST-2018

A scientific conference explores the developments of scientific research in the field of applied engineering sciences, technologies, material science, environmental and engineering management, in order to support inter-disciplinary work. The conference is being organized by Faculty of Engineering Garaboulli, and Faculty of Engineering, Al-khoms, Libya. The main objectives of this even are

- Focus on new developments in technical fields and display its key role in national development.
- Exchange ideas and experiences between the academics and technologists in engineering fields.
- Work among different engineering disciplines in design and implementation of projects.
- Role of engineering colleges and technical institutes in contributing effectively to development of Scientific research and link with related institutions.

A scientific conference explores the developments of scientific research in the field of applied engineering sciences, technologies, material science, environmental and engineering management, in order to support inter-disciplinary work. The following 43 but not limited to are the main tracks

1- Communication and Information Technology.

- Broad Band Communication
- Intelligent Communication.
- Mobile, Wireless and Optical Communication.
- Wireless Sensor Networks.
- Signal and Image Processing.
- Software Engineering and Cloud Computing.
- Computer Networks and Security.
- E-Government and E-Commerce.
- Education and Information Technology.

2- Electrical and Electronics Engineering

- Smart Grid Systems and Applications.
- Power Quality Improvement Techniques.
- Control System Technologies.
- Power System Modeling and Simulation.
- Power System Generation.

3- Oil and Chemical Engineering.

- Oil Exploration and Production Operations.
- Polymer Engineering and Technology
- Oil Refining Processes.
- Corrosion and Method of Prevention and treatment.

- Membrane science and Water Desalination.
- Modeling and Design in Chemical Processing.
- Separation processes and Petrochemical Production.

4- Industrial, Structural Technologies and Science Material

- Concrete and Building Technologies.
- Roads Engineering and survey.
- Design and Analysis of Mechanical and Structural.
- Production Processes, Welding Techniques and Heat Treatment.
- Rehabilitation of Engineering Facilities.
- Destructive and Non-destructive Tests.
- Engineering Materials and their Applications.
- Nano Technology in Engineering fields.

5- Engineering Systems and Sustainable Development

- Renewable and Alternative Energies.
- Water Purification and Water Distribution Networks.
- Feedback and Optimal Control Systems.
- Air Conditioning and Refrigeration Systems.
- Power System Generation.
- Hydraulic and Pneumatic Systems.
- Environmental waste management.
- Auditory and visual pollution.
- Auditory and visual pollution.
- Any other Topics on Architecture & Urban Planning

6- Engineering Management

- Risk Management.
- Design and Implementation Management.
- Quality Management Systems.
- Natural Resource Management.

Among about 145 contributed submissions, there were two keynote addresses, and 92 accepted research papers. The Conference started with reciting Quran and national anthem "Beladi" sung followed by inaugural speech delivered by Dr. Salhin Alaud, the organizing committee chair, faculty of Engineering, Elmergib University, Libya. The welcome speech was delivered by Dr. Mohamed Elalem, the scientific committee chair, Elmerghib university, followed by the Dean of the faculty of Engineering Dr. Farag Alsool. The Plenary talks were delivered by distinguished scientists; the details of which are available in the Scientific Program which is downloadable from the conference website http://cest2018.elmergib.edu.ly.

The Libya Iron and Steel Company, The Melleta Oil and Gas, Libya Export Promotion Center, Engineering Academy Tajoora, Zajel Libya and Elmergib University were the main Cosponsors of the CEST-2018.

About the Editor

Mohamed A. Elalem obtained his B.Sc. and M.Sc. in Electrical and Electronic Engineering (with specialization in Telecommunications) degrees in 1990 and 2006 respectively, and his Ph.D. in Electrical and Computer Engineering, Ryerson University, Toronto, Canada in wireless communications 2013. He is currently an assistant professor at telecommunications branch, faculty of Engineering, Elmergib University. He has contributed in a lot of conferences and committees (national and international). His main interesting areas are digital modulations schemes, cognitive radio, spectrum sharing, optimization techniques and RF design and evolution.

Elmergib University, Faculty of Engineering, Khoms, Libya.

Review Process

Authors were invited to submit abstracts which were peer reviewed by two specialists. The committee has received about (250) abstracts. The committee rejected about (40) abstracts. Then the authors were motivated to send their full-length papers for peer-review. CFP is managed by Easychair System. Each manuscript was peer-reviewed by two (2) technical specialists in fully blind base (the names and affiliation of the authors were hidden to the reviewers) The review process is conducted anonymously. To be published both reviewers were to agree separately that the manuscript met the standard required for publication in these proceedings.

Ignoring withdrawn papers, there were (160) papers submitted and (90) accepted for oral presentations. Three (3) papers were excluded from the proceedings according to their authors request. The committee and technical chairs would like to thank all the reviewers for their diligence and for contributing their time, effort and technical expertise to the review process.

The Committee

1	**Dr. Mohamed A. Elalem**	**Libya**	**Elmergib University**	**Assistant prof**	**Chair**
2	**Dr. Meftah Alfatni**	**Libya**	**Elmergib University**	**Lecturer**	**Track 1 Coordinator**
3	**Dr. Adnan S. Krzma**	**Libya**	**Elmergib University**	**Lecturer**	**Track 2 Coordinator**
4	**Dr. Ali Ebshish**	**Libya**	**Elmergib University**	**Assistant prof**	**Track 3 Coordinator**
5	**Dr. Hosen Jawan**	**Libya**	**Elmergib University**	**Professor**	**Track 4 Coordinator**
6	**Dr. Hatem Hadia**	**Libya**	**Elmergib University**	**Lecturer**	**Track 5 Coordinator**
7	**Dr. Mohamed A. Alaalam**	**Libya**	**Elmergib University**	**Professor**	**Track 6 Coordinator**
8	Dr. Abdullah Masrub	Libya	Elmergib University	Assistant prof	
9	Dr. Osama Alkishriwo	Libya	University of Tripoli	Assistant prof	
10	Dr. Khalid Alajel	Libya	Elmergib University	Assistant prof	
11	Eng. Ali Tamtum	Libya	Elmergib University	Assistant prof	
12	Dr. Ibrahim El Aziz	UK	University of Sheffield	Associate prof	
13	Dr. Bashir Saleh Younise	Libya	Elmergib University	Assistant prof	
14	Dr. Salah Aburawe	Libya	Elmergib University	Lecturer	
15	Dr. Ahmed Mohamed Hamruni	Libya	Elmergib University	Assistant prof	
16	Dr. Khaled Abdusamad	Libya	Elmergib University	Lecturer	
17	Dr. Ausama Hadi Ahmed	Libya	Elmergib University	Lecturer	
18	Dr. Mohamed K. Zambri	Libya	Elmergib University	Assistant prof	
19	Dr. Ali El Sharif	Libya	Elmergib University	Assistant prof	
20	Dr. Abdussalam M. Rifai	Libya	Elmergib University	Professor	
21	Dr. Faraj Farhat Eldabee	Libya	Elmergib University	Lecturer	
22	Dr. Abduel Majid K. Najjar	Libya	Elmergib University	Professor	
23	Dr. Mahmoud Y. Khamaira	Libya	Elmergib University	Lecturer	
24	Dr. Ali Elkais	Libya	Elmergib University	Assistant prof	
25	Dr. Ahmed Bshish	Libya	Elmergib University	Assistant prof	
26	Dr. Abubaker Alshuiref	Libya	Elmergib University	Assistant prof	
27	Dr. Abdussalam Addeeb	Libya	Elmergib University	Associate prof	
28	Dr. Ali Elghariani	Libya	University of Tripoli	Lecturer	
29	Dr. Ahmed Mohamed Goma	Libya	Elmergib University	Associate prof	

30	Eng. Abdulmajid Ferh	Libya	Elmergib University	Lecturer	
31	Dr. Abubkr Abdelsadiq	Libya	Elmergib University	Assistant prof	
32	Dr. Izziddien Alsogkier	Libya	Elmergib University	Lecturer	
33	Dr. Salem M. Sharif	Libya	Elmergib University	Assistant prof	
34	Dr. Abdelhamed I. Ganaw	Libya	Elmergib University	Assistant prof	
35	Dr. Mohamed El-Abboud	Libya	Elmergib University	Associate prof	
36	Dr. Mohamed S. Elforgani	Libya	Elmergib University	Assistant prof	
37	Dr. Bashir Ashhuby	UK	University of Sheffield	Lecturer	
38	Dr. Abdelrazak Ben Jaber	Libya	Nat. Standriz. Center	Assistant prof	
39	Dr. Salhin M. Alaud	Libya	Elmergib University	Lecturer	
40	Dr. Matouk M. Elamari	Libya	Engineering Academy	Assistant prof	
41	Dr. Khaled M. Dadesh	Libya	University of Tripoli	Assistant prof	

Program Schedule

Program of The First Conference for Engineering Sciences and Technology (CEST-2018)		
Day 1: Tuesday, September 25, 2018		
Room 1	09:00-10:00	
	10:00-11:30	
	10:30-	Open Ceremony
	11:45-	Oral Session [**Communication and Information Technology**]
	13:00-	Lunch Break
	14:30-	Oral Session [**Oil and Chemical Engineering**]
	15:45-	Coffee Break
	16:15-	Oral Session [**Engineering Systems and Sustainable**
Room 2	09:00-10:00	
	10:00-11:30	
	10:30-11:45	
	11:45-13:00	Oral Session [Electrical and Electronics Engineering]
	13:00-14:30	Lunch Break
	14:30-15:45	Oral Session [**Industrial, Structural Technologies and Science**
	15:45-16:15	Coffee Break
	16:15-17:30	Oral Session [**Industrial, Structural Technologies and Science**

September 25 - 27, 2018 – Garaboulli, Libya

Time	**Tuesday**	**Wednesday**	**Thursday**
09:00 - 10:00	Registration	Invited Speaker	Invited Speaker
10:00 - 10:30	Coffee Break		
10:30 - 11:45	Open Ceremony	Oral Sessions	Oral Sessions
11:45 - 13:00	Oral Sessions		
13:00 - 14:30	Lunch Time		
14:30 - 15:45	Oral Sessions	Oral Sessions	Oral Sessions
15:45-16:15	Coffee Break		
16:15 - 17:30	Oral Sessions	Oral Sessions	Close Ceremony

Tuesday, September 25, 2018 (11:45 – 13:00)

Room 1

Session: Communication and Information Technology			
Chai	Dr. Meftah Salem Alfatni and Dr. Khalid Mohamed Alajel		
Time	Paper ID	Paper Title	Author(s)
11:45-12:00	CEST_013	Fiber-Optic Temperature Sensor Design Adapted for Libyan	Mohamed Bin Saeed Mohamed Otman Twati
12:00-12:15	CEST_070	The performance of Space Time Block Coding (STBC) in MIMO Relay Network	Hamza Ali Jamal Elbergali
12:15-12:30	CEST_129	Hearing Protection System by Using a Simple Noise Reduction Strategy	Izziddien Alsogkier
12:30-12:45	CEST_136	Enhancement of Bandwidth of U-shape Loaded Microstrip Patch Antenna According to 802.11b Standard	Mohamed A. S. Alshushan Fadel A. M. Alaswad Marai M. Abousetta
12:45-13:00	CEST_185	Experimental Evaluation of the Humans' Health Hazards' Potential Due to Exposure to the Microwaves' Radiations in Garabouli City-Libya.	Abdurahman Altawil Mohamed Youssef Abdelbaset Karem Omran Majdi Masoud Alrajhi

Room 2

Session: Electrical and Electronics Engineering			
Chai	Dr. Adnan S. Krzma and Dr. Mohmoud Y. Khamaira		
Time	Paper ID	Paper Title	Author(s)
11:45-12:00	CEST_058	Micro Gas Turbine Simulation and Control	Ibrahim Sharif Mahmoud Mansour El-
12:00-12:15	CEST_217	Antenna Elevation Control using Multiple Switched Self-tuning Controllers Design	Othman E. Aburas Ahmed M. Alnajeh Youssef Amer Arebi
12:15-12:30	CEST_220	Control of a Three-phase Off-Grid Inverter for Renewable Energy Systems Applications	Ali M A Almaktoof Abdulsslam M Ashoor Shaouf
12:30-12:45	CEST_111	Optimal Power Loss Minimization using Optimal Size and Location of Shunt	Hesain Milad Alfrd

12:45-13:00	CEST_114	Experimental Investigation on the Performance Evaluation of Solar Tracking Photovoltaic System	A.Kagilik S. Mousa I.Enageem

Tuesday, September 25, 2018 (14:30 – 15:45)

Room 1

Session: Oil and Chemical Engineering			
Chair	Dr. Mohamed K. Zambri and Dr. Ali Elkaish		
Time	Paper ID	Paper Title	Author(s)
14:30-14:45	CEST_025	Synthesis gas Production with High Hydrogen Concentration Aspen Simulation.	Abdalhamed A. E. Musbah Salah.M.Algoul Abdalbaset M.R
14:45-15:00	CEST_040	A Stochastic Optimisation Technique for Tuning a Continuous Stirred Tank Reactor Controllers	Yousif Alsadiq
15:00-15:15	CEST_060	Verification of the reserves of Al-Hamada Oil Field V-NC6 Area by Application of Well Logs	Tariq Basher Essa Tabar Ali Omran
15:15-15:30	CEST_077	Boilers Performance Evaluation of Zuara Desalination Plant	Ali Muftah Mabruk M. Abugderah
15:30-15:45	CEST_116	Estimation of Original Oil in Place for Belhedan Oil Field by Using Volumetric Method, Material Balance Equation Method, and Reservoir Simulation Method	Ali Nasar Jibriel Abusaleem Essa M. Tabar

Session: Industrial, Structural Technologies and Science Material			
Chai	Dr. Hosen A. Jawan and Dr. Salem M. Sharif		
Time	Paper ID	Paper Title	Author(s)
14:30-14:45	CEST_015	The Effect of Using Ash Residues of Olive Fruits on the Properties of Cement Mortar	Hamza Almadani Mukhtar Muammar Aburawi
14:45-15:00	CEST_017	Study the Performance of Solar Water Heater with Various Loads	Ghassan Almasri Mustafa El-Musbahi
15:00-15:15	CEST_024	Effects of Reduction in Construction Temperature on Workability of Warm Mix Asphalt Incorporating Rh-Wma Additive	Bashir M. Aburawi

15:15-15:30	CEST_032	Seismic Response of Reinforced Concrete Buildings as Predicated by the Draft of Libyan Standard (DSLS-1977) and (IBC-	Issa. A. Mohammed Suleiman. A. Khatrush
15:30-15:45	CEST_035	Nonlinear Structural Dynamic Response of Multi-Story Buildings Under Seismic	Awatif Twil

Room 2

Tuesday, September 25, 2018 (16:15 – 17:30)

Room 1

Session: Engineering Systems and Sustainable Development			
Chai	Dr. Hatem Hadia and Dr. Khaled Abdusamad		
Time	Paper ID	Paper Title	Author(s)
16:15-16:30	CEST_062	Exergy Analysis Of A Brine Mixing Othrough MSF Distillation Plant	Usama Ezzeghni Mohamed Abduljawad
16:30-16:45	CEST_064	The Optimal Membrane Type for the Next Membrane Replacement of Tajoura SWRO Desalination Plant	Usama Ezzeghni
16:45-17:00	CEST_072	Feasibility Study of Cardboard Waste Recycling	Mahdi Esmieo Moad Shaklawon Omar Shaneb
17:00-17:15	CEST_103	Designing and Optimizing 10,000 M3/Day Conventional SWRO Desalination Plant	Usama Ahmed
17:15-17:30	CEST_120	Finite Element Modeling and Simulation of A Microstructure Silicon Beam Resonant	Mohamed Shaglouf Elharoshi Diryak Ahmed Abugalia

Room 2

Session: Industrial, Structural Technologies and Science Material			
Chairs:	Dr. Hosen A. Jawan and Dr. Abdelhamed I. Ganaw		
Time	Paper ID	Paper Title	Author(s)

16:15-16:30	CEST_038	Investigations of Kaolin Clay Collapse Behavior Using an Oedometer Apparatus	Musbah Hasan Gumaa Abdelazizi Hasan
16:30-16:45	CEST_059	Design of Reinforced Concrete Beams using Two Different Methods	Gumaa Hasan Mohammed A. Elsageer Musbah A. Hasan
16:45-17:00	CEST_082	High Density Polyethylene/Libyan Kaolin Clay Nanocomposites: Effect of Clay Particle Size on Rheological, Surface aMechanical Properties	Abdalbary Rhab Anour Shebani Abdalah Klash Abdelkader Aswei Khalid Omran Abdalbary Rhab
17:00-17:15	CEST_098	كيفية الاستفادة من مخلفات الخرسانة في حالتها الطازجة	م. علي عثمان مسعود م. محمد ميلاد الأشتر
17:15-17:30	CEST_167	A Review Study of The Effects of Air Voids on Asphalt Pavement Life	Ali Zaltuom

End of the 1st day

Day 2: Wednesday, September 26, 2018		
Room 1	09:00-10:00	Invited Speaker [Dr. Hamid H Sherwali]
	10:00-10:30	Coffee Break
	10:30-13:00	Oral Session [**Communication and Information Technology**]
	13:00-14:30	Lunch Break
	14:30-15:45	Oral Session [**Electrical and Electronics Engineering**]
	15:45-16:15	Coffee Break
	16:15-17:30	Oral Session [**Engineering Systems and Sustainable Development + Engineering Management]**
Room 2	09:00-10:00	
	10:00-10:30	Coffee Break
	10:30-13:00	Oral Session [**Industrial, Structural Technologies and Science Material**]
	13:00-14:30	Lunch Break
	14:30-15:45	Oral Session [**Engineering Systems and Sustainable Development**]
	15:45-16:15	Coffee Break
	16:15-17:30	Oral Session [**Industrial, Structural Technologies and Science Material]**

Wednesday September 26, 2018 (10:30 – 13:00)

Room 1

Session: Industrial, Structural Technologies and Science Material			
Chairs:	Dr. Abdussalam M. Rifai, Dr. Moamer Hmead and Dr. Bashir S. Younise		
Time	Paper ID	Paper Title	Author(s)

10:30-10:45	CEST_170	Modeling and Finite Element Analysis of Leaf Spring Using Pro-Engineer and ANSYS Softwares	Salem Fathi Elsheltat Abdulbaset Alshara
10:45-11:00	CEST_197	Influence of Plastic Bottles Fibre on Self Compacting Concrete	Abdelhamed Ganaw Basel Meghari Abdulnasir Alkoum Mohammed
11:00-11:15	CEST_212	Prediction of local concretes compressive strength using the maturity method	Mohammed Elsageer Wisam Elhmali Mansour
11:15-11:30	CEST_225	Design of Vertical Pressure Vessel Using ASME Codes	Najeeb A. Yahya Othman M. Daas Nureddin O.
11:30-11:45	CEST_226	Design Methodology for Supply Water Distribution Network; Case Study: Al-Hadeka District, Garaboulli-Libya	Abdulghani Ramadan Khairi Algrad
11:45-12:00	CEST_158	Static and Dynamic Analysis of Multistory RC Building with Various Heights in High Seismic Zone	Md. Shahnewaz Sarkar Ghusen Al-Kafri
12:00-12:15	CEST_140	Influence of Surface Roughness on Adhesion between the Existing and new plain concretes	Nurdeen Altwair Saad Jaber Abu Jarir
12:15-12:30	CEST_021	Thermal performance of a heat pipe with different working fluids	Ayad Alwaer Jasson Gryzagoridis
12:30-12:45	CEST_026	Effect of Corrugation Geometry And Shape On Energy Absorption of composite plate.	Fathi A.al ssahly Khalid A. Elbkory
12:45-13:00	CEST_132	Analysis of the Failure of Cylindrical Pressure Vessels	Osama Terfas Arwa M. Elambrouk Ahlam Y. Elraqiq

Room 2

Session: Communication and Information Technology			
Chairs:	Dr. Ahmed M. Goma, Dr. Khaled M. Dadesh and Dr. Abdullah A. Masrub		
Time	Paper ID	Paper Title	Author(s)
10:30-10:45	CEST_124	A Novel Chaotic Uniform Quantizer for Speech Coding	Osama Alkishriwo

10:45-11:00	CEST_125	Iterative Time--Varying Filter Algorithm Based on Discrete Linear Chirp Transform	Osama Alkishriwo Ali A. Elghariani Aydin Akan
11:00-11:15	CEST_131	Fast Efficient Transforms for Contour Extraction from Encrypted Medical Image	Ali Ukasha Ali Ahmed Ganoun
11:15-11:30	CEST_047	Employing Various Data Mining Techniques to Forecast the Success Rate of Information Technology Education Students	Mosbah Mohamed Elssaedi
11:30-11:45	CEST_187	Capability of Modified SIFT to Match Stereo Imagery System	Omar Abusaeeda Salah Naas Nasar Aldian Shashoa
11:45-12:00	CEST_144	Fast Efficient Transforms for Contours Extraction and Image Compression using Zonal Sampling Methods	Ali Ukasha Abdolhameed Ali Madi
12:00-12:15	CEST_049	Multiple Noises Removal from Computed Tomography (CT) Images	Abdelkader Salama Alrabaie Marwan M M El marmuri Emhimed Saffor
12:15-12:30	CEST_054	A New Technique to Encrypt-Decrypt Digital Color Images Using One-Dimensional Matrix	Khdega A.Yosef Galala
12:30-12:45	CEST_085	Using Triple Modular Redundant (TMR) Technique in Critical Systems Operation	Ali A. Tamtum Samira Abu Shernta
12:45-13:00	CEST_084	Building English Vocabulary Schema and Words Retention Using Review Value Calculation for English as Secondary Language Students	Mosbah Mohamed Elssaedi Burnhan Mustafa Tanis Melvin A. Ballera

Wednesday, September 26, 2018(14:30 – 15:45)

Room 1

Session: Electrical and Electronics Engineering

Cha — Dr. Adnan S. Krzma and Dr. Ali Tamtum

Time	Paper ID	Paper Title	Author(s)
14:30-14:45	CEST_168	Comparative Analysis of Electric Field and Potential Distributions over Porcelain and Glass Insulators Using Finite Element Method	Adnan S. Krzma Mahmoud Y. Khamaira Maruwan Abdulsamad
14:45-15:00	CEST_182	Long Term Peak Load Forecasting for the Libyan Network	Mahmoud Y. Khamaira Adnan S. Krzma A. M. Alnass
15:00-15:15	CEST_184	THD Investigation of Hybrid Cascaded Multilevel Inverter	A.Elzowawi Islam Saad Mustafa Elsherif
15:15-15:30	CEST_206	Impact of Wind Generation Location on Power System Losses	Ibrahim Naser
15:30-15:45	CEST_223	Excimer Laser Processing of IGZO Thin Films for Transparent TFTs	Khairi Abusabee Khalid .M. Alajel Salem .O. Elhamali

Room 2

Session: Engineering Systems and Sustainable Development

Ch — Dr. Mohamed A. Alaalam and Dr. Mohamed S. Elforgani

Time	Paper ID	Paper Title	Author(s)
14:30-14:45	CEST_157	Zero Energy and Low Water Schools: Case Study Building of Garaboulli Engineering Faculty-Libya	Salhin Alaud Khalid M. H. Jaballa Abdulghani M. Ramadan

14:45-15:00	CEST_155	Wind Energy Reliability Analysis based on the Monte Carlo Simulation Method	Khaled Abdusamad
15:00-15:15	CEST_174	Synthesis and characterization of magnetic CoFe1.9Cr0.1O4 nanoparticles by sol-gel method and their applications as an adsorbent for water treatment	Ibrahim Amar Abubaker Sharif Najat A. Omer Naght E. Akale Fatima Altobami
15:15-15:30	CEST_178	To What Extent Do Nursery Group Rooms Match with The Architectural Design Considerations?	Mustafa Zarigan Lutfi Senan Muftah Omeman
15:30-15:45	CEST_190	Solar Hydrogen Production System Simulation using Pscad	Matouk M. Elamari

Wednesday, September 26, 2018(16:15 – 17:30)

Room 1

Session: Engineering Systems and Sustainable Development + Engineering Management

Chairs: Dr. Mohamed A. Alaalam and Dr. Abdulghani M. Ramadan

Time	Paper ID	Paper Title	Author(s)
16:15-16:30	CEST_193	Performance Analysis of a Solar Driven Single Stage LiBr/H2O Absorption Refregiration System	Islam Shahboun Salem Omran Adeilla
16:30-16:45	CEST_205	Preserving. Architectural Heritage within the International Covenants and its Reflection in the Libyan Case	Hussein Ali Ashraf Laswad Latefa Wafa
16:45-17:00	CEST_219	Measuring urban clarity of the built environment	Fawzi Mohamed Agael
17:00-17:15	CEST_179	Key Performance Indicators in Libyan Oil and Gas Projects	Mahmoud Matoug Abdulbaset Frefer Haleema Omer
17:15-17:30	CEST_199	An Investigation of Corrosion Risks in the Oil and Gas Pipelines Using Analytical Hierarchy Process and Fuzzy Analytical Hierarchy Process	Abdulbaset Frefer Mahmoud M. Matoug Fatma L. Haddada

Room 2

Session Industrial, Structural Technologies and Science Material					
Chai	Dr. Bashir S. Younise and Ahmed M. Hamruni				
Time	Paper ID		Paper Title		Author(s)
16:15-16:30	CEST_029	Effects of Spring Stiffness on Suspension Performances Using Full Vehicle Models			Moamar Hamed M. Elrawemi
16:30-16:45	CEST_030	Influence of Coolant Concentration on Surface Roughness during Turning of Steel C-6			Abdulaziz Abodena Muhannad Alrzage Ibrahim K. Husain
16:45-17:00	CEST_039	Effects of outlet nozzle geometry on Swirling Flows in gas turbine			Hesham Baej Adel Akair Adel Diyaf Salem Adeilla
17:00-17:15	CEST_027	Mapping of Sea Water Intrusion in the Westren Libyan Coast using Geoelectric Method: Case Study			Abdel Hameed M. Salem Magdi A. Mountasir Husam Abdussalam R. Shames
17:15-17:30	CEST_028	Effects of Different Fluids Properties on Cavitation Performance in Centrifugal Pump			Saad Ghidhan Moamar Hamed Mansor Benaros

End of 2nd day

Day 3: Thursday, September 27, 2018		
Room 1	09:00-10:00	Invited Speaker [Dr. Tammam Ben Mousa] (apologized for coming)
	10:00-	Coffee Break
	10:30-13:00	Oral Session [**Industrial, Structural Technologies and Science Material]**
	13:00-	Lunch Break
	14:30-15:30	Oral Session [**Communication and Information Technology + Electrical and Electronics Engineering**]
	15:30-16:30	Close Ceremony
Room 2	09:00-10:00	
	10:00-	Coffee Break
	10:30-12:45	Oral Session [**Oil and Chemical Engineering**]
	13:00-	Lunch Break

Thursday, September 27, 2018 (10:30 – 13:00)

Room 1

Session: Industrial, Structural Technologies and Science Material			
Chai	Dr. Matouk M. Elamari, Dr. Mustafa A. Almusbahi and Dr. Salhin Alaud		
Time	Paper ID	Paper Title	Author(s)
10:30-10:45	CEST_122	The Effect of Adding Steel Slag and Lime on the Engineering Properties of a Sandy Soil	Mohammed Elsageer Ayad Abdelmoula
10:45-11:00	CEST_159	Capablity of Designing a Novel Smart Fluid Damper using a Mckibben Actuator	Haithem Elderrat Elganidi Elsaghier
11:00-11:15	CEST_050	Theoritical Invistigation Of An Indirect Evaporation Air Cooling System	Mohamed Alowa Gassem A. Azzain

11:15-11:30	CEST_041	Aerodynamic Effects Of Blade Positive Sweep In Axial Flow Cascades	Ali Kwedikha Abdul Azeam A. Elgayed Abelmalek N. Algaaoud
11:30-11:45	CEST_019	Built to Code Building Envelop Versus Sustainability of High-Rise Building Performance	Mohamed Ali Karim
11:45-12:00	CEST_020	Simple and Sustainable Constipate to Save Cost and Time for Constructions Structure	Abdualraouf Mohamed Mohamed Ali Karim
12:00-12:15	CEST_057	Monitoring Mis-Operating Conditions of Journal Bearings based on Modulation Signal Bispectrum Analysis of Vibration Signals	Osama Hassin Usama Haba Fengshou Gu Andrew Ball
12:15-12:30	CEST_083	Particle Size Dependence of MnO Reduction for Fabrication of 〖Al-AlMnO〗_X Composite vir Stir Casting	Khalid Almadhoni Sabah Khan
12:30-12:45	CEST_115	Nanotechnology: Concepts, Importance and the Current State of Scientific Research	Samieh Abu Saad Amani Elmahjubi
12:45-13:00	CEST_162	Investigation into Accuracy of LGD2006 for Medium-elevation Areas	Ahmed Hamruni Adel Alkilani

Room 2

Session: Oil and Chemical Engineering			
Chai	Dr. Abduel Majid K. Najjar, Dr. Ali S. Ebshish and Dr. Ibrahim M. El Aziz		
Time	Paper ID	Paper Title	Author(s)
10:30-10:45	CEST_045	CO_2 Corrosion Inhibitor Assessment Using Various Measurement Techniques in [illegible]	Abdelrazag Aziz
10:45-11:00	CEST_139	Pressure Transient Analysis by Using MS. Excel Sheet and Computer Programming	Essa M. Tabar Ali Omran Nasar Tariq Basher
11:00-11:15	CEST_141	Evaluation of Corrosion Resistance of Mild Steel and Aluminium Using Anodic Inhibitor Method and Passivity.	Ali Elkais Mohamed K Zambri
11:15-11:30	CEST_200	Optimum deposition of Tungsten Oxide on Titania Nanotubular and study Photoactivity of Nano-Composite Photoanode	Asma M. Husin Milad Soud Saad Awitil Mohammad B. Kassim Wan Ramli Wan Daud

11:30-11:45	CEST_208	Modeling the Effect of CO_2 on Thermodynamic Behavior of CO_2/Libyan Natural Gas Mixture	Almahdi Alhwaige Ali S. Bshish Salem M. Abdusalam Ahmed M. Ebshish
11:45-12:00	CEST_214	Novel Green Sorbents Derived from Mesembryanthemum-based Biomass for Wastewater Treatment Applications	Almaki Abushaina Abdelrahman Sultan Wael Elhrari Almahdi A. Alhwaige
12:00-12:15	CEST_215	Novel Green Photocatalysts Derived from Date-based biomass/TiO_2 for Photocatalytic Oxidation of Methylene Blue Dye in Aqueous Solutions	Almahdi Alhwaige Mohammed A. El-Ghweil Wael Elhrari
12:15-12:30	CEST_083	Particle Size Dependence of MnO Reduction for Fabrication of 〖Al-AlMnO〗_X Composite vir Stir Casting	Khalid Almadhoni Sabah Khan
12:30-12:45	CEST_227	Estimation of Empennage Design Weight in Conceptual Design Phase for Tactical Uavs	Abdulhakim Muhammad Essari

Thursday, September 27, 2018 (14:30 – 16:00)

Room 1

Session: Communication and Information Technology + Electrical and Electronics Engineering

Chai: Dr. Izziddien Alsogkier and Dr. Ausama H. Ahmed

Time	Paper ID	Paper Title	Author(s)
14:30-14:45	CEST_151	Bandwidth Optimization Through Hybrid Codecs G.711 and G.729 for VoIP Ethernet, FR and MP Networks	Abdullah Masrub Mohamed Alahemar AbdulSalam Addeeb
14:45-15:00	CEST_164	Modeling and Performance Evaluation of MapReduce in Cloud Computing Systems Using Queueing Network Models	Guzlan Miskeen
15:00-15:15	CEST_109	Handwriting Arabic Words Recognition Based on Structural Features	Salim Aloud
15:15-15:30	CEST_128	Color Image Encryption in the Spatial Domain Using 3-D Chaotic System	Osama Alkishriwo Hanan Salem Alzreghi

15:30-15:45	CEST_171	Combined Image Encryption and Steganography Algorithm in the Spatial Domain	Osama Alkishriwo Aya H. S. Abdelgader
15:45-16:00	CEST_224	Loss of Load Expectation of Alkhoms Generating Units	Mohamed Altaher Ben Mouhsen Ali A. Tamtum

Track 4

Industrial, Structural Technologies and Science Material

The Effect of using Ash Residues of Olive Fruits on the Properties of Cement Mortar

Mukhtar M. Aburawi[a], Hamza Mohammed Al-Madani[b*],

[a] Civil Engineering Department, El-mergib University, AlKhoms - Libya.
[b]Civil Engineering Department, Azzaytuna University, Tarhuna - Libya

DOI: https://doi.org/10.21467/proceedings.4.1
* Corresponding author email: hamza.almadani308@gmail.com

ABSTRACT

This research aims at studying the effect of the use of the burnt olive oil waste ash (OWA) resulting from olive plant wastes as a partial cement replacement (5%, 7% and 10%) on the properties of cement mortar. The ash burning temperature varies as 600, 700, 800 and 900˚C, and time as 6, 7, 8 hours. The mortar cured in air and water were prepared with 0.42 w/c ratio and sand to water ratio of 1.5 by mass.

The results showed that the 600˚C was efficient in terms of contribution to strength, specific gravity while 7% cement-OWA replacement mixture was found to favour flowability of the mortar compared to 5 and 10% substitution. Extending OWA burning time temperature to 900˚C and 8hrs increased its porosity and water absorption of the resulting mortar. The OWA slowed down the setting time which made it suitable in the hot weather concreting practice.

Keywords: cement; olive waste ash; mortar; curing; pozzolanic materials; compressive strength

1 Introduction

Large quantities of solid olive waste which contains organic minerals accumulate every year in the countries (Palestine. Tunisia and Libya) producing olive oil[1]. This causes great harm to the environment due to its interaction with heat and humidity thereby resulting in chemical hazards. For instance, the carbolic acid, and other strong life-threatening smell emanates from the decomposition[1]. There is increase in such waste accumulation at an alarming rate due to the lack of waste management techniques, such as recycling or re-use in a positive or productive environmental friendly manner with a view to reducing the environmental pollution risks and problems[1].

Concrete industry has seen significant development in the utilization of waste materials as partial replacement for ordinary Portland cement[1]. This research aims at exploring the performance of olive waste as alternative materials in concrete production for structures. Therefore, it is expected that such utilization could provide additional safety and longer service life to concrete structures.

Recently, a number of researchers focused on the use of agricultural material waste, as a partial replacement for cement mixtures so as to improve several properties of concrete and cement

mortar. A significant breakthrough was recorded especially on palm oil fuel ash, rice husk ash and date palm ash as regards their performances in OPC based concrete and geopolvmer or alkaline activated binder[25]. In this study, the burnt out and ground waste of olive fruits will be used as a partial replacement for OPC cement to see the effect of different replacement ratios on the properties of cement mortar in terms of the workability grade, absorption and compressive strength, and setting time of cement paste.

2 Experimental program

2.1 Materials

2.1.1 Ordinary Portland Cement and sand

The ordinary Portland cement, of specific weight of 3.15 and surface area of 273 m2/kg, in compliance with Libyan specifications No.340/1997m[2] was used in this study. The fine aggregate used was of specific weight 2.57, which is within the limit of fine aggregate in compliance with the British specifications (BS882-1992)[3].

2.1.2 Olive Oil waste treatment

The olive waste ash (OWA) was obtained through burning large quantities of olive fruit wastes at constant burning time of 6 hrs at temperatures of 600˚C, 700˚C, 800˚C and 900˚C, and in different burning times, 6 hrs and 8 hrs at the specific temperature of 900˚C. The rate of raising temperature inside the oven was 20˚C/Min. The ash was left for 24 hours in the air for cooling, and then ground in the grinding machine for 10 mins before sieving through sieve No. 200 (0.075mm). The surface area of the resultant ash was measured by Blaine device in accordance with the US standards (ASTM C204-92)[4].

2.2 Mix design and sample processing

The mixture of the samples was composed of cement of 0.42:1.5:1.0 by mass of cement, sand and water, respectively while OWA was used as a partial replacement for cement with 0wt.% (control), 5wt.%, 7wt.% and 10wt.% of cement. Mixing was done with an electric mixer for 5 mins while two-layer compaction was done in metal cube mould of dimension 50×50×50 mm in size with surface dressing and leveling using 16 tamping-rod blows, according to the approved US specifications steps (ASTM C109-92)[5]. Table 1 shows the details of percentages composition of materials in the prepared mortar. For each mix 21 cubes has been treated, as 9 cubes in the air at a temperature ranging from 20 to 24˚C, and 12 cubes in Jerry water according to US specifications (ASTM C109-92)[5] at a temperature ranging from 18 to

22°C, and to maintain the purity of the water used, the treatment water was changed every 15 days.

Table 1: Details of cement mortar mixing quantities

Batch No.	Sample code	Cement weight (gm.)	Ash percentage (%)	Ash weight (gm.)	Fine aggregate weight (gm.)	Water weight (gm.)
S1	OPC	2500	0	0	3750	1050
S2	OWA60085	2375	5	125	3750	1050
S3	OWA60087	2325	7	175	3750	1050
S4	OWA600810	2250	10	250	3750	1050
S5	OWA70085	2375	5	125	3750	1050
S6	OWA70087	2325	7	175	3750	1050
S7	OWA700810	2250	10	250	3750	1050
S8	OWA80085	2375	5	125	3750	1050
S9	OWA80087	2325	7	175	3750	1050
S10	OWA800810	2250	10	250	3750	1050
S11	OWA90085	2375	5	125	3750	1050
S12	OWA90087	2325	7	175	3750	1050
S13	OWA900810	2250	10	250	3750	1050
S14	OWA90065	2375	5	125	3750	1050
S15	OWA90067	2325	7	175	3750	1050
S16	OWA900610	2250	10	250	3570	1050

3 Results and discussion

3.1 Physical analysis of olive waste ash

With increase in burning temperature and time of olives waste, the specific weight and the surface areas of ash resulting from the burning process decreases as shown in Table 2. The decreases could be due to volatility of the amorphous fine particles like carbon or other debris there by leading volume and surface area reduction as temperature or duration increases. The physical properties and chemical composition of OWA are shown in Table 2.

Table 2: Physical properties of olive waste ash samples

Sample code	Surface area (cm^2/gm)	Specific weight
OWA6008	7461	2.28
OWA7008	5779	2.18
OWA8008	4439	2.12
OWA9006	4751	2.21
OWA9008	3310	2.09

The surface area and specific gravity (Table 2) reduced by 40.5% and 7.1%, respectively as the temperature increased from 600-800°C whereas at 900°C increasing the burning duration from

ISBN: 978-81-936820-6-7
Proceedings DOI: 10.21467/proceedings.4

Series: AIJR Proceedings

6-8hrs caused the reduction of 30.3% and 5.4%, respectively from original values of 4751 cm2/gm 2.21.

3.2 Oxide composition of olive wastes ash

Through the results of the chemical composition of olive wastes ash (OWA) samples by (XRF) device, shown in Table 3, it can be seen that temperature and burning hours have impact on the oxide composition of OWA. The sample burnt at 900˚C has more calcium and alumina contents while more burning duration favours the formation of silica at the same temperature. Besides, the increase in silica content from 18.22 to 31.98% (75.5% increment) as the temperature increases from 600 to 900˚C while potassium depleted significantly at that latter temperature.

Table 3: Oxide composition of olive waste ash samples

Chemical element	Sample code				
	OWA6008	OWA7008	OWA8008	OWA9006	OWA9008
Calcium %) CaO(	21.09	19.62	20.74	23.39	20.82
Silica %) SiO2(	18.39	23.6	22.94	18.22	31.98
Aluminum %) Al2O3(	1.23	1.27	1.26	1.21	1.44
Iron %) Fe2O3(	1.88	3.01	4.32	2.21	5.90
Potassium %) K2O(	44.96	42.24	40.99	42.2	31.25
Magnesium %) MgO(	0.64	0.75	0	0.79	0.53
Cobalt %) SO3(	5.45	3.88	3.95	4.93	2.78
Phosphorus) P2O5%(	6.19	5.46	5.6	6.87	4.99
Titanium) TiO2%(	0.18	0.17	0.2	0.17	0.26
Chlorides) Cl%(	1.42	2.15	1.81	1.03	0.55

3.3 Properties of fresh mortar and cement paste

3.3.1 Flowability and workability

From the results of the flow table for the workability values of the samples burnt at 600 deg C for 5, 7 and 10% shown in Figure 1. It is clear that 5% cement replacement percentage samples (OWA60085C) and 10% (OWA600810C) recorded a decline in workability values while OWA60087C (7%) were more homogeneous with high workability values, very close to the result of the reference sample (OWA0C). This suggests that less the presence of CaO, SiO2 and Al2O3 in the mortar with 10% OWA will definitely reduce the workability as seen in Figure 1. When the quantity of OWA was too low (5%) in concrete mixture, there could be excessive voids in the resultant mortar thereby increasing the interparticle sand grains friction which resulted in low workability as shown in the figure. The closeness of 7% OWA flowability to the control sample indicates that effective parking that ensured the control over

voids distribution. The quantity of CaO, SiO2 and Al2O3 is less than that of 10%OWA thereby causing the reduction in water demand in the mixture.

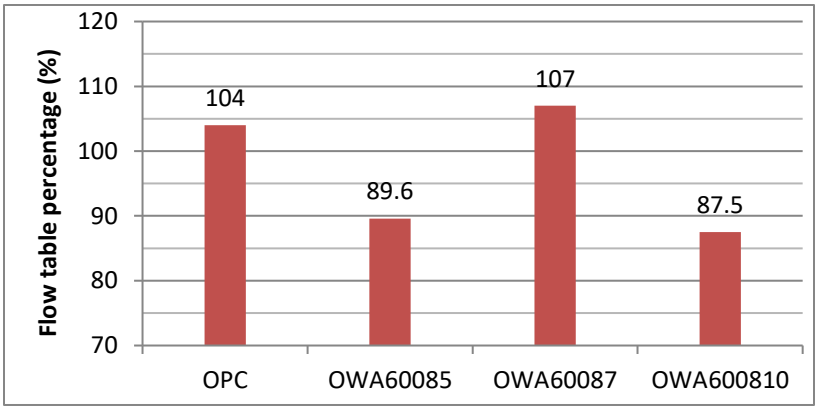

Figure 1: Effect of replacement percentage on flow

It was also observed in Figure 2 that the inclusion of OWA change the range of initial and final setting time which decreased from 135 mins of the control to 130.9 and 15 mins for 5.7 and 10% OWA additions, respectively as shown in Figure 2. This suggests that the more the quantity of OWA the more the delay of initial setting of the sample due to pozzolanic reaction and dilution of tricalcium aluminate portion of OPC that precede hydration reaction or the initial formation of forming calcium aluminium hydrate (CAH). The C3A in the composition increases with OWA content and reacted with gypsum to from calcium-sulfo-aluminate hydrate (CSAH) – a retarding product. CSAH deposits and forms a protection film on the cement particles to hinder the hydration of C3A and therefore delay the setting time of cement as noted in OWA 10% cement replacement. The hydration of alite and belite follows the initial setting spontaneously to form calcium silicate hydrate (C-S-H) in higher OWA content compared to low cement-OWA substitution.

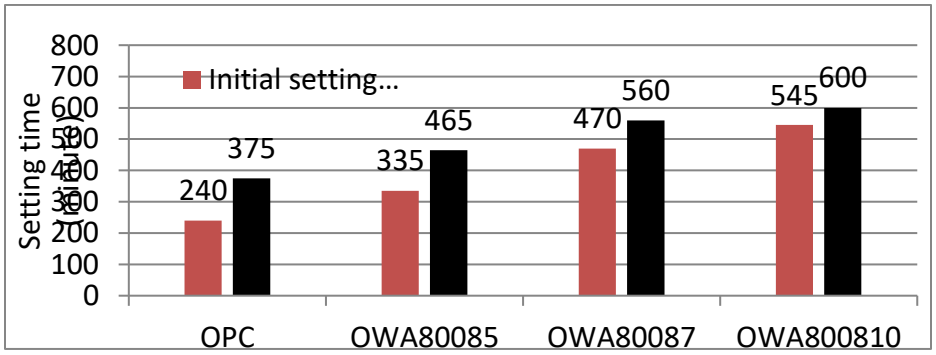

Figure 2: Effect of replacement percentage on setting time

ISBN: 978-81-936820-6-7
Proceedings DOI: 10.21467/proceedings.4

Series: AIJR Proceedings

Figure 3 shows the effect of burning time on setting time for the ash burned at temperature 900˚C and with replacement percentage 10%. The initial and final setting time of cement mortar decreased significantly, with increasing in burning time from 6 to 8 hours. The reason for this is due to increase in OWA particle surface area that resulted in more coating paste and enhanced particle reactivity as evidenced in earlier initial (485 mins) and final (540 mins) setting time in 8 hrs compared to 6 hrs of burning time of 555 and 675 mins, respectively.

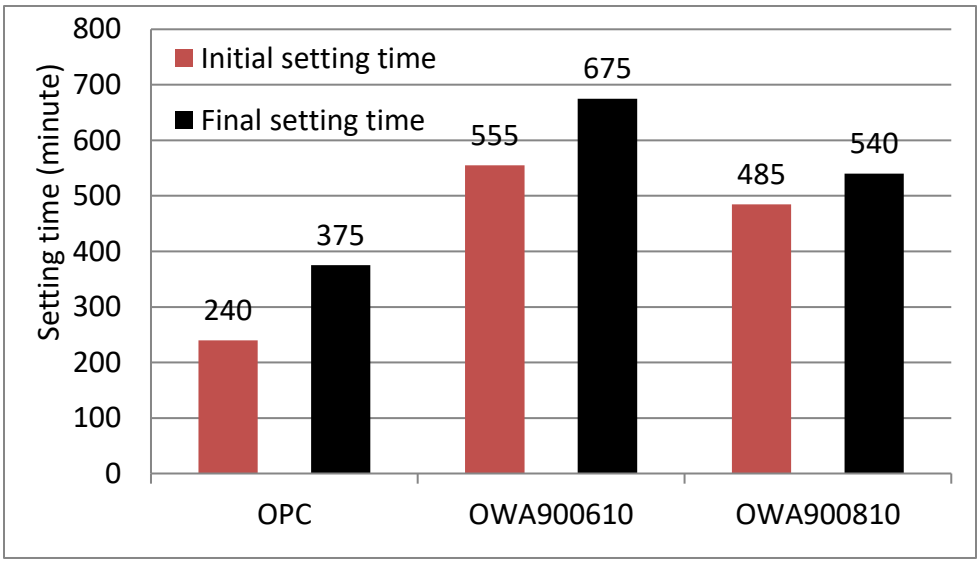

Figure 3: Effect of burning time on setting time for 10% replacement percentage

3.4 Compressive strength of mortar

Figure 4 shows the effect of burning temperature on the compressive strength for 5% cement replacement cured in the air. The OWA burnet at 600˚C appeared to perform better in compressive strength in comparison to those processed at higher temperatures. The rate of strength development was very close to the reference or control sample. However, the pozzolanic reactivity began to take effect at 28 days which indicates that about 20% of strength was gained as can be seen in Figure 4. However, there was no significant strength gained beyond 28 days in all the tested samples. This suggested that OWA underwent a limited pozzolanic reaction. This is more evident upon closely observing the OWA burnt at 700-900˚C for 8 hrs in Figure 4. Burning OWA beyond 600˚C appeared to have converted silica from amorphous phase to crystalline phase thereby affecting its reactivity.

With 100˚C margin from 600˚C, the 7, 28 and 90-day strengths were reduced by 40.1, 35.6 and 34.4%, respectively. The increment is closed to that observe at 900˚C when the difference

becomes 38.5%, 26.1% and 35.1%. These values reduced to 13.9, 32 and 13.4% when the temperature margin is 200˚C that is at 800˚C, which signifies better performance compared to 700˚C and 900˚C. This suggests that the proportion of amorphous and crystalline silica at that temperature (800˚C) is at optimum and since the samples burnt at 600˚C contains more amorphous silica, the strength was noted to be the highest observed within the blended and the reference or control samples at 28 and 90 days. The burnt ash samples at 600˚C recorded 90-day compressive strength of 18.8 MPa, which was higher than the reference sample value by 27.8%.

From Table 2, the higher strength recorded in the 600˚C burnt sample could be attributed to its higher specific gravity compared to others samples whose specific gravity decreased with increasing burning temperature.

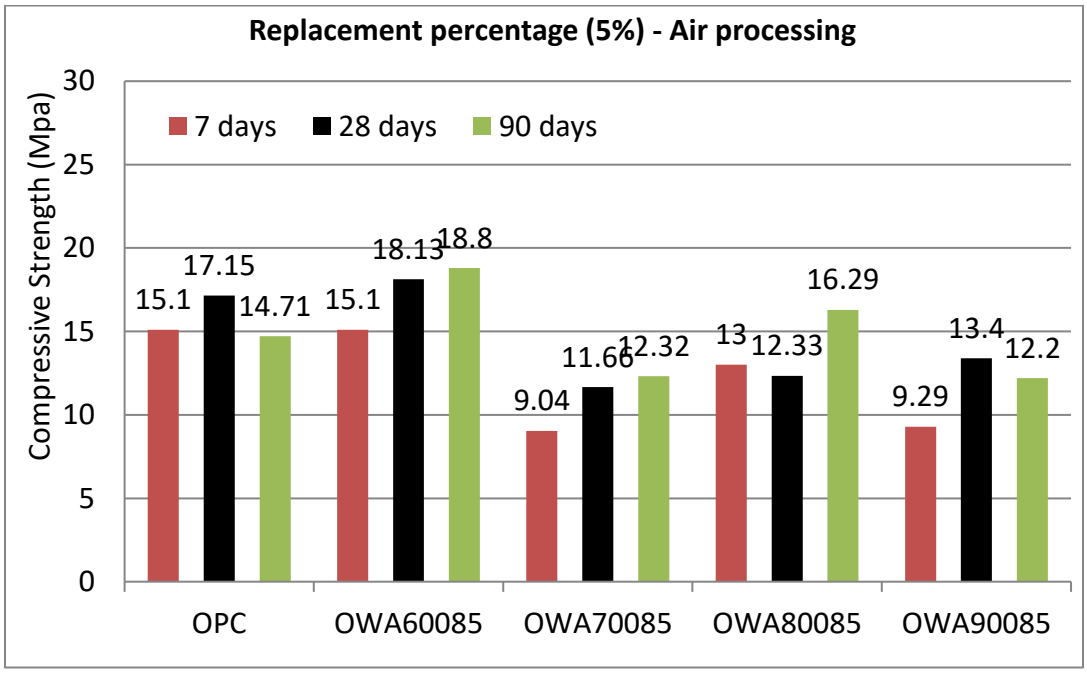

Figure 4: Effect of burning temperature on compressive strength

Figure 5 shows the effect of burning time on the absorption rate of replacement percentage of 7%. At 6 hrs duration at operating temperature of 900˚C, the absorption is found to be less than at 8 hrs by 15.4%. It implies that excessive exposure of the same leads to formation of more voids or pores with the interstices of the ash. The values recorded at 6 hrs is 4.5% higher than the control.

ISBN: 978-81-936820-6-7
Proceedings DOI: 10.21467/proceedings.4

Series: AIJR Proceedings

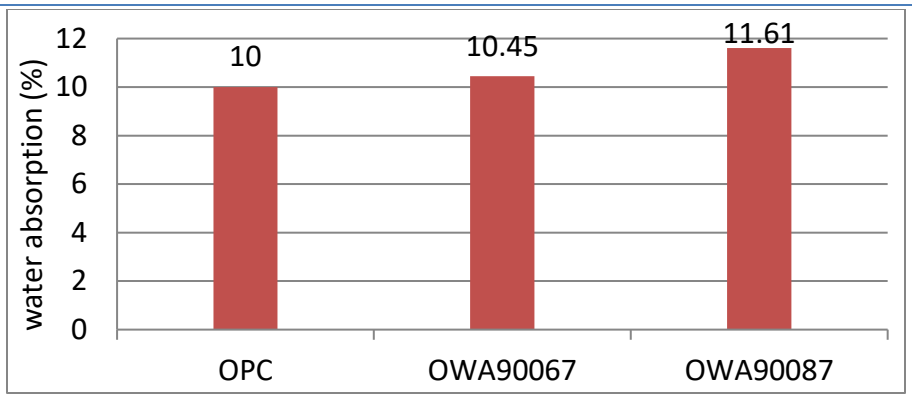

Figure 5: Effect of burning time on absorption at replacement percentage 7%

Figure 6 shows the effect of burning temperature on porosity at replacement of 10%. After 28 days of treatment in the water, it was noticed that the addition of burned ash at temperatures 600˚C, 700˚C and 800˚C led to decrease in porosity less than that of the reference sample, while adding the burnt ash at 900˚C led to increased porosity, that is increasing the proportion of air spaces inside the cement mortar, therefore leading to weakness in the compressive strength of the cement mortar.

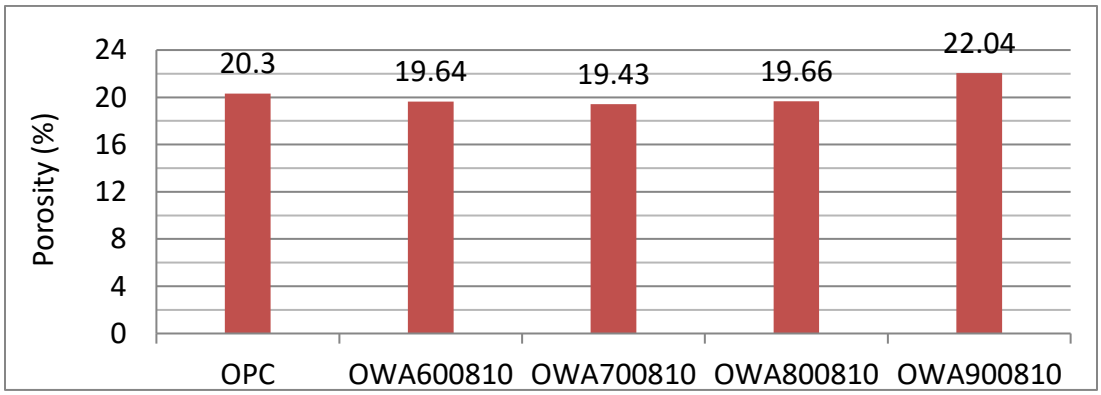

Figure 6: Effect of burning temperature on porosity at replacement percentage 10%

After 28 days of treatment in the water as shown in Figure 7, the effect of the burning temperature on the permeability at replacement percentage of 5%, was noticed to reduce at 600˚C (1.26×10^{-14}m/s) and it is 37% of the control sample (2.01×10^{-14}m/s). However, increment in permeability of the ash burnt at 700˚C (2.83x10-14 m/s) increased by 41% compared to the control and 124% with reference to that of 600˚C. It appears the porosity of the sample treated at the temperatures of 800 and 900˚C are equally distributed.

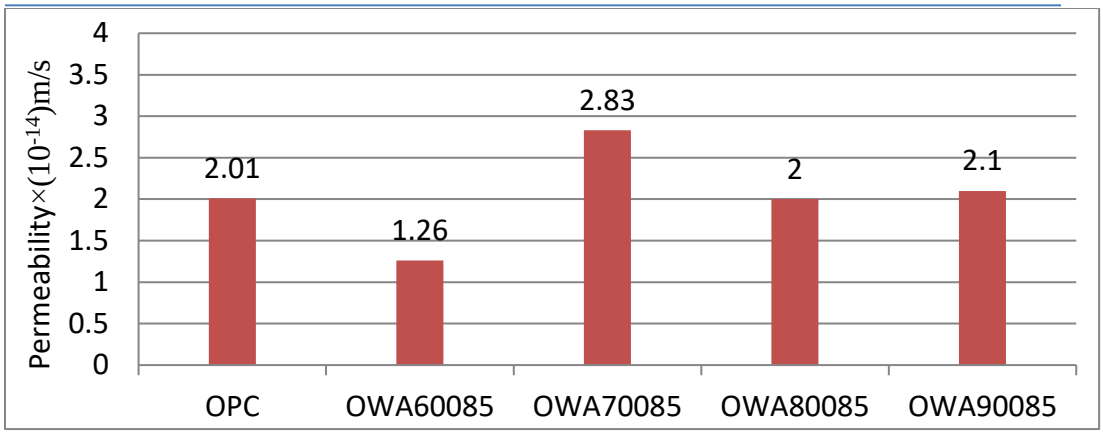

Figure 7: Effect of burning temperature on permeability coefficient at replacement percentage 5%

4. Conclusions

The following conclusions can be drawn from the results obtained from the treatment of olive waste ash (OWA) as partial cement replacement in blended mortar in terms of specific gravity, transport properties, workability and setting time:

- Burning temperature and burning time of OWA had an impact on the chemical composition and physical properties of the resulting ash most evidently, the specific gravity.
- With the increase in the replacement percentage of OWA, initial and final setting time of cement paste increased significantly due to prolonged or delayed pozzolanic reaction.
- Burning temperature had significant effect on the compressive strength of OWA blended cement mortar cured in the air. The ash was observed to perform better in terms of strength and permeability coefficient when it was treated at the 600°C.
- Even at maximum treatment temperature of 900°C, 6 hrs period of burning of OWA favored water absorption performance of OWA blended mortar than 8 hrs when the porosity was also noted to be worsened compared to lower treatment temperature and the control samples.

4 Acknowledgements

I would like to thank the personnel in the Chemistry lab, of the Industrial Research Center in Tajoura, and the personnel in the X rays and microscopic photographing labs, of the Oil Research Center in the city of Tripoli.

References

[1] Abdulwahid, M.Y.,(2009) "Effect of Olive Waste Ash on the Mechanical Properties Of Mortar". M.Sc. Thesis, Civil Engineering Department, Jordan University of Science and Technology.

[2] Libyan Standard Specifications No. 340 of 1997, of Portland Cement, National Center for Standard Specifications, Tripoli, Libya.
[3] BS 882, (1992) "Specification for aggregates from natural sources for concrete". British Standards Institution, 389 Chiswik high road, London, W4 4AL, UK.
[4] ASTM C204-92, (1992): "Standard Test Method for Fineness of Portland Cement by Air Permeability Apparatus". ASTM, 1916 Race St., Philadelphia, PA 19103, USA.
[5] ASTM C109-92, (1992): "Standard Test Method for Compressive Strength of Hydraulic Cement Mortars (Using 2-in. Or 50-mm Cube Specimens)". ASTM, 1916 Race St., Philadelphia, PA 19103, USA.
[6] ASTM C305-91, (1991): "Standard practice for mechanical mixing of hydraulic cement pastes and mortars of plastic consistency". ASTM, 1916 Race St., Philadelphia, PA 19103, USA.
[7] ASTM C191-92, (1992): "Standard Test Method for Time of Setting of Hydraulic Cement by Vicat Needle". ASTM, 1916 Race St., Philadelphia, PA 19103, USA.
[8] ASTM C642-97, (1997): "Standard Test Method for Density, Absorption, and Voids in Hardened Concrete". ASTM, 100 Barr Harbor Drive, West Conshohocken, PA 19428-2959, USA.
[9] AT315-EN 12390-8 (2000) "Testing hardened Concrete-Part 8: Depth of Penetration of Water Under Pressure".
[10] Haitham Abdel Hady Klob, 2009, "Study of the Impact of High Temperatures on Concrete Endurance". Master thesis, Civil Engineering Department- Al Mergeb University, Alkhoms-Libya.
[11] Libyan Standard Specifications No. 294 of 1988, of Water used in Concrete, National Center for Standard Specifications, Tripoli, Libya.
[12] Chindaprasirt, P., & Rukzon, S., (2008) " Strength, porosity and corrosion resistance of ternary blend Portland cement, rice husk ash and fly ash mortar ". Construction and Building Materials 22(2008):1601-1606.
[13] ASTM C618 (2005) "Standard Specification for Coal Fly Ash and Raw or Calcined Natural Pozzolan for use as a Mineral Admixture in Concrete". American Society for Testing and Materials, pp.310-313, USA.
[14] Mahmoud Imam, Mohamed Amin 2007, Materials Properties and Tests, Faculty of Engineering- El Mansoura University.
[15] Neville, A.M., (1995), "Properties of Concrete" 4th Edition, Prentice Hall.
[16] Rif'at Mahmoud Sallam 2004, "Causes of Concrete Damage and Methods of Repair and Protection" El Maarif Establishment, Cairo, Egypt.
[17] Merkhoufy Abdel Malek 2004, "Contribution in the Study of Fiber Concrete Characteristics and Distortions" Faculty of Sciences and Engineering Science- University of Quasedy Merbah Warkalah, Algeria.
[18] Ganesan, K., Rajagopal, K. & Thangavel, K. (2007) "Evaluation of bagasse ash as supplementary cementitious material". Cement and Concrete Composites, 29, 515-524.
[19] Shvarzman, A., Kovler, K., Schamban, I., Grader, G. & Shter, G. (2002) "Influence of chemical and phase composition of mineral admixtures on their pozzolanic activity". Advances in cement research, 14, 35-41.
[20] Bendapudi, S.C.K. & Saha, P. (2011) "Contribution of Fly ash to the properties of Mortar and Concrete". International Journal of Earth Sciences and Engineering, 4, 1017-1023.
[21] Malhotra, V.M. & Mehta, P.K. (1996) "Pozzolanic and cementitious materials". Taylor & Francis pp. 72.
[22] Bhatty, J.I. & Reid, K.J. (1985) "Use of thermal analysis in the hydration studies of a type 1 Portland cement produced from mineral tailings". Thermochimica Acta, 91, 95-105.
[23] Wild, S., Khatib, J. & Jones, A. (1996) "Relative strength, pozzolanic activity and cement hydration in superplasticised metakaolin concrete". Cement and Concrete Research, 26, 1537-1544.
[24] Hago, A.w., (2002) "Effect of the Fineness of Artificial Pozzolana on the Properties of Lime-Pozzolana Mix". Science and Technology, 7, pp.252-258.
[25] Al-Akhras, N., Al-Akhras, K., & Attom, M., (2009)" Performance of olive waste ash concrete exposed to elevated temperatures". Fire Safety Journal 44(2009):370-375.
[26] Tangchirapat, W., Jaturapitakkul, C., & Chindaprasirt, P., (2009) " Use of palm oil fuel ash as a supplementary cementitious material for producing high-strength concrete". Construction and Building Materials 23(2009):2641-2646.
[27] Tangchirapat, W., Jaturapitakkul, C., Chindaprasirt, P., & Saeting, T., (2007) " Evaluation of the sulfate resistance of concrete containing palm oil fuel ash". Construction and Building Materials 21(2007):1399-1405.
[28] Ayman Fathallah Mabrouk, 2014, The Impact of Burned and Ground Palm Tree Pips on the Mechanical Characteristics of Cement Mortar". Master thesis, Department of Civil and Architecture Engineering- Libyan Academy for Post Graduate Studies, Tripoli, Libya.
[29] J MENDHAM. R C DENNY. J D BARNES. M J K THOMAS. "VOGEL'S – Textbook of Quantitative Chemical Analysis". 6th Edition, Prentice Hall.
[30] ASTM C187-86, (1991): "Standard Test Method for Normal Consistency of Hydraulic Cement". ASTM, 1916 Race St., Philadelphia, PA 19103, USA.

Study the Performance of Solar Water Heater with Various Loads

Ghassan S. EL-MASRY*, Mustafa EL-MUSBAHI, Benur MAATUG

Department of Mechanical Engineering, Elmergib University, Garaboulli, Libya

DOI: https://doi.org/10.21467/proceedings.4.2

* Corresponding author email: gsalmasri@elmergib.edu.ly

ABSTRACT

The performance of a certain type of solar heater was studied by install, assemble solar heater and the installation of different measuring devices, such as water flow meter and temperature meters for water inside, outside, and measuring the temperature of the atmosphere and a measure of the amount of solar radiation, all of these devices connected to a device that stores this data every 5 minutes In the form of averages or totals.

The first tests were carried out by consumption of the water in the early morning (immediately after sunrise). In the second period, the consumption of water was at the end of the day (before sunset). The third period was at noon (midday)

TRNSYS, a specialized program in simulating solar thermal processes, TRNSYS can used to connect thermal system components in any form, solving differential equations and facilitating the output of information.

TRNSYS works to compensate the practical experience with a fully simulated theory that saves time and effort and gives us the desired results of the practical experiment. The program data is the solar heater characteristics of the experiment, the period to be tested and the amount of water to be consumed.

The study explains that the best time to increase the amount of energy extracted the water must drained at the afternoon period.

Keywords: solar heater, solar energy, simulation system, consumed period, change of loads, alternative energies

1 Introduction

A field study was conducted for a complex heater at the Solar Energy Research and Studies Centre in Tajoura, where integrated measuring devices were used to study and analyse the solar thermal performance of the solar heater. The study period lasted more than two months and was divided into three stages. The water was withdrawn in the first stage in the morning, the second stage just before sunset and then in the final stage, the drawn were during the afternoon. It will discuss the specifications of the solar heater, the measuring instruments and the methods of testing approved for the solar heater. In this study, it was based on the international standard for testing solar heaters, referred as ISO 9459-2 for the evaluation of solar heater under study, issued by the International Organization for Standardization (ISO)

 ISBN: 978-81-936820-6-7

2 Specifications

For data that helps to obtain the thermal performance of the heater, the solar heater is provided with measurement sensors connected to the Data Acquisition System, which can sensor data from sensors every 10 seconds and store it at the end of every five minutes in the form of cumulative or average values by The nature and characteristics of this data.

In this study, a range of variables were measured: the temperature of the water inlet to the reservoir T_i, the outlet temperature T_o, the temperature of the air surrounding the heater Tamp, the amount of hot water consumed M, and the intensity of the total solar radiation falling on the surface of the complex G_{sol}, For each five minutes throughout the day in the form of temperature averages and cumulative values of the radiation falling on the surface of the collector and water consumed. The data device calculates the amount of total thermal energy acquired for hot water Q_t.

3 Solar heaters

The heater consists of a compound with an assembly area of 3.024 m2 and a reservoir of horizontal type, with an auxiliary electric coil installed manually to meet the shortage of thermal energy resulting from the absence of the sun at night or in the days when the clouds are abundant. The collector and the reservoir are connected to each other by connecting pipes to suit the natural flow system. The system was directed to the true south at an angle of 40° from the horizontal

Table 1 *Specifications of solar heater*

Solar heater	
Type of heater	Natural flow closed circuit
The total capacity	200 liters
The solar collector area	3.024 m2
Collector pipe	15 mm diameter copper tube
Collector glass surface	glass thermally treated thickness of 3 mm
Absorption Surface Coating	Selective Coating (Black Chrome)
Collector insulation	glass wool thickness of 30 mm
Hot water tank	horizontal ring type
Hot water tank insulator	Polyurethane foam 45 mm thick

Figure 1 (a, b) shows the solar heater diagram used in the experiment

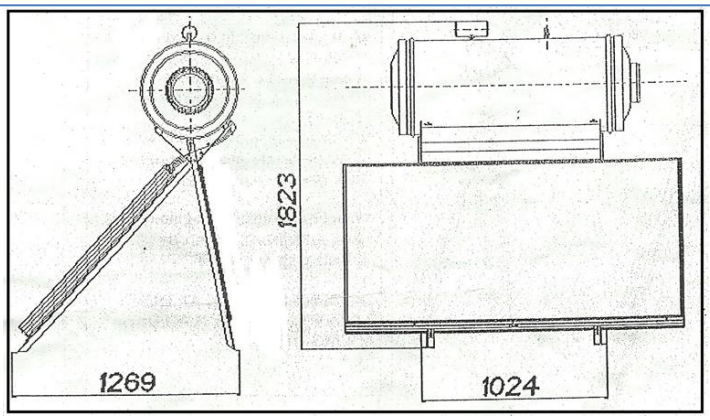

Figure 1a *Cross section of the solar heater (from catalog)*

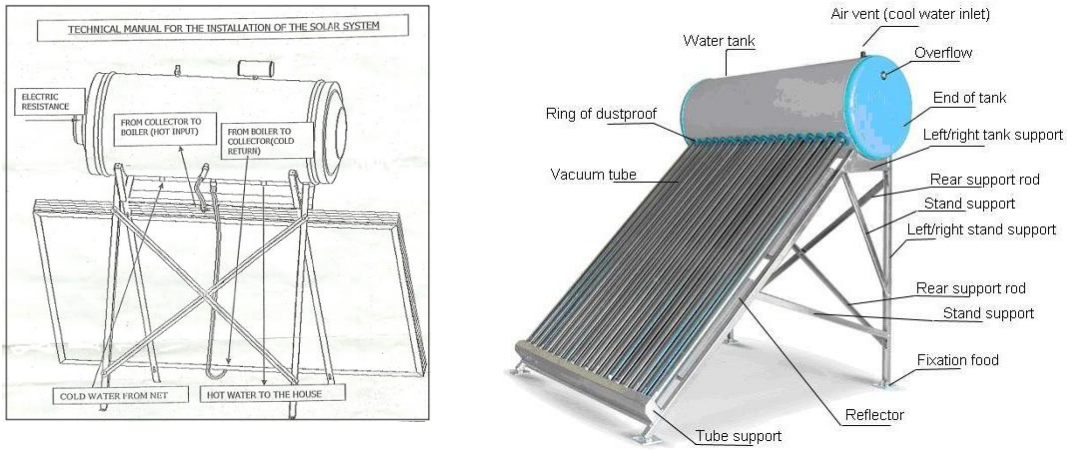

Figure 1b *a synthesis of the solar heater (the right figure from catalog)*

4 Range of test conditions

The test results are prepared in this system using a special model. The input / output graph and the temperature increase are also explained and presented.

Test results are not used to report on the performance of the heater under test. It is represented an intermediate stage in the test and is only used as entries for calculations.

Test results include daily system productivity for different values of H and ($T_{a\ (day)}$ - T_c). Therefore the performance of the solar water heating system can be represented by the following equation[2]

$$Q = a_1H + a_2 [T_{a\ (av)} - T_c] + a_3 \quad \text{..... (1)}$$

The coefficient (a_1, a_2, a_3) of the system is determined from the test results' using the linear correlation model, whereas (Q) means or refers to the net solar energy obtained by the thermal tank during the day, (Q) is calculated by total hot water drawn or extracted according to the test defined.

In addition, the results of the test containing the temperature ($T_{a\ (day)}$ - T_c) for water for different values of (H) and ($T_{a\ (day)}$ - T_c) by the following equation [2]:

ISBN: 978-81-936820-6-7
Proceedings DOI: 10.21467/proceedings.4

Series: AIJR Proceedings

$T_{d\,(max)} - T_c = b_1H + b_2\,[T_{a\,(day)} - T_c] + b_3$ .... (2)

The coefficients (b_1, b_2, b_3) are determined from the test results using the linear correlation model, while $T_{d\,(max)}$ in the equation refers to the maximum temperature of the extracted water. And the results and curves were as follows:

It was in the withdrawn curves for the morning period for three days as shown in Figure 2 (A, B, C):

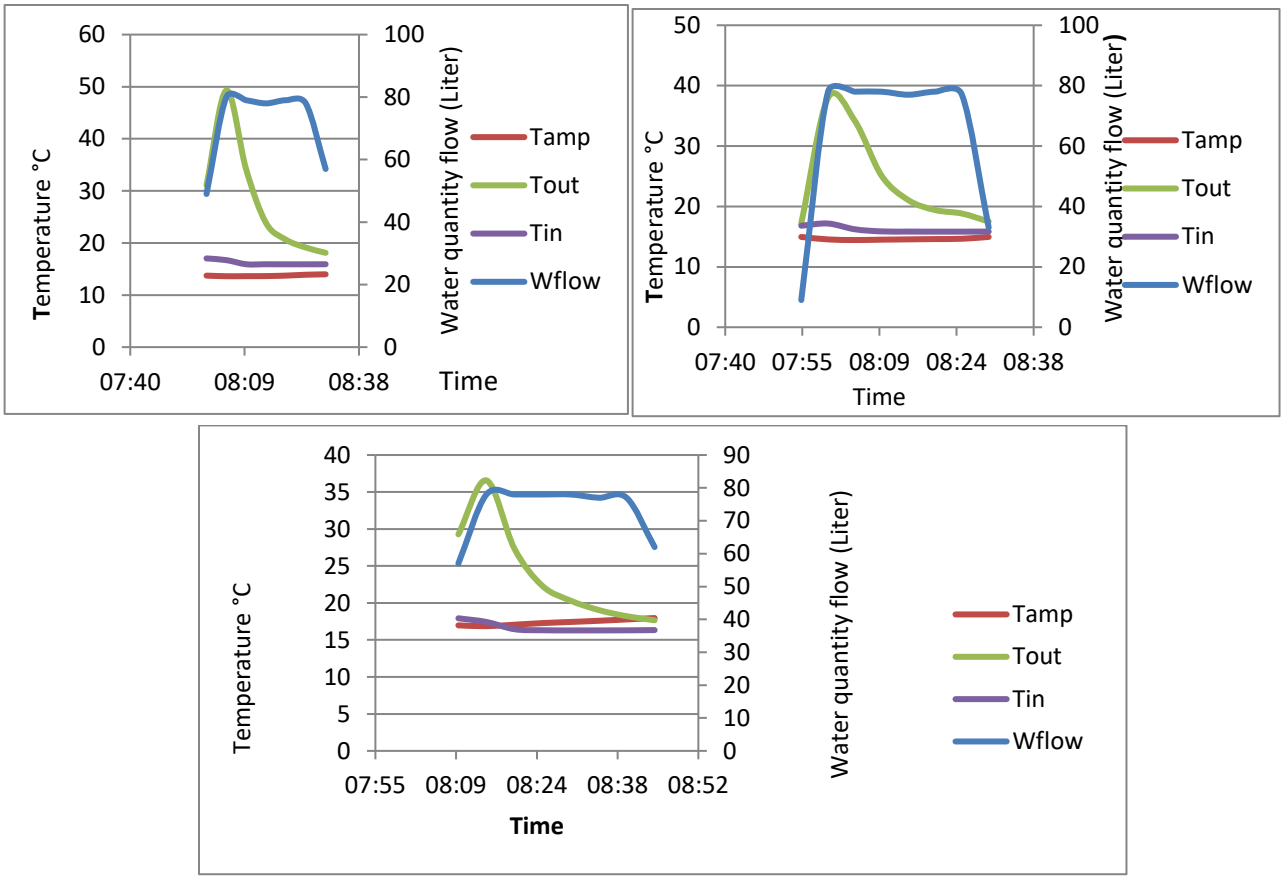

Figure 2 ***a,b,c*** *withdrawn curves for the morning period*

Then in the evening curves for three days as shown in Figure 3 (a, b, c):

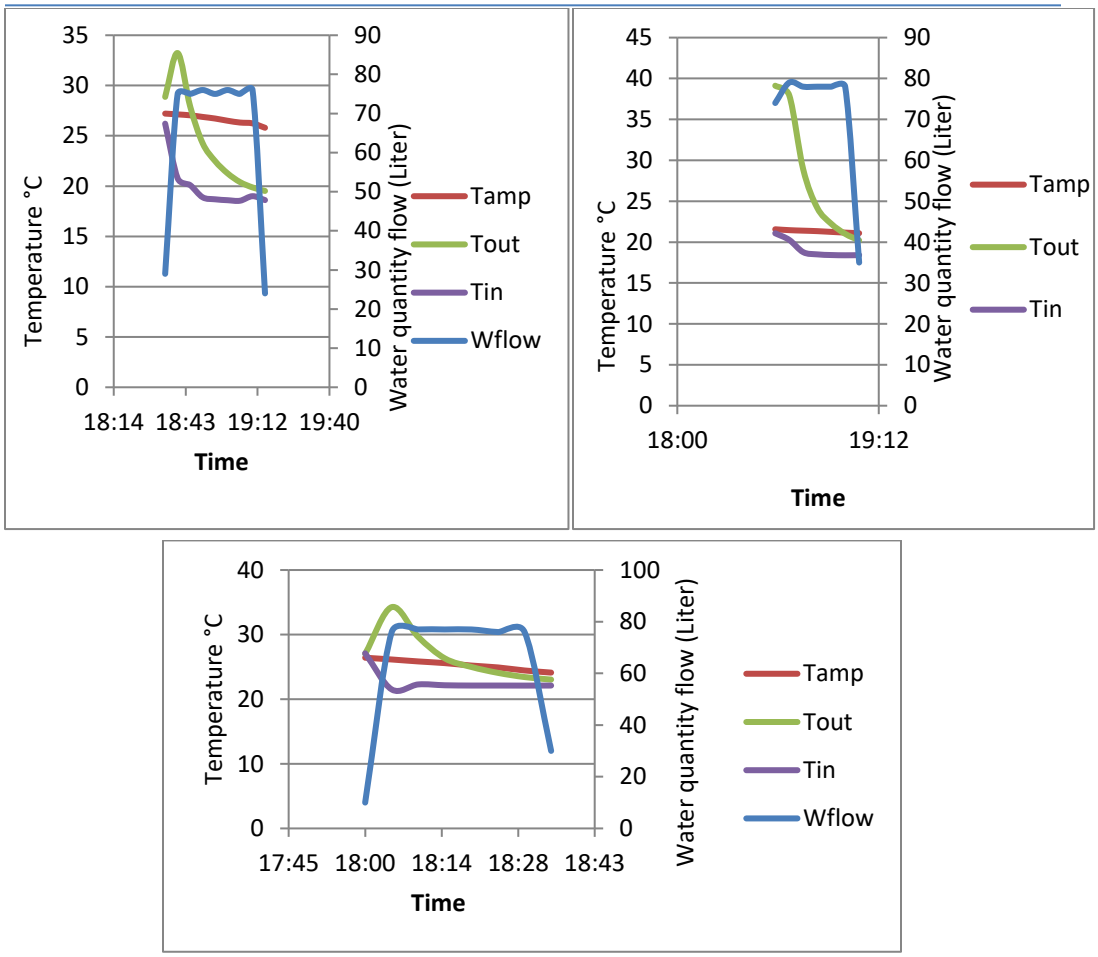

Figure 3 a,b,c *Draw curves during the evening*

In the afternoon for three days , as shown in Figure 4 (a, b, c):

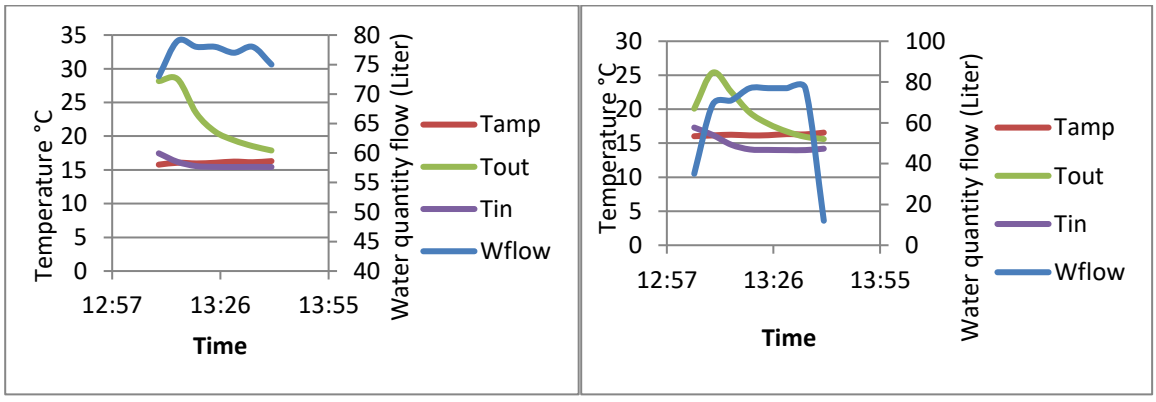

Figure 4a,b *Draw curves during the afternoon*

ISBN: 978-81-936820-6-7
Proceedings DOI: 10.21467/proceedings.4

Series: AIJR Proceedings

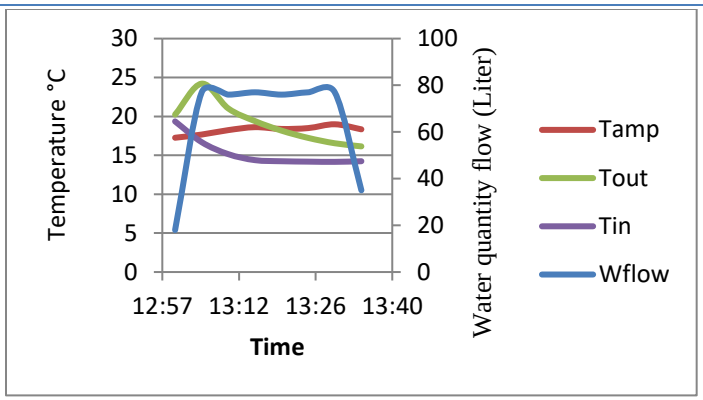

Figure 4c *Draw curves during the afternoon*

5 Representing the simulation program results

After introducing the specifications of the solar heater used in the experiment and determining the required temperature, as the temperature at which the draw water should come out, and give all the data to the program, the results are in curves as follows:

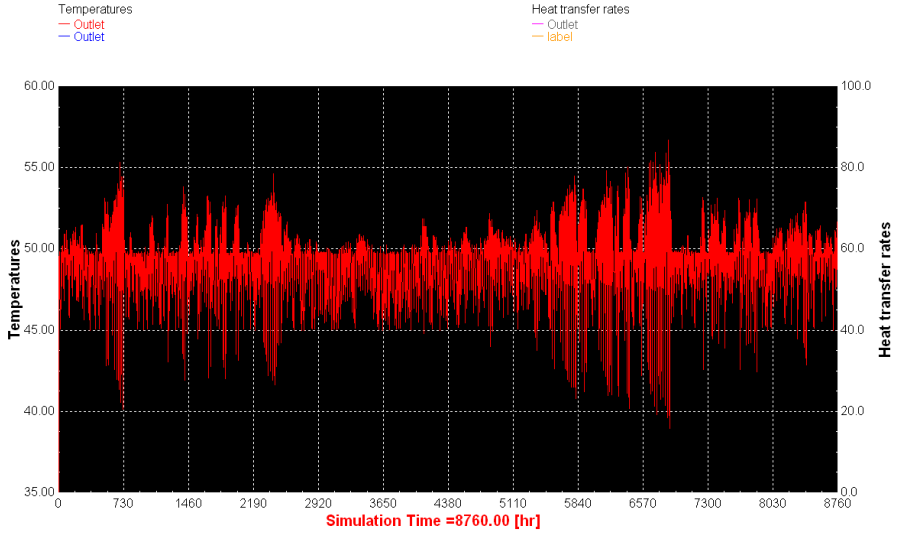

Figure 5 *Comparison between the temperature of the withdrawn water and the rate of heat transfer and the simulation time over a whole year*

Figure 5 shows that the higher the rate of heat transfer, the higher the temperature of the withdrawn water, that mean the relationship between the rate of heat transfer and the temperature of the withdrawn water is a direct relationship.

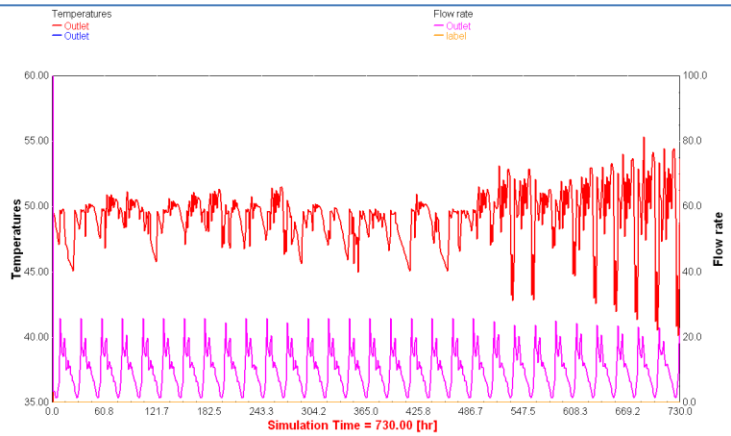

Figure 6 *The relation between the draw water temperature and the water flow rate (the drag rate) and the simulation time which is a full month*

In Figure (6), where the rate of drawn water was constant in the morning period over a whole month, but note that the temperature of withdrawn water increases by the end of the month, due to the fact that the solar radiation increases at the end of this month and based on the increase in The radiation increases the temperature of the drawn water.

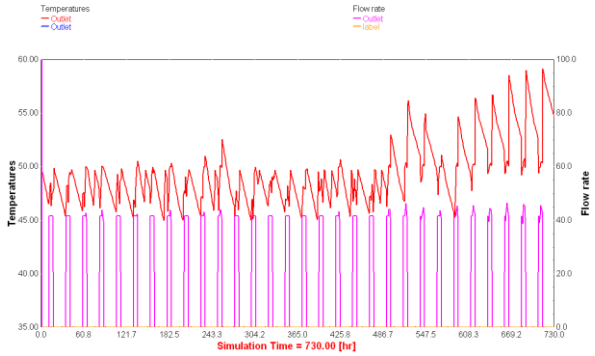

Figure 7a *The relationship between the temperature of the withdrawn water and the drag rate and the time that represents a full month and the draw were in the evening, ie before sunset*

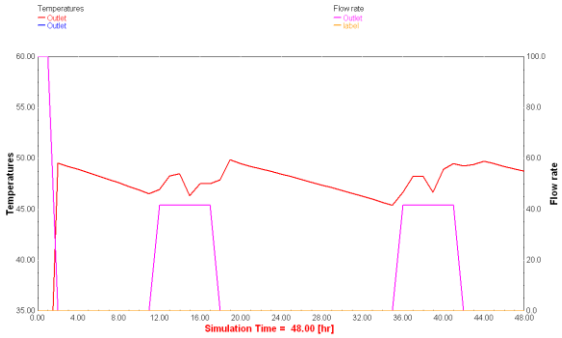

Figure 7b *The relationship between the temperature of the drawn water and the flow rate and the simulation time, which is two full days*

In Figure 7a,b, the draw here is a complete withdrawal of the load, i.e., a draw along the day from 11 am to 6 pm

ISBN: 978-81-936820-6-7
Proceedings DOI: 10.21467/proceedings.4

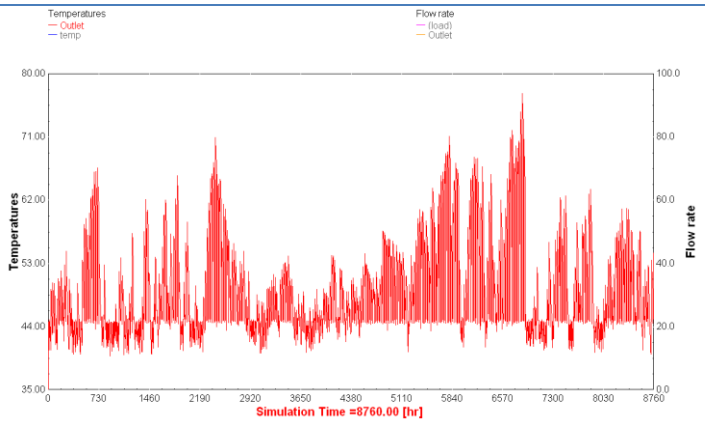

Figure 8 *The relationship between the temperature of the drawn water and the flow rate at afternoon and the simulation time which is equivalent to one year*

Figure 8 shows that at the afternoon there are increase of temperature of drawn water

6 Conclusion

This study explains the best time to drained the hot water from the solar collectors as shown in Figures 2,3,4 the experiment for three days for each period and the simulation program as shown in figure 7,8. This study shows the variation of results when the consumption of water is changed from morning, afternoon and evening. The best time to increase the amount of energy extracted and the temperature is at the afternoon period.

Reference

[1] Strategical report for renewable energy-Nation board for scientific research – Libya- Nation Week For scientific and Technology 2006

[2] ASHREA 93,77 fundamentals.

[3] ASHRAE. 1991a. Active solar heating systems installation manual.

Built to Code Building Envelop Versus Sustainability of High-Rise Building Performance

Mohamed ali karim *

Department of Civil Engineering, College of Engineering, Elmergib University, Libya

DOI: https://doi.org/10.21467/proceedings.4.3

* Corresponding author email: omgaon2x@yahoo.com

ABSTRACT

Global warming and climate change are major challenges facing the nation and the world. More than two thirds of the electric energy and one third of the total energy are used to heat, cool, and operate buildings, representing majority of all CO2 emissions. A reduction in building energy consumption will help to mitigate the energy security and climate change effects on buildings. The reduction in energy consumption is accomplished through the development of new technologies (for the building's envelope, mechanical, and lighting systems) that save energy and reduce CO2 emissions. However, an alternative approach is the use of passive systems that employ renewable energy sources. Passive systems avoid the need for heating or cooling through better design, construction, and operation. They utilize solar or wind energy to heat, cool, or light buildings. This study analyzes the sensitivity of energy demanded to build to code building's envelops. In other words, investigating whether building that meets the need of enveloping code can take advantage of the weather surrounding the building, in terms of cooling, or heating (comfort) the building as needed. Four high-rise office buildings (glazed curtain wall) with four different aspect ratios (1:1, 1:2, 1:3, and 1:4) are thermally analyzed in four climate zones: cool, temperate, arid, and tropical. The envelope of these high-rise buildings is modeled to meet International Energy Conservation Code (IECC) requirements, which references several American Society of Heating, Refrigeration, and Air Conditioning Engineers (ASHRAE) standards. As a result, the energy performance of high-rise office buildings is not sensitive to the passive solar gain as long as the exterior envelopes are built to IECC 2009 requirements, which does not allow the use of the ambient climate condition of the building to get comfort. This is not appropriate from the concept of sustainability of buildings as referred to above.

Keywords: Sustainability, High-Rise Building, Energy performance, Global warming

1 Introduction

One of the criteria for the development of countries is the urban renewal, especially the high-rise buildings in their cities. Thousands of years, tall buildings and towers have fascinated human beings; they have been built primarily for defensive or religious purposes as evidenced by the Pharaonic temples (pyramids) of Giza, Egypt, the Mayan temples of Tikal, Guatemala, and the Kutub Minar of Delhi, India. In the modern era, high-rise buildings are a reality of

 ISBN: 978-81-936820-6-7

contemporary life in cities and there are several reasons for this. Urban real estate is a premium due to the lack of available land; secondly, high-rise buildings (vertical construction) present an effective way to reduce traffic congestion in cities; thirdly, rapid population growth of urban communities, lastly, the limitations and the conditions of the terrain and topography [1, 2]. However meeting operational performance requirements and maintaining occupant comfort in high-rise buildings is a challenging design problem. The energy demands for large-scale HVAC system (Heating, Ventilating, and Air Conditioning) load is significant. Not only are the site energy costs are high, the attendant environmental consequences of using non-renewable energy sources are great. Improving the energy efficiency of high-rise buildings is a key component in increasing the sustainability of the environment. More than one-third of the world's energy consumption is attributed to the construction and building industry [3]. As a case, more than two thirds of the electric energy and one third of the total energy in the US are used to heat, cool, and operate buildings [4], representing roughly 18% of all U.S. CO2 emissions in one year. Given the current global energy crisis, there is a critical need to design and construct buildings that are more sustainable. Energy efficient buildings minimize building resource consumption, operations and life cycle costs, and can improve occupant health and comfort [5]. High-rise buildings should be designed in a manner to reduce the need for fossil fuels (oil, gas and coal) and promote greater reliance on renewable energy. This concept is reflected in what is known these days as sustainable architecture or green building. A green building is one that focuses on reducing the impact of buildings on the environment. In general, a green building is one that meets the needs of the present generation without compromising the ability of future generations to meet their needs as well [1]. For designers and architects such as William Reed, green buildings are designed, implemented, and managed in a manner that places the environment first[6]. In the state of Libya, the architectural renaissance will be an urgent necessity for the follow-up to the developed nations in this world; as the state of Libya adopts building specifications, which may not be compatible with the requirements of sustainability in terms of temperate climate. Moreover, the current standards of architectural systems do not adopt fully sustainable methods, since the concept of sustainability is a newborn concept and its implementation is economically expensive because of the cost of the techniques used. States are in a race to lay the foundations for sustainable construction. In keeping with the demand for the current architectural development, nations cannot wait for complete and integrated system to be built in sustainable ways. Thus, the idea of this research is to study if these specifications meet the requirements of sustainably performance of high building that are built according to these codes and standards (IECC code and ASHRAE standards) of the buildings envelope [7]. The study analyzes the sensitivity of energy demanded to build to code buildings envelopes. In other words, investigating whether a building that meets the need of envelop code can take advantage of the weather surrounding the building, in terms of cooling, or heating (comfort) the building as needed.

Four high-rise office buildings (glazed curtain wall) with four different aspect ratios (1:1, 1:2, 1:3, and 1:4) are thermally analyzed in four climate zones: cool, temperate, arid, and tropical. Energy demand is calculated for each model with respect to two opposing orientations (Figure1). The four high-rise buildings are modeled to meet IECC 2009 code requirements, which reference several ASHRAE standards, including Std. 90.1 for commercial building construction [7, 8]. The following sections describe the analytical method and the primary variables that will be measured against energy use in the four-modeled buildings. Then summarize the results and present the conclusion.

2 Building Materials and Basic Data

Four models of high-rise office buildings are considered in this study to evaluate the sensitivity of energy demands to variations in: (1) footprint aspect ratio (1:1, 1:2, 1:3, and 1:4), and (2) building orientation. Since the goal is to isolate the influence of built to code building's on energy demand, all other buildings descriptors such as the square footage, number of stories, building height(Figure 2), and occupancy for the four buildings are held constant across all four buildings. Specifically, the thermostat range, internal design conditions, occupancy, infiltration rate, and hours of operation as fixed control variables.

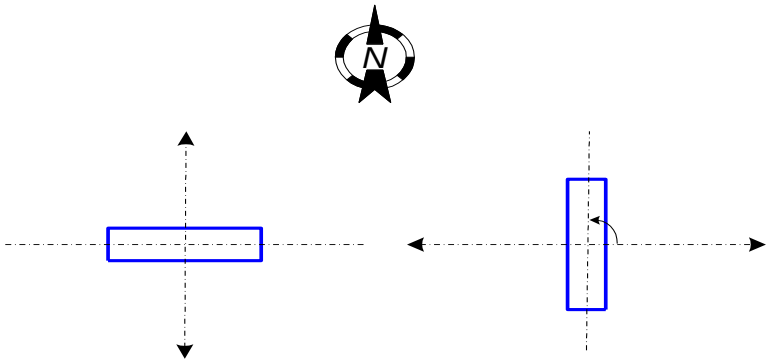

Figure.1. Building orientation considered in this study

The four buildings are 200 meters in height, 50 stories that are 4.0 m floor-to-floor height, with a total conditioned floor area of 135,000 square meters. The primary material for the meet the R-value specified for a climate according IECC 2009. To simplify the thermal analysis, the effect of surrounding buildings have been neglected assuming that the buildings were erected on flat open ground and are aligned with the cardinal directions.

ISBN: 978-81-936820-6-7
Proceedings DOI: 10.21467/proceedings.4

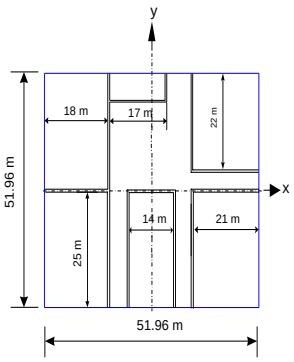

Plan view 1:1 configuration

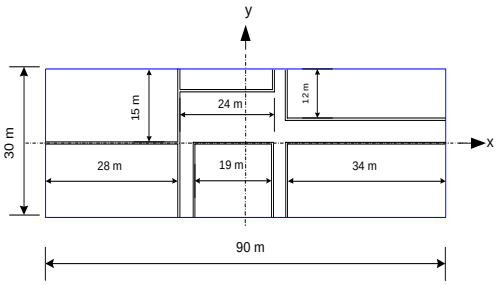

Plan view 1:3 configuration

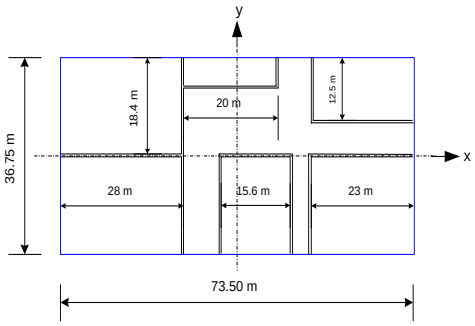

Plan view 1:2 configuration

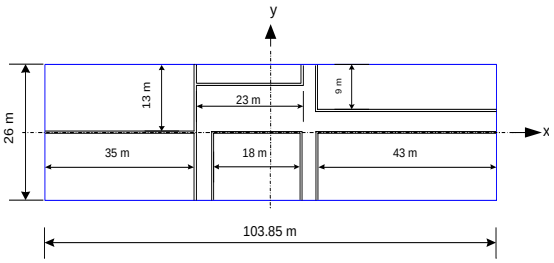

Plan view 1:4 configuration

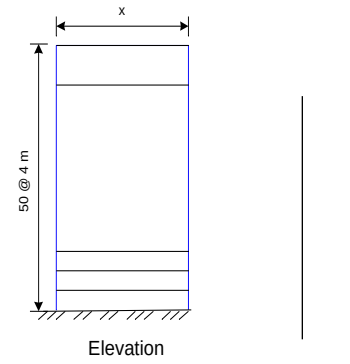

Elevation

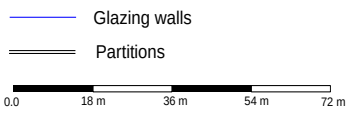

Figure 2: building plan view and envelope thermal properties

3 Thermal analysis

Autodesk's Ecotect energy simulation package was used for the thermal analysis. The thermal analysis involves examining each of the four models (1:1, 1:2, 1:3, and 1:4) in each of the four climatic zones (cool, temperate, arid, and tropical). That is, the only difference among the four runs for the same climate zone are the building width to length ratio (aspect ratio) for one orientation at a time. Ecotect calculates the overall heat gain/loss (Sun-path diagram Figure 3); and then with choose the way the comfort zones is calculated of each day of the year using the Flat Comfort Bands method, which sets upper and lower limits for comfort temperatures. If the internal zone temperature is either above or below the temperature limits for the prescribed comfort zone, then thermal environmental conditions are unacceptable to the majority of the occupants within that space. Factors that determine thermal environmental conditions are temperature, thermal radiation, humidity, air speed, and personal factors such as activity and clothing. Environmental factors are influenced by: (1) Direct solar gain, or radiant flow through transparent surfaces. (2) Internal (sensible) heat gain from lights, people, and equipment. (3) Conductive heat flow through opaque (envelope) elements. (4) Radiant flow through opaque (envelope) elements. (5) Ventilation and infiltration heat flow through cracks and openings. (6) Inter-zonal heat flow between adjacent zones, which for this analysis is negligible. Conductive and radiant flows through opaque elements are treated together and described as "Fabric" in Ecotect. Personal factors such as activity (metabolic rate) and clothing (insulation of clothing) are treated as constant for all building occupants.

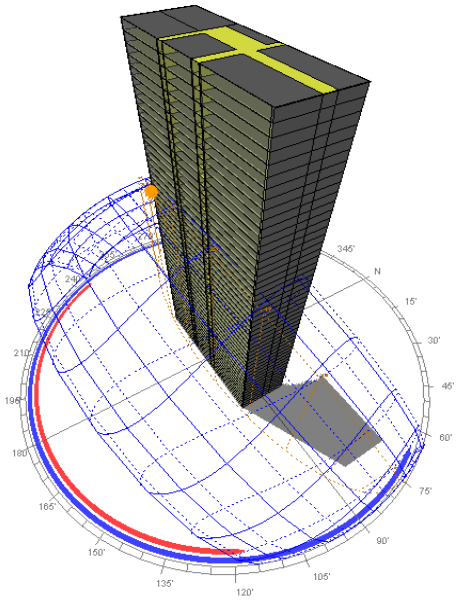

Figure 3: Sun-Path Diagram

ISBN: 978-81-936820-6-7
Proceedings DOI: 10.21467/proceedings.4

In this study, there are two main steps of the thermal analysis. The first step is to find the sensitivity of the energy demand (heating and cooling loads) to the change of the surface area ratio (SAR), which relates to floor-plan aspect ratio:

$$SAR = \frac{(floor\ perimeter \times floor\ height)}{floor\ plan\ area} \quad (1)$$

This analysis consists of thirty-two different simulation runs (of four models in two orientations in four climate zones), where annual cool and heating loads are calculated for each model. The results corresponding to the N-S orientation are provided in Table 1; and the difference in total energy demands between the N-S and E-W orientations is not significant.

Table 1: Energy demand verses SAR (N-S orientation)

Width to length ratio - increase in SAR												
Climate	1:1			1:2			1:3			1:4		
	Heating	Cooling	EUI	Heating	Cooling	EUI	Heating	Cooling	EUI	Heating	Cooling	EUI
	kwh/m^2			kwh/m^2			kwh/m2			kwh/m2		
Cool	49.8	9.4	59.2	51.9	9	60.9	53.6	8.7	62.3	55.9	8.4	64.3
Temperate	7.9	30.7	38.5	8.4	30.7	39.1	8.9	30.8	39.8	9.7	31	40.6
Arid	5.8	57	62.8	6.1	57.9	64.0	6.5	59	65.5	7	60.4	67.4
Tropical	0.0	62.5	62.5	0.0	62.75	62.6	0.0	63.4	63.4	0.0	64.1	64.1

.

Via the model of 1:4 aspect ratio as an example, the monthly and yearly energy demand ratios (EDR) for each of the four climate zones are shown in Table 2.

$$EDR = \frac{energy\ demand\ of\ East - West\ orientation}{energy\ demand\ of\ North - South\ orientation} \quad (2)$$

In addition, the passive solar heat gains ratio (PSHGR) of the model of 1:4 aspect ratio displayed in Figure 4. Moreover, the total heat gain and heat to gain ratio (HGR) of the month of July are broken down into individual sources of direct (solar) gain, internal gain, fabric, and ventilation.

Table 2: Energy demand ratio, EDR, (model of 1:4 aspect ratio)

Months	Energy demand ratio (EDR)			
	Cool	Template	Arid	Tropical
Jan	1.01	1.01	1.03	0.96
Feb	1.01	1.02	0.97	0.99
Mar	1.01	0.99	0.99	1.05
Apr	0.99	1.02	1.04	1.07
May	0.97	1.04	1.05	1.06
Jun	0.99	1.04	1.03	1.05
Jul	**1.011**	**1.034**	**1.026**	**1.055**
Aug	1.02	1.02	1.02	1.05
Sep	1.00	0.99	1.01	1.03
Oct	1.01	0.98	0.99	1.01
Nov	1.02	1.00	0.99	0.99
Dec	1.02	1.02	1.03	0.97
yearly	**1.01**	**1.02**	**1.02**	**1.03**

Table 3, presents the percentage of each of these heat sources and how they vary by orientation. The total energy demand for each orientation is not significantly different, even though the E-W oriented models has a much higher potential for passive solar heat gain

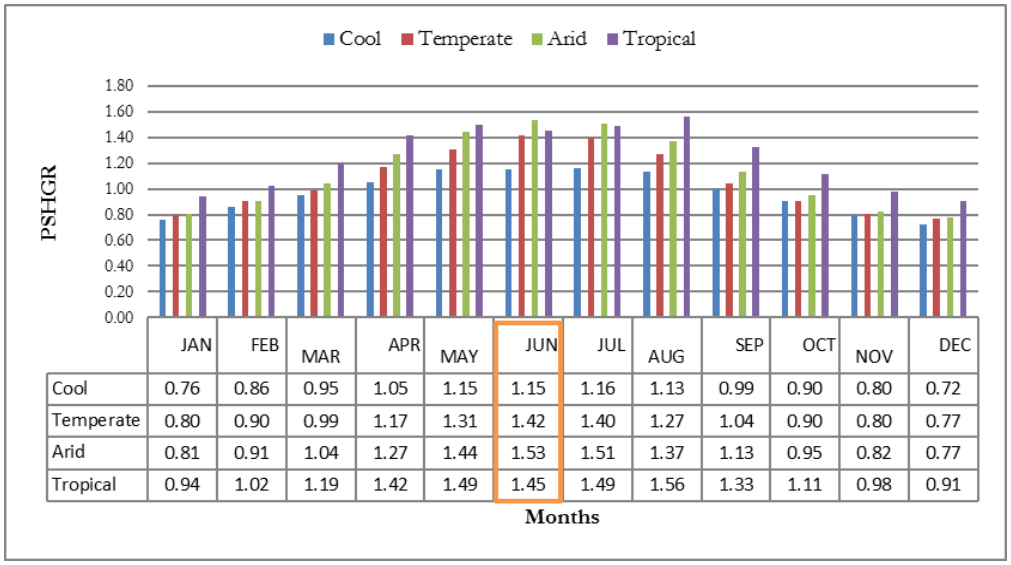

	JAN	FEB	MAR	APR	MAY	JUN	JUL	AUG	SEP	OCT	NOV	DEC
Cool	0.76	0.86	0.95	1.05	1.15	1.15	1.16	1.13	0.99	0.90	0.80	0.72
Temperate	0.80	0.90	0.99	1.17	1.31	1.42	1.40	1.27	1.04	0.90	0.80	0.77
Arid	0.81	0.91	1.04	1.27	1.44	1.53	1.51	1.37	1.13	0.95	0.82	0.77
Tropical	0.94	1.02	1.19	1.42	1.49	1.45	1.49	1.56	1.33	1.11	0.98	0.91

Figure 4: Monthly passive solar heat gain ratio (model of 1:4 aspect ratio)

ISBN: 978-81-936820-6-7
Proceedings DOI: 10.21467/proceedings.4

Series: AIJR Proceedings

The next stage of the thermal analysis investigates why the differences in the energy demand are negligible. One possible reason maybe because of the thermal properties of the IECC 2009 envelope. In the initial analysis, the glazing walls were modeled with U-factors and SHGC set according to the regional climate. These walls were subsequently modeled using single-pane glazing, which has inferior thermal properties (U=6.0 W/m²K & SHGC=0.94). The simulation was run again to evaluate the total energy demand for each of the two orientations. The results of the new simulation runs show that buildings oriented E-W require 12% more energy than those oriented N-S, and that the passive solar heat gain in July is significantly increased.

Table 3: Sources of heat gain (Wh) in July- built to code envelope (model of 1:4 aspect ratio)

Climate	**Cool**					**Temperate**				
Orientation	**θ=0**		**θ=90**		July HGR	**θ=0**		**θ=90**		July HGR
Direct	1.1E+8	17%	1.3E+8	20%	**1.16**	1.1E+8	8%	1.5E+8	11%	**1.40**
Internal	5.1E+8	78%	5.1E+8	75%	1.00	5.1E+8	40%	5.1E+8	38%	1.00
Fabric	2.1E+7	3%	2.3E+7	3%	1.11	2.8E+8	22%	2.9E+8	22%	1.02
Ventilation	1.3E+7	2%	1.3E+7	2%	1.00	3.8E+8	30%	3.8E+8	29%	1.00
Total	6.6E+8		6.8E+8		**1.032**	1.3E+9		1.3E+9		**1.038**
Climate	**Arid**					**Tropical**				
Orientation	**θ=0**		**θ=90**		July HGR	**θ=0**		**θ=90**		July HGR
Direct	1.1E+8	5%	1.6E+8	8%	**1.51**	9.9E+7	10%	1.5E+8	14%	**1.49**
Internal	5.1E+8	25%	5.1E+8	24%	1.00	5.1E+8	50%	5.1E+8	47%	1.00
Fabric	6.1E+8	30%	6.2E+8	29%	1.01	2.2E+8	21%	2.3E+8	21%	1.05
Ventilation	8.3E+8	40%	8.3E+8	39%	1.00	2.0E+8	19%	2.0E+8	18%	1.00
Total	2.1E+9		2.1E+9		**1.03**	1.1 E+9		1.1E+9		**1.057**

4 Results:

4.1 Demand sensitivity−glazing walls built to code.

For each building in the climate zones of Cool, Temperate, and Arid, the change in energy demand is slightly significant, where by increasing the surface area (up to 20%), energy demand is increased by 5.1-7.9% (Table 1) depending on the climate zone. In the tropical climate, however, the energy demands is insensitive to the variations in SAR, where the average increment percent is 0.4% and the total increase is 0.84%. Of course, an increase in the surface area (SAR) is likely to lead to an increase in the materials used, may influence construction costs and embodied energy. Furthermore, increases in the surface area may result in an increase in the area exposed to wind pressure, which might lead to the need of a larger size of structural element, which also influence construction costs and embodied energy. The differences in the total energy demand for two building orientations (N-S & E-W) in each climate zone are nearly negligible. Figure 4, demonstrating monthly breakdown solar heat gains and losses resulting from building oriented E-W are much greater than those if the building was oriented N-S. Table 3, clarifies that the influence of solar loads is small compared to internal, fabric, or ventilation loads. The amount of heat gain from passive sources represents 5-20% of the total heat gain. This is consistent for both orientations, and the effect is trivial compared to the total heat gain.

4.2 Demand sensitivity with non-code-compliant glazing on walls

The second stage of thermal analysis is an investigation of the sensitivity of built- to-code glazing systems on passive solar heat gain, compared to single-pane glazing, which has poorer thermal properties. The outcome demonstrates that code requirements for glazing systems results in reductions in direct heat gain to become to represent 5% rather than 24% of total heat gain(N-S),while become to represent 8% rather than 34% of total heat gain(E-W), (Table 3 & Table 4 for arid climate). Code-built glazing also reduces total energy demands by 12%, which also explains why there is such a small effect of varying building orientation on monthlies and yearly energy demand.

Table 4: Breakdown heat gain (Wh) in July in Arid climate – regular glass envelope (model of 1:4 aspect ratio)

	Heat gain (Wh)				July HGR
	θ=0		θ=90		
Direct	7.4E+08	24%	1.2E+09	34%	1.62
Internal	5.1E+08	16%	5.1E+08	14%	1.00
Fabric	1.0E+09	33%	1.0E+09	29%	1.01
Ventilation	8.3E+08	27%	8.3E+08	23%	1.00
Total	3.099E+09		3.564E+09		1.15

ISBN: 978-81-936820-6-7
Proceedings DOI: 10.21467/proceedings.4

5 Conclusions

By simulating each building configuration using Autodesk's Ecotect, two major conclusions regarding building energy demand can be drawn: (1) For the buildings in Cool, Arid, and Temperate climate zones, the energy demand may be considered marginally sensitive to changes in surface area ratio (SAR). Increasing the envelope surface area by 20% leads to energy demand increases of 5.1-7.9% depending on the climate zone. The energy demand for buildings in the Tropical climate zone is insensitive to variations in SAR. (2) The energy performance of high-rise office buildings is not sensitive to the passive solar gain as long as the exterior envelopes are built to IECC 2009 requirements for thermal performance. Finally, high quality thermal properties of code-built envelope systems offer more flexibility to designers with regard to the building site planning (geometry, layout, and orientation) without creating negative impacts on total energy demand. On the other hand, this limits the possibility of maximizing the advantages of passive heat gain. In addition, because built to code buildings are not significantly sensitive to direct solar gain; it leaves little room for other passive design strategies for energy conservation such as shading devices, landscaping, and thermal mass.

References

[1] K. Yeang, "The Green Skyscraper*," Prestel, Munich,* 1999

[2] M. Jenks, R. Burgess, "Sustainable urban forms for developing countries," *Spon Press,* NY, 2004.

[3] J. Straube, "Green building and sustainability," *Building science digest*, 5: 24, 2006

[4] WBDG. "Energy Codes and Standards," May, 2011. http://www.wbdg.org

[5] United States Green Building Council, "Green building research," June 2009. http://www.usgbc.org>

[6] W. Reed, "The Integrative design guide to green building". *Hoboken*, N.J, 2009

[7] The U.S. Department of Energy Building Energy Codes Program. *International Energy Conservation Code 2009*. International code council, INC., 2010

[8] ASHRAE STANDARED. *Energy Standard for Buildings Except Low-Rise Residential Buildings*. ASHRAE, Atlanta, 2010

Simple and Sustainable Constipate to Save Cost and Time for Structure Constructions

Abdualraouf Mohamed*, Mohamed Ali Milad

Department of Civil Engineering, College of Engineering, Elmergib University, Libya

DOI: https://doi.org/10.21467/proceedings.4.4

* Corresponding author email: raouf.amhir@gmail.com

ABSTRACT

The energy required producing the structural elements such as concrete, steel; wood, etc. have serious environmental and financial consequences. The energy analysis, therefore, must take into consideration the added cost of embodied energy, which is the energy consumed by all of the processes associated with the production of a building. Generally, highly processed material, the higher embodied energy is. Hence, concrete has the lowest re-use capability that makes it a less sustainable material. Thus, wisely, use construction material leads to avoid the use of materials that are associated with high-embodied energy. Moreover, choosing the optimal construction system is one of the elementary bases of sustainability through the possibility of recycling the materials used for building construction. This study presents guidance of the sustainable constipates based on the performance of building construction using masonry barring walls system against frame concrete structure system of residential buildings, Where finite element method was used to analyze the stresses on the masonry bearing walls, and structural analysis for the frame structure. Algebra calculation of the construction materials quantities, and known sources of embodied energy estimation. As a result, this comparison turns out that the masonry barring walls system procedure is offering good distribution of stresses, more economical, require lesser time to build, and highly recyclable, which making it more contributing to sustainability.

Keywords: Embodied energy, Sustainability, Masonry, Recycling, Construction

1 Introduction

The cost of structural elements of concrete construction work and materials used in the traditional methods of construction in the State of Libya may be high; some of it is not environmentally friendly. Moreover, the lack of natural resources for these materials and the high-embodied energy in their production and taking into account the non-use of sustainability methodology in construction makes us think more careful and thoughtful about the techniques used in construction in the State of Libya. In the construction of simple residential buildings, there is known two major structural systems: concrete rigid frame structure system; and masonry wall bearing system and there is great differences in the characteristics of each system [1]. Each has its advantages and disadvantages [2, 3]. Nevertheless, the concern is the

 ISBN: 978-81-936820-6-7

technique and performance of building that built according to these systems in the State of Libya at current era. Because of the method of implementation, where in realty construction is a mixed system between these two systems due to the embodied the concrete masonry into the rigid concrete frame. This method of construction might accidentally give very large capacity of the structural system compared to the capacity required, which leads to a non-economic building and is not sustainable for its more embodied energy and the effort of recycling materials used by the end of building's life span. On the other words, the presence and implementation of concrete masonry within the concrete rigid frame makes it an effective factor to carry forces and even change the behaviour of loads path. As result of mixing these two systems is a complex system that capable of resisting more than is required to resist. Nevertheless, unfortunately there is no need here to increase the capacity because the frame system designed to bear the whole loads alone. However, the main difference between the two systems is the mechanism of carrying loads safely through itself to the ground soil. Standers and cods commends that the characteristics of each of these structural systems individually and do not see the need to mix these two systems together because each of them is well alone [4, 5]. However, the reality of the situation in the State of Libya in the construction of simple private housing buildings, which mix these two systems made it important to know the advantages and disadvantages of this system to help the Libyan citizen to choose the optimal system to build his house in economic and sustainable way. Hence, the idea of this study evaluates the structural performance, and sustainability efficiency of each system then examines the effect mixing them [6]. Moreover, this study illustrates the behaviour of each of these known structural systems and simulate the system used extensively in the construction in the state of Libya, also compared between different systems in terms of stresses distribution, the amount of materials used, embodied energy, then evaluating these systems in terms of sustainability principle. The following sections demonstrate the method and the primary variables, then evaluates the results and present the conclusion.

2 Material and Research Methodology

The research studies a typical residential concrete building with components in line with the tradition and housing requirements of a middle-income family in Libyan society. It is single-story building of 165-square-meter footage print; Figure 1 shows the plan and 3D views of the house. 3D models of structural analysis were prepared for three structural systems. The first model is concrete rigid frame model and analyzed as line element by structural analysis method, the second model is masonry wall bearing and analyzed as surface element by finite element methods; the third is the mixed system model (concrete rigid frame and masonry wall bearing). Modeling and analysis are carried out using SAP 2000, Figure 2 shows the models as it appears on SAP 2000. Table 1 shows the characteristics of the materials used, and Table 2 shows the loads were applied [7]. Where these values simulate the properties of the materials used in practice and the application of standards and specifications in the Libyan state.

(a) (b)

Figure 1: (a) house plan view, (b) house 3D view

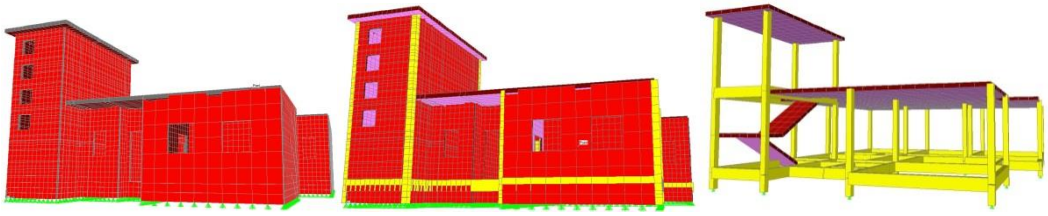

(a) (b)

(c)

Figure 2: (a) Concrete rigid frame model, (b) Masonry wall bearing model, (c) Mixed model

Table 1: Characteristics of materials for analysis and design

Material property	The value
Concrete (fc')	28 MPa
Rebar (fy)	280 MPa
Reinforced concrete density	24 kn/m^3
Masonry concrete density	20 kn/m^3

Table 2: Applied loads, dead and live

Model / Load type	Model 1	Model 2	Model 3
Self-weight of structural elements	SAP Calculated	SAP Calculated	SAP Calculated
Finishes loads on roof	2.50 kn/m^2	2.50 kn/m^2	2.50 kn/m^2
Wall loads	12 kn/m	SAP Calculated	SAP Calculated
Live load on roof	3 kn/m^2	3 kn/m^2	3 kn/m^2

ISBN: 978-81-936820-6-7
Proceedings DOI: 10.21467/proceedings.4

Series: AIJR Proceedings

3 Modeling

3.1 Concrete Rigid Frame Structure System

This system is used in the design of most residential buildings, so the loads carries by the slab, which is supported by beams (or beamless) on the columns then to the foundations. Walls here are partitions to separates building's components where its weight calculated, and it is applied as a distributed load on the beams, this allows mainly concentration loads on columns, moment and shear forces on the beams. The analysis results of the axial force were varied on the columns according to their share of loads, so the columns designed to have cross section of (20 x 20 cm) with 4 Ø 12 mm. Note that, the reinforcing percentage is the minimum value allowed by the code [5]. On the other hand, the concrete required for the columns is 3.0 m^3 while all beams designed to have cross section of (40x20 cm) and required concrete is 9.2 m^3.

3.2 Masonry Wall Bearing System

In this model, no columns or beams have been modeled on the fact that the concrete masonry walls alone carry and support the roof load and other loads to the soil safely [8]. The values of the stresses on the walls have changed slightly through wall's height and the stress distribution has become more uniformly in the absence of columns and beams, where concentration of stress was occurred at interfaces between walls and columns or beams. Note that in the presence of openings, the stresses in the corners of the openings were slightly larger. Generally, concrete masonry wall bearing as structural system showed good behavior of carrying loads and stress distribution. Figure 3 illustrates the stresses in some of the selected wall's surfaces in the building.

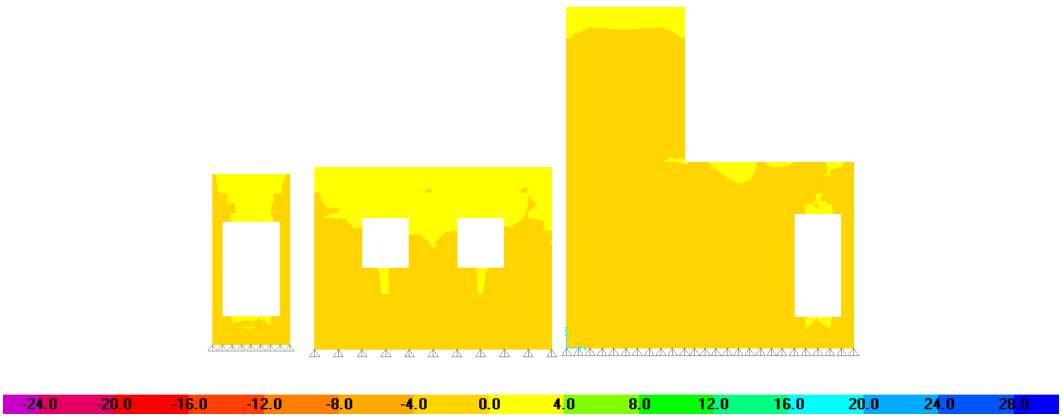

Figure 3: (a) Stresses in some of the selected wall's surfaces of the masonry wall-bearing model

3.3 Composite (Mixed) model

This model combines the first two models. The traditional way of building in the Libyan state is to embed walls in the concrete frames, where the walls are built then casting the columns

and the roof. This method makes the wall an effective structural part (unintentionally) of carrying most of the load to the soil directly, resulting in a very large shortage of supporting forces through columns. As a result of the analysis, the axial force decreased from the column with the largest forces (comparing with first model) to become a load 40.58 kn which is 10% of the designed load, while the other percentages of decrease in load on the rest of the other columns depending on the place in the building. Therefore, the 20 x 20 section is used with a minimum reinforce of 4Ø12 mm, which is more than enough compared to loads on all columns. So the reinforced concrete required for the columns and beams as seam as in rigid frame structure system. Thus, masonry wall that embedded in the rigid frame carried 90% of the loads that is supposed to be carried by the columns.

4 Results and Discussion

The performance of the three systems was good for supporting and carrying the loads applied to them. The concrete rigid frame system is very effective if the implementation methodology is followed as provided for standards and codes. Nevertheless, because of the embedded of the masonry walls during the implementation made the structural elements in this system is highly inefficient and thus non-economic and non-sustainable due to waste of energy and materials in the construction and energy and the cost of recycling Table 3 summarizes the results.

Table 3: Normalized results of structural analysis and energy, cost estimations

	Concrete Rigid Frame System	Masonry Wall Bearing System	Composite System	Extreme differences (%)	
				Min	Max
cost	1.57	1	1.57	-	36
Stress at top of footing level	8	1	0.69	31	87.5
Embodied energy	1.5	1	1.5	-	33

The evaluations normalized with respect to the values of masonry wall bearing system

Masonry wall system is respectable from an engineering field, and because the use of masonry walls is a basic concept in the housing of the Libyan state, where these walls used as partitions in the building, thus, it can use as structural elements as well. Hence that the wall capacity well

ISBN: 978-81-936820-6-7
Proceedings DOI: 10.21467/proceedings.4

Series: AIJR Proceedings

demonstrated, so that the maximum stress did not exceed at the interface with soil 1.5 MPa and gave a uniform and proportional distribution of loads to the entire building. The openings in the walls are somewhat in different form of the distribution of stress in the wall and caused a high concentration of stresses at the corners of these openings, whether for the doors or windows of the building. Concentrated stresses at the openings did not exceed 1.70 MPa. Thus, it is economy system compared to the other two systems. On the one hand, since building and construction, costs are determined mainly by the cost of materials, labor, framing, and placing or erection, and since the structural normal weight concrete cost is varying among countries and all over the world. However, for the Libya state it might be estimated 400/m^3 Libyan dinar including 100 kg rebar [9].Moreover, the embodied energy of normal-weight reinforced concrete with 100Kg rebar per cubic meter is 2.12 MJ/Kg (0.56 kwh/Kg) [10]. Therefore, using masonry wall bearing System leads to total saving resulting in cost non-use of normal-weight reinforced concrete (12.2 m^3) is 4900 Libyan dinars, in addition to 26 Mwh of the embodied energy. These values may be small at first sight, but it is represented cost of completely house in every 100 houses and is essentially important economically and environmentally if it is taken on an international scale.

5 Conclusions

Structural analysis and design using SAP200 and embodied energy, and cost estimation are performed to investigate the structural and energy performance. The results of the structural analysis showed good and effective performance for all studied systems. However, taking into consideration the economic and environmental aspects, the masonry wall bearing system model is the best performance. Where the maximum stress at the foundation level is small 1.5 MPa, which makes it possible to build on the lowest bearing capacity of acceptable foundation soils types. In addition, uniformly distribution of the load on the walls is desirable from an engineering point of view to ensure that uniform behavior occurs because of compressing the foundation soil within the permissible limits. Furthermore, this system is economically good and can save 36% of the cost of building structural elements. This system requires less time and labor than other construction systems; also, this system is environmentally friendly. It uses as little construction material as possible. It can save 26 Mwh of the embodied energy, as well as the possibility of recycling at the end building life span, because it is made of masonry that much easier in the grinding and recycle process compared to the reinforced concrete. Finally, the adoption of this system at an international level will achieve a perfect economic and environmental return.

References

[1] C. Russell Hibbeler. "Structural Analysis," *Prentice Hall*, N J, 2002.
[2] M. Nadim, "Structural concrete: theory and design," *Prentice Hall, Inc.*2002
[3] International Code Council "*International Building Code" IBC code*, US, 2012
[4] American Society of Civil Engineers, "*ASCE 7-10 Standard*," VI, US, 2010

[5] American concrete Institute, "*Building Code Requirements for Structural Concrete," ACI Code 318-2011.* American concrete Institute, MI, US. 2011

[6] M.A. Walker, "What about House Design and Room Location," *Virginia Cooperative Extension*, US.2009

[7] American Society of Civil Engineers, *"Minimum Design Loads for Buildings and Other Structures,"* ASCE/SEI 7-10, NJ, US, 2010

[8] H. Fathy, "Architecture for the poor," *The University of Chicago Press*.US.1973.

[9] RC Means, "*Means Cost Works*," .July, 2011.http:// www.meanscostworks.com.

[10] Council on Tall Buildings and Urban Habitat, "Tall building in numbers," CTBUH *Journal*, Issue III, 50-51, 2009.

[11] Technical Manual Design for lifestyle and the future, "*Australia's guide to environmentally sustainable homes*". March.2010. http://www.yourhome.gov.au

[12] Technical Manual. Embodied Energy. June 2010. http://www.yourhome.gov.au/technical/ fs52.html

[13] AISC. "Designing for Sustainability," *American Institute of Steel Construction*.US, 2011 *http://www.aisc.org/content.aspx?id=17560*

ISBN: 978-81-936820-6-7

Series: AIJR Proceedings
Proceedings DOI: 10.21467/proceedings.4

Thermal Performance of a Heat Pipe with Different Working Fluids

Ayad Alwaer*[1], Jasson Gryzagoridis[2]

[1]Department of Renewable Energies, Higher Institute of Science and Technology, Tarhuna, Libya
[2] Department of Mechanical Engineering, College of Engineering, Cape Peninsula University of Technology, Cape Town South Africa

DOI: https://doi.org/10.21467/proceedings.4.5

* Corresponding author email: GryzagoridisJ@cput.ac.za

ABSTRACT

The use of Heat pipes, for a variety of applications, has increased worldwide due to them achieving high thermal efficiencies. Heat pipes in evacuated tube solar collector systems, in modern domestic water heating, comprise of a sealed envelope of a copper pipe, which contain a small quantity of working fluid. The Heat pipe transfers energy by the latent heat of the evaporation of the working fluid in a heating section. This vapor travels to the cold portion of the heat pipe and condenses. The circulation is completed with the condensate flowing back through the container's inner wall to the heating section by gravity. Tests were conducted using a test apparatus specifically made for the purpose of comparing the relevant attribute of thermal performance of Heat pipes containing different working fluids. A commercially available heat pipe, with its proprietary working fluid, was used as a reference in comparing its thermal performance efficiency (57.1%) with those of identical heat pipes containing distilled water, methanol, acetone and ethanol as working fluids. The results from the experiments achieved thermal efficiencies of 63.1%, 60.5%, 57.6%, and 42.1% respectively.

Keywords: Heat pipe technology; working fluid; efficiency; solar energy; evacuated glass heat pipe collector

1 Introduction

The evacuated tube consists of an outer and inner glass tube with a vacuum trapped between these glass sections. This allows for radiation to penetrate into a centrally located heat pipe, but prevents heat loss via dissipation. The heat pipe is located centrally inside the inner tube. The heat pipe normally consists of a long copper tube containing a very small quantity of the working fluid (e.g., water, acetone, methanol, ethanol, etc.) which forms the vehicle for moving heat to the cooler section of the copper tube. Each collector is made up of a frame, a manifold and a set of tubes –either 8, 12, 18 or 24 tubes, depending upon the geyser size.

There are various forms of heat pipes, which are commercially used in the solar collector panels. As shown in Figure 1, the structure is basically very similar with variations in the shape and size of the (upper portion) condenser [1, 2].

 ISBN: 978-81-936820-6-7

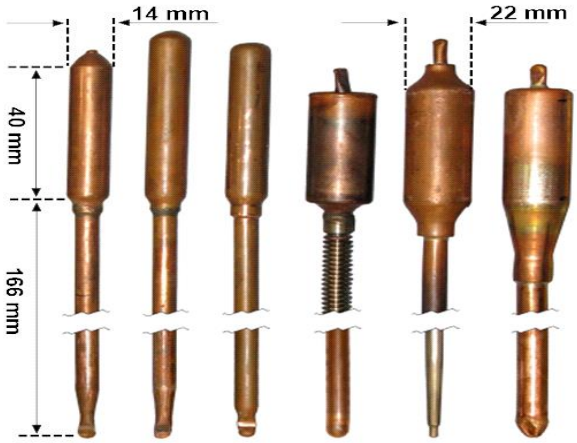

Figure 1: *Various geometrical forms of heat pipes* [1]

2 Heat Pipe Structure and Operation

The design of the heat pipe includes a long copper pipe with a larger diameter condenser at the top and welded at the other end. A small amount of working fluid is added into the heat pipe and then heated to high temperature, or a vacuum pump is used to remove the air from within the space. The result of either method is a vacuum in the copper pipe [3].

The vacuum inside the heat pipe allows the phase change of the fluid to a gas to occur at a lower temperature. The reason for this is to expedite the heat transfer process and create the continuous heat transfer cycle [4, 5&6]

The evacuated tube heat pipes typically found in solar collectors containing a small amount of working fluid have a boiling point of around 25 degrees Celsius as a result of the induced vacuum, so when heating the heat pipe above this temperature the working fluid begins to evaporate. The vapour rises to the condenser at the top of the heat pipe, where it condenses (giving off heat to the desired spot) and returns to the evaporation section at the bottom of the heat pipe. This process is repeated as a cycle [4, 5&7].

2.1 The Working Fluid

As stated before, the heat pipes can utilise various liquids as a working medium. Table 1 refers to the relevant properties of typical fluids that could be used.

Table 1: *Physical properties of Some Heat pipe working fluids* [8, 9].

Fluid	NBP (ºC)	ϱ(kg/m3)	Psat*(kPa)	μ**(kg/ms)	σ**(N/m)	λ (kJ/kg)
Water	100	1000	2.33	1.79×10^{-3}	7.56×10^{-2}	2256
Ethanol	78	789	5.95	1.77×10^{-3}	2.41×10^{-2}	846
Methanol	65	792	13.02	8.17×10^{-3}	2.45×10^{-3}	1100
Acetone	56	784	30	4.1×10^{-4}	2.4×10^{-2}	518

** The vapor pressure data are at 293 ºK., 20 ºC*

*** Surface tension and viscosity data are at 273 ºK., 0 ºC*

ISBN: 978-81-936820-6-7
Proceedings DOI: 10.21467/proceedings.4

Series: AIJR Proceedings

Some working fluids need a compatible vessel material to prevent and avoid chemical reactions or corrosion between the fluid used and the vessel. Chemical effects such as corrosion reduce the efficiency of the vessel, as a non-condensable gas can be produced by chemical reactions. For example, using ammonia as a working fluid in the heat pipe provides a temperature range from –70 to +60 ºC and is compatible with several vessel materials such as aluminum, nickel and stainless steel, but not copper [10]. In selecting a working fluid for use in a heat pipe application, the prime requirements are as follows, [11].

- Good thermal stability.
- Vapor pressures not too high or low over the operating temperature range.
- High latent heat.
- High thermal conductivity.
- Low liquid and vapor viscosities.
- Acceptable freezing or pour point.

The viscosity, sonic, capillary, entrainment and nucleate boiling limitations play important roles when selecting the working fluid [4, 5&6]. However, in the context of this research, the choice of the working fluid in the heat pipe will rest solely on the level of temperature achieved in the condenser part of the heat pipe. The reason adopted here is that this factor will govern the amount of heat that the heat pipe could transfer. In other words, the higher temperatures at the condenser will inherently be able to transfer more heat (comparatively speaking among heat pipes containing different working fluids) to the bulk of the fluid that is being heated. Therefore, internal heat pipe criteria such as the viscous limit, the sonic limit, the entrainment limit affecting the maximum heat flux, the capillary limit, etc., will be ignored and, the recommendation of which working fluid will best enhance the performance of the commercial evacuated heat pipe solar collector will depend entirely on calorific results [11, 12&13].

2.2 Energy Performance Analysis in the Heat Pipe Testing Apparatus

The energy performance indices to be obtained using a specially designed and constructed apparatus in this part of the study, will entail the energy collected from the sun simulator via the heat (using different working fluids) to equal the energy transferred by the heat pipe to the water in the apparatus's tank. In other words the efficiency of the heat pipe can be calculated in terms of heat transfer associated with the change of the internal energy of the water in the system. The heat input will be controlled using a solar simulator and the ambient temperature is not expected to change appreciably since the testing will be done in a laboratory.

2.3 Efficiency of Heat Pipe in Terms of Heat Transfer to Tank's Water

The efficiency of the heat pipe is calculated using the following formula, which involves the change of the internal energy of the water contained in the system's tank.

$$\eta_{hp} = \frac{(\Delta Q_u)/t}{I} m \times 100\%$$

Where η_{hp} is the heat pipe's efficiency (%) in terms of heat transfer to the tank's water, ΔQ_u is the change in the internal energy of the water in kJ/kg which is dependent on the temperature T and pressure P of the system, t is the solar irradiance time in hours, m is the mass in kg of water in the tank and I is the actual total solar radiation on the surface of the evacuated tube heat pipe, which is the irradiance kW/m^2 from the solar simulator multiplied by the heat pipe's actual receiving area of (0.08084 m^2).

3 A Rig for Testing the Performance of the Heat Pipe with Various Working Fluids

In order to test the performance of the heat pipe with various working fluids, an apparatus was designed and constructed consisting of a small geyser tank mounted on a frame. A heat pipe with its evacuated glass tube could easily be inserted and removed in a short turnaround time (see Figures 2 and 3). A single evacuated heat pipe assembly could be inserted in a dry bay attached to a tank which could accommodate four litters of water. Halogen floodlights mounted on a frame over the heat pipe assembly provided the heat source.

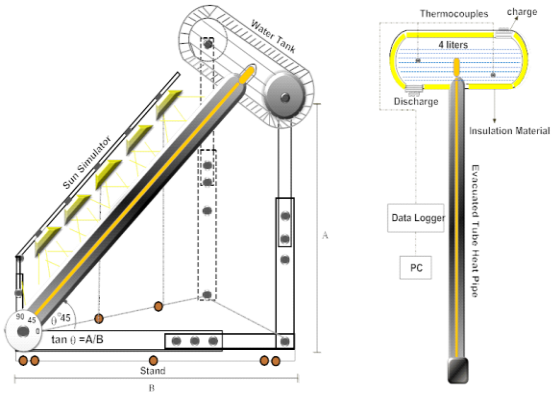

Figure 2: *Schematic diagram of the testing apparatus for the heat pipes.*

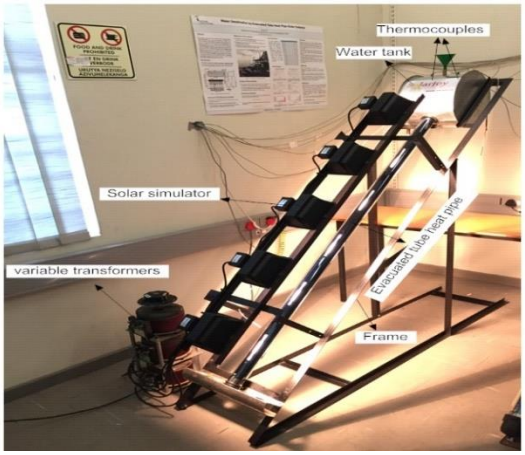

Figure 3: *The heat pipe's testing apparatus*

ISBN: 978-81-936820-6-7
Proceedings DOI: 10.21467/proceedings.4

Series: AIJR Proceedings

3.1 Tank Description

The cylindrical tank was made of 1.2 mm thick stainless steel sheet; with dimensions of 200 dia. and 150 mm long. An outer casing was built around the tank to cover the polyurethane insulation.

A brass heat pipe sleeve (14 mm internal diameter) was welded into the tank at a 45 degree angle to line up with the mounting frame of the heat pipe, tank and simulator.

In addition, two wells were built into the top of the tank to place thermo-couple sensors in order to record the temperature of the top and bottom fluid levels in the tank respectively. On the side of the tank a valve drain pipe was fitted with a 15 mm filling pipe fitted at the top. The halogen lights were controlled via a variable transformer thus regulating the simulated radiation on the heat pipe.

3.2 The Sun Simulator for the Heat Pipe Tester

The solar radiation simulator was used to heat the evacuated heat pipe. It consisted of an array of five halogen floodlights of 500 W each. The halogen lamps were distributed evenly over the length of the evacuated tube heat pipe, at a distance of 225 mm above it. The solar simulator's irradiance level was set to a level consistent with an average 800 watts per square metre, as measured over the evacuated heat pipe surface. The output of the sun simulator could be controlled by means of a variac (variable transformer) which controlled voltage supplied to the array of halogen lamps.

3.3 Frame

The frame was built using L shape mild carbon steel sections set for testing at a fixed angle of 45 degree.

4 Instrumentation for the Heat Pipe Tests

Two J-type thermocouples, one of them at the bottom and another at the top of the "geyser", were fitted to measure the water temperature in the storage tank, and, together with the ambient temperature, were recorded during the test period. A digital display data logger (Agilent-34972A) was used to record the temperature scale. All experiments were carried out for seven hours.

5 Testing the Heat Pipe Performance with Different Working Fluids.

The relatively elevated temperatures which are obtainable when using evacuated tube heat pipes in the field of water heating is the reason for the attempt to use them in the desalination of seawater.

The method followed in testing a set of working fluids in the heat pipe is described below:

Testing of the heat pipe's performance with various working fluids required a benchmark. This benchmark was obtained by first testing the commercial heat pipe (as it came from the manufacturer) with the original working fluid. Attempts to obtain information about the constitution of the working fluid, from the manufacturer in China, were unsuccessful. It was assumed that the liquid was water, but it had an orange/yellowish colour possibly because of some kind of additive. The fluid was drained and the heat pipe was charged with new fluid, after which the performance test was undertaken over the seven-hour period. It is worth mentioning here that the quantity of working fluid encountered in the commercial heat pipes varied considerably in the range of 5 to 10 ml; however this did not seem to affect their performance.

The raw data that was collected during each heat pipe experiment with the four working fluids consisted of recording the temperatures of the water at two locations in the tank's water, the irradiance from the solar simulator and the ambient temperature Ta. The duration of the individual tests was seven consecutive hours daily. The data displayed in Appendix A is a typical sample, where T_1 & T_2 are the tank's water temperatures (in degrees centigrade) recorded every 15 minutes via two thermocouples located at the top and bottom levels in the tank's water, using a data-logger. T_{a1}, T_{a2} and T_{a3} (Ambient temperature readings): these temperature readings, represented with their average value $T_{a\,avg.}$, were also recorded each 15 minutes via three thermocouples located around the heat pipe testing apparatus.

5.1 Results of the Heat Pipe Performance with Different Working Fluids

The purpose made testing apparatus was used in testing the performance of the heat pipes with four different working fluids. As already mentioned, the results from a test using one of the commercially available heat pipes was used as a benchmark in comparing their performance. The working fluids chosen were distilled water, methanol, acetone and ethanol. The experiments were conducted for the purpose of improving or better discovering the effect on the thermal performance and efficiency of the heat pipe, which was recharged with various working fluids at the same filling ratio by infusing always the same amount of working fluid (10 ml).

5.1.1 Results from the Experiments with the Testing Apparatus for the Heat Pipes

A summary of the results from testing the performance of the heat pipes with different working fluids appears in Table 2.

Figure 4 displays the behaviour of the temperature rise of the water in the tank of the heat pipe testing apparatus when testing each individual heat pipe, each containing a different fluid. Thus a direct comparison of their performance can be made.

ISBN: 978-81-936820-6-7
Proceedings DOI: 10.21467/proceedings.4

Table 2: *The initial and final temperatures of the water, ambient temperature and the efficiency% of each heat pipe containing a particular working fluid*

	Description of the test	Initial& final temp. °C	Ambient temp. avg. °C	Efficiency%
1	Original heat pipe (Commercial)	16.2-71.8	21.8	57.1
2	Heat pipe with Pure water (Working fluid)	16.3-77.7	19.3	63.1
3	Heat pipe with Methanol (Working fluid)	16.4-75.3	19.3	60.5
4	Heat pipe with Acetone (Working fluid)	16.4-72.5	19.3	57.6
5	Heat pipe with Ethanol (Working fluid)	16.5-57.7	21.9	42.1

The efficiency of each heat pipe, characterised by the working fluid that it contains, is presented for comparison purposes in Figure 5. The addition of the average ambient temperature data during each test enables an enhanced or more informed comparison on the performance of the heat pipes. The ambient temperature plays a major role in the heat loss from the tank of the testing apparatus. This fact affects the heat loss from the water tank and hence affects the water's peak average temperature, reflecting in the heat pipe's efficiency calculation.

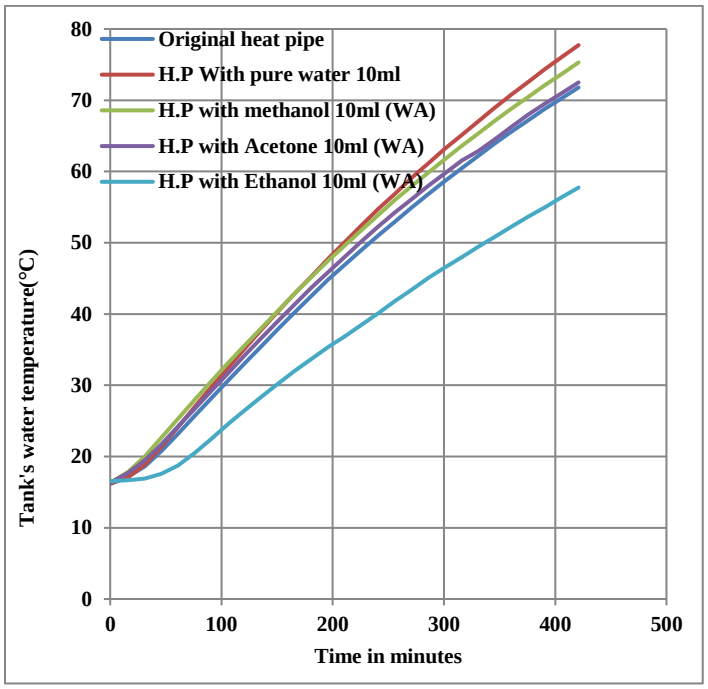

Figure 4: *Average water temperature in the tank of the testing apparatus for each heat pipe tested containing a different working fluid*

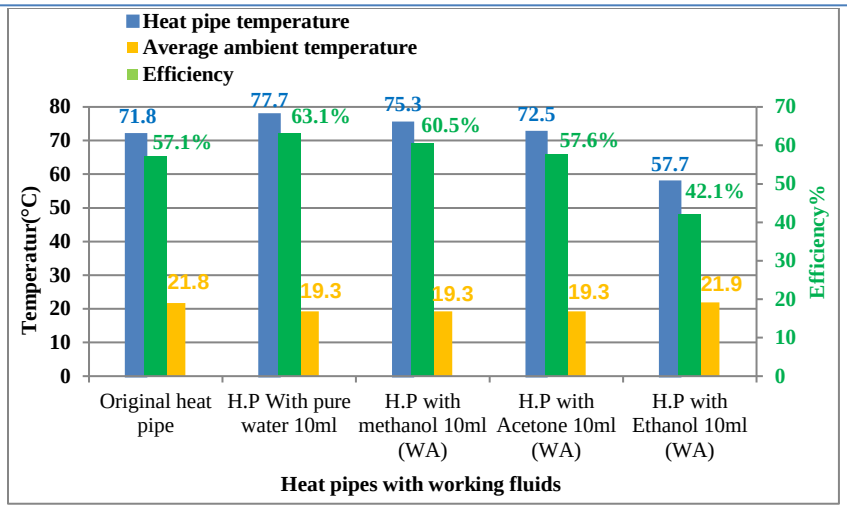

Figure 5: *Efficiencies of the heat pipe, bulk water temperatures in the heat pipe testing apparatus tank and average ambient temperatures*

5.1.2 Discussion of results with the testing apparatus for the heat pipes

The results of the experiments on different working fluids used in the evacuated tube heat pipe have shown that, of all the working fluids chosen in this study, i.e. pure water, methanol, acetone and ethanol, the former three performed well compared to the commercial working fluid.

In terms of ranking their performance, the pure water appeared superior to the others, with a thermal efficiency of 63.1%, followed by Methanol 60.5%, Acetone 57.6%, commercial working fluid 57.1% and Ethanol 42.1%. For a sample calculation of the heat pipe's efficiency in terms of heat transfer to the tank's water see Appendix B.

The averages of ambient temperatures during the tests when using methanol, water and acetone, as working fluids, were equal (19.3 ℃), which was colder/.lower than the average of ambient temperatures when testing with the commercial working fluid and ethanol in the heat pipe (21.8 ℃), as shown in figure 5.

It is not expected that such a small change in the ambient temperature would have affected the results significantly because the heat pipe's testing apparatus had a well-insulated tank. The additional heat losses to the environment (had all experiments been performed at the lower ambient temperature of 19.3 ℃), would be minimal and would have resulted in slightly lowering the efficiencies of the two heat pipes containing the commercial fluid and acetone respectively.

6 Conclusions

A totally separate, newly designed and constructed apparatus was used to test the performance of a heat pipe with various "working" fluids. The "commercial working fluid" inside the heat pipe was replaced each time with a different "working" fluid and individual experiments were

ISBN: 978-81-936820-6-7

Series: AIJR Proceedings
Proceedings DOI: 10.21467/proceedings.4

performed. The results of these experiments in terms of the thermal efficiency of the heat pipe were compared as follows:

The heat pipe containing the:

- "Commercial" working fluid – thermal efficiency 57.1%
- "Pure water" – thermal efficiency 63.1%
- "Methanol" – thermal efficiency 60.5%
- "Acetone" – thermal efficiency 57.6%
- "Ethanol" – thermal efficiency 42.1%

From these experiments it is concluded that the thermal efficiency of the heat pipe was improved by 6% when distilled water was used, as opposed to the commercial working fluid. In the context of the heat pipe being used in an evacuated tube solar energy collector it is expected that such a system will improve its thermal efficiency (compared to the currently commercially available units), with heat pipes containing pure water, methanol or acetone (in this order) as working fluids.

References

[1] S. Jack & G. Rockendorf, " Wärmerohre in Sonnenkollektoren– Wärmetechnische Grundlagen und Optimierung sowie neue Ansätze für die Integration," pp.1–190, November 2013.

[2] H .Barua, M. Ali, M. Nuruzzaman, M. Quamrul Islam & C. M. Feroz, "Effect of filling ratio on heat transfer characteristics and performance of a closed loop pulsating heat pipe," Procedia Engineering, 56, pp.88–95, 2013.

[3] F. N. Ashok & K. V. Mali, "Thermal Performance of Thermosyphon Heat Pipe Charged with Binary Mixture," International Journal of Science, Engineering and Technology Research, 4(1), pp.92–102, January 2015.

[4] R. S. Gaugler, "Heat transfer device," U.S., Patent No., 2350348, 6 June 1944.

[5] G. M. Grover, "Evaporation and condensation heat transfer device," U.S., Patent No., 3229759.

[6] G.M. Grover, T.P. Cotter & G.F. Erickson, "Structures of very high thermal conductance," J. App. Phys., Vol. 35, pp.1190-1191, 1964.

[7] R. S. Gaugler, "Heat transfer device," U.S., Patent No., 2350348, 6 June 1944.

[8] S. M. Peyghambarzadeh, S. Shahpouri, N. Aslanzadeh, & M. Rahimnejad,"Thermal performance of different working fluids in a dual diameter circular heat pipe," *Ain Shams Eng. J.*, Apr. 2013.

[9] E. W. Washburn,"International critical tables of numerical data, physics," chemistry and technology. Knoven, 2003.

[10] J. P. Holman, "Heat Transfer," Tenth Edit. USA 2010.

[11] P. Wallin, "Heat Pipe, selection of working fluid," pp. 1–7, 2012.

[12] R. Manimaran, K. Palaniradja, N. Alagumurthi, and J. Hussain, "FACTORS AFFECTING THE THERMAL PERFORMANCE OF HEAT PIPE – A REVIEW," *J. Eng. Res. Stud.*, III(II), pp.20–24.2012.

[13] D. A. Reay, & P.A. Kew, "Heat Pipes Theory, Design and Applications," Fifth Edit. 2006.

Appendixes

Appendix A

Typical data collected during the heat pipe tests for the various working fluids.

Testing the heat pipe containing pure water as a working fluid

	Date &Time	T_1 at top of the tank	T_2 at Bottom of the tank	Tavg.	Ta_1	Ta_2	Ta_3	$Ta_{avg.}$
		(°C)	(°C)	(°C)	(°C)	(°C)	(°C)	(°C)
1	09/09/2015 09:01:20:061	16.4	16.1	16.3	17.6	18.1	17.9	17.9
2	09/09/2015 09:16:20:046	17.9	16.2	17.1	23.4	19.7	19.0	20.7
3	09/09/2015 09:31:20:046	20.5	17.3	18.9	24.0	20.3	19.6	21.3
4	09/09/2015 09:46:20:046	23.3	19.4	21.3	24.4	20.6	19.9	21.7
5	09/09/2015 10:01:20:046	26.3	22.0	24.1	24.8	20.9	20.2	22.0
6	09/09/2015 10:16:20:046	29.1	24.8	27.0	24.9	21.1	20.4	22.1
7	09/09/2015 10:31:20:046	31.9	27.7	29.8	24.8	21.1	20.4	22.1
8	09/09/2015 10:46:20:046	34.5	30.4	32.5	24.9	21.1	20.4	22.2
9	09/09/2015 11:01:20:046	37.2	33.2	35.2	24.8	21.1	20.5	22.1
10	09/09/2015 11:16:20:046	39.8	35.9	37.8	24.8	21.2	20.4	22.2
11	09/09/2015 11:31:20:046	42.3	38.5	40.4	24.8	21.2	20.4	22.2
12	09/09/2015 11:46:20:046	44.8	41.0	42.9	24.8	21.2	20.4	22.1
13	09/09/2015 12:01:20:046	47.2	43.4	45.3	24.7	21.1	20.4	22.1
14	09/09/2015 12:16:20:046	49.7	45.9	47.8	24.7	21.1	20.3	22.1
15	09/09/2015 12:31:20:046	52.1	48.2	50.1	24.7	21.1	20.3	22.0
16	09/09/2015 12:46:20:046	54.4	50.5	52.4	24.9	21.0	20.3	22.1
17	09/09/2015 13:01:20:046	56.8	52.7	54.8	25.0	21.0	20.2	22.1
18	09/09/2015 13:16:20:046	58.8	54.9	56.9	25.0	21.0	20.2	22.1
19	09/09/2015 13:31:20:046	61.2	57.0	59.1	24.9	20.9	20.2	22.0
20	09/09/2015 13:46:20:046	63.2	59.1	61.1	25.0	20.9	20.2	22.0
21	09/09/2015 14:01:20:046	65.3	61.1	63.2	24.9	20.9	20.2	22.0
22	09/09/2015 14:16:20:046	67.2	63.1	65.2	25.0	20.9	20.2	22.1
23	09/09/2015 14:31:20:046	69.2	64.9	67.1	25.2	21.0	20.3	22.2
24	09/09/2015 14:46:20:046	71.2	66.8	69.0	25.5	21.0	20.3	22.3
25	09/09/2015 15:01:20:046	73.1	68.6	70.8	25.4	21.1	20.3	22.3
26	09/09/2015 15:16:20:046	74.9	70.4	72.6	25.4	21.1	20.4	22.3
27	09/09/2015 15:31:20:046	76.7	72.1	74.4	25.5	21.1	20.4	22.3
28	09/09/2015 15:46:20:046	78.4	73.7	76.1	25.4	21.1	20.4	22.3
29	09/09/2015 16:01:20:046	80.1	75.4	77.7	25.4	21.1	20.4	22.3

ISBN: 978-81-936820-6-7
Proceedings DOI: 10.21467/proceedings.4

Series: AIJR Proceedings

Appendix B

Sample calculation of the heat pipe efficiency in terms of heat transfer to the tank's water when the heat pipe containing pure water as the working fluid

The efficiency of the heat pipe is calculated using the following formula, which involves the change of the internal energy of the water contained in the system's tank.

$$\textbf{Efficiency} = \frac{\textbf{Output}}{\textbf{Input}} \times \textbf{100}\%$$

$$\eta_{hp} = \frac{(\Delta Q_u)}{I \times t} m \times 100\%$$

Where η_{hp} is the heat pipe's efficiency (%) in terms of heat transfer to the tank's water.

$\Delta Q_u\ (kJ/kg)$, is the change in the internal energy of the water in the tester's tank that depends on the temperature *T* and pressure *P* of the system.

t is the duration of the time for the test (7 h x 3600 h/s); $m(kg)$, is the mass of the water in the tank and $I(kW)$, is the total solar radiation on the evacuated tube heat pipe, which is the irradiance R, kW/m² from the solar simulator multiplied by the heat pipe's receiving area of ($0.08084\ m^2$).

1. Output

$$\Delta E(kJ) = \Delta Q_u \times m$$

$$\Delta E(kJ) = (Q_2 - Q_1)(kj/\text{kg}) \times m(kg)$$

This sample calculation refers to the case of the heat pipe containing pure water as the working fluid; the initial and final temperatures obtained were 16.3 and 77.7 $^\circ\ C$ respectively.

$\Delta E = (Q_{77.7} - Q_{16.3}) \times m$

Linear interpolation was used to find the energy transferred between the temperatures from a standard table of saturated water.

$\Delta \boldsymbol{E(J)} = (325.3192 - 68.42258) \times 1000 \times 4 = \boldsymbol{1027586.48\ J}$

2. Input

$R = 800\ W/m^2$

Assumed surface area of the evacuated tube heat pipe

$= 1.72m\ (length) \times 0.047m\ (dia) = 0.08084\ m^2$

$I = 800W/m^2\ \times 0.068\ m^2 = \boldsymbol{64.672\ W}$

$\boldsymbol{t = 7h \times 3600s = 25200\ s}$

$\boldsymbol{I \times t = 64.672\ w\ \times 25200\ s\ = 1629734.4J}$

$\eta\% = (\boldsymbol{1027586.48\ J/1629734.4J})\ \times 100 = \boldsymbol{63.1}\%$

Effects of Reduction in Construction Temperature on Workability of Warm Mix Asphalt Incorporating Rh-wma Additive

Bashir M. Aburawi*

Department of Civil, College of Engineering, Elmergib University, Libya

DOI: https://doi.org/10.21467/proceedings.4.6

* Corresponding author email: Aburawi2018@gamil.com

ABSTRACT

Conventional Hot Mix Asphalt (HMA) has been the primary material used in pavement in past decades. Recently, compared to conventional HMA, Warm Mix Asphalt (WMA) has shown great potential and offers benefits not given by HMA, since the WMA can be produced at lower temperatures without affecting pavement performance. The WMA technologies allow a significant reduction in construction temperatures of asphalt mixtures through lowering the viscosity of binders. In WMA, different types of additives are added to the binder depending on the technology used and such addition of these materials brings down the viscosity drastically thus reducing the temperature to which the aggregates and binders have to be heated during mixing and compaction. This study was limited to the effects of construction temperature on the workability performance of WMA incorporating RH-WMA additive. Binder namely 80/100 was used for preparation of all asphalt mixtures and RH-WMA used as warm mix asphalt additive. Asphalt mixtures were prepared using crushed granite aggregate for AC14 wearing course and compacted by using Servopac Gyratory Compactor (SGC). The Leeds Workability Method used to determine the workability index. The results show that increase in construction temperature improves the workability of both WMA and HMA. Workability Index (WI) of mixtures incorporating 3% RH-WMA is slightly higher than mixtures incorporating 2% RH-WMA. The increase in WI is more pronounced at higher RH-WMA contents.

Keywords: Warm Mix Asphalt, RH-WMA, Servopac Gyratory Compactor, The Leeds Workability Method, Workability Index.

1 Introduction

Asphalt is a pavement material that is brittle and hard in cold environments and soft at elevated temperatures. It has been historically employed as the most popular paving material for roadways [1]. Traditionally, Hot Mix Asphalt (HMA) has been widely used for road construction. The HMA production process requires a high temperature application. This requires the aggregates to be heated to very high temperature. The major disadvantage

 ISBN: 978-81-936820-6-7

associated with this process is that it consumes a lot of energy and discharges a large volume of toxic gasses and dust during its production and paving process. This has adverse effects on the health of the construction workers as well as the environment in particular.

Since Warm Mix Asphalt (WMA) additives can reduce the binder viscosity, the production temperatures can be lowered, compared to conventional HMA. It was reported that the mixing temperatures of WMA ranged from 100°C to 140°C compared to the mixing temperatures of 150°C to 180°C for conventional HMA [2]. Compared with HMA, WMA technology can significantly reduce mixing temperatures of asphalt mixture by 20°C to 30°C [3]. One of the additives used to produce WMA is a type of wax named RH-WMA. The additives improved asphalt binder coating, mixture workability and compactability at lower temperatures. Hesami [4] defined the workability of asphalt as the ease of handling, paving and compacting the mixture. Asphalt mixtures with higher workability are known to have higher compactability.

1.1 Warm Mix Asphalt Technology

To overcome the disadvantages associated with HMA, the WMA technology was introduced. WMA improves the energy efficiency by reducing the construction temperature. WMA uses additives that help reduce the viscosity of the asphalt binder, which in turn causes the asphalt mixing and construction to be carried out at relatively low temperatures while maintaining its performance similar to HMA [5]. Figure 1 shows different types of WMA additives and Figure 2 shows the other advantages of using WMA.

Figure 1: *Types of WMA Additives*

Figure 2: *Advantages of WMA*

One of the major advantages of WMA is the increased workability at conventional and lower compaction temperatures. Bennert. [6] defined the workability as the property of the asphalt mixture that describes the ease with which asphalt mixture can be placed and compacted to the desired mat density. Abdelgalil et al. [7] used a device that employed an electric transducer and heat regulator for evaluating mixing temperature in mixture workability and compatibility by determining the correlation between workability and compatibility. Zhao and Guo [8]

developed a test instrument to measure asphalt mixture workability. From the torque, the workability of the mixture can be judged and at lower mixing temperature, WMA exhibits similar workability with HMA [9]. Foaming materials can be used to produce WMA to increase the workability and compactibility of the mixture at lower temperatures [10]. Xiao. [11] reported that chemical additives improve asphalt binder coating, mixture workability and compactibility at lower temperatures. To lower the mixing temperature, organic or wax additives are utilised for reducing the viscosity of binder [12].

2 Materials and Methods

2.1 Materials

The conventional virgin 80/100 asphalt binder used was obtained from Shell Bitumen Company, Singapore and used as the control binder.Granite aggregate used in the preparation of all the mixtures were supplied by Kuad Kuari in Penang. The crushed granite was used in the mix design for Asphaltic Concrete mixture AC14 wearing course mix according to the Malaysian Public Works Department local specifications [13]. Aggregates and asphalt binder with properties similar to those used by Hamzah et al. [14] were also utilized for this study.

Pavement Modifier (PMD) was the filler used in this study. The PMD modifier was supplied by NSL Chemicals Ltd, Ipoh, Perak, Malaysia [15]. Figure 3 shows the PMD filler used. The RH-WMA warm mix modification technology was used to prepare WMA. RH-WMA is an organic based additive like wax developed in China. It can be utilized as an additive to be blended with reclaimed asphalt binder [16]. Figure 4 shows the RH-WMA that exists in the form of small white particles. The mixtures were compacted using the Servopac gyratory compactor (SGC) as shown in Figure 5 at 30 gyrations per minute at a compaction angle of 1.25° for 100 gyrations.

Figure 3: *PMD as Filler*

Figure 4 : *RH-WMA as Additive for WMA*

Figure 5: *Servopac Gyratory Compactor*

2.2 Leeds Workability Method

Asphalt mixtures must be workable so that it can be easily handled, spread and compacted to the required density. Unworkable mixtures will be difficult to compact without tearing under the paving machine screed and hence adequate compaction will not be achieved.

The Leeds Workability Method was developed by Cabrera and Dixon [17]. It was based on the relationship between mixture porosity and the associated compaction energy input applied by the Gyratory Testing Machine (GTM). Under the same field compaction effort, mixes with

ISBN: 978-81-936820-6-7
Proceedings DOI: 10.21467/proceedings.4

higher Workability Index (WI) shall lead to easy compaction and higher density compared to those with low workability. Mixes that achieve higher WI (workability) and lower CEI (compactability) are desirable. Higher WI is associated with easier and faster mat compaction during construction and lower CEI is associated with higher stability during trafficking. The WI can be used effectively to assess the influence of compaction temperature or mix composition, particularly binder content, coarse aggregate content, sand morphology and filler type [17]. Field experience has shown that mixes with a WI equal to or smaller than 6 are difficult to handle and compact. The mixtures were compacted at their OBC using the SGC. This compaction type is expected to realistically simulate the compaction in the field as compared to the impact compactor like Marshall compaction. Height changes and the number of its gyrations can be automatically recorded.

A high WI indicates a more workable mixture or mixture that is easier to compact. From the semi-logarithmic plot, air voids reduce with the number of gyrations. The straight line equation is defined in Equation (1).

$$Y = A - Bx \quad (1)$$

Where:

Y = Air voids, (%)

A, B = Constant

x = Log10, number of gyration

From Equation (2), the constant A is obtained by extrapolating the straight line to intersect with the Y-axis at zero gyration. The WI is defined as in Equation (2).

$$WI = 100/A \quad (2)$$

3 Results and Discussion

3.1 Effects of Compaction Temperature on Workability Index

The results show that increase in compaction temperature improves the workability of both WMA and HMA. This is true for all WMAs which demonstrate better workability than HMA. The compaction temperature of 125°C has a significant influence on the workability of WMA. It can be seen from Figure 7 that, as the number of gyrations increase, there is difference in the air voids of all mixtures. From Figure 7 (a) and (b), the air voids are highest for HMA and is more pronounced at 100 gyrations. This also infers that at 125°C and 110°C compaction temperatures, the increase in the number gyrations can result in lower air voids. This is not true for other temperatures as shows by no significant difference in Figure 7 (c) at 95°C compaction temperature. According to Figure 7 (c), there is no major changes in the air voids between HMA and WMA. The use of WMA additives has shown no significant benefit at 95°C compaction temperature. The WMA 2%, WMA 3% and HMA curves follow similar trend.

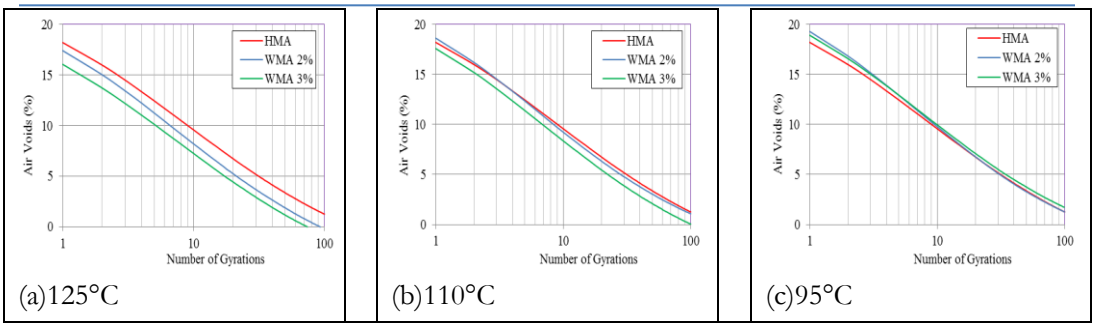

Figure 7 : Air Voids for WMA Compacted at Various Temperatures (HMA Compacted at 150°C)

All straight lines are plotted for every sample to determine the average WI. The regression value, R^2 for the straight line is above 0.90, implying good accuracy regression equations.

The effect of compaction temperature on WI can be seen by comparing WI in Figure 8. The WI increases as compaction temperature increases. The increase in WI with the increase in compaction temperature is due to the lubricating effects of asphalt mixture keeping the viscosity of the binder suitable for compaction. Higher WI values are preferred and are indicative of better mix workability. Mixture compacted at 125°C exhibited better workability than HMA. WMA has better workability characteristics than HMA. The WI reduces by 3-16%, for mixtures incorporating 2% RH-WMA when compaction temperature reduces to 110°C and 95°C, respectively. 3-19% for mixtures incorporating 3% RH-WMA when compaction temperature reduces to 110°C and 95°C, respectively.

3.2 Effects of RH-WMA Content on Workability

From Figure 8, the average WI of mixtures incorporating 3% RH-WMA is slightly higher than mixtures incorporating 2% RH-WMA. The increase in WI is more pronounced at higher RH-WMA contents.

3.3 Correlation between CEI and WI

Figure 9 shows the relationship between CEI and WI for different mixtures. Mixtures with high WI reflects low CEI and have better workability. Figure 9 shows linear relationships between CEI and WI. The WI is inversely proportional to CEI. High WI and low CEI are desirable.

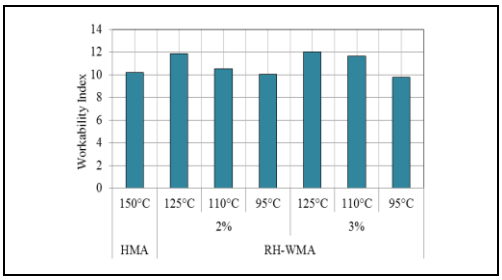

Figure 8: WI of Asphalt Mixtures Tested

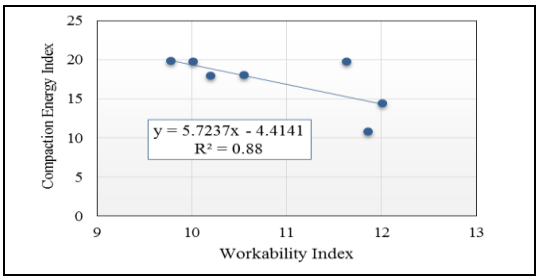

Figure 9 : Correlation between CEI and WI

ISBN: 978-81-936820-6-7
Proceedings DOI: 10.21467/proceedings.4

Series: AIJR Proceedings

4 Conclusions

The RH-WMA additive would either reduce the viscosity of the binder or allow better workability of the mix at lower binder content. For this case, the OBC of WMA is slightly lower than the OBC for HMA. The WI can be used effectively to assess the influence of production temperature.

5 Acknowledgment

The author would like to acknowledge the Universiti Sains Malaysia that has funded this research grant through the Research University Grant Scheme which enables this paper to be written.

References

[1] Sulyman, M., Sienkiewicz, M. and Haponiuk, J. Asphalt Pavement Material Improvement: A Review. *International Journal of Environmental Science and Development*, 5, 444-454, 2014.

[2] Kim, Y.-R., Zhang, J. and Ban, H.Moisture Damage Characterization of Warm-Mix Asphalt Mixtures Based on Laboratory-Field Evaluation. *Construction and Building Materials*, 31, 204-211, 2012.

[3] Wang, C., Hao, P., Ruan, F., Zhang, X. and Adhikari, S. Determination of the Production Temperature of Warm Mix Asphalt by Workability Test. *Construction and Building Materials*, 48, 1165-1170, 2013

[4] Hesami, E., Jelagin, D., Kringos, N. and Birgisson, B. An Empirical Framework for Determining Asphalt Mastic Viscosity as A Function of Mineral Filler Concentration. *Construction and Building Materials*, 35, 23-29, 2012.

[5] Kim, H., Jeong, K.-D., Lee, M. S. and Lee, S.-J. Performance Properties of CRM Binders with Wax Warm Additives. *Construction and Building Materials*, 66, 356-360, 2014.

[6] Bennert, T., Reinke, G., Mogawer, W. and Mooney, K. Assessment of Workability and Compactability of Warm-Mix Asphalt. Transportation Research Record: *Journal of the Transportation Research Board*, 2180(1), 36-47, 2010.

[7] Abdelgalil, S. M. K., Abdul Rahman, M. and Arshad, A. K. Development of Workability Measuring Device for Asphalt Mixture Using Electronic Transducer and Temperature Regulator. *Journal of Basic and Applied Scientific Research*, 1, 721-726, 2011.

[8] Zhao, G.-J. and Guo, P. Workability of Sasobit Warm Mixture Asphalt. Energy Procedia, 16, 1230-1236, 2012.

[9] Gudimettla, J. M., Cooley, L. A. and Brown, E. R. Workability of Hot Mix Asphalt. National Center for Asphalts Technology, Report, 03-03, 2003

[10] Martinez-Arguelles, G., Giustozzi, F., Crispino, M. and Flintsch, G. W. (2014). Investigating Physical and Rheological Properties of Foamed Bitumen. *Construction and Building Materials*, 72, 423-433, 2014.

[11] Xiao, F., Punith, V. S. and Amirkhanian, S. N. Effects of Non-Foaming WMA Additives on Asphalt Binders at High Performance Temperatures. *Fuel*, 94(5), 144-155, 2012.

[12] Sheth, N. M. Evaluation of Selected Warm Mix Asphalt Additives. Master Thesis, The University of Iowa, 2010.

[13] JKR. Standard Specification for Road Works in Malaysia, (Section 4: Flexible Pavements), Cawangan Jalan, Jabatan Kerja Raya Malaysia, Kuala Lumpur, 2008.

[14] Hamzah, M. O., Golchin, B. and Tye, C. T. Determination of the Optimum Binder Content of Warm Mix Asphalt Incorporating Rediset Using Response Surface Method. *Construction and Building Materials*, 47, 1328-1336,2013.

[15] Aman, M. Y. (2013). Water Sensitivity of Warm Porous Asphalt Incorporating Sasobit®. Ph.D Thesis, Universiti Sains Malaysia.

[16] Wang, H., Dang, Z., You, Zhanping. and Cao, D. Effect of Warm Mixture Asphalt (WMA) Additives on High Failure Temperature Properties for Crumb Rubber Modified (CRM) Binders. *Construction and Building Materials*, 35, 281-288, 2012

[17] Cabrera, J.G., Dixon, J.R. Performance and Durability of Bituminous Material, Proceeding of Symposium,University of Leeds, 1994

Effect of Corrugation Geometry and Shape on Energy Absorption of Composite Plate.

Khalid A. Elbkory[1], Fathi A.al ssahly[2]

[1] Department of Mechanical and Industrial Engineering, College of Engineering, Elmergib University, Libya

[2] Department of Marine Mechanical, College of Marine Resources Alasmarya Islamic University, Libya

DOI: https://doi.org/10.21467/proceedings.4.7

* Corresponding author email: khalidattia1981@gmail.com

ABSTRACT

It has been observed that there is a considerable interest in recent years regarding materials which have high crushing ability particularly in energy absorption in relation to car and allied industries . An important aspect of the crushing ability of materials is its specific energy absorption value which is much greater for polymer composite than conventional metallic material. In this research, series experiments were conducted including testing of the capabilities of composite material as an energy absorber with comparison to metallic materials. The method used in the current research is to fabricate and test a series of composite plate specimens with different corrugation profile, these are: sinusoidal, triangle and square. All these specimens were fabricated from glass fibers with hand layup technique. Each profile has three different types of specimens: single plate, double plates and triple plates. The corrugated plates are fixed over each other and subjected to the same kind of compression load. All these models have been exposed to lateral crushing load and then the collapse of these models have been observed and the results have been recorded. Finally; all the results obtained in this research were recorded and discussed. It is found that the highest value of specific energy absorption was (2.472Kj/Kg) recorded for level three square profile specimen. However, the lowest value (0.878Kj/Kg) was recorded for level two triangle profile specimen.

Keywords: Knitted Fabrics, Energy Absorption, Crashworthiness, Axial Crushing

1. Introduction

The performance of composite materials that have incurred damage has long been a topic of great interest and study. Today the use of composite materials in different kinds of applications is accelerating rapidly. Composite materials have become common engineering materials and are designed and manufactured for various application including automotive components, sporting goods, aerospace parts, consumer, and in the marine and oil industries [1].

The crashworthiness performance of automobile components to perform remarkably under crash conditions is very important to vehicle occupants. As stated by Reid [2] design of crashworthy structure requires both knowledge of structural geometry and understanding of the properties and deformation mechanism of the materials and components used. Work on

crushing behaviour of metal shell has advanced and well understood. Research groups have, since 1960s, carried out research, toward crashworthiness of metallic devices using empty thin-walled tube with different cross-sections[3–5]. The previous works on the axial crushing of fiber reinforced plastic composite tubes has indicated that significant specific energy absorption can be obtained from these materials, under some circumstances exceeding the ones that can be obtained from metal tubes [6-7].

In recent years there is an increasing demand in the use of composite materials for the automotive and aerospace industry. Composite material and in particular their anisotropy offers vast potential for optimally tailoring a design to meet crashworthiness performance requirements. Therefore, intensive research has been carried out to examine the failure mechanism of no hybrid and hybrid composite structure [8–13]. Looking back implementation of composite materials in the field of crashworthiness is attributed to Hull, who in 1980s and 1990s has studied extensively the crushing behaviour of fiber reinforced composite material. He found that the composite materials absorb high energy in the face of the fracture surface energy mechanism rather than plastic deformation as observed for metals[14,15]. Composite materials are playing a key role in the development of lightweight integral armor for military vehicles such as tanks or armoured personnel carriers. For future applications, revolutionary approaches are required to significantly reduce (up to 50%) the mass of these systems and improve their mobility and trans- portability without sacrificing survivability or main-trainability[16].

This paper experimentally investigating the effect of Corrugation geometry and shape on energy absorption of composite plates. Three different corrugation profile are tested which are sinusoidal, triangle and square. subjected to quasi-static compression load. All kind has three types of specimens referred to as level one, level two and level three. These tested models have been fabricated and tested under the same conditions.

2-Profiles Manufacturing

The corrugated profile are manufactured using metallic dies, Specifically iron. Hand lay-up process was used to fabricate all composite specimens. The material used for fabricating composite specimens are woven roving glass fiber and epoxy. The specification of the material used are given in table (1) the specimens were fabricated by placing the woven roving fiber glass in fabrication model as layers on each other . The woven roving fiber is passed through a resin bath, causing resin impregnation. The fabricated specimens were cured at room temperature for 24 hours to provide good hardness and shrinkage. Then the cured specimens were extracted from fabrication model to prepare them for the crushing test. Figure(1)-a shows

the three metallic dies used for the fabrication of corrugated composite specimens using hand layup process and Some of tested specimens are show in figure(1) b, c, and d.

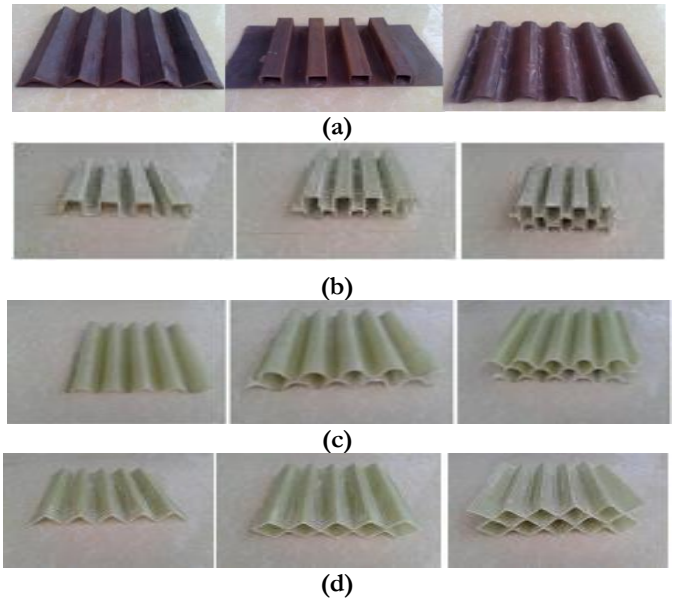

Figure 1.(a) different metallic dies used for specimens fabrication (b) square specimens (c) sinusoidal specimens and (d) triangular specimens

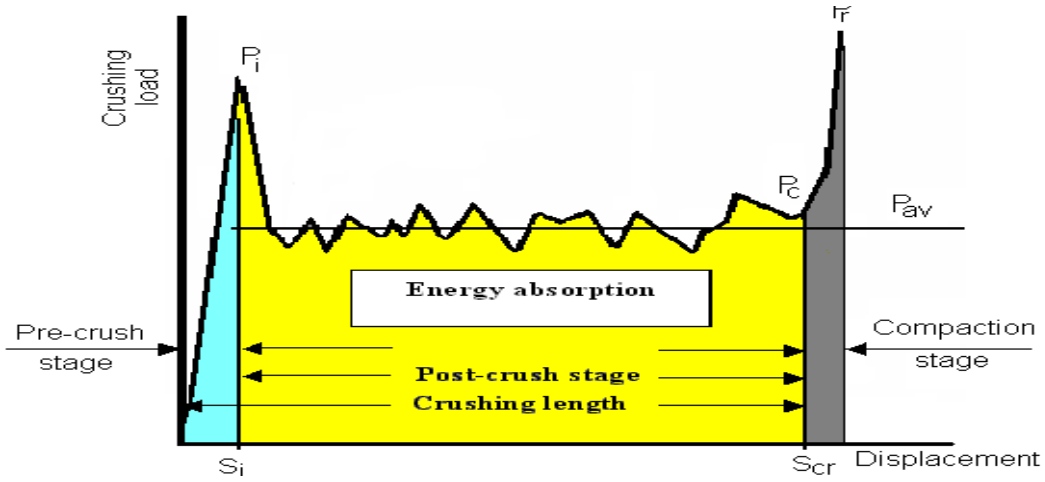

Figure 2: Schematic representation of a typical load-displacement curve of a corrugated composite with its main parameters

Table 1: Types of used constituents

2.1.1 Epoxy resin		UK Epoxy Resins UKH 137 Epoxy
Hardener		UK Epoxy Resins UKH 136 Hardener
Woven roving E-glass fiber		Synthetic fiber: 500g/m²
No. of layers of each specimens		Four layers

ISBN: 978-81-936820-6-7
Proceedings DOI: 10.21467/proceedings.4

Series: AIJR Proceedings

3-Test Procedure

The specimens were tested in quasi-static axial compression between two flat plates. ASTMD1621 standards, with full-scale load range of 4000kN was used. Three replicate tests were conducted for each type of models. All models were compressed at a rate of 2.5mm/min until limited crush, which implies complete compaction of tested specimen and load records increases sharply is reached. Load and displacement were recorded by automatic data acquisition system.

4-Results and Discussion

The tested specimens collapsed following the failure mode described by Hull[15]. As illustrated in figure (2). The load-displacement curve can be divided into three distinct regions. In region I the load P increases rapidly and reaches a maximum P_{max} before dropping. In region II the load oscillates about an average $\bar{P}$ and a series of folds form successively in the corrugated plate so that a folded zone grows progressively. For the last stage (region III), the load increases rapidly representing the end of the test. The detailed discussion of the results are presented in the proceeding section ,that involves crush stages and load displacement curve of composite specimens.

In this study, 27 specimens were made and tested under the same conditions. These types of specimens are divided to three levels. Level one has single corrugated plate, level two has two plates, and level three has three corrugated plates. Each level has three different profiles: Sinusoidal, triangular, and square profiles. The specimens that recorded the highest value and the lowest value of the specific energy absorption will be explained.

4.1-Three corrugated composite plate with square profile:

Typical load displacement curve for square under quasi-static compression load are shown in figure (3a). As it can be seen curve, the load increases gradually with the increase in the displacement up to initial failure where maximum load achieved 41KN at a displacement of 20 mm. Subsequently load drops down to 22KN at a displacement of 25mm. As compression load increases, it was observed that lateral split was formed (see figure 3b), and propagate causing fall down of load displacement curve. This case of crushing progress continues until the end of the test, where the specimen was completely crushed.

4.2-Two corrugated composite plate with triangular profile:

In general two triangular specimen crushed in the same manner as composed specimen except that no fracture occurred for two triangular specimen. As shown in Figure (4a) , the crushing load increases until the compression is about 14mm when full resistance is developed with 52KN load. Immediately after this stage start (plastic deformation) the load slow down until the compression is about 21mm when full resistance is developed with 16KN,after that increase resistance

the loading until compression 58KN at 25mm after that droop slow until the compression 20KN. Consequently load increases during this crushing stage followed by slight fluctuation the dramatic increase at the end of crushing test (see figure (4b).

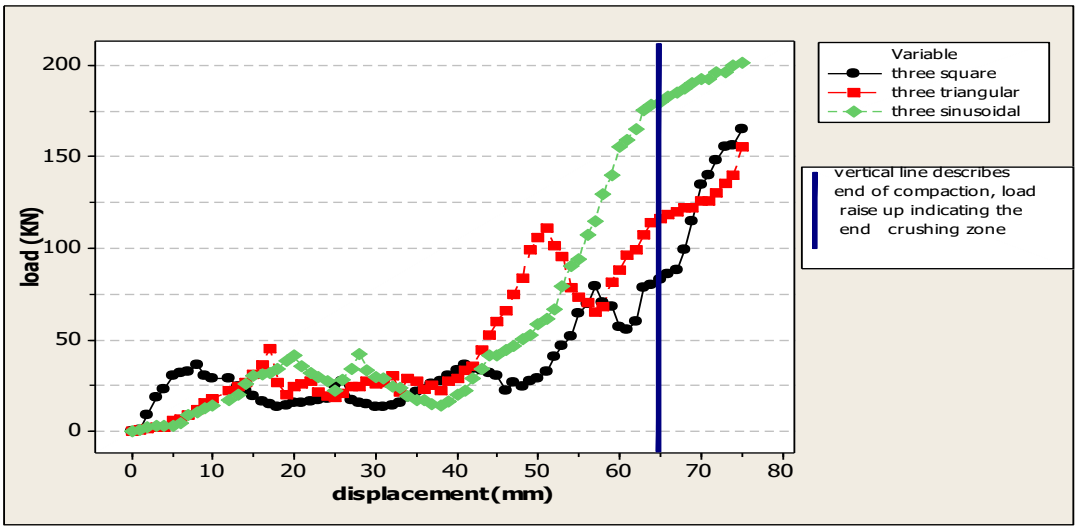

(a)

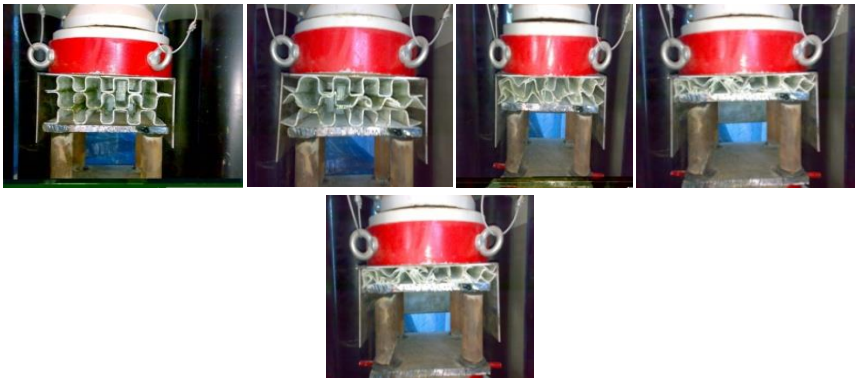

(b)

Figure 3. (a) load-displacement curve of level three of composite specimens, (b) deformation history of three level plate with square profile

ISBN: 978-81-936820-6-7
Proceedings DOI: 10.21467/proceedings.4

Series: AIJR Proceedings

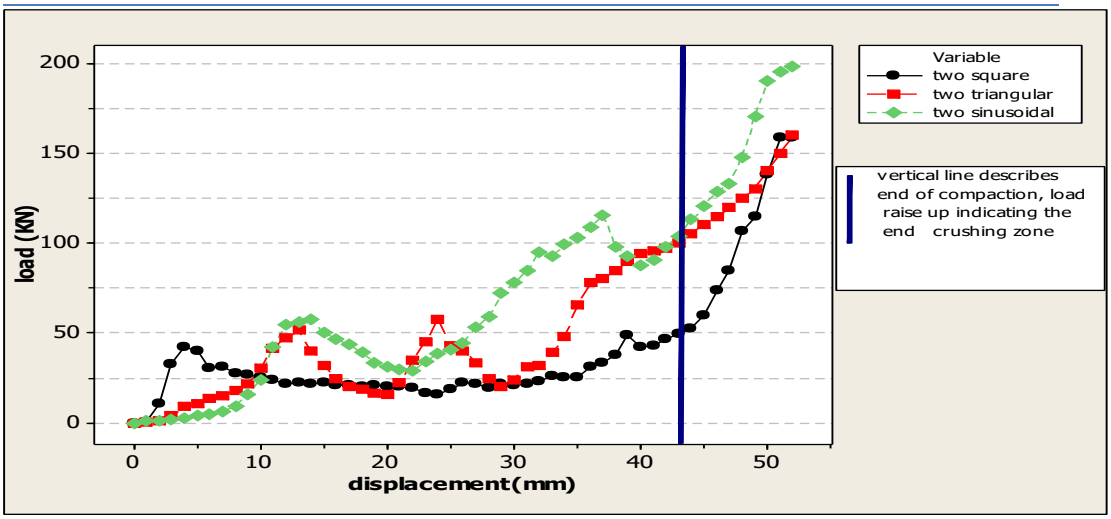

(a)

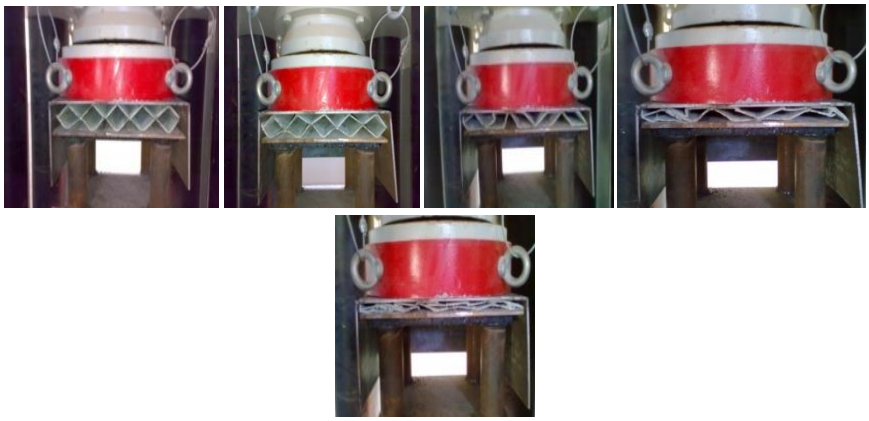

(b)

Figure 4. (a) load-displacement curve of level two of composite specimens, (b) deformation history of two level plate with triangular profile

5.Crushin Energy Absorption

The energy absorption capability can be estimated by knowing different parameter. These parameters are illustrated in the following section.

5.1 Total Energy Absorption (E): The total energy absorbed or the total work done, Wt, in crushing of composite specimens is the area under the load-displacement curve. It can be obtained by numerical integration of the load displacement curve.

$$Wt = \int_{Si}^{Scr} P_{av}\, dS = P_{av}(S_{cr} - S_i) \quad (1)$$

where, as they are indicated in figure 3, Si and Scr are the initial and final useful crush stroke and P_{av} is the mean crush load which obtained by averaging the applied loads during post

crush stage. The load-deformation characteristic is a measure of the energy absorption capacity. It differs from one structure to another, and it depends on the mechanism of deformation involved and the material used.

5.2 Specific Energy Absorption (Esp): To compare different materials or different geometry of specimens, it is necessary to consider the specific energy. The specific energy is defined as the amount of energy absorbed per unit mass crushed material (m). Therefore, the specific energy (Esp) that is dependent on the structure material was used for comparing the energy absorption of all specimen kinds. Specific energy absorption (Esp) can be calculated as;

$$Esp = \frac{W_t}{m} \quad (2)$$

After all the lateral cracking tests are completed, the results obtained from these tests can be seen in Table 2, and represented by the curve in Figure (5). Looking carefully to the results obtained with a specific absorption from the third-level samples, the square sample still has the highest values of initial failure load of (2,472 kj/kg). From the table, it can be seen that the triangular samples recorded the lowest value of (0.878kj/kg).

Table 2: Crashworthiness parameters of lateral tests for all specimens

The level	Sp-type	(KN)P_{max}	(KN)$\overline{P}$	(Kj)E_t	W (Kg)	(KJ/KN)E_{SP}	CFE* %	SE** %
One level	sinusoidal	113	65.66	0.525	0.470	1.117	58.1	90
	triangular	89	51.79	0.725	0.400	1.812	58.19	80
	square	68	40.62	0.649	0.370	1.754	58.69	66
Two level	sinusoidal	115.6	59.62	1.304	0.940	1.387	90	73
	triangular	58	31.95	0.703	0.800	0.878	61	60
	square	49	36.23	1.304	0.740	1.762	91	73
Three level	sinusoidal	48	44.67	1.608	1.410	1.140	86	62
	triangular	111	42.49	1.827	1.200	1.522	87	66
	square	79	44.26	2.744	1.110	2.472	95	75

(CFE*) Crush Force Efficiency (SE**) Stroke Efficiency

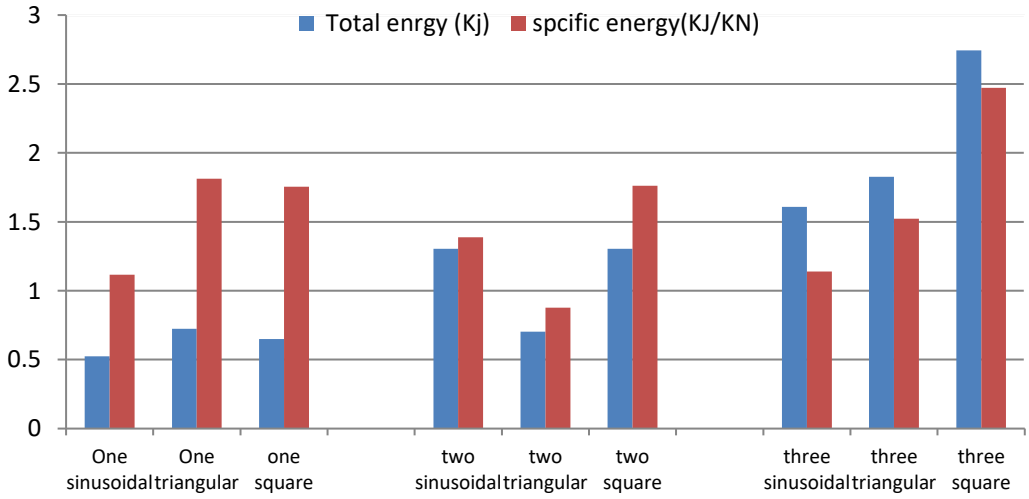

Figure 5. Total energy and specific energy of all specimens

ISBN: 978-81-936820-6-7
Proceedings DOI: 10.21467/proceedings.4

6-Conclusion

A series of composite plates with different corrugation profile (sinusoidal, square, and triangular) has been subjected to quasi-static compression load. The difference of the specimens' shape offer a compare between them in terms of the effect of the corrugation profile in energy absorption capability. Based on the results obtained, it can be noted that, the specimen geometry has a considerable affect on energy absorption capability and load carrying capacity; it has been observed that the change in corrugation profile has important affect on energy absorption capability, where the specimens of square profile recorded the highest values of energy absorption capability comparing to specimens with sinusoidal and triangular profile; the specific energy absorption and load carrying capacity increased with the increase of the number of corrugated plates and the relationship between the two factors is directly proportional; the highest value of specific energy absorption of group A specimens has been recorded by the level three square specimens to be (2.472KJ/Kg). However, triangular specimens come second with (1.812KJ/Kg), and specimens of two triangular recorded the lowest value of (0.878 KJ/Kg).

Reference.

[1] Elfetori F. Abdewi, S. Suliman, A.M.S. Hamouda, E.Mahdi. (2006), Effect of Geometry on the Crushing Behaviour of laminated corrugated Composite Tubes.journal of Materials Processing Technology 172 394-399.

[2] Reid SR. Plastic deformation mechanism in axially compressed metal tubes used as impact energy absorbers. Int J Mech Sci 1993;35:1035–52.

[3] Reddy TY, Al-Hassani STS. Axial crushing of wood filled square metal tubes. Int J Mech Sci 1993;35:231–46.

[4] Wu L, Carney JF. Experimental analysis of collapse behaviour of braced elliptical tubes under lateral compression. Int J Mech Sci1998;40(8):761–77

[5] Beardmore P, Johnson CF. Compos Sci Technol 1986;26:251–81.

[6] Hamada H, Coppola JC, Hull D, Maekawa Z, Sato H.Composites1992;23:245–52.

[7] Mamalis AG, Manolakos DE, Viegelahn GL. J ComposMater1990;25:72–90.

[8] Farely GL. Energy absorption of composite materials. J Compos Mater 1986;20:322–34.

[9] Mamalis GD, Manolakos E, Demosthenous GA, Ioannidis MB. Analytical modelling of the static and dynamic axial collapse of thin-walled fibreglass composite conical shells. Int J Impact Eng1997;19(5–6):477–92.

[10] Ramakrishna S, Hamada H. Energy absorption characteristics o crash worthy structural composite materials. Key Eng Mater1998;(141–143):585–620.

[11] Mahdi E, Sahari BB, Hamouda AMS, Khalid YA. An experimental investigation into crushing behaviour of filament wound laminated cone–cone intersection composite shell. Compos Struct2001;51(3):211–9

[12] Mahdi E, Sahari BB, Hamouda AMS, Khalid YA. Crushing behaviour of cone–cylinder–cone composite system. Mech Compos Mater Struct 2002;9(2):99–117

[13] Drzal LT. Composite property dependence on thefiber, matrix and interphase. In: Tough composite materials, Noyes; Park Ridge, 1985. p. 207±22.

[14] Hull D. Energy absorption of composite materials under crash conditions. In: Progress in Science and Engineering of Composites, Proceedings of the 4th International Conference on Composite Materials (ICCM/4), Tokyo, 25–28 October 1982. p. 861–70.

[15] Hull D. A unified approach to progressive crushing of fibre reinforced composite tubes. Compos Sci Technol 1993;35(3/4):231–46.

[16] Williams JG, James MR, Morris WL. Formation of the inter- phase in organic-matrix composites. Composites 1994;25:757±62.

Mapping of Sea Water Intrusion in the Western Libyan Coast Using Geo-electrical Method: Case Study

Abdel Hameed M. Salem[1*], Magdi A. Mountasir [2] , Husam Abdussalam R. Shames [3]

[1,3] Prospecting department, The Libyan Atomic Energy Establishment, Tripoli, Libya

[2] Scientific and technical matters department, Higher Institute for Sciences and Technology, Algaraboulli, Libya

DOI: https://doi.org/10.21467/proceedings.4.8

* Corresponding author email: Hameed.ehtman@gmail.com

ABSTRACT

As most of the Libyan population live in the north side of the country; mainly in the western coastal zone; the sea water intrusion is a vital phenomena that need to be studied to locate, measure its diffusion rate, and take a remediation actions [1]. Conventionally, water sampling of ground water wells is used to evaluate sea water intrusion in coastal areas [2]. Nevertheless, excessive use and cost of drilling should be avoided by relaying on advanced technologies [2]. Geo-electrical methods such as electrical resistivity and electromagnetic can be used for studying sub surface geophysics from the earth surface with no need for drilling, and can give a trusted results [3]. The huge contrast in resistivity between saline and fresh water makes measurement of the resistivity in the ground a useful technique for detecting and delineate the saline interface, consequently, using the electrical resistivity method is a successful technology for studying sea water intrusion [3]. Mapping sea water intrusion in a selected area located in the western coast of Libya is reported by this study, it covers about 120 Km² from Algrabouli to Elallus by 16 profiles perpendicular to shoreline with total number of 53 vertical electric sounding (VES). This study is considered as a case study to insure the need to cover the whole Libyan coast with more detailed studies, furthermore, it concluded that the sea water intrusion in Libya is truly a serious issue that will lead to pollute the groundwater in the coastal areas with salt and costal contaminated water in the case of not correcting the situation.

Keywords: Seawater intrusion in the western Libyan coast; Geo-electrical method to study sea water intrusion; Case study of sea water intrusion by electrical resistivity method.

1 Introduction

The phenomenon of sea water Intrusion occurs in coastal areas where the different densities of both the saltwater and freshwater allow the seawater to intrude into the freshwater aquifer. Equally important to the salinization of fresh water, the intruded seawater may be contaminated with sewage water [2].

For countries like Libya, that have coasts and their main resource of freshwater is the groundwater, a high potential of seawater intrusion exist in the coastal areas threatening the freshwater aquifer with salinization and contamination [1].

Before the improvements of geophysical methods to be used for geo-environmental investigations, water sampling was the only way to locate seawater intrusion. The need for a sufficient geo-environmental investigation techniques was high for areas where no wells exist. Drilling new wells to study seawater intrusion was not always applicable, economic and friendly to the environment [3]. Today, many geophysical methods such as geo-electrical are used to investigate seawater intrusion. These techniques deals with the electrical condition of earth and it investigate electrical properties of rocks and minerals under different geological circumstances.

Many studies world wide used electrical resistivity method for mapping the seawater intrusion for coastal areas [4], some of these studies in Europe are: Oteri [5] has delineated saline water intrusion in England since 1983. Antonio Satriani et al [6] have studied on Characterization of the Coastal Saltwater Intrusion in Metapontum Reserve Forest in Southern Italy. Soldal et al [7] have done Seawater in western Norway. Nowroozi et al [8] have carried out a study on saltwater intrusion into the freshwater aquifer in the eastern shore of Virginia (USA) by electrical resistivity survey using Schlumberger configuration. Abdul Nassir et al [9] have delineated and mapped the intrusion boundary between fresh water and saline water in northwest of Malaysia by geoelectrical imaging surveys. Shaaban F.F[10] has employed Vertical electrical soundings (VES) in a coastal area of north western Egypt. Sheriff et al [11] have carried out Geoelectrical studies for delineating seawater intrusion in UAE. Abdulaziz M. et al [12] have conducted seawater intrusion in southwest of Saudi Arabia. This study aims to map the seawater intrusion in around 120 Km² area between Algarboulli and Elallus at the western Libyan coast.

2 Study Methodology

2.1 The Scientific Theory

There are a high distinguish between saline and fresh water in resistivity, this difference made the measurement of the resistivity for the ground water a useful technique for detecting and delineating the saline interface. Knowing the formation resistivity will directly lead to appoint the total dissolved salt of ground water. The relation between formation resistivity and groundwater quality is demonstrated in Table 1. [2].

2.2 Data Acquisition

One of most used geophysical techniques for studying formation resistivity is the electrical resistivity method [2]. The main frequent used types of measurement are Vertical Electric Sounding (VES) and resistivity profiling [3]. A proper number of VES should be carried out in the survey area along on profiles perpendicular to shoreline. In this study, schlumberger

configuration has been adapted with maximum current electrode spacing of 400 m as illustrated in Figure 1. In this technique the electrical current by two electrodes AB is stepwise made to flow through deeper and deeper parts of the ground, otherwise the distances between the potential electrodes MN almost fixed. To measure apparent resistivity to subsurface layers, a resistivity meter (Saris) is used with equation (1).

$$\rho_a = \frac{\pi(s^2 - a^2/4)}{a}\frac{\Delta V}{i} \quad (1)$$

Where: ρ*a* = apparent resistivity, ohm-m; *a* = MN distance, m; s = AB distance, m; v = Voltage, volt; *i* = current, amp.

Table 1: *Relation between formation resistivity and groundwater quality*

Ground water quality group	Total Dissolved Salt TDS (mg /L)	Formation resistivity ρ (ohm meter)
Very fresh (VF)	< 200	>200
Fresh (F)	200 - 400	200 – 100
Moderately Fresh (MF)	400 - 800	100 -50
Weakly Fresh (WF)	800 - 1600	50 – 25
Moderately Brackish (MB)	1600 -3200	25 – 12.5
Brackish (B)	3200- 6400	12.5 – 6.25
Very Brackish (VB)	6400 -12800	6.25 – 3.12
Moderately salt (MS)	12800 - 25600	3.12 – 1.56
Salt (S)	> 25600	1.56<

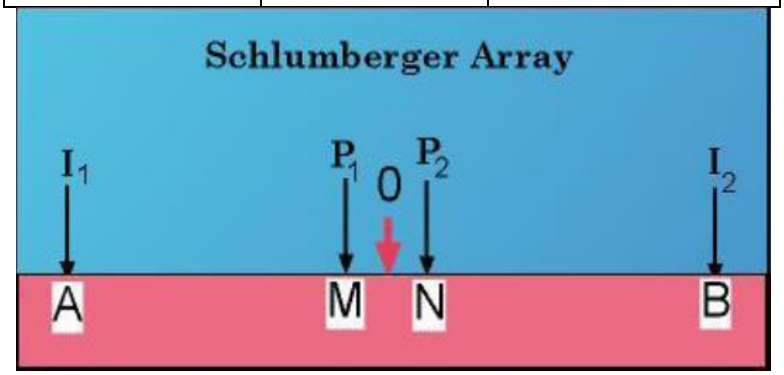

Figure 1: *Schlumberger array.*

ISBN: 978-81-936820-6-7
Proceedings DOI: 10.21467/proceedings.4

2.3 Data Processing and Interpretation

The VES curves were analyzed using the available software program (IpI2Win+ip) to generate pseudo cross sections, these sections shows distribution of resistivity with the depth. A resistivity values of less than 10 Ohm meter appears as dark blue and black color in the figures which means, depending on "Tab. 1", they were affected by sea water intrusion into ground water aquifer.

Iso- apparent resistivity maps were plotted by the help of the software (Oasis Montaj). These maps indicate distribution of apparent resistivity in the area against distance of current electrodes (AB) at a fixed depth. The depth was practically almost between (AB/3, AB/4).

3 The Case Study

3.1 Location of the Study Area

The study area is located approximately 60 km East of Tripoli. The site covers an area of about 120 km². It is bounded on the north by the Mediterranean Sea, and situated between Algarboulli and Elallus Figure 2. It lies between latitudes (32°46'57.10"N, 32°43'38.99"N), and longitudes (13°41'32.70"E, 14° 0'20.17"E).

Figure 2: Location of the study area.

3.2 Distribution of the Vertical Electrical Soundings and Profiles on the Study Area

The survey was accomplished with Fifty three VES configuration with a maximum current electrode spacing (AB) of four hundred meters. A sixteen pseudo cross sections perpendicular to the shore line were selected as illustrated in Figure 3.

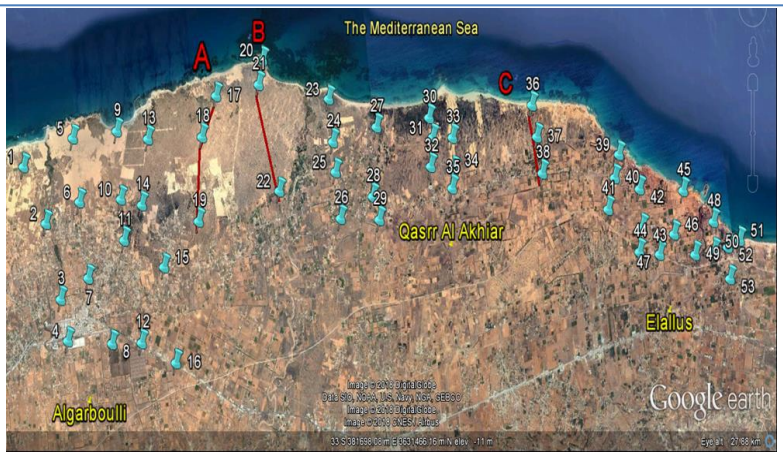

Figure 3: Distribution of the VES's and profiles on the study area.

4 Results and Discussions

4.1 Results Gained by (Ip I2wint +Ip) Software

As mentioned before, all sixteen pseudo cross sections have been processed using (Ip I2wint +Ip) software to show the distribution of resistivity with depth. Only three pseudo cross sections (referred to as A, B and C in Figure 3) have been selected as examples for these results in this paper. For cross section A Figure 4, the resistivity values ranged between (18 – 60 Ohm meter) at almost 75 meter depth which means there is no present of seawater intrusion according to Table 1. For resistivity obtained in Profile B, the lowest values ranged between (10 - 16 Ohm meter) at VESs (21, 22) to clearly indicate it was slightly effect by Sea water intrusion Figure 5. In cross section C, The lowest resistivity was located at VES 36 with (0-10 Ohm meter) value to declare the area as a highly effected by seawater intrusion Figure 6.

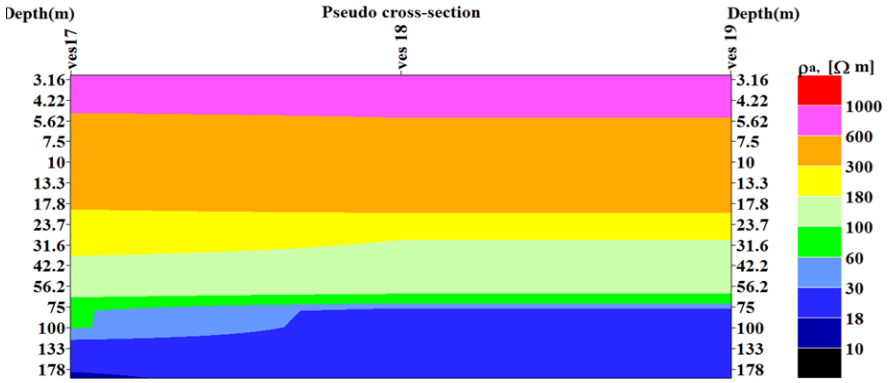

Figure 4: Profile A (VES's: 17, 18, 19).

ISBN: 978-81-936820-6-7
Proceedings DOI: 10.21467/proceedings.4

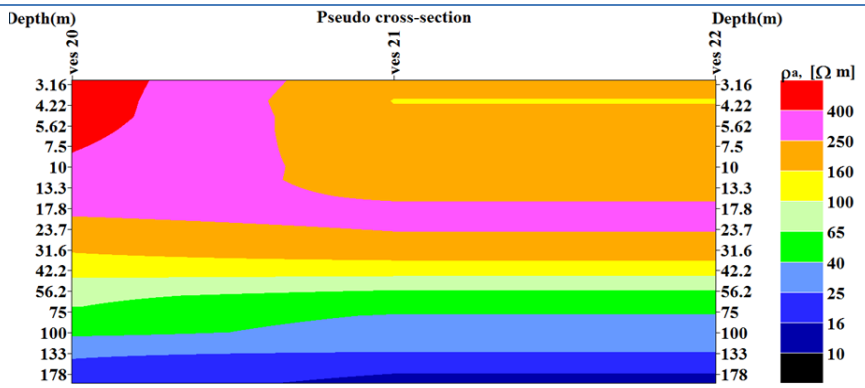

Figure 5: Profile B (VES's: 20, 21, 22)

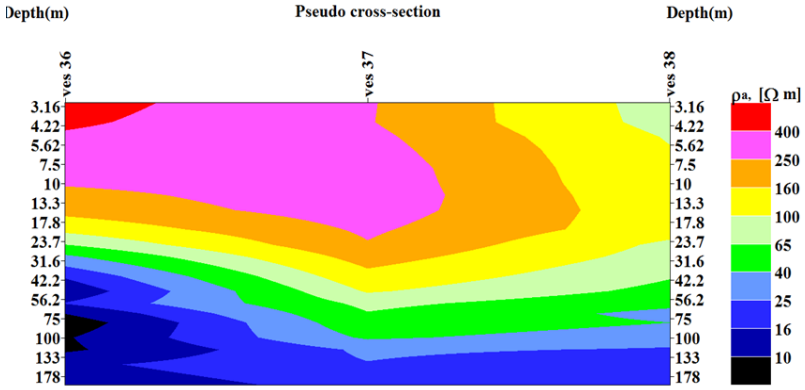

Figure 6: Profile C (VES's: 36, 37, 38)

4.2 Results Gained by Oasis Montaj Software

Three Iso-apparent resistivity maps have been generated to reflect lateral variation of apparent resistivity at a certain depth using the Universal Transverse Mercator (UTM) coordinate system, these maps indicate distribution of apparent resistivity in the area against distance of current electrodes (AB). The used AB values were: 200, 300 and 400 meters. In all three maps, the lowest resistivity values of less than (10 Ohm meter) were gained in certain VES's to specify the presence of seawater intrusion.

The iso-apparent resistivity map for AB = 200 meter at about (50 to 70 meters depth) are shown in Figure 7. , the lowest resistivity values were obtained at VESs (6, 7, 11, 30, 36, 51, 52).

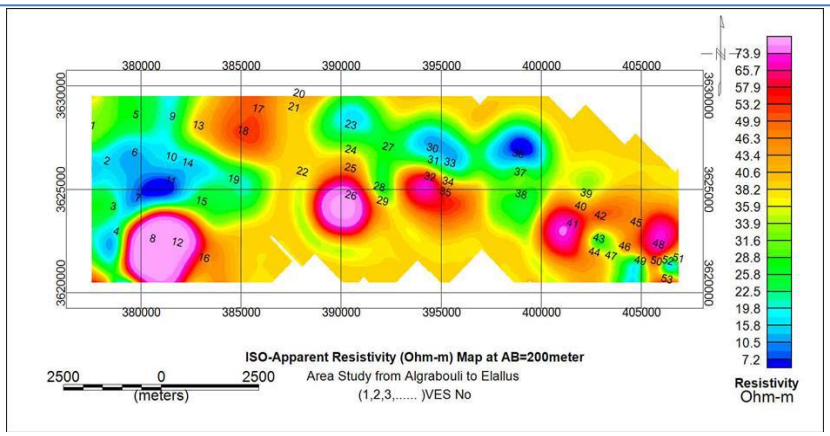

Figure 7: Iso-apparent resistivity map for AB = 200 m.

Figure 8 illustrated the iso-apparent resistivity map for AB = 300 meter at an approximate depth of (75 to 100) meters. the lowest resistivity values presented at VES's (3, 5, 6, 7, 10, 11, 14, 23, 24, 30, 31, 33, 36).

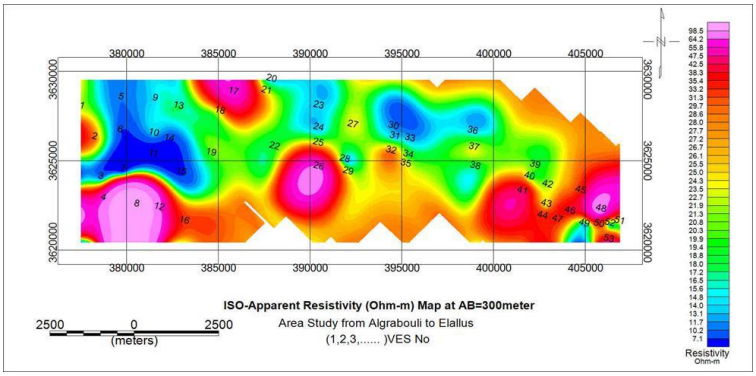

Figure 8: Iso-apparent resistivity map for AB = 300 m.

The map in Figure 9 shows iso-apparent resistivity for AB = 400 meter with almost (100 to 130) meters depth. the lowest resistivity values were considered at VES's (2, 7, 8, 11, 14, 23, 25, 27, 28, 30, 33, 34, 36, 51, 52).

ISBN: 978-81-936820-6-7
Proceedings DOI: 10.21467/proceedings.4

Series: AIJR Proceedings

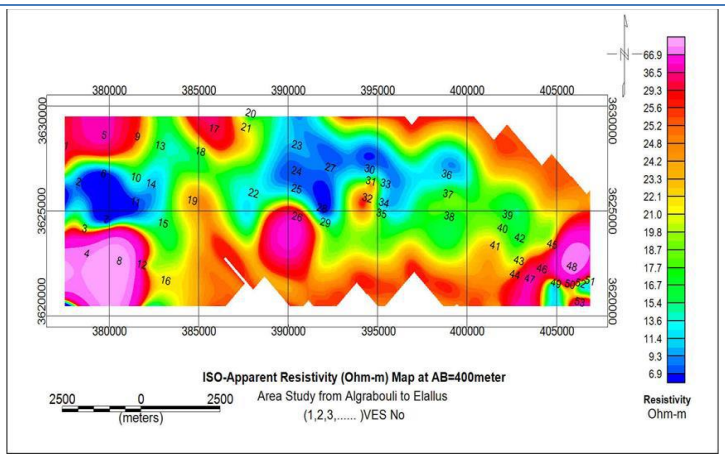

Figure 9: Iso-apparent resistivity map for AB = 400 m.

4.3 Mapping Seawater Intrusion in Western Libyan Coast

The interface between salt and fresh water is identified in the study area approximately as a red line in Figure 10. This map is evidently demonstrate and prove the occurrence of seawater intrusion in the area.

Figure 10: Mapping seawater intrusion in Western Libyan Coast.

5 Controlling and Minimizing Seawater Intrusion

Methods for controlling intrusion vary widely depending on the source of the saline water, the extent of intrusion, local geology, water use and economic factors. There are several methods for controlling seawater intrusion demonstrated with its advantages and disadvantages as follows: [13]

1- Reduction of pumping rates: needs public awareness with recycling and reuse of water. Advantages: reduction of abstraction rate. Disadvantages: private stockholders, temporary solution.

2- Relocation of pumping wells: movement of wells in more inland position. Advantages: decrease the occurrence of upconing of salt water. Disadvantages: costly, temporary solution, obstruction in relocation

3- Use of Sub surface Barriers: Reduce the permeability of aquifer; Sheet piling, Cement grout, or Chemical grout. Advantages: Reduce the intrusion of saline water. Disadvantages: Not efficient for deep aquifers, and costly.

4- Natural Recharge: Constructing dams and weirs to prevent the runoff from flowing to the sea. Advantages: Prevent the runoff to flow directly to the sea. Disadvantages: Depends on the soil properties , Take Long time, Unsuitable for confined and deep aquifers.

5- Artificial Recharge: Increase the ground water levels, using surface spread for unconfined aquifers and recharge wells for confined aquifers. Advantages: Increase the groundwater storage. Disadvantages: Ineffective in the areas where excessive ground water pumping occurs, Occupies a large area.

6- Abstraction of Saline Water: Reduce the volume of saltwater by extracting brackish water from the aquifer and returning to the sea. Advantages: Decreases the volume of saline water, Protects pumping wells from upconing. Disadvantages: private stockholders, temporary solution.

The best methodology to reduce the seawater intrusion in coastal aquifers is: Abstraction, Desalination and Recharge (ADR) [14]. This methodology aims to overcome all or at least most of the limitations of the previous methods. ADR consists of three steps; abstraction of brackish water from the saline zone, desalination of the abstracted brackish water using reverse osmosis (RO) treatment process and recharge of the treated water into the aquifer as shown in Figure 11. The reason of ranking this method as the best to control seawater intrusion is its unique ability to produce freshwater by using the saline groundwater which will directly lead to push the intrusion line back to the sea. The main disadvantage of this technique is the bad environmental effect resulted by using traditional energy sources.

ISBN: 978-81-936820-6-7

Series: AIJR Proceedings
Proceedings DOI: 10.21467/proceedings.4

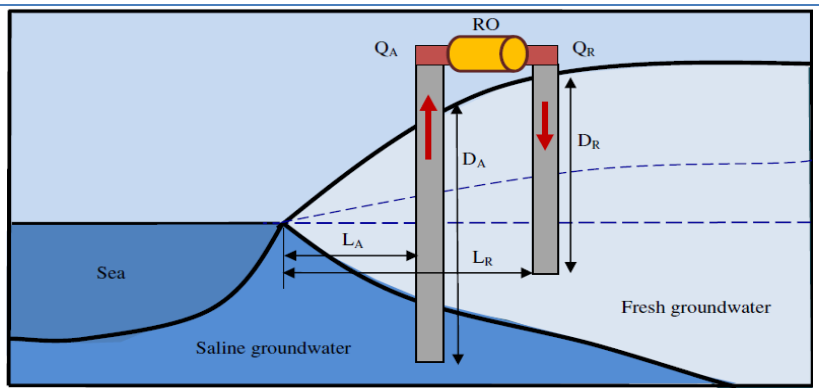

Figure 11: Diagram of the ADR Methodology.

6 Conclusion and Recommendations

- This paper was accomplished with Fifty three VES configuration with a maximum current electrode spacing (AB) of four hundred meters and sixteen pseudo cross sections perpendicular to the shore line were selected. The study evidently indicated the existence of seawater intrusion in the study area that covers about 120 Km^2 between Algrabouli and Elallus, moreover, highly express the need to map the whole country to precisely locate this phenomena.

- Establishing a national project to map ground water contamination for the whole shore line in Libya by using the electrical resistivity method to investigate the seawater intrusion.

- Using Abstraction, Desalination and Recharge (ADR methodology) to solve the problem of seawater intrusion in Libya depending on the national map for coastal ground water contamination.

- Using clean energy in desalination plants used for ADR methodology.

- Nuclear energy should be considered as one of the best choices when selecting the most proper energy technology for ADR and seawater desalination in Libya.

7 Acknowledgment

The authors would like to thank The Libyan Atomic Energy Establishment for her support and permission of using the Resistivity Meter (Saris) in this paper, moreover, deep thanks also extend to Fouzie Mohamed and Osama Osman at Geophysics Department, Science Faculty, Tripoli University for their contribution in obtaining the field data.

References

[1] O. Salem, "water resources management in Libya," April 2007 [workshop on Integrated Water Resources Management (IWRM) in Libya. Tripoli, Libya].

[2] Araguas, "Groundwater saline intrusion," Ed Madrid Instituto Geologic, Spain, First Edition, 2005.

[3] A. Telford, "Applied Geophysics," Cambridge university press, Great Britain, First Edition, 1990.

[4] J. Jansen, "Geophysical methods to map brackish and saline water in aquifers," April 2011 [Water Resources Conf. University of Georgia, USA].

[5] A. Oteri, "Delineation of saline intrusion in the Dungeness shingle aquifer using surface geophysics," 1983 [Quart. J. Engg. Geol]. Volume 16, pp. 43-5.

[6] A. Satriani, A. loperte, V. Imbrenda, and V. Lapenna, "Geoelectrical Surveys for Characterization of the Coastal Saltwater Intrusion in Metapontum Forest Reserve (Southern Italy)," 2012 [International Journal of Geophysics]. pp. 43-5.

[7] S. Oddmund, M. Eirik, H. Eirik, and R. Noralf, "Seawater Intrusion and Fresh Groundwater Hydraulics in Fjord Delta Aquifers Inferred from Ground Penetrating Radar and Resistivity Profiles -Sunndalsora and Esebotn, Western Norway" 1994 [Journal of Applied Geophysics]. Volume 32, pp.305-319.

[8] A. Nowroozi, S. Horrocks, and Henderson, "Saltwater intrusion into the freshwater aquifer in the eastern shore of Virginia: a reconnaissance electrical resistivity survey" 1999 [Journal of Applied Geophysics]. Volume 42, pp.1-22.

[9] S. Abdul Nassir, M. Loke, C, Lee and M, Nawawi, "Salt-water intrusion mapping by geoelectrical imaging surveys" 2000 [European Association of Geoscientists & Engineers, Geophysical prospecting]. Volume 48, pp. 647-661.

[10] F. Shaaban, "Vertical electrical soundings or groundwater investigation in northwestern Egypt: A case study in coastal area" 2001 [Journal of African Earth Sciences]. Volume 33, pp.673-686.

[11] A. Sherif, El. Mahmoudi, H. Garamoon, A. Kacimov, S. Akram, A. Ebraheemand, and A. Shetty, "Geoelectrical and hydrogeochemical studies for delineating seawater intrusion in the Outlet of Wadi Ham, UAE" 2006 [Environmental Geology]. Volume 49, pp.536-551.

[12] M. Abdulaziz, M. Al-Bassam, and T. Hussein, "Combined geo-electrical and hydro-chemical methods to detect salt-water intrusion: A case study from southwest Saudi Arabia" 2008 [Management of Environmental Quality: An International Journal]. Volume 19, pp.179-193.

[13] D. Todd, and L. Mays, "Groundwater Hydrology," Wiley, New York, USA,2005.

[14] F.Hany, H. Abd-Elhamid, and A. Javadi, "A Cost-Effective Method to Control Seawater Intrusion in Coastal Aquifers," J. of Water Resource Management, vol. 25, pp. 2755-2780, 2011.

ISBN: 978-81-936820-6-7

Series: AIJR Proceedings
Proceedings DOI: 10.21467/proceedings.4

Effects of Different Fluids Properties on Cavitation Performance in Centrifugal Pump

Saad Ghidhan [1*], Moamar Hamed[1] , Mansor Benaros[2]

[1] Mechanical and Industrial Engineering Department, College of Engineering, Elmergib University, Libya

[2] Mechanical and Industrial Engineering Department, Alasmarya University, Libya

DOI: https://doi.org/10.21467/proceedings.4.9

* Corresponding author email: saadgedan@yahoo.com

ABSTRACT

Cavitation, which is the formation and collapse of vaporous cavities in flowing liquids, can degrade the performance of pumps and other hydraulic equipment. The aims of the present research are to investigate the effect of different fluids properties on pump cavitation performance. Consideration is given to examine the effect of liquid viscosity and density on cavitation behavior. Experimental results are presented for a centrifugal pump operating in water, kerosene and diesel fuel with different disposal rates of flow. With references to the results, the water has affected by the cavitation at less Net Positive Suction Head (NPSH) than other liquids, also it can be conducted that the kerosene shares the closest cavitation behavior with diesel fuel. Therefore, the stress produced by cavitation bubbles decreases with increase of viscosity of the liquid.

Keywords: Water, kerosene, diesel fuel, cavitation performance, centrifugal pump, Net Positive Suction Head (NPSH)

1 Introduction

When a centrifugal pump handles liquids with different viscosity and specifications, there Net Positive Suction Head (NPSH) normally will be different. The simple definition of the NPSHA is the difference between pressure at the suction of the pump and the vapour pressure for the liquid being pumped [1]. An increase or decrease of NPSH will result in cavitation taking place in the pump. In result, the pump will be subject to abnormal operations, such as loud noise, violent vibration, performance degradation, impeller or other components damage. In fact, measuring or predicting NPSH of a centrifugal pump at various operating conditions is quite important for the hydraulic design optimization and engineering application when the pump handles different viscous liquids and it's important to know the situation of operating with this phenomena and how to avoid the problem of cavitation [2].

In almost of petroleum industries and chemical operations pumps will deal with liquids which have such different specifications, there are two sorts of liquid products, which need to be transported by centrifugal pumps. One kind of liquid is with a higher vapour pressure but with

nearly the same viscosity of water, and the other kind of liquid is with a lower vapour pressure but a higher viscosity than water [3].

Many researchers [4] [5] have discussed the inception of cavitation through the experiments and numerical simulations. The phenomena of cavitation are usually determined by the value of (NPSH). The physical properties of the liquid, its vapour and the flow conditions can affect the cavitation process and thus the cavitation performance of hydraulic equipment as well. The effects of the fluid properties, flow conditions, and heat transfer can improve cavitation performance for certain liquids and/or liquid temperatures, the net positive suction head (NPSH) requirements can be significantly less than that obtained for room-temperature water. As mentioned above NPSH is defined as the total pressure above vapour pressure at the inlet to a pump This improvement (decrease) in inlet pressure requirements is attributed to the varying degrees of evaporative cooling associated with the cavitation process. Because of the evaporative cooling, the cavity pressure and the vapour pressure of the liquid adjacent to the cavity are decreased relative to the vapour pressure of the bulk liquid. This decrease in cavity pressure retards the rate of further vapour formation, thereby allowing the pump to operate at lower values of NPSH than would otherwise be possible.

The NPSH requirement for a pump operating at a given head rise and flow condition is reduced by the amount corresponding to the decrease in cavity pressure. The accurate prediction of thermodynamic effects of cavitation is therefore essential to an optimum flow system that is designed to operate with cavitation.

2 Experimental Work

To determine the effect of fluid viscosity on the performance of centrifugal pumps and the phenomenon of cavitation which usually occur and negatively affect the performance of these pumps as explained previously. Laboratory experiments were carried out on a centrifugal pump using different liquids (water, kerosene and diesel fuel)

2.1 Test Rig Facilities

There are various ways to design the test rig to study the cavitation. The most important feature of any test-rig is the means of introducing cavitation into the pump system. In this research, the closed loop configuration was chosen for this testing as indicated in a schematic diagram shown in Figure 1. The flow system consists of 1 hp centrifugal pump using DC current motor, the flow orifice meter, pressure measuring devices, suction and delivery pipelines, speed control unit, and valves. Connecting pipes and control valves are assembled with (1 in) diameter plastic connections.

The suction line consists of a tube connected to a valve that controls the flow rate and a pressure gauge connection, at the end there is a nozzle valve.

The discharge line contains a valve that controls the flow rate and a connection pressure gauge and the orifice meter to measure the flow rate.

ISBN: 978-81-936820-6-7

Series: AIJR Proceedings
Proceedings DOI: 10.21467/proceedings.4

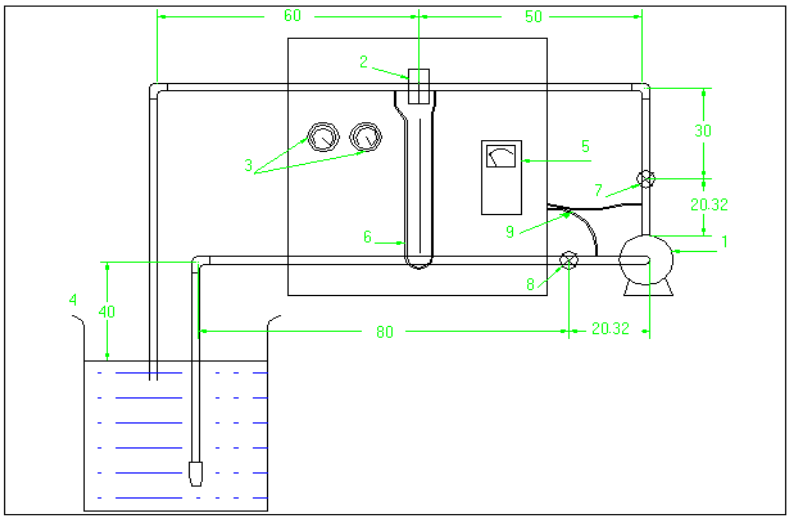

Figure 1: *Schematic diagram of test rig* [6].

Measuring devices are divided into, pressure gauge for the suction line and is used to measure the pressure of the water in the suction line from the type of tube Borden range from (0 to bar1) and the rate of (0.2 bar), the pressure gauge of the discharge line is also used to calculate the pressure of the water in the line using the Borden tube, measured from (0 to 6 bar). The other measuring devices are power measuring device; the capacity of the pump can be measured by a Watt meter where it is connected to the pump. This device is read from 0 to 1000 W and is rated at 2 W.

2.2 Test Procedures

The test procedure was conducted by assembling the system and connecting all the measuring devices, the driving pump is firstly operated with the water to carry out the pump performance test and cavitation test, and then the same steps of test had repeated with the kerosene and the diesel, each test has been carried out at different values of flow rate ratios.

The cavitation test on the pump has been carried out by keeping the pump running at the required speed, and flow rate ratio, and then reducing the inlet pressure step by step until the inception condition occurred. At each step, the flow rate was adjusted through the delivery valve, then the inlet pressure further reduced until developed cavitation and fall off head and efficiency was noticed. At each setting of inlet pressure and inception condition, the measurements of suction and discharge pressures and flow rate were recorded. The NPSH at each condition was calculated using the following equation: $NPSH = \left(\frac{P_{sg}}{\gamma} + \frac{V_s^2}{2g}\right) - \frac{P_v}{\gamma}$ also the head of the pump was calculated by the following equation: $= \left(\frac{P_d - P_s}{\gamma}\right) + 0.24$, efficiency of the pump was calculated by $\eta = \frac{\rho \, g \, Q \, H}{P}$ where ρ is density of the water, Q water flow rate, H head of the pump and P power [5].

3 Results and Discussion

In order to study the performance of the pump and also to examine the cavitation in the tested pump, three tests have been done, each test was conducted with different liquid, the first test the pump used the water and all the measurements have been taken with different flow rates, then the same procedures have been done for Kerosene and diesel.

3.1 Water Test

Firstly the performance of the pump was studied experimentally at different flow rates, the first test was conducted using the water, in this test the flow rate has been changed from 0.389 L/s to 1.4555 L/s, suction valve was totally opened and the level of the water in the tank was 40 cm from the centre of the pump.

Figure 2 presents the performance curves for the pump include power, head, efficiency and the NPSH. From Figure 2 it can be seen that the head of the pump starts decreasing with the increases of the flow rate, on the other hand the efficiency curve increase with increasing the flow rate until reached the maximum value of 26.1505 % then the efficiency start to drop, the NPSH was decreased with increasing of the flow rate and finally the power has risen with dropping the flow rate.

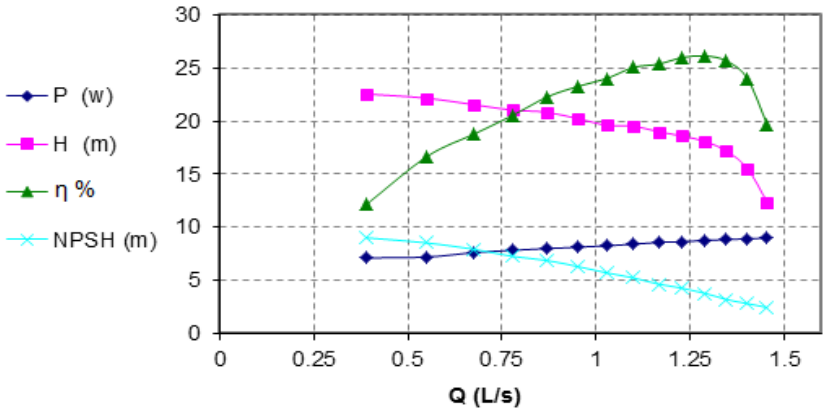

Figure 2: *The performance curves for the pump for water test*

Figure 3 shows the curves of NPSH at different flow rates. It can be noted that NPSH reach the collapse state, the point at which the lifting mark drops suddenly. It can be seen that, in the case of flow rate (Q = 0.30 L / s) the collapse occurs at the tenth point of the suction valve gradient when the net positive clouds (2.8693 m) and in the case of flow rate (Q = 0.60 L / s), the collapse occurs at the eighth point of the pull valve gradient when the net positive clouds (3.4282) m), as well as in the case of flow rate (Q = 0.90 L / s), these means the drops of the cavitation may occurs at different points with different flow rates.

ISBN: 978-81-936820-6-7
Proceedings DOI: 10.21467/proceedings.4

Series: AIJR Proceedings

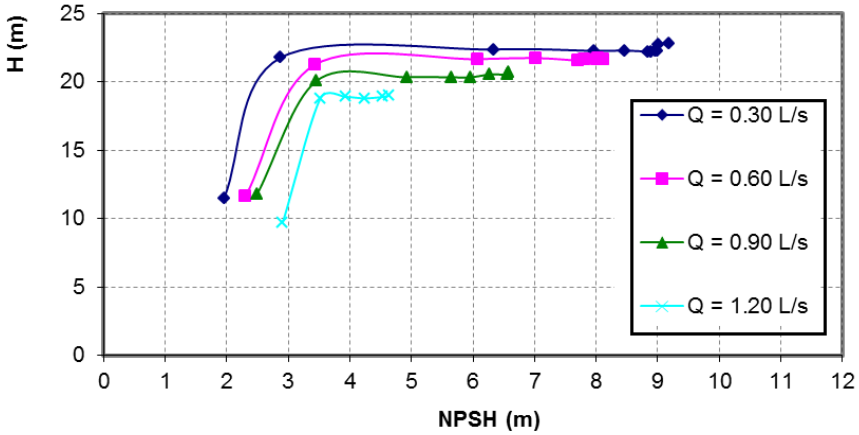

Figure 3: *NPSH with different flow rate for water test*

3.2 Kerosene Test

In this test the liquid in the test tank was changed to the kerosene, in order to study the performances of the pump and the cavitation. Figure 4 shows the performance curve of the centrifugal pump, it can be noted that, fluid starts to decrease as the flow rate and efficiency curve increases at a flow rate of (1.167 L / s). After that, the efficiency begins to decrease.

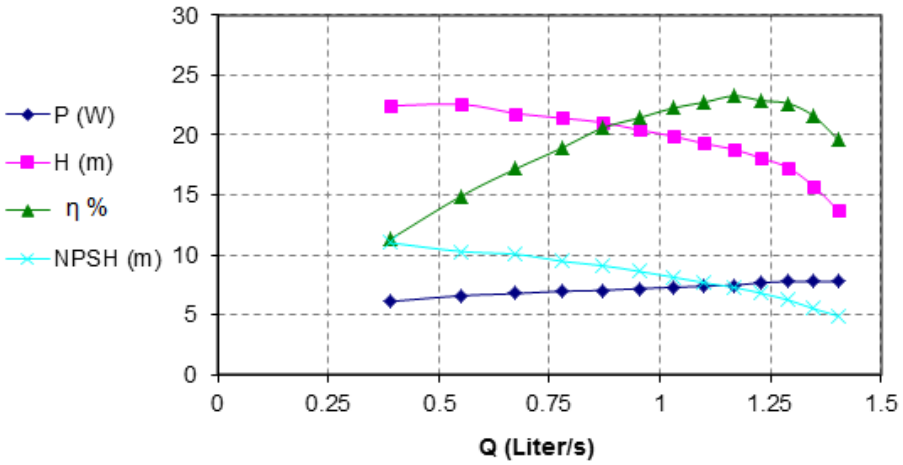

Figure 4: *Performance curves for the pump for Kerosene test*

Figure 5 shows the curves of NPSH at different flow rates. It can be noted that NPSH reach the collapse state, the point at which the lifting mark drops suddenly. It can be seen that, in the case of flow rate (Q = 0.30 L / s) the collapse occurs at the tenth point of the suction valve gradient when the net positive clouds (2.8693 m) and in the case of flow rate (Q = 0.60 L / s), the collapse occurs at the eighth point of the pull valve gradient when the net positive

clouds (3.4282) m), as well as in the case of flow rate (Q = 0.90 L / s), these means the drops of the cavitation may occurs at different points with different flow rates.

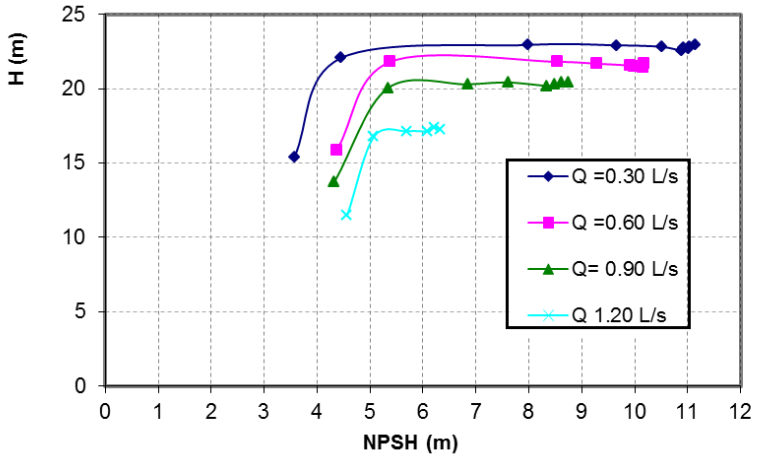

Figure 5: *NPSH curves for the pump in Kerosene test*

3.3 Diesel Test

In this test the liquid in the test tank was changed to diesel, in order to examine the effect of different viscosity on the pump performance and the cavitation. Figure 6 shows the performance curve of the centrifugal pump, it can be noted that the lifting properties begin to decrease as the flow rate and efficiency the higher the flow rate, the higher the flow rate, until it reaches its highest value (23.0136%) at a flow rate of 1.2301 L / s.

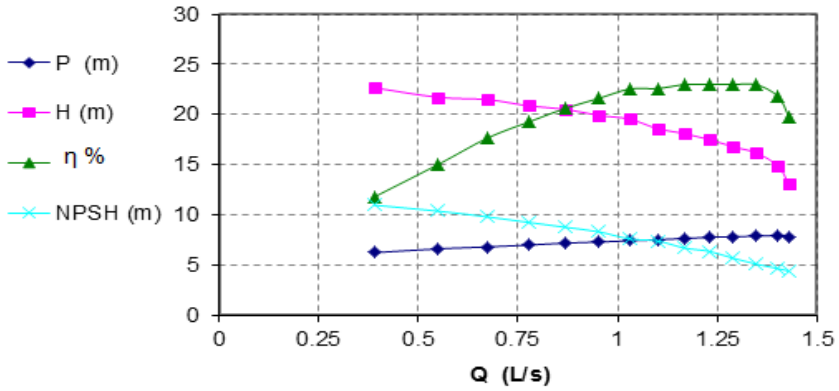

Figure 6: *Performance curves of the pump for diesel with different flow rates*

Figure 7 shows the curves of NPSH at different flow rates for the pump using diesel. It can be noted that NPSH reach the collapse state, the point at which the lifting mark drops suddenly. It can be seen that, in the case of flow rate (Q = 0.30 L / s) the collapse occurs at the tenth point of the suction valve gradient when the net positive clouds (2.8693 m) and in the case of flow rate (Q = 0.60 L / s), the collapse occurs at the eighth point of the pull valve gradient when the net positive clouds (3.4282) m), as well as in the case of flow rate (Q = 0.90

ISBN: 978-81-936820-6-7
Proceedings DOI: 10.21467/proceedings.4

L / s), these means the drops of the cavitation may occurs at different points with different flow rates.

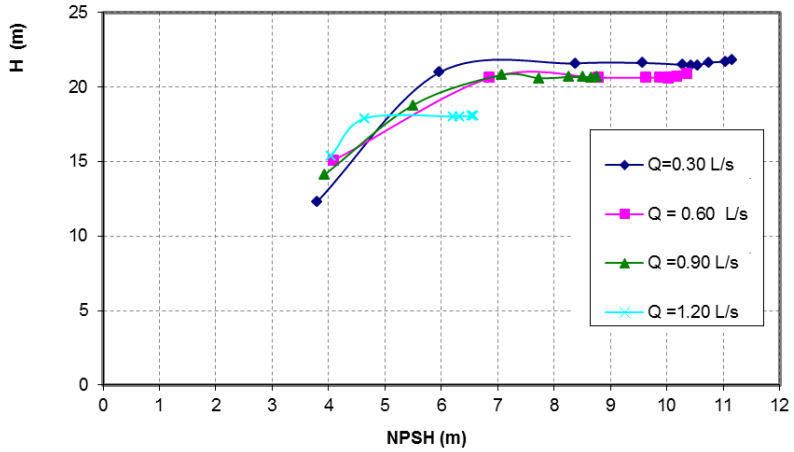

Figure 7: *NPSH curves of the pump for diesel test with different flow rates*

4 Comparison of the Performance of the Pump for the Liquids Used With Different Viscosity

The efficiency of the pump when operated with water is higher than its efficiency when operated with kerosene and diesel as shown in the Figure 8, so it is the highest efficiency in the case of water (26.1505%) at a flow rate equal to the maximum efficiency of kerosene (23.2624%) at a flow rate of (1.167 L / s) and the maximum efficiency of diesel (23.0136%) at a flow rate equal to 1.2301 L / s. The state of the water is different from the efficiency of the pump in the cases of kerosene and diesel where their efficiency is close to each other, and also finds that the difference between the efficiency of the pump at the small flow rates are close and increases as the flow rate is increased.

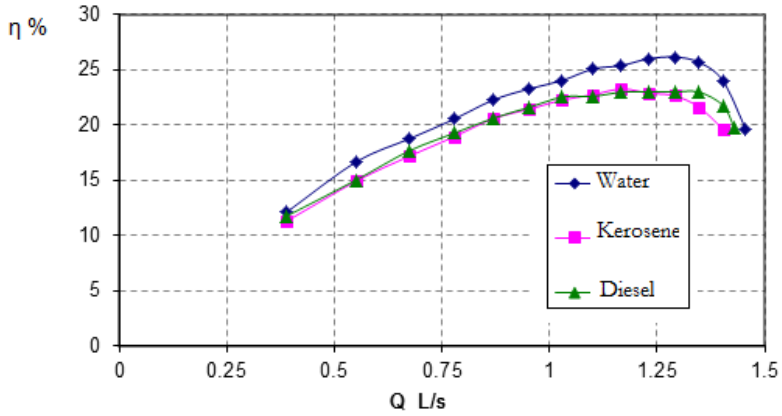

Figure 8: *Efficiency curves of the pump for water, Kerosene and Diesel*

Figure 9 shows the NPSH of the pump in the case of water, kerosene and diesel. It can be seen from the figure that the NPSH for the pump in the case of water is lower than in the case of kerosene and diesel to start in water from (8.9964 m) and then gradually decrease to (2.4208) m), as well as in the case of kerosene and diesel from (11,019 m), (10.9479 m) respectively, and then start to decrease to (4.9136 m), (4.3899 m), respectively.

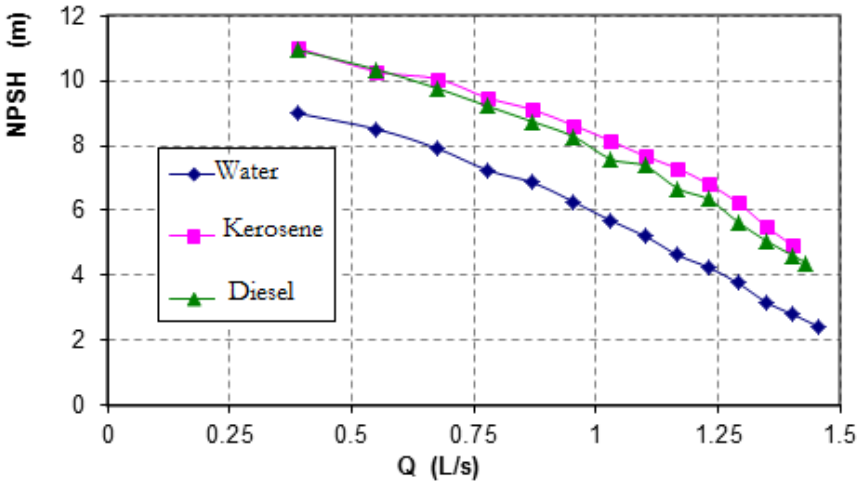

Figure 9: *NPSH curves of the pump for water, Kerosene and Diesel*

5 Conclusions

Experimental was conducted for different flow rates, and with different liquids, these results are presented for a centrifugal pump operating in water, kerosene and diesel fuel with different disposal rates of flow, to examine the effect of liquid viscosity and density on cavitation behaviour. Based on the experimental results, the water has affected by the cavitation at less Net Positive Suction Head (NPSH) than other liquids, also it can be conducted that the kerosene shares the closest cavitation behaviour with diesel fuel. Therefore, the stress produced by cavitation bubbles decreases with increase of viscosity of the liquid.

References

[1] Al-Hashmi, S, Gu, F, Li, Y, Ball, A, Fen, T and Liu, "Cavitation detection of a centrifugal pump using instantaneous angular speed," *ASME 7th Biennial Conference on Engineering Systems Design and Analysis,* vol. 3 Manchester, England, July 19–22, 2004, pp. 185-190.

[2] Ahmed A. B. Al-Arabi and Sobeih M. A. Selim, "Reality of Cavitation Inception in Centrifugal Pumps," *8th Internal Conference on Sustainable Energy Technologies*; Aachen, Germany 31th August – 3rd September, 2009, pp 1-11.

[3] Schiavello B., Visser F C, "Pump Cavitation-Various NPSHR Criteria, NPSHA Margins, and Impeller Life Expectancy," *Proc. of the 25th Int. Pump Users Symp*. (Houston, Tex, 23-26 Feb) 2009, pp 113-144

[4] Spraker W. A. "The Effects of Fluid Properties on Cavitation in Centrifugal Pumps." *J. Eng. Power*, vol. 87, no. 3, July 1965, pp. 309-318.

[5] Maxime Binama, Alex Muhirwa, Emmanuel Bisengimana. "Cavitation Effects in Centrifugal Pumps- A Review" *Binama Maxime.Int Journal of Engineering Research and Applications,* vol. 6, Issue 5, (Part-1) May 2016, pp.52-63.

[6] M. A. Hosien, S. M. Selim., "Experimental study of cavitation criterion in centrifugal pumps". *J Visual 2013*; 16:99–110.

ISBN: 978-81-936820-6-7
Proceedings DOI: 10.21467/proceedings.4

Effects of Spring Stiffness on Suspension Performances Using Full Vehicle Models

M. Hamed[1*],M. Elrawemi[1] ,F.Gu[2], and A.D.Ball[2]

[1] Mechanical and Industrial Engineering Department, College of Engineering, Elmergib University, Libya

[2]Centre for Efficiency and Performance Engineering, University of Huddersfield, UK

DOI: https://doi.org/10.21467/proceedings.4.10

* Corresponding author email: moamar.ehmied@gmail.com

ABSTRACT

Suspension system has significant influence on the passenger safety, providing comfortable ride, stability, and handling of the vehicle. The aims of the present research are to investigate and quantify the effect of spring weakness on suspension performance. This is based on a MATLAB simulation analysis of a seven degree-of-freedom (7-DOF) model for a full vehicle. In the simulation, the suspension faults were seeded by reducing the spring stiffness by 25%, 50% and 80%. The model was validated using experimental data, collected by driving the vehicle across bumps.

The simulation results for varying degrees of spring stiffness indicated that the ride comfort was decreased as the spring stiffness was increased for excitation frequencies close to resonant frequencies of the vehicle body (approximately 1 Hz). As spring stiffness was increased at excitation frequencies below 1 Hz, the suspension travel was reduced. Within the zone of resonant frequency of sprung mass, the deformation amplitudes were increased as the spring stiffness increased. Moreover, Frequency Response Functions analysis has been used for fault detection of reduction of spring's stiffness by 25%, 50% and 80%.

Keywords: Ride comfort; Road handling; vehicle stability; Vibration measurement; spring stiffness.

1 Introduction

The main function of suspension system is to support and carry the vehicle weight, to protect drivers and passengers from vibrations, and to maintain significant contacts between the tyre and the road surface [1]. For vehicles, it is a difficult challenge to consistently maintain a high standard of ride comfort and vehicle handling under a range of driving conditions. Between October 2010 and September 2011, the Ministry of Transport (M.O.T) collected data [2] in the UK in respect of MOT tests for approximately 24.2 million vehicles. These data was illustrates that lighting and signalling problems accounted for the highest number of re-tests (19.79%), followed by suspension faults (13.18%) and 8.75% (the fourth most common fault) were tyre faults. Early detections of abnormal events in automotive suspension systems can reduce the damage caused to the vehicle in driving situations, in addition to improving

 ISBN: 978-81-936820-6-7

passenger comfort and security. The performance of a vehicle is often downgraded due to the appearance of faults with the suspension [3]. The common faults associated with suspension components are damaged or leaking shock absorbers, spring weakness, wearing down of the pivot and bushing and damage to the main support member assembly, as shown in Figure 1.

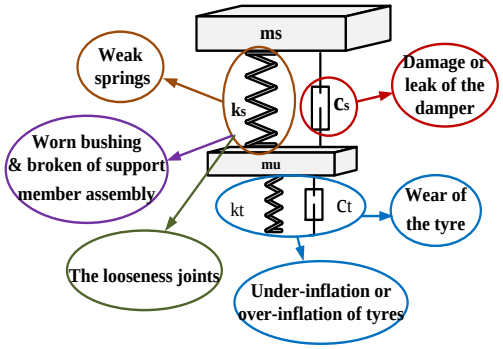

Figure 1: *common faults in suspension systems*

Faults occurring in the damping system can be as a result of one or more of the following factors: worn seals, a reduction in the oil volume due to leakages, broken mounts and extruded or worn bushings. All of the aforementioned causes can lead to a decline in the performance of the shock absorber, resulting in longer braking distances. This then causes the tyres to wear away reducing the car handling during cornering [4].

In order to study the performance of the suspension in terms of ride quality, handling and stability of the vehicle, some important parameters must be considered. These parameters are: wheel deflection, suspension travel and the vehicle body acceleration, with the aim of achieving a small amplitude value for each of the same [3]. Road handling is associated with the relative displacement between the suspension and the road input (Zu - Zr). This is represented as wheel deflection. Suspension travel is defined as the relative displacement between the vehicle body and the wheel (Zs – Zu). This can be used for assessing the space required to accommodate the suspension spring. Ride comfort is related to the vehicle body motion sensed by the passenger. This requires the acceleration of the vehicle body (sprung mass) to be relatively small. According to ISO: 2631-1-1997[5] proper road handling must be in the region of 0.0508 m, whilst the standard value for suspension travel must be in the region of 0.127m (as a minimum value). The passenger is thought to feel highly comfortable if the RMS acceleration is below 0.315 m/s2.

A number of researchers have investigated suspension performance using modelling/simulation and experimental investigation. Faheem [6] investigated a mathematical model for a quarter car with 2-DOF and a half car with 4-DOF. Rao[7] developed a mathematical model of a 3-DOF quarter car with a semi-active suspension system. This model was used for the testing of skyhook and other strategies involving semi active suspension systems. Esslaminasa et al [8] developed a semi-active twin-tube shock via the modelling of one and two DOF, for a quarter car design. Darus [9] adopted a state space approach in

ISBN: 978-81-936820-6-7
Proceedings DOI: 10.21467/proceedings.4

developing a mathematical model for both a quarter car and a full car using MATLAB packages. Metallidis [10], applied a statistical system identification technique to perform parametric identification and fault detection of nonlinear vehicle suspension systems. Kashi [11] applied model-based fault detection on a vehicle control system, which relied on mathematical descriptions of the system, yielding robust fault detection and an isolation of faults affecting the system. Agharkakli et al [12] presented a mathematical model for passive and active quarter car suspension systems. Ikenaga et al [13]conducted a research study to improve road handling and ride comfort. An active suspension control system was presented based on a full vehicle model which included the performance of the suspension system. Lu et al [14]discussed the effect of truck speed on shock and vibration levels indicating that the effect of truck speed on the root mean square acceleration of the vibrations, were strong at a lower speed but weak at a higher speed.

Sekulic et al[15] present a research to study the effects of spring stiffness and shock absorber damping on the vertical acceleration of the driver's body, suspension deformation and dynamic wheel load, with the purpose to define recommendations for selecting oscillation parameters while designing the suspension system of a (intercity) bus. Results of this research indicated that, the parameters which ensured good rid comfort of the driver were conflicting with the parameters which ensured the greatest stability of the bus and the corresponding wheel travel. Breytenbach [16] discussed the ride comfort versus handling argument for off-road vehicles. This research investigated a new approach of a semi-active suspension mode called "4 State Semi-active Suspensions", allowing a switch between low and high damping.

The objective of the present research is to investigate the effect of spring weakness on suspension performance, in addition to developing suspension condition monitoring based on a full vehicle mathematical model

2 Suspension System Model and Dynamics

Development of the vehicle model operates under the assumptions that the vehicle is a rigid body, represented as sprung mass (ms), and the suspension axles are represented as unsprung mass (mu) as shown in Figure 2. The suspension between the vehicle body and wheels are modelled by linear spring and damper elements and each tyre is modelled by a single linear spring and damper.

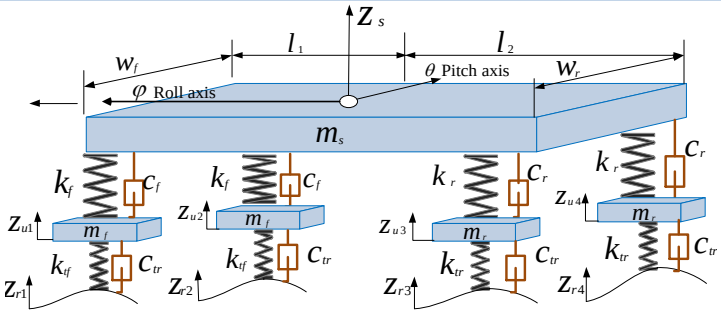

Figure 2: *Full vehicle models*

The equations of all motions are derived separately resulting in the equations of the body motions [8].

Equation of motion for bouncing of sprung mass:

$$m_s \ddot{z_s} = k_f(z_{u1}-z_{s1}) + k_f(z_{u2}-z_{s2}) + k_r(z_{u3}-z_{s3}) + k_r(z_{u4}-z_{s4}) + c_f(\dot{z_{u1}}-\dot{z_{s1}}) + c_f(\dot{z_{u2}}-\dot{z_{s2}}) + c_r(\dot{z_{u3}}-\dot{z_{s3}}) + c_r(\dot{z_{u4}}-\dot{z_{s4}}) \quad (1)$$

For pitching of sprung mass

$$I_P\ddot{\theta} = k_f l_1(z_{u1}-z_{s1}) + k_f l_1(z_{u2}-z_{s2}) - k_r l_2(z_{u3}-z_{s3}) - k_r l_2(z_{u4}-z_{s4}) + c_f l_1(\dot{z_{u1}}-\dot{z_{s1}}) + c_f l_1(\dot{z_{u2}}-\dot{z_{s2}}) - c_r l_2(\dot{z_{u3}}-\dot{z_{s3}}) - c_r l_2(\dot{z_{u4}}-\dot{z_{s4}}) \quad (2)$$

For rolling motion of sprung mass

$$I_R\ddot{\varphi} = k_f\frac{w_f}{2}(z_{u1}-z_{s1}) - k_f\frac{w_f}{2}(z_{u2}-z_{s2}) + k_l\frac{w_r}{2}(z_{u3}-z_{s3}) - k_r\frac{w_r}{2}(z_{u4}-z_{s4}) + c_f\frac{w_f}{2}(\dot{z_{u1}}-\dot{z_{s1}}) - c_r\frac{w_f}{2}(\dot{z_{u2}}-\dot{z_{s2}}) + c_r\frac{w_r}{2}(\dot{z_{u3}}-\dot{z_{s3}}) - c_r\frac{w_r}{2}(\dot{z_{u4}}-\dot{z_{s4}}) \quad (3)$$

For each wheel motion in vertical direction

$$m_f\ddot{z_{u1}} = -k_f(z_{u1}-z_{s1}) - c_f(\dot{z_{u1}}-\dot{z_{s1}}) + k_{tf}(z_{r1}-z_{u1}) + c_{tf}(\dot{z_{r1}}-\dot{z_{u1}}) \quad (4)$$

$$m_f\ddot{z_{u2}} = -k_f(z_{u2}-z_{s2}) - c_f(\dot{z_{u2}}-\dot{z_{s2}}) + k_{tf}(z_{r2}-z_{u2}) + c_{tf}(\dot{z_{r2}}-\dot{z_{u2}}) \quad (5)$$

$$m_r\ddot{z_{u3}} = -k_r(z_{u3}-z_{s3}) - c_r(\dot{z_{u3}}-\dot{z_{s3}}) + k_{tr}(z_{r3}-z_{u3}) + c_{tr}(\dot{z_{r3}}-\dot{z_{u3}}) \quad (6)$$

$$m_r\ddot{z_{u4}} = -k_r(z_{u4}-z_{s4}) - c_r(\dot{z_{u4}}-\dot{z_{u4}}) + k_{tr}(z_{r4}-z_{u4}) + c_{tr}(\dot{z_{r4}}-\dot{z_{u4}}) \quad (7)$$

The equation variables are defined and summarized in Table 1 (adopted from [9]), along with the parameters of the suspension system. This is with the exception of the damping coefficient of the tyres for different pressures, which were adopted from [17]. Amendments were also made to some of the variables in order to meet the specifications of the vehicle used in the

ISBN: 978-81-936820-6-7
Proceedings DOI: 10.21467/proceedings.4

Series: AIJR Proceedings

experiment. The road profile was calculated and created according to vehicle speeds and the height and width of the bumps by the following equation:

$$u(p) = 1/2a\sin(2\pi f_p t) \quad (8)$$

The road profile was also assumed to be a single bump with a sin wave shape. Where a is the bump height (50)

Table 1: *Defines the equation variables and parameters of suspension*

Variables	Definition	Units	variables	Definition	Units
ms= 1200	Sprung mass	Kg	wf=90	Front vehicle width	m
mf=90	Unsprang mass	kg	wr=1.70	Rear vehicle width	m
kf=36279	Front spring stiffness	N/m	Zs≤0.06	Displacement of the vehicle body	m
kr=19620	Rear spring stiffness	N/m	zu1-zu4≈0.0508	Displacement of each wheel	m
cf=3924	Front damper coefficient	Nm/sec	Ir=5340	Roll and pitch of moment of inertia	$Kg.m^2$
cr =2943	Rear damper coefficient	Nm/sec	Ip =6430	Pitch of moment	$Kg.m^2$

3 Experimental Set up and Test Procedure

To validate the theoretical model, a front wheel drive Vauxhall ZAFIRA (2001) car, equipped with two different sensors was used. The sensors mounted on the car include: (1) a vibration sensor with a sensitivity of (3.770 pc/ms-2) mounted on the upper mounting point of the front left shock absorber, and (2) a dynamic tyre pressure sensor (DTPS) with a sensitivity of (11.43 Pc/0.1Mpa) connected to the valve stem of the front left wheel. The pressure sensor was situated in the centre rim of the front left wheel and the vibration sensor on the inside of the car. They were placed in these positions after being assembled and connected to the wireless sensor nodes (transmitters).The gateway (receiver) was equipped with a laptop inside the car. In order to ensure a sound installation of the sensors, two different adapters were designed and manufactured at the University of Huddersfield. In addition to this, a wireless measurement system was also designed and installed on the car, to offer a complete remote measurement for the vibration and pressure data being extracted. The most fundamental aim of the test was to obtain the acceleration (vibration) response of the suspension system to validate the model and also to enable a thorough analysis of the effects that different spring rates have on the performance of the suspension system. The test was conducted with the standard tyre pressure (2.3bar) and a vehicle speed of 8km/h.

4 Results and Discussion

The model was validated using experimental data collected when the vehicle was being driven, at a speed of 8km/h, over Bump 1 (located within the premises of The University of Huddersfield. The bump profile was 5.80 m width, 0.50 m length and 0.050 m height and this was assumed to be the input for the system. MATLAB software was used to analyze the vehicle response. Figure 3 depicts the acceleration of the vehicle body in the time domain based on the model simulation and experiments. Upon a comparison of the experimental results, it can be noted that the model fairly predicts the suspension performance.

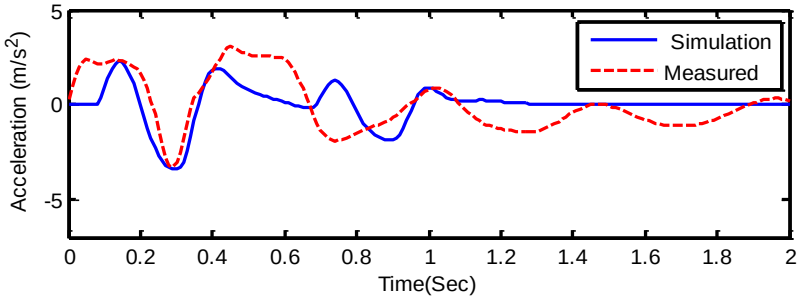

Figure 3 *Vibration (acceleration) of suspension simulation and experimental*

Figure 4(a) shows the plots of the road profile in the time domain for both the front and rear wheels of the vehicle. For the simulation study, road disturbance is assumed to be the input for the system. Figure 4(b) shows the effect of varying the spring rates on the vehicle body response. From these results, it was observed that decreases in spring stiffness causes a resultant decrease in the amplitude of the relative displacement of the car body. Figure 5 depicts the displacement of four wheels (unsprung mass) with different spring stiffness in the time domain. The results show that the amplitude/peak value of the wheels decreases with a corresponding decrease in the stiffness value. This indicates that the performance of the suspension may be affected by the changes made to the spring stiffness.

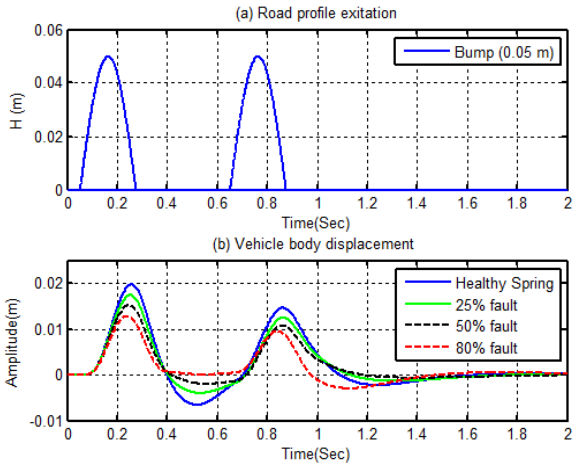

Figure 4 (a): *Road profile excitation and* **(b):** *Displacement of vehicle body for different spring stiffness.*

ISBN: 978-81-936820-6-7
Proceedings DOI: 10.21467/proceedings.4

Series: AIJR Proceedings

An analysis of different parameters such as: wheel deflection, suspension travel and acceleration of the vehicle body was carried out in order to consider the different effects the spring stiffness level has on the performance of the suspension, which includes, the ride quality and handling and stability of the vehicle. The road handling profile (wheel deflection) for a vehicle is associated with the contact forces between the road surface and the vehicle tyre (zu – zr).

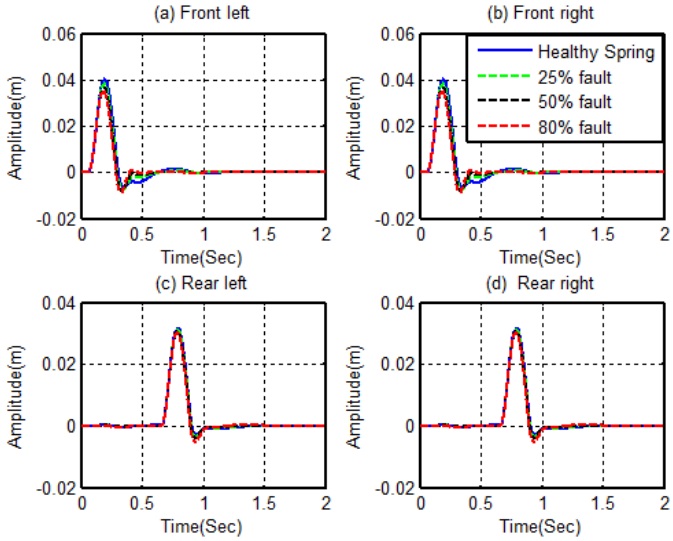

Figure 5 *Vehicle wheel's displacement with different spring stiffness*

For this simulation, the wheel deflections were approximately 0.015 m, 0.012 m, 0.008 m and 0.006 m for a healthy, 25%, 50%, 80% faulty spring respectively, as presented in Figure 6. From this figure, a noticeable change in the peak value of the wheel deflection can be observed. However, it can be noted that the vertical deflection does not decay quickly with the healthy spring, in particular, those with healthy and 25% faults. When compared with proper road handling as per ISO: 2631-1-1997 [4] (which must be in the range of m) this range is acceptable.

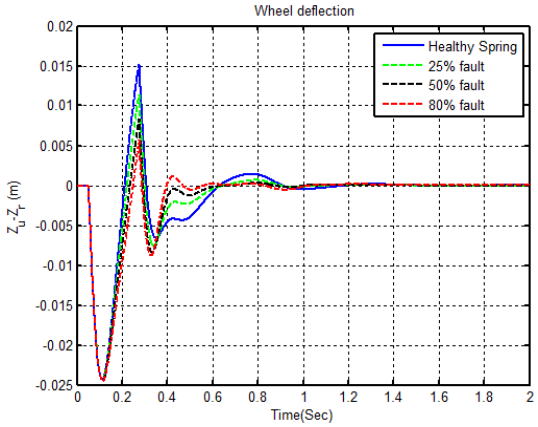

Figure 6 *Wheel deflections for different spring stiffness*

The suspension travel can be defined as a relative displacement between the vehicle body and the wheel (zs – zu) as shown in Figure 7. From this figure, it can be observed that lower spring stiffness provides for a lower suspension travel therefore to reduce the suspension travel a soft spring is required. In accordance with ISO: 2631-1-1997 [4] the passenger is thought to feel highly comfortable if the RMS acceleration is below 0.315 m/s^2.

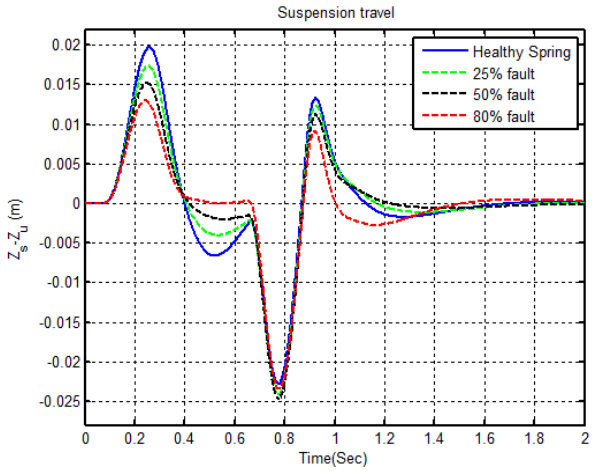

Figure 7 *Suspension travel for different spring stiffness*

In Figure 8 the amplitudes of the vertical acceleration were increased within the domain of the vehicle body (sprung mass) as the spring stiffness was increased. Lower values for the spring stiffness provided better oscillatory comfort for the passenger at excitation frequencies approximating the resonant frequency of the vehicle body. However, the vertical acceleration decays quickly with the reduction of the stiffness.

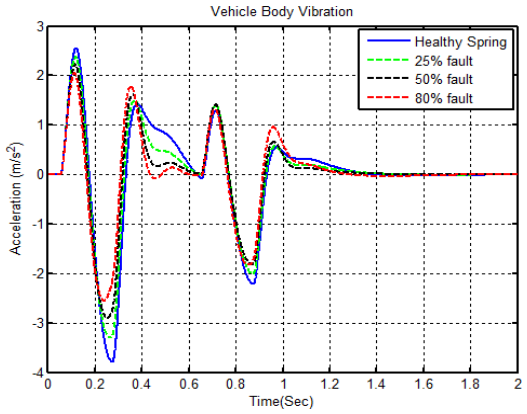

Figure 8 *Acceleration of the vehicle body for different spring stiffness*

To develop conditioned monitoring tools for suspension faults, detect the level of spring stiffness and also to predict potential suspension faults which may arise in the future, the Frequency Response Function (FRF) technique was used. The FRF is a fundamental measurement that isolates the inherent dynamic properties of a mechanical structure and also describes the input-output relationship between two points on a structure as a function of

ISBN: 978-81-936820-6-7
Proceedings DOI: 10.21467/proceedings.4

frequency. Figure 9 shows the amplitude-frequency characteristic curves for the changes to the spring stiffness of the suspension in four different output cases (vehicle body vertical displacement, vehicle body velocity, displacement of front and rear wheel) and the front left road input. The results show that decreasing the stiffness affects and reduces the value of the suspension displacement at the sprung mass natural frequency. A change in the amplitudes of displacement was more significant within the domain of resonant frequency of sprung mass (around 1Hz). A change of spring stiffness did not produce any effect on the change of the displacement and velocity of the vehicle body within the domain of resonant frequency of unsprang mass of the vehicle (around 10 Hz). However, the area under the curve does not necessarily decrease with a reduced peak value of the suspension displacement. From this, it can be concluded that in the frequency range close to the natural frequency of the vehicle body, a soft stiffness is required. However, lower stiffness also affects and produce vibrations in the mid- to high frequency range as shown in the front wheel responses.

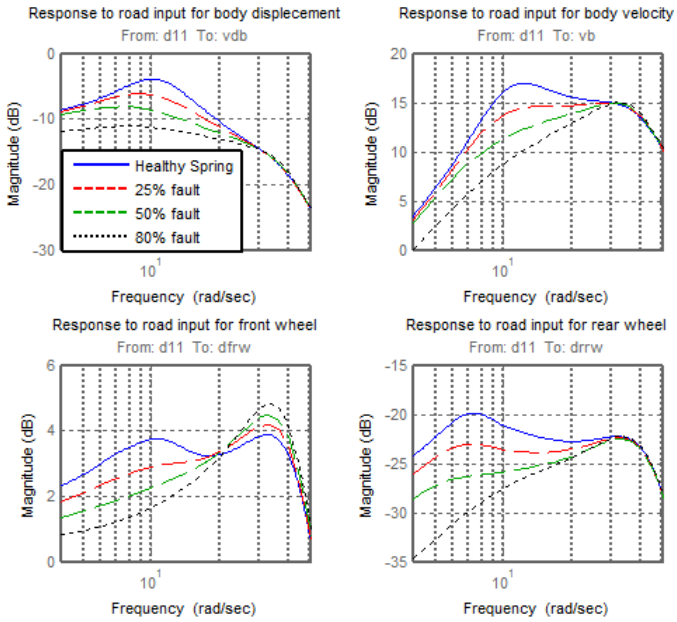

Figure 9 *Transfer function response for the vehicle body and vehicle wheels*

5 Conclusions

After collecting the relevant data using the full vehicle model, an analysis of the findings illustrates the effects on suspension performance when applying a range of spring stiffness. MATLAB was used to develop the full vehicle model with 7-DOF. Following this, analyses were carried out on the time and the frequency response of the vehicle. The analyses focus on the performances of the suspension in terms of ride comfort, road handling and stability of the vehicle. This study considered the faults of spring stiffness which were simulated by reducing the spring stiffness by 25%, 50% and 80%.

The simulation results indicated that the various parameters of suspension performance such as, ride comfort, road handling and vehicle stability need a design optimization due to the need to balance their conflicting requirements. For instance, the simulation results for varying of spring stiffness indicated that the ride comfort was decreased as the spring stiffness was increased for excitation frequencies close to resonant frequencies of the vehicle body (approximately 1 Hz).

FRF results show that, decreasing the stiffness affects and reduces the value of the suspension displacement at the sprung mass natural frequency. A change in the amplitudes of displacement was more significant within the domain of resonant frequency of sprung mass (around 1Hz). A change of spring stiffness did not produce any effect on the change of the displacement and velocity of the vehicle body within the domain of resonant frequency of unsprang mass of the vehicle (around 10 Hz). It can be concluded that, FRF methods can be effectively used for fault detection of suspension system.

References

[1] B. K. N. Rao, Handbook of condition monitoring. Oxford, UK: Elsevier Advanced Technology, 1996.

[2] H. John, "Good Garages | Honest John."

[3] B. L. Zohir, "Ride Comfort Assessment in Off Road Vehicles using passive and semi-active suspension."

[4] T. Weispfenning, "Fault Detection and Diagnosis of Components of the Vehicle Vertical Dynamics," Meccanica, vol. 32, no. 5, pp. 459–472, Oct. 1997.

[5] A. Mitra, N. Benerjee, H. Khalane, M. Sonawane, D. JoshI, and G. Bagul, "Simulation and Analysis of Full Car Model for various Road profile on a analytically validated MATLAB/SIMULINK model," IOSR J. Mech. Civ. Eng. IOSR-JMCE, pp. 22–33.

[6] Ahmad Faheem, Fairoz Alam, and V. Thomas, "The suspension dynamic analysis for a quarter car model and half car model," Dec-2006.

[7] R. Rao, T. Ram, k Rao, and P. Rao, "Analysis of passive and semi active controlled suspension systems for ride comfort in an omnibus passing over a speed bump," Oct-2010.

[8] N. Eslaminasab, M. Biglarbegian, W. W. Melek, and M. F. Golnaraghi, "A neural network based fuzzy control approach to improve ride comfort and road handling of heavy vehicles using semi-active dampers," Int. J. Heavy Veh. Syst., vol. 14, no. 2, pp. 135–157, Jan. 2007.

[9] R. Darus and Y. M. Sam, "Modeling and control active suspension system for a full car model," in 5th International Colloquium on Signal Processing Its Applications, 2009. CSPA 2009, 2009, pp. 13–18.

[10] P. Metallidis, G. Verros, S. Natsiavas, and C. Papadimitriou, "Fault Detection and Optimal Sensor Location in Vehicle Suspensions," J. Vib. Control, vol. 9, no. 3–4, pp. 337–359, Mar. 2003.

[11] K. Kashi, D. Nissing, D. Kesselgruber, and D. Soffker, "Diagnosis of active dynamic control systems using virtual sensors and observers," in 2006 IEEE International Conference on Mechatronics, 2006, pp. 113–118.

[12] A. Agharkakli, G. Sabet, and A. Barouz, "Simulation and Analysis of Passive and Active Suspension System Using Quarter Car Model for Different Road Profile," Int. J. Eng. Trends Technol.-, vol. 3, no. 5, 2012.

[13] K. B. Arıkan, Y. S. Ünlüsoy, İ. Korkmaz, and A. O. Çelebi, "Identification of linear handling models for road vehicles," Veh. Syst. Dyn., vol. 46, no. 7, pp. 621–645, Jul. 2008.

[14] F. Lu, Y. Ishikawa, H. Kitazawa, and T. Satake, "Effect of vehicle speed on shock and vibration levels in truck transport," Packag. Technol. Sci., vol. 23, no. 2, pp. 101–109, 2010.

[15] D. Sekulic and V. Dedovic, "The Effect of Stiffness and Damping of the Suspension System Elements on the Optimisation of the Vibrational Behaviour of a Bus," Int. J. Traffic Transp. Eng., vol. 1, no. 4, Dec. 2011.

[16] B. Breytenbach and P. S. Els, "Optimal vehicle suspension characteristics for increased structural fatigue life," Dec. 2011.

[17] J. Y. Wong, Theory of Ground Vehicles. John Wiley & Sons, 2001.

ISBN: 978-81-936820-6-7

Series: AIJR Proceedings
Proceedings DOI: 10.21467/proceedings.4

Influence of Coolant Concentration on Surface Roughness during Turning of Steel C-60

Abdulaziz Abodena, Muhannad Alrzage, Ibrahim K. Husain

Faculty of Engineering, University of Gharyan, University, Libya

DOI: https://doi.org/10.21467/proceedings.4.11

* Corresponding author email: abodena65@gmail.com

ABSTRACT

During recent years, considerable attention has been paid to the during turning operations, to improve forming the outer layer, such as surface cooling which enhances some of the surface characteristics and producing a good surface finish. In this experimental work, the effect of cutting fluid concentrations on surface roughness has been studied because of its importance in the cutting process. The general aim of the work in this paper was to investigate the surface roughness of the workpiece when machining high carbon steel with tungsten inserts during wet machining conditions. In the experimentation, five different velocities, five feeds, five depths of cut and five coolant-oil content percentages were used to evaluate the surface roughness with these parameters. Design of experiments is a very efficient method for developing valuable research while saving time in the process. The technique used in this study for designing experiments was introduced by Box and Hunter. A rotatable factorial design of experiments with a central composite of second order can be used to enhance the reliability of investigation work. The package of design of experiments and analysis of variance used in this study has been used widely in experimentation work. The tests were performed using a traditional lathe machine. The results of this process were obtained, analyzed, and discussed using three-dimensional relationships between roughness and the cutting parameters mentioned above. The conclusions from this work show a general trend for a decrease in surface roughness as the percentage of oil in the coolant increases.

Keywords: Turning, surface roughness, cutting fluids.

1 Introduction

The nature of the surface region generated in metal machining may be quite different from that of bulk material. The surface may contain topographical features such as surface roughness. The subsurface may contain other features in the form of residual stress, plastic deformation and variation in microstructural characteristics such as hardening tempering over tempering, chemical composition and grain size [1]. Metal cutting is one of the vital processes and widely used manufacturing processes in engineering industries. Highly competitive market

 ISBN: 978-81-936820-6-7

requires high quality products at minimum cost. Improvement of productivity with good quality of the machined parts is the main challenges of metal industry; there has been more concern about monitoring all aspects of the machining process. Surface finish is an important parameter in manufacturing engineering and it can influence the performance of mechanical parts and the production costs[2]. During recent years, considerable attention has been paid to the turning operations, to improves forming the outer layer, such as surface cooling which enhances some of the surface characteristics and producing a good surface finish[1]. Cooling and lubrication are important in reducing the severity of the contact processes at the cutting tool-workpiece interfaces. Historically, more than 100 years ago, water was used mainly as a coolant due to its high thermal capacity and availability. Corrosion of parts and machines and poor lubrication were the drawbacks of such a coolant. Oils were also used at this time as these have much higher lubricity, but the lower cooling ability and high costs restricted this use to low cutting speed machining operations. Finally, it was found that oil added to the water gives good lubrication properties with the good cooling and these became known as the soluble oils[3, 4]. The main objective of this work is to study the effect of coolant concentration on the surface roughness of Carbon-Steel (C60) during the turning process, with other operating variables such as cutting speed, feed rate, and cutting depth, to determine the most suitable operating conditions to achieve the best surface smoothness. Even when considering the current trend towards research into minimum quantity lubrication processes, in many cases a flood of liquid is still directed over the tool with the aim of preventing the tool and workpiece from overheating, increasing tool life, and improving surface finish [5]. Selecting a suitable fluid for a particular application among the large number of commercially available fluids is an issue, and a significant challenge due to the fact it is often an empirical process.

2 Experimental work

In this study carbon steel alloy C60 was used as workpiece material. The chemical analyses, in weight percent, of this material is shown in Table (1). The material was received in the form of cylindrical bars with diameter of 60 mm and length of 70 mm.

Table 2: Chemical composition of the C60 [6]

Element	Si	Mo	Cu	Mn	Ni
Weight%	max. 0.40	max. 0.10	0.61	0.75	max. 0.40

2.1 Cutting Conditions

In this work, all of cutting tests are performed under lubricated conditions on (Al-pin 180N) type model of the lathe machine. In order to study in depth the effects of each parameter on the surface characteristics of workpiece, four cutting parameters were chosen namely; oil concentration, cutting speed, feed and cutting depth. The values of the actual and coded variables of the testing condition are listed in the following table

ISBN: 978-81-936820-6-7

Series: AIJR Proceedings
Proceedings DOI: 10.21467/proceedings.4

Table 3: Coding of cutting test Parameters

Parameters	Symbol	Levels				
		-2	-1	0	1	2
Coolant composition (%)	X_1	3	6	9	12	15
Speed, (m/min)	X_2	56	120	150	412	840
Feed (mm/rev)	X_3	0.055	0.09	0.18	0.3	0.4
Depth of cut (mm)	X_4	0.2	0.6	1	1.4	1.8

2.2 Design of Experiments

Traditional experimentation involves considerable effort and time, particularly when a wide range of investigation work is needed. Design of experiments is a very efficient method for developing valuable research while saving time in the process and for achieving results in a much more economical manner. As a rule, an experiment designed to find the optimum condition of a process is described adequately by a second order polynomial. The technique used in this study for designing experiments was introduced by box and Hunter.
Experimental work involves the study of the relationships between different factors at different levels and a certain response and this is where the design of experiments technique is helpful. There is a big opportunity to study the individual effects of each parameter and their interactions using the factorial design of experiments.

The package of design of experiments and analysis of variance used in this study has been used widely in experimentation work [7, 8]. The spherical variance function designs are preferable since these designs provide a constant variance for the response at all points of the experiment since they are at the same radius from the centre of the design. These kinds of designs are known as rotatable designs.

2.3 Postulation of Mathematical Model:

A functional relationship between the response surface roughness of the workpiece produced by turning process in dependent variable (oil concentration, cutting speed, cutting feed and depth of cutting) can be fitted into the following polynomial response equation of second-order.

$$Yu = b_o + b_1x_1 + b_2x_2 + b_3x_3 + b_4x_4 + b_{11\,x_1^2} + b_{22}x_2^2 + b_{33}x_3^2 + b_{44}x_4^2 + b_{12}x_1x_2 + b_{13}x_1x_3 + b_{14}x_1x_4 + b_{23}x_2x_3 + b_{24}x_2x_4 + b_{34}x_3x_4$$

where; $x_1, x_2, x_3 and\ x_4$ are the coded values of the variables. These variables are coded for convenient identification and for easy calculation.
The regression coefficients b_o, b_1, b_3, …etc can be calculated by the method of least squares using the related equations.

2.4 Analysis of Variance (ANOVA):

The relationship between the response and the cutting process parameters were quantitatively determined using empirical equations (the proposed model). The evaluation and the analysis of the experimental data were made by adopting polynomial response of second-order equations in terms of the process variables by establishing their interactions.

In the present work the variance for each of the regression coefficient is given by the related equations. The F-ratio for each term can then be determined from the variance analysis. In such an analysis, it is of interest to partition the sum of squares of the Y's into the contribution due to the first-order (Linear) term. An additional contribution due to the second-order (quadratic and interaction) terms, lack-of-fit terms (which measure the deviations of the response from the fitted surface), and the experimental error obtained from the replicated points at the center.

3 Results and Discussion

The model is developed in terms of Coolant concentration (%) cutting speed, cutting depth and cutting feed by utilizing Response Surface Methodology. As it was mentioned above, the variables are investigated using the experimental design matrix instead of the conventional one-variable at a time method. The evaluation and the analysis of the experimental data is made by adopting a polynomial response surface of second-order in terms of the process variables by establishing their interaction. The results are tested statistically using the ANOVA technique presented previously. The F-ratio test as a tool of the analysis of variance is used to check the adequacy of the model. To determine whether the final equations are a good fit to the experimental observations, the F-ratio test is carried out. The standard valued of F-ratio for the significance level a = 0.05 and degrees of freedom 4 and 6 is F0.05(4,6) = 4.53 and at degrees of freedom 10 and 6 is F0.05(10,6) = 4.06.

$$\begin{aligned} Ra = 0.619 + 0.708x_1 - 0.882x_2 + 0.98x3 - 0.08x4 + 2.14{x_1}^2 + 2.06{x_2}^2 \\ + 0.317{x_3}^2 + 0.32{x_4}^2 - \ 0.42x_1x_2 + 0.57x_1x_3 - 0.11x_1x_4 \\ - 0.54x_2x_3 - 0.38x_2x_4 + 0.49x_3x_4 \end{aligned}$$

3.1 Relation between roughness, oil content and speed

Cutting speed and oil content are important parameters that effect on the roughness in cutting process. The figure (1) shows the result of the effect of oil content and speed on the roughness based on the empirical equation shown up. From the figure it is noticed that there is a change in the roughness value whenever the speed and the concentration of the oil change. It was noted that when the concentration of oil and speed is at the lowest levels, the roughness is the highest levels. When the concentration of oil increased to about 9% and the speed to about 150 m/min, it was noticed a decrease in the value of roughness until it reached its lowest value.

ISBN: 978-81-936820-6-7

Series: AIJR Proceedings
Proceedings DOI: 10.21467/proceedings.4

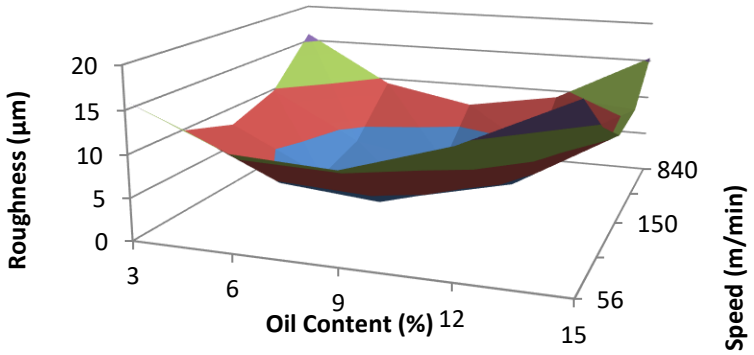

Figure 3: Relationship *between roughness, oil content and cutting speed*

3.1.1 Effect of oil content and feed on roughness

Figure (2) show the results of roughness versus different oil concentrations and cutting feed. The roughness is influenced by feed and oil concentration change. The best result of the number of smoothness is obtained at the minimum of the cutting feed and at concentration of oil about 9% used in this work.

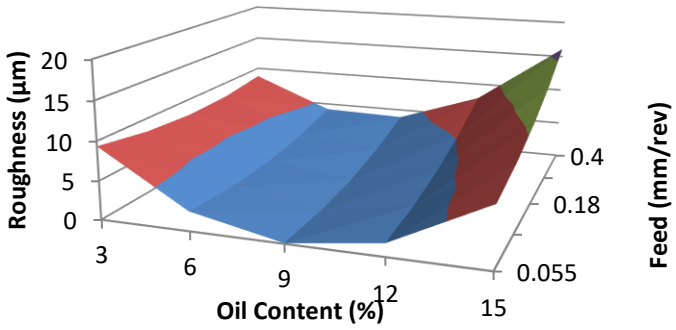

Figure 4: Relationship *between roughness, oil content and cutting feed*

3.2 Relationship between roughness, oil content and depth

Figure (3) shows the roughness versus different of oil content and depth of cut. The change in depth of cutting and oil content leads to change in roughness, low values of roughness is observed when oil concentrations are between 6% and 12% and the lowest value is at 9% and low depth of cut.

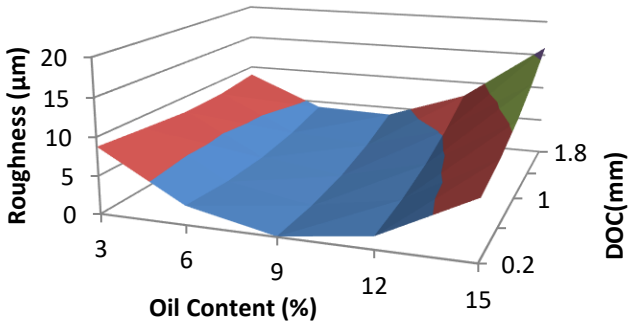

Figure 5: Relationship *between roughness, oil content and depth of cutting*

4 Conclusions

In this study 31 tests were made with different variables (oil concentration, cutting speed, cutting depth and feed) to reach the best value for surface smoothness. All these processes were applied to a group of samples of (C60). The following can be concluded; the results obtained from this work have shown that oil concentration has different effect on the response studied. An increase in oil concentration leads to improvement in surface finish up to a certain level. The recommended cutting feeds that result in good surface finish are from 0.055 to 0.18 mm/rev when concentration of oil is 9%. At speed of medium range 150 m/min and concentration oil of 6 to 9%, good surface finish can be obtained.

References

[1] EL-XEER, M.E.-K.M., EFFECT OF SOME BURNISHING PARAMETERS ON RESIDUAL STRESSES AND FATIGUE LIFE 2002.

[2] Bhavsara, H.Y.V.S.N., Experimental Investigation of Surface Roughness and Power Consumption in Turning Operation of EN 31 Alloy Steel. 2014: Elsevier Ltd.

[3] Machado, A., The effect of extremely low lubricant volumes in machining. 1997.

[4] McCoy, J., Tracing the historical development of metal workingfluids. 1994: New York: Marcel Dekker.

[5] Abodena, A.M. An Investigation into the Effect of Coolants' Concentration and Cutting Conditions on the Coefficient of Friction during Turning of Aluminum 6082-T6. in 1st Conference of Industrial Technology CIT2017. 2017. Misurata.

[6] Ravne., M. *steel data*. 2005; Available from: http://www.metalravne.com/selector/steels/C60.html.

[7] Joyce, R.M., Experiment optimization in chemistry and chemical engineering, S. Akhnazarova and V. Kafarov, Mir Publishers, Moscow and Chicago, 1982, 312 pp. Price: $9.95. Journal of Polymer Science: Polymer Letters Edition, 1984. **22**(6): p. 372-372.

[8] Allus, M.A., R.G. Brereton, and G. Nickless, The use of experimental design, multilinear regression, ANOVA, confidence bands and leverage in a study of the influence of metals on the growth of barley seedlings. Chemometrics and Intelligent Laboratory Systems, 1989. **6**(1): p. 65-80.

ISBN: 978-81-936820-6-7
Proceedings DOI: 10.21467/proceedings.4

Seismic response of reinforced concrete buildings as predicated by the draft of Libyan standard (DSLS-1977) and (IBC-2009)

Issa. A. Mohammed, Suleiman. A. Khatrush

Department of Civil Engineering, Faculty of Engineering, Benghazi University

DOI: https://doi.org/10.21467/proceedings.4.12

* Corresponding author email: eng.iessa@yahoo.com

ABSTRACT

The draft of suggested Libyan Standard (DSLS-1977) is the only code of practice for designing and construction of earthquake resistant buildings in Libya, was first proposed by the Ministry of Housing in 1977, it is still used by Libyan engineers and several other foreign firms operating in Libya. The draft is suffering from many limitations and shortcomings, it has not been subjected to any development for a long period to be consistent with modern codes. DSLS-1977 divided Libya into 5 hazard zones and suggested a basic model for seismic analysis for regular buildings limited to 40 m high, suggesting linear elastic behavior of the building, and adopting the equivalent lateral force procedure associated with the fundamental mode of vibration for the determination of the resulting base shear force. The assessment and examination of the ability of DSLS-1977 for predicting an appropriate seismic forces for reinforced concrete building system was made by conducting a comparison study with the international building code IBC-2009. Special attention was made to the effect of soil structure interaction involved in the analysis when using IBC-2009 model on the resulting base shear.

KEYWORDS Earthquakes in Libya, seismic analysis, equivalent lateral force procedure soil structure interaction

1 Introduction

Following the earthquake of Al-Marj(1963), Dr. Minaml, the UNESCO expert in anti-seismic engineering was invited to study the damage and to submit a report on the relocation and reconstruction of the town. In that report, Minaml also presented certain recommendations regarding the earthquake resistant regulations for design and construction of buildings and other structures in the Al-Marj region of Cyrenaica and other seismic parts of the country [1]. In 1973, a research programme was started in the civil engineering department of the faculty of engineering university of Tripoli supervised by Professor Mallick to make a seismic study of Libya and to prepare seismic zoning map. Based on the available data on the geology and tectonic structure of the country, fault location, past earthquake history and economic important of the region, Libya has been divided into four earthquake zones, The panel of

experts in the Ministry of Housing in 1977 slightly modified Mallick proposed zoning map of Libya to five zones as shown in figure.1 [2]. And producing, a first draft of a code of practice for designing and construction of earthquake resistant buildings entitled "Criterion and practice for design and construction of earthquake resistant buildings". denoted here as (DSLS-1977). Most of the contents of the proposed standard have been extracted from the Indian Standard Code of Practice, IS-1893-1975 [3].

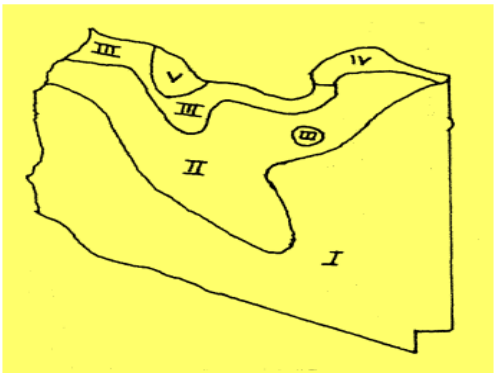

Zone	I	II	III	IV	V
Seismic coefficient	0.01	0.02	0.04	0.05	0.06

Figure.1: *Seismic zoning map adopted proposed by Ministry of Housing* [2].

Al-Geroushi & Ben Amir (1992) proposed a model for the development a Libyan specification for the calculation of seismic loads on the buildings named as (Garyounis model-1). They made a comparison with the proposed Libyan Specification (DSLS) , the forces obtained from the(Garyounis model-1) were found to be larger than the (DSLS) [4].

By mid -1999, a complete final first draft of IBC was assembled and ready to processed through the new procedures of the International Committee Council ICC, the first edition introduced in 2000. Subsequent IBC code editions were introduced in 2003,2006,2009 and 2012.In the IBC ,the seismic zones of the Unified Building Code UBC1997 were replaced by contour maps giving Maximum Considered Earthquake (MCE) spectral response accelerations at short period (S_s) and 1-second (S_1)for class B soil. The probabilistic MCE spectral response accelerations shall be taken as the spectral response acceleration represented by a 5% damping acceleration response spectrum having a 2% probability of ecceedance within a 50-year period.

It is aimed in this work to use the DSLS-1977 model for seismic analysis of building of reinforced concrete moment resisting frame assembly, illustrate the shortcoming in DSLS-1977 using IBC-2009 as a base code, show suitable conditions in order to use Equivalent Lateral Force Procedure of IBC-2009 applied for the Libyan case, and discuss the effect of soil condition and soil structure interaction (SSI).

ISBN: 978-81-936820-6-7
Proceedings DOI: 10.21467/proceedings.4

Series: AIJR Proceedings

2 Static analysis procedures in DSLS -1977 and IBC-2009

The several analytical methods usually adapted for earthquake analysis are mentioned in DSLS-1977, however only detailed steps of, the coefficient method employing equivalent static method ESLF is available. [2],

In the IBC-2009, the American Society of Civil Engineering (ASCE7-2005) remains the primary reference for determining earthquake, snow and wind loads [5], hence the "equivalent lateral force" analysis (ELF) according to ASCE7-2005 may be applied to all structures with S_{Ds} less than 0.33g and S_{D1} less than 0.133g. as well as structures subjected to higher design Spectral response accelerations. If the structures do not meet certain requirement, more sophisticated dynamic analysis procedures must be used otherwise. Table.1 contains the required parameters to be evaluated for the application of the two codes related to the calculated steps for the evaluation of base shear in each case .

Table 1*: Basic requirements of DSLS -1977 and IBC-2009 (Static Analysis)*

Code	DSLS	IBC
Method	ESLF	ELF
Main equation	$V = C\,\alpha_h W$	$V = S_{DS}/(R/I)W$
Seismic Coefficient	α_0 (one value)	S_s & S_1 (contour lines)
Site class	3 Classes (TI,TII&TIII)	5 Classes (S_A, S_B, S_C, S_D & S_E)
Soil coefficient	β_0	F_a & F_v : site coefficient Table 11-4-1& Table 11-4-1
Important factor I	I	I
Time period fundamental period	$T = \frac{0.09\,H}{\sqrt{D}}$ H: height of the structure. D: dimension parallel to flexibility of the structure	$T = C_t\,h_n^x$ h:height ,C_t & x: coefficient Table 12-8-2
Ductility	$C = \frac{0.50}{T^{1/3}}$	response modification factor (R) Table 12-2-1
Limitations of base shear equation	-	$Cs_{max} = S_{DS}/(R/I)$ for $T \le TL$ $Cs_{max} = S_{DS}/(R/I)$ for $T > TL$ $Cs_{min} = 0.01$
Building Height	Not exceeding 40 m	$S_{Ds} < 0.33g$ $S_{D1} < 0.133g$

Seismic weight	W: Total dead load + portion from live load to the frame defined as follow: - if (L.L ≤ 3 KN/m²) portion of L.L =25% if (L.L > 3 KN/m²) portion of L.L = 50%.	W: Total dead load + portion from live load to the frame defined as follow: - in areas used for storage, a minimum of 25 % of the floor live load ere provisions for partitions is required in the floor load design, the actual partition weight or a minimum

3 Application of DSLS-1977 and IBC-2009.

The assessment of Draft of Suggested Libyan Standard (DSLS-1977) is suggested to be carried out by testing its adequacy to produce comparable results with a well known code such as IBC-2009. Prior to IBC code, the Uniform Building Code (UBC 1997) was used in many countries as a code for calculating seismic forces, and Section 1653 Division III Volume II in UBC 1997 used to determine seismic zone for areas outside USA, values for seismic zone for Libya were illustrated in appendix(C) in UBC 1977 [6].

3.1 Considered spectral response acceleration

The most important factors in the use of IBC code was Ss and S_1. In this work , for the sake of comparison and since there are no mapped values available for Libya in the (IBC-2009). After searching, two methods were found to evaluate S_{Ds} and S_{D1} for the regional map of Libya [7].

Method 1

In this method the design spectral response acceleration S_{Ds} and S_{D1} can be calculated using the following
equivalency relationships:-

$S_{Ds} = 2.5\ C_a$ $S_{D1} = C_v$

According to appendix of chapter16 in UBC-1997 Libya and Tripoli are classified as 2A, and according to Table 16-I the seismic coefficient Z equal (0.15) from Tables 16-Q

Table 2: *Values of S_{Ds} and S_{D1} calculated by Method 1*

Seismic Zone	Seismic Zone Factor Z	Soil Type	C_a	C_v	$S_{Ds} = 2.5C_a$	$S_{D1} = C_v$
TRIPOLI 2A Section 1653 Division III Volume II UBC 1997	0.15	S_A	0.12	0.12	0.300	0.12
		S_B	0.15	0.15	0.375	0.15
		S_C	0.18	0.25	0.450	0.25
		S_D	0.22	0.32	0.550	0.32
		S_E	0.30	0.50	0.750	O.50

ISBN: 978-81-936820-6-7
Proceedings DOI: 10.21467/proceedings.4

Series: AIJR Proceedings

and 16-R C_a and C_v can be calculated for each soil type and then calculate S_{Ds} and S_{D1}using the equivalency relationships, the values of S_{Ds} and S_{D1} are presented in Table.2.

Method 2

In this method the values of maximum considered earthquake S_s and S_1 can be obtained from those references which given values of Ss and S_1 for the location outside USA. Table G-1 in reference [8] gives values of S_s and S_1 for Tripoli illustrated in Table.3.

Table 3: *Earthquake loading data at additional locations outside of the united states*

Continent/Region	Country	Base/ City	Ss(%g)	S_1 (%g)	10/50* S_s(%g)	10/50* S_1(%g)
Africa	Libya	Tripoli	57.1	22.9	28.6	11.4

*10/50 it means ground motions with 10% chance of exceedance in 50 years, and the corresponding mean return period (the average number
of years between events of similar severity is 500 year.

these values were used to calculate S_{Ds} and S_{D1} the results are tabulated in Table.4. The comparison between Method 1 and Method 2 are illustrated in Table .5 , it is noticed that the values calculated by method 1 are generally higher and range from 65% to 97% .

Table.4: *Values of S_{Ds} and S_{D1} evaluated by method 2*

10/50 S_s (%g)	10/50 S_1 (%g)	Site class	F_a	F_v	$S_{Ms}= F_vS_s$	$S_{M1}= F_vS_1$	$S_{Ds}=$ 2/3 S_{Ms}	$S_{D1}=$ 2/3 S_{M1}
		S_A	0.8	0.8	0.229	0.091	0.152	0.060
0.286	0.114	S_B	1.0	1.0	0.286	0.114	0.190	0.076
		S_C	1.2	1.69	0.343	0.192	0.228	0.128
		S_D	1.57	2.34	0.449	0.266	0.299	0.177
		S_E	2.38	2.38	0.680	0.394	0.453	0.262

Table 5: *Comparison between Method 1and Method 2 values.*

	Method 1		Method 2	
Site class	S_{Ds} = 2.5 Ca	S_{D1}= Cv	$S_{Ds}=$ 2/3 S_{Ms}	$S_{D1}=$ 2/3 S_{M1}
S_A	0.300	0.12	0.152	0.060
S_B	0.375	0.15	0.190	0.076
S_C	0.450	0.25	0.228	0.128
S_D	0.550	0.32	0.299	0.177
S_E	0.750	0.50	0.453	0.262

3.2 Proposed values

In this work the values evaluated by (Method 2) are adopted. However, based on the values proposed for Tripoli and correlating them with that based on seismic zoning map adopted by Ministry of Housing 1977, using linear interpretation between the zones it became possible to propose an approximate values for the whole zones of Libya as shown in table.6.

The values proposed in this work for Libya was compatible with classification of S_s and S_1 for Region of Seismicity illustrating in reference [9] .Take into consideration Libya classifying as region of low to moderate seismic activity. Housing and Infrastructure Board and its consulting American company referred as (ACEOM) prepare a guidance document and they suggested a zoning map of Libya illustrated in figure 2., and propose a values for S_s and S_1 in each zone [10]. Table .6 showing the comparison of the proposed values in this work and those proposed (ACEOM).

Table.6: *Proposed values of S_s and S_1 and comparison with AECOM values*

LIBYAN MAP ZONE	Values proposed in this work		Values Proposed by AECOM	
	S_s	S_1	S_s	S_1
1	0.0715	0.0285	0.06	0.02
2	0.143	0.057	0.125	0.04
3	0.286	0.114	0.25	0.08
4	0.3575	0.1425	0.31	0.09
5	0.4290	0.171	0.37	0.11

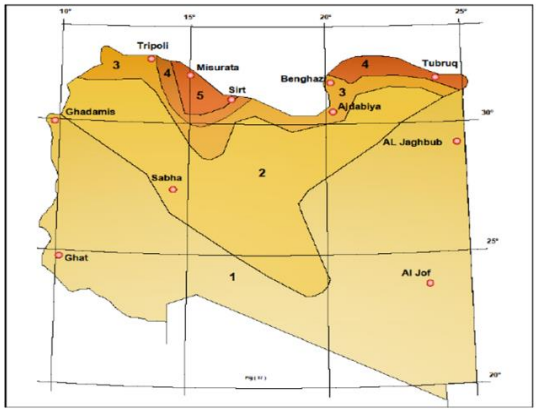

Figure.2. *Libyan map and seismic zones[10].*

ISBN: 978-81-936820-6-7
Proceedings DOI: 10.21467/proceedings.4

4. Case Study

The investigated buildings are located in Tripoli and consist of a multistory reinforced concrete moment resisting frame structure, with an area 7 bays in X-direction 5m center to center and 3 bays in Y-direction 6m center to center. The plan is shown in figure. 3 and elevation heights of 5, 9 and 13 floors are shown in

figure.4. The problem analyzed using both Draft of suggested Libyan standard (DSLS-1977) and the International Building Code (IBC-2009) .

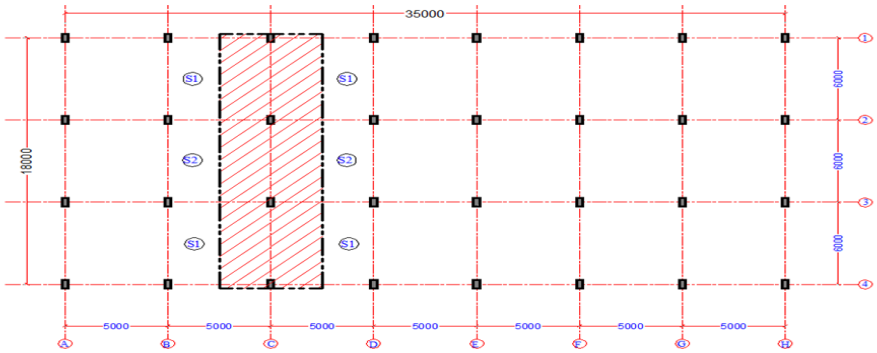

Figure. 3 : *Plan configuration (all dimension in mm)*

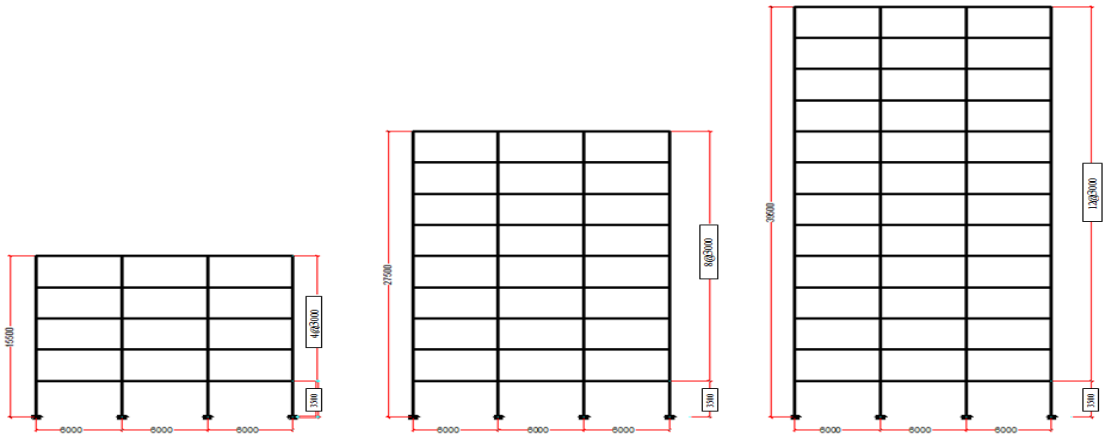

Figure .4: *Elevation configuration (all dimension in mm)*

4.1 Problem description

Element dimensions and planer aspect ratio are selected to satisfy the requirement of both codes for equivalent static analysis, The structures are regular in both vertical and horizontal directions consist of frame system of beams and columns supporting reinforced concrete hollow block slabs of (30 to 35cm) thick and column dimensions (25x60cm) ,(30x70cm) &

(40x80cm) for 5,9 and 13 floors respectively ,the frame spacing is 5m and the type of the foundation condition adopted as raft foundation.

5 Site class consideration

The three types of soil in the Draft of suggested Libyan standard (DSLS- 1977), are corresponding to five types of soil in the International Building Code (IBC-2009) and presented in Table.7 and fairly matching them to allow reasonable comparison between the two codes.

Table 7: *Soil type in DSLS -1977 and corresponding type in IBC-2009*

DSLS- 1977		IBC -2009	
SOIL TYPE	SOIL DESCRIPTION	SOIL TYPE	SOIL DESCRIPTION
-	-	S_A	Hard rock
TYPE (I)	Rock or Hard Soils.	S_B	Rock
TYPE (I)	Rock or Hard Soils.	S_C	Very dense soil and soft rock
TYPE (II)	Medium Soils.	S_D	Stiff soil profile
TYPE (III)	Soft Soils.	S_E	Soft soil profile

5. Base shear calculations

The ground motion parameters required by the two codes for the calculation of base shear using static procedure were derived according to the governing equations previously explained. The calculations are presented in two spread sheets, Table.8 illustrating the base shear evaluated by Equivalent Static Lateral Force (ESLF) stated in (DSLS-1977), the results indicate that the resulting base shear is directly function of height of the building and no effect by the foundation soil. Table.9 illustrating the base shear evaluated by (ELF) and it can be clearly shown that the resulting base shear magnitude is a function of both building height and also significantly affected by foundation soil**.** A general overview of the results show that the base shear produced by IBC-2009 in all cases of greater magnitude than that predicted by DSLS-1977

Table 8*: Base shear calculated by ESLF*

$V_b = C\alpha hW$												
	Step 1	Step2			N	h m	Step3 T sec	Step4 C	Step5 I	Step6 $C\beta I\alpha_o$	Step7 W KN	Step8 V KN
CASE	α_o	*Soil*	Foundation system	β								
5-Storey	0.04	T(I) Rock or Hard soils	Raft	1	5	15.5	0.5	0.6298	1.00	0.0252	34544	870
5-Storey		T(II) Meddium soils	Raft	1			0.5	0.6298	1.00	0.0252	34544	870
5-Storey		T(III) Soft soils	Raft	1			0.5	0.6298	1.00	0.0252	34544	870
9-Storey	0.04	T(I) Rock or Hard soils	Raft	1	9	27.5	0.9	0.5179	1.00	0.0207	62627	1297
9-Storey		T(II) Meddium soils	Raft	1			0.9	0.5179	1.00	0.0207	62627	1297
9-Storey		T(III) Soft soils	Raft	1			0.9	0.5179	1.00	0.0207	62627	1297
13-Storey	0.04	T(I) Rock or Hard soils	Raft	1	13	39.5	1.3	0.4582	1.00	0.0183	90710	1662
13-Storey		T(ID) Meddium soils	Raft	1			1.3	0.4582	1.00	0.0183	90710	1662
13-Storey		T(III) Soft soils	Raft	1			1.3	0.4582	1.00	0.0183	90710	1662

ISBN: 978-81-936820-6-7
Proceedings DOI: 10.21467/proceedings.4

Series: AIJR Proceedings

Table 9: *Base shear calculated by ELF*

$V = S_{DS}/(R/I)$

CASE	Step1	Step2	Step3		Step4				Step5A		Step5B		Step 6	Step 7	Step 8	Step 9							Step 10	Step 11
	Occ Fac	Imp (I)	S_s	S_1	site class	Soil profil name	F_a	F_v	$S_{MS}=F_aS_s$	$S_{M1}=F_vS_1$	$S_{DS}=2/3(S_{MS})$	$S_{D1}=2/3(S_{M1})$			R	h m	Ct	x	T sec	$C_S=S_{DS}/(R/I)$	$C_{S_{max}}=S_{D1}/T(R/I)$	W KN	V KN
5-St	II	1.0	0.2860	0.1140	SA	Hard Rock	0.80	0.80	0.2288	0.0912	0.1525	0.0608	SDCB	SDCB	5	15.5	0.0466	0.90	0.5491	0.0305	0.0221	34544	765
5-St		1.0			SB	Rock	1.00	1.00	0.2860	0.1140	0.1907	0.0760								0.0381	0.0277		956
5-St		1.0			SC	Very dense soil and soft	1.20	1.69	0.3432	0.1927	0.2288	0.1284								0.0458	0.0468		1581
5-St		1.0			SD	Stiff Soil Profile	1.57	2.34	0.4490	0.2668	0.2993	0.1778								0.0599	0.0648		2068
5-St		1.0			SE	Soft Soil	2.38	3.46	0.6807	0.3944	0.4538	0.2630								0.0908	0.0958		3135
9-St		1.0			SA	Hard Rock	0.80	0.80	0.2288	0.0912	0.1525	0.0608			5	27.5			0.9200	0.0305	0.0132	62627	828
9-St		1.0			SB	Rock	1.00	1.00	0.2860	0.1140	0.1907	0.0760								0.0381	0.0165		1035
9-St		1.0			SC	Very dense soil and soft	1.20	1.69	0.3432	0.1927	0.2288	0.1284								0.0458	0.0279		1749
9-St		1.0			SD	Stiff Soil Profile	1.57	2.34	0.4490	0.2668	0.2993	0.1778								0.0599	0.0387		2421
9-St		1.0			SE	Soft Soil Profile	2.38	3.46	0.6807	0.3944	0.4538	0.2630								0.0908	0.0572		3580
13-St		1.0			SA	Hard Rock	0.80	0.80	0.2288	0.0912	0.1525	0.0608			5	39.5			1.2745	0.0305	0.0095	90710	865
13-St		1.0			SB	Rock	1.00	1.00	0.2860	0.1140	0.1907	0.0760								0.0381	0.0119		1082
13-St		1.0			SC	Very dense soil and soft	1.20	1.69	0.3432	0.1927	0.2288	0.1284								0.0458	0.0202		1828
13-St		1.0			SD	Stiff Soil Profile	1.57	2.34	0.4490	0.2668	0.2993	0.1778								0.0599	0.0279		2532
13-St		1.0			SE	Soft Soil Profile	2.38	3.46	0.6807	0.3944	0.4538	0.2630								0.0908	0.0413		3743

5.1 Consideration of soil structure interaction (SSI) by IBC code.

Buildings are subjected to different earthquake loading and behave differently with diversification in the types of soil condition. The process in which the response of the soil influences the motion of the structure and the motion of the structure influences the response of the soil is termed as SSI. In the IBC-2009, and the American Society of Civil Engineering (ASCE7-2005) a methodology for the design of building structure including the effect of soil structure interaction (SSI). The application of this methodology in sequence steps for considering the effect of SSI on base shear values using the equivalent lateral procedure (ELF), are illustrating in Table.10.

Table 10: *Steps for calculating reduction in base shear*

Step	Description	Formula	source
1	Previous parameters	S_{D1}, T ,C_s	Table 9
2	Effective building height and weight	$\bar{h}$: the effective height 0.7 h $\bar{W}$:the effective seismic weight= 0.7 W.	Section 19.2 ASCE 7-05
3	Shear wave velocity	(Vs / Vso),	Table 19-2-1 ASCE 7-05
4	average unit weight of the soils and the average shear wave velocity	Calculated or assumed	Table 19-2-1 ASCE 7-05
5	relative weight density of the structure and soil	$\alpha = \bar{W} / (\gamma A_O h)$	Eqs 19-2-6 ASCE 7-05
6	dynamic foundation stiffness modifier for rocking	α_θ	Table 19-2-2. ASCE 7-05

7	the effective period of the structure	$\overline{T}=T\sqrt{1+\frac{25\propto r_a\bar{h}}{v_s^2T^2}\left(1+\frac{1.12r_a\bar{h}^2}{\propto_\theta r_m^3}\right.}$	Eqs 19-2-5 ASCE 7-05
8	$\overline{Cs}$ using the fundamental natural period of the flexibility supported structure($\overline{T}$)	$\overline{Cs}=\frac{S_{D1}}{T\frac{R}{I}}$	Eqs 12.8-3 ASCE 7-05
9	effective damping factor for the structure-foundation system	$\overline{\beta}=\beta_0\frac{0.05}{(\frac{\overline{T}}{T})^3}$	Eqs 19-2-9 ASCE 7-05
10	reduction in the base shear	$\Delta V=\left[C_s-\overline{C}_s(\frac{0.05}{\overline{\beta}})^{0.4}\right]\overline{W}\leq 0.3W$	Eqs 19-2-2 ASCE 7-05
11	Reduced Base shear	$\overline{V}=V-\Delta V$	Eqs 19-2-1 ASCE 7-05

5.2 Overview of the Results and the effect of SSI.

The general overview of the resulting base shear presented in Table.11 indicate that the values of base shear calculated by IBC-2009 is mostly higher than that which is calculated by DSLS-1977. However, when SSI is considered in IBC-2009, the reduced base shear sometimes becoming lower than DSLS-1977 specifically when soil condition is hard. The values of base shear calculated by IBC-2009 increase when the type of the soil generally change from hard to soft, whereas the values of base shear calculated by DSLS-1977 are not affected by the change of ground condition, this related to the dependency only on the height of structure (Number of floors). However, by taking the base shear values produced by DSLS-1977 as a base for comparing the difference in percent between the results of the two codes, the equation will be in the following form: -

$$\frac{\mathbf{IBC_{value}\text{-}DSLS_{value}}}{\mathbf{DSLS_{value}}}$$

The results are presented in Table 11, they indicate wider range of differences between IBC-2009 and

DSLS-1977 as soil becoming weaker. The percent differences are getting lesser with increasing building height.

For 5-stories case as in Table 11a the percent difference is (9.89) corresponding to soil type T(I)&S_B, and gradually increases to reach (259.2) corresponding to soil type T(III)&S_E. For 9-stories case as in Table 11b the percent difference is (-19.64) corresponding to soil type T(I)&S_B and gradually increases to reach (177.95) corresponding to soil type T(III)&S_E. For 13-stories case as in Table 11c the percent difference is (-34.42) corresponding to soil type T(I)&S_B, and gradually increases to reach (126.85) corresponding to soil type T(III)&S_E. However, by considering the effect of SSI the base shear reduced by considerable amount as shown in Table.11 . For 5-storey case as in Table 11a the percent difference is (-14.88)

ISBN: 978-81-936820-6-7
Proceedings DOI: 10.21467/proceedings.4

Series: AIJR Proceedings

corresponding to soil type T(I)&S_B and gradually increases to reach (152.24) corresponding to soil type T(III)&S_E. For 9-storey case as in Table 11b the percent difference is (-34.75) corresponding to soil type T(I)&S_B, and gradually increases to reach (94.57) corresponding to soil type T(III)&S_E. For 13-storey case as in Table 11c the percent difference is (-54.1) corresponding to soil type T(I)&S_B, and gradually increases to reach (58.79) corresponding to soil type T(III)&S_E, but still keeping higher values than DSLS-1977, except for hard ground condition.

Table 11a: *Comparison of base shear values (DSLS-1977&IBC-2009) for 5-storey*

	DSLS SOIL TYPE	BASE SHEAR DSLS-1977	IBC SOIL TYPE	BASE SHEAR without SSI IBC-2009 (KN)	BASE SHEAR with SSI IBC-2009(KN)	Percent difference without SSI%	Percent difference with SSI %
			S_A HARD ROCK	765	587		
	T(I) ROCK OR HARD SOIL	870	S_B HARD ROCK	956	741	9.89	-14.88
	T(I) ROCK OR HARD SOIL	870	S_C VERY DENSE SOIL	1581	1132	81.72	30.12
	T(II) MEDIUM SOIL	870	S_D STIFF SOIL PROFIL	2068	1448	137.70	66.39
	T(III) SOFT SOIL	870	S_E SOFT SOIL PROFIL	3125	2195	259.20	152.24

Table 11b: *Comparison of base shear values (DSLS-1977&IBC-2009) for 9- storey*

			S_A HARD ROCK	828	580		
	T(I) ROCK OR HARD SOIL	1288	S_B HARD ROCK	1035	725	-19.64	-43.75
	T(I) ROCK OR HARD SOIL	1288	S_C VERY DENSE SOIL	1749	1224	35.79	-4.95
	T(II) MEDIUM SOIL	1288	S_D STIFF SOIL PROFIL	2421	1695	87.97	31.58
	T(III) SOFT SOIL	1288	S_E SOFT SOIL PROFIL	3580	2506	177.95	94.57

Table 11c: *Comparison of base shear values (DSLS-1977&IBC-2009) for 13- storey*

			S_A HARD ROCK	865	606		
	T(I) ROCK OR HARD SOIL	1650	S_B HARD ROCK	1082	757	-34.42	-54.10
	T(I) ROCK OR HARD SOIL	1650	S_C VERY DENSE SOIL	1828	1280	10.79	-22.45
	T(II) MEDIUM SOIL	1650	S_D STIFF SOIL PROFIL	2532	1772	53.45	7.42
	T(III) SOFT SOIL	1650	S_E SOFT SOIL PROFIL	3743	2620	126.85	58.79

The results are also illustrated in graphical form in figure.5 (a,b &,c).

It is clearly shown that the values of base shear calculated by IBC-2009 are generally higher, and is increasing as

ground condition getting softer, this is more pronounced

in the cases without consideration of SSI.

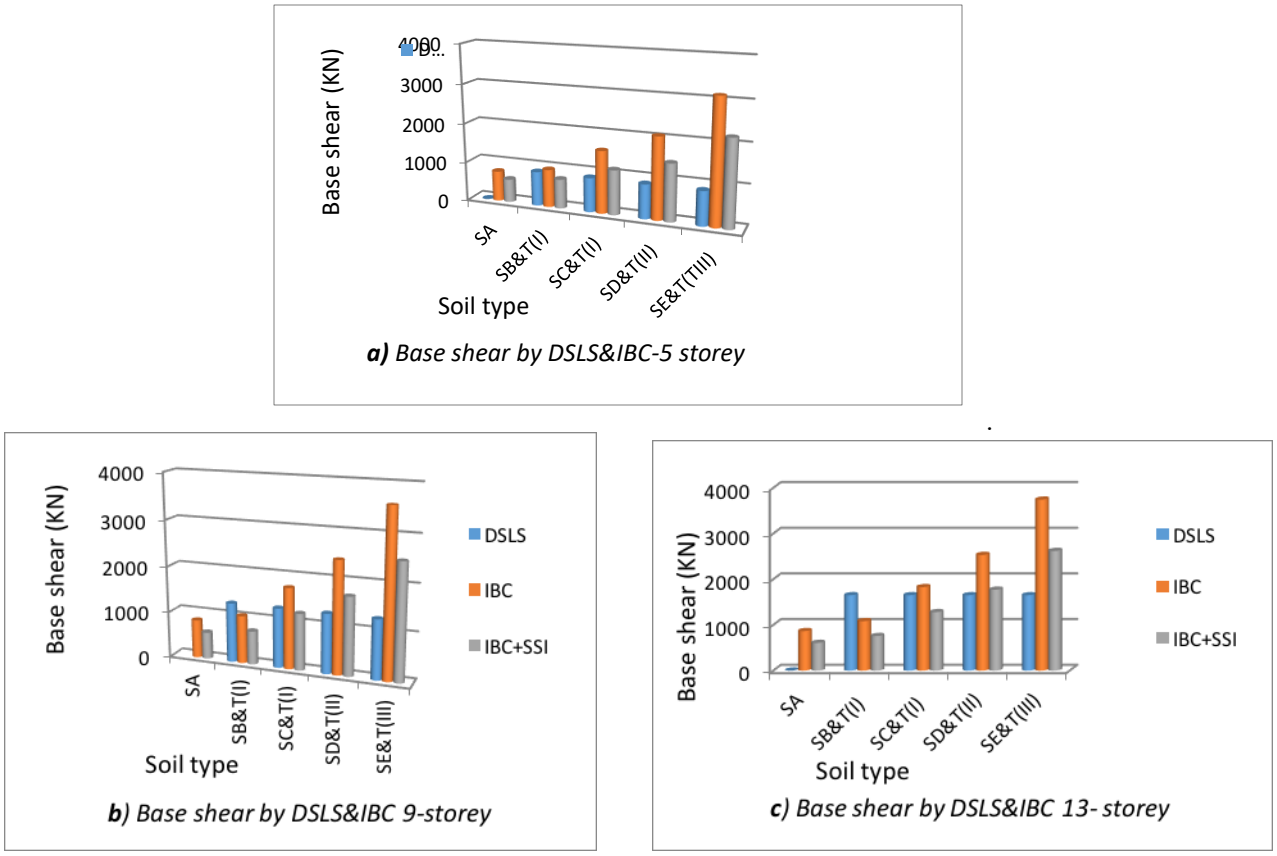

Figure .5: *Base shear calculation by DSLS-1977&IBC-2009 (5,9 and 13 storey)*

6 General Discussion

The present study does not consider many factors related to structural aspects such as irregularity, ductility, structure system etc., It is essentially focused more on building height, soil condition and SSI, nevertheless, the application procedure experienced in this work for both code requirement allow us to encounter several shortcomings in DSLS-1977 that many modern codes have already overcome, such limitations could be responsible for the differences in the obtained results. The study indicate that for all the investigated cases the resulting base shear, calculated by IBC-2009 is generally higher than the values produced by DSLS-1977. Furthermore, the consideration of soil structure interaction (SSI) by the IBC-2009 has a significant effect on the reduction of base shear even though, it is limited to a

ISBN: 978-81-936820-6-7
Proceedings DOI: 10.21467/proceedings.4

Series: AIJR Proceedings

maximum base shear reduction due to SSI to only 30% in order to guarantee conservative solution. Current codes and seismic provisions recognize the important rule that the soil structure interaction (SSI) can play on the seismic response of building structures [11], while in DSLS-1977 there is no addressing of SSI and the foundation soil system under the structure is rigid and hence represents a fixed base condition. The type of the soil in IBC-2009 has great influence in base shear values, while in DSLS-1977 the base shear values are not affected by the change of the soil type.

This is due to the soil condition is expressed by DSLS-1977 in terms of the factor β_o which is constant in case of raft foundation and depends only on the type of foundation rather than the type of soil.

7 Conclusion

This study investigates some aspects of the seismic response of reinforced concrete buildings, with emphasize to the effect of soil structure interaction. Special focus is made to local Libyan situation with the aim of evaluating the results obtained from the application of the proposed Libyan specification DSLS-1977, by conducting a comparison with one of the well-known specifications which widely used, specifically the International Building Code IBC-2009. The proposed Libyan specification DSLS-1977 containing many shortcomings and deficiencies, it is not considering many conditions and important factors which are necessary for conducting seismic analysis. It is not including a clear criteria of structural resisting system , structural aspect , structural configuration and soil condition. Furthermore, no consideration by DSLS-1977 for the effect of soil structure interaction SSI which regarded by the present study as very significant and having an important impact in reducing the base shear especially with low strength foundation soil.

References

[1]. Minami, Kazuo. " *Relocation and reconstruction of the town of Barce, Cyrenaica*, Libya ", damaged by the earthquake of 21 February 1963. Unesco, (1965).

[2]. Mallick, D. V., and S. Y. Barony. "*Earthquake resistant design practice in Libyan Jamahiriya*." Proceedings of the World Conference on Earthquake Engineering. Vol. 7. No. 9. publisher not identified, (1980).

[3]. Jain, Sudhir K. "*Review of Indian seismic code*, IS 1893 (Part 1): 2002." Indian concrete journal 77.11

(2003): 1414-1422.

الجروشى . رجب و بن عامر . محمد (مقترح تطوير المواصفات الليبية لحساب الأحمال الزالزالية على المبانى- نموذج قاريونس1) [4] .

(1993) نوفمبر 27 -30 , طرابلس , المؤتمر الخامس للهندسة الانشائية ,

[5]. Leyendecker, Edgar V., et al. "*Development of maximum considered earthquake ground motion* maps." Earthquake Spectra 16.1 (2000): 21-40.

[6]. Code, Uniform Building. "Volume 2." *Structural engineering design provisions*" (1997).

[7]. S. K. Ghosh, "Seismic ground motion values for locations outside the United States", Civil + Structural engineer.**http://csengineermag.com/artic/seismic-ground-motion-values-for-locations-outside** the united states.

[8]. Unified facilities criteria (UFC), "Structural Engineering", UFC 3-301-01,27 January (2010).

[9]. Department of Veterans Affairs, H-18-8, Office of Construction& Facilities Management, Strategic Management Office "Seismic design requirements." February (2011)**.**

[10]. Guidance Document, "*Design Criteria for Housing Projects, Housing and Infrastructure Board* ", Program Management Department, June (2009).

[11]. Nikolettos, G. S., and C. C. Spyrakos. "*Seismic analysis and design of building structures including* SSI." WIT Transactions on The Built Environment 41 (1970).

ISBN: 978-81-936820-6-7

Series: AIJR Proceedings
Proceedings DOI: 10.21467/proceedings.4

Nonlinear Structural Dynamic Response of Multi-Story Buildings Under Seismic Loading

Awatif Othman Twil

Department of Civil and Structural, Engineering, Gharyan University, Libya

DOI: https://doi.org/10.21467/proceedings.4.13

* Corresponding author email: Eng_awatif@yahoo.com

ABSTRACT

A study of earthquakes in the world is performed, and also a study of methods of dynamic analysis suitable for use with linear and nonlinear systems is made with a stress on the nonlinear response of buildings due to moderate or high seismic loading.

The response of a building to a seismic load severe enough may induce inelastic deformations and the building behavior is expected to be nonlinear. Consequently, it is necessary to develop a method of analysis suitable for use with nonlinear systems. A step-by-step method is well suited to the analysis of nonlinear systems rather than using the method of superposition. The total structural response is due to each response contribution within the step. The Wilson-θ method is the step- by- step unconditionally stable method which is used for this aspect of nonlinear dynamic analysis and it is introduced in the present work.

Keywords— Large earthquake; nonlinear system; unconditionally stable.

1 Introduction

About 50,000 earthquakes occur annually over the entire earth, approximately 100 are of sufficient size to produce substantial damage if their centers are near areas of habitation. When a large earthquake occurs it may induce inelastic deformations and the building behavior is expected to be nonlinear. It is important to note that linear response analysis, whether formulated in the time domain or in the frequency domain involves the evaluation of many independent response contributions that are combined to obtain the total response. Hence, superposition technique is employed.

These methods employed only superposition method for linear systems. Neither one of them is suited for use in the analysis of nonlinear systems.

The step-by-step method is only conditionally stable and for numerical stability of the solution may require such an extremely small time step as to make the method impractical if not impossible. The Wilson-θ method serves to assure the numerical stability of the solution process regardless of the magnitude selected for the time step. For this reason, such a method is *unconditionally* stable. [1] [4] [6]

2 Linear and Nonlinear Behavior of Materials

Linear behavior is always elastic while nonlinear material behavior may be elastic or inelastic. If the spring is elastic then its force-displacement line or curve will follow the same curve, in unloading case as shown in Figures 1 and 2.

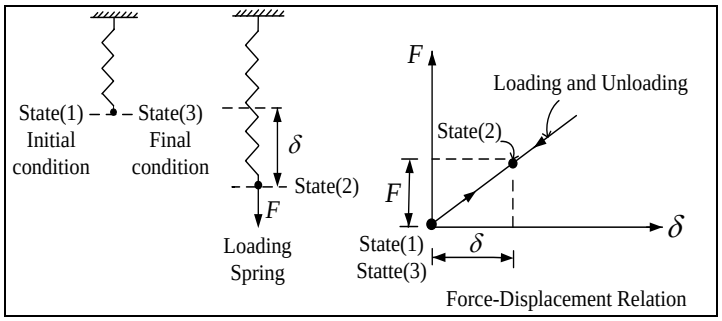

Figure 1: Linear spring: Elastic behavior

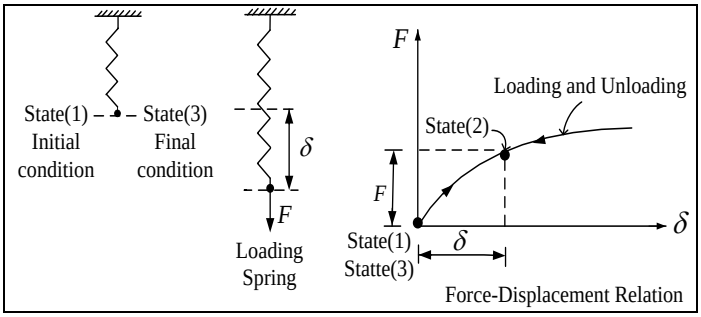

Figure 2: Nonlinear spring: Elastic behavior

If the material is inelastic and nonlinear as shown in Figure 3. Then in case of unloading, it does not follow the loading curve but follows a line parallel to the initial tangent of the loading curve. Permanent deformation δ^* will result.

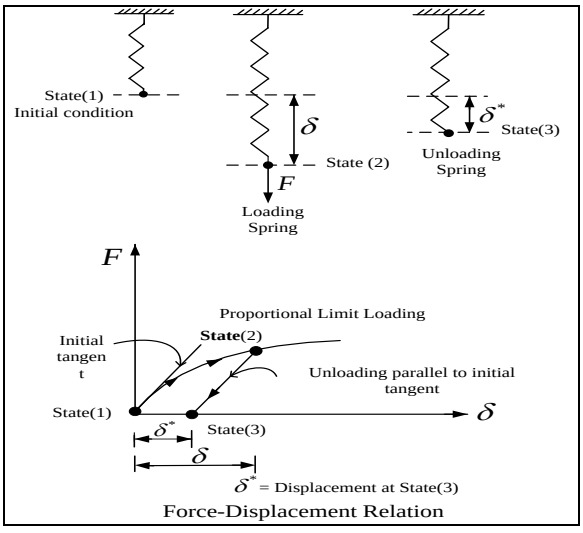

Figure 3: Nonlinear spring: Inelastic behavior

ISBN: 978-81-936820-6-7
Proceedings DOI: 10.21467/proceedings.4

3 Linear and Nonlinear Behavior of Structures

Linear and nonlinear behavior of springs, under loading conditions are shown in the following two examples:

A. Linear Springs

Linear spring behaves linearly under loading conditions. Loading sequence is not important in case of linear material as shown in Figure 4. The resulting displacement is the same.

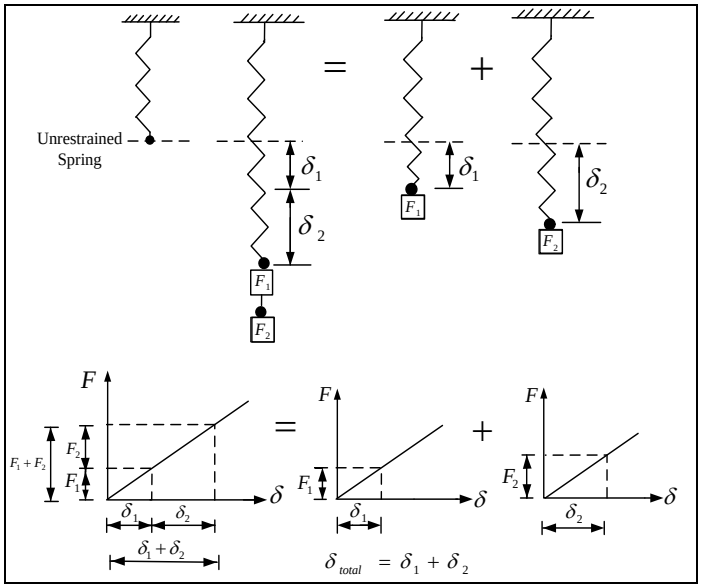

Figure 4: Superposition method applies to linear systems

Loading history is not relevant to the effect of a particular force. For example, force F_2 will always cause the same displacement δ_2 , no matter what loads are placed on the spring before it is applied.

B. Nonlinear Springs

Nonlinear spring is shown in Figure 5 the addition of loading does not result in the same effect in terms of displacements. Here, the effect of the forces F_1 and F_2 when applied together is not the same as the sum of the effects of these forces when each of them is applied separately. Therefore, superposition is not applicable to nonlinear springs. Loading history is relevant to the effect of a particular loading. The displacement due to a given load depends on the total force that is presently acting on a structure system or spring. Hence, superposition does not apply to nonlinear springs, which have the nonlinear force-displacement relationship.

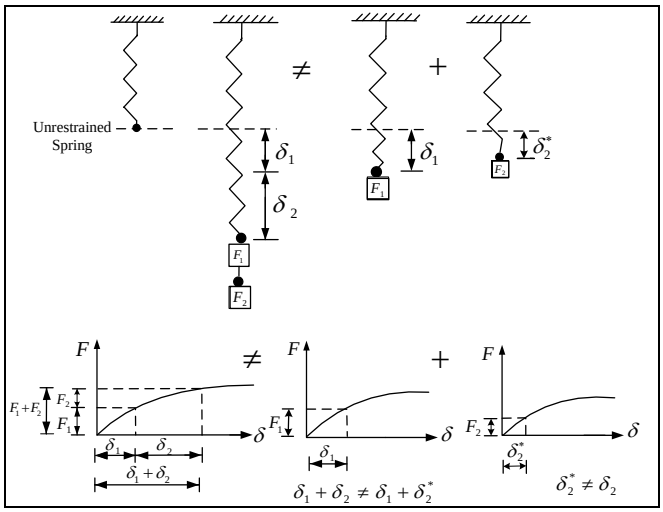

Figure 5: Superposition method does not apply for nonlinear systems

There are many important classes of structural dynamic problems which cannot be assumed to be linear. The response of a building to a seismic load severe enough to induce inelastic deformations makes the building behavior nonlinear.

The step-by-step linear acceleration method is well suited to the analysis of nonlinear systems. The response for each time step is an independent analysis problem, and there is no need to combine response contributions within the step. This method is an explicit solution which is only *conditionally stable* and for numerical stability of the solution may require such an extremely small time step. The modification introduced to the method by Wilson serves to assure the numerical stability of the solution process regardless of the magnitude selected for the time step. For this reason, such a method is *unconditionally stable* and is suitable for this aspect for nonlinear dynamic analysis. [1] [4] [6]

4 Wilson-θ Method

The basic assumption of the Wilson-θ method is that the acceleration varies linearly over the time interval from t to $t+\theta\Delta t$ where $\theta \geq 1.0$. The value of the factor θ is determined to obtain optimum stability of the numerical process and accuracy of the solution. It has been shown by Wilson that for $\theta \geq 1.38$, the method becomes unconditionally stable. [6] [7]

Using the difference between dynamic equilibrium conditions defined at time t_i and $t_i+\tau$, where $\tau = \theta\Delta t$, we obtain the incremental equations

$$M\hat{\Delta}\ddot{u}_i + C(\dot{u})\hat{\Delta}\dot{u}_i + K(u)\hat{\Delta}u_i = \hat{\Delta}P_i \tag{1}$$

In which the circumflex over Δ indicates that the increments are associated with the extended step $\tau = \theta\Delta t$. Thus

$$\hat{\Delta}u_i = u(t_i+\tau) - u(t_i) \tag{2}$$

ISBN: 978-81-936820-6-7
Proceedings DOI: 10.21467/proceedings.4

Series: AIJR Proceedings

$$\hat{\Delta}\dot{u}_i = \dot{u}(t_i + \tau) - \dot{u}(t_i) \tag{3}$$

$$\hat{\Delta}\ddot{u}_i = \ddot{u}(t_i + \tau) - \ddot{u}(t_i) \tag{4}$$

$$\hat{\Delta}P_i = P(t_i + \tau) - P(t_i) \tag{5}$$

The stiffness coefficient and damping coefficient are obtained for each time step

$$K_{ij} = dF_{Si}/du_j \tag{6}$$

$$C_{ij} = dF_{Di}/d\dot{u}_j \tag{7}$$

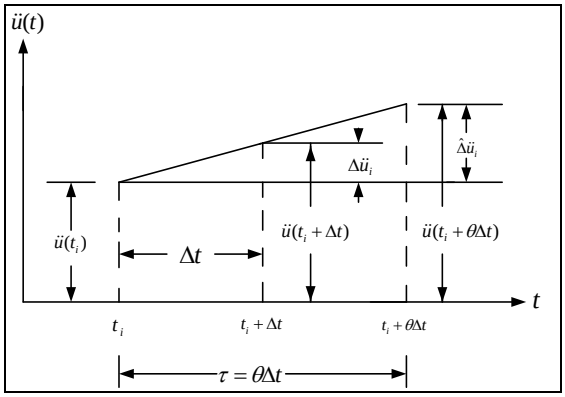

Figure 6: Linear acceleration assumption in the extended time interval.

From Figure 6, we can write the linear expression for the acceleration during the extended time step as

$$\ddot{u}(t) = \ddot{u}_i + \frac{\hat{\Delta}\ddot{u}_i}{\tau}(t - t_i) \tag{8}$$

In which $\hat{\Delta}\ddot{u}_i$ is given by (4), integrating (8) twice yields

$$\dot{u}(t) = \dot{u}_i + \ddot{u}_i(t - t_i) + \frac{1}{2}\frac{\hat{\Delta}\ddot{u}_i}{\tau}(t - t_i)^2 \tag{9}$$

$$u(t) = u_i + \dot{u}_i(t - t_i) + \frac{1}{2}\ddot{u}_i(t - t_i)^2 + \frac{1}{6}\frac{\hat{\Delta}\ddot{u}_i}{\tau}(t - t_i)^3 \tag{10}$$

Evaluation of (9) and (10) at the end of the extended interval $t = t_i + \tau$ gives

$$\hat{\Delta}\dot{u}_i = \ddot{u}_i\tau + \frac{1}{2}\hat{\Delta}\ddot{u}_i\tau \tag{11}$$

$$\hat{\Delta}u_i = \dot{u}_i\tau + \frac{1}{2}\ddot{u}_i\tau^2 + \frac{1}{6}\hat{\Delta}\ddot{u}_i\tau^2 \tag{12}$$

Equation (12) is solved for the incremental acceleration $\hat{\Delta}\ddot{u}_i$ and substituted in (11), we obtain

$$\hat{\Delta}\ddot{u}_i = \frac{6}{\tau^2}\hat{\Delta}u_i - \frac{6}{\tau}\dot{u}_i - 3\ddot{u}_i \tag{13}$$

$$\hat{\Delta}\dot{u}_i = \frac{3}{\tau}\hat{\Delta}u_i - 3\dot{u}_i - \frac{\tau}{2}\ddot{u}_i \tag{14}$$

Substituting (13) and (14) into (1), results in an equation for the incremental displacement $\hat{\Delta}u_i$ which may be conveniently written as

$$\overline{K}_i\hat{\Delta}u_i = \hat{\Delta}\overline{P}_i \tag{15}$$

where

$$\overline{K}_i = K_i + \frac{6}{\tau^2}M + \frac{3}{\tau}C_i \tag{16}$$

$$\hat{\Delta}\overline{P}_i = \hat{\Delta}P_i + M(\frac{6}{\tau}\dot{u}_i + 3\ddot{u}_i) + C_i(3\dot{u}_i + \frac{\tau}{2}\ddot{u}_i) \tag{17}$$

To obtain the incremental acceleration $\hat{\Delta}\ddot{u}_i$ for the extended interval, the value of $\hat{\Delta}u_i$ obtained from the solution of (15) is substituted into (13). The incremental acceleration $\Delta\ddot{u}_i$ for the normal time interval Δt is then obtained by a simple linear interpolation

$$\Delta\ddot{u} = \hat{\Delta}\ddot{u}/\theta \tag{18}$$

To calculate the incremental velocity $\Delta\dot{u}_i$ and incremental displacement Δu_i corresponding to the normal interval Δt use is made of (11) and (12) with the extended time interval parameter τ substituted for Δt, that is

$$\Delta\dot{u}_i = \ddot{u}_i\Delta t + \frac{1}{2}\Delta\ddot{u}_i\Delta t \tag{19}$$

$$\Delta u_i = \dot{u}_i\Delta t + \frac{1}{2}\ddot{u}_i\Delta t^2 + \frac{1}{6}\Delta\ddot{u}_i\Delta t^2 \tag{20}$$

The displacement u_{i+1} and velocity $\dot{u}_{i+1}$ at the end of the normal time interval are calculated by

$$u_{i+1} = u_i + \Delta u_i \tag{21}$$

$$\dot{u}_{i+1} = \dot{u}_i + \Delta\dot{u}_i \tag{22}$$

The initial acceleration for the next step should be calculated from the condition of dynamic equilibrium at time $t + \Delta t$, thus

$$\ddot{u}_{i+1} = M^{-1}\{P_{i+1} - C_{i+1}\dot{u}_{i+1} - K_{i+1}u_{i+1}\} \tag{23}$$

5 Earthquake Applications

El Centro of 1940 Earthquake Excitation Cases of Study

The excitation data were obtained from the acceleration original record of the first second for El Centro earthquake of 1940 shown in Table 1. And the plot of this record is shown in Figure

ISBN: 978-81-936820-6-7
Proceedings DOI: 10.21467/proceedings.4

Series: AIJR Proceedings

7. Note that the ground acceleration is varies with time in units of g, where g is the gravitational acceleration $\left(g = 386\,in/\sec^2\right)$. [6]

Table 1: The acceleration record for El Centro earthquake of 1940. [6]

t,sec	$\ddot{u}_g(t), g$	t,sec	$\ddot{u}_g(t), g$	t,sec	$\ddot{u}_g(t), g$
0.000	0.1080	0.429	-0.0237	0.872	-0.0232
0.221	0.0189	0.665	0.0138	0.997	-0.0789
0.374	0.020	0.794	-0.0568	0.161	-0.0001
0.623	0.0094	0.946	-0.0603	0.332	-0.0012
0.789	-0.0387	0.097	0.0159	0.581	0.0425
0.941	-0.0402	0.291	0.0059	0.725	-0.0256
0.042	0.0010	0.471	0.0076	0.877	-0.0343
0.263	0.0001	0.72	-0.0088	1.066	-0.0666

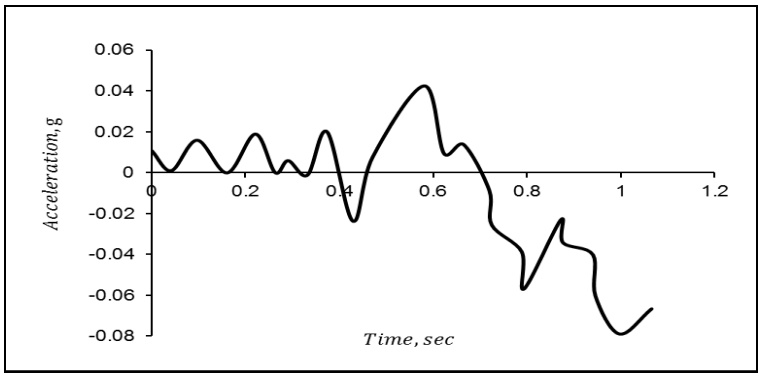

Figure 7: The acceleration record for El Centro earthquake of 1940.

Application 1: Elastic Multi Degree of Freedom System

The analysis of a two-story building system shown in Figure 8. under the effect of the same earthquake. The excitation data were scaled down from the acceleration record for El Centro earthquake of 1940 by a factor of a half, as shown in Table 1. The plastic moment for the columns on the first or second story is $M_P = 154.942\ \ kip.in$.

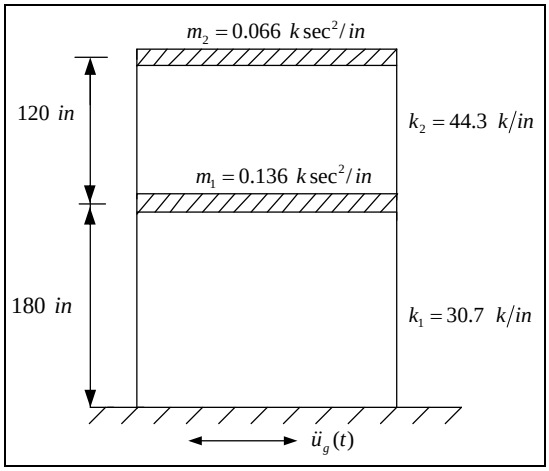

Figure 8: Two-story shear building under earthquake load.

Application 2: Elastoplastic Multi Degree of Freedom System

The analysis of a multi-story building system shown in Figure 8 with elastoplastic behavior. The input data for application (2) is the same as the input data for application (1), but the excitation data for El Centro earthquake of 1940, is used without reduction as listed in Table1.

The Wilson- θ method was used as the method of analysis for applications (1) and (2).

The results for application (1) are plotted in Figures 9 and 10 for stories (1) and (2) respectively. And for application (2) are plotted in Figures 11 and 12 for story 1 and story 2 respectively.

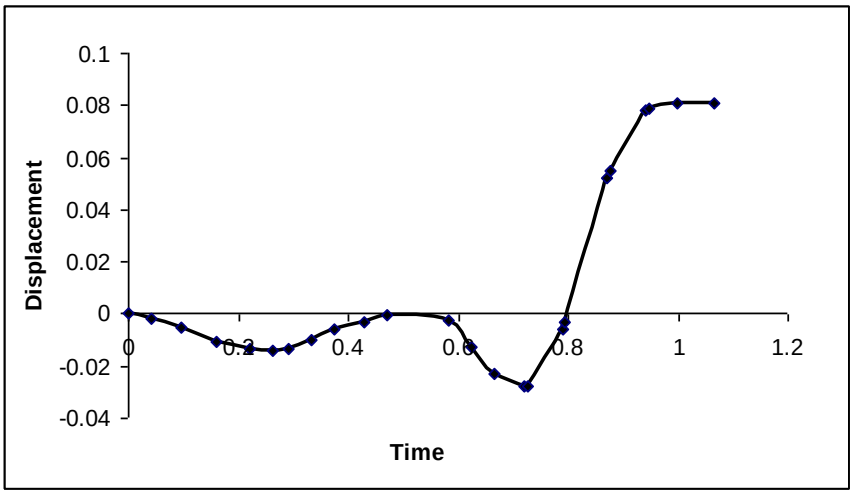

Figure 9: Displacement for earthquake application (1), elastic behavior for Story 1.

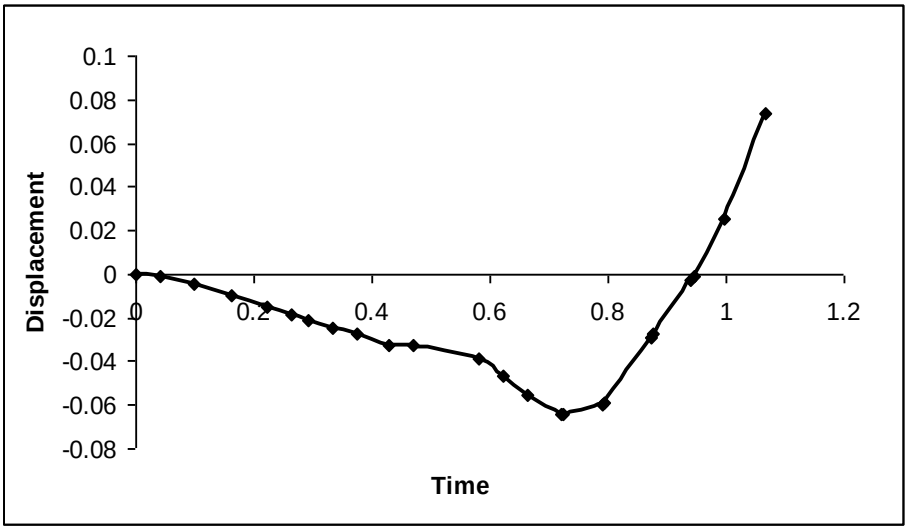

Figure 10: Displacement for earthquake application (1), elastic behavior for Story 2.

ISBN: 978-81-936820-6-7
Proceedings DOI: 10.21467/proceedings.4

Series: AIJR Proceedings

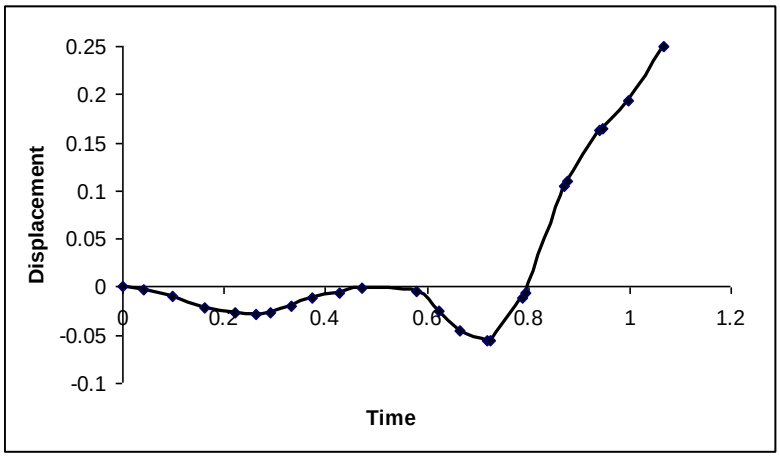

Figure 11: Displacement for earthquake application (2), elastoplastic behavior for Story 1.

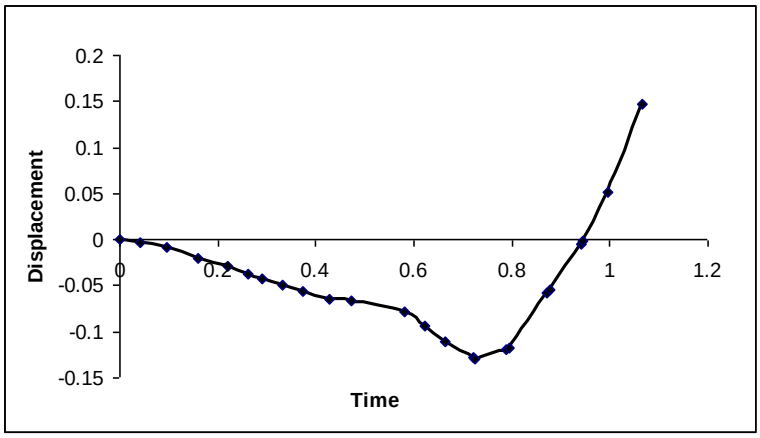

Figure 12: Displacement for earthquake application (2), elastoplastic behavior for Story 2.

Comparison between elastic and elastoplastic displacement response for story (1) and (2) are given in Figures 13 and 14 respectively.

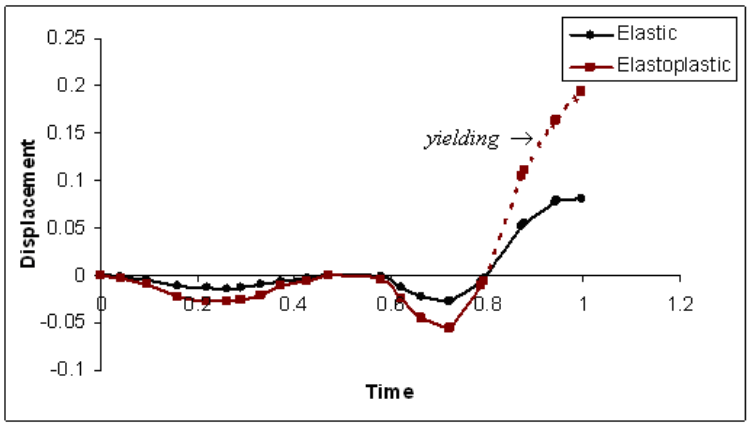

Figure 13: Comparison of elastoplastic behavior with elastic displacement response, story 1 for El Centro earthquake (applications 1 and 2).

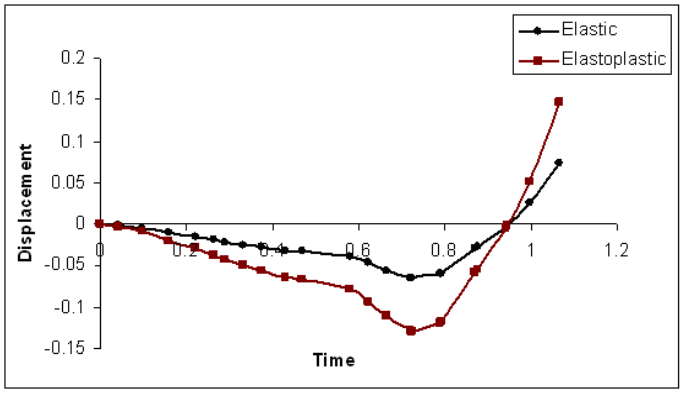

Figure 14: Comparison of elastoplastic behavior with elastic displacement response, story 2 for El Centro earthquake (application 1 and 2).

6 Conclusion

Nonlinear behavior of structures may be due to the inherent nonlinear stress-strain relationship of the material which is called material nonlinearity or due to the changes to geometry (dimensions and configuration) caused by the load, which is called geometrical nonlinearity. The Wilson-θ method as an unconditionally stable method, serves to assure the numerical stability of the nonlinear solution process regardless of the magnitude selected for the time step. For this reason, Wilson-θ method was chosen as unconditionally stable method for this aspect of nonlinear dynamic analysis. The basic assumption of the Wilson-θ method is that the acceleration varies linearly over the extended interval $\tau = \theta\Delta t$ in which $\theta \geq 1.38$ for unconditional stability.

References

[1] Anil K. Chopra, "Dynamics of Structures ", Second Edition, Pearson Education, 2003.
[2] Alan Weary, "Designer's Guide to the Dynamic Response of Structures", 1997.
[3] Ray W. Clough and Joseph Penzien, "Dynamics of Structures ", McGraw Hill, First Edition, 1975.
[4] Ray W. Clough and Joseph Penzien "Dynamic of Structures ", Computers and Structures, Second Edition, 2003.
[5] Norman B. Green, "Earthquake Resistant Building and Construction", Litton Educational Publishing, 1978.
[6] Mario Paz, "Structural Dynamics ", Van Nostrand Reinhold Environmental Engineering Series, 1980.
[7] Mario Paz, "Structural Dynamics ", Van Nostrand Reinhold Environmental Engineering Series, 1985.

ISBN: 978-81-936820-6-7
Proceedings DOI: 10.21467/proceedings.4

Investigations of Kaolin Clay Collapse Behavior Using an Oedometer Apparatus

Musbah A. Hasan*, Gumaa Abdelazizi Hasan

Department of Civil Engineering, College of Engineering, Sirte University, Libya

DOI: https://doi.org/10.21467/proceedings.4.14

* Corresponding author email: abormila@gmail.com

ABSTRACT

Geotechnical engineers face serious problems when construction sites contain collapsible soils, which are known by their strength when dry and experience sudden excessive settlement when inundated. Response-to-wetting oedometer tests can be used to obtain estimates of collapse settlements of structures founded on collapsible soil deposits. Generally, the collapsibility of soils is governed by the amount of water within the sample and the magnitude of the applied pressure. In this paper, an experimental study was performed, by using the one-dimensional compression test (single and double oedometer tests), to investigate the effect of the change in initial water content (IWC) and void ratio on the collapse potential of kaolin clays upon wetting. The test results confirmed that, the collapse potential value decreases with the decrease of initial void ration at a low vertical load increment. However, for the samples with different initial water content, the increase of initial water content leads to a decrease of the collapse potential values.

Keywords: Collapse potential, Kaolin clay, Water content, Void ratio, Oedometer test.

1 Introduction

When the soil has a collapsible grain structure, it can be defined as a soil that can resist moderately large applied stresses with a low value of settlement at a small amount of water content. However, a significant reduction in volume can be observed with the increase of water content, as the applied stresses remain constant. Collapsibility is limited not only to cohesive soils, but also to some cohesionless soils and constructed fills, where the collapse can occur suddenly as a result of the increase of moisture content, as the total vertical stress remains constant (M. Reznik, 2007). As is known, the density of soil plays a main role in the effect of soil collapsibility; i.e. porous fills and soils collapse once it is subjected to loads smaller than the denser fills or soils. However, in many countries, it appears, according to some official documents such as that of Rookovodstvo (1977), that the engineers and designers focus only on the effect of moisture content on soil collapsibility. The document (Rookovodstvo, 1977) designates the value of moisture content and vertical loads at which the loaded soil starts collapsing, as initial collapse moisture content and initial collapse pressure respectively. Once

 ISBN: 978-81-936820-6-7

the applied load exceeds the initial collapsible pressure specified for particular values of water content and void ratio, the collapse of soil can be noticed. (Vilaret al., 1998) studied the collapse behaviour of a compacted lateritic soil by using the conventional loading−wetting oedometer tests and suction-controlled tests. The influence of dry unit weight, moulding water content and overburden stress on collapse strains is analyzed, and it is shown that the drier samples were the most susceptible to collapse upon wetting. The bearing capacity of collapsible soils decreased to about 50% due to soaking process, hence, the author recommends using twice the factor of safety stated in different codes to account the soaking effect in collapsible soils. The bearing capacity of collapsible soils when compacted to 95% of its dry density is larger than that of natural soil by about 24–30%. For both undisturbed and compacted soil samples, as the initial water content increases the collapse potential of soil decreases (K.E.Gaaver 2012). For the same moisture content, the collapse potential decreases when increasing the degree of compaction. Conversely, it increases in the case of soils where the percentage in fine particles is high. Also, with the same energy of compaction, the collapse decreases when increasing the moisture content and this is valid for water, and oil. Conversely, it grows in the case of soils containing more fines. The collapse by water flooding is the fastest and the most accentuated more than that oil. This is valid for all energies of compaction and moisture contents and at any moment (Rachid et al., 2010). Pre-wetting with applying the dynamic compaction at the same time will result in higher efficiency for the compaction. The determination of the most favourable moisture content is required, because the compaction of soils at upper moisture contents can lead to liquefaction, which can cause stopping of volume reduction (Kenneth et al., 1993).

2 Experimental Programe

Nine one-dimensional oedometer tests were performed on compacted soil specimens in order to study the influence of initial water content (IWC) and the initial void ratio on collapsibility of kaolin clay. In addition, specimens were saturated at different applied stresses and the amount of collapse deformation was measured.

Table 1. *Laboratory testing program*

Test type	Test Number	Initial Water Content w (%)	Saturated at	Void Ratio (e)
Double Oedometer test	1	10	-	2
	2	10	5KPa	2
	3	10	-	1.7
	4	10	5KPa	1.7
	5	20	-	2
	6	20	5KPa	2
Single Oedometer test	7	10	100KPa	2
	8	10	100KPa	1.7
	9	20	100KPa	2

ISBN: 978-81-936820-6-7
Proceedings DOI: 10.21467/proceedings.4

Series: AIJR Proceedings

2.1 Physical properties of soil

Tests were performed on specimens of kaolin clay to determine its physical properties. The kaolin clay was supplied by Whitfield & Son Ltd., England. Properties of the material were obtained according to (BS) standard. Compaction tests on the soil samples were carried out in accordance with the Standard Proctor test procedure, BS 1377. The maximum dry unit weight of kaolin clay was found to be 15.58 kN/m3 and the corresponding optimum moisture content was about 23.8%. Determination of the distribution of the silt/clay particles was achieved using a hydrometer test, BS 1377. Table 2. summarizes the recorded geotechnical properties obtained from liquid limit, plastic limit, hydrometer, specific gravity and compaction tests. Also, the tested soil sample was classified as (MH) according to the Unified Soil Classification System (USCS).

Table 2. *Physical properties of kaolin clay:*

Liquid limit: %	**Plastic limit: %**	**Specific gravity**	**Silt fraction: %**	**Clay fraction: %**	**Soil classification**	**Maximum dry density, γ_{dmax} (kN/m^3)**	**Optimum water-content: %**
0.088**55.0**	31.4	2.64	58	42	MH	15.57	23.8

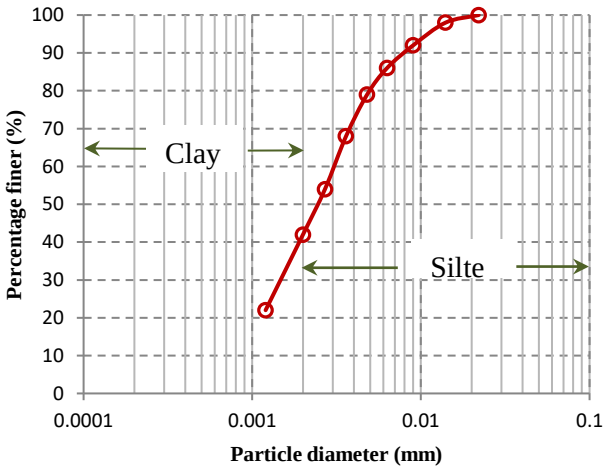

Figure 1. *Kaolin clay particle size distribution curve*

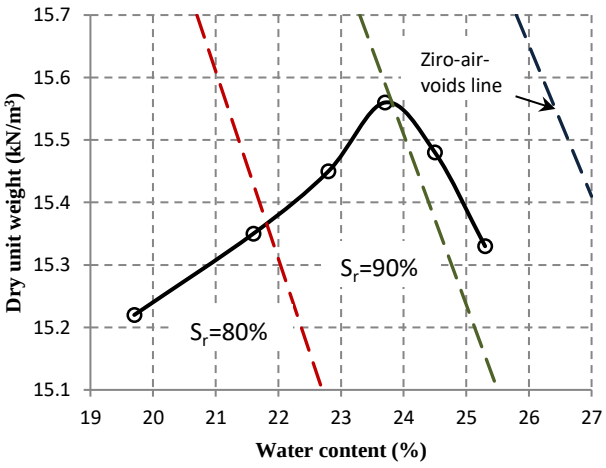

Figure 2. *Standard Proctor compaction curve*

2.2 Sample preparation

Soil specimens of kaolin clay were prepared by compacting moist soil, having a predetermined water content of (10 and 20 %) and an initial void ratio of (1.7 and 2), into an oedometer apparatus metal ring as shown in Figure 3. The soil was compacted into the metal ring using a small hammer. Change in the specimen initial water content, when the test is running, was prevented by cealing the odometer cell with a plastic sheet as illustrated in Figure 4. For the

present investigation four groups of soil specimens were prepared, each group has a certain initial water content and void ratio. Table 1 shows the initial condition of the soil specimens.

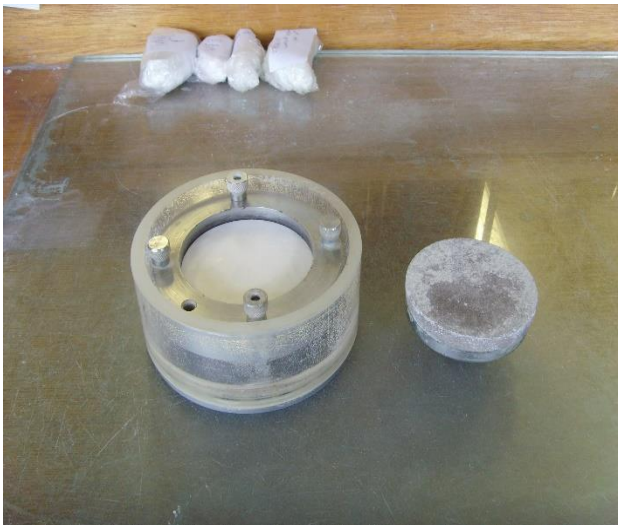

2.3 Oedometer Test Procedure:

A mass of kaolin clay is placed in the oedometer ring and allowed to reach equilibrium under a small hunger load. A series of load increments (5, 25, 50, 100 and 200 KPa) were applied and the dial gauge reading is recorded at the beginning and after equilibrium is reached for each load increment. The next load is applied and the changing of dial gauge reading is recorded once the entire consolidation is achieved. Inundation of the tested samples is taken place at 5 and 100 kPa load increment for double and single oedometer tests respectively. In this paper, the determination of collapse potential was calculated by taking the difference in volumetric strain (%) between the as-compacted and inundated specimens using Equation (1), by conducting the double and single oedometer tests considering different soil conditions in terms of the moisture content and void ratio, (BS 1377: Part 5: 1990).

$$CP = \left(\frac{e_i - e_f}{1 + e_o} \right) \tag{1}$$

Where CP = the collapse potential, e_o = the initial void ratio, e_i = the void ratio caused by the applied load at constant water content and e_f = the void ratio caused by the applied load after saturation.

3 Results and Discussion

3.1 Influence of initial water content

Figure 5 compares the compression curves of double oedometer tests at different initial water contents (IWC) of (10 and 20%). Soil specimen inundated at 5 kPa and subsequently loaded in the soaked condition up to 200 kPa. The magnitude of collapse in the specimen when (IWC

ISBN: 978-81-936820-6-7
Proceedings DOI: 10.21467/proceedings.4

Series: AIJR Proceedings

= 10%) is higher than that when (IWC = 20%). Where, the reduction in void ratio at vertical stress of 100 kPa was about 39 % higher when the initial water content increases from 10 to 20%. Figure 6 shows a similar comparison between compression curves using a single oedometer test for two moist kaolin clay specimens inundated at 100 kPa. On wetting, the specimens collapse would increase approximately (28%) as the initial water content decreased from 20 to 10% at a vertical stress of 100 kPa. This could be attributed to, a portion of the fine-grained fraction of the soil exists as bonding material for the larger-grained particles. These bonds undergo local compression in the small gaps between adjacent grains. Therefore, these soils compress slightly at low moisture contents due to increase of pressures.

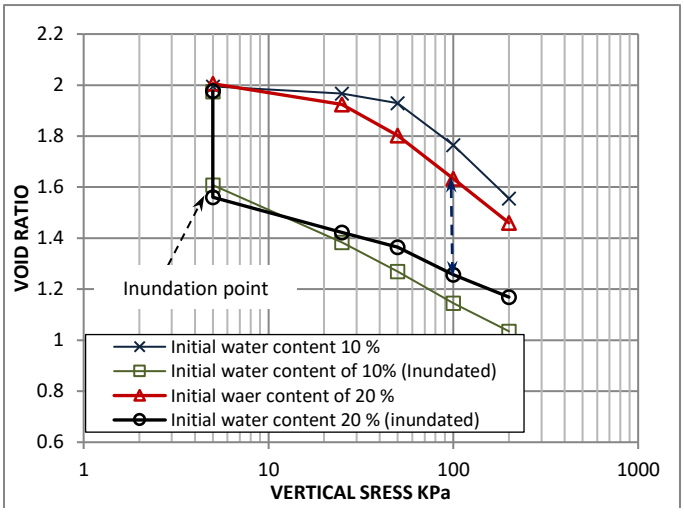

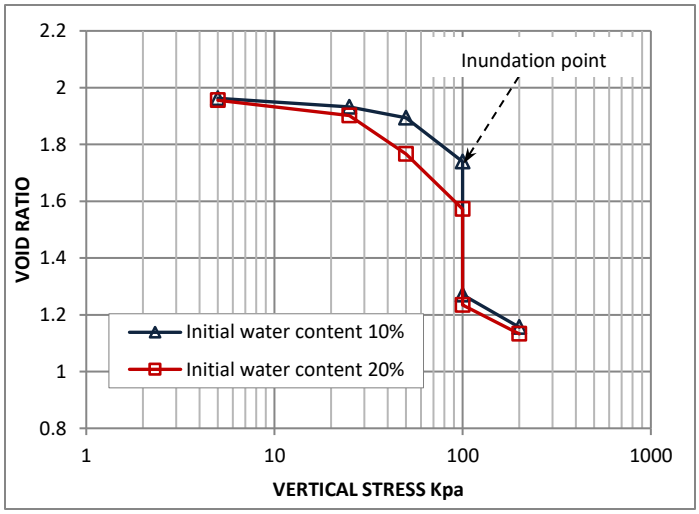

When a collapsible soil is allowed to moisture, the fine binder that is providing the bonding mechanism between the large-grained particles will soften, weaken, and/or dissolve to some extent. Therefore, increasing the value of initial water content leads to the bonding materials start to gradually deteriorate. Consequently, a part of these bonds will undergo an earlier destruction prior to inundation.

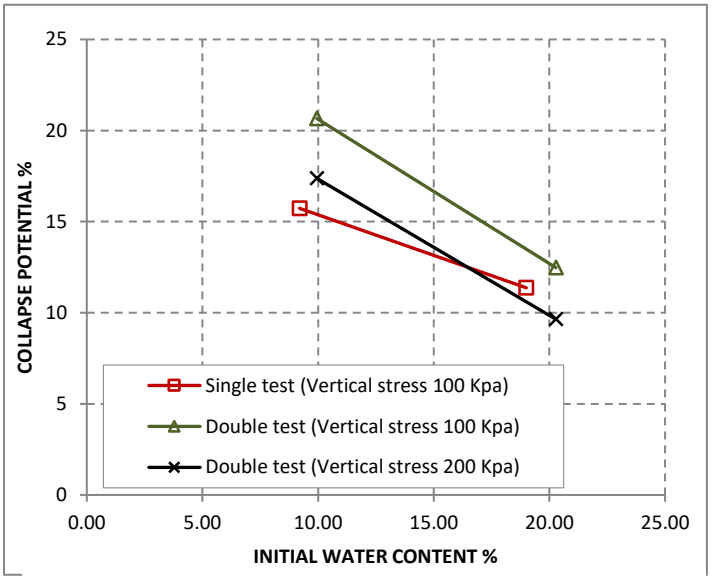

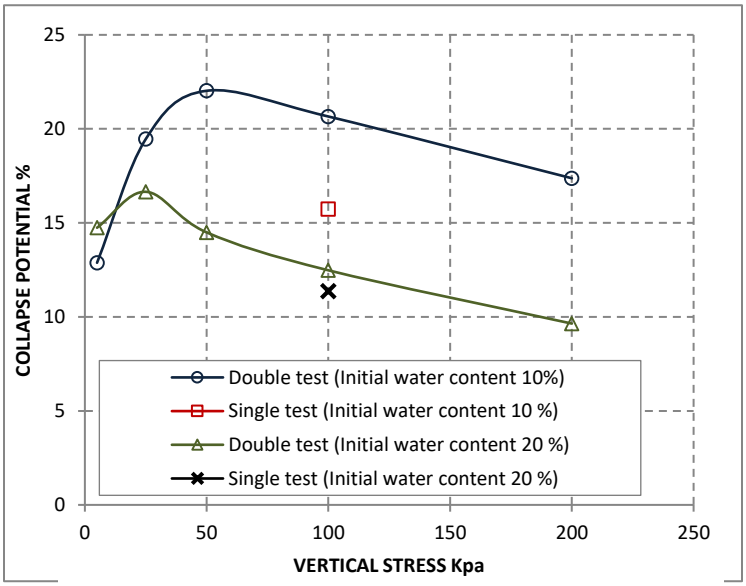

Figure 7 presents the relation between collapse potential (CP) and initial water content (IWC) of kaolin clay sample. At higher values of vertical stress, the magnitude of collapse potential,

ISBN: 978-81-936820-6-7
Proceedings DOI: 10.21467/proceedings.4

Series: AIJR Proceedings

would record a significant decreasing when the initial water content is increased. Considering a double oedometer test, at a vertical stress of 100 KPa, the collapse potential decreases from 20.65% to 12.47% as the initial water content increases from 10 to 20%. According to (Jennings et al 1975), the severity of the problem changes from severe trouble to very severe trouble based on the decrease in initial water content. Furthermore, results of variation of collapse potential versus vertical stress are expressed in Figure 8.

Compressing the specimens under constant initial void ratio of 2 and various initial water contents of (10 and 20%) will result in different values of (CP) as the magnitude of compression force varies. The curve representing the double oedometer test with initial water content of 10% shows that, the highest collapse potential value was observed at 50KPa load increment (CP=22.025). The collapse potential starts increasing with the increase of loads until it reaches its maximum value at a critical pressure (pre-consolidation pressure): "pressure at which collapse of a soil begins and the soil changes its response from low to high compressibility" (Phien-wej's et al., 1992) of 50KPa; then it begins to decrease with the increase of the loads being continued. Comparing this curve to the curve obtained from a similar test, having the value of initial water content increased to 20%, a significant reduction of collapse potential is observed. Also, the influence of test type, (single and double oedometer tests), was investigated to compare the results of collapse potential at a certain load increment. Figure 8 shows that, the value of collapse potential, obtained from single oedometer test, was always lower than that obtained from double oedometer test. Where, (CP = 15.73%) for single oedometer test and (CP=20.66%) for double oedometer test under the same nominal stress of 100 KPa and initial water content of 10%. This could be attributed to that, friction forces acting along the interfaces between soil specimens and oedometer ring may not decrease to the same degree during single oedometer testing as it could happen if soil specimens were inundated prior to stress application in double oedometer test. Furthermore, it is easier to inundate the unloaded soil specimens (Y.M.Reznik 2000). In addition, the difference between the results obtained from single oedometer test and double oedometer test decreases as the initial water content increases.

3.2 Influence of initial void ratio

Figures 9 and 10 show that, the decrease in void ratio upon wetting is quite small at the beginning of the loading process; however, it starts increasing rapidly with the increase of vertical loads being continued. The collapse potential values also increase with the increase of vertical loads upon wetting, where it starts from (CP=6.7%), which means trouble, at (5KPa) vertical stress, to end up with (CP=27.10%) which means a very severe trouble, at (200KPa) vertical stress as shown in Figure 11. Also the single oedometer test results show that, the value of collapse potential, at a certain point of a 100 KPa load increment, increases from (CP=15.73%) to (CP=18.89%) by reducing the value of void ratio from 2 to 1.7. This proves the fact that, the collapse potential, for kaolin clay soil, increases with the decrease of the initial

void ratio at later stages of load increment. This was observed when the same sample subjected to a double oedometer test show in Table (1) [tests (1 and 2) and (3 and 4)], where (CP=20.65%) from tests (1 and 2) at 100KPa vertical stress and (CP=25.91%) from tests (3 and 4) at the same vertical stress.

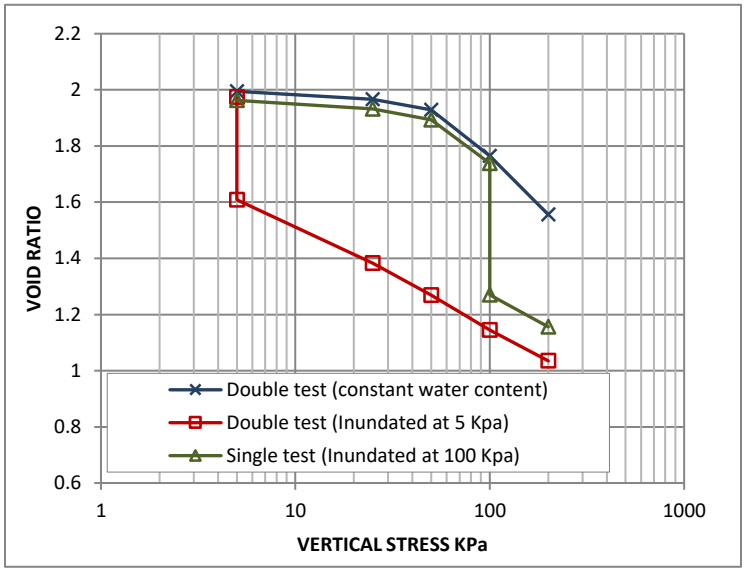

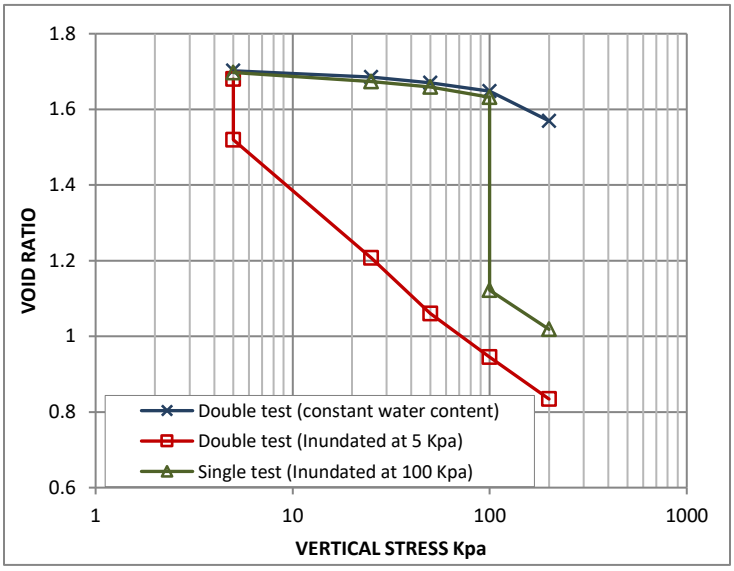

In Figure 11 and 12, a comparison, between the results obtained from double and single oedometer tests, is drawn in order to investigate the effect of the change in void ratio, from 2

ISBN: 978-81-936820-6-7
Proceedings DOI: 10.21467/proceedings.4

Series: AIJR Proceedings

to 1.7 with constant initial moisture content of about 10%, on the collapse potential of kaolin clay. It is observed that, the collapse potential values obtained when considering a void ratio of 2 are higher than those obtained using a void ratio of 1.7 at vertical loads of (5 and 25KPa) and constant water content of 10%. However, a further increase in the vertical stress results in the opposite of that, where the values of collapse, potential obtained from both tests, become bigger for higher vertical stresses of (50, 100, and 200KPa) as shown in Figure 12. The reason for that might be that the rearrangement of kaolin clay particles for a specimen with a high initial void ratio is faster than a specimen with lower initial void ratio, under loads being increasingly added, for the same specimen volume and initial water content. Therefore, from Figure 11, the sample with an initial void ratio of (2) becomes more compacted and stable than the sample with an initial void ratio of (1.7) after load increment of (50KPa). This leads to the collapse potential for the sample with an initial void ratio of (2), starting to decrease after exceeding this point, because a high percentage of compaction occurred in earlier stages of load increment as shown in Figure 10. Whereas, the other sample, a low percentage of compaction has occurred in earlier stages of load increment Figure 9, so that the (CP) value keeps increasing after exceeding the point of 50KPa vertical load. Accordingly, the outcome of this comparison is that the collapse potential value decreasing with the decrease of the initial void ratio under low values of vertical stress (earlier stages of load increment).

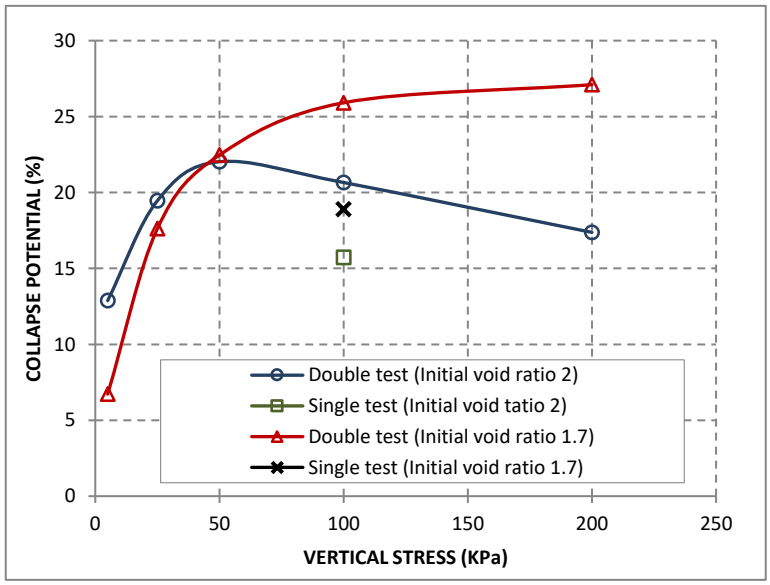

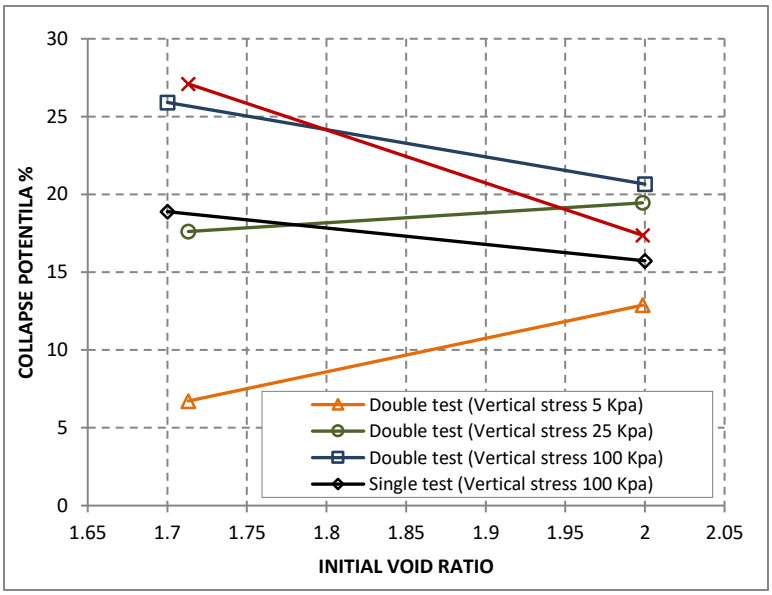

4 Conclusions

1) Under a low in situ water content (w.c. =10%) and void ratio of 2 the kaolin clay soil will pose a very severe trouble upon wetting (the collapse potential index at 50 kPa is as high as 22.03%). However, rising the initial water content (IWC) as high as 20%, resulting in a reduction in the collapse potential index to 14.49%.
2) At an initial water content of 10% and constant void ratio of 2, a considerable difference between the collapse potential index obtained from double and single oedometer tests is observed when subjected to a vertical load increment of 100 KPa. However, this difference will decrease as the initial water content increases at the same vertical load increment and void ratio.
3) the collapse potential values obtained when considering a void ratio of 2 are higher than those obtained using a void ratio of 1.7 at vertical loads of (5 and 25KPa) and constant water content of 10%. However, a further increase in the vertical stress results in the opposite of that, where the values of collapse potential index obtained from both tests, become bigger for higher vertical stresses of (50, 100, and 200KPa).

References

[1] British Standards Institution. Methods of Test for Soils for Civil Engineering Purposes.
[2] J.E. Jennings, K. Knight, A guide to construction on or with materials exhibiting additional settlements due to collapse of grain structure, in: Proceedings, Sixth Regional Conference for Africa on Soil Mechanics and Foundation Engineering, Johannesburg, 1975, pp. 99–105.

ISBN: 978-81-936820-6-7
Proceedings DOI: 10.21467/proceedings.4

[3] Jennings, J.E. and Knight, K. (1975) "A guide to construction on or with materials exhibiting additional settlement due to collapse of grain structure". Proceedings 6th African Conference on Soil Mechanics and Foundation Engineering. 99 – 105.

[4] Kenneth D. Walsh, William N. Houston, and Sandra L. Houston. Evaluation of in-place wetting using soil suction measurements. J. Geotech. Engrg. 119, 862 (1993).

[5] Khaled E. Gaaver. Geotechnical properties of Egyptian collapsible soils. Alexandria Engineering Journal (2012).

[6] Phien-wej, N., Pientong, T., Balasubramaniam, A.S. In: collapse and strength in characteristics of loess in Thailand, Engineering Geology vol. 32. Elsevier Science, Amsterdam, pp. 59-72. 1992.

[7] Rachid Benkadja, Brahim Belouahri. Influence of Oil on the Magnitude and Rate of Collapsible Soils. Journal of Civil Engineering Research and Practice, Vol. 7 No.1, April 2010, pp. 1 - 12

[8] Reznik, Y.M. Engineering approach to interpretation of oedometer tests performed on collapsible soils. Engineering Geology Vol 57, Issues 3–4, Pages 205-213 (July 2000)

[9] Reznik, Y.M., 1994a. Evaluation of collapse potential using singleoedometer test results. Bulletin of the Association of EngineeringGeologists XXXI (2), 255–261.

[10] Reznik, Y.M., 1994b. Comment: Evaluation of collapse potential using single oedometer test results. Bulletin of the Association of Engineering Geologists XXXI (3), 279.

[11] Vilar, O.M., Machado, S.L. and Bueno, B.D.S. Collapse Behavior of a Compacted Lateritic Soil; 1998.

[12] Yakov M. Reznik, influence of physical properties on deformation characteristics of collapsible soils. Engineering Geology, vol. 92, pp 27-37, (2007).

[13] Lawton, E. C., Fragaszy, R. J., and Hetherington, M. D. (1992). "Review of wetting-induced collapse in compacted soil." J. Geotech. Eng., 118(9), 1376–1394

Modeling Effects of Outlet Nozzle Geometry on Swirling Flows in Gas Turbine

Hesham Baej*, Adel Akair ,Adel Diyaf , Salem Adeilla, Abdurahman Kraiem

Department of mechanical engineering , College of Engineering, Higher institute of science and technology,Gharyan- Libya

DOI: https://doi.org/10.21467/proceedings.4.15

* Corresponding author email: heshamttt@gmail.com

ABSTRACT

Swirl stabilised combustion is one of the most successful technologies for flame stabilisation in gas turbine combustors. Lean premixed combustion systems allow the reduction of NOx coupled with fair flame stability. The swirl mechanism produces an aerodynamic region known as central recirculation zone (CRZ) providing a low velocity region where the flame speed matches the flow velocity, thus anchoring the flame whilst serving to recycle heat and active chemical species to the root of the former. Another beneficial feature of the CRZ is the enhancement of the mixing in and around this region. However, the mixing and stabilisation processes inside of this zone have shown to be extremely complex. The level of swirl, burner outlet configuration and combustor expansion are very important variables that define the features of the CRZ. The complex fluid dynamics and lean conditions pose a problem for stabilization of the flame. The problem is even more acute when alternative fuels are used for flexible operation.

Therefore, in this paper swirling flame dynamics are investigated using computational fluid dynamics (CFD) with commercial software (ANSYS). A new generic swirl burner operated under lean-premixed conditions was modelled. A variety of nozzles were analysed using isothermal case to recognize the the behavers of swirl. The investigation was based on recognising the size and strength of the central recirculation zones. The dimensions and turbulence of the Central Recirculation Zone were measured and correlated to previous experiments. The results show how the strength and size of the recirculation zone are highly influenced by both the shear layer surrounding the Central Recirculation Zones (CRZ) and outlet configurations

Keywords: Central Recirculation Zone, swirling flow, CFD, turbulent.

1 Introduction

A proved technology to reduce the impact of NOx is the use of lean premixing with swirl-stabilized combustion. Swirling flow technologies have shown to give high flame stability taking advantage of coherent structures such as corner and central recirculation zones which anchor the flame, recirculating hot products and active chemical species whilst also increasing

their residence time, allowing the use of low equivalence ratios thus giving lower flame temperatures and NOx emissions [1].

However, premixed combustion is not perfect because fuel and air mix just before entering the combustion chamber, thus leading to a significant degree of un-mixedness. These create complex instabilities that would feedback into the mixing-reaction combustion process. Combustion instabilities remain a critical issue limiting the development of low emission, lean premixed gas turbine combustion systems. Strong efforts are currently undertaken for the numerical simulation of swirl-stabilized flames with the intention of designing improved gas turbine combustors [2-3]. The biggest challenge to fuel-flexibility of most combustors is the large differences between natural gas and the proposed replacement fuels. Moreover, gas turbines must meet the current emissions regulations, which often mean running very near lean blowoff. However, blowoff continues to be a phenomenon that is difficult to predict across reactor types and fuel compositions. To describe the lean blowoff behaviour of swirl combustors under various fuel compositions, correlations have to be determined and simplified models developed to allow the implementation of fuel flexible technologies [4].

The crucial feature of swirl burners is the formation of a central recirculation zone (CRZ) which extends blowoff limits by recycling heat and active chemical species to the root of the flame in the burner exit [5-6]. Thus, the CRZ is one of the mechanisms for flame stabilization that through an aerodynamically decelerated region creates a point where the local flame speed and flow velocity match [7]. A vast amount of literature exists on measuring, correlating and predicting blowoff limits for bluff body and swirl stabilized combustors. There are three basic characterizations of the physical phenomena responsible for blowoff. Longwell et al. [8] suggested that blowoff occurs when it is not possible to balance the rate of entrainment of reactants into the recirculation zone, viewed as a well stirred reactor, and the rate of burning of these gases. A different view is that the contact time between the combustible mixture and hot gases in the shear layer must exceed a chemical ignition time. This leads to scaling the characteristic dimension by the recirculation zone length, leading to a similar Da criterion [9]. Current theories are based on a flamelet based description upon local extinction by excessive flame stretch [10]. Flame stretching starts blowoff with the initiation of holes in the flame, that are healed by the same flame creating stretching in areas that otherwise would have been unaffected. Flame will extinguish when flame stretch rate exceeds a critical value. However, it is also recognized that this mechanism is not the one causing the final blowoff, as it is clear from data that the flame can withstand some extinction [11]. Therefore, it is considered that the "critical extinction level" must be somehow influenced by other mechanisms [8-9]. Regarding the central recirculation zone, the use of different configurations has demonstrated that the shape and strength of the CRZ can change drastically depending on these alterations [12-13]. Valera- Medina et al. [13] have observed how the change of the combustor nozzle can produce different central recirculation zones under the same injection conditions.

2 Numerical Methodology

CFD modelling was used to simulate the isothermal of swirl burner. A 100kW swirl burner constructed from stainless steel was used to examine the flow behave limits at atmospheric conditions (1 bar, 293 K) based to the previous experiments conducted at Cardiff University's Gas Turbine Research Centre (GTRC). Different nozzles were used with various angles: 15°, 25°, 35°, 45°, with swirl numbers of 1.05 . A single tangential inlet (a) feeds the premixed air and fuel to an outer plenum chamber (b) which uniformly distributes the gas to the slot type radial tangential inlets (c). Swirling unburned fuel then passes into the burner body (d), then into the burner exhaust (e) where the gases pass around the flame stabilizing central recirculation zone. The central diffusion fuel injector (f) (which was not used for fuel during the course of this study) extends centrally through the combustor body to the exhaust, Figure1.

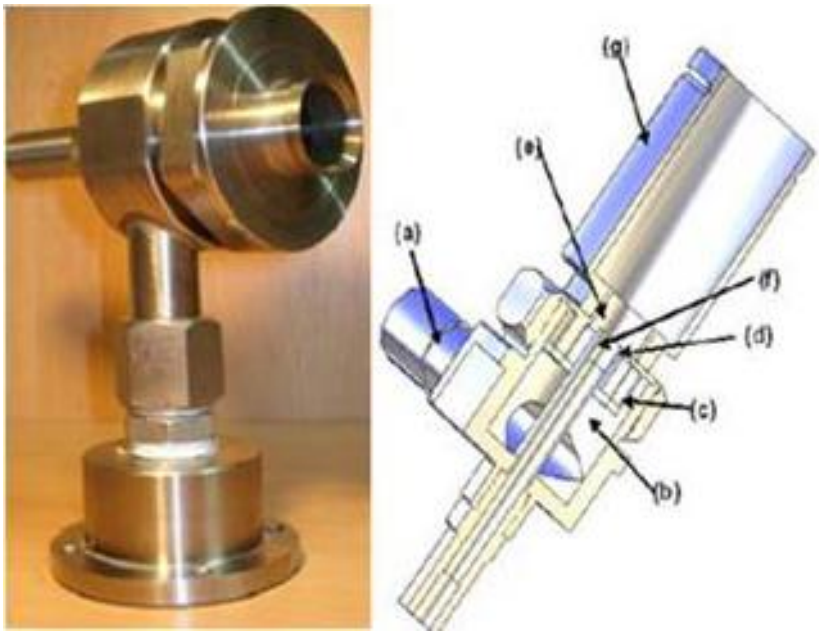

Figure 1: Swirl *burner and schematic diagram, respectively.*

CFD modelling is initially performed to simulate at the isothermal and atmospheric pressures conditions with 300 K . Isothermal conditions with no combustion were used to calibrate the system and indicate the flow pattern, although it is well known that there are also 3D time, dependant coherent structures, thus the results are of an indicative nature. During the simulation, various types of solvers were investigated and conclusions drawn as to which were the most effective. Based on the experimental results obtained the best turbulent option for the present work was the $\varkappa$-ω SST model [11, 14-16].

Swirl combustor and burners are usually characterized by the degree of swirl, via a swirl number (S). For this particular project, the swirl element of 1.05 has four tangential inlets symmetrically distributed. The swirl burner produces a CRZ that extends back over the central fuel injector, allowing the flame to propagate into this region. This effect can be reduced by

ISBN: 978-81-936820-6-7
Proceedings DOI: 10.21467/proceedings.4

fitting a divergent of the exhaust nozzle of the burner, as shown in Figure 2, producing a different CRZ.

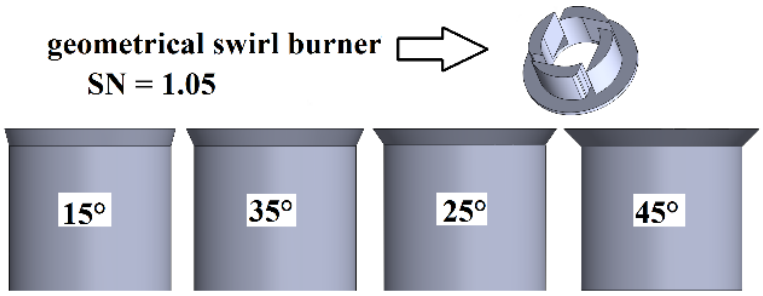

Figuer 2 Geometrical *swirl number 1.05 and various divergent angles nozzles, respectively*.

3 Turbulence modelling

The turbulence model used was the shear-stress transport (SST) k-ω model, so named because the definition of the turbulent viscosity is modified to account for transport of the principal turbulent shear stress. It has features that give the SST k- ω model an advantage in terms of performance over both the standard K- ω model and standard k-ε model. Other modifications include the addition of a cross-diffusion term in the ω equation and a blending function to ensure that the model equations behave appropriately in both the near-wall and far field zones. The turbulence kinetic energy, k, and the specific dissipation rate, ω, are obtained from the following transport equations:

$$\frac{\partial}{\partial t}(\rho k) + \frac{\partial}{\partial_{xi}}(\rho k u_i) = \frac{\partial}{\partial x_i}\left(\Gamma_k \frac{\partial}{\partial x_j}\right) + G_k - Y_K + S_K$$

$$\frac{\partial}{\partial t}(\rho \omega) + \frac{\partial}{\partial x_i}(\rho \omega u_i) = \frac{\partial}{\partial x_i}\left(\Gamma_\omega \frac{\partial \omega}{\partial x_j}\right) + G_\omega - Y_{K\omega} + D_\omega + S_\omega$$

Calculations for all previous terms have been fully described in [17].

4 Mesh distribution and Boundary Conditions

A fresh air at normal conditions was used to simulate the behaviours of the flow pattern based on previous works [18-19]. The air flow mass flow rate and the operating conditions of the burner are given in Table 1,

Table 1: *Inlet boundary conditions for all nozzles*.

Test	Pressure	Temperature	Inlet velocity
1	1 bar	300K	2.5 m/s
2	1 bar	300K	5 m/s

FLUENT 15.0 was used to achieve the modelling and simulation [20]. The pre-processor used to construct the model grid was ICEM 15.0The computational mesh consists of 1700162

elements, with a structured grid created with a higher density of nodes in areas where the fluid flow was expected to considerably change and where a finer grid resolution was assumed to be beneficial for achieving an accurate resolution.

This was essentially done close to the burner exit and around the fuel nozzles, Figure 3.

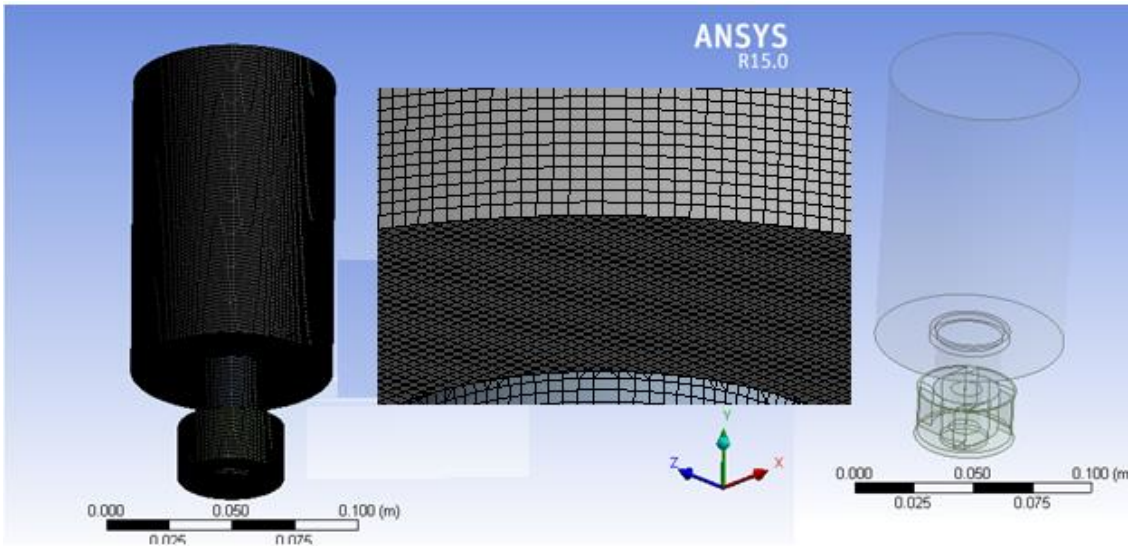

Figure 3. *Mesh distribution swirl numbers 1.05 and 1.50, respectively*

5 Results and Discussions

The comparison of the CFD simulation presented in Figure 4(a) and (b) reveals the effects of outlet configurations on the flow pattern. The predicted and measured boundaries of the CRZ for isothermal flows show a longer CRZ extending up to the combustor exit, as expected. However, the usage of different nozzles showed the reduction of both the size and the strength of the CRZ, Table 2.

Table 2. *Comparison of isothermal patters of the CRZ using different nozzle angles*.

nlet velocity		15°	25°	35°	45°
2.5 m/s	Width	1.15 D	1.20 D	1.26 D	1.31 D
	length	2.58 D	2.60 D	2.63 D	2.80 D
5 m/s	Width	1.37 D	1.38 D	1.40D	1.37 D
	length	3.24 D	3.24 D	3.29 D	3.62 D

The flow rate increases with the intensity of the shear layer. This will converge into a new structure called High Momentum Flow Region (HMFR), highly correlated to the CRZ [19]. This will increase the strength of the CRZ but reduce its dimensions, as observed in table 2. The changing of nozzle angles affects the velocity of the flow, thus showing slower profiles than with nozzle 45°. At the same time, it seems that the dimensions of the CRZ with 45°

ISBN: 978-81-936820-6-7
Proceedings DOI: 10.21467/proceedings.4

Series: AIJR Proceedings

angle have increased to a width of 1.37D and height of 3.62D, compared to a width of 1.15D and a height of 2.58D with nozzles of 15°, 45° under similar conditions, Figure 5. show the progression of the CRZ and its boundaries, defined as a region of greater turbulence compared to the low velocity case. It is clear that the CRZ using high velocity has increased the turbulent intensity with both nozzles 35° , 45° while the observed reduction with the 25° nozzles at the same conditions as shown in table 3 .

Table 3: *Comparison of turbulent intensity of all cases.*

Turbulent intenisity	15°	25°	35°	45°
2.5 m/s	60.3%	61.8%	63.5%	63.8%
5 m/s	129%	66%	135%	135%

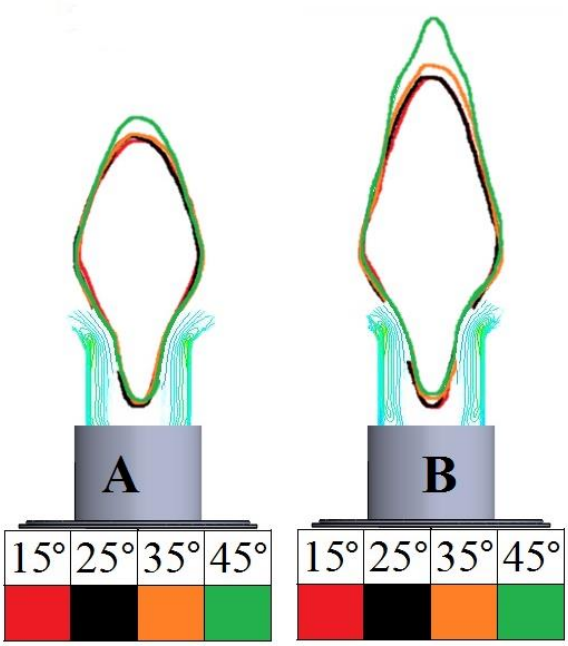

Figure 4. Comparison *of CRZ size of all nozzles A at 2.5 m/s and B at 5 m/s*

The usage of deferent nozzles alters the size and inner turbulence of the structure; in Table 3 and Figures 5 it is clear that the turbulence intensity inside the CRZ with high velocity blends is higher than with low velocity . The increase of the nozzle divergence from the 15 degree up to 45 degree will increases in almost 7-10% the turbulence of the structure, whilst augmenting its width and length in ~10% for all cases, Figure 4. The length of the recirculation zone increases due to the reduced reaction time of the blend and the higher turbulence inside of the structure.

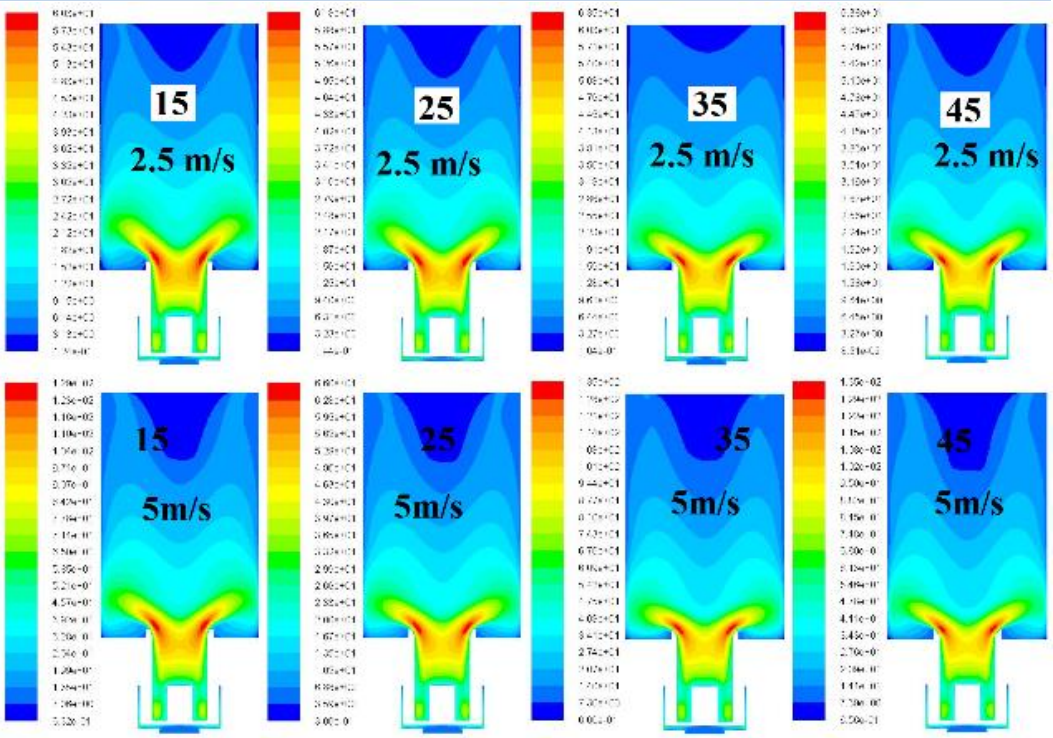

Figure 5 *Comparison of turbulence intensity of different velocity 2.5m/s and 5 m/s.*

The flow rate increases with the intensity of the shear layer. This will converge into a new structure called High Momentum Flow Region (HMFR), highly correlated to the CRZ [19]. This will increase the strength of the CRZ but reduce its dimensions, as observed in table 2. At the same time, it seems that the dimensions of the CRZ with 35° have increased to a width of 1.40D and height of 3.29D, compared to a width of 1.37D and a height of 3.62D with 45° nozzle under similar conditions, Figure 4-5. show the progression of the CRZ and its boundaries, defined as a region of greater turbulence compared to the low flow rate.

Figure 6 illustrates the axial velocity using different nozzle angles at a constant mass flow rate. The smallest CRZ width size was observed using the 15^0 geometry, as expected. Also the 45^0 nozzle produces higher outlet velocities than the 25° and 35° divergent angles due to the sharp sudden expansion. The 45° nozzle generates axial velocities 25% slower than the straight 15° geometry, thus allowing a better recuperation of the CRZ. This causes an increase in size of CRZ, Figure 6.

ISBN: 978-81-936820-6-7
Proceedings DOI: 10.21467/proceedings.4

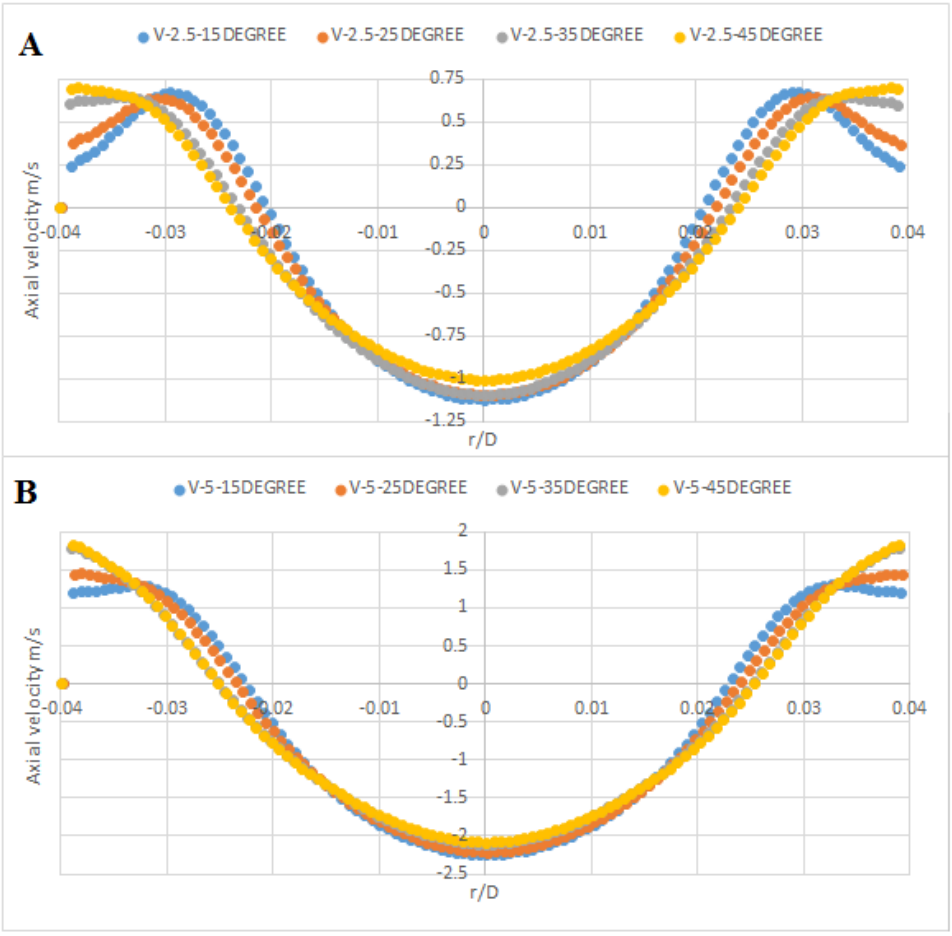

Figure 6 comparison *of two velocities A 2.5 m/s and B 5 m/s*

The high momentum shearing flow region illustrated in Figure 7 with swirl numbers of 1.05 shows the divergence of the flow at the outlet of the nozzle. It is clear that the increase in the velocity will produce higher stretch in the radial and tangential direction with a faster decay of velocity in azimuthal direction and wider CRZs.

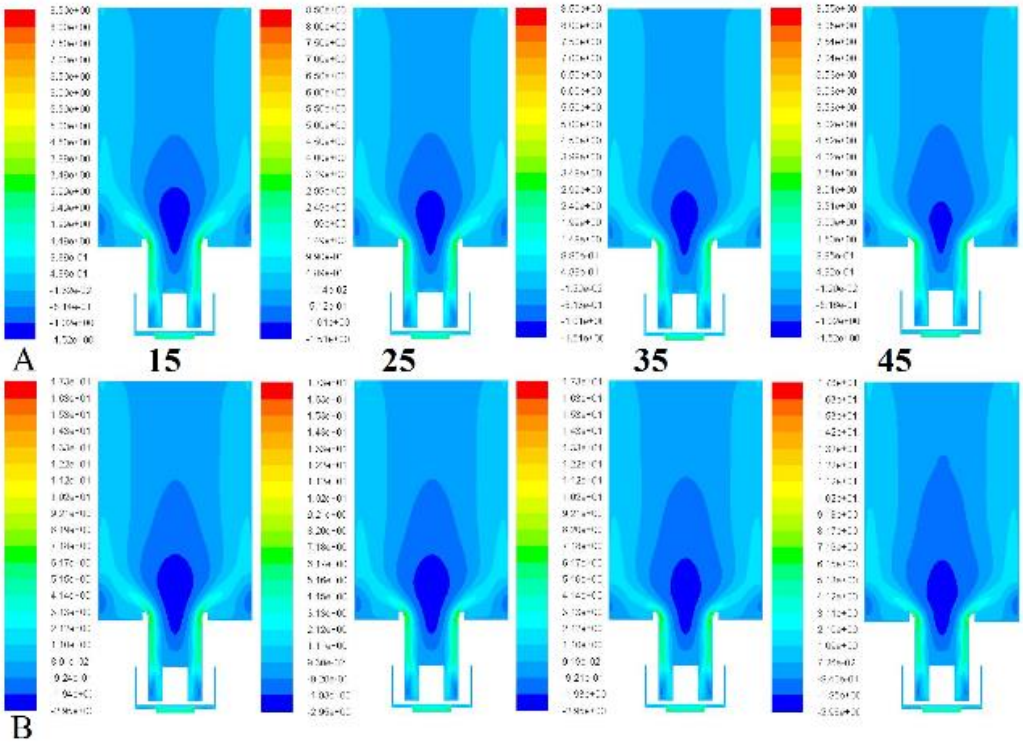

Figure 7 comparison *of HMFR using all nozzles*

6 Conclusion

The CFD predictions of swirl burner aerodynamics show how variable outlet configurations change the CRZ patterns. The changing of the geometry could be have the important factor of great importance to the change of the CRZ. It is clear that the CRZ is increased with the usage of 45° compared with another outlet nozzles angles. Changing the angle of the nozzle will control the direction of shear layer. This in return could be beneficial for new blends and the increase of the residence time of the products/reactants of the fuels/diluent compositions. The results showed that for all nozzles produced different central recirculation zones under the same power loads. Measurements indicate that the 45° nozzle produced the largest, and shorter CRZ structure, while the nozzle with the 25° nozzle produced the narrowest CRZ.

7 Acknowledgment

I am gratefully acknowledges the support of the Cardiff university and Libyan Embassy and the Libyan Cultural and Education Bureau in London during my research.

References

[1]Sadanandan R., Stohr M., Meier W: "Simultaneous OH-PLIF and PIV measurements in a gas Turbine model Combustor",*Applied Physics B*, vol. 90, 609-618 (2008).

[2]Huang, Y., and Yang, V: "Dynamics and stability of lean-premixed swirl stabilized combustion," Progress in Energy and Combustion Science, 35(4), 293-364 (2009).
[3]Syred N,: A review of oscillation mechanisms and the role of the PVC in swirl combustion systems, Prog Energy Combust Sci 32 (2), 93-161(2006).
[4] Megan Karalus: An Investigation of Lean Blowout of Gaseous Fuel Alternatives to Natural Gas, PhD Thesis, University of Washington,(2013).
[5] Lieuwen T, Yang V: Combustion Instabilities in Gas Turbine Engines, Prog. In Astronautics Aeronautics, AIAA, U.S.A., vol. 210, 213-276 (2005).
[6] Tuttle SG, Chaudhuri S, Kotska S, Koop-Vaughan KM, Jensen TR, Cetegen BM, Renfro MW: Time-resolved blowoff transition measurements for two-dimensional bluff body-stabilized flames in vitiated flow. Combust Flame 159, 291-305(2012).
[7] Lieuwen T: Unsteady Combustor Physics, Cambridge Press, U.S.A., pp. 430(2012).
[8] Longwell JP, Frost EE, Weiss MA: Flame stability in bluff body recirculation zones. Indust Eng Chem 8, 1629-1633 (1953).
[9] Shanbhogue SJ, Husain S, Lieuwen T: Lean blowoff of bluff body stabilized flames: Scaling and dynamics, Prog Energy Combust Sci, 35, 98-120 (2009).
[10]Driscoll J: Turbulent premixed combustion: flamelet structure and its effect on turbulent burning velocities, Progress in Energy and Combustion Science 34 (1), 91-134(2008).
[11] Poinsot T, Veynante D: Theoretical and Numerical Combustion, R.T. Edwards, U.S.A., pp. 522(2005).
[12]Valera-Medina A, Syred N, Bowen P :Central Recirculation Zone Analysis using a Confined Swirl Burner for Terrestrial Energy, J AIAA Propulsion and Power 29 (1), 195-204 (2013).
[13]Valera-Medina A, Syred N, Griffiths A Visualization of Coherent Structures in a Swirl Burner under Isothermal Conditions. Combustion and Flame 159,1723-1734 (2009).
[14] Versteeg HK and Malalasekera W, An Introduction to Computational Fluid Dynamics – The Finite Volume Method, Longman Group Ltd (1995).
[15] Date A W: Introduction to Computational Fluid Dynamics, Cambridge University Press (2005).
[16] Syred, N.J M.Beer: Combustion in swirling flows: A review combustion and flame 23,143-201(1974)
[17] ANSYS FLUENT 12.0 Theory Guide 2009 [Online]. Available:at www.scribd.com/doc/191713736/Ansys-Fluent-12-0-Theory-Guidem
[18] Baej H., Valera-Medina A., Bowen P., Syred N., O'Doherty T., Marsh R ., Impacts on Blowoff by a variety of CRZs using various gases for Gas Turbines
[19] Vigueras-Zuniga MO, Valera-Medina A, Syred N, Bowen P: High Momentum Flow Region and Central Recirculation Zone Interaction in Swirling Flows, SOMIM. Approved
[20] Zimont V, Gas Premixed Combustion at High Turbulence. Turbulent Flame Closure Model Combustion Model. Exp Thermal Fluid Sci 21:179– 186 (2000).

Aerodynamic Effects of Blade Positive Sweep in Axial Flow Cascades

Ali R. Kwedikha*, Abdul Azeam A. Elgayed, Abelmalek N. Algaaoud

Department of Mechanical Eng., College of Engineering, University of Zawia, Libya

DOI: https://doi.org/10.21467/proceedings.4.16

* Corresponding author email: ali.kwedikha@zu.edu.ly

ABSTRACT

In this work, the effects of sweep applied to rotor of axial flow turbomachines were investigated by means of applying computational fluid dynamics (CFD) tools. Low-aspect-ratio rotors of positive sweep (**PSW**) have been studied and compared to unswept datum (**USW**) rotors, at one flow rate and different spanwise locations.

Comparative studies have been carried out on positive sweep and upswept rotors at the design flow rate, by means of developing structured fully hexahedral mesh of the entire computational domain. The structured meshing technique offers the moderation of cell number and skewness, and makes possible cost-effective CFD investigations. Investigations of inlet and outlet flows field were carried out at the design flow rate.

It was pointed out that the efficiency for the positive sweep rotor is deteriorated near the tip and near the hub at the design point.

Keywords: Three-dimensional turbomachinery flow, blade sweep, structure meshing.

1 Introduction

In the turbomachinery manner, blade positive sweep may possibly give opportunity to control the flow and to demonstrate the impact of blade positivity on rotor aerodynamics, thus contributing to a more comprehensive understanding of the effects of consequences. This paper presents an investigation using computer codes for studying the blade sweep positivity effects on the Three-Dimensional (3-D) flow of axial fan.

A comparative investigation using a computational Fluid Dynamics (CFD) tool for Positive Sweep (**PSW**) and Unswept (**USW**) blades is carried out. **Figure 1** shows the front views of these blades.

Low-aspect-ratio rotor of **PSW** sweep has been studied and compared to unswept datum rotor, at the design flow rate and different spanwise locations. Sweep is a non-radial blade stacking technique. Sweep is forward or backward if a blade section at a given radius is upstream or downstream of the adjacent blade section at lower radius respectively, and termed positive or negative if a blade section under consideration is upstream or downstream of the adjacent inboard blade section, respectively [1].

 ISBN: 978-81-936820-6-7

In the literature, several studies have been carried out for axial flow turbomachinery in order to investigate the effect of backward or forward sweep on the 3-D flow of axial fan. These studies have focused on the interblade and downstream flow phenomena e. g. Yamaguchi et al. [2]. Others report negligible effects of pure positive sweep on the upstream flow field, as in Clemen et al. [3]. Few researches focused on the pure positive sweep of the turbomachinery rotors. Therefore, lack of information appears in the literature concerning positive sweep rotor designs. This has made some difficulty to compare with the results of other research projects. According to Braembussche and Vad [1], no generally valid concept for aerodynamically optimum prescription of blade sweep angle along the span has been published in the open literature.

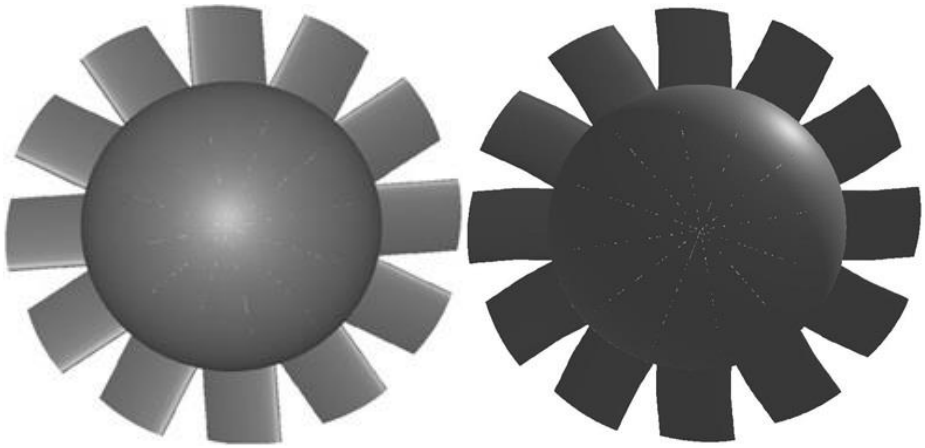

USW rotor PSW rotor

Fig. 1. Front views of USWand PSW rotors

The study presented here contributes to a more comprehensive understanding of the positive sweep effects. The aim is to provide some answers not presented by the available literature. This study provides a comparative study between **USW** and **PSW** rotors using CFD tools. The numerical simulation was carried out using ANSYS Student Release 17.2, the code is a state-of-the-art computer programs for modelling fluid flow in complex geometries, using Finite Volume Method (FVM).

Some assumption used in this work such as: the flow is considered steady state, incompressible, with swirl-free inlet, no entrance guide vane and negligible heat transfer.

2 Blade positive sweep geometry

The stacking line (SL) is the line passing through the centres of gravity of the blade airfoil sections enclosed in cylindrical stream tubes. The chord line is the straight line connecting the two points of leading edge (LE) and trailing edge (TE) of each blade section. Blade sweep is known as technique of non-radial blade stacking. Sweep can be provided if the blade sections

of a datum blade of radial stacking line (RS) are displaced parallel to the chord [4] as sketched in **Figure 2a.** A blade is swept forward (FSW) or backward (BSW) at a given radius if the blade sections of a radially stacked datum blade are shifted parallel to their chord in such a way that a blade section under consideration is upstream or downstream of the neighbouring blade section at lower radius, respectively [5], Sweep is said to be positive near an endwall when a blade section under consideration is upstream of the adjacent inboard section, as shown in **Figure2**.

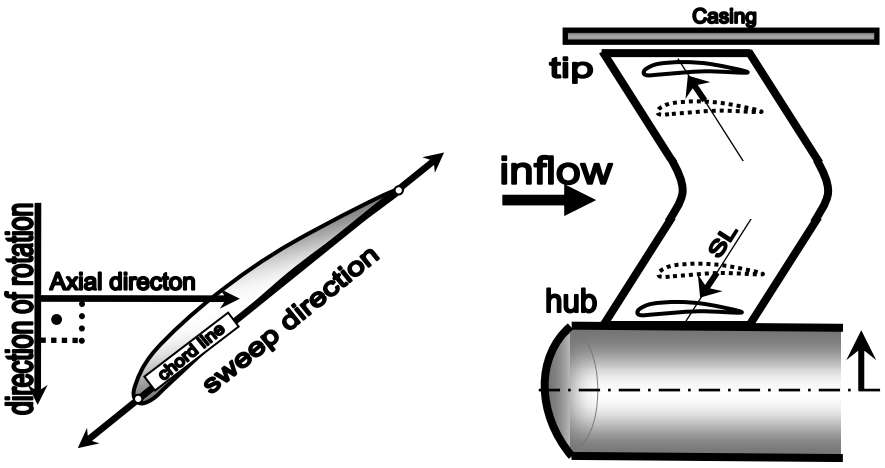

a) Direction of sweep **b) Schematic drawing for PSW**

Fig. 2. Sweep direction and schematic drawing for PSW

In this case study, reference [**6**] is taking as preliminary reference. The rotor blade sections has C4 (10%) profile along the entire span, with circular arc camber lines. The Reynolds number (Re) determined using speed of blade tip, characteristic length of chord tip and the kinematical viscosity of air at 20 °C is approx. 1.074x10^6.

Taking the reference velocity (u_{ref}) as the tangential velocity of the blade tip (u_t), the global flow coefficient (Φ_D) is defined as the area-averaged axial velocity in the annulus divided by u_{ref}. Hub-to-tip ratio (ν) is defined as the ratio of blade hub diameter to the blade tip diameter, while the tip clearance (τ) is defined as the ratio of rotor tip clearance to the blade span. The main fan characteristics are summarised in **Table 1.**

Table 1. Main fan characteristics[6]

Casing diameter	2000 mm
Hub-to-tip ratio ν	0.6
Rotor blade count N	12
tip clearance τ (%span)	5
flow coefficient Φ_D	0.33

ISBN: 978-81-936820-6-7
Proceedings DOI: 10.21467/proceedings.4

Series: AIJR Proceedings

The rotor blades are arranged in such a way that, the blades are assembled in an annular cascade with cylindrical and part of spherical as well as cylindrical casing, as shown in **Figure3.**

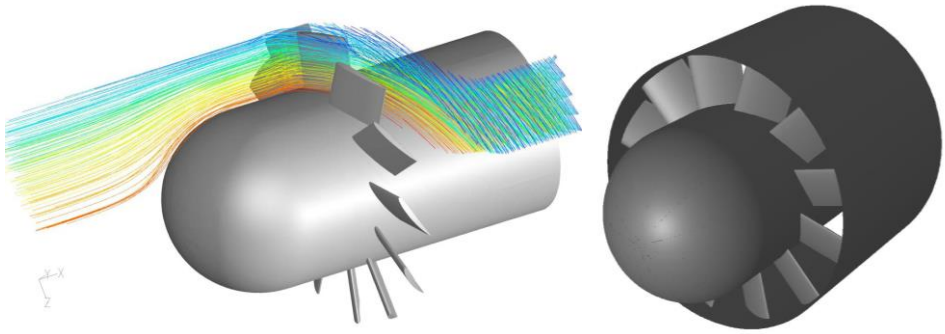

Fig. 3. Virtual isometric of USW rotor

In this study, to create positive sweep the blade sections are swept upstreamlly from the middle of the blade span to the both endwalls by 3.5 degree.

3 CFD technique

The CFD investigations were carried out by using the commercial available finite-volume ANSYS-17.2 code. 3-D geometry was constructed by split volumes and meshed using multiblocks structured grids. This technique used to provide hexahedral meshes for the whole geometry of both rotors. It must be noted as Wenneker stated that, discretization of the flow equations on unstructured grids is considered to be more difficult than on structured grids [7]. 2-D structured meshes take place in two essential forms H-grids and C-grids. With consideration of periodicity, one computation domain instead of all geometry has been created to avoid the mesh size and time consuming. Typical computational domain for **USW** rotor is presented in **Figure 4.**

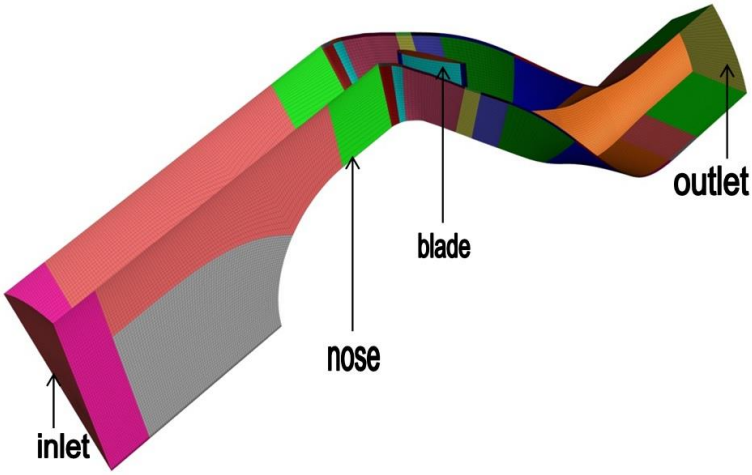

Fig. 4. Typical computational domain for USW rotor

The domains extend to approx. 7 and 4 midspan axial chord lengths in the axial direction upstream and downstream of the rotor blading, respectively. The coordinates of domain in x-axis started from (-1750 to 2000 mm). Sector shape is inlet face with 30 degree central angle. Cone and hub sectors with one blade in the middle of the domain are provided next to the downstream of inlet face.

3.1 Boundary Conditions

- **Inlet boundary condition**: the inlet is set as a velocity inlet with magnitude of 9.2 [m/s]. The flow direction is parallel to the rotational x-axis.
- **Wall boundary condition**: the blade, hub and outer cassing have been defined as wall.
- **Outlet boundary condition**: outflow is used for the condition of outlet boundary.
- **Interior boundary condition**: the remaining part of the domain is set as default interior and the air fluid is applied with density of 1.225 kg/m^3.
- **Periodic condition**: all the side surfaces of the domain are defined as rotational periodic.

The standard k-ε model with enhanced wall treatment has been used as the turbulence model. The nondimensional wall normal cell size y+ values mostly fell within the range of 30 to 100, which agreeable with the requirements of the applied law of the wall. The discretisation of the convective momentum and turbulent quantity fluxes were carried out for both rotors by the second Order Upwind method. Typical computations required approximately 5000 iterations. The solutions were considered converged when the scaled residuals reached to 10^{-8} .

3.2 Meshing

To provide hexahedral meshes, the domain has been spitted to 31 volumes for both rotors and meshed using multiblocks structured grids. Biswas and Strawn stated that, hexahedral meshes provide a more accurate solution than their tetrahedral counterparts for the same number of edges [8], in this work; all the volumes have been meshed by the method of "Cooper". The most of the domain was meshed with "Hexahedral" structured meshing. Before starting with 3-D meshing, two types of grid meshing are applied in 2-D topology, C-type meshing applied for the vicinity of blade LE and TE, whereas H-type applied in most of the left. Dense meshing near the blade LE and TE as well as near the hub and tip is applied as in work of Kamenik et al [9]. The structured grid is usually applied to a relatively simple configuration. However, the swept blade geometry is being considered as a relatively complex design, in which a result of applying 3-D annular cascade instead of linear cascade. The total number of cells for **USW** and **PSW** rotor are 498889 and 469410 hexahedral cells, respectively. To develop annular cascade configuration and to take advantages of the periodicity, boundary condition of periodicity for one domain was applied, so that each meshing points and arrangement of each periodic face were created just identical with corresponding matching

ISBN: 978-81-936820-6-7

Series: AIJR Proceedings
Proceedings DOI: 10.21467/proceedings.4

face. Acceptable equiangle skewness of cell volume was achieved; the maximum skewness values are 0.82 and 0.75 for **USW** and **PSW** rotors, respectively.

4 Results and Discussion

4.1 Comparative flow survey of PSW and USW rotors at design flow rate

Results of valuable analysis by means of CFD technique for a comparison between **PSW** and **USW** rotors can be achieved, which is the purpose of this section.

Pitchwise averaged data

The inlet and outlet planes have positioned closely to the blade at the axial direction of -20% and 113% midspan axial chord, respectively, where the zero axial position indicates the LE at midspan as shown in **Figure 5a**. Another investigations located at the spanwise locations of 20%, 50% and 90% measured from the hub are shown in **Figure 5b**. The flow field will be surveyed at these five locations where significant 3-D results of the fluid mechanical behaviour can be achieved.

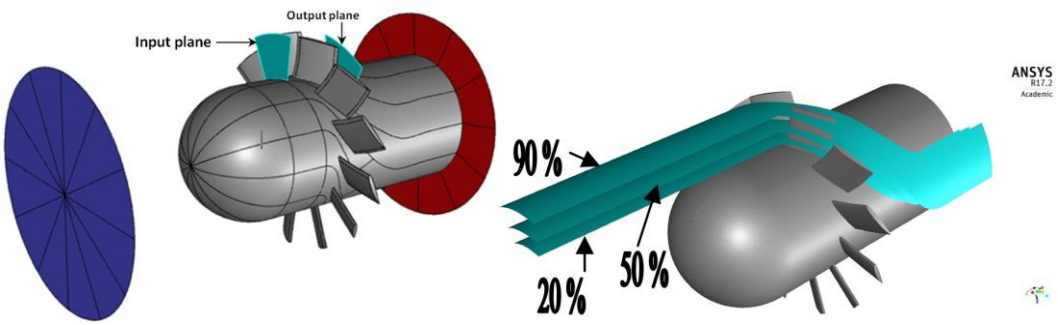

a) input and output planes **b) 20% ,50% and 90 % span**

Fig. 5. Location of results

The reference velocity (u_{ref}) or (u_t) in [m/s] can be defined as blade tip speed = ($d_t \pi n$) where, d_t is the blade tip diameter and n is the rotor speed (in revolutions per second). The definition of local flow coefficient (φ) is the ratio of axial velocity (v_x) to u_t

Figure 6a shows the distribution of local inlet axial velocity at the inlet plane and **Figure 6b** presents the spanwise distribution of pitchwise-averaged values for outlet axial velocity. **Figure 6b** indicates the two rotors having nearly similar pitch-averaged outlet axial velocity performance; which is possibly due to the small sweep angle. It was observed, that in **Figure 6a, PSW** decreases inlet axial velocity near the tip at **PS**, this acts to reduce the axial velocity downstream of the inlet especially at pressure side (**PS**) and blade LE as it is visible on the **Figure 7.**

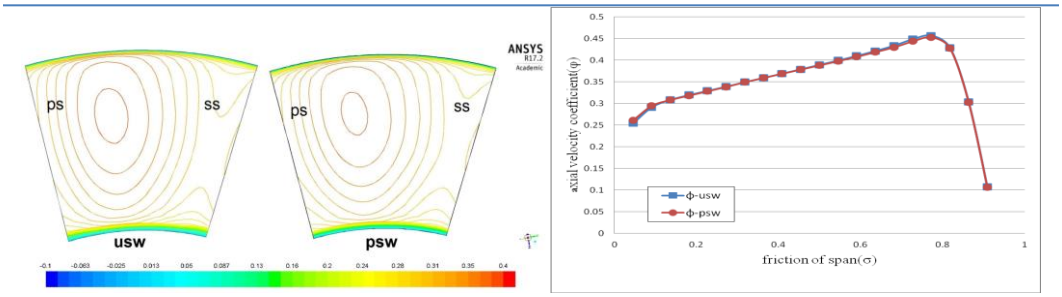

a) distribution of inlet φ **b) pitchwise-averaged outlet φ**

Fig. 6. Inlet and outlet of axial velocity coefficients.

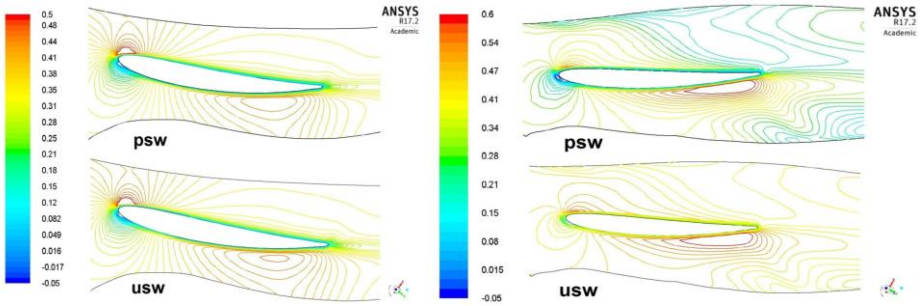

at 20% span **at 90% span**

Fig. 7. Distribution of local axial velocity coefficient

The definition of ideal total pressure rise coefficient (ψ_{id}) is $\psi_{id}=\Delta p_{t\,id}/(\rho\, u_{ref}{}^2/2)$. Where, $\Delta p_{t\,id} = \rho\, r\, \omega\, v_{u2}$, v_{u2} is the tangential pitchwise mass-averaged tangential velocity, r is radial coordinate, ω is rotor angular speed and ρ is the air density. For inviscid flow, the ideal total pressure rise (ψ_{id}) of turbomachines is assumed swirl-free inlet flow according to the Euler equation. Also according to effects of the so called "controlled vortex design (**CVD**)" in both rotors, the ideal total pressure rises gradually increased along the blade spanwise especially above midspan, the ideal total pressure rise increases significantly at TE of the **PSW** which is due to the blade positivity, as visibly shown in **Figure 8a**. As zhang et al.[10] concluded that, the pressure fluctuation of forward sweep blade is decreased while the pressure fluctuation of backward sweep blade is increased, likewise to our case that, **PSW** blade tip acts to increase ideal total pressure rise near the cassing compared to **USW** as shown in **Figure 8b**, this is due to decreasing the axial velocity at higher radii especially at the blade pressure side. However, **PSW** reduces ideal total pressure compared to **USW** along the spanwise except near the blade tip.

ISBN: 978-81-936820-6-7
Proceedings DOI: 10.21467/proceedings.4

Series: AIJR Proceedings

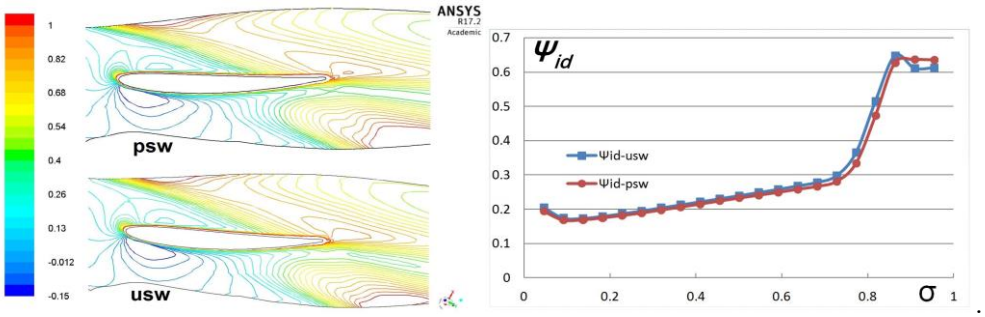

a) at 90% span **b) at span wise distributions**

Fig. 8. Ideal total pressure rise coefficient

The definition of the local total pressure rise coefficient (ψ) is Δp_t / ($\rho\, u_{ref}{}^2/2$), where Δp_t is the pitchwise mass-averaged local total pressure rise. The local total efficiency (η) and total pressure loss coefficient (ω) can be defined as $\eta = \psi / \psi_{id}$ and $\omega = \psi_{id} - \psi$, respectively. **Figure 9b** shows the local total efficiency (η) profiles along the span. By employing the positivity of sweep, the total local efficiency is observed to be decreased compared to the unswept rotor. **PSW** blade sweep showed reduced local efficiency especially at lower the midspan and close to the blade tip, this is due to the increased ideal total pressure rise and increased losses where the aerodynamic benefits of blade positivity would be expected on the basis of Clemen and Stark[4]. Furthermore, the local total efficiency is found almost similar to **USW** within the range of 70% to 85% of the spanwise otherwise. **PSW** exhibits the worst local total efficiency, especially at the part of the blade tip in suction side (**SS**) as shown in **Figure9a**.

It is pointed out that the local efficiency for **PSW** rotor is deteriorated near the tip which considered as a disadvantage of applying positive blade rotor at the case of design flow rate.

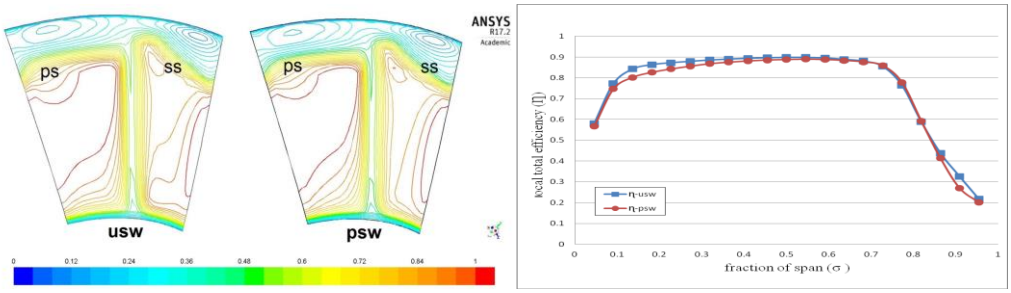

a) at outlet plane **b) at span wise distributions**

Fig. 9. Local total efficiency.

Increased total pressure loss for both rotors was found for both rotors above 80 percent span due to the existing tip clearance. At the blade tip, developing the local losses can be exist, the reason is that due to the combined effects of endwall tip-clearance, re-arrangement of the axial velocity and increased ideal total pressure rise, and can further increase by existing of positive

sweep near the endwalls especially at SS, as shown in **Figure 10**. Clemen and Stark mentioned that, increased losses can be expected near the endwall in the case of negative sweep, due to opposite tendencies. By this means negative sweep and positive sweep can cause the shift of blade load toward the **LE** and toward the **TE** near the endwall, respectively [4]. By applying the positivity of sweep, the local total pressure loss observed to be increased at the blade tip, this causes to increase losses and decrease local total efficiency at the endwall.

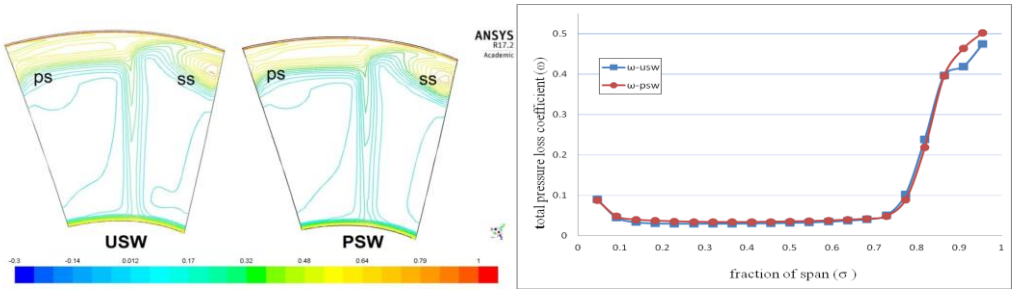

a) at outlet plane **b) at span wise distributions**

Fig. 10. Total pressure loss coefficient

5 Conclusions

The aim of this study was to investigate the effects of positive sweep applied to rotor of axial flow turbomachines using CFD tools. In this work, it is concluded that, the **PSW** rotor exhibits the lowest local total efficiency along the entire span, especially near the blade tip and near the hub at the design point, where as **USW** exhibits the highest local total efficiency along the entire span. It is pointed out generally that positive sweep gives a potential near-tip to increase of losses.

These results, therefore, demonstrate that the **PSW** rotor is considered as a disadvantage of applying positive blade rotor at the design flow rate.

Since, there is a deterioration of efficiency by using positive sweep near the tip and near the hub. It is recommended that, other investigations on a negative sweep should be carried out.

References

[1] Van Den Braembussche, R. A. and Vad, J. *"Challenges in optimisation of axial flow turbomachinery blades for 3D flow, including sweep and dihedral effects. In Modelling Fluid Flow"*, Springer Verlag Heidelberg, 2004, pp. 99-103.

[2] Yamaguchi, N., Tominaga, T., Hattori, S., and Mitsuhashi, T., *"Secondary-Loss Reduction by Forward-Skewing of Axial Compressor Rotor Blading,"* Proceedings Yokohama International Gas Turbine Congress, Yokohama, Japan, 1991,pp. II.61-II.68.

[3] Clemen, C., Gümmer, V., Goller, M., Rohkamm, H., Stark, U. and Saathoff, H., *"Tip-aerodynamics of forward-swept rotor blades in a highly-loaded single-stage axial-flow low-speed compressor."* 10th International Symposium on Transport Phenomena and Dynamics of Rotating Machinery (ISROMAC10), Honolulu, 2004, Paper No. 027. (CD-ROM Proceedings)
https://www.researchgate.net/publication/274636618_Tip-aerodynamics_of_forward_swept_rotor_blades_in_a_highly-loaded_single-stage_axial-flow_low-speed_compressor

[4] Clemen, C. and Stark, U. *"Compressor blades with sweep and dihedral: a parameter study"*. 5th European Conference on Turbomachinery Fluid Dynamics and Thermodynamics, Prague, 2003, Proceedings pp. 151-161.

ISBN: 978-81-936820-6-7

Series: AIJR Proceedings
Proceedings DOI: 10.21467/proceedings.4

[5] Corsini, A. and Rispoli, F., *"Using Sweep to Extend the Stall-Free Operational Range in Axial Fan Rotors",* Proc. Instn Mech. Engrs, Part A, J Power and Energy, 2004, Vol. 218, pp. 129-139.

[6] Vad, J., Kwedikha, A. R. A., Horváth, Cs., Balczó, M., Lohász, M. M., and Régert, T., *"Combined Aerodynamic Effects of Controlled Vortex Design and Forward Blade Skew in Axial Flow Rotors"*. Proceedings of the Institution of Mechanical Engineers – Part A: Journal of Power and Energy, 2007, Vol. 221, pp. 1011-1023.

[7] Wenneker, Ivo, *" Computation of flows using unstructured staggered grids"* Dissertation at Delft University of Technology. 2002, Delft, the Netherlands.

[8] Rupak Biswas, Roger C. Strawn, *"A dynamic mesh adaption procedure for unstructured hexahedral grids."* Paper 96-0027, 34th AIAA Aerospace Sciences Meeting, Reno, NV, 1996.

[9] Kamenik, Jan, Keane, Andrew, Toal, David and Bates, Ron, *"Application of sweep to transonic compressor rotor blades for low-order statistical moment averaging in robust design".* In Proceedings of the 1st Global Power and Propulsion Forum: GPPF, 2017, 7 pp.
https://eprints.soton.ac.uk/406744/

[10] Di Zhang, Jiao-Bin MA, and Qi Jing , *"Numerical Study Of Unsteady Flow And Exciting Force For Swept Turbomachinery Blades"*. Thermal Science, year 2016, vol. 20, suppl. 3, pp. s669-s676.
http://thermalscience.vinca.rs/pdfs/papers-2016/tsci160205199z.pdf

Theoretical Investigation of an Indirect Evaporative Air Cooling System

Mohamed I. Alowa, Gassem A. Azzain

Department of Renewable Energies, Faculty of Energy and Mining Engineering,
Sebha University, Libya

DOI: https://doi.org/10.21467/proceedings.4.17
* Corresponding author email: moh.alowa@sebhau.edu.ly

ABSTRACT

In this paper an indirect evaporative cooler theoretically investigated. Because of its low cost and low environment pollution, the indirect evaporative coolers have great potential as an alternative to conventional air conditioning in an arid hot climates such as southern of Libya where the temperature and relative humidity reach 45°C and 20 % respectively. The present investigated system consists of cooling tower, cross unmixed heat exchanger, air blower, circulating pump, air filter, humidifier, and air duct. The main factors that affect on the temperature output of the system are presented. The affect of air conditions input to the cooling tower and air duct were clarified by solving the control equations using Matlab program. The results show that the air dry bulb temperature directly proportion to the outlet dry bulb temperature, and air input relative humidity notable proportion to the outlet dry bulb temperature. The water flow rate in the cooling tower affect on the outlet air temperature, were as it increases the outlet air temperature decreases. Also the air flow rate through the cooling tower contributes in the outlet air temperature, while the increasing in the air flow rate leads to decreasing in the outlet air temperature. Furthermore as the flow rate of the air inside the air duct increases, the outlet temperature decreases. Moreover investigation proves that the indirect evaporative cooling successfully can be used in the southern of Libya.

KEYWORDS: Indirect evaporative cooling, Cooling tower, Arid hot climates

1 Introduction

An indirect evaporative air cooler (IEC) is one of the promising solution for air conditioning specially in the arid hot climates, which encouraging the researchers to taken up different studies concerning of this subject. The analysis for theoretical and experimental works takes place over a wide world locations even in the cold weather State, such as European countries where the experimental analysis of (IEC) system studied [1]. The components of the (IEC) have factors effecting on the system performance, [2] investigated the conductivity of metal, fibers, ceramics and how they impact on the (IEC) system. The (IEC) acts as an energy recovery device in air conditioning systems which called a semi-indirect evaporative cooler [3]. The outdoor conditions have a most effect on the (IEC) availability applications that provide

 ISBN: 978-81-936820-6-7

a comfort conditions, [4]. The review of (IEC) [5] technology was undertaken from a variety of aspects including background, history, current status, concept, standardization, system configuration, operational mode, research and industrialization, market prospect and barriers, as well as the future focuses on commercialization indicated that (IEC) technology has potential to take up the air conditioning duty for buildings. The (IEC) systems has been modified to increase its cooling performance one of modification is an effectiveness- number of transfer unit (Ɛ-NTU) method analysis using an indirectly pre-cooling the working air before it inters the wet passage that could be based on (Ɛ-NTU) heat exchanger by redefining the potential gradients, transfer coefficient, heat capacity rate parameters [6]. The thermodynamic characteristics of (IEC) experimentally and theoretically research works on feasibility studies, performance test and optimization as well as transfer analysis reviewed [7]. The advantages of the (IEC) is the low energy consumption and the environmental friendly and very low warming impact, the disadvantage is the water consumption [8]. For the (IEC) system, the main equipment is the cooling tower where the cold water produced. The principle of the cooling tower is the process of heat and mass transfer by direct contact between air and water in the tower packed by means of the coefficient of both heat and mass transfer. The simultaneous heat and mass transfer between water and air experimentally investigated [9] where the effect of air and water flow rates on the global heat and mass transfer coefficient clarified. In this paper the effect of the air conditions and the flow rates of both air and water on the air out of (IEC) that mainly consists of cooling tower, cross unmixed heat exchanger, air blower, circulating pump, humidifier, and air duct is investigated by solving the control equations using Matlab computer program.

2 System Description

The investigated (IEC) system is shown in Figure 1,and it can be described as following.

Air Blower: It is a centrifugal fan type that supply the air from an ambient air to the conditioning duct where the processing equipments of the system assembled.

Heat Exchanger: The heat exchanger is the equipment where heat transfer between the water from the cooling tower and the air inlet to the system is taken place. The heat exchanger type is staggered order find tube unmixed cross flow and its effectiveness is 75%.

Humidifier : The humidifier is a bank of atomizer nozzles that spry the cooled water from the cooling tower into the stream of the cooled air that is outlet from the heat exchanger.

Duct System: Duct is a passage where the ambient air flows onto the equipments of blower, filter, heat exchanger, humidifier, and eliminator. Duct cross section area, and length are 64×64 cm^2, and 1.3 m respectively.

Cooling Tower : The cooling tower is the equipment where the heat and mass transfer occurring by direct contacting between the air and to produce the cold water. The cooling tower type is the forced counterflow. The tower consists of a draft axial fan mounted at the

top of the tower. The nozzles spray water on the dick for enlarging the contacting area between the air and water to maximize the heat and mass transfer rate. The bottom of the tower body is a water sump which collects the cold water. The tower height is 2 m, cross section is area, 1×1 m^2.

Cooling Water Circulating System : The cooling water is circulated by means of a centrifugal pump and water flow rate is controlled by three valves.

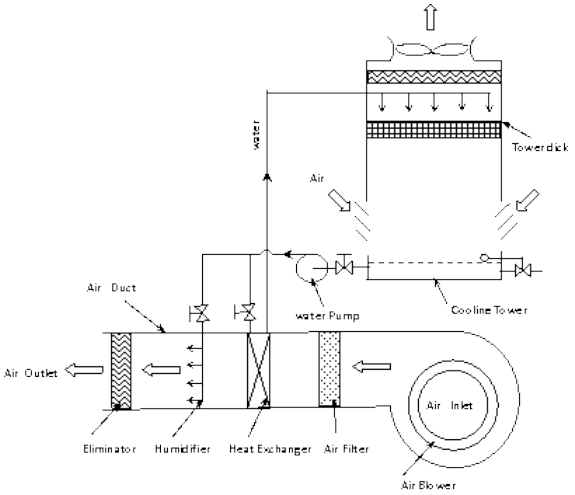

Figure 1: Indirect evaporative air cooler system.

3 Theory

The main processes are occurred first in the cooling tower where the mass and heat transfer takes place to produce the cold water, next the heat transfer between the air and cold water through the heat exchanger for air cooling, then the air humidified by the cold water. For the cooling tower, from Figure 2, ignore water loosing and heat transfer through the tower walls, the energy balance equation for the process of direct contact of heat and mass transfer in cooling tower is [10]

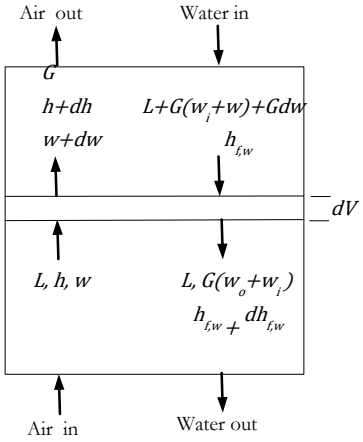

Figure 2 : Counterflow cooling tower diagram.

ISBN: 978-81-936820-6-7
Proceedings DOI: 10.21467/proceedings.4

$$Gdh = -[L - G(w_2 - w)]dh_{f,w} + Gdwdh_{f,w} \quad (1)$$

where G is the air flow rate, (kg/s), h is the moist air enthalpy, (kJ/kg), L is the water flow rate, (kg/s), w, is humidity ratio of moist air, (kg_w/kg_a), $h_{f,w}$ is water enthalpy at its temperature, (kJ/kg).

(w_2- w) is small and it can be ignored so,

$$Gdh = -Ldh_{f,w} + Gdwdh_{f,w} \quad (2)$$

For water energy balance in terms of the heat and mass transfer coefficients, K_C(kw/m^2 ^{o}C) and, K_D(kg/s.m^2) respectively

$$-Ldh_{f,w} = K_C A_V dV(t_w - t) + K_D A_V dV(w_{s,w} - w)h_{fg,w} \quad (3)$$

where, A_V, is water surface area per unit volume, (m^2/m^3), t_w , water temperature (^{o}C), t, moist air dry-bulb temperature, (^{o}C), $w_{s,w}$, humidity ratio of saturated air at t_w, (kg_w/kg_a), $h_{fg,w}$= $h_{g,w}$- $h_{f,w}$.

$h_{g,w}$, is the enthalpy of saturated water vapor at t_w (kJ/kg).

The air side water vapor mass balance is

$$-Gdw = K_D A_V dV(w_{s,w} - w) \quad (4)$$

Introducing Lewis number $Le = \frac{K_C}{K_D c_{pa}}$ in equation (3) gives,

$$-Ldh_{f,w} = K_D A_V dV[Lec_{pa}(t_w - t) + (w_{s,w} - w)h_{fg,w}] \quad (5)$$

Combining equs. (2), (4),and (5)

$$\frac{dh}{dw} = Lec_{pa}\frac{t_w - t}{w_{s,w} - w} + h_{g,w} \quad (6)$$

The enthalpy of moist air for constant C_{pa},

$$h = c_{pa}dt + wh_g$$

$$dh = c_{pa}dt + dwh_g$$

$$h_{s,w} - h = c_{pa}(t_w - t) + h_g^o(w_{s,w} - w)$$

where $h_{s,w}$, is the enthalpy of saturated air at t_w, h_g^o is the enthalpy of saturated water vapor at 0^{o}C.

From equ. (6)

$$\frac{dh}{dw} = Le\frac{h_{s,w} - h}{w_{s,w} - w} + (h_{g,w} - h_g^o Le) \quad (7)$$

For $Ldh_{f,w} = LC_w dt_w$ so by equs. (5) and (7), we have

$$-\frac{dt_w}{h_{s,w} - h} = \frac{G}{LC_w}\left[Le + \frac{h_{fg,w} - h_g^o Le}{(h_{s,w} - h)/(w_{s,w} - w)}\right]\frac{dw}{(w_{s,w} - w)} \quad (8)$$

For the Heat exchanger the effectiveness is $\varepsilon = \frac{t_o - t_i}{t_i - t_{w,i}}$ (9)

The humidifier control equations are.

$$h_{ih} = \acute{t}_o + w_i(2501 - 1.805t_{ih}) \quad (10)$$

$$h_{f,w} = 0.204266 + 4.18609t_w \quad (11)$$

$$l = g(w_o - w_i) \quad (12)$$

$$h_o = \frac{l}{g+l} \times h_{f,w} + \frac{g}{g+l} \times h_{ih} \quad (13)$$

$$t_o = \frac{h_o - 2501w_o}{1+1.805w_o} \quad (14)$$

h_{ih}, t_{ih}, w_i, enthalpy, temperature, and humidity ratio of air input to the humidifier respectively, $\acute{t}_o$, is the air temperature out of the heat exchanger, l, g, water, and air flow rates through the humidifier respectively (kg/s), t_o, w_o , temperature, and humidity ratio of the air output.

4 Results and Discussion

The above control equations (8) through (14) solved using Matlab computer program for steady state and assuming no heat and water loss from the cooling tower and air duct. Input the system specifications, and G, L, input t_w, for Le =1, the solution is starting with the initial conditions and applying trial and error procedure to get the air outlet conditions. The process bath of the air through the air duct is shown in Figure 3 where, the air sensible temperature dropping in heat exchanger by the cold water from the cooling tower. The temperature dropping takes place as a result of the operation conditions. Finally the cold air is humidified by the humidifier which increases the air humidity as well as slightly deceases its temperature.

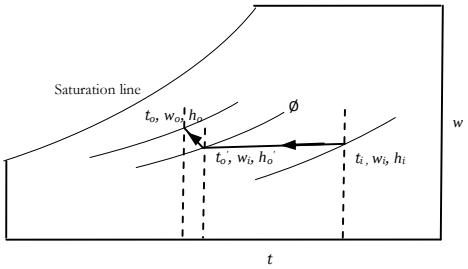

Figure 3 : Processes bath of the air through the air duct.

The effect of the conditions of the inlet air to the system for a constant air relative humidity(RH) Ø, and water, air flow rates in the cooling tower are L= 0.65 kg/s, G= 2.6, respectively, and air flow in condition duct g=1.5 kg/s is shown in Figure 4 which reveals that as inlet dry bulb air temperature t increases, its outlet temperature increases t_o. But as (RH) decreases for constant air dry bulb temperature, the outlet air temperature deceases, that because, for the low (RH) which means low wet bulb temperature more amount of water evaporated in the cooling tower due to the high mass an heat transfer coefficient and as a result the water heat capacity between inlet and out let lowered hence, the water temperature

ISBN: 978-81-936820-6-7
Proceedings DOI: 10.21467/proceedings.4

from the cooling tower that flow to the heat exchanger and the humidifier causing air temperature drop.

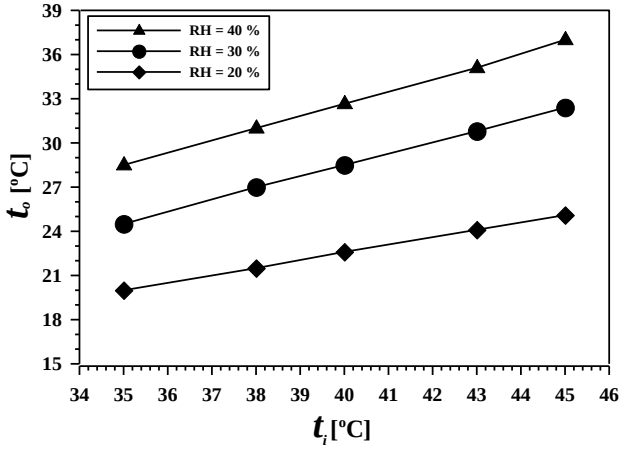

Figure 4: Effect of inlet air conditions on the outlet air at *L*= 0.65 kg/s, G= 2.6 kg/s, and *g* =1.5 kg/s.

The water flow rate plays noticeable effect on the water temperature outlet from the cooling tower which then supplied to the heat exchanger. The effect of cold water flow rate from the cooling tower on the air temperature exit from the duct is shown in Figure 5 which illustrates that as the flow rate of water increases, the exit temperature from the duct decreases that because higher water flow rate enables heat and mass transfer between the air and water to increase as well as the increasing of the water flow rate into the heat exchanger, increases the heat transfer rate.

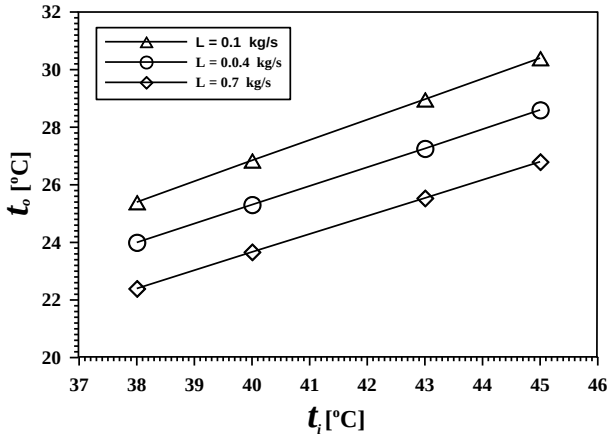

Figure 5: Effect of the water flow rate in the cooling tower on the outlet air at G= 2.6 kg/s, *g* =1.5 kg/s, and Ø=25%.

From Figure 6, it's clear that when the air flow rate increases into the cooling tower the air out let of the duct decreases due to water temperature drop in the tower and consequently in

the heat exchanger as a result of enlargement of heat and mass transfer area between air and water that gives big chance of the transferring process to take place.

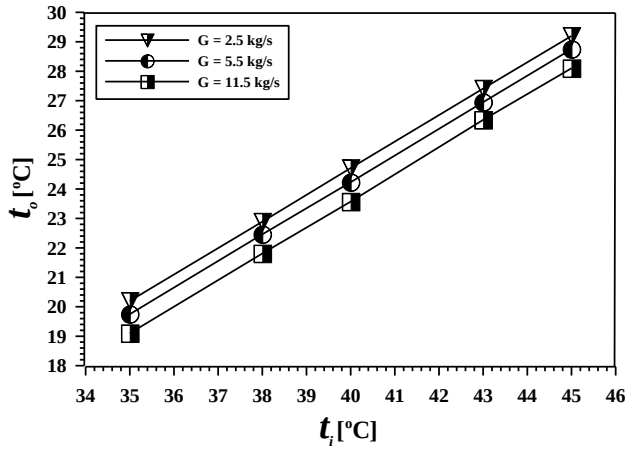

Figure 6 : Effect of the air flow rate in the cooling tower on the outlet air at L= 0.65 kg/s, g =1.5 kg/s, and Ø=25%.

The air velocity in the air duct has a manifest effect on the outlet air temperature as shown in Figure 7, from which it can be deduced that as the air velocity increases the air temperature outlet decreases due to the increasing in the NTU of the air-water heat exchanger.

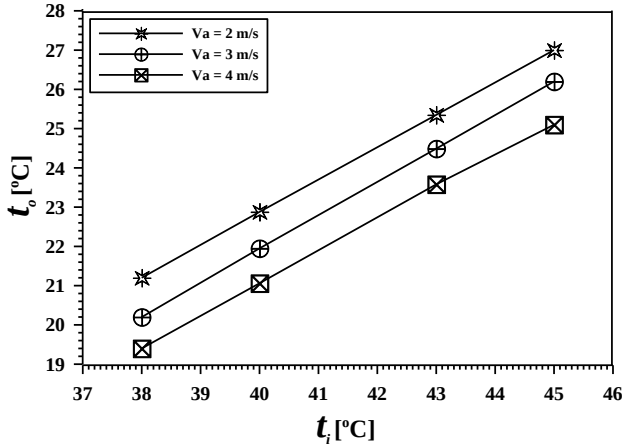

Figure 7 Effect of the air velocity in the air duct on the outlet air at L= 0.65 kg/s, G= 2.6 kg/s, and Ø=25%.

5 Conclusion

The (IEC) system have been investigated which reveals that the main principles of the (IEC) system depends on the direct contact between the air and water where both heat and mass transfer between the air and water takes place in the cooling tower. The factors that effect on the performance of the (IEC) system are the inlet air conditions mainly inlet air wet bulb temperature or (air relative humidity) as its decreases the air temperature outlet decreases for constant water and air flow rates, also the flow rates of both the air and water in the cooling

ISBN: 978-81-936820-6-7

Series: AIJR Proceedings
Proceedings DOI: 10.21467/proceedings.4

tower have highly impact on the (IEC) system and whenever these flows increases the air temperature out of the system decreases due the simultaneous of heat and mass transfer raising up. Likewise as air velocity in the duct increases the outlet of air temperature decreases due the heat exchanger effectiveness improvement. The (IEC) systems may successfully used as air cold conditioners at the arid climates such as Libya particularly southern regions. more studies on the (IEC) systems required to be done to improve their performance.

References

[1] B. Costelloe, D. Finn, "Indirect Evaporative Cooling Potential in Air - Water Systems in Temperate Climates", *Energy and Buildings* Vol. 35 (2003) 573-591.

[2] X. Zhao, Shuli Liu, S. B. Riffat, "Comparative Study of Heat and Mass Exchanging Materials for Indirect Evaporative Cooling Systems", *Building and Environment* Vol. 43, Issue 11, Nov. 2008, Pag. 1902-1911

[3] R. Herrero Martin, "Numerical Simulation of a-Semi-Indirect Evaporative Cooler", *Energy and Buildings* Vol. 41, Issue 11 Nov. 2009, Pag. 1205-1214.

[4] G. Heidarinejad, M. Bozorgmehr, S. Delfani, J. Esmaeelian, "Experimentally Investigation of Two-Stage Indirect/Direct evaporative Cooling System in Various Climatic Conditions", *Building and Environment* Vol. 44, Issue 10, Oct. 2009, Pag. 2073-2079.

[5] Z. Duan, et al., "Indirect Evaporative Cooling: Past, Present and Future Potentials", *Renewable and Sustainable Energy Reviews"*, Vol. 16, Issue 9, Dec. 2012, Pag. 6823-6850.

[6] Ala Hasan, "Going Below the Wet-Bulb Temperature by Indirect Evaporative Cooling: Analysis Using a Modified Ɛ-NTU Method", *Applied Energy*, Vol. 89, Issue 1, Jan. 2012, Pag. 237-245.

[7] Y.M. Xuan, et al., "Research and application of Evaporative Cooling in China: a Review (1)-Research", *Renewable and Sustainable Energy Reviews*", Vol. 16, Issue 5, Jun. 2012, Pag. 3535-3546.

[8] Bogdari Porumb, et al., "A Review of Indirect Evaporative Cooling Technology", *Energy Procedia* , Vol. 85, Jan. 2016, Pag. 461-471.

[9] M. Lemouari, M. Boumaza, and A. Kaabi, "Experimental Analysis of Heat and Mass Transfer Phenomena in a Direct Evaporative Cooling Tower", *Energy Conversion and Management*, Vol. 50, Issue 6, Jun. 2009, Pag. 1610-1617.

[10] T. Kuehen, J. Ramsey, and J. Threlkeld, "Thermal Environmental Engineering", *Prentice Hall*, 1998.

Monitoring Mis-Operating Conditions of Journal Bearings based on Modulation Signal Bispectrum Analysis of Vibration Signals

Osama Hassin[1*], Usama Haba[1,2], Fengshou Gu[2], Andrew Ball[2]

[1] Department of mechanical, College of Engineering, University of Gharyan, Gharyan, Libya
[2] School of Computing and Engineering, University of Huddersfield, Huddersfield, UK

DOI: https://doi.org/10.21467/proceedings.4.18
* Corresponding author email: osamingo@yahoo.com

ABSTRACT

Journal bearings are widely used to undertake a wide range of operating conditions. Under high radial load, low rotating speed and thin lubrication films, asperity collisions between the journal and the bearing surfaces may occur. These self-excitations can create wideband random vibrations due to asperity contact and asperity churn. On the other hand, under low radial load and high rotating speed they can have instable operations due to oil whirls and shaft fluctuations. In addition, because of high lubricant viscosity, fluid shearing forces can be dominant, which may also result in wideband vibrations. These types of excitations together with structural responses can be coupled to produce nonlinear modulation phenomena. In this paper, modulation signal bispectrum (MSB) is used to analyses the vibration responses in order to identify the vibration signals values under different operating conditions and hence achieve condition monitoring of journal bearings. Furthermore, MSB coherences display clear regular modulating components in the high carrying frequency range due to coupling between shaft frequencies and the wideband compounds. In associating MSB-Coh. with normalising of MSB magnitude makes possibility to differentiate responses between asperity collision vibration and instability vibration. Thereby, it is possible to identify optimal operating conditions and detect abnormal operations caused by degraded lubrications or worn surfaces.

Keywords: Journal bearings, vibration condition monitoring, MSB, optimal operating conditions.

1 Introduction

A self-aligning spherical journal bearing has been designed for applications such as high speed fans and other similar applications. One usage of the journal bearing is to support radial load under high speed. It also designed to work at hydrodynamic lubricant regime in which thick oil film formed between the shaft and the bearing. Because of lubricant stiffness and damping coefficients, journal bearings are considered the best element for absorbing vibration, resisting shock, quietness and long life. In contrast, high radial load, low rotating speed, and weak of oil film may lead the journal bearing to work at boundary lubricant regime which causes metal-to-metal contact.

 ISBN: 978-81-936820-6-7

The idea of condition monitoring is monitoring the asset behaviour to detect, diagnose and prognoses faults and mis-operating conditions that have reached a certain symptomatic level to provide system breakdown. Vibration monitoring analysis is one of the main techniques used to diagnose and predict various defects [1]. Vibration monitoring is to break down a composite signal which generated from different vibration sources in which each source has a unique signal characteristic. Therefore, when the analyses of the journal bearing vibration signals carried out, many different sources of vibrations should be considered. The most well know external excited vibration sources of journal bearing are mechanical unbalance and misalignment. Furthermore, oil coefficients and asperity collisions also causes self-excited vibrations of journal bearing [2]. In this paper, vibration monitoring analysis is used to detect mis-operating conditions. When the machine operating conditions changes, the vibration signal changes accordingly. Modulation Signal Bispectrum (MSB) is a technique used to analyse the vibration of the composite signal which is a combination of the information and the carrier signals. This research found that MSB magnitude and MSB coherence are useful to identify vibration caused by internal and external excitations. MSB magnitude directed to vibration caused by self-excitation forces, in contrast, MSB coherence indicated to vibration caused by external-excitation forces. Finally, optimal operating conditions have been identified by coupling mean values of both MSB-Mag. and MSB-Coh. spectrums. Because the journal bearing does not contain any rotating element as a rolling bearing, vibration signals correlated to shaft rational speed and random asperity collisions.

2 The Lubrication Regimes

In 1846, Stribeck reported that the friction coefficient was inversely proportional to speed. Thus, he presented the characteristic curve of the coefficient of friction versus speed. Figure 6 illustrations the Stribeck curve, this shows the relationship between the coefficient of friction and bearing parameter or modulus $\eta N/p$, where η is the absolute viscosity of the lubricant in kg/m.s, N is the shaft speed in rpm and p is the pressure on the projected area in Pa. The Stribeck curve shows how the coefficient of friction changes with lubrication regime: boundary lubrication, mixed-film lubrication and hydrodynamic lubrication. The optimum point of the curve is when the coefficient of friction passed through a minimum point from mixed to hydrodynamic lubrication [4]. Many parameters influence the friction coefficient such as the operating condition (speed and pressure), the material properties (roughness of surface) and the viscosity of the lubricant. Later, the Stribeck curve application extended to a number of tribology component besides journal bearing. For example, ball bearing, seals and wet clutches have applied the Stribeck curve idea.

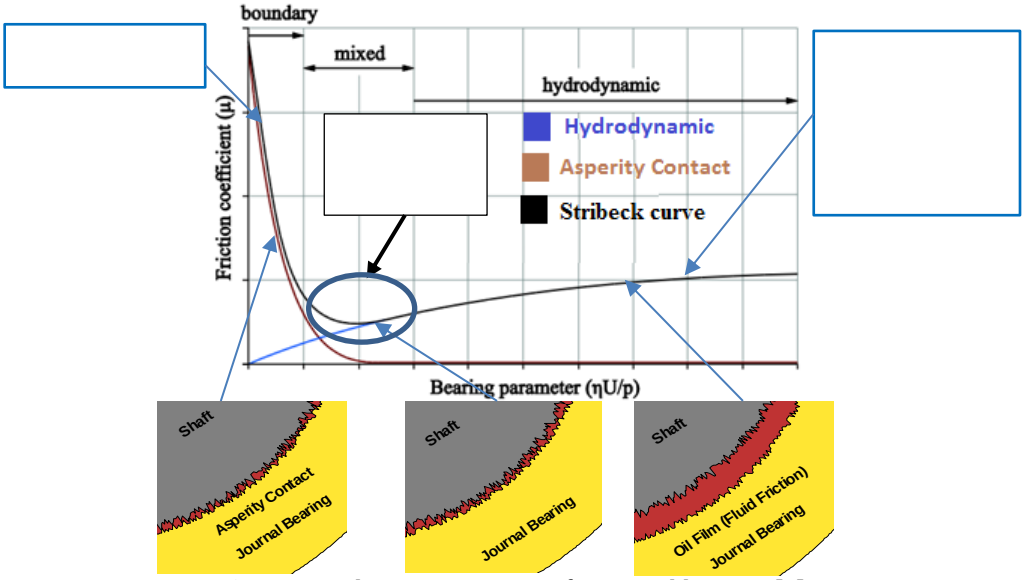

Figure 6: Lubrication *regimes of a journal bearing [3]*

3 Vibration of Journal Bearing

Vibration responses of a self-aligning journal bearing directly linked to the radial load, rotating speed, lubricant viscosity, oil film thickness, eccentricity, surface asperity characteristics and material of the bearing. Different forces placed on journal bearing affect the vibration responses and produce both low and high frequency vibrations. For example, the low journal whirling frequency is influenced by shaft fluctuating. Likewise, high random frequency bands of the vibration signals are occurred by asperity collisions and churns [5]. At hydrodynamic regime, journal bearing vibration sources often are generated by mechanical contact between the rotating shaft and stationary bearing [6]. High clearance causes looseness of bearing which generates more of a square wave than a sinusoid wave [7] and, many harmonics are generated from these signals. In the case of severe looseness, it is stretched all the way across the spectrum and half-harmonics are even generated in extreme cases (one-time, double times, three times, four times, five times, six times, etc.) rpm [7]. Another type of excitations is mechanical unbalance which causes a pure sinusoid and therefore generates a peak at one time rpm [8]. Journal bearing is often generate vibration peaks at frequencies lower than one time rpm. Another problem of the journal bearing is oil whirl. In which oil whirl is a phenomenon that vibrations are excited by oil film between frequency from 0.38 time rpm to 0.48 time rpm. Changes in viscosity and pressure of the oil and related loads can affect oil whirl [9]. Asperity collisions and churns interactions are sources of self-excitation, which result in high responses at structure resonances. The random high frequency of vibration responses is mainly related to two frictional effects. High frequency bands around 10kHz of the bearing are related with both asperity contacts and fluid friction through the method of clustering spectrum of vibration signals, [10]. The response frequency of self-excited vibration is very close to one of the system's natural frequencies [11]. Finally, the interaction between periodic responses and

ISBN: 978-81-936820-6-7
Proceedings DOI: 10.21467/proceedings.4

Series: AIJR Proceedings

resonant responses produce modulation signals. The equation bellow presents different sources of vibration in a journal bearing [12].

$$m_s\ddot{x} + \overbrace{k[p(x),\omega,\mu]x}^{\text{Hydrodynamic}} + \overbrace{\sum_{i=1}^{n} k_i \Gamma[p(x),\omega,\mu]x}^{\text{Asperity churns}} + \overbrace{\sum_{i=1}^{n} k_i \Psi[p(x),\omega,\mu]x}^{\text{Asperity collisions}}$$

$$= \overbrace{F_r}^{\text{Static radial load}} + \overbrace{\sum_{i}^{n} A_i \cos(i\omega t + \alpha_i)}^{\text{Unbalance+misalignment}} \quad (1)$$

where m_s is the mass of the shaft; k_i denotes the bending stiffness of an arbitrary micro asperity; k is the stiffness coefficients due to hydrodynamic pressure effect which includes inherent surface defects and journal elastic deformations of micro asperities and main load zones.

4 Modulation Signal Bispectrum

Understandably, high forces of external and internal excitation will generate massive vibration responses. Any mechanical problem will produce vibration with low frequency correlated to shaft rotational speed. Contrast, random asperity collisions will produce high band frequency. Due to a low frequency (information signal) is superimposed on a high frequency (carrier signal) modulation signal of vibration will be generated in journal bearing. Bispectrum is a non-linearity signal generated by interact two waves. MSB is used to detect coupling signal between shaft frequencies and the wideband compounds. The modulation signal of vibration is formed by nonlinear of two components, periodic and random signal. Thus, it is anticipated that bispectrum can give a more accurate representation of the vibration signal for mis-operating diagnosis [13]. The Discrete Fourier Transform (DFT) $X(f)$ of a vibration signal $x(t)$ is defined in the form of Modulation Signal Bispectrum (MSB),

$$B_{MS}(f_x, f_c) = E\left\langle X(f_c + f_x)X(f_c - f_x)X^*(f_c)X^*(f_c)\right\rangle \quad (2)$$

The phase relationship of MSB is

$$\begin{aligned}\varphi_{MS}(f_x, f_c) &= \varphi(f_c + f_x) + \varphi(f_c - f_x) - \varphi(f_c) - \varphi(f_c) \\ &= \varphi(f_x) + \varphi(-f_x)\end{aligned} \quad (3)$$

where f_x is information frequency; f_c is the carrier frequency, $f_c + f_x$ and $f_c - f_x$ are the higher and lower sideband frequencies respectively. It takes into account both $f_c + f_x$ and $f_c - f_x$ simultaneously in Equation above for quantifying the nonlinear effects of modulation signals. If they are due to the modulation effect between f_c and f_x, a bispectral peak will be

at bifrequency $B_{MS}(f_x, f_c)$. On the other hand, if these components such as various noises are not coupled but have random distribution, their magnitude of MSB will be close to zeros. In this way, the wideband noise and aperiodic components of vibration signals can be suppressed effectively so that the discrete components relating modulation effects can be represented sparsely and characterised more accurately.

A normalized form of MSB, also named as modulated signal bicoherence, is introduced as,

$$b^2{}_{MS}(f_x, f_c) = \frac{|B_{MS}(f_x, f_c)|^2}{E\left\langle |X(f_c)X(f_c)X^*(f_c)X^*(f_c)|^2 \right\rangle E\left\langle |X(f_c+f_x)X(f_c-f_x)|^2 \right\rangle} \quad (4)$$

It is to measure the degree of coupling between three components against noise influences, in the same way as the conventional bicoherence [14, 15].

5 Experimental Procedure

A self-aligning spherical journal bearing, SA35M shown in Figure 7, has been tested. In this experimental, three types of lubrication are used to generate different operating conditions denoted as lube 22, 37 and 46 VG. Also, three different speed 1500, 1200 and 900 rpm are used. Furthermore, four different radial loads 1, 5, 10 and 20 bar are exerted on the shaft supported between two bearings. These different viscosities, rotation speed and radial load will lead journal bearing to work under different lubricant regimes. Figure 7 shows the journal bearing test rig. An accelerometer sensor is fixed horizontally to collect the vibration signals. Also, an encoder and a pressure sensor are placed to measure the output rotating speed and radial load, respectively.

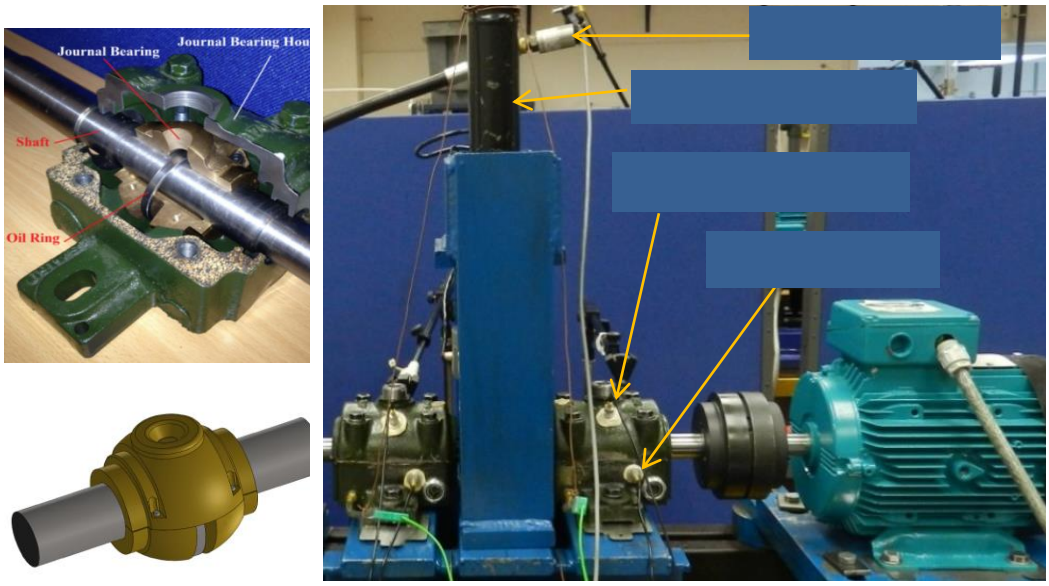

Figure 7: Self-aligning *journal bearing components and test rig [12]*

ISBN: 978-81-936820-6-7
Proceedings DOI: 10.21467/proceedings.4

Series: AIJR Proceedings

6 Experimental Results

RMS values are proportional to speeds, loads but do not show any significant difference between lubrication types because of instability distribution of the oil by oil ring and non-linearity distribution of the temperature. In theory, low speed causes more friction especially at high load but in the RMS results, Figure 8, show that the high speed always has high vibration and high load conditions generate high vibration energy. Also, different viscosities generate nonlinear RMS values of the vibration signals Thus in this study; the RMS values do not provide any good indication to present the bearing condition at different lubricant regimes. Therefore, these values do not consider to be a good indicator to obtain optimum operating conditions because they are always proportional to loads and speeds.

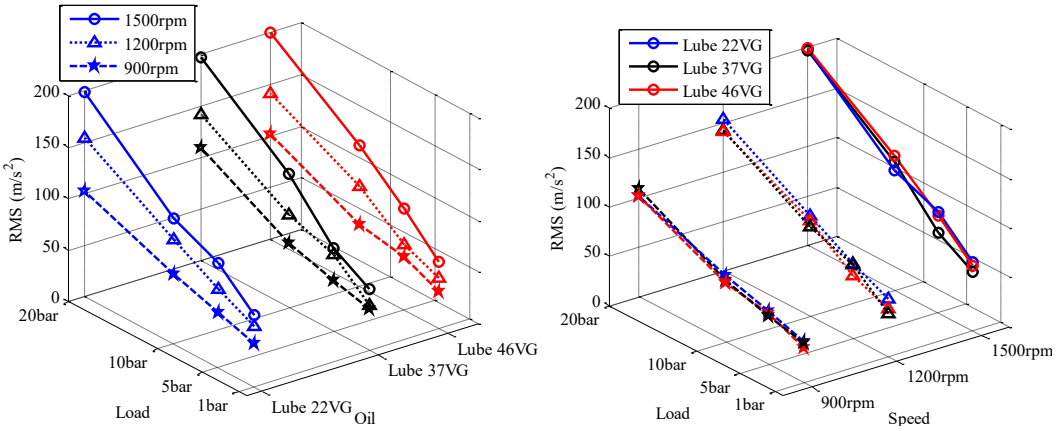

Figure 8: RMS *values of vibration signals under different operating conditions*

6.1 MSB Magnitude and MSB Coherence Results

Modulation signal bispectrum is dealing with coupled signals. In this manner, the wideband noise and periodic components of vibration signals can be suppressed effectively so that the discrete components relating modulation effects can be represented sparsely and characterised more accurately. MSB-Mag. and MSB-Coh. can provide a more clear representation of the journal bearing operation under different operating conditions. From Figure 10, it can be found that there is a high frequency band sensitive to changing radial load in MSB-Mag. These bands might be correlated with the friction of asperity collision caused by increasing the radial loads, which decrease the contact point at hmin and leads to metal-to-metal contact. In MSB-Coh. Figure 12, there is clear frequency band related to shaft speed. As a result of that, the small wedge may decrease fluctuating of the shaft and make it rotates more stable. High viscosity lubricant has high damper coefficient to absorb more vibration than low viscosity, but it loses its ability to move easily into the gap between surfaces. Moreover, high viscosity might cause asperity churns at high radial clearance in load zone.

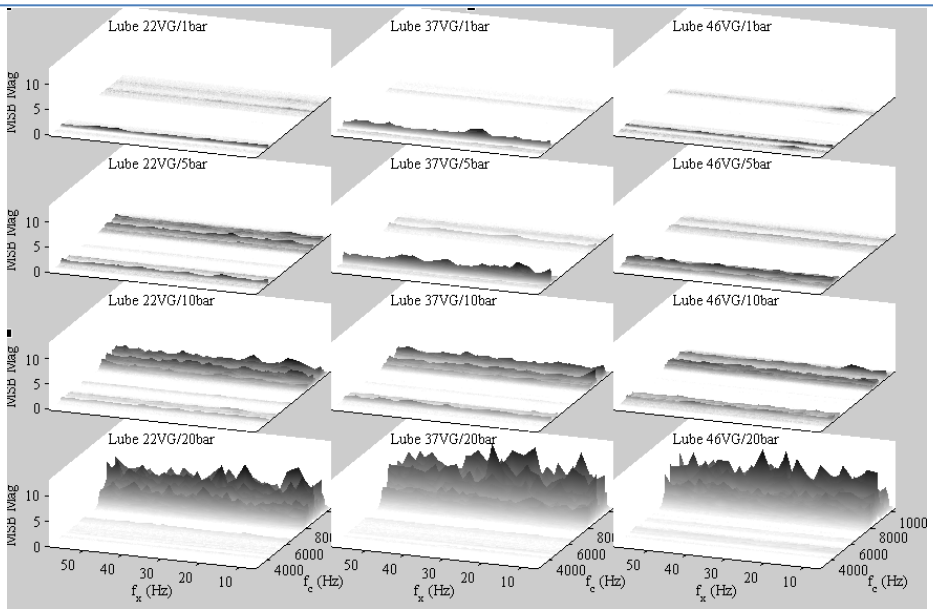

Figure 9: MSB-Mag. *at 900rpm under different loads and viscosities*

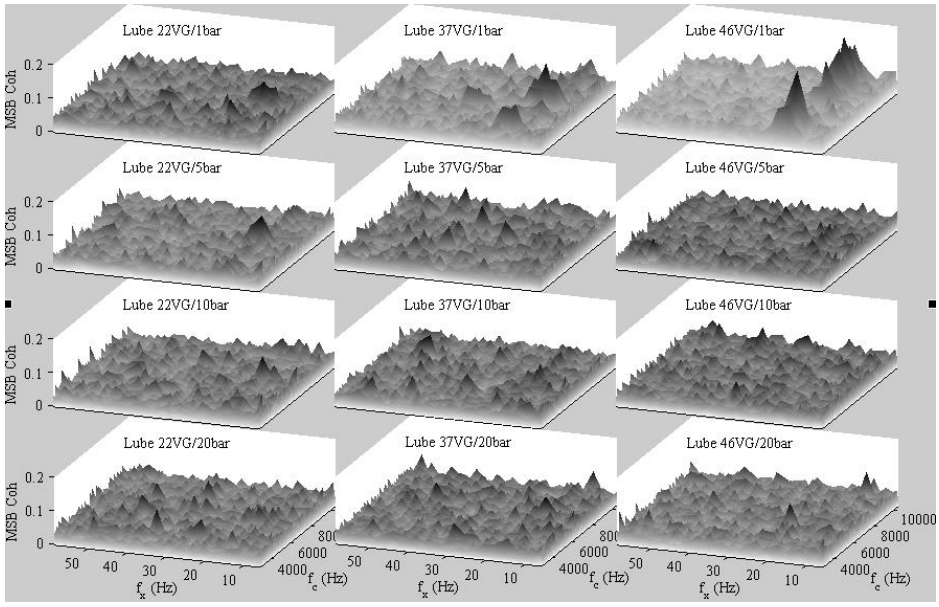

Figure 10: MSB-Coh. *at 900rpm under different loads and viscosities*

6.2 Mean Values of MSB Magnitude and MSB Coherence Results

MSB-Mag. manly presents asperity collision. In contrast, MSB-Coh. presents stability of the shaft. By calculating mean values of both MSB-Mag. and Coh. It can be found that the low load has the lowest mean of MSB-Mag., and at the same time has a higher mean value of MSB-Coh. In contrast, high load has less value of MSB-Coh. and high value of MSB Mag. as can be seen in Figure 11 That means, high load makes shaft more stable but causes asperity collision.

ISBN: 978-81-936820-6-7
Proceedings DOI: 10.21467/proceedings.4

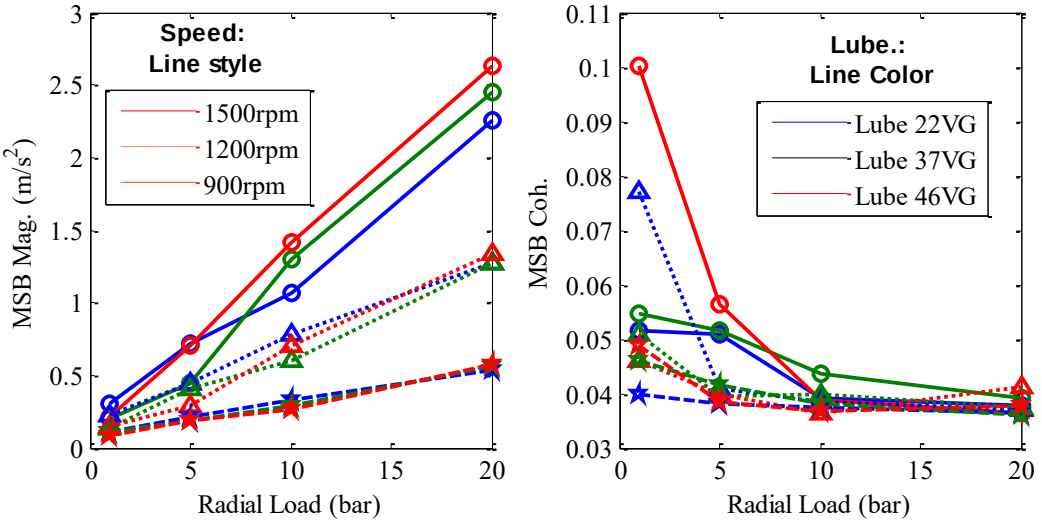

Figure 11: Mean *values of MSB-Mag. and MSB-Coh.*

Figure 12 shows gathering results of mean values of normalized MSB-Mag. and mean values of MSB-Coh. Examine the Figure representation; this operating condition could be considered as an acceptable operating conditions of the journal bearing compared with Stribeck curve in Figure 6. So, less mean value of MSB-Mag. and less value of MSB-Coh can be identified as an optimum operating condition.

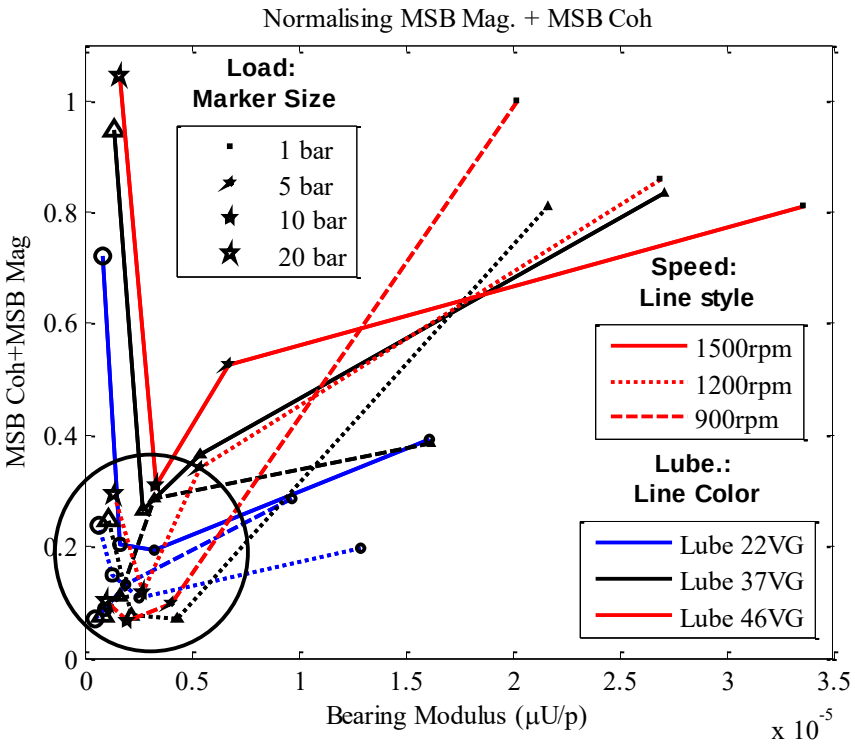

Figure 12: Representative *Stribeck curve by coupling MSB-Mag. and MSB-Coh.*

The optimum operating conditions in this experiment is at speed 1200 rpm and under 5 bar load of oil 37. The worst operating condition at hydrodynamic regime is at speed 1500rpm under load 1 bar and oil 46. The worst operating condition at boundary regime is at speed 900 rpm under load 20 bar and oil 22. These results prove the theory of Stribeck curve.

7 Conclusion

When the shaft rotates under a different operating condition, vibration signals manifests rich frequency components due to various vibration excitations such as mechanical problem, asperity collisions and asperity-fluid interactions. The mechanical problem, unbalance, occurs when the radial clearance is too large. To avoid this instability, a small radial load should be applied, or radial clearance should be decreased. However, if the radial load exceeds a certain level, metal-to-metal contacts will occur and generate more unneeded frictions, so the radial load should be carefully chosen.

RMS values of raw data are not convenient to obtain optimum operating conditions and do not differentiate between speeds and oil viscosities under different loads. On the other hand, mean values of MSB-Mag. and MSB-Coh. are found to be effective to determine the optimum operating condition. Abnormal conditions such as high loads, low viscosities and low speeds have high mean values of MSB-Mag. In the meantime, un-wanted operating conditions such as low load, high viscosity and high speed have high means value of MSB-Coh. Finally the mis-operating conditions have been found by analysing vibration signals based on coupling MSB-Mag. and MSB-Coh.

References

[1] Sethiya, S., Condition Based Maintenance (CBM). Secy. to CME/WCR/JBP, 2006.

[2] Raharjo, P., An Investigation of Surface Vibration, Airbourne Sound and Acoustic Emission Characteristics of a Journal Bearing for Early Fault Detection and Diagnosis. University of Huddersfield, May 2013.

[3] Tomanik, E. and A. Ferrarese. Low friction ring pack for gasoline engines. in ASME 2006 Internal Combustion Engine Division Fall Technical Conference. 2006. American Society of Mechanical Engineers.

[4] Frene, J., et al., Hydrodynamic lubrication: bearings and thrust bearings. Vol. 33. 1997: Elsevier.

[5] Raharjo, P., et al., Vibro-Acoustic Characteristic of A Self Aligning Spherical Journal Bearing due to Eccentric Bore Fault. 2012.

[6] Kim, M., et al., Experimental identification of abnormal noise and vibration in a high-speed polygon mirror scanner motor due to mechanical contact of plain journal bearing. Microsystem technologies, 2010. **16**(1-2): p. 3-8.

[7] Looseness - Bearing - VibrationSchool.com. 17 Nov 2015

[8] Unbalance - Single Plane - VibrationSchool.com. 11 Nov 2015.

[9] Journal bearing problem . VibrationSchool.com. 27 Nov 2015

[10] Osama Hassin, et al., Journal bearing lubrication monitoring based on spectrum cluster analysis of vibration signals in CMADEM 2015. 2015.

[11] Muszynska, A., Free, forced, and self-excited vibration. December 1997.

[12] Osama Hassin, Condition Monitoring of Journal Bearings for Predictive Maintenance Management Based on High Frequency Vibration Analysis**,** PhD thesis**,** May 2017.

[13] Gu, F., et al., Electrical motor current signal analysis using a modified bispectrum for fault diagnosis of downstream mechanical equipment. Mechanical Systems and Signal Processing, 2011. **25**(1): p. 360-372.

[14] Gu, F., et al., A new method of accurate broken rotor bar diagnosis based on modulation signal bispectrum analysis of motor current signals. Mechanical Systems and Signal Processing, 2015. **50**: p. 400-413.

[15] Gu, F., et al., A Novel Method for the Fault Diagnosis of a Planetary Gearbox based on Residual Sidebands from Modulation Signal Bispectrum Analysis. COMADEM 2014 16th-18th Sep. Brisbane, Australia., 2014.

ISBN: 978-81-936820-6-7

Series: AIJR Proceedings
Proceedings DOI: 10.21467/proceedings.4

Design of Reinforced Concrete Beams Using Two Different Specification

Gumaa A. Hasan*,Mohammed A. Elsageer, Musbah A. Hasan

Department of Civil Engineering, College of Engineering, Sirte University, Libya

DOI: https://doi.org/10.21467/proceedings.4.19

* Corresponding author email: Gumaa.hasan@yahoo.com

ABSTRACT

Nowadays, reinforced concrete beams are designed using traditional specification, such as BS8110 and Eurocode2 based on truss action. In this research BS8110 and Eurocode2 specification of designing a beam for flexure and shear are studied and compared with each other, to provide an in depth understanding of the two approaches. Two beams are designed, the first beam using BS8110 and the second beam using Eurocode2. The designs based on BS8110 and Eurocode 2 at the ultimate and serviceability limit states are discussed and the approach used to predict deflections is described and checked using standard relationship based on statics. Secondly the BS8110 and Eurocode2 approaches to designing a beam for shear and deflection are compared with each other. the two test beams are tested and the test results are compared with predicted results. The results from the laboratory tests have shown that the Eurocode2 beam carried a higher load and gave a higher central deflection compared to BS8110.

Keywords: Reinforced Concrete, Beam analysis, shear and deflection.

1 Introduction

Concrete is the most important construction material in the construction industry [1, 2]. There are approximately 2,000,000 billion tonnes of concrete being produced yearly [2]. Although concrete is good in compression and a durable material, it is weak in tension, where its tensile strength is approximately 10% of its compressive strength [3]. Concrete fails in tension when it is exposed to tensile stresses that are greater than its tensile strength capacity. So concrete on its own cannot resist these tensile stresses and it needs to be reinforced with another material that is good in tension, such as steel bars, to prevent failure of concrete in tensile region. Current design approaches for structural concrete beams are based on truss action [4]. In these design approaches the beam is designed firstly for flexure and then forshear independently of each other.

2 Comparison Between Provisions for Shear in BS8110 And Eurocode2

2.1 Shear

In the design for shear the basic principles behind the approaches in BS8110 and Eurocode2 are the same [5], and they are as follows

If the applied shear is less than the shear resistance of the concrete, minimum shear reinforcement should be provided, If the applied shear is higher than the concrete shear strength and less than the maximum design shear, designed shear reinforcement should be provided and if the applied shear is higher than the maximum design shear then a larger section must be chosen.

2.1.1 Shear Strength of Concrete

vc in BS8110 is equivalent to $\frac{VRd}{bd}$ in Eurocode2, where vc is design shear stress for concrete, VRd is the shear stress in concrete, b is the width of the section, and d is the effective depth of tension reinforcement

In BS8110 and Eurocode2 the strength of the concrete without shear links is dependent on the percentage of tensile reinforcement steel, the concrete grade and the effective depth of section and any axial forces are ignored [5, 6, 7].

Expression In BS8110

$$\mathrm{vc} = \frac{0.79\left[\left(100\frac{\mathrm{As}}{\mathrm{b.d}}\right)^{\frac{1}{3}}\times\left(\frac{400}{\mathrm{d}}\right)^{\frac{1}{4}}\times\left(\frac{\mathrm{fcu}}{25}\right)^{\frac{1}{3}}\right]}{\gamma_{\mathrm{m}}} \quad (1)$$

where vc is Shear stress in concrete, As is Area of tensile reinforcement, fcu is Characteristic strength of concrete, and γ_{m} is Factor of safety

Expression In Eurocode2

$$v_{Rd,c} = 0.18 \times \left(1 + \sqrt{200/d}\right) \times (100\rho_1 \times fck)^{1/3}/\gamma_m \quad (2)$$

where ρ_1 is Longitudinal reinforcement ratio, and fck is Characteristic of concrete

The limitations associated with each of these equations are as follows:

Expression In BS8110:

The percentage of tensile reinforcement should not be greater than 3% [BS8110]

The effective depth d should not be greater than 400 mm [8]. According to BS8110 the concrete shear capacity increase with depth less than 400 mm.

The ultimate concrete strength f_{cu}should not be greater than $40N/mm^2$[BS8110, 8]

The factor of safety is 1.25 [BS8110, 8]

Expression In Eurocode2:

The percentage of tensile reinforcement should not be greater than 2% [7, 8]

The effective depth d should not be greater than 600 mm

There is no limit placed on the concrete strength (f_{ck}) [8]

The factor of safety is 1.5 [7, 8]

Tables 1 and 2 show the shear stresses for a concrete with a cube strength of $30\ N/mm^2$using BS8110 and Eurocode2

ISBN: 978-81-936820-6-7
Proceedings DOI: 10.21467/proceedings.4

Series: AIJR Proceedings

Table 1: *Shear Strength of Concrete BS8110 [8]*

	d (mm)				
100As/bd	150	250	300	400	600
0.15%	0.46	0.4	0.38	0.36	0.36
0.3%	0.57	0.51	0.48	0.45	0.45
1%	0.86	0.76	0.72	0.67	0.67
3%	1.24	1.09	1.04	0.97	0.97

Table 2:*Shear Strength of Concrete Eurocode2 [8]*

	d (mm)				
100As/bd	150	250	300	400	600
0.15%	0.40	0.35	0.34	0.32	0.29
0.3%	0.51	0.44	0.43	0.40	0.37
1%	0.75	0.66	0.63	0.60	0.55
3%	1.09	0.96	0.92	0.86	0.80

2.1.2 Strength of Concrete Section With Shear Links

Designing concrete beam in shear using Eurocode2 can lead to significant economies in shear links compared to a beam designed using BS8110 [5, 7]

BS8110 – Assumptions:

- The angle between the notional compressive struts and the axis of the beam is constant and fixed at an angle $45°$ [5]
- The lever arm is assumed to be equal to the effective depth of the section [5]

Eurocode2 – Assumptions:

- The angle $\theta°$ between the notional compressive struts and the axis of the beam has a value within the range of 22° to 45° [5, 7].
- The lever arm is assumed to be equal to $0.9d$ [5, 7].

The resulting equations are as follows:

BS8110

$$\frac{Asv}{b \times Sv} = \frac{(v - vc)}{fyv/\gamma_m} \tag{3}$$

where Asv is the area of shear reinforcement, v is the Shear stress, Sv is the Spacing between links and fyv is Characteristic strength of links

Eurocode2

$$\frac{Asw}{b \times S} = \frac{\gamma_m \times v_{Ed}}{0.9.fyk.\cot\theta} \qquad \text{where } v_{Ed} = \frac{V_{Ed}}{b.d} \tag{4}$$

where v_{Ed} is the Shear forces at the ultimate limit state, fyk is the Characteristic strength of reinforcement and S is the Spacing between links

it should be noted that in BS8110 the shear reinforcement does not resist the total applied shear but only resists the shear in excess of that which can be resisted by the concrete $(v - vc)$ [7], where v is the design shear stress and vc is the design concrete shear stress. In Eurocode2 all the shear must be carried by the shear links, when shear links are required [5, 7]

2.1.3 Maximum Shear Strength of Section

The maximum allowable shear force is limited by placing a limit on the crushing strength of the diagonal compression member to prevent excessive stress from occurring in the diagonal compressive strut and hence prevent compressive strut failure of the concrete.

In BS8110 the maximum allowable shear is dependent on the strut angle and concrete strength, and since the angle of inclination of the strut has a constant value, the maximum shear is dependent only on the concrete strength [7].

$$v_{max} = 0.8\sqrt{fc} \quad \leq 5N/mm^2 [BS8110]. \qquad (5)$$

where fc is the Compression stress of concrete

In Eurocode2 the angle $\theta°$ has a value within the range of 22° to 45° , and hence the maximum shear is a function of the angle $\theta°$ and the concrete strength [7].

$$v_{Rd,max} = \frac{0.36(1-{fck}/{250})\times fck}{\cot\theta - \tan\theta}\,[7] \qquad (6)$$

A comparison of the maximum shear stress permitted within BS8110 and Eurocode2 is shown in Table 3.

Table 3: *Maximum Shear Stress Limitation in BS8110 and Eurocode2 [5].*

Cube strength (N/mm^2)	Eurocode2		BS8110
	$\theta°$		
	27°	35°	
25	2.91	3.38	4
30	3.38	3.92	4.38
40	4.19	4.87	5
50	4.85	5.64	5
60	5.36	6.22	5

2.1.4 Enhanced Shear Near Supports

BS8110 and Eurocode2 allow greater shears to be resisted by a concrete section which is close to the supports of a beam. The enhancement is a function of the av/d ratio where d is the effective depth of the section and av is the distance from the section considered to the face of the beam support. In BS8110, the design concrete shear stress vc, can be enhanced by $2d/av$ where $2d$ is greater than av. In Eurocode2 the shear which can be resisted by the concrete without shear links, can be enhanced by $2.5d/av$ where $2.5d$ is

ISBN: 978-81-936820-6-7
Proceedings DOI: 10.21467/proceedings.4

Series: AIJR Proceedings

greater than av[5, 6]. Eurocode2 allows a slightly higher enhancement of the shear capacity than BS8110 , so benefits are less in the case of BS8110 compared to Eurocode2 [8]

2.1.5 Spacing Of Links

BS8110

"The spacing of links in the direction of the span should not exceed 0.75d. At right-angles to the span, the horizontal spacing should be such that no longitudinal tension reinforcing bar is more than 150 mm from a vertical leg; this spacing should in any case not exceed d"[9]

Eurocode2

In Eurocode2 the spacing is a function of the applied shear. The rules are shown in Table 4.

Table 4: *Spacing between Links [5, 6]*

Applied Shear	Spacing (mm)	
	Lateral Spacing	Longitudinal Spacing
$v < v_{max} \times 1/5$	$d \leq 800$	$0.8d \leq 300$
$v_{max} \times 1/5 < v < v_{max} \times 2/3$	$0.6d \leq 300$	$0.6d \leq 300$
$v > v_{max} \times 2/3$	$0.3d \leq 200$	$0.3d \leq 200$

2.1.6 Additional Tensile Forces

In Eurocode2 the tensile force in the bottom tension member is given by:

$$Fs = M/Z + 1/2 \times V_{Ed} \times \cos\theta \quad (7)$$

where Fs is the Tensile stress of reinforcement, M is the Design ultimate moment, and Z is the Lever arm.

The second term in this equation is related to the shear forces in the links, so Eurocode2 takes into account the tensile forces which are caused by the bending and shear force in the links.

BS8110 takes into account only the first term in this equation (the bending term) and ignores the tensile force which is caused by shear force (second term in this equation).

2.2 Deflection

1- The assumptions which are required to define the behavior of a section under any loading condition are as follows:

BS8110

In an un-cracked section the reinforcement and the concrete in tension and compression are assumed to behave elastically. The modulus of elasticity of the reinforcement may be taken as 200 $kN/mm^2$and for the concrete may be taken from BS8110-2:1985, Section 3.5

In a cracked section the reinforcement in tension and compression is assumed to behave elastically and the concrete in compression is also assumed to behave elastically but in the tension region the concrete is assumed to behave linearly from zero stress at the neutral axis

to a limiting stress of $1\ N/mm^2$ at the centroid of the tensile reinforcement for short term loading and $0.5\ N/mm^2$ for long term loading. [9].

Eurocode2

In an un-cracked section the reinforcement and concrete in tension and compression are assumed to behave elastically [5]. The modulus of elasticity for the reinforcement can assumed to be $200 kN/mm^2$.

In a cracked section the reinforcement in tension and compression is assumed to behave elastically and the concrete in compression is assumed to behave elastically but in tension the concrete stress is ignored. [7].

Where BS8110 assumes that the tensile strength of concrete is approximately 1 $N/mm^2$and Eurocode2 uses a significantly higher value than BS8110 [5].

2- Curvature

According to Narayanan [18], see Figure 1 (a parameterized moment-curvature diagram), when M/bd^2 is in between 0.3 and 0.6, BS8110 gives higher curvature values than Eurocode2. This is because BS8110 uses a value for the tensile strength of concrete of approximately 1 N/mm^2 and Eurocode2 uses a much higher value. In general terms BS8110 and Eurocode2 are more or less equivalent.

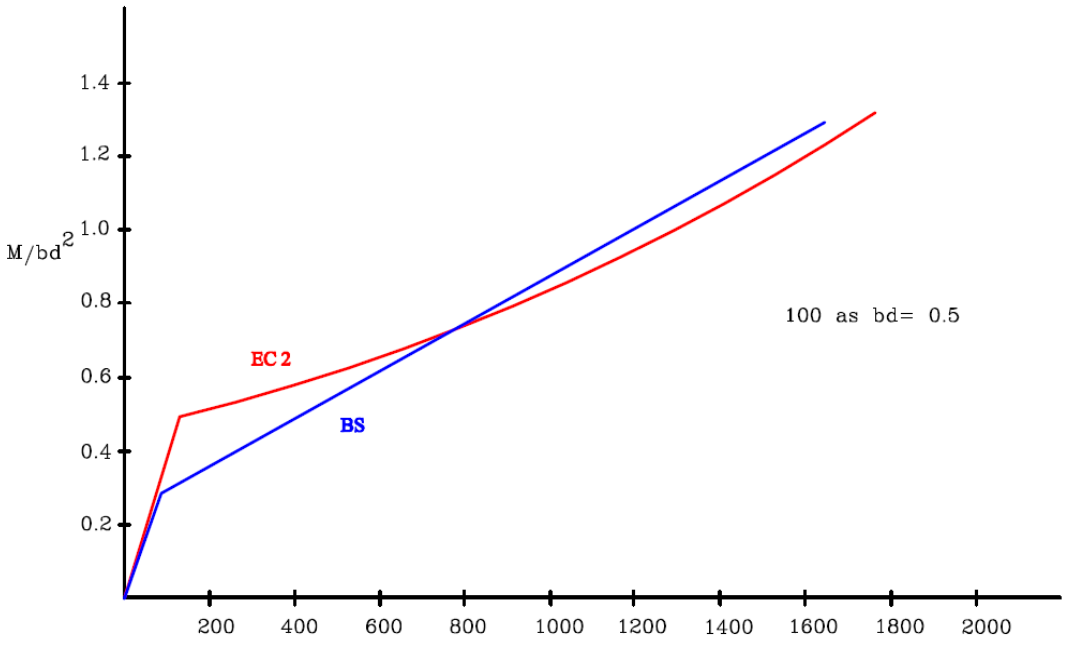

Figure 1: *Comparison of Curvatures Predicted by BS8110 and Eurocode2 [18]*

ISBN: 978-81-936820-6-7
Proceedings DOI: 10.21467/proceedings.4

Series: AIJR Proceedings

2.3 Economic Study

The Table 5 shows that the traditionally designed beams, which have been designed using BS8110 and Eurocode2, the weights of the reinforcement are 38.48 kg and 39.78 kg respectively.

Table 5: *Weight and Cost of Reinforcing Bars in Beam*

	Size of bar	No. Of bars	Length of bar (m)	Total length of bars (m)	Density of bar	Weight of bar (kg/m)	Total weight of bars (kg)	Weight of beam (kg)
Beam (1) BS8110	6	23	1.178	27.094	7.8	0.220	5.97	38.48
	10	2	3.45	6.9	7.8	0.612	4.225	
	20	3	3.85	11.55	7.8	2.45	28.297	
Beam (2) Eurocode2	6	28	1.178	32.984	7.8	0.220	7.27	39.78
	10	2	3.45	6.9	7.8	0.612	4.225	
	20	3	3.85	11.55	7.8	2.45	28.297	

3 Details of Materials and Test Procedure

3.1 Description of Beams and Loading Arrangement

Two beams were prepared for the laboratory based test programme with a rectangular cross-section of$200mm \times 300mm$, an overall length of 3500 mm, an effective span of 3000 mm and a minimum cover of 25 mm.

The two beams were tested using a four point loading arrangement the loading points were located at distance equal to 662.5 mm from the centerline of each support, see Figure 2, the spacing was based on Kani's Valley.

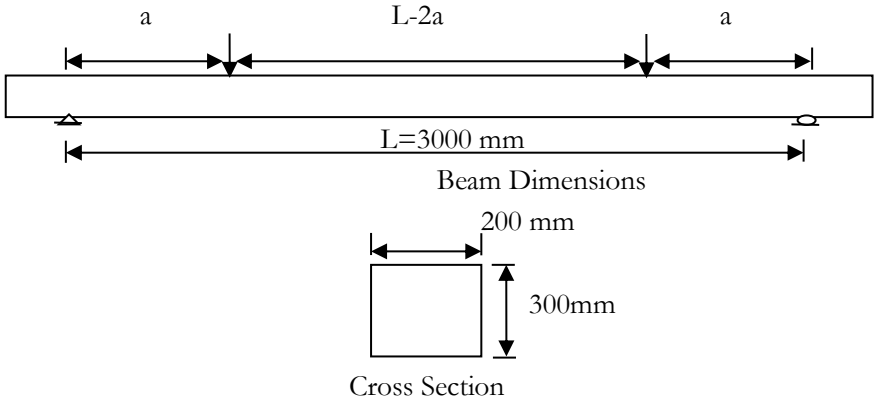

Figure 2: *Details of Beam and Loading Arrangement*

3.2 Design Of Test Beams

The beams were designed using two design approaches i.e. BS8110 Part 1 [1] and Eurocode2 [7]. The first beam was designed using the approach described in BS8110 and the secondbeam was designed using the approach in Eurocode2. Table 6 provides details of the three beams.

Table 6: *Beam Specifications*

Beam	Cross-section (mm^2)	Tensile bars (mm^2)	Spacing of links (mm)
BS8110	(200×300)	$3T20$	$T6\ at\ 150$
Eurocode2	(200×300)	$3T20$	$T6\ at\ 100$

3.3 Details of Reinforcement

Three sizes of reinforcing bars were used and they are as follows:

- 6mm diameter reinforcing bars were used as shear reinforcement in all three beams.
- 10mm diameter reinforcing bars were used as hanger bars for the links in all three beams.
- 20mm diameter reinforcing bars were used as tensile reinforcement in all three beams.

The three barsizes were tested to obtain the mechanical properties using of the steel. Tables 7, 8 and 9 show the tensile test results. All reinforcing bars were high yield steel.

Table 7: *Tensile Test Results for 6mm Diameter Reinforcing Bars*

Test	Maximum load (kN)	Tensile strength (N/mm^2)	Young's modulus (N/mm^2)
Test 1	16.61	588	196
Test 2	16.51	584.1	194
average	16.015	567	195

Table 8: *Tensile Test Results for 10mm Diameter Reinforcing Bars*

Test	Maximum load (kN)	Tensile strength (N/mm^2)	Young's modulus (N/mm^2)
Test 1	49	624	197
Test 2	47.98	611	202
average	48.49	617.5	199.5

Table 9: *Tensile Test Results for 20mm Diameter Reinforcing Bars*

Test	Maximum load (kN)	Tensile strength (N/mm^2)	Young's modulus (N/mm^2)
Test 1	203.2	647	211
Test 2	199.47	635.25	205
average	201.33	641.13	208

ISBN: 978-81-936820-6-7
Proceedings DOI: 10.21467/proceedings.4

Series: AIJR Proceedings

3.4 Details Of The Concrete

Six cubes and six cylinders were taken from the concrete mix in order to obtain the concrete crushing strengths at the time the beams were tested. These results were used to obtain the best estimate of the flexural/shear capacities of the beams and also the deflection values for the beams i.e. two sets of calculation were prepared one set assuming the concrete strength to be 30 N/mm^2 and the second set using actual concrete strength obtained from the cubes and cylinders. The material and load safety factors were moved from all the calculations used to predict the flexural and shear carrying capacities and the deflections of the beams. Tables 10 and 11 show the results obtained from the cube and cylinder tests carried out at the time the beams were tested.

Table 7:*Concrete Cube Crushing Test Results*

Ten day strength	Weight of cube (g)	H_1 (mm)	H_2 (mm)	H_3 (mm)	Applied loading (kN)	f_{cu} (N/mm^2)
Cube 1	2417	100	100	100	182	18.2
Cube 2	2518	100	100	100	200.4	20.04
Cube 3	2442	100	100	100	195.3	19.53
Cube 4	2421	100	100	100	211	21.1
Cube 5	2420	100	100	100	180.7	18.07
Cube 6	2400	100	100	100	203.4	20.34

Table 8: *Concrete Cylinder Crushing Test Results*

Ten day strength	Weight of cube (kg)	Diameter (mm)	high (mm)	Applied loading (kN)	f_{cK} (N/mm^2)
Cylinder 1		150	300	214.5	12.4

Average cube strength = $19.54 \quad N/mm^2$
Average cylinder strength = $12.4 \quad N/mm^2$

4 Results From Laboratory Based Test Programme

4.1 BS8110 Beam

According to the results from the laboratory based test, the maximum failure load was 80kN and the maximum deflection at mid span was 11.64 mm. Figure 3 shows the relationship between the applied load and central deflection of the beam.

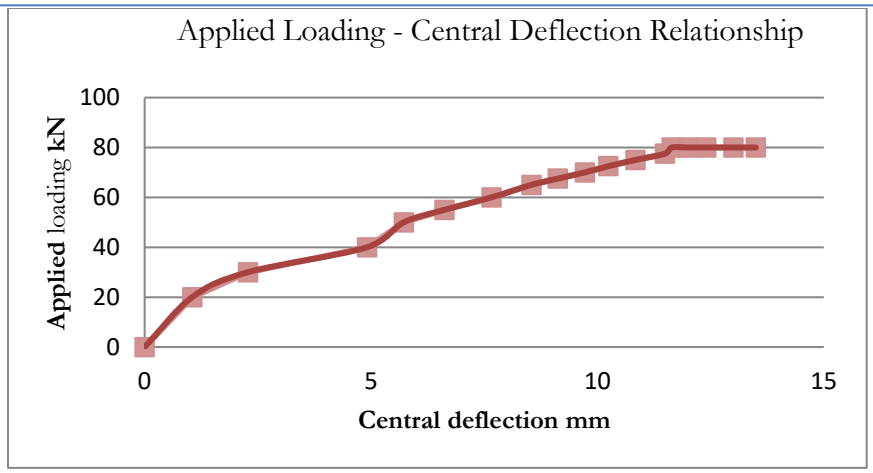

Figure 3: *Applied Load- Central Deflection Relationship*

4.2 Eurocode2 Beam

The maximum applied load at failure for the Eurocode2 Beam was 95kN and the maximum deflection at mid span at failure was 24 mm. Figure 4 shows the corresponding applied load - deflection relationship.

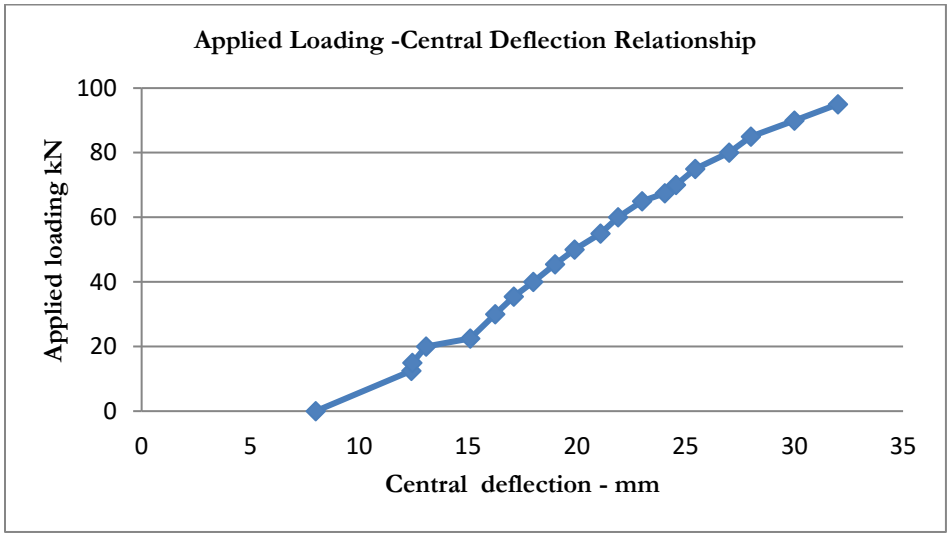

Figure 4: *Applied Loading-Central Deflection Relationship*

5 Conclusion

1. The BS8110 and Eurocode2 beams failed in shear before reaching their ultimate flexural capacity.
2. The Eurocode2 specification is much easier to follow than the specification detailed in BS8110
3. The Eurocode2 specification requires less shear reinforcement than the BS8110 specification
4. BS8110 and Eurocode2 are similar in that

ISBN: 978-81-936820-6-7
Proceedings DOI: 10.21467/proceedings.4

- The shear stress depends on the effective depth and tensile reinforcement ratio and the concrete strength
- There is a shear stress below which only minimum shear reinforcement need be provided

5. BS8110 and Eurocde2 are different in that
    - In BS8110 the shear reinforcement does not resist all the applied shear but resists only the shear in excess of that which can be resisted by the concrete $(v - vc)$ [18], where v is the design shear stress and vc is the design concrete shear stress. In Eurocode2 the shear must be carried by the shear links, when the shear links are required
    - The BS8110 specification gives a higher value of v_c than is obtained from Eurocode2 for C30 concrete
    - Eurocode2 permits significantly higher shears to be resisted by a section than does BS8110
    - The scope of the approach in Eurocode2 is more extensive than the specification used in BS8110 for instance in Eurocode2 there is no limit placed on the concrete strength and designer is free to chosen any angle of inclination of the compression strut between 22° and 45° [8].
    - In Eurocode2 the designer can seek out economies in the provision of shear reinforcement.
6. The results from the laboratory tests have shown that the Eurocode2 beam carried a higher load ($95kN$) and gave a higher central deflection (24mm) compared to BS8110 beam which failed under a load of 80 $kN$and a maximum central deflection of 13.5mm.

References

[1] MacGinley T J, Choo B S, Reinforced concrete, design theory and examples. Second edition, 1990.

[2] Royal Society of Chemistry, The Concrete conundrum. Available on: http://www.rec.org/chemistryworld/restricted/2008/Msrch/TheConcreteConundrum. asp.

[3] Gambhir M L, Concrete Technology, 2004.

[4] Kuttab, A S and Haldane, Detailing for shear with the compressive force path concept. Proceeding of the IABSE Colloquium. Structural Concrete, Vol 69 No: 6, pp74-150, 1991.

[5] Narayanan R S, Concrete structures: Eurocode EC2 & BS8110 Compared, 1994.

[6] Hulse R, Monypenny P C, An instruction to EC2 and comparison with BS8110, 1993.

[7] Mosley W, Bungey J, and Hulse R, Reinforced concrete design to Eurocode2. Sixth Edition, 2007.

[8] Moss, R. EN1992-Eurocode and BS8110 Compared. Proceedings of the Institution of Civil Engineers - Civil Engineering, Volume: 156 Issue: 3, Aug 2003.

[9] British Standard BS8110, Structural use of concrete of concrete – Part 1: Code of practice for design and construction, 1997.

High Density Polyethylene/Libyan Kaolin Clay Nanocomposites: Effect of Clay Particle Size on Rheological, Surface and Mechanical Properties

Anour Shebani[1], Wael Elhrari[2*], Abdalah Klash[3], Abdelkader Aswei[4], Khalid Omran[5], Abdalbary Rhab[6]

[1,2,3,6] Polymer Research Center, Tripoli, Libya

[4, 5] Higher Institute for Comprehensive professions Al garaboulli, Libya

DOI: https://doi.org/10.21467/proceedings.4.20

* Corresponding author email: wael@prc.ly

ABSTRACT

This research work focuses on the effect of Libyan Kaolin clay particle size on the reheological, surface and mechanical properties of high density polyethylene (HDPE)/clay nanocomposites. Three polymer clay nanocomposites (PCNs) using 2 wt.% clay with different particle size (< 75, 75-150 and 150-300 μm) and 2 wt.% polyethylene grafted maleic anhydride (PE-g-MA) were prepared by melt processing method. The rheological (viscosity and melt flow rate), surface (wettability/hydrophilicity), and mechanical properties (tensile strength, elongation at break, Young's modulus, hardness and impact strength) were investigated. The obtained properties of PCNs were compared with HDPE. A better enhancement in the rheological properties properties was observed when clay particle size of < 75 μm was used. It was exhibited lower viscosity and higher MFR value, which provide better processing properties in comparison to HDPE and other PCNs. PCN with clay particle size of (75-150 μm) had more wettability and/or hydrophilicity than HDPE and other PCNs. Mechanical properties results showed significant improvement only in the impact properties as compared to HDPE. In short, PCN made with Libyan kaolin clay with particle size 75-150 μm appears to has comparatively better overall properties in comparison to other PCNs.

Keywords: polyethylene/clay nanocomposites, particle size, rheological properties, mechanical properties, Surface properties

1 Introduction

Polymer nanocomposites (PNs) are termed as multiphase systems in which the nanofillers with at least one dimension in the nanoscale regime are dispersed in the polymer matrix [1]. One of the most promising PNs is the nanocomposites based on polymers and clay or clay minerals. This a special class of composites known as polymer/clay nanocomposite (PCN). PCNs have attracted great interest, because they exhibit significant improvement in polymers properties when compared with virgin polymer or conventional micro- and macro-composites

 ISBN: 978-81-936820-6-7

[2]. Superior mechanical, thermal, electrical, rheological, barrier and optical properties are achievable with these nanocomposites [3-5]. PNCs are very promising materials for various applications and their demand increases in modern material industries such as aerospace, automobile, barrier materials, construction, and biomedical [6-7]. It is noteworthy, that the most important polymers that are employed in the PCNs are polyethylene, polypropylene, polyvinyl chloride, polyamide, polysulfone, polycarbonate, polyaniline, and poly(ethylene oxide). On the other hand, number of clay types have been used in PCNs include Kaolinite, Illite, Bentobite, Chlorite, and Montmonillonte.

Although, Libya rich in clay, there is no attention has been paid to use local clay as reinforcing filler for PNCs. In our previous work [8], the influence of Libyan Kaolin clay on the impact strength properties of high density polyethylene (HDPE)/clay nanocomposites was investigated. In that study, the effect of clay loading, compatibilization, and clay particle size on impact properties of HDPE/clay nanocomposites was studied. We found that the addition of Libyan Kaolin filler has resulted in an improvement in the impact strength properties of HDPE. Maximum improvement in the impact strength properties was obtained at low clay loading (2 wt.%) using clay with particle size 75-150 μm and 2 wt.% PE grafted maleic anhydride (PE-g-MA) as a compatibilizer. To gain more understanding about the influence of Libyan Kaolin clay on PCNs properties, this study aims to investigate the effect of clay particle size on rheological, surface and other mechanical properties (e.g. tensile strength, elongation at break, Young's modulus, and hardness) using HDPE/clay nanocomposites with 2 wt.% clay with different clay particle size and 2 wt.% PE-g-MA. As it was declared in our previous work [8], we hope that the obtained results will encourage Libyan scientists to start using of Libyan kaolin clay and other clays in the field of PCNs.

2 Materials and Methods

Materials

HDPE was used as the matrix polymer (SABIC Saudi Arabia, HDPE F00952, melt flow index 0.05 g/10 min and density 952 g/cm^3). PE-g-MA prepared in our lab according to reference [9], was used as a compatibilizer. Kaolin is supplied by Industrial Research Center Tripoli (collected from Jarmah Member, Sabha city in Libya). Kaolin was sieved to remove impurities and then passed through different sieves size to get particle size of (< 75, 75-150 and 150-300 μm). The plate thickness of this type of kaolin ranges from 26.5 to 40.5 nm [11]. *p*-Xylene (Alfa Aesar 99%) was used to melt HDPE before compounded process.

Composite Preparation

HDPE was used as received. kaolin was dried in an air circulating oven at 85 °C for 24 hr. The HDPE of desire amount was melt in small amount of xylene and then mixed with 2 wt.% kaolin and 2% PE-g-MA in a separate bowl. The mixture then dried in an air circulating oven at 85°C for 24hr. Then the final mixing was carried out using twin screw extruder (Brabender)

(L/D ratio 48) with screw speed of 70 r.p.m. at temperature from 140-190 °C (140 °C for zone1, 160 °C for zone 2, 170 °C for zone 3, 180 °C for zone 4, and 190 °C for zone 5 and zone 6). The extruded composites were cooled in air and then granules to small pieces. Specimens for impact strength were prepared in an injection molding (Xplore 12ml) at temperature 230 °C, and injection pressure of 14 bar. Details of the composites and codes are reported in Table 1.

Table 1: *Composites composition and codes*

No	Composite name	HDPE, wt. %	Clay, wt. %	Compatibilizer wt.%	Clay's particle size μm
1	HDPE	100	0	0	---
2	Composite 1	98	2	2	< 75
3	Composite 2	98	2	2	75-150
4	Composite 3	98	2	2	150-300

Characterization

Rheological properties

Examples of desirable rheological properties may include: viscosity and melt flow rate (MFR). Thus, MFR and viscosity of the melt were studied using CEAST modular line melt flow models 7024 according to ASTM D 1238P. The tests were carried out at 190 °C under specified load of 5.0 kg.

Wetting properties and surface characteristics

The measurement were carried out using Contact angle ramè-hart instrument co. model 200-F4 at room temperature. 3 μl volume drops of water were deposited on the surface of the HDPE and the three PCNs with a syringe. Pictures of the water drops were acquired through a digital camera positioned on a static contact angle analyzer. The θ of the contact angle was measured automatically from the image setup. Each contact angel value is an average of 5 measurements.

Mechanical properties

The tensile strength, elongation at break and young modulus were determined using SATRA tensile tester for HDPE and the three PCNs. Tensile test were performed at room temperature. Four specimens (73mm- 4mm-2mm) were tested for each sample under speed test (100mm/min). The hardness of molded HDPE and all composite materials were determined using a Shore D durometer RayRan in accordance with ISO 868:2003. Hardness value for each sample is an average of 8 measurements. The charpy impact test was carried out to determine the impact strength of the HDPE, and all composite materials using (CEAST Resil Impactor tester), with impact energy of 15 J. The specimens for impact test were prepared and notched according to ASTM (D256-87). Four specimens were tested for HDPE and each composite.

ISBN: 978-81-936820-6-7

Series: AIJR Proceedings
Proceedings DOI: 10.21467/proceedings.4

3 Results and Discussion

Rheological properties

Results of rheological properties of HDPE and the three PCNs are presented in Figures 1 (a,b). The obtained results indicate that the particle size of Libyan Kaolin clay clearly affects the rheological properties of PCNs. Generally, the PCNs performance depends on a number of nanoparticles features such as the size, aspect ratio, specific surface area, volume fraction used, compatibility with the matrix and dispersion [12]. As shown in Figures 1 (a,b), it is apparent that the addition of Libyan Kaolin to HDPE caused decrease of the viscosity and thus an increase of the MFR in comparison to HDPE. It is known from the literature [12] that the organically clay can undergo degradation, which cause radicals formation and result chain scission. This normally reduces the molecular weight and viscosity and increases the MFR. On the other hand, the decrease viscosity of PCNs in comparison to neat polymer can be due to the reorientation of the nanoclay [13]. It is important to know that the high viscosity means a high molecular weight polymer with low MFR. Low viscosity offers better processing properties, while high viscosity is recommended for better mechanical properties. It has been reported that the addition of small amounts of nanofiller can enhance the composite properties and reduce the processing problems [14]. Kerstin et. al. [11] declared that introducing nanoparticles into the polymer might be a solution to fulfill both requirements: mechanical stability and simple processability. Therefore, it is important to describe PCNs, not only mechanically and morphologically but also rheologically as well.

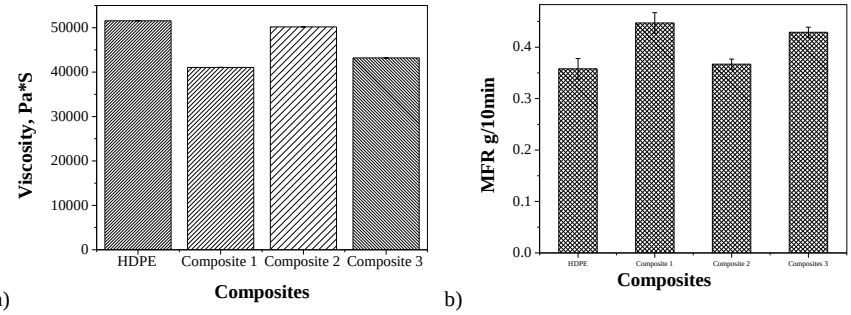

Figure 1: *a) Viscosity for HDPE and the three PCNs, b) MFR for HDPE and the three PCNs.*

As illustrated in Figures 1 (a,b) HDPE showed to has the highest viscosity and the lowest MFR values in comparison to the three PCNs. PCN with clay particle size of (< 75 μm) exhibited lower viscosity and higher MFR, which provide better processing properties in comparison to HDPE and other PCNs. Whereas PCN with clay particle size of (75-150 μm) showed higher viscosity and lower MFR in comparison to other PCNs. Strong interaction between filler particles and the polymer results in immobilized polymer chains on the surface of the filler, which leads to an increase in viscosity [15]. It seems that PCN with clay particle size of (75-150 μm) may have the strongest interaction between the clay and HDPE in

comparison to other PCNs. Additionally, PCN with clay particle size of (150-300 μm) displayed viscosity and MFR values which are intermediate between the values of the other PCNs. These results are in fair agreement with literature because MFR showed to be inversely proportional to viscosity [16]. However, such a behaviour is explained by an increase in polymer chain mobility and more free volume obtained in the nanocomposites samples [17]. According to Agboola [18], rheological behaviors of PCNs are strongly influenced by the material structure and the interfacial characteristics. Mackay et al. [19], suggested that the decrease in viscosity can be related to the free volume introduced by the clay nanoparticles. The effect of the nanoclay particles on the free volume depends on the clay/polymer interactions [9]. According to Gholizadeh et al. [20], the addition of nanoclay decreases the free volume, while opposite tendency was observed by Yu et.al. [21]. To clear this contradiction further investigations on the effect of the addition of nanoclays to polymer matrices are required.

Wetting properties and surface characteristics

Wetting properties and surface characteristics of HDPE and the three PCNs were studied using contact angle measurements (CAMs). CAMs are often used as an empirical indicator of wettability and interfacial tension. For polymer production where particulates or fibers are used for reinforcement, colorant, flame retardancy or stability, understanding the wetting phenomena has considerable value in relation to the material performance [22]. In practical, wettability and hydrophilicity are closely related phenomena. More wettability means more hydrophilicity. The results of the CAMs in Figure 2 revealed some information on the wettability of the HDPE and the three PCNs. Wettability and contact angle are inversely related: the lower the contact angle, the greater the wettability. The contact angle depends on several factors, such as surface energy, wettability of the surfaces, viscosity of the liquid, roughness, the manner of surface preparation, and surface cleanliness [23,24].

The HDPE represented more hydrophobicity behavior, which means less wettability property than the three PCNs because its contact angle above 90° and the water droplet was tended to ball up and run off the HDPE surface. HDPE is basically a hydrophobic polymer and thus the high value of contact angle is justifiable. A surface is hydrophilic if the value of the contact angle is less than 90°, whereas the surface is hydrophobic if the value of the contact angle is greater than 90° [30]. The contact angle of HDPE was decreased by the addition of Libyan kaolin clay in the three PCNs. This means that the wettability and/or hydrophilicity is increased for the HDPE. This is because the surface of each PCN contains some of the nanoclays [25].

The clay particle size has apparent effect on the contact angle. It decreased from 91.4 (for neat HDPE) to around 88.3 when clay with particle size of (< 75 μm) was added to the HDPE, while it decreased to about 85.2 when clay with particle size of (75-150 μm) was added to the HDPE. It decreased finally to approximately 85.9 when clay with particle size of (150-300 μm)

ISBN: 978-81-936820-6-7

Series: AIJR Proceedings
Proceedings DOI: 10.21467/proceedings.4

was added to the HDPE. This indicates that PCN with clay particle size of (75-150 μm) had more wettability and/or hydrophilicity than other PCNs. On the other hand, PCN with clay particle size (< 75 μm) was exhibited lower wettability and/or hydrophilicity than other PCNs. In short, the ultimate enhancement in the wettability and/or hydrophilicity which observed when clay with particle size of (75-150 μm) means that the surface of HDPE became more polar in comparison to the other PCNs. This enhances the above finding and explanation. As declared above, strong interaction between filler particles and the polymer results in immobilized polymer chains on the surface of the filler, which leads to an increase in viscosity. Hence, the improvement in wettability and/or hydrophilicity of PCNs's surface can be attributed to the enrichment of the HDPE surface with nanoclays. Good wettability is often a predictor of high quality adhesive bonding. Indeed, wettability is of importance in adhesion, surface coating, water repellency, and waterproofing [26]. To our knowledge, the effect of clay's particle size on the wettability and/or hydrophilicity properties of PCNs has so far not been extensively studied.

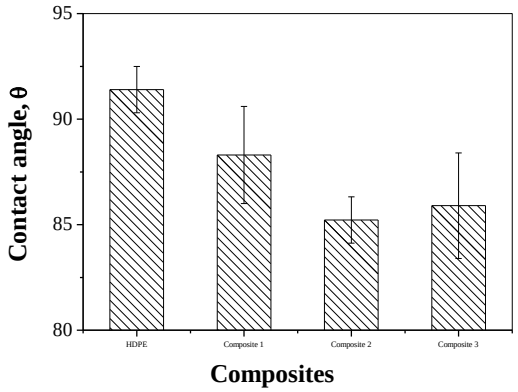

Figure 2: *Contact angle for HDPE and the three PCNs.*

Mechanical properties

Table 2 shows experimental data obtained for some mechanical properties of the HDPE and the three PCNs. It is important to note that the standard deviations are given in parentheses next to the values of the mechanical properties. Experimental results in Table 2 proved that clay particle size can notably affect the mechanical behavior of HDPE matrix. It was found that tensile strength, elongation at break, Young's modulus and hardness decreased, whilst impact strength increased with the addition of clay in all cases.

Table 2: *Mechanical properties of HDPE and the three PCNs.*

Sample	Tensile strength, MPa	Elongation at break, %	Young's modulus, MPa	Hardness	Impact strength, $KJ.m^{-2}$
HDPE	29.68 (3.13)	2.39 (0.16)	794.23 (2.40)	60.4 (1.34)	12.18 (1.57)
Composite 1	19.45 (1.06)	2.30 (0.16)	734.21 (1.91)	58.20 (20.20)	25.03 (4.10)
Composite 2	19.86 (1.03)	2.20 (0.05)	760.15 (1.17)	57.70 (0.28)	39.13 (5.34)
Composite 3	22.11 (1.31)	2.28 (0.08)	599.79 (5.17)	52.70 (0.28)	38.85 (4.36)

The tensile strength of HDPE decreased approximately 34% when clay with particle size of (< 75 μm) was used (composite 1), while it decreased about 33% when clay with particle size of (75-150 μm) was used (composite 2). The lowest decrease (about 25%) in the tensile strength of HDPE was observed when clay with particle size of (150-300 μm) was used (composite 3). In the case of PNs, most studies report the tensile properties as a function of clay content [27]. This is because the degree of crystallinity is dependent of the clay content [28]. This is important since the tensile properties are mainly dependent on the crystallinity of the polymer. Also, composite strength is very much dependent on the interface adhesion quality between the clay and polymer matrix [29].

Addition of Libyan kaolin clay caused a little reduction in the elongation at break of HDPE. The elongation at break for HDPE decreased approximately 4%, 8%, and 5% when clay with particle size of (< 75 μm), (75-150 μm) and (150-300 μm) were used, respectively. This is because nanoclay particles are stiff materials with no elongation properties; therefore, their addition can lower composites elongation [30]. Similar findings were reported by many studies [31,32]. According to Ahmadi et. al. [32], the reduction in the elongation at break may be attributed to the fact that ductility decreases when stiffness is increased by reinforcement.

The experimental measurements of Young's modulus (also known as the elastic modulus) of the three PCNs in Table 2 illustrates that the addition of Libyan kaolin clay caused a reduction in the stiffness of HDPE matrix. This is because Young's modulus is a measure of the stiffness of a solid material. Particularly, a stiff material has a high Young's modulus and changes its shape only slightly under loads. The decrease in the Young's modulus in composite 1 and composite 2 was approximately 7.6% and 4.3%, respectively. More reduction in the Young's modulus (about 24.5%) was observed when clay with particle size of 150-300 μm was used. It is well known that the elastic modulus "Young's modulus" is a stiffness parameter which governs by the size and amount of the dispersed phase [25].

Table 2 represents also the Shore D hardness results of pure HDPE and its nanocomposites. The hardness of HDPE decreases with incorporation of nanoclay. The average value of the Shore D hardness is observed to be ~ 60, 58, 57 and 52 for pure HDPE, composite 1, composite 2 and composite 3, respectively. This means that the hardness was deceased by 3.6 % for composite 1, 4.5% for composite 2 and 12.7% for composite 3 as compared to pure HDPE. This indicates that the hardness showed to decrease with increasing the clay particle size. Hardness is found to be based on the clay loading [33].

Impact strength properties in Table 2 was published and discussed elsewhere [8]. The results show that particle size has considerable effect on the impact strength properties of HDPE/clay nanocomposite. The three PCNs showed better impact strength properties than pure HDPE. Maximum impact strength value (39.125 KJm^{-2}) for the composites was obtained at particle size of 75-150 μm (composites 2). Composite with particle size of 150-300 μm (composites 3) exhibited impact strength value (38.851 KJm^{-2}) close to that of composites 2.

ISBN: 978-81-936820-6-7

Series: AIJR Proceedings
Proceedings DOI: 10.21467/proceedings.4

Proper particle size of kaolin at given filler content probably decreases the level of stress concentration in the composites with the resultant increase in impact strength. However, the proper particle size cannot be predicted, it depends on the particle shape, matrix and particle/matrix adhesion [25]. However, quality dispersion of nanoparticles in matrix plays key role for an improvement of impact properties of nanocomposites [34].

As shown in Figure 3, PCN made with Libyan kaolin clay with particle size 75-150 μm appears to has comparatively better overall mechanical properties in comparison to other PCNs. It can be noted from the above results that the addition of 2% of Libyan kaolin clay with different particle sizes to HDPE did not cause improvement in the mechanical properties, such as strength, elongation at break, Young's modulus and hardness. On the other hand, it has resulted in an improvement in the impact strength properties of HDPE. The properties of PCNs not only depends on the adhesion and compatibility of the organoclay with the matrix, but also on other factors such as processing conditions and clay loading. For example, George et. al. [35] studied the effect of kaolin clay particles on the mechanical, morphological and processing features of kaolin clay reinforced PS/HDPE blends and found that the tensile strength and tensile modulus of PCNs was increased with 2% clay loading, while the impact strength was increased at 3 % of clay loading.

Generally, better interfacial bonding imparts better properties to a PCN, such as tensile strength, hardness and high modulus, as well as resistance to fatigue, tear, corrosion and cracking. Since, the mechanical properties of PCNs can be altered by various factors: properties of the polymer matrix, clay particle size and morphology, particle loading and distribution, interfacial adhesion between clay and matrix, etc.. According to this it seems that the addition of 2% of Libyan kaolin clay seems to be not enough to produce the expected reinforcement in the PCNs. For example, in the case of biodegradable PCNs, most studies report the tensile properties as a function of clay loading, as mentioned above. This is because clay content effects the crystallinity which have an effect on the tensile properties. Moreover, Libyan kaolin clay appears to need special treatment to obtain clay in nanometer dimensions with narrowed particle size distribution. It is important to reveal here that nanoclays with smaller particle size distributions exhibit better dispersion in the polymer matrix. This because smaller particles have a higher surface area for a given particle loading. High surface area means more contact area available, and therefore have a higher potential to reinforce the polymer matrix. Therefore, the preparation of PCNs by using clay with smaller and more uniform particle sizes can lead to nanocomposites with better properties.

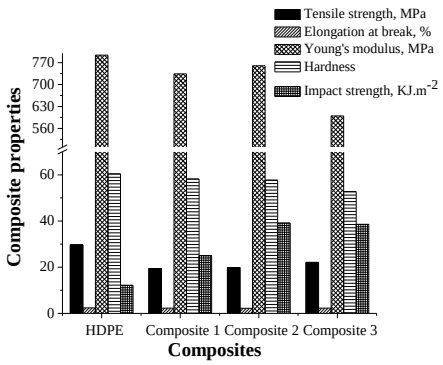

Figure 3: *Comparison between the mechanical properties of HDPE and the three PCNs.*

4 Conclusions

PCNs were produced using HDPE, 2% Libyan kaolin clays with different particle sizes (< 75, 75-150 and 150-300 μm) and 2% PE-g-MA as a compatibilizer. PCNs were prepared by melt-mixing technique using mini-twin-extruder. The effects of the kaolin clay particle size on the rheological, wetting and mechanical properties PCNs were studied. PCN made with Libyan kaolin clay with particle size 75-150 μm appears to has comparatively better overall properties in comparison to other PCNs. The effects of the kaolin clay particle size on some desirable rheological properties such as viscosity and MFR was studied. HDPE showed to has the highest viscosity and the lowest MFR values in comparison to the three PCNs. PCN with clay particle size of (< 75 μm) exhibited lower viscosity and higher MFR value, which provide better processing properties in comparison to HDPE and other PCNs. Whereas PCN with clay particle size of (75-150 μm) showed higher viscosity and lower MFR in comparison to other PCNs. Additionally, PCN with clay particle size of (150-300 μm) displayed viscosity and MFR values which are intermediate between the values of the other PCNs.

Wetting properties and surface characteristics of HDPE and the three PCNs were studied using CAMs. The contact angle of HDPE decreased by the addition of Libyan kaolin clay in the three PCNs, which resulted in an improvements in the wettability and/or hydrophilicity. PCN with clay particle size of (75-150 μm) had more wettability and/or hydrophilicity than other PCNs. On the other hand, PCN with clay particle size (< 75 μm) exhibited lower wettability and/or hydrophilicity than other PCNs. the improvement in wettability and/or hydrophilicity of PCNs's surface could be attributed to the enrichment of the HDPE surface with nanoclays.

Mechanical characterization tests including tensile strength, hardness and impact strength tests have been performed. The results showed that the addition of 2% of Libyan kaolin clay with different particle sizes to HDPE did not cause improvement in the mechanical properties, such as strength, elongation at break, Young's modulus and hardness. On the other hand, it has resulted in an improvement in the impact strength properties of HDPE. According to these results, it seems that the addition of 2% of Libyan kaolin clay not enough to produce

ISBN: 978-81-936820-6-7

Series: AIJR Proceedings
Proceedings DOI: 10.21467/proceedings.4

the expected reinforcement in the PCNs. Moreover, Libyan kaolin clay appears to need special treatment to obtain clay in nanometer dimensions with narrowed particle size distribution. In this regard, more attention will be given to study the effect of clay loading and optimizing the clay particle size and distribution on the properties of HDPE/clay made by Libyan kaolin clay in future.

Acknowledgment

The authors would like to thank Industrial Research Centre who performed the tensile strength test.

References

[1] A. Tatyana, S. Ilya, K. József, "Polymers and related composites via anionic ring-opening polymerization of lactams: recent developments and future trends: review", *Polymers*, vol. 10, no. 4, pp. 357-404, 2018.

[2] K. Behzad, "Nanofiller reinforcement effects on the thermal dynamic mechanical, and morphological behavior of HDPE/rice husk flour composites", *Bioresources*, vol. 6, no. 2, pp. 1351-1358, 2011.

[3] M. A. Rajan, A. Ramasubbu, A. Thaddeus, V. F. Latha, T. S. Vivekanandam, S. Umapathy, "Thermal properties of PMMA/Montmorillonite clay nanocomposites", *Journal of Nanoscience and Nanotechnology*, vol. 6, no. 12, pp. 3993-3996, 2006.

[4] B. Xu, W. M. Huang, Y. T. Pei, Z. G. Chen, A. Kraft, R. Reuben, J. M. Hosson, Y. Q. Fu, "Mechanical properties of attapulgite clay reinforced polyurethane shape-memory nanocomposites", *European Polymer Journal*, vol. 45, no. 7, pp. 1904-1911, 2009.

[5] R. Sudip, Y. Q. Siew, E. Allan, D. C. Xiao, "The potential use of polymer-clay nanocomposites in food packaging", *International Journal of Food Engineering*, vol. 2, no. 4, pp. 1-11, 2006.

[6] D. R Paul., L. M Robeson., "Polymer nanotechnology: nanocomposites", *Polymer*, vol. 49, no. 15, pp. 3187-3204, 2008.

[7] G. Sagheer, K. Ayesha, M. Bakhtiar J. Saira, "Research Progress on Properties and Applications of Polymer/Clay Nanocomposite", *Polymer-Plastics Technology and Engineering*, vol. 55, no. 7, pp. 684-703, 2015.

[8] A. Shebani, W. Elhrari, A. Klash, A. Aswei, O. Khalid, R. Abdalbary, "Effects of Libyan kaolin clay on the impact strength properties of high density polyethylene/clay nanocomposites", *International Journal of Composite Materials*, vol. 6, no. 5, pp. 152-158, 2016.

[9] M. Ghaemy, S. Roohina, "Grafting of maleic anhydride on polyethylene in a homogeneous medium in the presence of radical initiators", *Iranian Polymer Journal*, vol. 12, no. 1, pp. 21-29, 2013.

[10] A. M. A. Shiwa, A. Hussin, "Sabha clay deposit, Libya: its mineralogy and impending industrial significance", *Electronic Journal of Geotechnical Engineering*, vol. 18, pp. 3803-3811, 2013.

[11] M. Kerstin, B. Elodie, L. Marcos, J. Maria, E. S. Yolanda, M. José, M. Oliver, B. Alvise, H. Steve, B. Uwe, P. Germán, J. Marius, L. Martina, S. Zuzana, C. Sara, S. Markus, "The Influence of New Hydrophobic Silica Nanoparticles on the Surface Properties of the Films Obtained from Bilayer Hybrids", *Nanomaterials*, vol. 7, no. 2, pp. 1-10, 2017.

[12] A. Sahar, S. Husam, "An overview of the oxidation and stabilization of polymer nanocomposites", *Nanocomposites MoDeSt Workshop*, Warsaw-Poland, 2013.

[13] B. Farida, K. Nadir, B., Catherine, T. Francois, E. Ruiz, "A comparative study of dispersion techniques for nanocomposite made with nanoclays and an unsaturated polyester resin", *Journal of Nanomaterials*, vol. 2011, pp. 1-12, Article ID 406087, 2011.

[14] M. Joshi, B. S. Butola, G. Simon, N. Kukaleva, 'Rheological and viscoelastic behavior of HDPE/octamethyl-POSS nanocomposites", *Macromolecules*, vol. 39, no. 5, pp. 1839-1849, 2006.

[15] J. Sapkota, "Influence of clay modification on curing kinetics of natural rubber nanocomposites", Master of Science Thesis, Tampere University of Technology, Finland, 2011.

[16] Y. Basel, "Simple rheological analysis method of spinnable-polymer flow properties using MFI tester", *Indian Journal of Materials Science*, vol. 2015, Article ID 790107, pp. 1-8, 2015.

[17] S. H. Jin, D. K. Choi, D. S. Lee, "Electrical and rheological properties of polycarbonate/multiwalled carbon nanotube nanocomposites", *Colloids and Surfaces A*: *Physicochemical and Engineering Aspects*, vol. 313-314, pp. 242-245, 2008.

[18] O. S. Agboola, E. R. Sadiku, A. T. Adegbola, O. F. Biotidara, "Rheological properties of polymers: structure and morphology of molten polymer blends", *Materials Sciences and Applications*, vol. 2, no. 1, pp. 30-41, 2011.

[19] M. E. Mackay, T. T. Dao, A. Tuteja, D.L. Ho, B. V. Horn, H. Kim, and C. J. Hawker, "Nanoscale effects leading to non-einstein-like decrease in viscosity", Nature Materials. vol. 2, pp. 762-766, 2003.

[20] B. Gholizadeh, Arefazar A., and Barzin J., "Polycarbonate/polyamide 6/nanoclay ternary nanocomposite membranes: preparation, characterisation, and gas separation properties", Polymers and Polymer Composites, vol. 17, no. 3, pp. 181-187, 2009.

[21] D. Yu, H. Wang, Y. Feng, and Z. P. Fang, "Investigation of free volume, interfacial, and toughening behavior for cyanate ester/bentonite nanocomposites by positron annihilation", Journal of Applied Polymer Science, vol. 102, no. 2, pp. 1509-1515, 2006.

[22] S. P. Thomas, S. Thomas, R. Abraham, and S. Bandyopadhyay, "Polystyrene/calcium phosphate nanocomposites: Contact angle studies based on water and methylene iodide", eXPRESS Polymer Letters, vol. 2, no. 7, pp. 528-538, 2008.

[23] A. W. Adamson, and A. P. Gast, "Physical chemistry of surfaces", John Wiley & Sons, Inc., USA, 1990.

[24] J. N. Israelachvili, 'Intermolecular and surface forces", 2ed, Academic Press, UK, 1992.

[25] A. I. Alateyah, H. N. Dhakal, and Z. Y. Zhang, "Contact angle measurement of the vinyl ester matrix nanocomposites based on layered silicate", International Journal of Materials and Metallurgical Engineering, vol. 7, no. 12, pp. 976-981, 2013.

[26] C. Piao, J. E. Winandy, and T. F. Shupe, "From hydrophilicity to hydrophobicity: a critical review: part 1. wettability and surface behavior", Wood and Fiber Science, vol. 42, no. 4, pp. 490-510, 2010.

[27] W. M. Yiu, and Z. Y. Zhong, "Polymer nanocomposites", Woodhead Publishing and Maney Publishing, England, 2006.

[28] R.K. Gupta, and S.N. Bhattacharya, "Polymer-clay nanocomposites: current status and challenges", Indian Chemical Engineer, vol. 50, no. 3, pp. 242-267, 2008.

[29] S. Y. Fu, X. Feng, B. Lauke, Y. Mai, "Effects of particle size, particle/matrix interface adhesion and particle loading on mechanical properties of particulate-polymer composites", Composites: Part B, vol. 39, 933-961, 2008.

[30] E. Selver, and S. Adanur, "Processing and property relationship of polypropylene monofilaments containing nanoclay", Journal of Industrial Textiles, vol. 40, no. 2, pp. 123-137, 2010.

[31] A. Pegoretti, A. Dorigato, and A. Penati, "Tensile mechanical response of polyethylene-clay nanocomposites", eXPRESS Polymer Letters, vol. 1, no. 3, pp. 123-131, 2007.

[32] S. J. Ahmadi, H. Yudong, and W. Li, "Synthesis of EPDM/organoclay nanocomposites: effect of the clay exfoliation on structure and physical properties", Iranian Polymer Journal, vol. 13, no. 5, pp. 415-422, 2004.

[33] B. Sharma, S. Mahajan, R. Chhibber, and R. Mehta, "Glass fiber reinforced polymer-clay nanocomposites: processing, structure and hygrothermal effects on mechanical properties", Procedia Chemistry, vol. 4, pp. 39-46, 2012.

[34] R. Valek, and H. Jaroslav, "Impact properties of polymeric nanocomposites with different shape of nanoparticles", 1st Nano conference, Brno-Czech Republic, 2011.

[35] T. S. George, K. K. Asha, R. Anjana, and K. E. George, "Studies on nano kaolin clay reinforced PS-HDPE nanocomposites", Indian Journal of Advances in Chemical Science, vol. 1, no. 4, pp. 201-206, 2013.

ISBN: 978-81-936820-6-7

Series: AIJR Proceedings
Proceedings DOI: 10.21467/proceedings.4

Particle Size Dependence of MnO Reduction for Fabrication of Al − $AlMnO_X$ Composite vir Stir Casting

Khalid Almadhoni[1], Sabah Khan[2]

[1]Dr. Engineer, Department of Mechanical Engineering, Faculty of Engineering, Sabratha University, Sabratha, (Libya)

[2] Dr. Assistant Prof., Department of Mechanical Engineering, Faculty of Engineering and Technology, JMI, Jamia Nagar, New Delhi-110025 (India)

DOI: https://doi.org/10.21467/proceedings.4.21

* Corresponding author email: K_almadhoni@yahoo.com

ABSTRACT

In the present work, a composite of Al matrix reinforced with 10% MnO particles has been developed using stir casting technique. MnO with particles size of range of 53 to 90 μm for composite (A) and 188 to 250 μm for composite (B) as reinforcement and pure Mg powder as wetting agent to improve the wettability of MnO particulates with molten Al were used for production of Al-MnO composites having 10 wt.% of MnO. The pouring temperature and stirring speed have been set to 750 ℃ and 900 RPM, respectively. The main purpose of this work is to study the dependence of MnO reduction on particle size for fabrication of Al matrix composite via stir casting route. For structural analysis, fundamental material characterization like SEM, EDX, XRD and OM was carried out for developed composite samples. The results reveal that an in-situ formed finer alumina (Al_2O_3) particles and an intermetallic precipitate of Al-Mn as a result of chemical reaction between molten Al and MnO particles have been observed using SEM with EDX of both developed composite samples. SEM with EDX analysis has detected that the composition of reinforcement particles of composite sample of A contains Al and O, which indicates presence of in-situ generated Al_2O_3. While the composition of reinforcement particles of composite samples of B contains high percentage of Mn, high percentage of O and low percentage of Al, which indicates presence of unreacted MnO and generated in-situ Al_2O_3 to form in-situ ($AlMnO_x$) intermediate compound. This has been also confirmed by elemental mapping SEM analysis. SEM analysis of in-situ $AlMnO_x$ particles at high magnification has detected that their structure is porous. Optical micrographs have shown that a good bonding between particles and the matrix in both developed composite samples with presence some aggregations of particles and pores. For both developed composite samples, the amount of (Al-Mn) phases formed in the specimens may be too little to be detected directly from the bulk specimens by XRD. Phase identification by X-ray diffraction technique verifies of presence Al and Al_2O_3 phases in composite sample of A, while it verifies of presence Al and MnO phases in composite sample of B.

Keywords: Al, MnO, Morphology, microstructure, $AlMnO_x$, Al-Matrix Composite.

 ISBN: 978-81-936820-6-7

1 Introduction

The low density, environment resistance and adequate mechanical and physical properties of Al metal matrix composites (AMMC's) make them one of the most interesting material alternatives for the manufacture of lightweight parts for many types of modern engineering equipments.. Composites are classified by matrix into metal matrix composites (MMC's), ceramic matrix composites (MMC's) and polymer matrix composites (MMC's) while by filler type are classified into particle reinforced composite, fiber reinforced composites and structural composites [1-2], Figure 1.1.

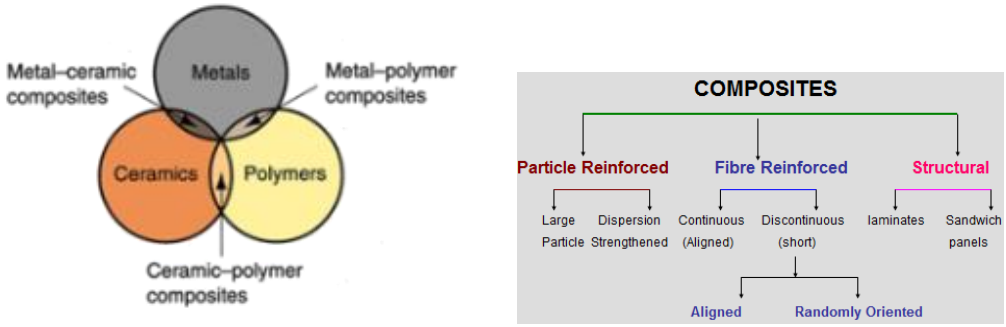

(a) (b)

Figure 1.1: Classification of composites (a): by matrix type and (b): by filler type (1-2)

Al and its alloy are the most commonly used metal matrix materials in the production of MMC's because of their preferred properties such as lightness, corrosion resistance and ductility and easy availability. Reinforcing of AMC with whiskers, short fibers or particulates of various kinds of ceramic materials such as SiC, SiO_2, Al_2O_3, MgO, ZnO, BeO, MnO_2, TiO_2, TiC, etc., provide properties compared to monolithic base alloy [3]. MMC's as compared to other MMCs have superior values of refractoriness, compressive strength, hardness and show excellent wear resistance [2-4-5]. Thermal characterization is one of the prime physical characterization of composites, which also include electrical, magnetic and optical properties. Heat is transferred at a higher rate across materials of high thermal conductivity than across materials of low thermal conductivity [6]. Melt stir casting has a good potential in all-purpose applications as it is a low cost MMC's production method. Its advantages lie in its simplicity, flexibility and applicability to large quantity production. This route is also attractive because, in principle, it allows a conventional metal processing method to be used, and hence reduces the final cost of the product [7-8]. The particle size and orientation have greater effect on the properties of the composite. Zhou et al. [9] used Al_2O_3 with different size to fill silicone rubber, and reported that nano-sized Al2O3 composite exhibited higher thermal conductivity and mechanical properties than the micro-sized one. Many researchers have reported that at the same percentage of reinforcement, smaller particle size leads to lower inter-particle distance and more chances for the formation of thermal conductive 'pathway' [10]. When the average inter-particle distance is in a suitable range, extensive plastic deformation in the matrix

ISBN: 978-81-936820-6-7
Proceedings DOI: 10.21467/proceedings.4

Series: AIJR Proceedings

can be easily induced [11–12]. Operating temperature should be kept at semisolid stage to improve the wettability of reinforcements with the matrix, this is attributed to interactions among the particles themselves, between solid Al and particles and between remaining liquid phases of Al with particles [13]. Manganese has been known as an alloying element of Al alloys which contributes to uniform deformation. The effect of Mn on the mechanical behavior of Al alloys is investigated by S. W. Nam and D. H. Lee. It was found that as the Mn content increases over 0.5 wt% in Al alloys, both yield and ultimate tensile strength increased significantly without reduction of ductility. Adding Mn to aluminum alloys also improves both low-cycle fatigue resistance and corrosion resistance [14]. Release of manganese (Mn) in the matrix, intermetallic compound of Al-Mn precipitated in the matrix in different phases. Results showed that the porosity was evident in the micrographs and with increase in Al_2O_3-MnO_2 wt%, the strength improved and the ductility decreased [15]. Adding Mg improves the wettability of MnO_2 with molten Al and thus increases the amount of reinforcing phase in the composite material [16]. A. Agarwal, S. Singh and others prepared hybrid composites using both in-situ and ex-situ approaches together by dispersing powder mixture of alumina (Al_2O_3) and manganese dioxide (MnO_2) in a ratio of 1:1 but with different sizes, by stir casting method in Al matrix. They investigated and compared the microstructures and mechanical properties of Al-Al_2O_3, Al-MnO_2 and Al-Al_2O_3(MnO_2) composites. Results showed that fine Al_2O_3 particles were formed as result of reduction of MnO_2 by Al and Mn was released in the matrix, which combined with Al to form intermetallic compounds of Al-Mn precipitate in the matrix in different phases of Al-Mn and reinforce it. It was also found that with increase in wt.% of Al_2O_3- MnO_2, mechanical properties of the composite enhanced with decrease in ductility, however they reported evidence of porosity in the micrographs [17].

2 Manganese Oxide Mesoporous Solids (MOMS)

As we know mesoporous material contain pores with diameters between 2 and 50 nm. These materials are classified into according to their size by IUPAC. The microporous materials have pore diameters of less than 2 nm and macroporous materials have pore diameters of greater than 50 nm; the mesoporous category thus lies in the middle. Manganese oxide mesoporous solids (MOMS) are gaining popularity and are characterized by a high surface area mesoporous and /or microporous mixed oxidic solid [16]. Researchers have found that the surface area of Al$x$$MnO_2$ is 711 m^2/g, while the mean pore diameter was 3.6 nm. Results showed that the extreme surface area value of Al$x$$MnO_2$ is attributed to the existence of an open network interconnected particles forming features medium height with no preferential orientation [18].

3 Material Selection

The composite of Al-AlMnOX was fabricated by stir casting method. Pure aluminum (AA-1070) with 99.77% purity is used as the matrix for fabrication of the composite. Table 3.1 gives the chemical composition of the matrix

Table 3.1 Chemical composition of Matrix Al (wt %)

Si%	Cu%	Mg%	Fe%	Zn%	Ni%	Mn%
0.0637	0.0152	0.0017	0.0874	0.0130	0.0056	0.0026
Cr%	V%	Ti%	Sn%	Bi%	Pb%	Al%
0.0024	0.0105	0.0071	0.0033	0.0023	0.0040	99.77

Manganese (II) oxide, also called Manganese monoxide, is used as reinforced material, in the particle size range of 53 to 90 µm for composite (A) and 188 to 250 µm for composite (B) and with 10% RVR. The purity of the powder, its density and the size of the particles selected for the present l study is given in the Table 3.2.

Table 3.2: Specifications of MnO powder selected for present study

Purity %	Density (g/mL) at 25 °C(lit.)	Size of particles selected
99	5.45	(188-250) microns
99	5.45	(53-90) microns

Additive material:

Pure Mg powder was used 1% by weight as wetting agent to increase the wettability of MnO particulates with molten Al. Mg is added to in order to help wetting of particles in molten Al and to retain the particles inside the melt [19-20].

4 Experimental Setup and Fabrication of Composite

The experimental setup consist of conical shaped silicon carbide (SiC) crucible for melting of Al, as it withstands high temperature up to [1700°C]. The crucible is placed in electric melting furnace made up of high ceramic alumina around which heating element is wound. The coil which acts as heating element is K thermocouple (Nickel-Chromium / Nickel-Alumel). Due to the high affinity of Al at liquid stage to react with atmospheric oxygen, the process of stirring is carried out in closed chamber with an inert gas such as nitrogen or argon. Closed chamber is formed. Due to corrosion resistance to atmosphere, silver steel is selected as stirrer shaft material. One end of shaft is connected to 0.05 HP motor, while at the other end blades are welded. Four blades are welded to the shaft at 90°C. The speed can be varied from (0 - 4000) RPM. A permanent mould made of cast iron used to pour the fabricated composite. Figure 4.1 shows a setup of stir casting apparatus developed in the lab.

Figure 4.1: Stir-Casting-Apparatus Set-up

ISBN: 978-81-936820-6-7
Proceedings DOI: 10.21467/proceedings.4

Series: AIJR Proceedings

The impurities and thick oxide layers on the surface are removed by mechanical cleaning by grinding on grinding belt machine, polishing on polishing machine followed by chemical etching by immersing the part in 50% nitric acid aqueous solution at room temperature for 15 min. The part is then rinsed in cold water, followed by hot water and blow dried, as suggested by R. Gadag, 2010 and G. Totten, 2003 [21-22] .The procedure of preparing the composite was carried out by initially setting the temperature at 500°C and then gradually increasing up to 850°C. The pure Al (purity 99.77 %) matrix was cleaned to remove impurities, weighed and then kept in the crucible for melting. Nitrogen gas was used as inert gas to avoid oxidation. Required quantities of 1% pure Mg powder as wetting agent and 10% MnO as reinforcement particles in the size of range of 53 to 90 μm for composite (A) and 188 to 250 μm for composite (B) are weighed to be added. In order to remove any gases and moisture present in reinforcing material, MnO is preheated for half an hour at temperature of 200°C [19-20]. After the matrix completely melts, it was stirred for one minute for homogeneity. Temperature is set to 630°C which is below the melting temperature of the matrix. While stirring semisolid Al, a preheated the wetting agent Mg is added followed by preheated particulate MnO. Dispersion of preheated reinforcements at the semisolid stage of the matrix enhances the wettability of the reinforcement, thus preventing the particles from settling at the bottom of the crucible [23]. Measured flow rate of reinforcements was about 0.2 gm/s. Dispersion time was taken as 4 minutes. Stirrer rpm is gradually increased from 0 to 900 RPM with the help of speed controller. Immediately, after completion of dispersion of particles with continued stirring at semisolid stage, slurry was reheated up to 750°C to make sure slurry is fully liquid. Total stirring time was 8 minutes. Composite slurry was poured in a cast iron preheated mold. Preheating of mold at 500°C was done to remove the entrapped gases from the mold which could reduce the porosity and improve the mechanical properties of composite [20].

4 Results

The specimen were removed from the mold and taken for morphological characterization. The morphological studies of the composite were carried out using the following techniques:

4.1 Scanning Electron Microscopy (SEM/EDX)

The morphology of the composite was observed by scanning electron microscopy (SEM),using a SEM-EDX Oxford INCA 400 model at an acceleration voltage 10 kv. The micrographs were taken at a magnification of 1000.

Composite A:

Figure 5.1 (a) shows un-etched SEM micrograph of Al-10wt.%MnO composite A at 600X and its chemical composition of entire area is given in Figure 5.1 (b) at an encircled spot by EDX analysis. Figure 5.1 (a) indicates white string phase. It also shows dark gray phase.

These phases are identified as Al and O, as well as a virtually non-existent ratio of Mn by EDX in Figure 5.1 (b).

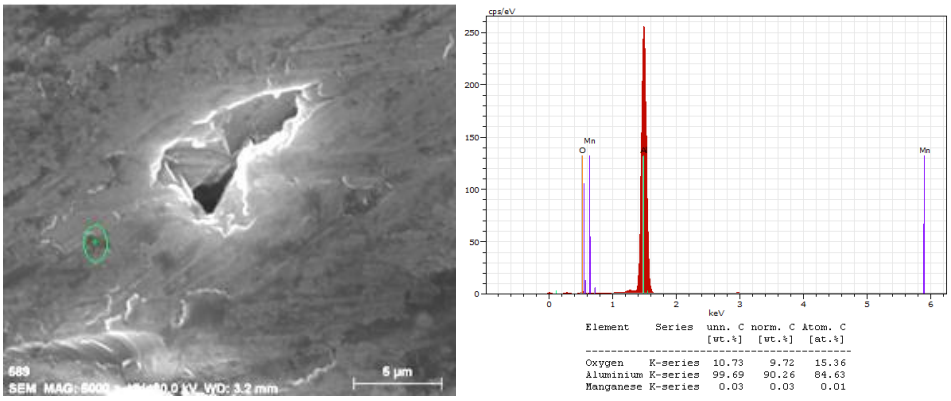

(a) (b)

Figure 5.1: (a) Un-etched SEM micrograph of Al-10wt.%MnO composite A at 600X and (b) composition of encircled spot by EDX

Presence of Mn traces in the Al-matrix is attributed to the result of the reduction of MnO with Al melt. Mn released in the matrix reacts with Al-rich matrix to make Al_2O_3 and an intermetallic precipitate of Al-Mn as is suggested by the following chemical reaction taking place in the (Al-MnO) composite system: Figure 5.3 (a) indicates SEM micrograph of the Al-10wt.%MnO composite B at 600X and its chemical composition is given in Figure 5.3 (b) at a encircled spot by EDX analysis.

$2Al + 3MnO = 3Mn + Al_2O_3$ (1),

$Al+Mn = AL(Mn)$ ppt. (2).

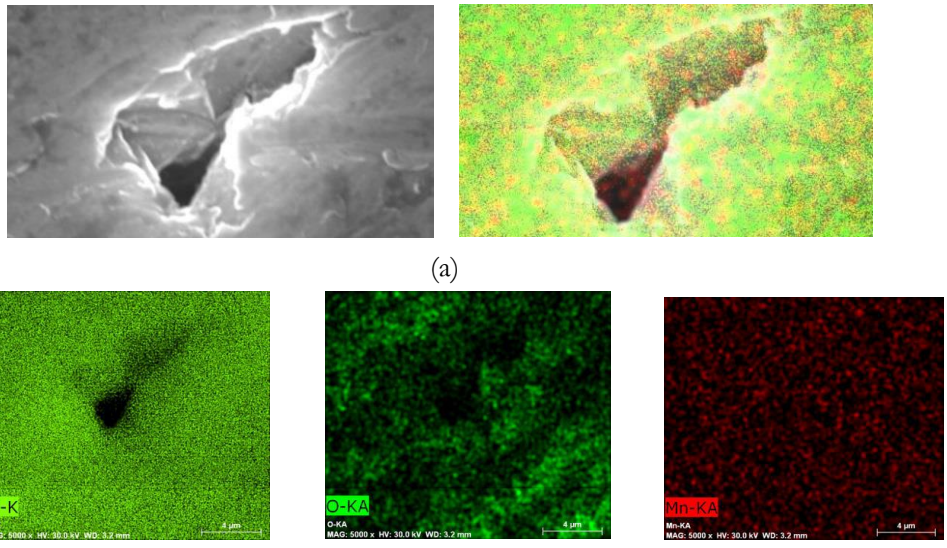

(a)

(b)

Figure 5.2: Un-etched elemental mapping SEM micrograph (Al, O and Mn) of Al-10wt.%-MnO composite A at 5000X. at 300X, (a) Collectively and (b) Separately

ISBN: 978-81-936820-6-7
Proceedings DOI: 10.21467/proceedings.4

Series: AIJR Proceedings

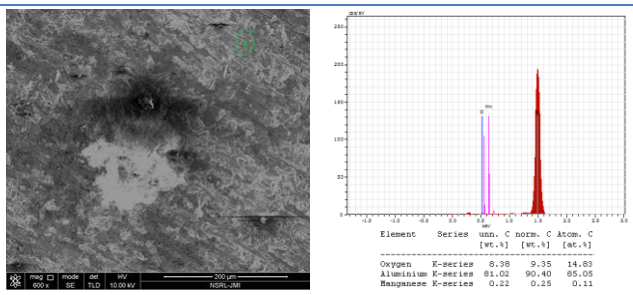

(a) (b)

Figure 5.3: (a) Un-etched SEM micrograph of Al-10wt.%MnO composite B at 600X and (b) composition of encircled spot by EDX.

Figure 5.3 (a) indicates fine bright particles in the Al matrix identified as Al_2O_3 particles by EDX in Figure 5.3 (b) and traces of Mn is detected by EDX which indicates presence of Mn in the Al matrix to make an intermetallic precipitate of Al-Mn. Presence of Al_2O_3 and Al-Mn is attributed to the result of the chemical reaction between Mn released in matrix by reduction of MnO with molten Al and Al-rich matrix itself in the composite system as is suggested by the reactions referred to in equations (1) and (2).

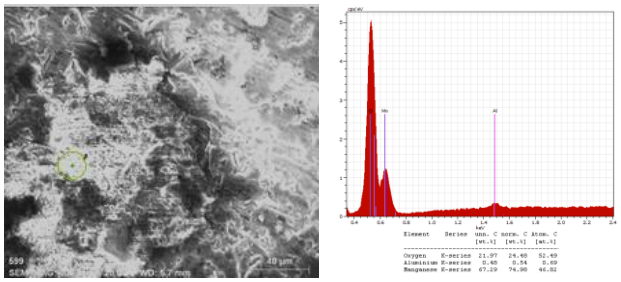

(a) (b)

Figure 5.4: (a) Un-etched SEM micrograph of Al-10wt.%MnO composite B at 600X and (b) composition of encircled spot by EDX

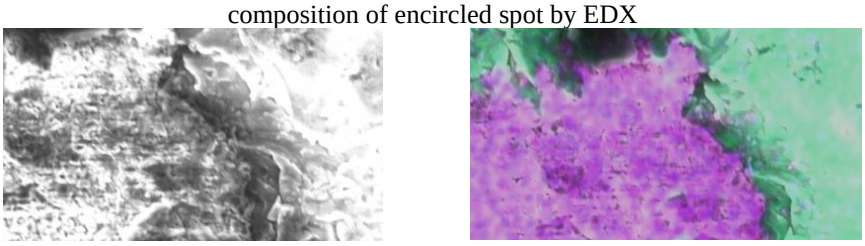

(a)

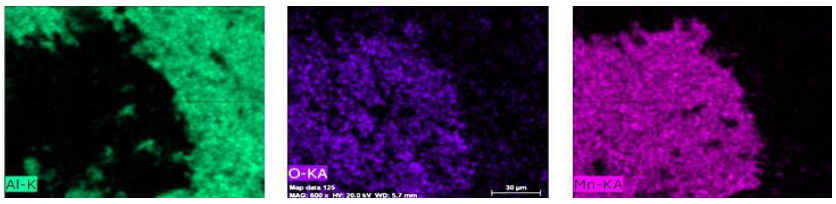

(b)

Figure 5.5: Un-etched elemental mapping SEM micrograph (Al,O and Mn) of Al-10wt.%-MnO composite B at 600X, (a) Collectively and (b) Separately

Figure 5.4 (a) shows un-etched SEM micrograph of the reinforcement particle in the matrix of composite B at 600X and its chemical composition is recorded by EDX in Figure 5.4 (b). EDX analysis indicates presence of Mn in the Al matrix to make an intermetallic precipitate of Al-Mn.

Figure 5.5 illustrates un-etched elemental mapping SEM micrograph (Al, O and Mn) of composite B at 600X. Figure 5.9 (a) illustrates presence of Al (green), O (cyan) and Mn (Pink) collectively in the matrix. More O and Mn with little Al are seen to form porous AlMnOx particle, thus confirming Al_2O_3 (light green) embedded in an unreacted MnO particle (light pink) in the Al-matrix (green). More O at the matrix-reinforcement boundary is clearly visible to appear as dark green Al_2O_3 layer from matrix side and dark pink MnO layer from reinforcement side. Distribution of Al, O and Mn is shown in Figure 5.5 (b) separately, thereby confirming what has been indicated in Figure 5.5 (a).

4.2 Optical Microscopy

Optical microscopic technique was applied for the analysis of microstructure of the composite samples. The magnified images of the samples were obtained using a microscope digital camera Leica DM 2500 M. Optical images of composites were taken at different points of the samples surfaces. All of the analyses were carried out at room temperature. The maximum magnification obtained with the optical microscope was about 500X.

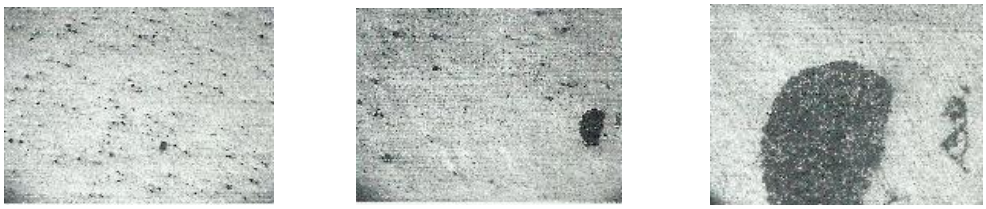

(a) (b) (c)

Figure 5.6: Un-etched OM of Al-10wt.%MnO composite A at (a): 25X, (b): 100X and (c): 500X

On macroscopic scale at low magnification, at 25X in Figure 5.6 (a), un-etched optical micrograph of Al-10wt.%MnO composite A is shown. The density of small dark spots in the matrix is less than those observed in composite samples of A. In Figure 5.6 (b) at higher magnification of 100X, few small light spots are inside the bigger particles. Figure 5.6 (c) at higher magnification of 500X indicates big reinforcement particle containing more small light spots than those indicated in composite samples of A1, which may indicate formation of porous alumina (Al_2O_3) particle or agglomerated cluster of alumina particles. It also shows a good bonding between the particles and matrix.

ISBN: 978-81-936820-6-7
Proceedings DOI: 10.21467/proceedings.4

Series: AIJR Proceedings

(a) (b) (c)

Figure 5.7: Un-etched OM of Al-10wt.%MnO composite B at (a): 25X, (b): 100X and (c): 500X.

Figure 5.7 (a) shows un-etched optical micrograph of Al-10wt.%MnO composite B at 25X. It indicates reinforcement particles surrounded by small dark spots in the matrix. Small light and dark spots are inside the bigger particles are visible in Figure 5.7 (b) at higher magnification of 100X, which could be pores and in-situ formed Al_2O_3 particles embedded in MnO particles. It also shows an aggregation of the particles. On microscopic scale, at magnification of 500X in Figure 5.7 (c), big aggregated reinforcement particles containing small light and dark spots is shown. This could be indication of in-situ formed alumina particles embedded in MnO particles to form porous in-situ generated intermediate compound (AlMnOX) particle. It also shows a good bonding between the particle and matrix.

4.3 X-ray diffraction (XRD)

XRD analysis is based on constructive interference of monochromatic X-rays and a material sample. The characteristic x-ray diffraction pattern generated in the XRD analysis provides a unique "fingerprint" of the crystals present in the sample. In the present analysis as part of morphological characterization, a comparative XRD analysis is carried out between the Matrix Al and the developed composite.

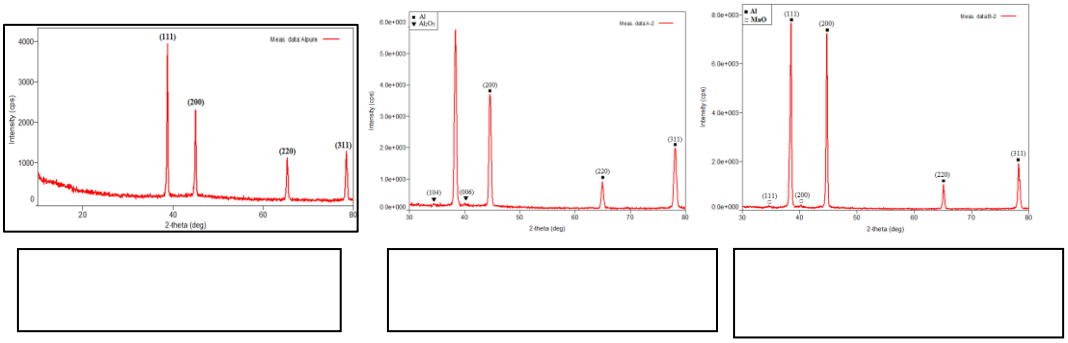

The Figure 5.8 illustrates the XRD result of the matrix (Al). The result reveals that the main phases present belong to Al, which is present in the form of phases e.g.,Al(111), Al(200), Al(220) and Al(311). The Figure 5.9 illustrates the XRD result of developed Al-10%MnO composite A. The result shows that the main phases present belong to Al (largest peaks) and Al_2O_3 (lower peaks). The Al is present in the form of phases i.e. Al (111), Al (200), Al (220)

and Al (311), while Al_2O_3 is present only in the form of phases i.e. Al_2O_3 (104) and Al_2O_3 (006) phases. Peaks are identified by using JCPDS software. The peak intensities of Al in the manufactured composite are changed. There is a significant increase in peak intensities of Al (111) and Al (200) phases, and slight increase in peak intensity of Al (311) phase. However, the peaks are of only of Al and Al_2O_3 phases, which confirms that MnO particles have been completely reduced with molten Al forming in-situ Al_2O_3 particles and little amount of an intermetallic (Al-Mn) compound phases that can be detected directly from the bulk specimen as indicated by XRD. The Figure 5.10 illustrates the XRD result of developed Al-10%MnO composite B. The result shows that the main phases present are Al (largest peaks) and MnO (lower peaks). The Al is present in the form of phases i.e. Al(111), Al(200), Al(220) and Al(311). MnO is present in the form MnO(111) and MnO(200). Peaks are identified by using JCPDS software. The peak intensities of Al in the manufactured composite are changed. There is a significant increase in peak intensities of Al(111) and Al(200) phases, and moderate increase in peak intensity of Al(331). Manganese oxide was indicated in low intensities of MnO(111) and MnO(200) phases. However, there are peaks corresponding to Al and MnO phases. This confirms that MnO particles have been partially reduced with molten Al forming little amount of in-situ Al_2O_3 particles and an intermetallic (Al-Mn) compound phases to be detected directly from the bulk specimen as indicated by XRD.

6 Conclusion

Results show that the use of manganese oxide (MnO) as reinforcing ceramic particles in pure aluminum can produce (Al-Al_2O_3) or (Al-$AlMnO_X$) in-situ particulate composite via stir casting method. The composite can be developed by controlling the particle size. There is appreciable reaction between MnO particles and melted Al matrix, producing in-situ finer Al_2O_3 particles and an intermetallic precipitate of Al-Mn compound, which could be in various phases with uniform distribution in Al to make Al-alloy as matrix. Some portion of Al diffuses into MnO particles to react with oxygen and generate Al_2O_3 particles forming MnO porous intermediate compound ($AlMnO_X$). Fine alumina (Al_2O_3) particles and an intermetallic precipitate of Al-Mn as a result of chemical reaction between molten Al and manganese oxide (MnO) particles have been observed using scanning electron microscopy (SEM) with energy dispersive X-ray analysis (EDX) of entire area of both developed composite samples. EDX analysis of the reinforcement particles of developed composite sample B has detected that their composition contains high percentage of Manganese (Mn) and Oxygen (O) with low percentage of Al, which indicates presence of unreacted MnO and generated Al_2O_3 particles. SEM analysis of in-situ formed $AlMnO_X$ particles at high magnification has detected a characterized porous structure. EDX Analysis of the reinforcement particles of composite sample of A has detected that their composition contains high percentage of (Al) and (O) without presence of (Mn), which indicates presence of generated Al_2O_3 only. This has been also confirmed by elemental mapping SEM analysis.

ISBN: 978-81-936820-6-7

Series: AIJR Proceedings
Proceedings DOI: 10.21467/proceedings.4

Optical micrographs have indicated presence of porosities in the both composite samples, but their density varies from A to B, depending on the reinforcement particles size. Optical micrographs have shown that a good bonding between particles and the matrix of both developed composite samples.

XRD analysis has indicated that the main phases present in both developed composite samples are Al (largest peaks). It is present in the form of phases Al(111), Al(200), Al(220) and Al(311), but with various intensities. Al_2O_3 (lower peaks) has only been indicated in composite sample of A. It is present in the form of phases Al_2O_3(104) and Al_2O_3(006). MnO (lower peaks) has been indicated in composite sample B,. It is present in the form of phases MnO(111) and MnO(200) of composite sample B. MnO phases of composite sample B have shown low intensity peaks, which indicates that less amount of unreacted MnO particles. Amount of intermetallic compound (Al-Mn) phases formed in the specimens of both developed composites may be too little to be detected directly from the bulk specimen by XRD.

Thus, the morphological structure analysis using XRD of developed composite samples indicates the presence of a porous $AlMnO_X$ embedded in pure Al matrix in developed composite sample B only.

References

[1] ASM International Handbook Committee: "Composite, Engineered Materials Handbook," Volume 1, Third Printing, August 1989.

[2] K. Surappa, "Aluminium matrix composites: Challenges and opportunities". Sadhana. 28: 319-334, 2003.

[3] Sabah Khan, "Analysis of Wear Rate and Tribological Behavior of Aluminum Cast Alloy A356 and Granite Composite at Different Speeds", (IJEAT), Volume-5, Issue-3, February 2016, Pp 128 – 131.

[4] Khedera, G. Marahleh and D. Al-Jameaa, "Strengthening of Aluminum by SiC, Al2O3 and MgO". Jordan Journal of Mechanical and Industrial Engineering. Volume 5, Number 6, Dec. 2011.

[5] D. Ramesh, R. Swamy and T. Chandrashekar, "Effect of weight percentage on mechanical properties of frit particulate reinforced Al6061 composite". ARPN Journal of Engineering and Applied Sciences. Vol. 5, No. 1, January 2010.

[6] K. Almadhoni and S. Khan," Evaluation of the effective thermal properties of aluminum metal matrix composites reinforced by ceramic particles", International journal of current engineering and technology, E-ISSN 2277 – 4106, P-ISSN 2347 – 5161, Vol.5, No.4, 2015.

[7] R. Calin, M. Pul and Z. Pehlivanli, "The Effect of Reinforcement Volume Ratio on Porosity", Materials Research, 15(6): 1057-1063, 2012.

[8] N. Jit, A. Tyagi and N. Singh, Al-Cu-Si - (Al_2O_3)p composites using A 384.1 Al Alloys.. Vol. 21, No. 10, S066-071, 2009.

[9] Zhou W. Y., Qi S. H., Tu C. C., Zhao H. Z., Wang C. F., Kou J, "Effect of the particle size of Al_2O_3 on the properties of filled heat-conductive silicone rubber" Journal of Applied Polymer Science, 104, 1312–1318 (2007).

[10] Ling W., Gu A. J., Liang G. Z., Yuan L." New composites with high thermal conductivity and low dielectric constant for microelectronic packaging", Polymer Composites, 31, 307–313 (2010).

[11] R. Gadag and A. Shetty, Handbook of engineering chemistry, Department of chemistry, National institute of technology, Karnataka, Shurathkal, 2010.

[12] J. Hashim, L. Looney and M. Hashmi, "The wettability of SiC particles by molten aluminum alloy", Journal of Materials Processing Technology, 119(1-3):324-328, 2001.

[13] K. Almadhoni and S. Khan, "Review of effective parameters of stir casting process on metallurgical properties of ceramics particulate Al composites", Journal of mechanical and civil engineering (IOSR-JMCE), Vol. 12, Issue 6, Ver. IV, PP 22-40, 2015.

[14] S. Nam and D. Lee, "The effect of Mn on the Mechanical Behavior of Al Alloys, Metals and materials", Vol. 6, No. 1, pp. 13-16, 2000.

[15] V. Tirth, "Process parameters and improvements in properties of metals and alloys by squeeze casting", IJNSTEEES, International Science Press 2, pp 26- 61, 2009.

[16] C. Singh and K. Mer, "Wear characterization of Al- Al_2O_3 in-situ particulate composite synthesized in open hearth furnace with manually controlled stirring method", Proceedings of international conference on innovation & research in technology for sustainable development (ICIRT), 2012.

[17] Agarwal, S. Singh and others, "Development of Al- Al_2O_3 (MnO_2) hybrid MMCs and their characterization for mechanical properties", MIT international journal of mechanical engineering, Vol. 2, No. 1, pp. 62-69, 2012.

[18] G. Kreysa, J. Baselt and K. Unger, Novel Mn-based Mesoporous mixed oxidic solids, Technology & Engineering, Elsevier, 2000.

[19] D Saheb, "Aluminum silicon carbide and aluminum graphite particulate composites", ARPN, Journal of engineering and applied sciences, Vol. 6, No. 10, ISSN 1819-6608, 2011.

[20] P. Sharma, "Production of AMC by stir casting – An overview", International journal of contemporary practices, ISSN: 2231-5608, Vol.2, Issue 1, 2013.

[21] R. Gadag and A. Shetty, Handbook of engineering chemistry, Department of chemistry, National institute of technology, Karnataka, Shurathkal, 2010.

[22] G. Totten and D. Scott, Handbook of aluminum, Physical metallurgy and processes, Vol. 1, 2003.

[23] J. Hashim, L. Looney and M. Hashmi, "The wettability of SiC particles by molten aluminum alloy", Journal of Materials Processing Technology, 119(1-3):324-328, 2001.

ISBN: 978-81-936820-6-7

Series: AIJR Proceedings
Proceedings DOI: 10.21467/proceedings.4

Nanotechnology: Concepts, Importance and the Current State of Scientific Research

Samieh Abu Saad[1*], Amani Elmahjubi[2]

[1] Head of Engineering Department, Industrial Research Centre Tajoura, Libya

[2] Head of Chemicals& Glassware Storage Unit, Industrial Research Centre Tajoura, Libya

DOI: https://doi.org/10.21467/proceedings.4.22
* Corresponding author email: samieh7@yahoo.com

ABSTRACT

In nowadays, research in nanoscale science has been greatly developing and obtaining more interests. Numerous research activities in the last two decades focus on exploring nanoscience, understanding the fundamentals, and developing technical solutions. Materials in nanoscale showed remarkable and superb properties that are completely different from those when the material in the bulk condition. This makes nanotechnology to hold a great promise in effecting profound scientific, medical, energy, economic and even cultural change on society. Almost all countries are placed long and short term strategic plans as to obtain more experience and carefully examine the potential implications of nanotechnology and its strategic benefits. Consequently, research indicators on this technology indicate that some developing countries compete with the world's largest countries in the control of this technology. This paper, however, provides an introduction to the nanotechnology, and also discovers the current status of the research on this particular field globally and in the Arabic region. The real status of the scientific research on the nanotechnology in Libya correspondingly is realised. Steps required by the Libyan authorities and research principles to fill in the gape in this area are also expressed.

Keywords: Nanotechnology; Nanoscience; Research in Nanotechnology; Nanotechnology Applications.

1 Introduction

Nanotechnology has become a competitive scientific technology that most of developed countries competed to control. The research and development in this particular field of technology has impacted every aspect of modern human life. More and divers areas of research have been continuously increasing and gaining the interest of researchers and scientists to apply this kind of technology and benefit from [1]; e.g. energy; agriculture; petroleum industry; food industry; and probably the strongest field is medicine and healthcare. Nanotechnology refers to the science and technology of which a matter is controlled in a nanoscale. It is commonly attributed for the technologies leading to produce nanoscale materials at nanometre dimension (10-9 m) [2, 3]. The nanoscale is consensually considered to cover the range of 1

 ISBN: 978-81-936820-6-7

to 100nm. According to the US National Nontechnology Initiative (NNI), the nanotechnology is '*the understanding and control of matter at dimensions between approximately 1 and 100 nanometres, where unique phenomena enable novel applications. Encompassing nanoscale science, engineering, and technology, nanotechnology involves imaging, measuring, modelling, and manipulating matter at this length scale*'. Yet, numerous definitions of nanotechnology have migrated and expanded with the passage of time. For instance, in [4], the definition is expressed as '*nanotechnology is the design, characterization, production and application of materials, devices and systems by controlling shape and size of the nanoscale*'. While in [5], a slightly different nuance is given by '*the deliberate manipulation, precision placement, measurement, modelling and production of matter at the nanoscale in order to create materials, devices and systems with fundamentally new properties and functions*'. Another different definition, though floating around, is introduced in [6] that is '*the design, synthesis, characterization and application of materials, devices and systems that have functional organization at least one dimension on the nanometre scale*'. Obviously, the definitions, however, should provide some form of proactive engineering to the term nanotechnology. Nevertheless, to avoid the debate about the definition as it is not the particular scope of this paper, it would be better to suggest that a certain technology can be considered nanotechnology only if it involves all of the following three attributes: first, research and technology development at the atomic, molecular or macromolecular levels, in the scale of approximately 1–100 nm range; second, creation and use of structures, devices and systems that have novel properties and functions because of their small and/or intermediate size; and finally, an ability to control or manipulate on the atomic or the nanoscale [7].

This paper provides an introduction to the basic principles and applications of nanotechnology. It also discovers the current status of research on this particular field globally and in Arabic countries. The real situation of the scientific research on nanotechnology in Libya is finally concluded, and steps required by authorities and research principles to motivate the research in this area are expressed.

2 Importance of Nanotechnology

Nanotechnology is considered as a powerful tool and technique in medical technology as well as almost every filed life. This kind of technology develops so fast; while its applications diverse to touch all branches of science, engineering and industries. The momentum of nanostructures stems from the fact that new materials with absolutely new properties can be developed. Properties of a matter depend strongly on how atoms are arranged in space; e.g. if atoms in coal (Carbon) is rearranged, it could make diamond. Therefore, nanotechnology holds great opportunities for innovation in, virtually, every industry and application. New materials and advanced devices of a desirable properties and functions can be developed for numerous applications using this technology. The main aspects that make nanotechnology attractive to researchers are the fact that it is relatively cheap, can be manufactured in bulk with lower energy; the ability to control the material's properties by controlling its particles

ISBN: 978-81-936820-6-7

Series: AIJR Proceedings
Proceedings DOI: 10.21467/proceedings.4

size and structural form as well as controlling the conditions and methods of preparation; and relatively safe in terms of use for people and environment [8]

3 Influence of Size on the Materials' Properties

Owing to the small size of the building blocks (particle, grain, or phase) nanomaterials demonstrate unique mechanical, optical, electronical, and magnetic properties [3]. Properties of nanomaterials depend on [9]: fine grain size and size distribution (<100 nm); the chemical composition of the constituent phases; the presence of interfaces, more specifically, grain boundaries, hetero-phase interfaces, or the free surface; and lastly interactions between the constituent domains.

Changes in the size-dependent properties of a matter are observed due to the fact that wave-like properties of electrons inside the matter and atomic interactions are influenced by the size of materials at the nanometre scale. Confinement of the DeBroglie wavelength of charge carriers inside nanomaterials could also lead to quantization effect [3]. As the size decreases, the ratio of atoms on the surface increases. Such atoms are high energy surface atoms and very reactive. This also creates a high surface to volume ratio leading to a tremendous improvement in chemical properties. Platinum nanoparticles, for example, are efficient catalysts for many reactions whereas platinum bulk sheets are sufficiently inert [8, 9]. Large surface to volume ratio means subtle changes to the surface due to addition of numerous atoms or molecules leading to dramatic alterations of physical properties. Number of fields, including magnetism, luminescence and renewable/alternative energy to sensors as well as photo-catalysis, will benefit from capitalizing on the surface–volume relationship. The possible enhancement of physical properties is therefore due to quantum size and clustering interface effects [10]. Figure 1 shows how surface volume ratio changes with particle size.

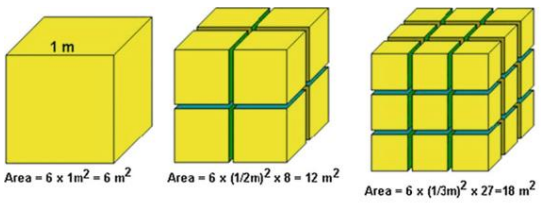

Figure 1: The *surface volume ratio changes with particle size.*

4 Nanofacture

There is a wide variety of technologies that have the potential to produce nanomaterials with different degrees of quality, speed and cost. Yet, grain size, shape and structure of the required nanomaterials are the main factors restrict the selection of the technology [11]. Almost all of these techniques fall into the main categories described in Figure 2. The top-down methods mostly require large (and also expensive, needs considerable concentrations of capital) installations [11]. Traditionally, scaling-down processes are based on process that include

grinding or etching and utilise an ultraprecision engineering. Mechanical stiff parts are used to ultra-precisely shape objects. While on the other hand, for semiconductor processing a very high-quality thin films are deposited, either physical vapour deposition (PVD) or chemical vapour deposition (CVD), with nanometre control, perpendicular to the plane of a substratum [11, 12]. Sophisticated technologies, e.g. exposure to a plasma, or ions implantation, are employed to modify existing surfaces of materials [12].

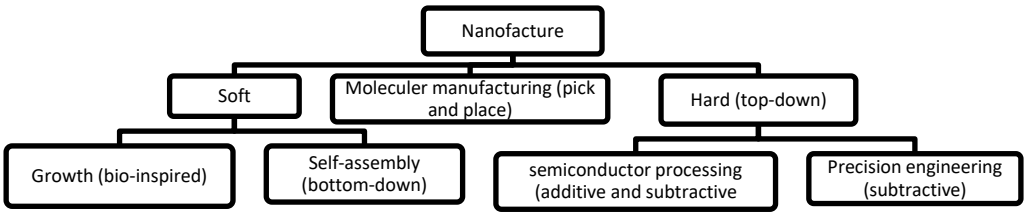

Figure 2: Different *modes of nano-manufacture (nanofacture).*

The other approach is known as molecular manufacturing; also known as "pick and place" or bottom-to-bottom methods, literally construct things atom-by-atom [11, 12].

The third approaches, known as bottom-up or self-assembly, are based on creating objects that capable of spontaneously assembling into useful structures. Precursors are gathered in random positions and orientations, and supply energy to allow them to sample configuration space. Once the precursors are in position, the bonds connecting them are strengthened and the final object is fixed permanently [11, 12].

5 The Current Situation of Research in Nanotechnology

To study the development trends of the research in nanotechnology, the outcomes of nanotechnology related research is examined. Indicators; namely, funding, publications and patents are presented, investigated and analysed. The results of such studies would also help policy makers in assessing their past policies, forecasting future trends based on the previous and contemporary trends [14], and take new valuable actions to succeed.

5.1 Globally

Governmental funding plays a critical role in establishing and stimulating nanotechnology research and development (R&D). Based on the Global Funding of Nanotechnologies & its Impact report [15], since 1997 the United States (US), followed by most countries in the European Union (EU), and other countries have announced series of policies and heavy funding to support academia for the field of nano-innovation R&D. Since then, as denoted in Figure 3, this budged was gradually increasing. Remarkably, the US outspends every country else. Yet Japan and Russia have managed to take a temporary lead in 2000-2003 before fall back. Also, it points out that the funding trend in EU grows gradually; while on the other hand faster growth rates are observed in Asia.

ISBN: 978-81-936820-6-7
Proceedings DOI: 10.21467/proceedings.4

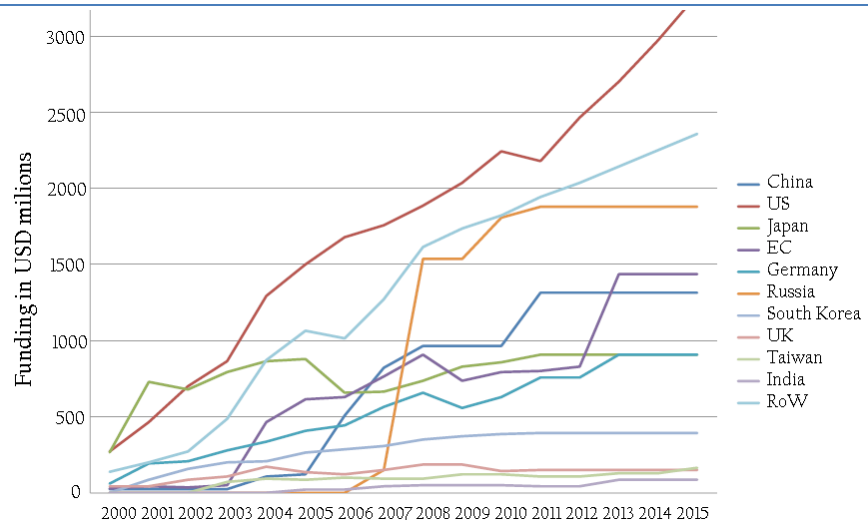

Figure 3: Funding of nanotechnologies by country [15]

Such funding is expected to positively reflect on the nanotechnology related R&D activities. This can be observed in the number of nanotechnology related articles and the number of granted patents annually. These two figures are mainly considered when examining the outcomes of R&D activities [14]. Visibly, scientific articles are the major source of knowledge production and transfer from academic research to industrial applications and developing innovations [14].

In this work, statistics of published scientific articles are obtained from the Thomson Reuters Web of Science (WoS) which are usually used for retrieving and analyzing academic research outputs [15]. Additionally, to avoid confusion and for better understanding only the top 5 countries are considered for the period of 2010-2017 as represented in Figure 4. It reveals that China possesses the highest rate of growth with about 47% while the US comes second with mostly half growth rate. Remarkably, India, South Korea and Iran rank in the list with growth rate of about 24%.

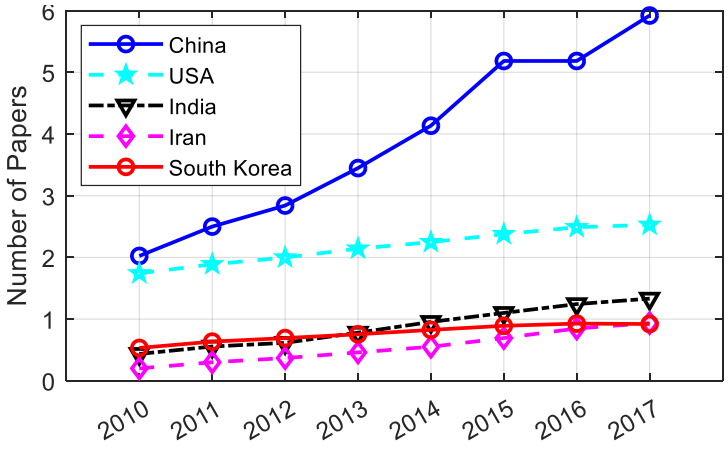

Figure 4: The *number of nanotechnology article in 2010-2017*

Nevertheless, number of articles need to be carefully analysed when used as an indicator for nanotechnology developing. Obviously, it is related to other figures such as population, stage of development, percentage of R&D expenditures, and some other important factors. Therefore, to reliably analyse data, another index is deployed to study the growth of nanotechnology research globally; i.e. the local share of nano-articles to total articles published by each country. Figure 5 shows the top 5 shares (%) in 2010-2017. It represents that Asian countries have the highest share in this indicator, and almost all of them have shares higher than the world average (9.5%). Iran and Saudi Arabia have consist increasing share and achieved their highest shares in 2017. Both have experienced huge growth in the published nano-articles by giving propriety to nanotechnology research. Noticeably, Bahrain is in this particular list indicating the level of interest paid to this technology.

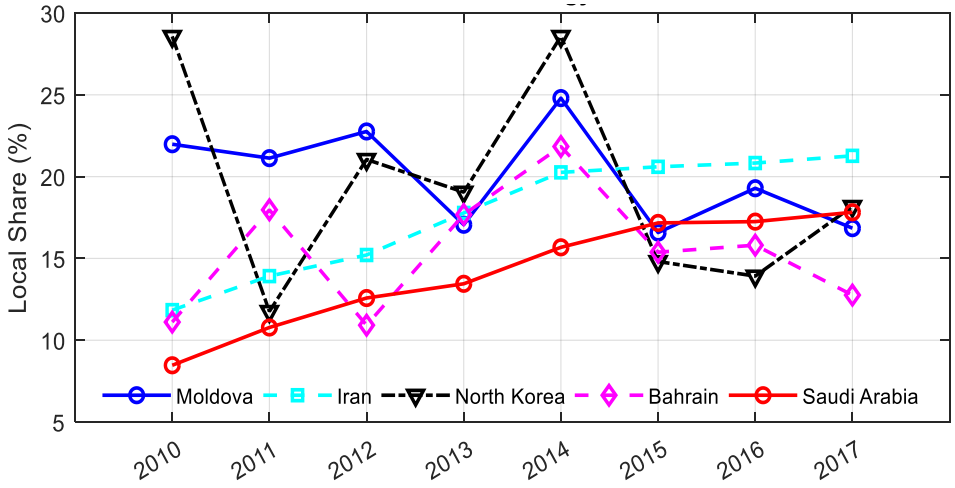

Figure 5: The *local share in nanotechnology articles in 2010-2017*

It is worth mentioning that although US is ranked 2nd in published nano-articles, it possesses an average share of around 6 % in 2010-2017. While India ranked 6th in this list explaining the reason they both are not appearing in Figure 5. To further analyse the global development in nanotechnology, patents number is employed as a technology and innovation indicator. Patent data were retrieved from the United States Patent and Trademarks Office (USPTO) and European Patent Organisation (EPO). Figure 6 represents the nanotechnology patents granted in the USPTO in 2010-2017. It shows that US ranks 1st by possessing 60% of all nanotechnology patents. Noticeably, South Korea has consistent increasing patents and ranked 2nd in 2017 moving Japan 3rd with a gap of 500 patents.

ISBN: 978-81-936820-6-7
Proceedings DOI: 10.21467/proceedings.4

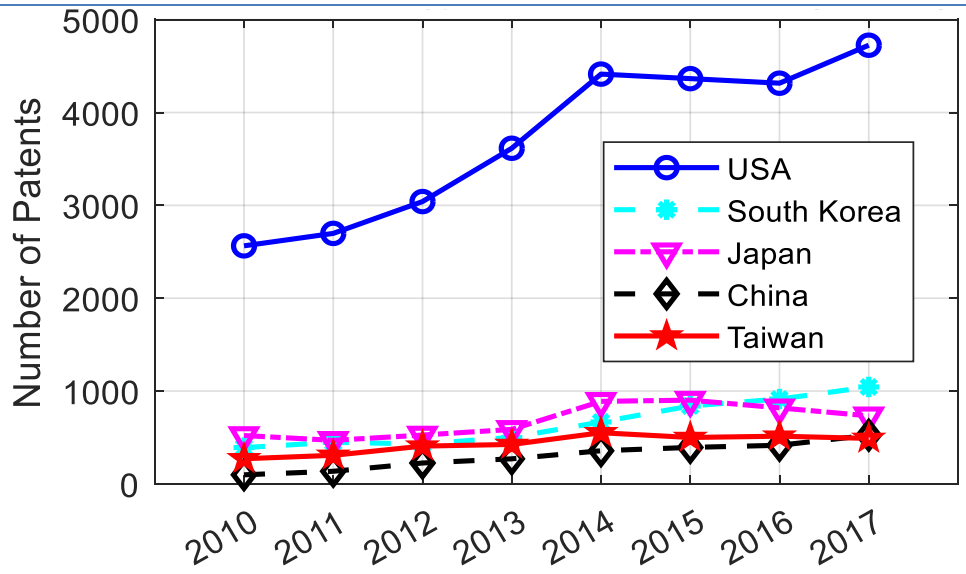

Figure 6: Nanotechnology *related patents in USPTO*

The EPO also shows that US possesses the highest patents granted in 2010-2017 as denoted in Figure 7. Apart from France and Japan, the gap between each country and other is visible.

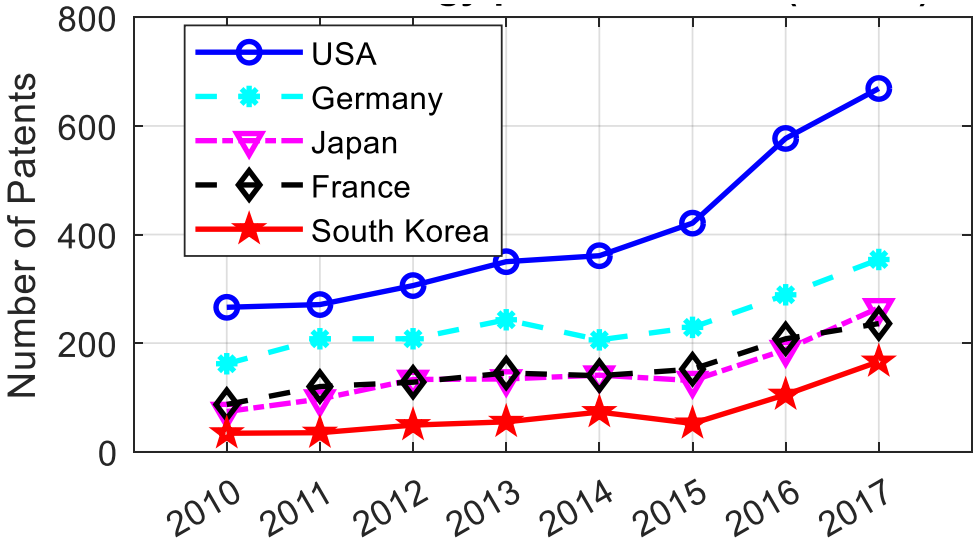

Figure7*:* Nanotechnology *related patents in EPO*

5.2 The Arabic countries

Similarly, the current situation of research in the field of nanotechnology in Arabic countries is explored using both the number of publications and corresponding local share. It is worth mentioning that trusted resources about the exact funding spend on nanotechnology related R&D by most Arabic governments is not available. Hence only publications number and local

share are explored. Additionally, due to the fact that published articles are very small in contrast to that published globally, the accumulative number in 2000-2017 is used instead, as denoted in Figure 8. Saudi Arabia has the highest accumulative number with more than 8000 articles, followed by Egypt with about 7750 articles. The rest are all either around 1500 articles or reasonably lower; whereas Libya stands in the back with less than 100 articles.

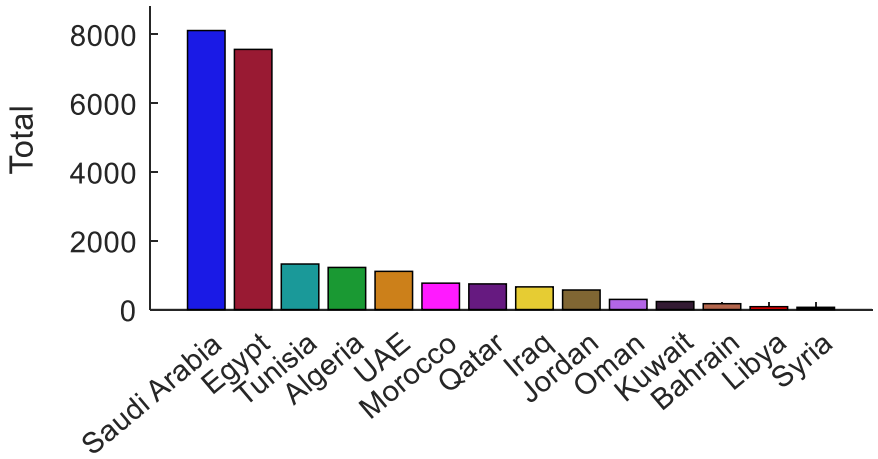

Figure 8: Published *nanoarticles in Arabic countries, total in 2000-2017*

The local share is also calculated for every single Arabic country and represented in Figure 9. It appears that Saudi Arabia leads the list with about 8% share; Qatar comes 2nd with 6%. UAE, Iraq, Bahrain, Kuwait and Egypt have close shares of about 5%. Libya has no share calculated as a trusted total number of articles is not available.

More, apart from Saudi Arabia patents granted in USTPO by Arabic countries is as small as less than 8, see Figure 10. In fact Saudi Arabia has been ranked 12th globally in USPTO.

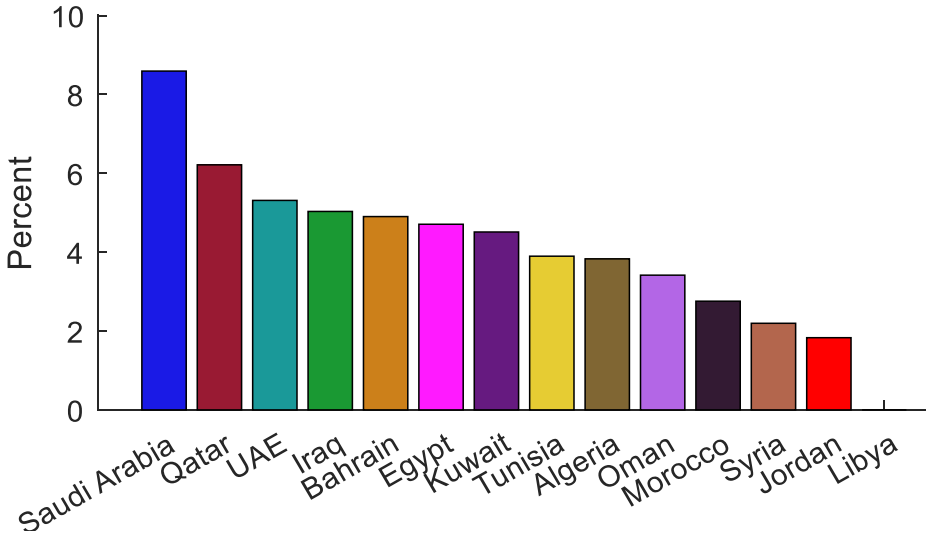

Figure 9: Local *share of nanoarticles in the Arabic countries*

ISBN: 978-81-936820-6-7
Proceedings DOI: 10.21467/proceedings.4

Statistics from EPO showed similar results to that of the USPTO indicating that research activities in nanotechnology is still in early stages in Arabic countries. However; Saudi Arabia represents the best performance and possesses advanced position globally.

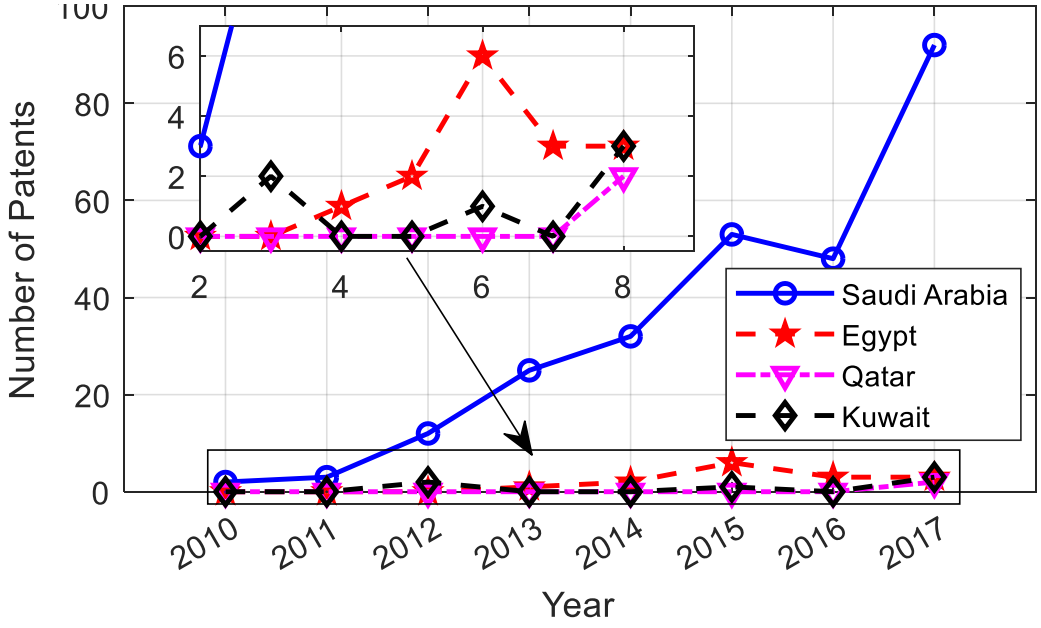

Figure 10: Arabic *nanotechnology related patents in USPTO*

To further analyse the current situation in Arabic countries, the Global Innovation Index (GII) [16] in 2013-2017 is discovered. This would also provide detailed metrics about the innovation performance in Arabic countries. Table 1 represents the ranking of GII of top 10 Arabic countries. It illustrates that UAE ranks first mostly in 2013-2017. Particularly it possesses the 35th globally in 2017. Qatar also showed good performance in that it moved from the 50th globally in 2016 to 49th Saudi Arabia also develops gradually, although its rank decayed from 49th in 2016 to 55th in 2017 globally moving to 3rd in the Arabic GII list. Kuwait, Bahrain and Morocco have systematic improvement in the GII globally. The table indicates that the some Arabic countries keen interest in innovation. In fact, innovation is the main pillars for a high-productivity knowledge economy. It is worth mentioning that these countries have made important progress by localization of nanotechnology research in universities and research bodies as well as establishing specialized research centres in the field of nanotechnology. For instance, Saudi Arabia established 6 institutes specialised in nanotechnology and at least three companies in the field of Nanotechnology industries; while almost all universities have departments educate nanoscience and nanotechnology. Egypt also possesses the highest number of specialized organizations, institutions and research centres in Arabic countries; i.e. more than 10 [17].

Table 1: *Global rankings of Arabic contries in GII.*

Country	Arabic countries GII ranking				
	2013	2014	2015	2016	2017
UAE	38	36	47	41	35
Qatar	43	47	50	50	49
Saudi Arabia	42	38	43	49	55
Kuwait	50	69	77	67	56
Bahrain	67	62	59	57	66
Morocco	92	84	78	72	72
Tunisia	70	78	76	77	74
Oman	80	75	69	73	77
Lebanon	75	77	74	70	81
Jordan	61	64	75	82	83

6 Development of Nanotechnology in Libya

Pessimistically, the concern for this technology in Libya, formally, is not yet clear. Despite the attempts from scholars, research centres and universities to concretize it; yet these efforts are solitary and not comprehensive. Figure 8 showed that only around 85 articles were published globally. Governmental actions are urged to initiate programs that involve different institutions, focuses on the R&D, the creation of human capacity, the provision of infrastructure. Steps need to be taken may include but not limited to:

- Establish clear and objective policies as well as national initiative with obvious objectives and visions for excellence in this particular field to create a favorable investment environment;
- Establish and implement an objective plan for scientific and technological research and innovation in the field of nanoscience and technology. The plan should include the foundations of joint cooperation to maximize the benefit from the scientific and human resources available in R&D centres, institutes and universities;
- Provide the necessary long term resources for the constitution of capacities; and suitable funds toward R&D to motivate the development in this field;
- Encourage (i.e. by funds, special policies and targeted intermediaries) to involve scientists, researchers, and scholars in the nanotechnology field, and establish clusters or networks to adapt and develop rapidly;
- Promote management in mediators to focus on linking academic and industrial organisations together, in order to motivate collaborative research and innovation;

7 Conclusions

This work has provided a brief introduction to the nanotechnology, including definition, the basic principles, applications, and manufacturing methods. It is also expanded to identify the

ISBN: 978-81-936820-6-7
Proceedings DOI: 10.21467/proceedings.4

Series: AIJR Proceedings

global pattern of nanotechnology related indicators, i.e. articles number, patents number and GII, in a developmental context in 2010-2017. Based on the analysis, the results reveal that the most of developed countries have made a considerable funding to support and encourage academia for the R&D in the field of nanotechnology. The USA and china have the highest indicators; while countries in Asia, generally, have showed the fastest growing rate. The study also showed that some Arabic countries have dramatically improved nanotechnology indicators. Namely, Saudi Arabia has identified increasing trend and systematic development in most indicators studied. Qatar, UAE, Kuwait, Bahrain and Egypt have also experienced developing trends. On the other hand Libya stands back in almost all indicators. Libyan policy makers must take serious actions to initiate strategies, make funds available and initiative programs that involve institutions focus on R&D, creation of human capacity, and the provision of infrastructure to encourage scientists and researchers to develop their related nano-activities.

References

[2] Carolina Fracalossi Rediguieri, "Study on the development of nanotechnology in advanced countries and in Brazil," *Brazilian Journal of Pharmaceutical Sciences* vol. 45, n. 2, abr.jun. 2009

[3] Kannaparthy R., Kanaparthy A. "The changing face of dentistry: nanotechnology". *Int J Nanomedicine* 6: 2799-804. 2011

[4] Iadiz MAR, Bamedi M, Fakour SR "Periodontal Diseases and Recently Applied Nano-Technology: A Review Article." *Health* 9: 345-51. 2017

[5] E. Abad et al "Nano Dictionary. Basel: Collegium Basilea" 119-146, 2005

[6] Jeremy Ramsden "Essentials of Nanotechnology".*Ventus Publishing ApS*, SBN-13: 9788776814182, 2009

[7] Lubick N; Betts ،Kellyn "Silver socks have cloudy lining" *Environ Sci Technol*. 42 (11): 3910, 2008.

[8] RocoMC "Building foundational knowledge and infrastructure for nanotechnology: 2000-2030". Chapter 4. In: Cheng et al (eds) '*anotechnology: delivering the promise'*, vol 1. ACS, Washington, DC, pp 39–52, 2016

[9] Liming Dai (Ed.) "Carbon Nanotechnology: Recent Developments in Chemistry, Physics, Materials Science and Device Applications", *Elsevier: Amsterdam*, 2006.

[10] Hari Singh Nalwa, "Nanostructured Materials and Nanotechnology", *Elsevier*, ISBN: 0080537278, 2001

[11] Günter Schmid "Nanotechnology. Volume 1: Principles and Fundamentals" *WILEY-VCH Verlag GmbH & Co. KGaA,Weinheim*ISBN: 978-3-527-31732-5. 2008

[12] Jeremy R. Ramsden, "Applied Nanotechnology", *Elsevier Inc*, ISBN: 978-0-8155-2023-8, 2009

[13] Jeremy R. Ramsden, "Nanotechnology: An Introduction", *Elsevier Inc*, ISBN: 978-0-08-096447-8, 2011

[14] Wang J, Shapira P "Funding acknowledgement analysis:an enhanced tool to investigate research sponsorshipimpacts: the case of nanotechnology". *Scientometrics87*(3):563–586, 2011

[15] Gorjiara T, Baldock C "Nanoscience and nanotechnologyresearch publications: a comparison between Australia andthe rest of the world". *Scientometrics* 100(1):121–148, 2014

[16] http://cientifica.com/wp-content/uploads/downloads/2011/07/Global-Nanotechnology-Funding-Report-2011.pdf; accessed on 14/06/2018 @ 12:01PM

[17] https://www.globalinnovationindex.org/

[18] ALECSO "A diagnostic study to survey the possibilities in the field of nanoscience and technology in the Arabic world", A study launched by the *Arab Organization for Industrial Development and Mining*, 2017.

The Effect of Adding Steel Slag and Lime on The Engineering Properties of a Sandy Soil

Ayad Abdelmoula Mohammed, Mohammed Ali Abdalla Elsageer*

Department of Civil Engineering, Faculty of Engineering, Sirte University, Libya

DOI: https://doi.org/10.21467/proceedings.4.23

* Corresponding author email: drmohammedalsger@gmail.com

ABSTRACT

Compaction is the process of mechanically densifying a soil which increase its density to meet engineering requirements. Unstable soils can create significant problems for pavements or structures ,therefore soil stabilization techniques are necessary to ensure the good stability of soil so that it can successfully sustain the load of the superstructure especially in case of soil which are highly active, also it saves a lot of time and millions of money when compared to the method of cutting out and replacing the unstable soil. This research describes a study of the effect of adding steel slag and lime on the engineering properties of a sandy soil. A series of laboratory experiments have been implemented and varieties of samples were made by mixing steel slag and lime with soil. different percentages of steel slag and lime were used as stabilization materials. Test results show that adding steel slag and lime can improve the properties of compacted sandy soil, and has a great effect on the behavior of compaction of stabilized soil, the maximum dry unit weight increased gradually at the low addition ratios and the maximum increase occurred at steel slag and lime content equals to 25% and 15% respectively.

KEYWORDS: Steel Slag, Compaction, Sandy Soil

1 Introduction

The availability of build able land is fast drifting away each day due to scarcity of lands with good natural bearing capacity. This leads to construction of building on poor soils which eventually lead to structural foundation failures. It has become very imperative to improve soil or the quality of grounds by the adoption of suitable improvement methods depending on the materials available . however, during soil or ground improvement, cost effectiveness is one of the major factors. Consequent upon this, there is paramount need to adopt the use of admixture during steel slag/soil improvement or stabilization. However, steel slag which is a waste product from steel production could replace some proportions of sand/soil. This admixture not only replaces some proportions of soil for cost effective soil improvement. this review work exposes those qualities and applications that make steel slag a good replacement or not during mixing with soil, to find out how improvement and for a more economic approach for stabilization soil. The present review also gives researchers and geotechnical engineering a clue on the application of steel slag and the limit for its usage. Different

 ISBN: 978-81-936820-6-7

methods can be used to improve and treat the geotechnical properties of the problematic soils (such as strength and the stiffness) by treating it in situ , these methods include dandifying treatments (such as compaction or preloading). The chemical stabilization of the soils (soft fine-grained soils) is very important for many of the geotechnical engineering applications such as pavement structures, roadways, building foundation, channel and reservoir linings, to avoid the settlement of soft soil.

Many materials and items discarded by organizations, companies and people have the potential to be reused for their original purposes or for new ones. Reuse discarded materials and items allows companies to get the most out of it. Additionally, reusing products conserves natural resources and saves valuable landfill space. Use of environment friendly materials in any industry is of paramount importance. limited waste landfill space, increasing cost of waste disposal in combustion facilities and landfills, depletion of the natural resources, and the need for sustainable development have all amplified the need to reuse the materials that were once regarded as wastes as substitutes for natural resources. In 2002, 50 million metric tons of steel slag was estimated to be produced worldwide [1] and 12 million tons was estimated to be produced in Europe [2]. Currently, the world annual production of steel slag is estimated to range between 90-135 million metric tons. Approximately 15 to 40% of the 10-15 million metric tons of steel slag generated in the United States in 2006 was not utilized [3] and a larger percentage of the 0.35-0.45 million metric tons of steel slag estimated by Akinwumi et al. [4].

GGBS or GGBFS (Ground Granulated Blast Furnace Slag) is a waste product drawn by the rapid cooling of molten iron slag. It is obtained from steel manufacturing process. In order to make use of GGBS, an attempt has been made for adopting it in soil stabilization. From the previous studies, it is clear that the GGBS induces the strength of cement and is extensively used as cement additives. This can be implemented in the soil for stabilization.

Addition of these wastes in stabilization technique makes proper utilization of these wastes and solves the problem of disposal. Steel slag is a by-product produced during the conversion of iron ore or scrap iron to steel.

Numerous studies have been conducted by various researchers for the use of steel slag to improve the engineering properties of weak soils .

The use of steel slag has been established in a number of applications in the construction industry. Slag can be applied as a material in cement, as road base course material due to large bearing capacity and excellent in wear resistance [5] as aggregate material for the asphalt concrete mixture [6] as fine and coarse aggregates in cement concrete mixture [7] and as improvement weak soil due to high angle of internal friction and high particle density.

Osinubi, et al. [8] studied the effect of using Blast Furnace Slag (BFS) to stabilize a lateritic soil to be used as hydraulic barrier. It was observed that inclusion of BFS increased the CBR value to 10% of the soil treated with 9% BFS and it became suitable for the use as hydraulic barrier.

Oormila and Preethi [9] examined the properties of black cotton soil stabilized using fly ash (FA) and Ground Granulated Blast Furnace Slag (GGBFS).Different percentages of FA and GGBFS were added. They found that the stabilizers have significantly improved the index properties of the soil and to achieve the maximum CBR value, the soil was blended with 20% GGBFS.

Golakiya and Savani [10] investigated the effect of Electric Arc Furnace Dust (EAFD) and Dolime fine addition on black cotton soil to improve geotechnical properties. Electric arc furnace dust generated during steel production and considered as hazardous waste. Dolomite stone is a type of lime stone and additive for slag formation. During the crushing process of Dolomite stone, fine particle is generated known as Dolime fine and regarded as industrial waste. They found that addition of 30% EAF dust and 12% Dolime to the black cotton soil had shown a good result.

Akinwumi [11] who studied soil improvement using electric arc furnace (EAF) steel slag. Various percentages of pulverized steel slag were applied to the soil. It was observed that pulverized steel slag improved the plasticity, uncured strength and drainage characteristics of the soil at the optimum percent of slag 6%.

Biradar, et al. [12] investigated the effect of using Fly ash and Steel slag to stabilize clay soils. Fly ash and Steel slag were mixed at different percentages 0, 10, 20, 30, 40 and 50% by weight of the soil to obtain the optimum percentage of admixture required. The study results showed that addition of steel slag and fly ash decreased the consistency limits and increased the CBR value of the soil.

1.1 Objective

The objective of the study is to improve the proctor compaction test properties of the soil, through the addition of steel slag and lime as stabilizers to become able to withstand the loads located

2 Experimental Work

Proctor compaction tests are conducted using equipment and procedures. The soil is brought to a desired moisture content and compacted in layers in the selected mold. After compaction, the moist unit weight and moisture content are determined and the dry unit weight calculated. These procedures are repeated at a sufficient number of moisture contents to establish a relationship between dry unit weight and moisture content at compaction. This data, when plotted, represents a curvilinear relationship known as the compaction curve or moisture-density curve. The values of maximum laboratory dry unit weight (Ɣd-max) and optimum moisture content are determined from the compaction curve.

2.1 Materials

2.1.1 Water

Tap water was used for mixing and increase moisture content.

ISBN: 978-81-936820-6-7
Proceedings DOI: 10.21467/proceedings.4

Series: AIJR Proceedings

2.1.2 Soil

Soil was collected from Sirte and used in this research. The soil was stored in dry place and passed through U.S. sieves and the results of sieve analysis (D 6913) test are shown in Figure 1.

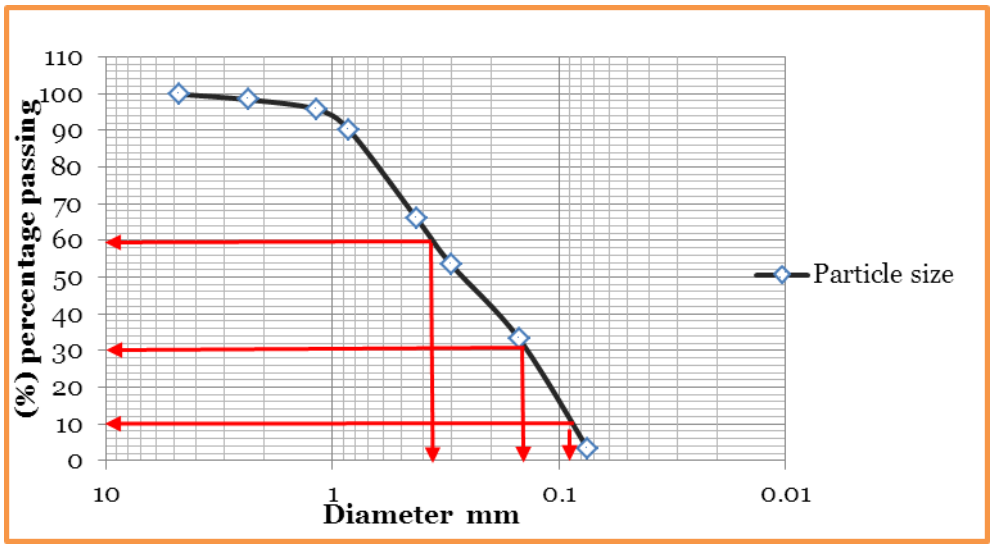

Figure 1: Particle Size Distribution of Tested Soil

According to the sieve analysis results and Unified Soil Classification System soil experimented in this work is classified as granular materials , and the type of soil is **SP** : sand poorly graded.

2.1.3 Steel Slag – Blast Furnace Slag (GGBS) :-

Steel slag was collected from Libyan iron and steel company (Misurata) and used in this research. Six ratio 5, 10, 15, 20, 25 and 30%, by weight of the soil used. The steel slag samples were crushed to reduce its particle size down to less than 0.425 mm.

2.1.4 Lime

Commercially available lime which was used in this study, passed through sieve No 200 and mixed with soil in varying percentages 5, 10, 15, 20, 25 and 30%.

2.2 Sample Preparation

To prepare sand soil . it was first oven –dried at 105ºC approximately 24 hours. Then , it was taken out of the oven and compacted. After that, 5000 gm of these soil were taken and mixed with lime, steel slag in varying percentage 5, 10, 15, 20, 25 and 30%. The lime and steel slag were passed through sieve No 200 before to be mixed with soil.

3 Results and Discussion

3.1 Compaction Test on Non-Treated Soil

Figure 2 shows the results of standard proctor test on the natural soil , which shows a typically shaped curve with a single peak, with maximum dry density of 1.95 g/cm^3 at optimum moisture content of 11%.

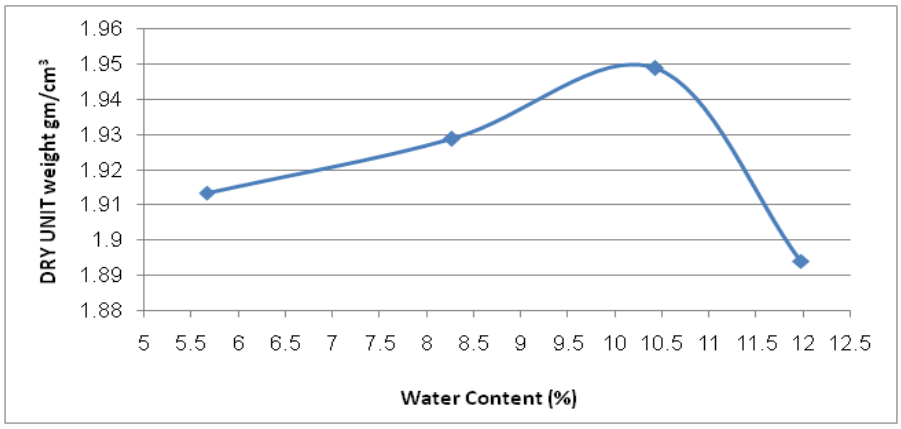

Figure 2: Standard Proctor Test Results on Natural Soil

3.2 Standard Proctor Test on GGBS Treated Soil

In order to investigate the effect of addition of steel slag on optimum water content and maximum dry unit weight of the selected soils, a series of standard proctor tests on GGBS treated soils 5, 10, 15, 20, 25 and 30% GGBS content by weight of selected soil were conducted according to ASTM D(698). Selected soil was dried in a oven and mixed until uniform color was observed before compaction. Figure 3 shows the effect of replacing GGBS on the soil with the investigated percentages, which shows that at the beginning of GGBS replacement, the maximum dry unit weight increased gradually. The highest value of dry unit weight was obtained at GGBS content equal 25%. On the contrary, increasing the GGBS content more than 25% (GGBS>25%) decreased the maximum dry unit weight of stabilized soil.

It is clear also from the figure that the optimum water content varied with GGBS content. The optimum water content fluctuated with the increase of GGBS content. This can be attributed to the change of surface area of treated soil than that in natural sandy soil.

3.3 Standard Proctor Test on Lime Treated Soil

Figure 4 shows the effect of adding Lime on compaction characteristics of the tested soil samples. it is clear that the effect of replacing five different percentage of lime to soil had nearly similar results, However, the replacement of lime to sandy soil was important to develop the behavior of stabilized soil. It also shows that at the beginning of replacing lime the maximum dry unit weight is almost stay the same, then the maximum dry unit weight was achieved at lime content equal 15% dry unit weight of stabilized soil then decreased by replacing more lime.

ISBN: 978-81-936820-6-7
Proceedings DOI: 10.21467/proceedings.4

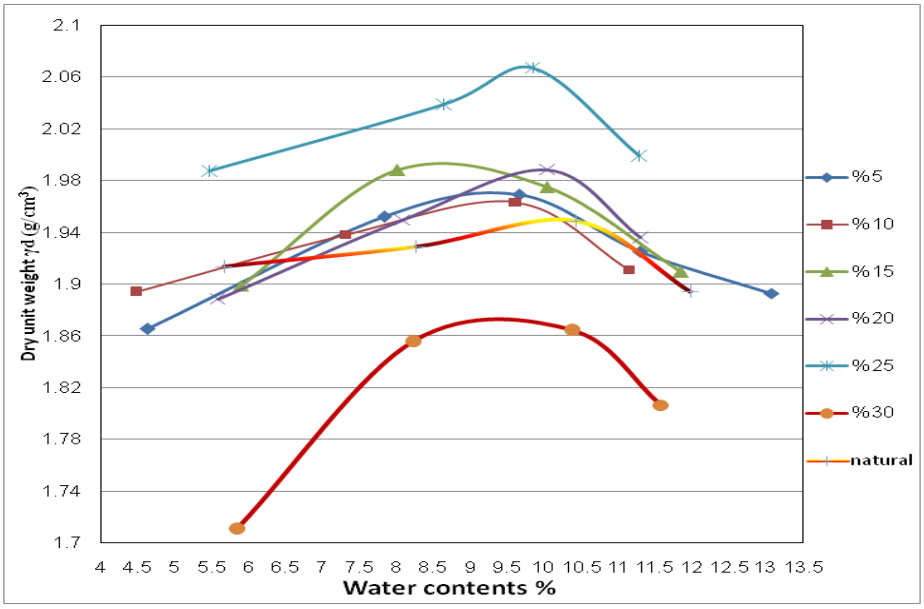

Figure 3: Standard Proctor Test Results on Soil With Various GGBS Content

It is also from the below result that the optimum water content varied with lime content. The optimum water content fluctuated with increasing of lime content. Figure 5 shows that the values of the max dry unit weight of soil increase with the increase of the both additives (GGBS and lime) and the highest values of dry unit weight (γdmax) is obtained at GGBS content equal to 25% and 15%for lime. Furthermore the replacement of GGBS has a marked effect on the increase of max dry unit weight of soil comparing with the replacement of lime at the different tested percentages.

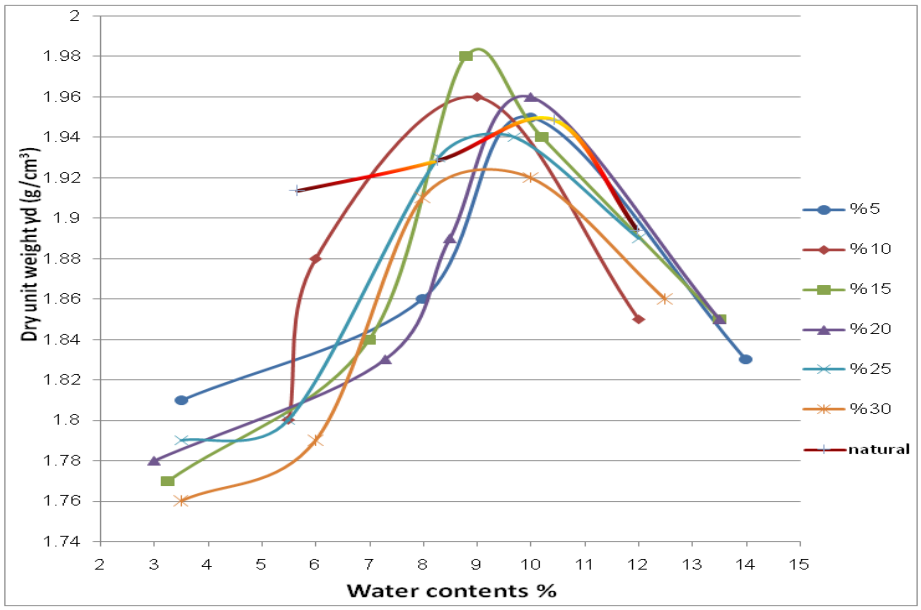

Figure 4: Standard Proctor Test Results on Soil With Various Lime Contents

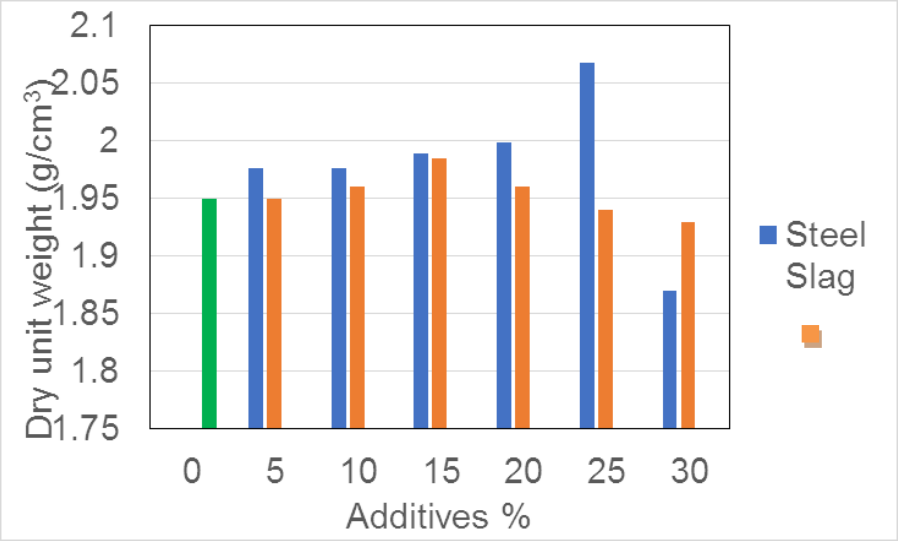

Figure 5: Comparison Between The Effect of Percentage of Additives on Maximum Dry Unit Weight

From Figure 6 it is obvious that the highest value of the optimum moisture content is obtained at natural soil , and the lowest at GGBS ratio (15%).

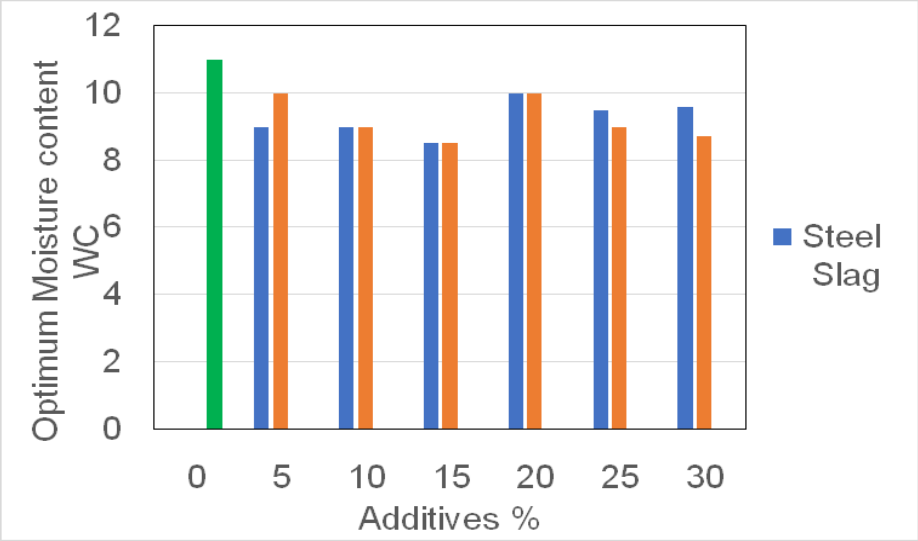

Figure 6: Comparison between the effect of percentage of additives on optimum moisture content

4 Conclusions

An extensive laboratory testing program was carried out to investigate the effect of addition of the steel slag and lime on the compaction characteristics of a sandy soil. The obtained results from both additives and were compared the following conclusions are made. The replacement of steel slag to sandy soil has a marked effect on the behavior of compaction of stabilized soil. The maximum dry unit weight increased gradually at the beginning of replacement of steel slag and the maximum dry unit weight increased by about 4.655% when

ISBN: 978-81-936820-6-7
Proceedings DOI: 10.21467/proceedings.4

the steel slag content increased from 5% to 25%. Increasing the steel slag content more than 25% (GGBS>25%) decreased the maximum dry unit weight, where steel slag content equal to 30% the maximum dry unit weight of treated soil decreased significantly by about 9.57% than that at 25%. The optimum water content varied with steel slag content. the optimum water content fluctuated with the increase of steel content. The comparison between the effect of both replacement shows that steel slag is more effective than lime on the improvement of the max dry unit of the soil, while the effect of the both replacement on the OMC is almost the same at different used percentages. In addition of that steel slag has advantage of its low cost and easy availability in large quantities.

Acknowledgment

First and foremost, we thank Allah. This paper based on undergraduate project during the Academic year 2017/2018 done by the students, Abdelkader Hatim Abdelkader, Awad Zhran Awad and Abdalslam Musbah Alsdaiunder under the supervision of MSc. Ayad Abdelmoula Mohammed. The authors are gratefully and sincerely thank the students for their hard work on the experimental and theoretical parts of the project. Special thanks are due to Mr. Suliman Ahmed the technicians in the Soil Mechanics lab for his assistance with the laboratory work.

References

[1] Altun A, Yilmaz I, Study on steel furnace slags with high MgO as additive in Portland cement, Cement and Concrete Research, 32(8), (2002), 1247–1249, DOI 10.1016/S0008-8846(02)00763-9.

[2] Motz H, Geiseler J, Products of steel slags an opportunity to save natural resources, Waste Management, 21(3), (2001), 285–293, DOI 10.1016/S0956- 053X(00)00102-1.

[3] Yildirim IZ, Prezzi M, Chemical, Mineralogical, and Morphological Properties of Steel Slag, Advances in Civil Engineering, 2011(2011), (2011), 1–13, DOI 10.1155/2011/463638.

[4] Akinwumi II, Adeyeri JB, Ejohwomu OA, Ee cts of Steel Slag Addition on the Plasticity, Strength, and Permeability of Lateritic Soil, International Conference of Sustainable Design, Engineering and Construction 2012, In: Chong WKO, Gong J, Chang J, Siddiqui MK (eds.), ICSDEC 2012, ICSDEC Conference Proceedings, American Society of Civil Engineers; Texas, United States, 2013, pp. 457–464, DOI 10.1061/9780784412688.055.

[5] K. Horii, T. Kato, K. Sugahara, N. Tsutsumi, and Y. Kitano, "Overview of iron and steel slag application and development of new utilization technologies," Nippon Steel and Sumitomo Metal Technical Report No. 1092015.

[6] J. Emery, "Steel slag utilization in asphalt mixes. National Slag Association, MF 186-1." Retrieved from www.nationalslagassoc.org, 1984.

[7] G. Singh, S. Sangwan, and M. Usman, "Experimental study of blast furnace slag concrete," International Journal of Engineering Sciences and Research Technology Experimental, vol. 9655, pp. 475–480, 2015.

[8] K. J. Osinubi, A. O. Eberemu, and A. A. Amadi, "Compacted lateritic soil treated with blast furnace slag as hydraulic barriers in waste containment systems," International Journal of Risk Assessment and Management, vol. 13, pp. 171-189, 2009. View at Google Scholar | View at Publisher

[9] R. Oormila and T. V. Preethi, "Effect of stabilization using fly ash and GGBS in soil characteristics," International Journal of Engineering Trends and Technology, vol.11,pp.284-289,2014.

[10] H. D. Golakiya and C. D. Savani, "Studies on geotechnical properties of black cotton soil stabilized with furnace dust and dolomitic lime," International Research Journal of Engineering and Technology, vol. 2, pp. 810-823, 2015.

[11] I. Akinwumi, "Soil modification by the application of steel slag," Rperiodica Polytechnica Civil Engineering, vol. 58, pp. 371–377, 2014. View at Google Scholar | View at Publisher.

[12] K. B. Biradar, U. Arun, and P. V. V. Satyanarayana, "Influence of steel slag and fly ash on strength properties of clayey soil : A comparative study," International Journal of Engineering Trends and Technology, vol. 14, pp. 61–64, 2014. View at Google Scholar | View at Publisher.

Analysis of the Failure of Cylindrical Pressure Vessels

Osama A. Terfas*, Arwa M. Elambrouk, Ahlam Y. Elraqiq

Department of marine and offshore engineering, University of Tripoli, Libya

DOI: https://doi.org/10.21467/proceedings.4.24
* Corresponding author email: o.terfas@uot.edu.ly

ABSTRACT

This study investigates the failure of cylindrical pressure vessels and examines their integrity in the presence of cracks using von-Mises (Distortion Energy) yielding criterion and fracture mechanics methodology. The design Code of ASME-VIII section-2 was used to determine safe thickness and maximum allowable working pressure. The fracture stress, the critical stress intensity factor, the critical crack length and maximum pressure were determined. The results showed that yielding criterion with factor of safety of "2" for materials proposed in this study are applicable to design and construct pressure vessels under considered internal pressure and vessel size. The study revealed that cracked pressure vessels can be fit for service under some conditions of crack size and internal pressure. It can be concluded that pressure vessels that are safe under yielding theories could be safe as well where the crack exists under restricted conditions of the applied internal pressure, shell thickness, and material property.

KEYWORDS: Fracture mechanics, pressure vessels, structural integrity, yielding criterion.

1 Introduction

The continued and prolonged use of pressure vessels for power plants, nuclear reactor vessels, storage vessels for liquefied gases such as LPG or chemical reactions, industrial processing, and oil refineries storage tanks requires them to withstand severe conditions of pressure, temperature, and other environments. Such environmental conditions include corrosion, neutron irradiation, and hydrogen embrittlement. Pressure vessels are required to operate at a temperature as high as 600 C to as low as -20C, with design pressures as low as 0.1MPa to as high as 15MPa [1]. To ensure safe design, installation, operation, and maintenance, the pressure vessels must be in accordance with codes such as American Society of Mechanical Engineers (ASME) Boiler and Pressure Vessel code. Therefore, great emphasis should be placed on analytical and experimental methods for determining their operating stresses [2]. When the pressure vessel is exposed to internal pressure, the material comprising the vessel is subjected to stresses acting in all directions. The normal stresses resulting from this pressure are functions of the radius and the shape of the pressure vessel, open ended cylinder, closed end cylinder as well as the applied pressure [3].

Furthermore it also needs to understand the significance of these stresses on the structural integrity of the pressure vessel by considering the material properties of the vessel [4]. In this

 ISBN: 978-81-936820-6-7

context a major achievement in the theoretical foundation of the linear fracture mechanics was the introduction of the stress intensity factor (SIF) as a parameter for the intensity of stresses close to the crack tip. The stress intensity factor (K_a) is compared with the critical stress intensity factor K_{IC} (material fracture toughness) to determine whether or not the crack will propagate. This fracture parameter depends on size, shape and location of the defect; the applied load and geometry of the structure [5]. The presence of cracks on the walls of a pressure vessel can severely reduce the strength of the vessel and can cause sudden failure at nominal tensile stresses less than the material's yield strength [6]. Therefore, to ensure the integrity of a structure when a crack is present, the designer should understand and adequately apply the mechanics of fracture, particularly the relation between applied stress, the flaw size and the fracture toughness.

For the purpose of developing the design philosophy and the related operational limitations of various approaches, the yielding strength of the vessel is used as the criterion of failure [7]. In this context, failure theories of Von-Mises, Tresca, and maximum principle stress in conjunction with software and finite element method are widely adopted to design pressure vessels [8]. In addition, the numerical analysis of thin walled pressure vessel design parameters, material properties and temperature are found effective tools, and the maximum stress criteria is in good agreement with Von-Mises criteria for the failure of pressure vessels [9]. The analysis method applied in this work is the thin-walled pressure vessels theory for a ratio of inner radius to wall thickness $r/t>10$.

2 Materials

The materials selected for pressure vessels for the present work are shown in Table 1[10-11].

Table 1. *Mechanical properties and chemical composition of materials used.*

Material	σ_{uts} MPa	σ_y MPa	C %	Cr %	Ni %	Cu %	Mn %	Mo %	Si %
SS 316L	482	172	0.03	16	14	-	2	2.5	0.75
A 283-GR.C	455	207	0.24	-	-	0.2	0.9	-	0.4
SS 304N	551	241	0.03	18	8	-	2	-	0.75
A106-GR.C	485	276	0.30	0.4	0.4	0.4	0.67	0.15	0.1

3 Pressure Vessel Design Procedure

3.1 Stresses Developed in Thin-Walled Pressure Vessels

Thin-walled pressure vessels provide an application of the analysis of plane stress condition. The stresses developed due to the hydrostatic pressure are longitudinal stress (axial) σ_L and hoop stress σ_h in the circumference direction. The analysis of stresses in thin-walled pressure vessels will be limited to cylindrical pressure vessels as these are used widely and easy to

manufacture in contrast to spherical vessels. For a cylindrical pressure vessel shown in Figure 1 with length "L", radius "r" and thickness "t", the stress σ_L in the axial direction of a cylindrical vessel with closed ends is[12]:

$$\sigma_L = \frac{p.r}{2.t} \quad (1)$$

The hoop stress σ_H, acts in the vessel wall in the circumferential direction can be written as:

$$\sigma_H = \frac{p.r}{t} \quad (2)$$

Note that the hoop stress is twice the axial stress.

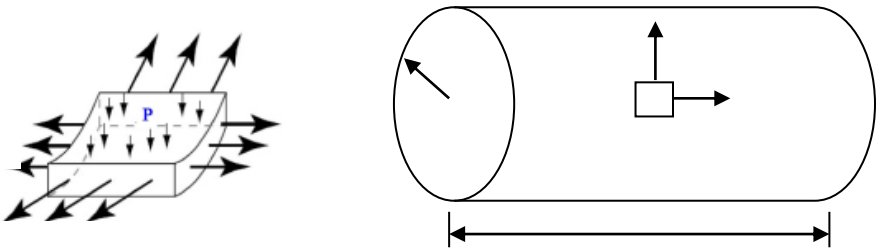

Figure 1: *Longitudinal and hoop stresses in a cylindrical closed-end vessel.*

3.2 Code Selection

There are many engineering standards which give information on the design. It is emphasized that any standard selected for manufacture of the pressure vessels must be followed and complied with in entirety and the design must not be based on provisions from different standards [13]. The ASME is normally followed cross the world, but other national or international standards may also be used. For this design, ASME VIII (division 2) "Construction of Pressure vessel Codes" are selected.

3.3 Implementation of ASME Code (section VIII-division 2)

The minimum thickness or maximum allowable working pressure of cylindrical shells shall be the greater thickness or lesser pressure as given by (3) or (4).

Circumferential Stress (Longitudinal joints)

When the thickness does not exceed one-half of the inside radius, or P does not exceed 0.385SE, the following formulas shall apply [14]:

$$t = \frac{PR}{SE-0.6P} \quad \text{or} \quad P = \frac{SEt}{R+0.6t} \quad (3)$$

ISBN: 978-81-936820-6-7
Proceedings DOI: 10.21467/proceedings.4

Series: AIJR Proceedings

Where R is the inside radius, t is the shell thickness, E is the welded joint efficiency, S is the material strength, P is internal pressure.

Longitudinal Stress (Circumferential joints)

When the thickness does not exceed one-half of the inside radius, or P does not exceed 1.25SE, the following formulas shall apply[14]:

$$t = \frac{PR}{2SE+0.4P} \quad \text{or} \quad P = \frac{2SEt}{R-0.4t} \tag{4}$$

4 Failure Assessment Analysis

4.1 Yielding Criterion

Yielding criterion of Von-Mises is applied in order to assess the integrity of the pressure vessels considered in this study. In von-Mises theory of failure, the yielding occurs when the von-Mises stress σ_v is equal to the yielding stress [15]:

$$\sigma_v = \sqrt{\sigma_1{}^2 - \sigma_1.\sigma_2 + \sigma_2{}^2} = \sigma_y \tag{5}$$

Where, $\sigma_1=\sigma_H$ is hoop stress, and $\sigma_2=\sigma_L$ is longitudinal stress, and σ_y is yielding strength.

4.2 Fracture Mechanics Criterion

The cracked cylindrical pressure vessel subjected to a longitudinal crack considered for the present work is shown in Figure 2.

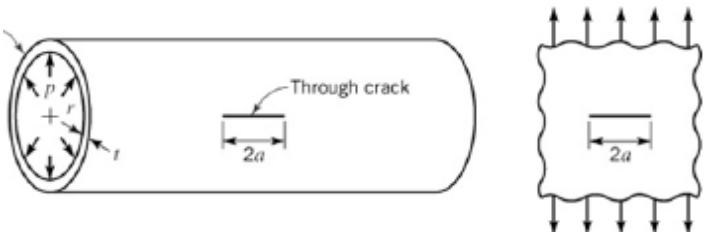

Figure 2: *A cylindrical pressure vessel with a longitudinal crack.*

The corresponding fracture stress σ_f (MPa) required propagating the crack is [16]:

$$\sigma f = \frac{K_{Ic}}{\sqrt{\pi.a_c}} \tag{6}$$

Where, K_{Ic} (MPa.√m) is the material fracture toughness, and "a" is the crack length. This can also be re-written in terms of the applied stress intensity factor (K_a), and the crack propagates when:

$$K_a = \frac{p.r}{t}.\sqrt{\pi.a} \geq K_{Ic} \qquad (7)$$

4.3 Software Developed

A computer program has been constructed and used to assess the integrity of cracked and uncracked pressure vessels. The program is based on the von-Mises theory and fracture mechanics method by considering the von-Mises stress, yielding strength, critical fracture toughness and critical crack depths. Figure 3 shows the front window of the program where the input data are: crack depth (a), internal pressure (p), shell thickness (t), vessel radius (r), and (K_{Ic}). The output results are the von-Mises stress (σ_v) which is compared with the yielding strength, and fracture stress (σ_f) as a function of the fracture toughness and crack depth, and applied stress intensity factor (K_a).

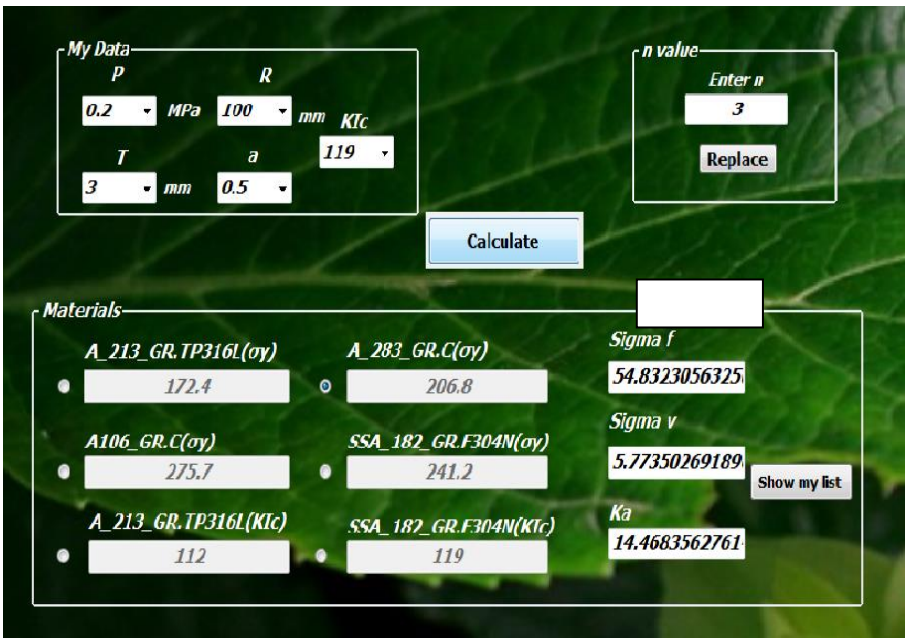

Figure 3: *A view for the input and output data of the program.*

5 Results and Discussion

Figure 4 shows the von-Mises stress (σ_v) as a function of vessel diameter for different shell thicknesses. The figure shows very conservative results with factor of safety greater than one ($\sigma_y > \sigma_v$). It is shown that the yielding does not occur for all materials considered in this study for vessels diameters of 200 to 1000 for shell thickness 3mm to 20mm under designed pressure varies between (14.5psi-130.5psi) 100 to 900KPa.

ISBN: 978-81-936820-6-7
Proceedings DOI: 10.21467/proceedings.4

Series: AIJR Proceedings

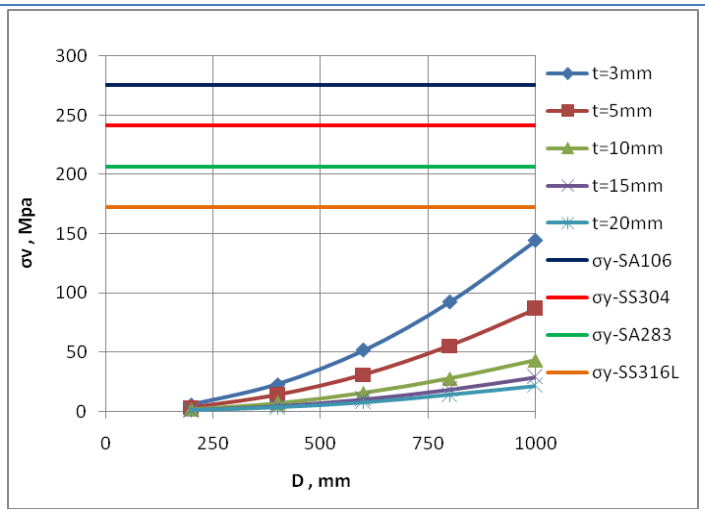

Figure 4: *The von-Mises stress (σ_v) as a function of vessel diameter and thickness.*

Figure 5 shows pressure vessels yield criterion using factor of safety of 2. For shell thickness of 5mm or greater, all used materials are safe for diameters from 200mm to 1000mm, while vessels with shell thickness of 3 mm are safe as long as the diameter less than 800mm.

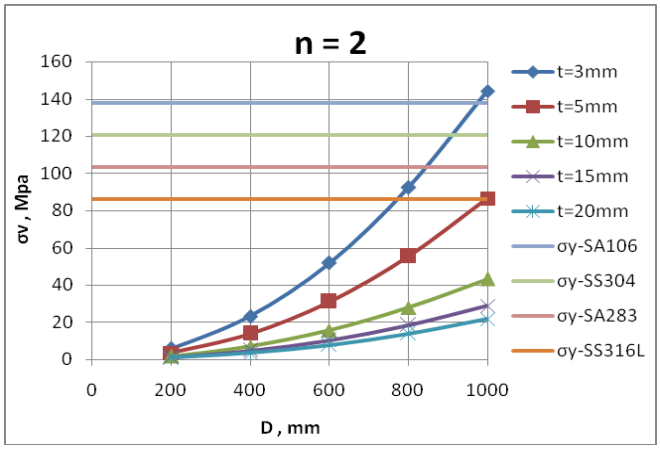

Figure 5: *Pressure vessels yield criterion using factor of safety of 2.*

Figure 6 shows the assessment of the pressure vessel in terms of applied stress intensity factor (K_a) and the material fracture toughness (K_{Ic}) of SS A-F304N with material strength of 241.2MPa and fracture toughness of K_{Ic}=119MPa.√m, for a crack length (a = 0.5 t). It is shown that thin pressure vessels with 3 and 5 mm thickness can be run safely under a considered pressure of (1 to 9 bar) for vessel diameters less than 600mm for a crack depth less than 0.5t. For thicker vessels, bigger vessels can be made from this type of material.

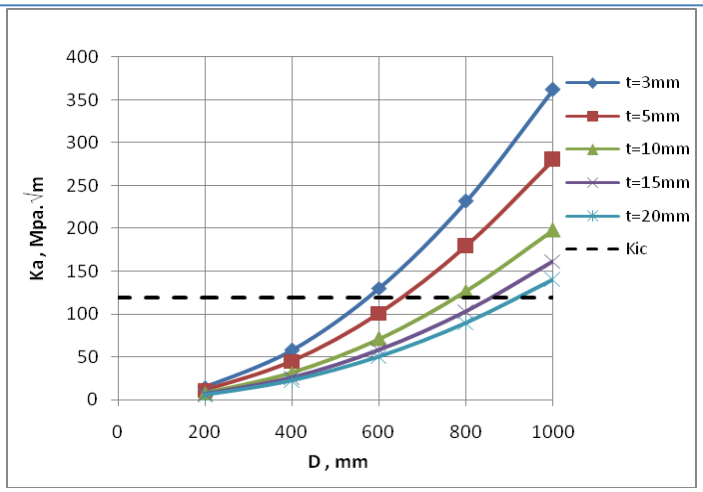

Figure 6: *The applied stress intensity factor as a function of vessel diameter for a=0.5t.*

Figure 7 shows the assessment of the cracked pressure vessel made of SS F304N of material strength of 241.2MPa and k_{Ic}=119MPa.√m, based on a crack depth (a=0.2t). The assessment is considered safe when values of the applied stress intensity factor (K_a) are less than the fracture toughness of the material (k_{Ic}). Therefore, vessels with diameters ranges from 200mm to 1000mm are safe as long as their thickness is greater than 10mm. However, thinner vessels having 3 and 5 mm thickness can be operated safely under a pressure considered for vessel diameters less than 720mm for a crack depth less than 0.2t.

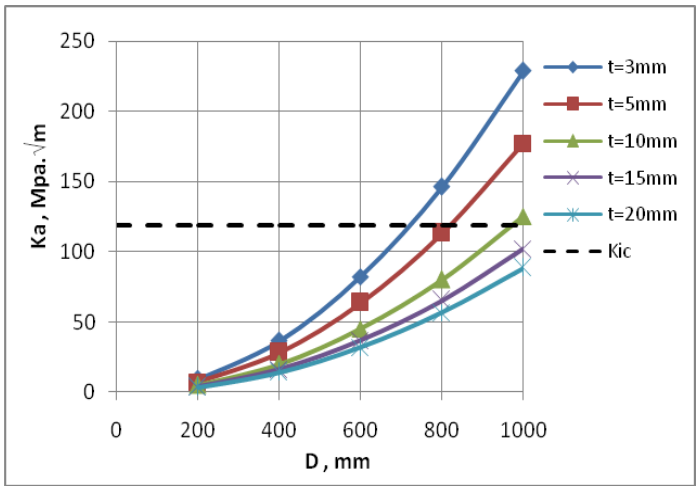

Figure 7: *Applied stress intensity factor as a function of vessel diameter for a=0.2t.*

Figure 8 shows the applied stress intensity factor for cracked pressure vessels of (a = 0.5 t), made of SS316L of k_{Ic}=112 MPa.√m. It is shown that cracked vessels are safe as long as the crack depth is less than 0.5t for specific vessel diameter and thickness. For example, cracked vessels with diameters of 600mm are safe with thickness greater than 5mm.

ISBN: 978-81-936820-6-7
Proceedings DOI: 10.21467/proceedings.4

Series: AIJR Proceedings

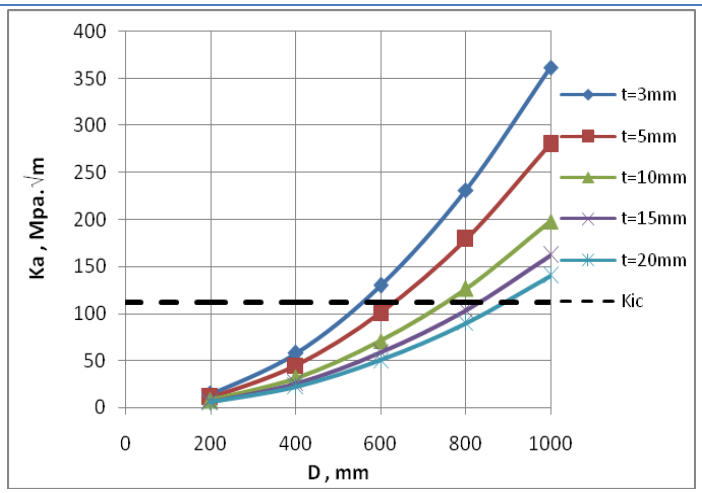

Figure 8: *Applied stress intensity factor as a function of vessel diameter for a=0.5t.*

Figure 9 shows the applied stress intensity factor for cracked pressure vessels of (a=0.2t), made of SS316L with K_{Ic}=112MPa.√m. It is obvious that the majority of K_a values are below the horizontal line of K_{Ic} which means these vessel sizes are safe except for thin vessels (t=3, 5mm) with large vessel diameter (D=700, 1000mm).

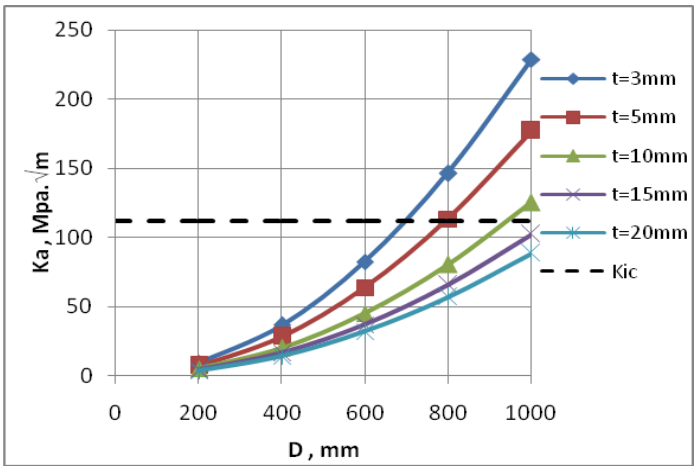

Figure 9: *Applied stress intensity factor as a function of vessel diameter for a=0.2t.*

Figure 10 shows the fracture stress as a function of crack length. This figure is used in conjunction with Figures 11 and 12 to determine the fracture stress required to propagate the crack, critical crack length and maximum pressure. The SS304 steel vessel having diameter of 1000mm, shell thickness of 15mm and 20mm is safe under maximum pressure of 9bar when the crack length is less than 6mm. For vessels of 10mm thickness, the largest acceptable crack length is 3mm. However, vessels with shell thickness of 5mm are not safe under a pressure of 9bar, unless the pressure is reduced below 5bar for (a<2mm). For vessel diameters of 500, the shell thickness of 5mm is safe as long as the crack length is less than 3mm at the maximum pressure used.

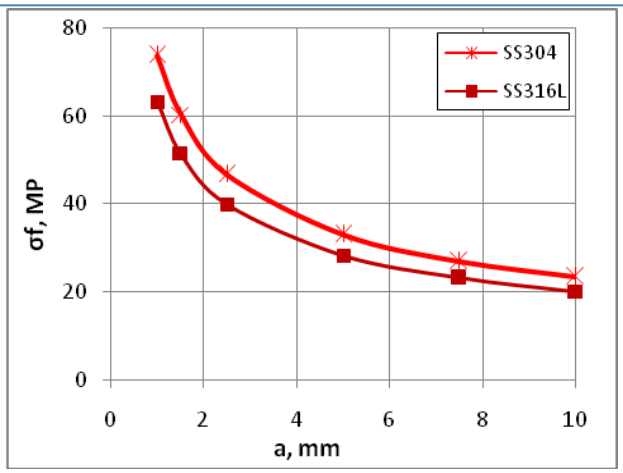

Figure 10: *Fracture stress as a function of crack length for steel used.*

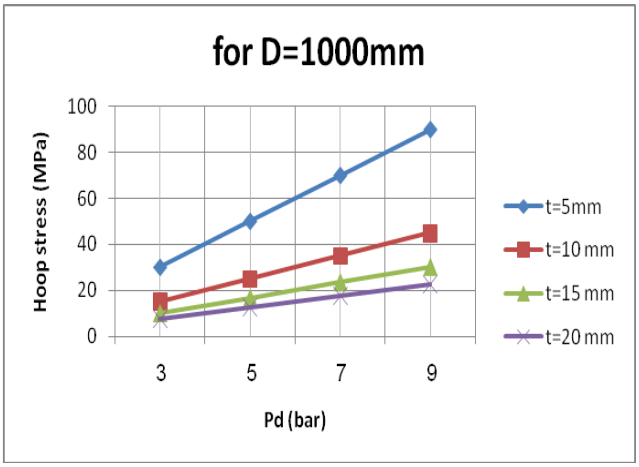

Figure 11: *Hoop stress as a function in design pressure for vessel diameter of 1000mm.*

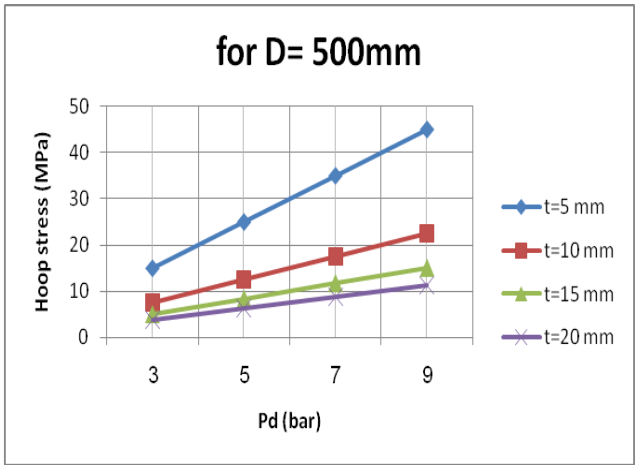

Figure 12: *Hoop stress as a function in design pressure for vessel diameter of 500mm.*

ISBN: 978-81-936820-6-7
Proceedings DOI: 10.21467/proceedings.4

Series: AIJR Proceedings

For SS316L, a vessel with diameter of 1000mm and the shell thickness of 5mm is safe if pressure reduced below 6bar and the crack length is less than 1.5mm. For 10mm thickness the largest acceptable crack length is 2mm under pressure of 9bar. However, for pressure less than 6bar cracked pressure vessels with diameter of 1000mm and shell thickness of 15mm and 20mm are safe as long as crack length is shorter than 7.5mm and 10mm respectively. For vessel diameters of 500 with shell thickness of 5mm is safe as long as the crack length is less than 2mm at the maximum pressure. While for 10mm thickness the vessel is safe as long as the crack length is less than 5mm.

6 Conclusions

This research investigated the effects of design parameters in terms of material strength and internal pressure on the integrity of pressure vessels. Both yielding criterion of von-Mises, and fracture stress theory were used to assess the integrity of pressure vessels. The von-Mises stress (σ_v) method showed that all materials used in this study are safe for dimensions and thicknesses considered and ensures factor of safety greater than one. However, for factor of safety of 2 only a very thin vessel with t=3mm and D>800mm is subjected to yielding. In the presence of a crack with the length of (0.2t) vessels with diameters greater than 700mm associated with thickness less than 10mm become unsafe. However, vessels with diameters ranges from 200mm to 1000mm with thickness of 15mm and 20mm are safe under considered conditions.

References

[1] Somnath Chattopadhyay, Pressure Vessels: Design and Practice, CRC press, 2005.
[2] Ahmed Ibrahim, Yeong Ryu, Mir Saidpour, Stress Analysis of Thin Walled Pressure Vessels, Modern Mechanical Engineering, Scintific Research Publishing, V5, 01-09, 2015.
[3] Busuioceanu Paraschiva, Stefanescu Florentinab, Ghencea Adrianc, Study of Stresses and Stress Concentrations in Pressure Vessels, Journal of Bussiness economics and Information Technology, V3, 2016.
[4] Dennis H. Moss, Pressure Vessel Design Manual. 3rd edition, Elsevier, 2004.
[5] Kuna, M. Finite Elements in Fracture Mechanics: Theory - Numerics - Applications (Solid Mechanics and Its Applications, 2013.
[6] S. Kotrechko,Yu. Meshkov, A new approach to estimate irradiation embrittlement of pressure vessel steels, pressure vessel and piping, 2007.
[7] Analysis of a thick and thin walled pressure vessel for different materials. Qayssar S. Masikh, Mohammad Tariq, Prabhat K. Sinha. International Journal of Mechanical Engineering and Technology, V5, 09-19, 2014.
[8] Thin Z. Hlaing, Htay H. Win, Failure Analysis of A Thin-walled CNG Cylindrical Pressure vessel, International Journal of Scientific Engineering and Technology Research, V3, 1874-1879, 2014.
[9] Özmen S. Eruslu, Sencer S. Karabeyodlu, Failure Analysis of thin Walled Pressure Vessels, International Scientific Conference, Gabrovo, 22-24 Nov. 2007.
[10] Carbon Steel Handbook, Electric Power Research Institute (EPRI), Palo Alto, CA: 2007.
[11] Stainless Steel Grade Datasheet, Atlas Steel Technical Department, 2013.
[12] Apurva P., Mahesh G., Nitin D., Rajkumar P., Design and analysis of pressure vessel, International Journal of Innovative Research in Technology & Science(IJIRTS), V2, 28-34, 2013.
[13] B.S.Thakkar, S.A.Thakkar, Design of pressure vessel using ASME code Section VIII, Division-1, International Journal of Advanced Engineering Research and Studies, 2012.
[14] ASME-VIII Code, Division 2, Boiler and Pressure Vessel, Alternative Rules for Construction Pressure Vessels, 2010.
[15] Hibbeler, C., Mechanics of materials, 8th edition, prentice hall (pearson), 2011.
[16] Anderson, T. L. Fracture Mechanics: Fundamentals and Applications, Third Edition. CRC Press, 2012.

Influence of Surface Roughness on Adhesion Between the Existing and New Plain Concretes

Nurdeen Mohamed Altwair [1*], Saad Jaber Abu Jarir [2]

Civil Engineering Department, College of Engineering, Elmergib University, Libya

DOI: https://doi.org/10.21467/proceedings.4.25

* Corresponding author email: nmaltwair@elmergib.edu.ly

ABSTRACT

The bonding that exists between the old concrete and the new concrete depends largely on the quality of substrate surface preparation. The accurate representation of substrate surface roughness can help determine very precisely the correct bonding behavior. In this work, the experimental program aimed to investigate the bond strength between two plain concretes, the first one is a concrete substrate as existing concrete, the second one is a new concrete overlay. Four types of original concrete substrate surface preparation were used: as-cast (without surface preparation) as a reference, wire-brushed, grooves and drilled holes. Adhesion strength is quantified at 30 days based on the results of the slant shear test and splitting cylinder tensile test, as well as shrinkage test which was made after 56 days of casting the new overlay concrete. The results generally indicate that the surface roughness of the concrete substrate is very much required to obtain superior mechanical bond of the composites; whereby the concrete with grooves and drilled holes substrate providing the most superior mechanical bond.

Keywords: Bond strength; New concrete overlay; Original concrete substrate; Slant shear test; Splitting tensile test; Surface roughness; Shrinkage.

1 Introduction

Developed infrastructure is a vital factor of economic growth and the prosperity of human life in many countries around the world. Many structures which make up the entire infrastructure and especially those made of reinforced concrete, such as buildings, bridges and pavements, etc. be suffered from severe deterioration. In the structural elements, these problems lead to cracks and breakdown in the concrete elements due to aggressive environmental impact such as exposing to different types of salts, freeze-thaw cycles and increase in unexpected live loads, etc. [1].

Nowadays, the most important and main challenges facing civil engineers are saving and rehabilitation of degraded constructions, as well as, developing and enhancing the durability and efficiency of these constructions. Furthermore, rehabilitation and repairing methods of the concrete are beneficial to the owner as compared to rebuilding [2]. The idea of rehabilitating and strengthening of the concrete structures is to apply a new concrete layer over an existing concrete to increase the resistance of the structural component and thereby

 ISBN: 978-81-936820-6-7

increase the durability over time [3]. The linkage between the existing and new concrete layers is often weak [3,4]. Bonding quality of these layers is the main successful objective of the restructuring process being repaired. Furthermore, the successful development and performance of the structure directly depend on the roughness of the surfaces [5,6].

It has been recently observed that a numerous number of concrete structures existing in some regions around the world which had been repaired are still facing the risks of collapse and failure. It has been observed that the main reasons for this failure are the chemical bonding and interaction between the two layers materials. In addition, the physical and mechanical bonding depends on the porosity and roughness of the surfaces, as well as the shear and tensile strengths between two surfaces [7]. The problem of study lies in the inefficiency of bonding between the existing and new concrete layers at the maintenance of concrete structures, as a result of the surrounding environmental conditions, such as the difference in temperature as well as excessive loads. For this reason, many researchers interested in the repair of concrete structures have conducted several experiments to bond the existing and new concrete layers. The results were varied due to the difference in the use of bonding material, the method of bonding the existing concrete, the smoothness of the surface to be repaired, environmental effects and differences of expansion and shrinkage between both concretes. Therefore, the study will seek to increase the bond between the existing and new concrete when changing the roughness of existing concrete. Thus, reducing the use of chemical additives which are used to improve adhesion between existing and new concrete, especially since the use of such materials are considered a high cost. In addition, identifying the best mechanical methods that improve adhesion, will reduce the cost of repair, strengthening the structural elements and extending the age of the concrete members.

2 Materials and Methods

2.1 Materials

Ordinary Portland cement (OPC) that complies with the requirements of BS EN 197-1:2011 was used. The physical properties and chemical compositions of OPC is provided in Table 1.

Table 1. *Chemical compositions and physical properties OPC.*

Chemical composition (mass %)		Physical properties	
Items	Value	Items	Value
Silicon dioxide (SiO_2)	20.14	Specific gravity	3.15
Aluminum oxide (Al_2O_3)	5.91	Specific surface area(m^2/g)	2977
Ferric Oxide (Fe_2O_3)	2.99	Strength activity index at 3 days (MPa)	26
Calcium oxide (CaO)	62.9	Strength activity index at 28 days MPa	44
Magnesium Oxide (MgO)	1.59		
Sodium oxide (Na_2O)	0.18		
Potassium oxide (K_2O)	0.88		
Sulfur oxide (SO_3)	2.11		
Phosphorus oxide (P_2O_2)	0.9		
LOI	0.4		

Coarse aggregate of different maximum size viz; 19 mm, 14 mm was obtained from the quarries of Al-Alus in Al-Kums area. The coarse aggregate has a specific gravity of 2.72, water absorption of 0.41 % and bulk density of 1530 kg/m^3. Natural sand with maximum size of 1.2 mm, used as a fine aggregate was collected from Zlitan area. The fine sand has a fineness modulus of 2.7, specific gravity of 2.66 and water absorption of 0. 85 %.

2.2 Mix Proportion

Each of the composite specimens consists of the same material, i.e existing (concrete substrate) and new concrete overlay were designed as normal concrete. The design method used for normal concrete mixtures is based on absolute volume method, and the target strength of the normal concrete used was approximately 30 MPa. Samples representing the existing and new concrete were prepared using the mix proportions shown in Table 2.

Table 2. *Mix proportions for plain concrete.*

Items	Cement	Water	Fine aggregate	Coarse aggregate
Quantity (kg/m^3)	396	185	425	1344

2.3 Preparation and Processing of Samples

In order to gain proper bond strength the surface must be prepared prior to performing the overlay. In this study, each test specimen consisted of two equal layers of thickness; normal strength concrete (plain concrete substrate) will be used as original substrate material which represents the existing concrete, the other layer is also composed of the same type of concrete (the difference in casting time) which represents the new concrete (plain strength concrete overlay). Original concrete substrate specimens are placed in lubricated half piece of specimen mold. After casting, the fresh specimens were left at room temperature in their molds for 24 hours. After one day, the specimens were demoulded, cleaned from suspended parts of concrete or oil or any particles and dust, and cured for 28 days in a water curing tank. At 28 days of casting and curing in the water, specimens were taken out from the water tank for surface preparation. Four types of concrete substrate surface preparation were used: as-cast (without surface preparation) (CS) as a reference, wire-brushed (WS), grooves (GS), and drilled holes (DS), as shown in Figure 1. After surface preparation, all the concrete substrate specimens were left to dry for 1 month. Thus, the total period applied to the concrete substrate specimens before casting the new concrete as a repair material was 58 days. Before casting the new concrete overlay, the concrete substrate specimens were saturated in the water for one day, followed by 25 minutes of drying. The concrete substrate specimens were then placed into their moulds; in the case of the slant shear and shrinkage samples, the slanting side was facing upward to be overlaid with the new concrete overlay. For the tensile splitting samples, the substrate halves with different surface roughness were placed vertically at one side of the cylindrical moulds, and the moulds were then filled with new concrete (Figure 2). The composite specimens were left at room temperature in their molds for 24 hours. After 24 hours, the specimens were demoulded, and cured in water (for slant shear and tensile splitting

ISBN: 978-81-936820-6-7

Series: AIJR Proceedings
Proceedings DOI: 10.21467/proceedings.4

samples) for 30 days. The specimens for the shrinkage test were left at room temperature until the testing days.

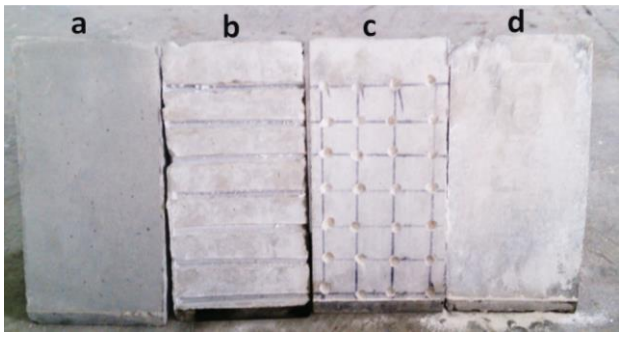

Figure 1: *Different surface roughness of concrete substrate specimens. (a) as-cast (b) grooves (c) drilled holes (d) wire-brushed.*

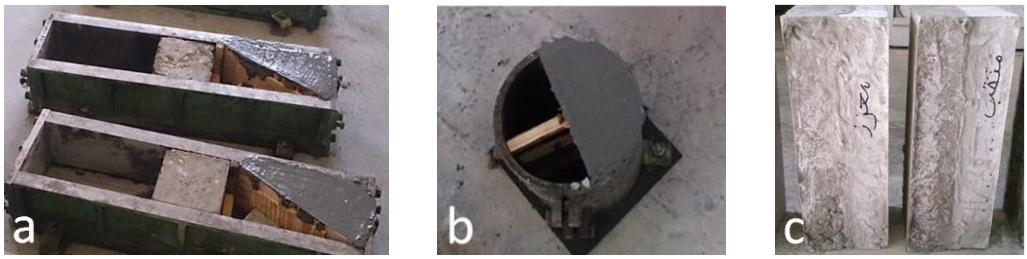

Figure 2: *Specimens preparation. (a) Slant shear test specimen (b) Splitting tensile test specimen (c) shrinkage test specimen.*

2.4 Testing of Specimens

The study of the surface quality is quantified by slant shear test, splitting cylinder tensile test and shrinkage test.

Slant shear test has been selected for being sensitive to roughness. The adopted geometry for the slant shear specimens was a 15 cm x15 cm x 30 cm prism with the interface line of 30° to the vertical (Figure 3). The specimens were tested under compression using the standard procedure for the testing of cubes of compressive strength according to ASTM C 882 standard [8].

The nominal shear strength between the concrete over layer can be calculated as follows.

$$\text{Slant shear strength (MPa)} = \frac{F}{A} \quad (1)$$

Where:

F is the maximum force recorded (in N), and A is the area of the slant surface (in mm^2). The slant surface area can be taken as a nominal value of 150 x 150/sin 30°.

The splitting tensile test was conducted to determine the bond strength between two layers of concrete, according to ASTM C496 [9]. In the present study, new concrete overlay was cast

and bonded with the concrete substrate specimens to form a cylindrical composite cylinder (300 mm height x 150 mm diameter) as shown in Figure 4. The splitting tensile strength was calculated using the following equation:

$$\text{Splitting tensile strength (MPa)} = \frac{2F}{\pi A} \quad (2)$$

Where:

F is the maximum force recorded (in N), and A is the area of the bond plane (in mm^2). The bonded area can be taken as a nominal value of 300 *150 = 45,000 mm^2.

As for shrinkage test, three composite specimens with dimensions of 12 cm×12 cm×35 cm were prepared. After casting the new concrete overlay as shown in paragraph no 2.3, approximately 24 hours after shrinkage test composite specimens cured at room temperature in their molds, they were demolded as ASTM C596 [9]. After composite specimens removed from the mold, using a super glue, stainless steel discs were adhered onto all four surfaces of each composite specimen centred about the length and width, where the measurement direction was perpendicular to the specimen composite specimen axis as shown in Figure 5.

Figure 3: *Slant shear test set-up.*

Figure 4: *Splitting tensile test set-up.*

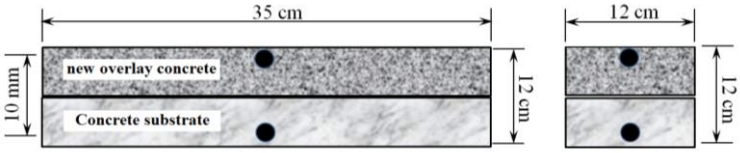

Figure 5: *The shape and dimensions of the shrinkage test sample***.**

The initial shrinkage reading was taking after 6 days of curing in the air. All specimens were exposed to drying conditions up to 56 days. Initial shrinkage reading was taking using stain gauge and length comparator complying with ASTM C596 (the gauge length is 100 mm). The drying shrinkage measurements were taken at the periods of exposure of 3, 5, 10, 15, 20, 25, 30, 35, 40, 45, 50 and 56 days, and the results of average for each of two opposite surfaces reading of three specimens were taken.

ISBN: 978-81-936820-6-7
Proceedings DOI: 10.21467/proceedings.4

3 Results and Discussions

3.1 Slant Shear Test Properties

Over the year, slant shear test is the most common type of tests to determine the bonding strength under combined state of compression and shear stresses. This test has become the most acceptable method and has been officially adopted in many international standards.

The experimental slant shear strength test results were shown in Table 3. As demonstrated in Table 3, the average slant shear bond strength was the highest in the grooved surface (12.26 MPa) and then wire brush and drill holes surfaces which were 7.79 MPa, 7.15 MPa respectively. Compared with the control specimen which represented by CS, the slant bond strength increases in the order of as cast surface (CS), drilled holes (DS), wire-brushed (WS) and finally grooved (GS) as shown in Figure 6. The relative percentage increases in bond strength were found to be around 81.9 % for DS, 95.9 % for WS and 210.4 % for GS.

Table 3. *Slant shear strength and failure modes for different types of surface treatment.*

Surface preparation	Sample No.	Max. force F (kN)	Comp. stress (MPa)	Shear Stress τ (MPa)	τ Average (MPa)	S.D.	C.V.	Failure mode
As-cast	CS1	155.6	6.92	3.46	3.99	2.9	0.75	A
	CS2	59.7	2.65	1.33				
	CS3	323.3	14.4	7.18				
Wire brush	WS1	461.3	20.5	10.3	7.79	2.17	0.28	A
	WS2	275.3	12.2	6.12				
	WS3	312.6	13.9	6.95				
Drill holes	DS1	156.9	6.97	6.97	7.15	2.17	0.28	A
	DS2	199.6	8.87	8.87				
	DS3	126.3	5.61	5.61				
Grooves	GS1	482.7	21.5	10.7	12.26	2.02	0.17	B
	GS2	656.8	29.2	14.6				
	GS3	516.5	23	11.5				

τ = Slant shear bond strength; S.D. = standard deviation C.V.= Coefficient of variation.
A = Interface failure; B = Interface failure with partially substrate failure.

Thus, the different roughness surfaces improve the slant bond strength by between 81.9 and 210.4 %, with the grooved surface presenting the highest value of increase; i.e. the most efficient. Hence, this confirms that the surfaces with different roughness provide significant improvement in slant bond strength of the composites in comparison to the control. The minimum acceptable slant bond strength which set out in the ACI Concrete Repair Guide in the range of 6.9–12 MPa [10]. Thus, the results obtained show that the surfaces treated in this study are actually required in order to fulfill the minimum prescribed slant bond strength of the composite. In conducting the slant shear test on the studied specimens, the failure modes can be classified into two types, type (A) is the interface failure; type (B) is the interface failure with partially substrate failure. The observations refer that the control specimen, drilled holes

and wire-brushed exhibit type A failure; i.e. a total interfacial failure or complete de-bonding of the composite, while the grooved surface reveals a type (B) failure mode which is interface failure with partially new concrete overlay failure. Hence, low slant bond strength shown in the specimens with different roughness mentioned is compatible with failure mode of these specimens. However, the highest slant bond strength shown by the grooved surface is compatible with the observed failure mode; i.e. Interface failure with partially substrate failure.

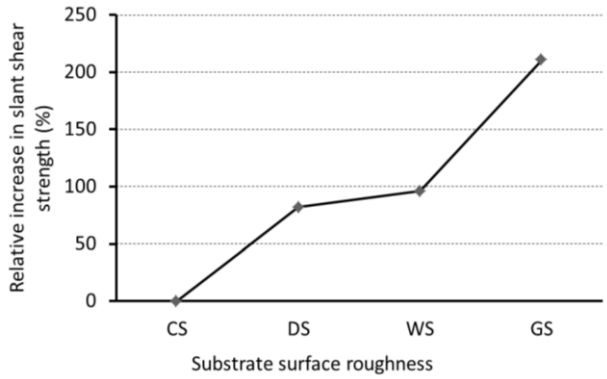

Figure 6. *Relative increase in slant shear bond strength for the different types of surface treatment.*

3.2 Splitting Tensile Test Properties

The splitting tensile test supplies measure of the indirect tensile capacity of the composite interface. The splitting tensile test results are shown in Table 4, whereas the percentage increase in the splitting tensile strength of the different types of surface treatment relative to that of the reference composite is shown in Figure 7. The results show that different types of surface treatment were able to significantly increase the splitting tensile strength of the composites when compared to the control composite (SC). Compared with the control composite, with the use of rough interface surface, the splitting tensile strength significantly increased for example, with about 1.44 %, 4.02 % and 7.62 % for WC, DC and GS, respectively. Hence, the grooved surface was the most efficient types of surface treatment, as it gave the highest increase in the splitting tensile strength among the composites in comparison with the reference composite, which indeed agree with the trend for slant bond strength results given and explained previously. Two types of failure modes of the splitting tensile test can be spotted, namely A = pure interface failure; B = interface failure with partially substrate failure. Obviously, the results reveal the relationship between the types of surface treatment and splitting bond tensile strength and the failure mode in the splitting tensile test. The observation show that the control composite (as-cast) and wire-brushed surfaces exhibit type (A) failure; i.e. a pure interface failure, while both the grooved and drilled holes surfaces reveal a type (B) failure mode which is interface failure with partially new concrete overlay failure. Based on the ACI concrete repair guide [10], which shows the classification of

ISBN: 978-81-936820-6-7
Proceedings DOI: 10.21467/proceedings.4

minimum acceptable bond tensile strength, whereby all of the results obtained in this study were excellent, since the splitting bond tensile strength was higher than 2.1 MPa.

Table 4. *Splitting tensile strength and failure modes for different types of surface treatment*.

Surface preparation	Sample No.	Max. force F (kN)	Ten. strength T (MPa)	T Average (MPa)	S.D.	C.V.	Failure mode
As-cast	CS1	447	9.5	9.71	0.28	0.029	A
	CS2	473	10.03				
	CS3	452.7	9.6				
Wire brush	WS1	451	9.57	9.85	0.3	0.03	A
	WS2	480	10.18				
	WS3	462	9.8				
Drill holes	DS1	488.8	10.37	10.1	0.21	0.021	B
	DS2	475.6	10.1				
	DS3	469.5	9.96				
Grooves	GS1	477	10.2	10.45	0.35	0.034	B
	GS2	481	10.4				
	GS3	510	10.8				

T = Splitting tensile strength; S.D. = standard deviation C.V.= Coefficient of variation.
A = Pure interface failure; B = Interface failure with partially substrate failure.

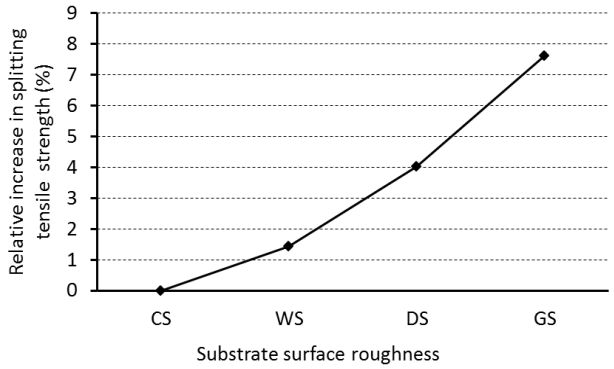

Figure 7. *Relative increase in splitting tensile strength for the different types of surface treatment*.

3.3 Shrinkage (Volume Changes)

When shrinkage is restrained, permanent tensile stresses develop in the new concrete that result in the formation of tensile cracks in the new concrete material itself, or in splitting at the interface of the new concrete overlay and the concrete substrate. Since most of the repair materials, including new concrete are applied to an older concrete substrate that has negligible shrinkage, new concrete overlay with very low shrinkage potential should be chosen to minimize the compatibility problems between concrete overlay and substrate concrete. Shrinkage values for the different types of surface treatment whether the direction of the measurement is perpendicular to the long axis or short axis of specimen, are shown in Figure 8 and Figure 9. In both cases and at all measurement durations (i.e. at 3, 5, 10, 15, 20, 25, 30,

35, 40, 45, 50 and 56 days), it can be observed that the composite specimens with grooved and drilled holes surfaces showed low shrinkage compared with the control and wire-brushed surfaces composites. The significant reduction in shrinkage values for composite specimens with grooved and drilled holes surfaces could be attributed to the strong overlap between old concrete substrate and new concrete overlay (penetration of the concrete material into the grooves and holes) leading to prevents the new concrete overlay from the movement. Shrinkage values for the different types of surface treatment at 56 days are demonstrated in Figure 10. Compared with the control composite, with the use of rough interface surface, shrinkage values significantly decreased for example, with about 48 % and 24 % and for DC and GS, respectively, and when calculating the shrinkage values with the direction of the long axis, about 53 %, and 43 % and 32 % for DC, GS and WS, respectively with the direction of the short axis of composite specimen. However, according to Emmons et al. [11], shrinkage values of repair materials in excess of 0.05%, and 0.1% at 30 days are considered to represent moderate and high levels of drying shrinkage, respectively, that can potentially result in premature failures, whereby all of the shrinkage values obtained in this study were less than the mentioned values.

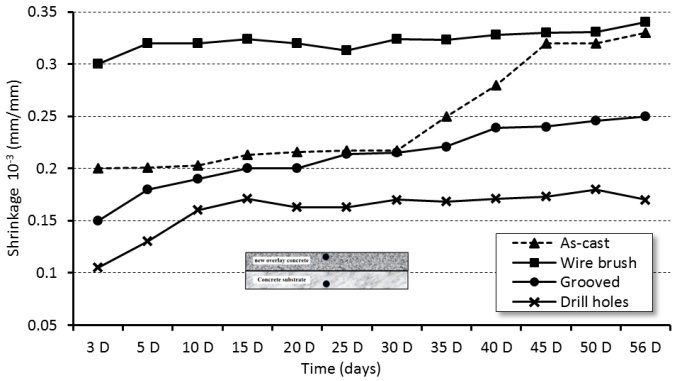

Figure 8.*Shrinkage values for the different types of surface treatment; The direction of the measurement is perpendicular to the long axis.*

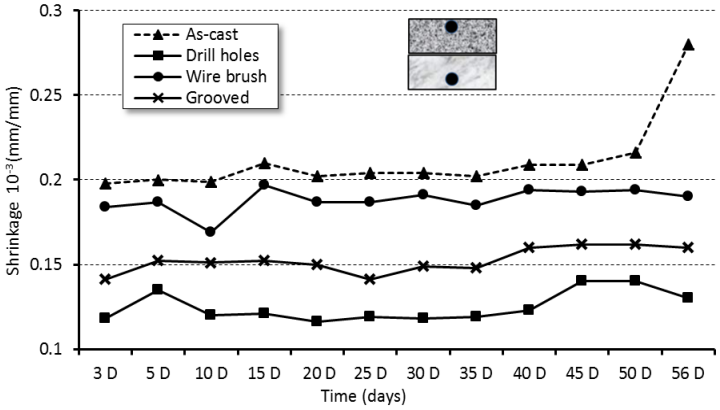

Figure 9.*Shrinkage values for the different types of surface treatment; The direction of the measurement is perpendicular to the* short axis.

ISBN: 978-81-936820-6-7
Proceedings DOI: 10.21467/proceedings.4

Series: AIJR Proceedings

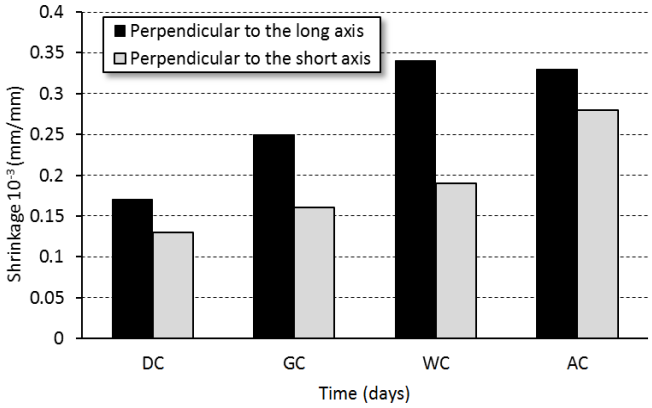

Figure 10. *Shrinkage values for the different types of surface treatment* at 56 days.

4 Conclusions

Based on the results and observations, the following conclusions can be drawn:

- The surface roughness suggested in this study; i.e. wire-brushed, grooves and drilled holes significantly affect adhesion with new concrete overlay, since all concrete substrate surface preparation methods revealed higher bond strengths compared with that of the as-cast (control specimen).
- Grooved and drilled holes surfaces were the preparation method of the substrate surface that presented the highest values of bond strength in shear and in tension, from all the considered techniques.
- Based on ACI Concrete Repair Guide, the results obtained show that the surfaces treated in this study are indeed required in order to achieve the minimum prescribed slant bond strength of the composite.
- All the results obtained from the split tensile strength test shows that new plain concrete overlays have excellent bond quality, since the splitting bond tensile strength was higher than 2.1 MPa.
- The observations of failure mode in the slant shear test show that the control specimen, drilled holes and wire-brushed exhibit a total interfacial failure, while the grooved surface reveal interface failure with partially new concrete failure. In addition, the failure mode in the split cylinder tensile strength test show that the control composite (as-cast) and wire-brushed surfaces exhibit a pure interface failure, while both the grooved and drilled holes surfaces reveal interface failure with partially new concrete overlay failure.
- The composite specimens with grooved and drilled holes surfaces showed low shrinkage compared with the control and wire-brushed surface composites. However, all the shrinkage values obtained in this study were less than the permissible limit according to Emmons et al. (0.1% at 30 days).

References

[1] B. A. Tayeh, B.H. Abu Bakar, M. A. Megat Johari, "Characterization of the interfacial bond between old concrete substrate and ultra-high performance fiber concrete repair composite", *Materials and Structures*, vol. 46, no 5, pp. 743-753, 2014.

[2] B. A. Tayeh, B.H. Abu Bakar, M. A. Megat Johari, "Assessment of adhesion between RPC overlay and existing concrete substrate", *Applied Mechanics and Materials*, vol. 802, pp. 95-100, 2015.

[3] A. Momayez, M.R. Ehsani, A.A. Ramezanianpour, H. Rajaie "Comparison of methods for evaluating bond strength between concrete substrate and repair materials", *Cement and Concrete research*, vol. 35, no. 4, pp.748-757, 2005.

[4] I. S. Wall, N. G. Shrive, "Factors affecting bond between new and old concrete,, *Materials Journal*, vo. 85, no. 2, pp. 117-125,1998.

[5] Y. A. Ali, R. Ambalavanan, "Flexural behavior of reinforced concrete beams repaired with styrene–butadiene rubber latex, silica fume and methylcellulose repair formulations", *Magazine of Concrete Research*, vol. 51, no. 2, pp.113-120, 1999.

[6] N. Gorst, L. Clark, "Effects of thaumasite on bond strength of reinforcement in concrete", *Cement and Concrete Composite*, vol. 25, no. 8, pp.1089–1094, 2003.

[7] A. Rahman, A. Changfa, " State-of-the-art review of interface bond testing devices for pavement layers: toward the standardization procedure", *Journal of Adhesion Science and Technology*, vol. 31, no 2, pp. 109 -126, 2016.

[8] ASTM-C882, "Standard test method for bond strength of epoxy-resin systems used with concrete by slant shear", *West Conshohocken*, American Society for Testing and Materials, 1999.

[9] ASTM-C496, "Standard test method for splitting tensile strength of cylindrical concrete". *West Conshohocken*, American Society for Testing and Materials, 1996.

[10] G. Chynoweth, R.R. Stankie, W.L. Allen, R.R. Anderson, W.N. Babcock, P. Barlow, J.J. Bartholomew, G.O. Bergemann, R.E. Bullock, F.J. Constantino, "Concrete repair guide", ACI committee, concrete repair manual, vol. 546, ACI, Farmington Hills, pp 287–327, 1996.

[11] P.H. Emmons, A.M. Vaysburd, J.E. Mcdonald, "A Rational Approach to durable concrete repairs", *Concrete International*, vol.15, no. 9, pp. 40-45,1993.

ISBN: 978-81-936820-6-7

Series: AIJR Proceedings
Proceedings DOI: 10.21467/proceedings.4

Static and Dynamic Analysis of Multistory RC Building with Various Heights in High Seismic Zone

Ghusen Al-Kafri[1], Md. Shahnewaz Sarkar[2*] , Md. Shaizuddin Sarkar[3]

[1] Department of Civil Engineering, College of Engineering, Sirte University, Libya
[2, 3] Department of Civil & Architecture Engineering, College of Engineering and Applied Science, Libyan Academy, Libya

DOI: https://doi.org/10.21467/proceedings.4.26
* Corresponding author email: shahnewaz2020@gmail.com

ABSTRACT

The earthquake ranks as one of the most destructive natural disasters recorded all over the world. It has taken millions of lives and caused vast damages to infrastructures through the ages. Since the earthquake forces are random in nature and unpredictable, the engineering tools are needed to be sharpened for analyzing structures under the action of these forces. This paper deals with the comparison of static and dynamic analysis of four RC multistory building models with different height in high seismic zone. The considered structure is modeled as 5, 10, 15 & 20 story structure and analyzed by commercial software Autodesk ROBOT Structural Analysis 2018. Equivalent Lateral Force (ELF) Procedure is used for static analysis and Response Spectrum (RS) Procedure is used for dynamic analysis. All the analyses are conducted according to ASCE7-10. Then results are compared based on different parameters such as: Displacement, Story Drift, Base Shear, Story Shear and Story Moment. Finally, a comparative study has been carried out between static and dynamic analysis. It was found that ELF procedure provides higher displacement, story drift and base shear compared to RS procedure. Based on the findings of the study it is recommended to use dynamic analysis (RS) instead of static analysis (ELF) specially in high rise building.

Keywords: Equivalent lateral force; response spectrum; static analysis; dynamic analysis; displacement; story drift; base shear.

1 Introduction

Nowadays, it is very popular for constructing low to high-rise buildings in the world due to increasing population that is required to resist the lateral dynamic loads caused by earthquake. Earthquake effects are more intense than wind effects. From past intense disaster, it can be proved that many structures are totally damaged because of earthquakes, that is natural and unpredictable, which gives intense ground shaking. Therefore, earthquake analysis and design are very important in today's world. There are various types of structural analysis used to analyse high-rise buildings subjected to seismic load such as Equivalent Lateral Force (ELF) procedure, Response Spectrum (RS) procedure, Time History Analysis etc. In the present study, ELF & RS procedures have been carried out according to ASCE7-10.

 ISBN: 978-81-936820-6-7

A research work was carried out on two methods of seismic analysis namely static and dynamic for 14 story RC building under Equivalent static and dynamic loads according to Egyptian code 2012. (Mahmoud and Abdallah, 2014). Another study (Tafheem *et al.*, 2016) investigated the seismic performance of a 10 story reinforced concrete moment resisting framed building under static and dynamic loading as per Bangladesh National Building Code (BNBC 2006). Furthermore, a study was carried out on the seismic analysis of two reinforced concrete moment resisting frame buildings (G+10 and G+25) using ELF and RS (Kakpure and Mundhada, 2017).

The objective of this study is to make a comparative study between static (ELF) and dynamic (RS) analysis by investigating a reinforced concrete multistory building with different heights located in high seismic zone according to ASCE7-10. For this purpose, four models with different heights are modelled and analysed using ROBOT 2018 and the results are compared together based on five parameters: Displacement, Story Drift, Base Shear, Story Shear and Story Moment.

2 Project Description

For this study, a regular reinforced concrete building is considered as shown in Figure 1. The floor area of the structure is 625 sqm (25m x 25m) with 5 bays along each side (each span 5m). The structure is modelled four times as 5, 10, 15 & 20 storied structure. Height of each story is 3m.

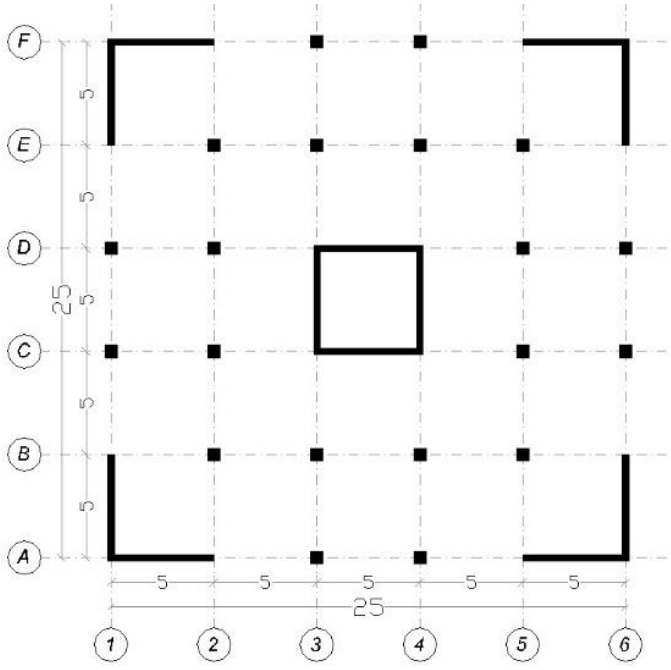

Figure 1: *Plan view of considered structure*

For the structures with different height, different dimensions are taken for structural elements. Table 1 shows the dimensions taken for different structural elements in this study.

ISBN: 978-81-936820-6-7
Proceedings DOI: 10.21467/proceedings.4

Series: AIJR Proceedings

Table 1: *Dimension of structural elements*

Structure	Story	Column		Shear Wall Thickness (cm)	Slab Thickness (cm)
		b (cm)	h (cm)		
5 Story	1 to 5	40	40	30	17
10 Story	1 to 5	50	50	35	17
	6 to 10	40	40	30	17
15 Story	1 to 5	60	60	40	17
	6 to 10	50	50	35	17
	11 to 15	40	40	30	17
20 Story	1 to 5	70	70	45	17
	6 to 10	60	60	40	17
	11 to 15	50	50	35	17
	16 to 20	40	40	30	17

While designing any building, different loads acting on it play a major role. An error in estimation of these loads can lead to the failure of the structure. Therefore, a careful study of loads that are acting on the structure becomes necessary. The loads in particular area must be selected properly and the worst combination of these loads must be evaluated.

The dead load in a building should be comprised of the weight of all walls, partitions, floors, roof and should include the weight of all other permanent constructions in that building. Based on the materials used in the building, the dead load (DL) is calculated as 2.96 KN/m^2. Live Load (LL) is taken 1.92 KN/m^2 according to ASCE 7-10. The structure is assumed to be located in high seismic area, Los Angeles, USA. The seismic parameters used in this study are taken according to ASCE 7-10 and are shown in Table 2.

Table 2: *Seismic parameters*

Site Class	D
Acceleration Parameter for 1-sec Period, S_1	0.857g
Acceleration Parameter for short Period, S_s	2.442g
Risk Category	III
Importance Factor, I	1.25
Long-Period Transition Period, T_L	8s
Response Modification Factor, R	4.5

3 Modeling and Analysis

All the structures with different heights are modeled and analyzed by ROBOT 2018 using Equivalent Lateral Force Procedure (ELF) as static analysis and Response Spectrum Procedure (RS) as dynamic analysis according to ASCE7-10. Figure 2 shows the modelling of different structure in software.

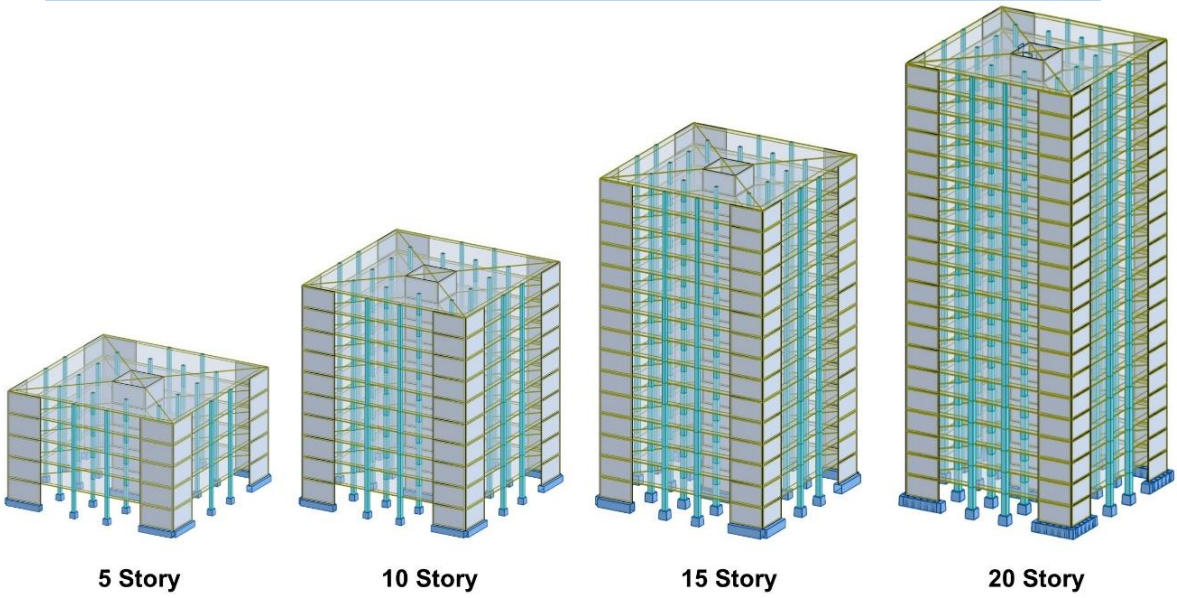

Figure 2: *Modelling of different structures in ROBOT*

4 Results and Discussion

After performing static and dynamic analysis for all the structures with different height, the obtained results were compared based on five factors i.e. Displacement, Story Drift, Base Shear, Story Shear and Story Moment as shown in Table 3, 4 and 5.

Table 3: *Comparison of static and dynamic analysis results for structures with different height*

Analysis Type	Story	Displacement		Story Drift		Base Shear (KN)
		X (mm)	Y (mm)	X (mm)	Y (mm)	
Static (ELF)	20	626.1	626.9	41.8	41.9	28,955.96
	15	278.0	278.3	24.3	24.4	26,146.06
	10	88.3	88.4	11.2	11.2	22,929.92
	5	9.8	9.8	2.3	2.3	13,249.58
Dynamic (RS)	20	230.2	233.0	21.6	21.6	24,612.55
	15	136.1	137.3	16.7	16.7	22,224.15
	10	54.1	54.4	9.6	9.6	19,490.45
	5	6.2	6.2	2.0	2.0	11,262.14

ISBN: 978-81-936820-6-7
Proceedings DOI: 10.21467/proceedings.4

Series: AIJR Proceedings

Table 4: *Comparison of story shear by static and dynamic analysis*

Story	Story Shear (KN)							
	5 Story		10 Story		15 Story		20 Story	
	Static (ELF)	Dynamic (RS)	Static (ELF)	Dynamic (RS)	Static (ELF)	Dynamic (RS)	Static (ELF)	Dynamic (RS)
20							2,974.31	4,210.68
19							5,760.18	7,362.71
18							8,360.33	9,394.46
17							10,777.60	10,564.48
16							13,014.92	11,127.95
15					3,423.83	4,252.66	15,194.91	11,323.35
14					6,581.28	7,399.56	17,191.20	11,361.80
13					9,475.63	9,451.15	19,007.36	11,432.03
12					12,110.39	10,761.86	20,647.19	11,705.20
11					14,489.29	11,679.13	22,114.70	12,298.83
10			4,221.94	4,407.09	16,739.76	12,518.70	23,491.35	13,293.21
9			7,996.56	7,983.76	18,728.39	13,459.21	24,694.82	14,649.53
8			11,326.96	10,705.45	20,460.20	14,558.22	25,730.36	16,228.88
7			14,216.65	12,836.90	21,940.73	15,813.74	26,603.67	17,900.87
6			16,669.60	14,588.58	23,176.18	17,174.57	27,321.05	19,549.00
5	4,416.53	4,169.75	18,807.60	16,140.21	24,232.81	18,614.09	27,923.85	21,137.28
4	7,949.75	7,323.97	20,494.13	17,477.58	25,045.93	19,990.81	28,377.28	22,538.90
3	10,599.66	9,448.09	21,736.31	18,523.31	25,625.99	21,130.25	28,691.40	23,627.42
2	12,366.27	10,729.12	22,543.54	19,205.56	25,986.35	21,897.39	28,878.64	24,326.07
1	13,249.58	11,262.14	22,929.92	19,490.45	26,146.06	22,224.15	28,955.96	24,612.55

Table 5: *Comparison of story moment by static and dynamic analysis*

Story	Story Moment (KN.m)							
	5 Story		10 Story		15 Story		20 Story	
	Static (ELF)	Dynamic (RS)	Static (ELF)	Dynamic (RS)	Static (ELF)	Dynamic (RS)	Static (ELF)	Dynamic (RS)
20							1,143.16	791.00
19							1,1136.82	14,077.26
18							29,416.71	36,541.46
17							55,426.77	64,715.80
16							88,619.46	95,841.93
15					1,315.93	806.09	129,431.64	128,513.13
14					12,800.99	14,219.26	175,905.76	159,936.16
13					33,657.25	36,764.99	228,288.50	189,837.86
12					63,096.80	65,007.07	286,041.15	217,799.96
11					100,342.28	96,465.39	348,636.52	243,860.43

10			1,622.68	803.25	145,699.15	130,303.77	416,982.90	268,966.56
9			15,739.27	14,722.66	196,804.40	164,477.01	488,064.27	292,969.36
8			41,008.96	39,114.70	253,761.11	199,630.81	562,671.32	317,602.45
7			76,100.49	71,297.33	315,801.32	236,174.80	640,303.13	344,371.08
6			119,693.23	109,344.04	382,173.93	274,740.72	720,476.17	374,719.91
5	1,697.47	782.95	171,674.31	152,899.15	453,606.01	316,857.23	804,326.29	410,516.61
4	16,305.02	13,937.24	228,848.50	199,482.62	526,714.78	361,504.58	888,352.36	451,154.66
3	41,172.74	36,257.31	290,884.32	249,383.45	602,145.28	409,858.20	973,660.53	497,472.17
2	73,650.71	64,569.95	356,452.89	301,995.35	679,205.10	461,923.30	1,059,839.85	549,152.21
1	111,089.01	96,363.00	424,255.66	356,609.80	757,244.76	517,266.35	1,146,519.18	605,417.63

Figure 3 & Figure 4 show the displacement for different structures by static and dynamic analysis. From the figures it can be observed that the displacement obtained by static analysis (ELF) is higher than that obtained by dynamic analysis (RS) for all structures. Static analysis gives 58.1% to 172% higher displacement than dynamic analysis. It can be also noticed that the difference in displacement calculated by static and dynamic analysis increases with the increase of height of the structure.

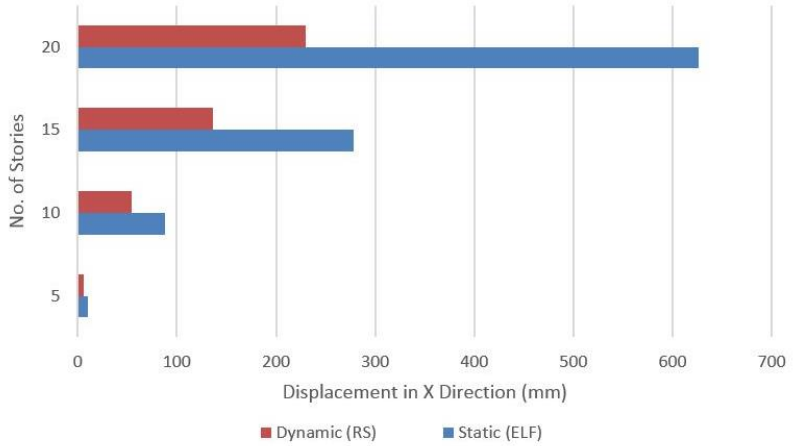

Figure 3: *Displacement in X Direction by Static and Dynamic Analysis*

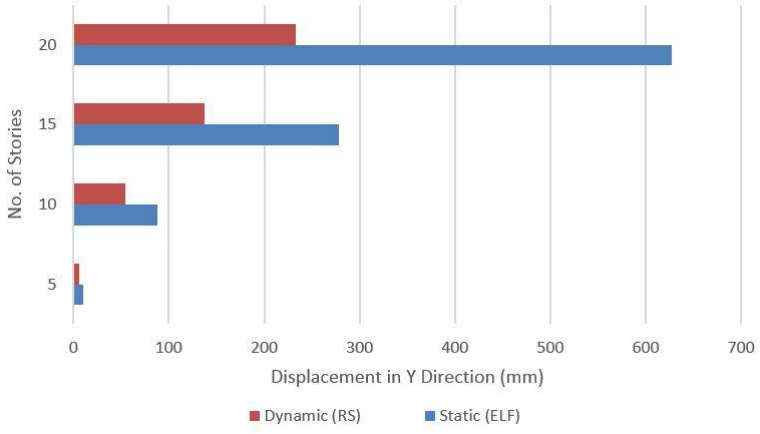

Figure 4: *Displacement in Y Direction by Static and Dynamic Analysis*

ISBN: 978-81-936820-6-7

Series: AIJR Proceedings
Proceedings DOI: 10.21467/proceedings.4

Figure 5 & Figure 6 show the story drift for different structures by static and dynamic analysis. According to the code ASCE 7-10 the story drift for this study is limited to 45 mm. It can be noticed that the story drift for all structures is within permissible limit. The figures show that the story drift calculated by dynamic analysis is lower than static analysis, where it gives 15% to 94% less drift. It can be noticed that the difference increases gradually with the height of the structure. This indicates that static analysis may lead to uneconomical design as it gives higher drifts.

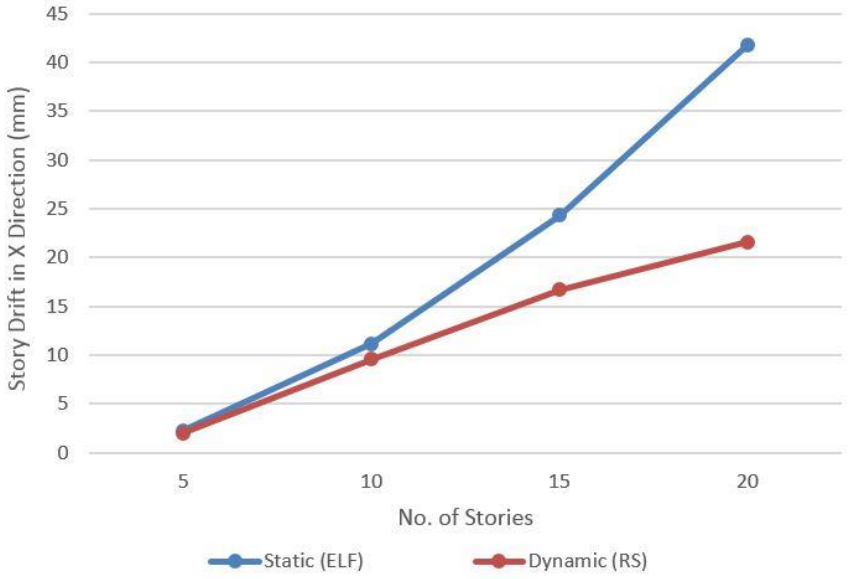

Figure 5: *Drift in X Direction by Static and Dynamic Analysis*

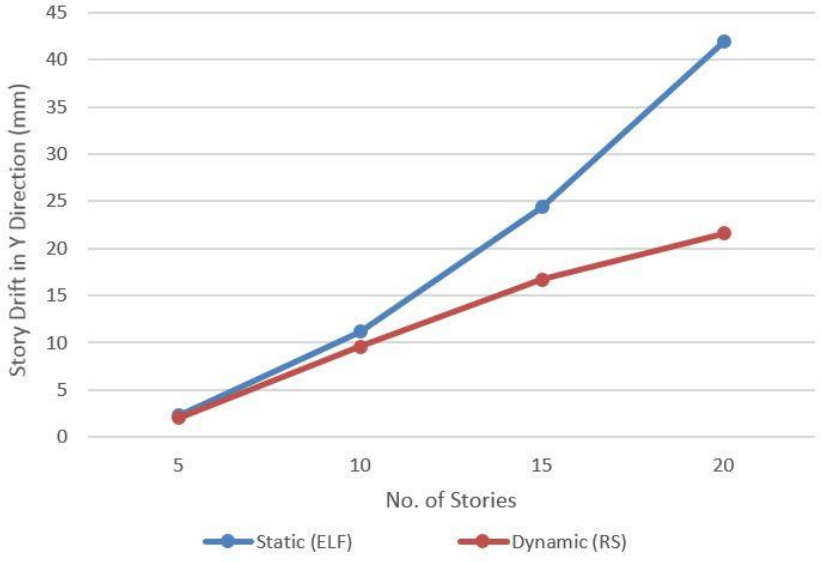

Figure 6: *Drift in Y Direction by Static and Dynamic Analysis*

Figure 7 indicates the base shear for different structures by static and dynamic analysis. From this figure along with Table 3 it can be noticed that the base shear obtained from dynamic analysis is about 85% of static analysis. A study (Mahmoud and Abdallah, 2014) showed that the total base shear obtained from static analysis is about 8% higher than that of dynamic analysis. On the other hand, another study (Tafheem *et al.*, 2016) found that the total base shear obtained from static analysis is about 17% higher than that of dynamic analysis. Similarly, in the present study, it has been found that in case of static analysis, the base shear is 17.6% higher than that of dynamic analysis.

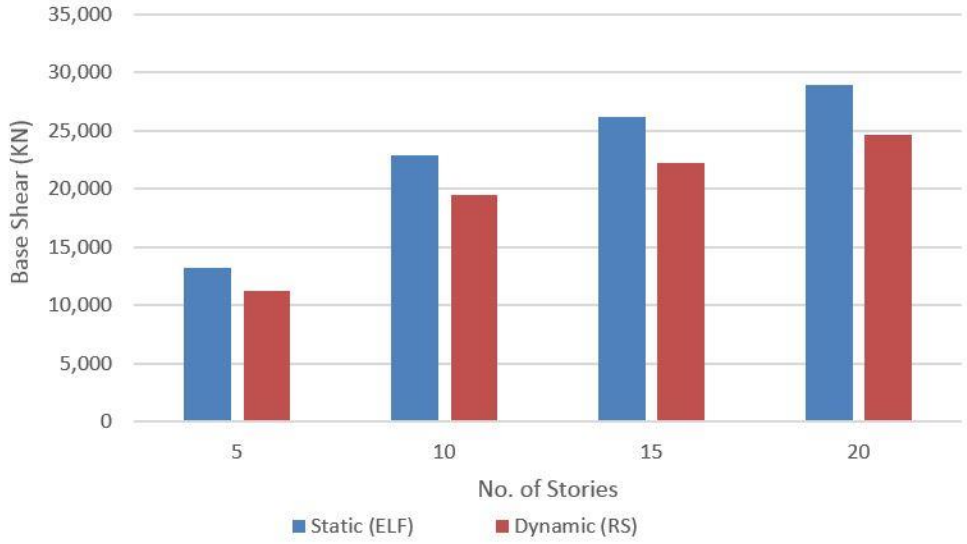

Figure 7: *Base Shear by Static and Dynamic Analysis*

Figure 8 shows the story shear for different structures by static and dynamic analysis. From the figure it can be observed that the story shear obtained by static analysis (ELF) is higher than dynamic analysis (RS) for all stories of all structures except for top stories of 10, 15 & 20 storied structure, where dynamic analysis gives slightly higher story shear compared to static analysis. It can also be noticed that the difference in story shear obtained by static and dynamic analysis gradually decreases with the increase of height for 5 and 10 storied structure, while for 15 and 20 storied structure the difference in story shear is high in middle stories and decreases in upper & lower stories. Maximum difference in story shear is 17.6% for 5 & 10 storied structure while the difference is 40.5% & 79.8% for 15 & 20 storied structure respectively.

Figure 9 shows the story moment for different structures by static and dynamic analysis. From the figure it can be clearly noticed that the difference in story moment obtained by static and dynamic analysis gradually decreases with the increase of height of the structure. It can also be observed that the story moment obtained by static analysis (ELF) is higher (upto 116.8%) than dynamic analysis (RS) for all structures except for some top stories of 15 & 20 storied structure, where dynamic analysis gives higher story moment (upto 26.4%).

ISBN: 978-81-936820-6-7

Series: AIJR Proceedings
Proceedings DOI: 10.21467/proceedings.4

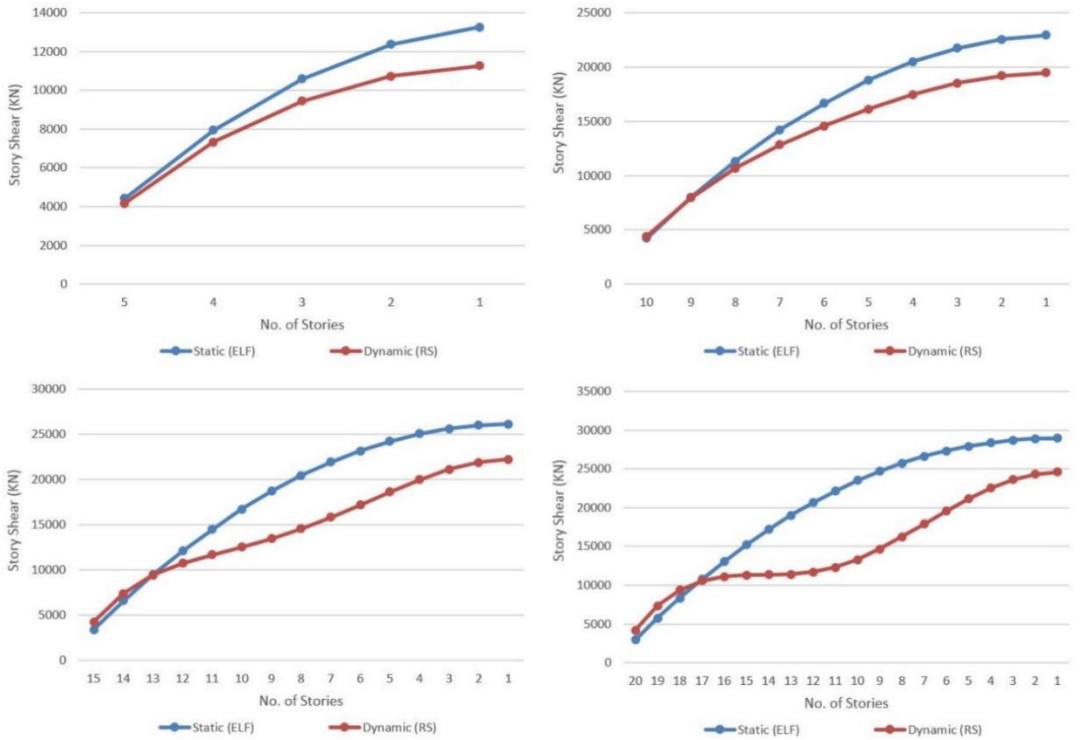

Figure 8: Story Shear for *5, 10, 15 & 20 storied structure by Static and Dynamic Analysis*

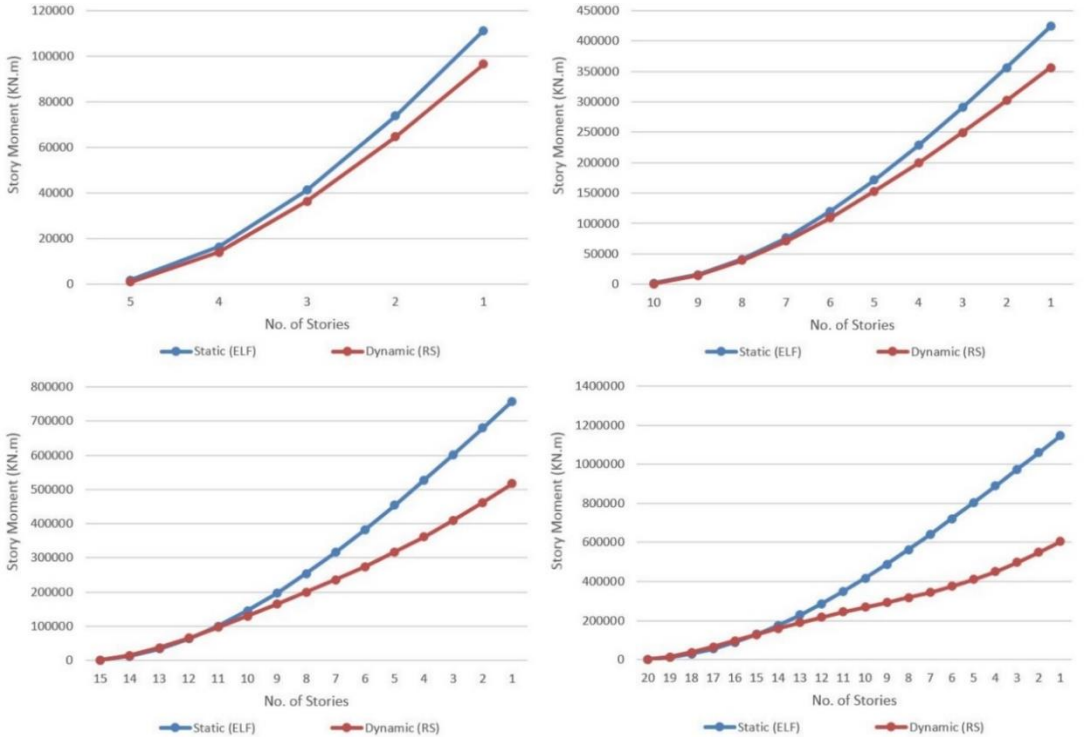

Figure 9: Story Moment for *5, 10, 15 & 20 storied structure by Static and Dynamic Analysis*

5 Conclusions

From the results of the study it is found that Response Spectrum Analysis is an important dynamic analysis tool and it does not require high level of modelling and in the same time it provide better results compared to static analysis. Although Response Spectrum Analysis (dynamic) preferred over Equivalent Lateral Force Procedure (Static), it is very important to engineers and researchers to understand that the RS analysis is an approximate method and has limitations, as it is restricted to linear elastic analysis only. For more accurate and exact results, other advanced dynamic analysis tool such as Non-linear time history analysis can be used, but this method is more complex and time consuming. Finally, in terms of practical application, it is recommended to use dynamic analysis (RS) instead of static analysis (ELF) specially in high rise building, as it requires less computational efforts while it gives reasonably better results, leading to more economic and safe design.

References

[1] Autodesk, Robot Structural Analysis 2018, Structural Analysis Software, version 2018.

[2] B. S. Taranath, "Reinforced Concrete Design of Tall Buildings", CRC Press, New York, USA, 2010.

[3] G. G. Kakpure and A. R. Mundhada, "Comparative Study of Static and Dynamic Seismic Analysis of Multistoried RCC Buildings by ETABS," *International Journal of Engineering Research and Applications*, vol. 7, Issue 5, pp. 06-10, 2017. DOI: 10.9790/9622-0705050610.

[4] "Minimum Design Loads for Buildings and Other Structures" (ASCE/SEI 7-10), American Society of Civil Engineers, USA.

[5] Seismic Design Tool. Access online on 10 June 2018 at https://earthquake.usgs.gov/designmaps/us/application.php

[6] S. Mahmoud and W. Abdallah, "Response Analysis of Multi-Storey RC Buildings under Equivalent Static and Dynamic Loads According to Egyptian Code," International Journal of Civil and Structural Engineering Research, vol. 2, Issue 1, pp. 79-88, 2014.

[7] Z. Tafheem, J.I. Jihan, T. Samdanee, M.Z. Islam and A.S.M. Tarin, "Earthquake Response Analysis of a Multistoried RC Building Under Equivalent Static and Dynamic Loading as per BNBC 2006," *Malaysian Journal of Civil Engineering*, vol. 28, Issue 1, pp. 108-123, 2016.

ISBN: 978-81-936820-6-7
Proceedings DOI: 10.21467/proceedings.4

Capability of Designing a Novel Fluid Damper Using a McKibben Actuator

Haithem Elderrat[1*], Elganidi Elsaghier[2]

[1] Department of Mechanical Engineering, Faculty of Engineering, Misurata University, Libya
[2] Department of Industrial Engineering, Faculty of Engineering, Misurata University, Libya

DOI: https://doi.org/10.21467/proceedings.4.27
* Corresponding author email: h.elderrat@eng.misuratau.edu.ly

ABSTRACT

Flow fluid between moving parts is providing the damping force. Such characteristic can be utilized to build fluid dampers for a wide variety of vibration control systems. Most previous works have studied the application of fluids damper in pistons/cylinders actuator, where the kinetic energy of a vibrating structure can be dissipated in a controllable fashion. The reduction of the friction can cause a sudden jump in the velocity of the movement. Stick-slip friction is present to some degree in almost all actuators and mechanisms and is often responsible for performance limitations. To overcome this problem, this report investigates the capability of designing a fluid damper that seeks to reduce the friction in the device by integrating it with a McKibben actuator. It is also reduced the total weight of such damper. In this paper, the concept of McKibben actuator has been reviewed, the modelling of device made is also presented. Also, the model has been validated experimentally. It is founded that the model predicts the behavior of the test rig with accuracy 85%. Also, the total weight could be reduced to 50% from the original weight.

Keywords: Viscus fluid, Stick-slip friction, McKibben actuator.

1 Introduction

A vibration isolator is a device inserted between the source of vibration and the primary device to reduce unwanted vibration [1]. The basic constituents of anti-vibration devices are the resilient load-supporting means and the energy dissipation means or the damping elements. Damping force exists if there is a relative velocity between two ends of the damper, and it refers to three types which are coulomb, viscus and material damping. In a coulomb damping, energy is absorbed via sliding friction (friction between rubbing surfaces that are either dry or have insufficient lubrication) [2]. Viscous damping is an energy loss occurs in liquid lubrication between moving parts or in a fluid forced through a small opening by a piston [3, 4]. A material damping where the material is deformed due to an applied force, and some energy is absorbed and dissipated by the material due to the friction between the its internal planes [5].

The majority of anti-vibration devices have studied the application of fluids damper in piston and cylinder actuator, where the kinetic energy of a vibrating structure can be dissipated in a

controllable fashion. Although the friction has a positive effect in the damping devices, the dry sealing friction makes a vibration transmission to the equipment; this tiny vibration may cause poor accuracy for sensitive devices [6]. Friction could have a bad effect on the system when applied force is close to overcoming the static friction. The behaviour is called stick-slip motion. Stick-slip motion occurs at close to zero velocity and is in the form of a sudden jerking motion. Typically, the static friction coefficient between two surfaces is larger than the kinetic friction coefficient. If an applied force is large enough to overcome the static friction, the friction reduces from static to dynamic friction. The reduction of the friction can cause a sudden jump in the velocity of the movement. Stick-slip friction is present to some degree in almost all actuators and mechanisms and is often responsible for performance limitations [7]. Using a McKibben actuator instead of a hydraulic actuator could reduce the friction in the device. Such actuator has advantages over cylinder and piston dampers for instance: high power/weight ratio and low cost, also there is no stick-slip phenomena in such actuator [8]. This report investigates the possibility of designing a fluid damper by using a McKibben actuator instead of piston and cylinder actuator.

2 McKibben Actuators

The McKibben actuator is a device that converts fluid pressure to force; it consists of an internal rubber tube inside a braided mesh shell. When the inner tube is pressurized, the internal volume of the actuator changes causing the actuator to expand or contract axially as shown in Figure 1. The McKibben actuator is usually used to mimic the behaviour of skeletal muscle [9]. It is also used in medical equipment [10] and industrial applications [11]. Although the working fluid in a McKibben actuator is usually air, there are some applications using water as a working fluid, especially in exoskeleton devices and devices working in a water medium, such as an actuator for an underwater robot introduced by Kenneth et al. [12]. Shan et al. developed a variable stiffness adaptive structure based upon fluidic flexible matrix composites (F2MC) and water as the working fluid [13]. The fibres in an F2MC actuator can be placed at any one angle or combination of angles. This material can be designed to bend and it also provides a greater axial force.

The advantages of the McKibben structure tubes are that it uses inexpensive and readily available materials, and it can easily be integrated into a structure. A McKibben actuator also offers others advantages such as being light weight and with low maintenance costs when compared to traditional cylinder actuators [13]. A comparison of the force output of a pneumatic McKibben actuator and a pneumatic cylinder was made, and the result shows that the McKibben actuator produces a higher ratio of power to weight than the pneumatic cylinder actuator [8].

ISBN: 978-81-936820-6-7
Proceedings DOI: 10.21467/proceedings.4

Series: AIJR Proceedings

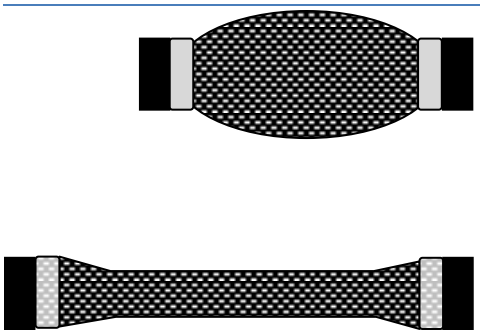

Figure 1: Concept of McKibben actuator.

3 Modelling of McKibben Actuator

To predict the behaviour of the test rig under static load, there is no effect of viscous damping of the valve, and the test rig could be modelled similar to a McKibben actuator. The variable parameters of this device are: a force applied to the test rig, internal pressure of the McKibben tube, type of internal material, and length of the McKibben tube. There are several techniques used for predicting the behaviour of this actuator and to provide a relationship between variable parameters. The technique of energy analysis, where input work (W_{in}) is equal to the output work (W_{out}), will be used in this research. It is assumed the shape of the McKibben tube is cylindrical. By neglecting the effect of the inner tube at this stage, the input work is done on this actuator by applying compressed air; this air moves the inner rubber surface, so the work is:

$$dW_{in} = P'dV \quad (1)$$

Where: dV volume change, and P' gauge pressure. The output work from this pressure is tension in the actuator, which leads to a decrease in the length of the tube:

$$dW_{out} = -FdL \quad (2)$$

Where: F axial force, and dL axial displacement. From the principle of virtual work, we could reach to the next expression [13]

$$F = P'\left(\frac{3L^2-b^2}{4\pi n^2}\right) \quad (3)$$

Where: n number of turn, and b uncoiled length of fibre. Now, the effect of elastic energy of inner tube will be accounted. So,

$$dW_{in} = dW_{out} + V_r dW \quad (4)$$

Where: Vr the volume is occupied by the inner tube, and W is the strain energy density function. From the previous analysis of input work and output work:

$$P'dV = -FdL + V_r dW \quad (5)$$

To determine the strain energy density of the inner tube, the rubber tube will be assumed to behave as a Neo–Hookean solid. The strain energy function of the actuator W could be expressed as a function of the first invariant of strain [14].

$$W = \frac{\mu_r}{2}[I_1 - 3] \tag{6}$$

μ_r is the shear modulus for infinitesimal deformations [14], and I_1 strain invariants which could be expressed:

$$I_1 = \lambda_1^2 + \lambda_2^2 + \lambda_3^2 \tag{7}$$

λ_i (i=1,2,3) are the principle stretches. $\lambda_1 = \frac{L}{L_0}$, $\lambda_2 = \frac{D}{D_0}$ and $\lambda_3 = \frac{1}{\lambda_1 \lambda_2}$.

Where L and D, are instantaneous length and diameter, while L_0 and D_0, are initial length and diameter of the tube, respectively. The diameter of the tube could be expressed in terms of length of tube [12]:

$$D^2 = \frac{b^2 - L^2}{\pi^2 n^2} \tag{8}$$

Therefore, strain energy density of inner tube W is determined by using the equation:

$$W = \frac{\mu_r}{2}\left[\frac{L^2}{L_0^2} + \frac{b^2 - L^2}{D_0^2 \pi^2 n^2} + \frac{D_0^2 L_0^2 \pi^2 n^2}{L^2(b^2 - L^2)} - 3\right] \tag{9}$$

The derivative strain energy density regarding the length:

$$\frac{dW}{dL} = \frac{\mu_r}{2}\left[\frac{2L}{L_0^2} + \frac{-2L}{D_0^2 \pi^2 n^2} + \frac{-2D_0^2 L_0^2 \pi^2 n^2 (b^2 - 2L^2)}{L^3 (b^2 - L^2)^2}\right] \tag{10}$$

Therefore, the force output of the actuator could be expressed:

$$F = P'\left(\frac{3L^2 - b^2}{4\pi n^2}\right) + \frac{V_r \mu_r}{2}\left[\frac{2L}{L_0^2} + \frac{-2L}{D_0^2 \pi^2 n^2} + \frac{-2D_0^2 L_0^2 \pi^2 n^2 (b^2 - 2L^2)}{L^3 (b^2 - L^2)^2}\right] \tag{11}$$

The equation illustrates that there are four variable parameters of this device: an applied force, internal pressure, and the length of the tube and type of internal material.

4 Experimental Work

The rig used in this research is shown in Figure 2; it consists of a McKibben tube, valve and accumulator. The McKibben tube is sealed at one end, and it is able to carry load at this tip, while the tube is attached to an accumulator via a valve at another end. Pressurizing the McKibben tube could be achieved at the top of the accumulator. By applying force to the end of the volume of actuator is changed, consequently the pressure inside tube is increased. Then, the fluid is able to flow in and out of the tube, and energy is eliminated through the viscous effect of the controlled valve. The total weight of such device is less than the half weight of similar piston/cylinder damper, the same results were found in previous researches [12-13].

To validating of the model, the isotonic test was carried out in this report. The actuator was loaded to known load, then internal pressure was increased 0.5 bar increments, and the internal pressure P, length of tube L are recorded. Changing in the pressure is causing to chaining length of the actuator. So, these parameters are governed by equation 11.

ISBN: 978-81-936820-6-7
Proceedings DOI: 10.21467/proceedings.4

Series: AIJR Proceedings

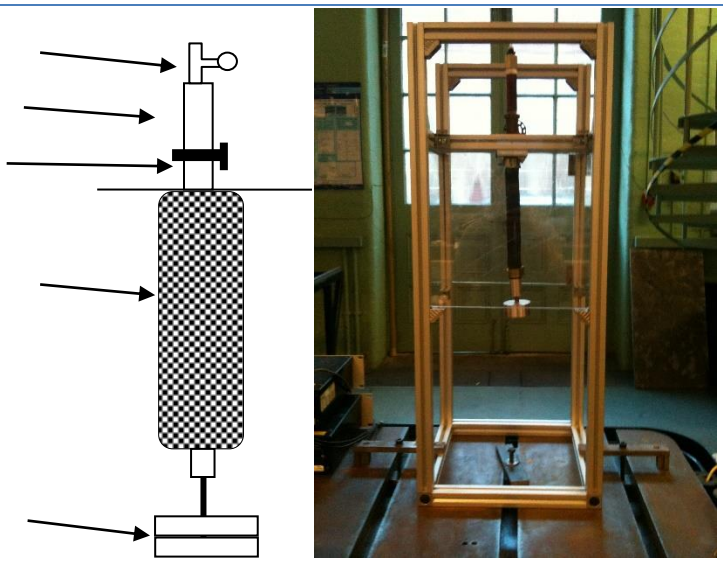

Figure 2: Test rig.

The length of McKibben actuator was 0.12m with diameter 0.011m. when uncoiled fibre the Length was 0.138m. Such actuator has 2.15 turns. The inner tube was made by rubber with thickness is 0.0003m and Shear modulus is 0. 6MPa.The procedures were examined at two constant loads which are 25N and 50N. Figure 3 shows the experimental results which are compared with the modelling results at a constant load. The figures show the model gives acceptable results in comparison with experimental data. Although there are differences between the modelling results and experimental results, the accuracy of this model is above 85%.

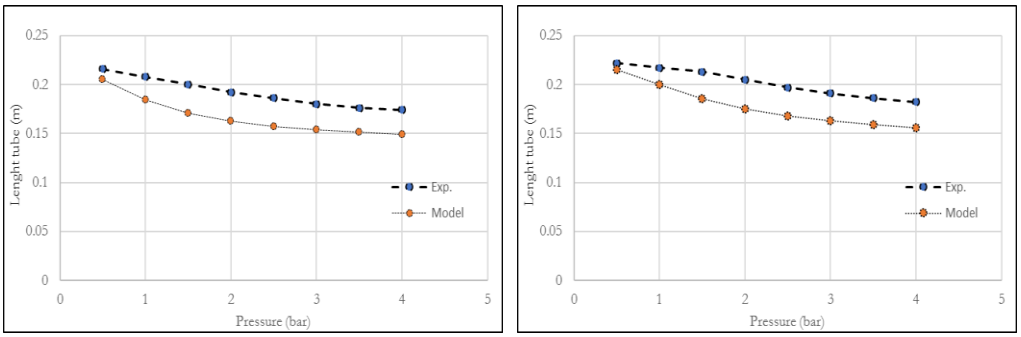

a b

Figure 3: Model and experimental result of rig: a) force is 25N; b) force is 50N.

To minimize these differences, it is important to consider the realistic shape rather than ideal cylindrical shape, also to account the force losses in the system due to friction between fibres and friction between the inner tube and outer tube.

Moreover, it is noticed, the model is shown to have less accuracy at low pressure, and the error is bigger when applying higher loads. To minimize such error, the end effects of the tube should be captured. The end effects changes in the output of the force at the length limits. When the actuator is reaching the length saturation L_s (length saturation), the stretching will be occurring in the fibres; therefore, the output force will be dependent on stiffness of the fibre material. While the force is zero if the length of actuator is less than minimum length L_m, this model is shown in next equations [15].

$$F = \begin{cases} P\left(\frac{3L^2 - b^2}{4\pi n^2}\right) + \frac{V_r \mu_r}{2}\left[\frac{2L}{L_0^2} + \frac{-2L}{D_0^2 \pi^2 n^2} + \frac{-2D_0^2 L_0^2 \pi^2 n^2 (b^2 - 2L^2)}{L^3 (b^2 - L^2)^2}\right] + K_f(L - L_s) & L > L_m \\ 0 & L < L_m \end{cases} \quad (12)$$

Where: K_f stiffness of fibre material.

5 Conclusions

Flow fluid is considered as one of the most superior means of control of vibration, and there are many of applications which profit from the characteristics of viscus fluid, which have been employed successfully. However, a conventional fluid damper has dry sealing frictions which cause a vibration transmission to the equipment. To reduce the friction in a device, a McKibben actuator could be used instead of a hydraulic actuator. Also, using such actuator could be reduced more than half of total weight of devices. A model of a McKibben actuator has been developed and then, it is validated experimentally. The model predicts the behaviour of the test rig with accuracy about 85%.

References

[1] R.A. Ibrahim, "Recent advances in nonlinear passive vibration isolators". *Journal of Sound and Vibration*, 2008. 314(3-5): p. 371-452.

[2] D.J. Mead, "Passive vibration control," 2000: John Wiley and Sons Ltd.

[3] M.R. Jolly, J.W. Bender, and J.D. Carlson, "Properties and Applications of Commercial Magnetorheological Fluids," . *Journal of Intelligent Material Systems and Structure*, 1999. 10(1): p. 5-13.

[4]. D.H.Wang,. and W.H. Liao, "Magnetorheological fluid dampers: a review of parametric modelling". *Smart Materials and Structures*, 2011.

[5] Y. A. Yu, et al., "Automotive vehicle engine mounting systems: A survey". *Journal of Dynamic Systems, Measurement and Control, Transactions of the ASME*, 2001. 123(2): p. 186-194.

[6] M.S. Seong, S.-B. Choi, and C.-H. Kim, "Design and Performance Evaluation of MR Damper for Integrated Isolation Mount". *Journal of Intelligent Material Systems and Structures*, 2011. 22(15): p. 1729-1738.

[7] Karnopp, D., "Computer Simulation of Stick-slip Friction in Mechanical Systems". Journal of Dynamic Systems, Measurement and Control, *Transactions of the ASME*, 1985. 107(1): p. 100-103.

[8] K.L.Hall, "Dynamic Control For a Pneumatic Muscle Actuator to Achieve Isokinetic Muscle Strengthening" 2011, Wright State University.

[9] E. J. Koeneman, et al. "A pneumatic muscle hand therapy device. in Engineering in Medicine and Biology Society*", 26th Annual International Conference of the IEEE*. 2004.

[10] D. G.Caldwell., et al., "A pneumatic muscle actuator driven manipulator for nuclear waste retrieval". *Control Engineering Practice*, 2001. 9(1): p. 23-36.

[11] K.K.Kenneth, and R. Bradbeer, "Static Model of the Shadow Muscle under Pneumatic Testing". Department of Electronic Engineering, City University of Hong Kong, Kowloon, Hong Kong, 2006.

ISBN: 978-81-936820-6-7

Series: AIJR Proceedings
Proceedings DOI: 10.21467/proceedings.4

[12] Y. Shan et al., "Variable Stiffness Structures Utilizing Fluidic Flexible Matrix Composites". *Journal of intelligent material system and structures* 2009. 20: p. 443.

[13] S, Lightner, "The Fluidic Muscle: A 'New' Development". *The International Journal of Modern Engineering*, 2002. 2.

[14] M.S. Chou-Wang, and C.O. Horgan, "Cavitation in nonlinear elastodynamics for neo-Hookean materials". *International Journal of Engineering Science*, 1989. 27(8): p. 967-973.

[15] R.W. Colbrunn, G.M. Nelson, and R.D. Quinn. "Modeling of braided pneumatic actuators for robotic control ". *Intelligent Robots and Systems*, 2001.

Investigation Into Accuracy Of LGD2006 for Medium-Elevation Areas

Adel Alkilani [1], Ahmed Hamruni [2]*

[1] Faculty of engineering technology, Misallata, Libya

[2] Department of Civil Engineering, Faculty of Engineering, Elmergib University, Libya

DOI: https://doi.org/10.21467/proceedings.4.28

* Corresponding author email: elhamrouni@hotmail.com

ABSTRACT

This paper presents a study about the Libyan Geodetic Datum 2006 (LGD2006) where a triangulation network has been established in a medium-elevation area in Libya. The network is consisted of braced quadrilaterals of 45 km lines in direction of meridians and 7 km lines in direction of parallels. The network distances and angles were accurately measured and then the coordinates were computed. In addition, coordinates of the major traverses points were measured using static GPS observation technique for several hours to ensure the maximum accuracy. GPS measurements were conducted using the World Geodetic System of 1984 (WGS84). Inverse geodetic methods were used to compare the achieved results with those of the Libyan ordinance survey. The results show that the best fit datum for medium-elevation areas (300-500m) in Libya is LGD2006 whereas WGS84 is best for low-elevation areas.

Keywords: LGD2006, triangulation, static GPS, accuracy, inverse geodetic problems.

1 Introduction

1.1 Background

As the surface of the earth is irregular and complex, for many centuries geodesists tried to determine the shape of the earth. They found that the most complex model of the earth is the geoid and the simplest model is the ellipsoid. This has led to many different reference ellipsoids around the world. Each country takes the newest reference ellipsoid as its reference datum for surveying purposes. Using an incorrect datum to express coordinates can result in position errors of hundreds of meters. As a result, countries modify the global datums to best fit their topographic relief by minimising the geoid undulations. The resulted new datum is known as the local datum [7].

European datum of 1950 (ED1950) had been used in Libya in late fifties and early sixties of last century. This datum best fits Europe not North Africa. European-Libyan datum of 1979 (ELD1979) is another datum that has been used in Libya. Nowadays the Libyan Geodetic Datum of 2006 (LGD2006), which is based on the international ellipsoid of 1924, is the most used datum for surveying applications in Libya [5].

 ISBN: 978-81-936820-6-7

Several researches found that the used ellipsoid for Libya fits only the northern part of the country because of deformations in the datum and that the used ground control points had been established by different companies using different measuring methods.

1.2 Aim and Objectives

The overall aim of this paper is to investigate the accuracy of using the LGD2006 for the medium-elevation areas in Libya. This aim will be assessed through investigating the following objectives:

- Choosing study area where ordinance survey ground control points are available.
- Establishment of a triangulation network of braced quadrilaterals of 45 km lines in direction of meridians and 7 km lines in direction of parallels.
- Using static GPS to measure the coordinates of Laplace station.
- Using geodetic formulas to compute distances and comparing results with those obtained by field observations.
- Establishment of new accurate ground control points to be used in other surveying applications.

2 Test site and Apparatus Used

2.1 Test Site

The test site is located in a medium-elevation area (300 to 400m above mean sea level) close to the city of Tarhuna. The site is between longitudes of 13° 30′ E and 13° 54′ E and latitudes of 31° 21′ N and 31° 52′ N. The test site is shown in Figure 1 while Figure 2 illustrates the topography of the site.

This site was chosen according to its elevation and to availability of two ground control points from the ordinance survey of Libya. These control points are called GPS 12-3 and GPS 12-4 and are located close to the site. Their coordinates are in LGD2006.

2.2 Apparatus Used

The instruments used in this research are:

- 1″ Total station from Trimple
- Prism
- Leica dual frequency GPS receiver
- Communication equipment

3 Trials, Results and Analysis

3.1 Observation Techniques

A total number of two accurate ground control points were available from the ordinance

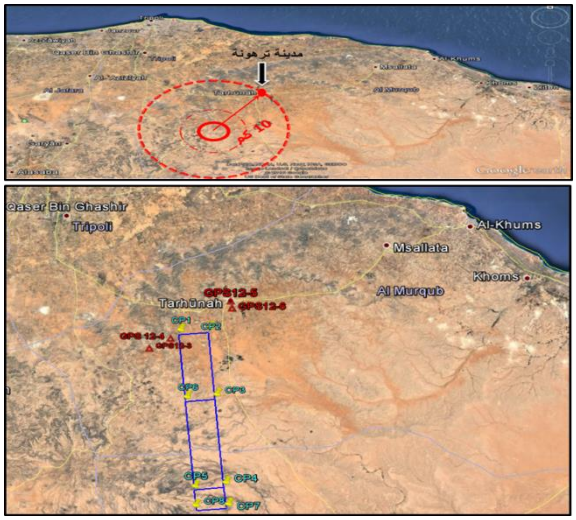

Figure 1: *Test site (source: Google earth)*

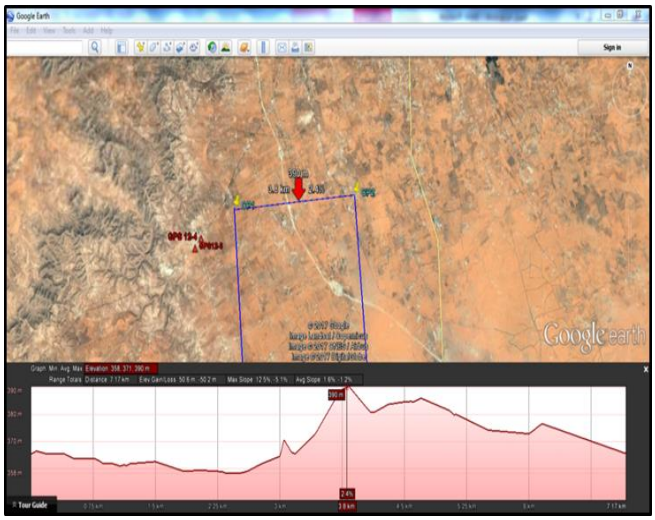

Figure 2: *Topography of the test site*

survey of Libya. These points were collected using static GPS with an estimated accuracy of 0.0068 m. These points were used as starting points to establish the network's other points. The number of established control points is 8 and were called CP_1 to CP_8 . In-between, points were called X_1, X_2, ……., X_n . Figure 3 depicts the established control points.

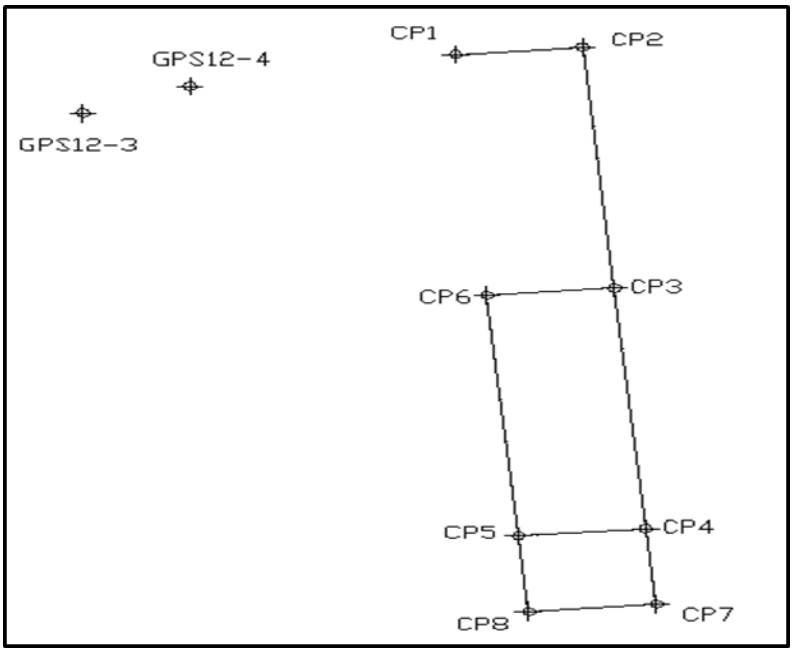

Figure 3: *Established control points*

ISBN: 978-81-936820-6-7
Proceedings DOI: 10.21467/proceedings.4

Series: AIJR Proceedings

The lines' length of the established triangulation network is 45km in the direction of meridians and 7km in the direction of parallels. These lengths were chosen so that the curvature of the earth will be taken into account. The chosen shape of the network is the braced quadrilateral. The control point GPS 12-4 was occupied by the total station and back sight was taken on GPS 12-3 to determine the true north. Then using the total station, the coordinates of all points, azimuths of lines and lengths of network lines were computed. In addition, static GPS observation technique, for several hours, was used to get the coordinates of the control points in WGS84.

3.2 Results and Discussion

The obtained coordinates for the control points in LGD2006 (UTM6º) and in WGS84 are shown in Table 1.

Table 1: *coordinates of control points*

Coordinates of network points in LGD2006 (UTM6º)			Coordinates of network points in WGS84		
point Id	Easting (m)	Northing (m)	Latitude (φ)	Longitude (λ)	Ellip.Hgt (m)
GPS12-3	356678.648	3578390.064	32° 19' 57.82" N	13° 28' 38.18" E	410.66
GPS12-4	357214.163	3578344.043	32° 19' 56.58" N	13° 28' 58.68" E	402.41
CP1	359198.744	3579582.980	32° 20' 38.92" N	13° 30' 11.68" E	400.12
CP2	366328.401	3580205.442	32° 21' 02.28" N	13° 34' 44.03" E	402.12
CP3	368067.873	3560281.212	32° 10' 16.13" N	13° 36' 00.50" E	418.49
CP4	369830.714	3540088.677	31° 59' 21.40" N	13° 37' 17.63" E	468.53
CP5	362699.684	3539466.102	31° 58' 58.15" N	13° 32' 46.33" E	541.94
CP6	360936.841	3559658.352	32° 09' 52.84" N	13° 31' 28.68" E	488.91
CP7	370308.386	3534617.252	31° 56' 22.78" N	13° 37' 40.67" E	492.14
CP8	363177.398	3533994.688	31° 55' 59.56" N	13° 33' 9.52" E	489.86

3.2.1 Transformation of Cartesian coordinates to geodetic coordinates

As the used coordinate system in the network is the Cartesian system and the ellipsoid represents the geodetic coordinate system, it's necessary to represent the relationship between the two systems mathematically according to the theory of cylindrical conformal projection as follows [6]:

$\varphi = f(X, Y)$, $\lambda = f(X, Y)$, $X = f(\varphi, \lambda)$, $Y = f(\varphi, \lambda)$

Conformal projection has two projection parameters, forward and reverse.

1- Forward (direct) parameters to get Cartesian coordinates

The assumptions put by Kruger to solve the projection equation are to keep the longitudes constant function and to make latitudes variable function as follows:

$$X = X_0 + C_2\lambda^2 + C_4\lambda^4 + C_6\lambda^6 + C_8\lambda^8 + C_{10}\lambda^{10} + \cdots$$

$$y = C_1\lambda + C_3\lambda^3 + C_5\lambda^5 + C_7\lambda^7 + C_9\lambda^9 + C_{11}\lambda^{11} + \cdots$$

2- Reverse (inverse) parameters to get geodetic coordinates

$$\varphi = B_x + C'_2 y^2 + C'_4 y^4 + C'_6 y^6 + C'_8 y^8 + \cdots$$
$$\lambda = C'_1 y + C'_3 y^3 + C'_5 y^5 + C'_7 y^7 + C'_9 y^9 + \cdots$$

where $C_1, C_2, C_3, C_4, C_5, \ldots$ are the forward parameters and

$C'_1, C'_2, C_{,3}, C'_4, C'_5, \ldots$ are the reverse parameters

In addition, Bidshivalf theory was used to get the reverse parameters as following [4]:

$P'_0 = 1 \quad , \quad Q'_0 = 0$

$P'_1 = dx \quad , \quad Q'_1 = y$

$P'_2 = P'^2_1 - Q'^2_1 \quad , \quad Q'_2 = 2P'_1 Q'_1$

$P'_3 = P'_1 P'_2 - Q'_1 Q'_2 \quad , \quad Q'_3 = P'_1 Q'_2 + Q'_1 P'_2$

$P'_n = P'_1 P'_{n-1} - Q'_1 Q'_{n-1} \quad , \quad Q'_n = P'_1 Q'_{n-1} + Q'_1 P'_{n-1}$

The values of $P'_1, P'_2, P'_3, \ldots P'_n$ are substituted back into the following formula to transform Cartesian coordinates to geodetic ones:

$$q = q_0 + \sum_{j=1}^{n} C'_j P'_j \quad \rightarrow \quad q = q_0 + C'_1 P'_1 + C'_2 P'_2 + C'_3 P'_3 + \cdots$$

$$L = L_0 + \sum_{j=1}^{n} C'_j Q'_j \quad \rightarrow \quad L = l_0 + C'_1 Q'_1 + C'_2 Q'_2 + C'_3 Q'_3 + \cdots$$

$$q_0 = ln\sqrt{\left[\frac{1+sin\varphi}{1-sin\varphi}\right]\left[\frac{1-e*sin\varphi}{1+e*sin\varphi}\right]^e}$$

Latitude can be obtained from the following new formula developed by the geodesist Bidshivalf

$$B = 2\,arctan\left[\sqrt{\left[\frac{1-esinB_0}{1+esinB_0}\right]^e}.Exp(q)\right] - \frac{\pi}{2}$$

Where C' represents the reverse parameters, L represents the longitude, B is the latitude and B_0 is the central latitude.

The process is iterative so a Matlab program was developed to perform the conversion of coordinates from Cartesian to geodetic and the reverse process with the possibility to change datums as required. The program has been tested using the ordinance survey control point (GPS 12-3), the discrepancies in coordinates were close to zero and they were as a result of using 8 parameters in the program while the ordinance survey used only 5 parameters.

The Matlab program was used to convert the LGD2006 (UTM6º, International Hayford1924) network coordinates to geodetic coordinates, the results are shown in Table 2.

ISBN: 978-81-936820-6-7
Proceedings DOI: 10.21467/proceedings.4

Series: AIJR Proceedings

Table 2: *Network Cartesian and geodetic coordinates in LGD2006 (UTN6º)*

point Id	Longitude (λ)	Latitude (φ)	Easting (m)	Northing (m)
GPS12-3	13.47727320 º	32.33272965 º	356678.648	3578390.064
GPS12-4	13.48296802 º	32.33238317 º	357214.163	3578344.043
Control Point 1	13.50386317 º	32.34380816 º	359198.782	3579582.981
Control Point 2	13.57951374 º	32.35029741 º	366328.427	3580205.404
Control Point 3	13.60075344 º	32.17081670 º	368067.856	3560281.184
Control Point 4	13.62217705 º	31.98894569 º	369830.460	3540092.809
Control Point 5	13.54681925 º	31.98249019 º	362700.774	3539470.353
Control Point 6	13.52524994 º	32.16434433 º	360938.280	3559658.728
Control Point 7	13.55264639 º	31.93321194 º	370307.987	3534622.442
Control Point 8	13.62796417 º	31.93966278 º	363178.325	3533999.995

3.2.2 Comparing obtained results and ordinance survey results using geodetic formulas

The reverse geodetic formulas were used to compute the lengths of network lines to compare them to those of the ordinance survey to determine the accuracy of LGD2006 in medium-elevation areas.

To compute the distance between two points, first a number of parameters has to be calculated as following [6]:

$$e' = \sqrt{\frac{a^2 - b^2}{b^2}} \quad , \quad e = \sqrt{\frac{a^2 - b^2}{a^2}} \quad , \quad C = \frac{a^2}{b} \quad , \quad \rho = \frac{pi}{180} \quad , \quad fm = \frac{\varphi_1 + \varphi_2}{2 * \rho} \quad ,$$

$$ff = \frac{\varphi_2 - \varphi_1}{\rho} \quad , \quad Lm = \frac{\lambda_2 - \lambda_1}{\rho}$$

$$W_1 = \sqrt{(1 - e^2 \sin^2 \varphi_1)} \quad , \quad W_2 = \sqrt{(1 - e^2 \sin^2 \varphi_2)} \quad , \quad N = \frac{C}{\sqrt{(1 + H)}} \quad ,$$

$$M = \frac{N}{1 + H} \quad , \quad H = e'^2 * COS^2(fm)$$

$$\sin u_1 = \frac{\sin \varphi_1 . \sqrt{1 - e^2}}{W_1} \quad , \quad \sin u_2 = \frac{\sin \varphi_2 \sqrt{1 - e^2}}{W_2} \quad \cos u_1 = \frac{\cos \varphi_1}{W_1} \quad ,$$

$$\cos u_2 = \frac{\cos \varphi_2}{W_2}$$

$$P = \cos u_2 . \sin w \quad , \quad q = \cos u_1 . \sin u_2 - \sin u_1 . \cos u_2 \cos w$$

$$\cot x_1 = \cot u_2 . \cos \Delta w \quad , \quad \cot x_2 = \cot u_1 . \cos \Delta w$$

$$\tan \Delta\beta_{12} = \frac{\tan q}{\tan p} = \frac{\cos x_1 . \tan \Delta w}{\sin(x_1 - u_1)} \, , \, \beta_{21} = \frac{\tan q_1}{\tan p_1} = -\frac{\cos x_2 . \tan \Delta w}{\sin(x_2 - u_2)}$$

$$\beta_{21} = \beta_{12} \pm 180 + \Delta\beta$$

Using the above parameters, distances can be computed using two methods, one for short distances and the other is for long ones.

1- Geodetic formulas for short distances

$$Z = Lm\,.N\,.COS(fm)\left(1 + (1 - 9.e'^2 + 8.H^2).\frac{ff^2}{24} - \frac{(Lm\,.Sin(fm))^2}{24}\right)$$

$$Q = ff.M\left(1 - (e'^2 - 2H^2).\frac{b^2}{8} - \frac{(1+H^2)\ (Lm.COS(fm))^2}{12} - \frac{(Lm.COS(fm))^2}{8}\right)$$

$$S = \sqrt{Z^2 + Q^2}$$

2- Geodetic formulas for long distances

If the azimuth is less than 45º, the formula used is: $\tan\sigma = \frac{\tan p}{\cos\beta_{12}}$

If the azimuth is more than 45º, the formula is: $\sin\sigma = \frac{\sin q_2}{\sin\beta_{12}} = \frac{\cos u_2.\sin\Delta w}{\sin\beta_{12}}$

Where:

e, e': first and second eccentricity

u_1, u_2: reduced latitude of the point

β_{12}, β_{21}: forward and back azimuth

Δw: difference between longitudes

S: measured short distance on ellipsoid

M: meridional radius of curvature

N: radius of curvature in the prime vertical

$\Delta\beta$: convergence of meridians

p , *q*: lines lengths from spherical triangle

$\boldsymbol{\sigma}$: measured long distance on ellipsoid

Another Matlab program was developed using the above formulas to solve the reverse geodetic problems of short and long distances using LGD2006. The results are presented in Table 3.

Table 3: *Distances between network points using LGD2006*

Distance	points	$\boldsymbol{\varphi}$	$\boldsymbol{\lambda}$	Distance measured by total station	Reverse formulas for short distances	Reverse formulas for long distances
S_{6-3}	Point(cp6)	32.16434433	13.525249944	7158.019	7157.938	7157.939
	Point(cp3)	32.17081670	13.600753444			
S_{3-4}	Point(cp3)	32.17081670	13.600753444	20269.338	20268.990	20268.991
	Point(cp4)	31.98894569	13.622177055			
S_{4-5}	Point(cp4)	31.98894569	13.622177055	7158.155	7158.091	7158.092
	Point(cp5)	31.98249019	13.546819250			
S_{5-6}	Point(cp5)	31.98249019	13.546819250	20269.055	20268.500	20268.502
	Point(cp6)	32.16434433	13.525249944			
S_{4-7}	Point(cp4)	31.98894569	13.622177055	5492.236	5492.220	5492.220
	Point(cp7)	31.93966292	13.627964358			
S_{7-8}	Point(cp7)	31.93966292	13.627964358	7158.112	7158.076	7158.077
	Point(cp8)	31.93321203	13.552646394			
S_{8-5}	Point(cp8)	31.93321203	13.552646394	5492.129	5492.086	5492.086
	Point(cp5)	31.98249019	13.546819250			

ISBN: 978-81-936820-6-7
Proceedings DOI: 10.21467/proceedings.4

Series: AIJR Proceedings

Using the same Matlab program the distances were computed using the WGS84 datum, the results are shown in Table 4.

Table 4: *Distances between network points using WGS84*

Distance	points	φ	λ	Distance measured by total station	Reverse formulas for short distances	Reverse formulas for long distances
S_{6-3}	Point(cp6)	32.16467923	13.52463410	7158.019	7157.908	7157.909
	Point(cp3)	32.17115206	13.60014078			
S_{3-4}	Point(cp3)	32.17115206	13.60014078	20269.338	20268.888	20268.889
	Point(cp4)	31.98927792	13.62156647			
S_{4-5}	Point(cp4)	31.98927792	13.62156647	7158.155	7158.056	7158.057
	Point(cp5)	31.98282194	13.54620554			
S_{5-6}	Point(cp5)	31.98282194	13.54620554	20269.055	20268.401	20268.402
	Point(cp6)	32.16467923	13.52463410			
S_{4-7}	Point(cp4)	31.98927792	13.62156647	5492.236	5492.195	5492.195
	Point(cp7)	31.93999427	13.62735433			
S_{7-8}	Point(cp7)	31.93999427	13.62735433	7158.112	7158.042	7158.043
	Point(cp8)	31.93354290	13.55203324			
S_{8-5}	Point(cp8)	31.93354290	13.55203324	5492.129	5492.062	5492.062
	Point(cp5)	31.98282194	13.54620554			

3.3 Discussion of results

The field measurements by the total station is considered as a reference for the purpose of comparison. Comparing the field observations by the total station using the reverse geodetic problems, ordinance survey measurements using LGD2006, and GPS measurements using WGS84, it's clear from Table 3 and Table 4 that there are some differences between the above mentioned measurements. The distances using LGD2006 are closer to reference distances. From Table 3, the biggest difference between reference distances and short distances computed by reverse geodetic problems is 55cm which is between control points 5 and 6 and the smallest difference for short distances is 16mm which is between control points 4 and 7. For long distances using LGD2006, the results are almost the same for short distances. When WGS84 datum was used to compute the distances, either short or long, using geodetic problems (Table 4), the differences between the resulted distances and the reference ones are bigger than those obtained when using LGD2006 datum. The biggest difference is 65cm between control points 5 and 6 and the smallest difference is 41mm between control points 4 and 7.

4 Conclusion and recommendations

A triangulation network was established on a large lot of medium-elevation land using UTM6º (zone 33) and a number of field and office trials and tests were conducted to check the accuracy of LGD2006 in medium-elevation areas. The results show that the best fit datum for areas of elevations 300 to 500m is the LGD2006 and WGS84 is best for areas of low elevations.

Based on the research findings, the following recommendations are being made for possible future work.

- Another study should be made on high-elevation areas to check the suitability of LGD2006 in those areas.
- Continuing studies on the ellipsoid used in Libyan datum and its conformance with the geoid.
- Using static GPS to establish high accuracy first class ground control point in all regions of Libya.

References

[1] Edward M. Mikhail, Analysis and adjustment of survey measurements, School of Civil Engineering Purdue University-1981.
[2] Paul R. Wolf ,Elementary Surveying Ninth Edition, Civil and Environmental
[3] Saudi authority of geological survey, 1994, geodetic datum for maps and ground data systems, Saudi Arabia
[4] Bidshivalf, 2004, principles of coordinate transformation in new techniques, university of boltsk, Belorussia
[5] Ordinance survey of Libya,2006, geodetic project and map projection systems, Libyan datum, Libya.
[6] Ikreesh, Mohamed, 2012, Advanced geodetic surveying and new mapping for GIS, Libya.
[7] Dawod, Gomaa, 2012, geodetic surveying, Saudi Arabia.

ISBN: 978-81-936820-6-7
Proceedings DOI: 10.21467/proceedings.4

A Review Study of The Effect of Air Voids on Asphalt Pavement Life

Ali Mohamed Zaltuom

Department of Civil Engineering, College of Engineering, Elmergib University, Libya

DOI: https://doi.org/10.21467/proceedings.4.29
* Corresponding author email: amzaltuom@elmergib.edu.ly

ABSTRACT

Roadways play a main role in the development of the countries and societies by providing the essential links between the different parts of the country, to facilitate the transport of goods and movement of people. Compaction is one of the most critical factors associated with the performance of asphalt pavements. When the asphalt content is too high, the compact of mixture might too easily, moreover resulting in low air voids. When the asphalt content is too low, the compact of mixture may be stiff and difficult to the specified density. Asphalt pavements are constructed with initial air voids of 6-8 % depending on the type of mixture and pavement layer. Asphalt mixtures has high air voids content during constructed, it is expected to reduce and this densification can be considered as a predominant cause of rutting during initial periods of traffic. Due to air voids reduction, the material becomes stiffer leading to increase rut resistance. Such increase could also be contributed due to age hardening of the material. Inadequate compaction is one of the leading causes of early deterioration and failure of these pavements. The purpose of this paper is to review the importance and the effect of air voids on asphalt pavement lifespan. The result indicated poor compaction of the mix will leave a high percentage of air voids making it susceptible to moisture infiltration and cracking. Conversely, over compaction may cause mixes to have very low air voids making it subject to asphalt bleeding in hot weather environments.

Keywords: Asphalt Pavements, Air Voids, Fatigue , Rut Resistance.

1 Introduction

Road pavements are one of the largest infrastructure components in most of the developed nations of the world and vitally important to a country's economic development. The construction of a high quality road network directly increases a country's economic output. Roads are constructed to provide fast and safe access between important cities, the construction process will have the added effect of stimulating the construction market [1]. Everything in the life has limited age. For road pavements, wearing surfaces have a life expectancy of between 10-20 years [2]. Asphalt concrete pavements have a short life cycle [3]. Fatigue damage is one of the primary distresses in asphalt concrete pavements besides thermal cracking and rutting [4]. Asphalt consists of four main materials: bitumen, aggregate, fillers

(fine particles) and air. Asphalt without sufficient air entrapped in the layer will deform under traffic and result in a rutted and rough surface. Field air voids represent the amount of entrapped air in an asphalt layer that has been placed on-site. The objective of asphalt mix design is to achieve an asphalt mix with the lowest practicable air voids without compromising long term performance. Too many air voids and the asphalt becomes permeable to water and air, which causes reduced service life. Too few air voids and the asphalt becomes rutted and deformed under trafficking [5].

Porous asphalt is designed to provide the optimum functional and structural performance particularly the mixture's permeability, modulus and durability. However, these properties are not proportional. High air void content provided in the mixture will improve the permeability but reduces its modulus and durability [6].

2 Compaction Importance and Pavement Performance

Construction of high quality roads can help minimize pavement distresses such as rutting, cracking, and other forms of distresses, and improve the long-term performance of the pavement [7]. Compaction is one of the most important factors affecting the performance of asphalt pavements. The asphaltic layer is the most susceptible layer as it is in direct contact with the environment and traffic [8]. The volume of air in a pavement is important because it has a profound effect on long-term pavement performance [9]. Compaction is the process by which the asphalt and aggregate are compressed into a reduced volume. It is generally conceded that the compaction of asphalt concrete is one of the most critical factors associated with the performance of flexible pavements [10].

2.1 Stability

Stability can be defined as the resistance to deformation of an asphalt concrete pavement when subjected to traffic loadings under a variety of environmental conditions. A stable pavement maintains its shape and smoothness under repeated loading. In general, the stability increases as density increases with air voids decrease [13]. In this case stability is reduced by five or more points for each percent decrease in air voids [10].

2.2 Durability

The durability of asphaltic concrete has been defined as the resistance to weathering and the abrasive action of traffic (These factors can be the result of weather, traffic or a combination of the two). Good durability can be described as the ability to provide long-term performance without premature cracking or ravelling [10] [13]. The durability of asphalt concrete is largely a matter of the durability of the asphalt cement. Reduction in penetration or increase in viscosity with time. Research has shown that for a given asphalt the rate at which an asphalt hardens is related to the total air voids in the asphalt concrete. If the volume and interconnection of voids in a pavement is such that water is transmitted to the base course, the pavement may fail due to loss of strength in the base material [13].

ISBN: 978-81-936820-6-7

Series: AIJR Proceedings
Proceedings DOI: 10.21467/proceedings.4

2.3 Rutting

Figure 1 shown that at low air voids (less than 2%) the binder almost totally fills the void space between the aggregate particles, so that the mix acts as a fluid and is less resistant to rutting when subjected to heavy traffic. Poorly compacted mixes also have less resistance to rutting due to a weaker structure under traffic.

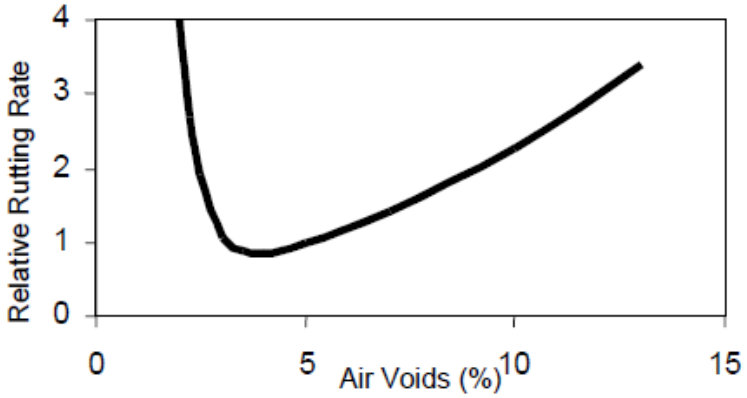

Figure 1: *Relative Rutting Rate vs Air Voids*

2.4 Fatigue Life

The air void content is important on the fatigue behaviour of asphalt concrete. Previous studies results show that high air void contents produce mixes with comparably short fatigue lives. These data suggest that variations in air void content create greater changes in fatigue life [13]. Laboratory investigations indicate that the fatigue life of asphalt concrete could be reduced by 35 percent (or more) for each one percent increase in air voids [10]. Fatigue life or resistance to cracking under repeated load, is directly proportional to the compaction level, Figure 2 shows results of fatigue testing. In this case an increase of air voids from 5% to 8% has resulted in a 50% reduction in fatigue life[15].

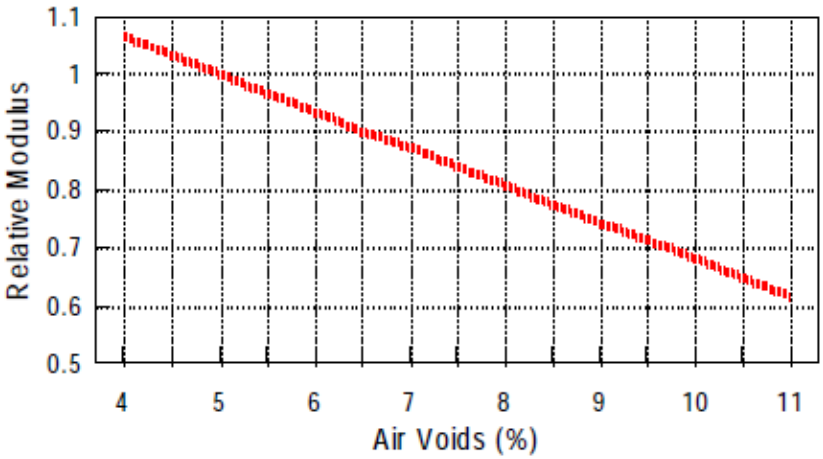

Figure 2: *Relative Fatigue Life vs Air Voids*

2.5 Strength or Stiffness

Stiffness has been shown to be dependent upon density. The investigators presented the stiffness increases with density suggesting that a more dense mixture results in greater load supporting capabilities of the material [13]. The structural strength of an asphalt mix as measured by its stiffness or modulus, is also related to compaction level. Figure 3 shows strength relative to 5% air void. In this case an increase in voids from 5% to 8% has resulted in a 20% reduction in stiffness or load carrying capacity [15].

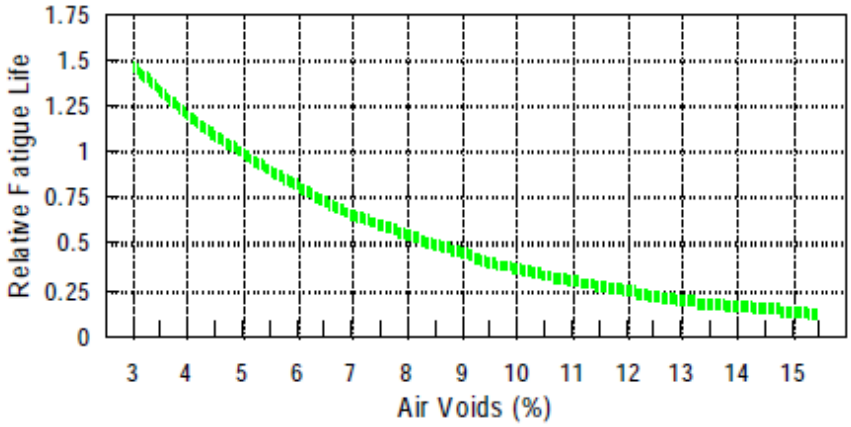

Figure 3: *Relative Strength vs. Air Voids*

2.6 Flexibility

The flexibility of an asphalt paving mixture is defined as the ability of an asphalt pavement to adjust or the ability of the mixture to conform to long-term variations in base and subgrade elevations. In general, those mixtures of acceptable stabilities with high asphalt contents and high air voids will produce mixtures with the greatest flexibility without cracking [13].

Sometimes the need for flexibility conflicts with stability requirements. For example, an open-graded mixture, which is generally more flexible, is designed to be water permeable. A dense graded mix is relatively impermeable, but is less flexible. Both can affect stability.

3 Factors effecting compaction

The purpose of compacting asphalt pavements is to density the asphalt concrete and thereby improve its mechanical properties as well as to provide a watertight segment for the underlying materials in the pavement structure [13].

Asphalt compaction is a densification process during which air voids are reduced and compaction in the field is commonly performed using vibratory compactors through the application of combined static and dynamic forces. It is necessary to reduce the air void content of asphalt as the properties of the pavement depends on its density [14].

Impact compaction relies on a high impact force. Most premature failures of asphalt pavement are concerned with poor compaction [12].

ISBN: 978-81-936820-6-7
Proceedings DOI: 10.21467/proceedings.4

Series: AIJR Proceedings

4 Design air voids

Air voids are small airspaces or pockets of air that occur between the coated aggregate particles in the final compacted mix. A certain percentage of air voids is necessary in asphalt mixes to allow for some additional pavement compaction under traffic and to provide spaces into which small amounts of asphalt can flow during this compaction [15]. Air-voids have significant influence on the properties of asphalt pavement, they causes the fatigue damage under repeated load and aggravates the strength of asphalt mixture, causing the macro crack appears in asphalt pavement [16].

Porous asphalt mixture is an open graded gradation that consists of low composition of fine aggregates to allow the mixture to have large quantity of interconnected air voids. These interconnected voids forms capillary channels for the water to flow through and reduce the water runoff from the pavement surface. This shows that the presence of air voids (interconnected and isolated voids) within the mixture is the most significant factor that influences its permeability [17].

Too much air voids also can cause the mixture having excessive aging and stripping problems , that submergence of flexible pavement in moisture over a period of time can damage the fatigue life considerably before design life is achieved [18]. On the other hand, inadequacy of air void within the mixture will lead to the loss in permeability and clogging problem [6].

Least fine materials mixture has caused the mixture to become sensitive towards the changes in voids content as shown by the sudden drop in resilient modulus and large increase in permeability and abrasion loss at high voids content. fine aggregate mixture indicates it is more durable and resilient to deformation but produces low coefficient of permeability. Therefore, any combination of materials (aggregate composition and binder) used should possess strong cohesion and adhesion properties so that a stabilized mixture can be achieved but simultaneously maintaining an open structure of the porous mixture [6].

The range of design air void values in laboratory compacted asphalt mixes is included in asphalt mix design standards. Different types of asphalt include different design air voids as shown in Table 1.

Table 1: *Design air voids [9]*

Mix Type	Marshal Method Mix Design
	Air Voids range %
L	3.8 - 4.2
H	4.9 - 5.3
V	5.9 - 6.3

Asphalt with high design air voids (H) is used for locations with heavy traffic volumes where there is potential for further compaction of the asphalt mix after placing. (V) asphalt has higher design air voids and is used for heavily trafficked intersections where there is significant

potential for further compaction of the asphalt mix after placing. As a result of the higher air voids.

Asphalt with lower design air voids (L) is used for locations with light traffic volumes where there is very little further compaction of the asphalt mix after placing. This type of asphalt achieves high levels of durability and fatigue resistance as a result of the lower air voids and provides long service life. That air void content was the most significant factor affecting on pavement performance [19]. Clearly, the in-place air voids and therefore the in-place density have a significant impact on the pavement life [20].

5 Importance of Air Voids

The asphalt should be flexible enough to resist distress. Also, compaction locks the asphalt-coated aggregate particles together to achieve stability and provide resistance to different types of deformation while simultaneously reducing the permeability of the mixture and improving its durability [14].

Previous research has shown that air-voids have significant influence on the strength and durability of asphalt mixture [16]. There is considerable evidence that dense graded mixes should not exceed 8 percent nor fall below 3 percent air voids during their service life. This is because high air void content (above 8 percent) or low air void content (below 3 percent) can cause the following pavement distresses [9].

It was also observed that the frequency of loading inversely affected the fatigue life of the asphalt concrete mixture. In other words as the rate of loading was increased the life of the pavement was decreased [18]. Reducing in density could result in reduced the air voids for asphalt mixture ,therefore could have the opposite effect leads to a loss of fatigue life and serviceability of the pavement [19].

Achieving good density of the hot mix asphalt optimizes all desirable mix properties. The result showed that as the percent of air voids increased the number of load cycles to failure representing fatigue life decreased. Thus fatigue decreases with increasing air voids.

6 Conclusions

The quality of compaction is important to the performance of asphalt pavement . Air voids are generally described as the most effective parameter to explain the behavior of the mix. High level of air voids always results in a high expectations of moisture flow within mixtures. Most premature failures of asphalt pavement are concerned with poor compaction. Increase of air voids in asphalt mixture by 1% than that of design may cause 35% decrease of pavement fatigue life and double the permeability [12].

Previous study showed that a 1% increase in air voids (above the base air void level of 7%) tends to produce about a 10% loss in pavement life [21]. The results clearly reflect the importance of air voids when drilling in the AC layer. From the figures we can see that looking at the 4% central air voids can reduce the gradual response of the material [22].

ISBN: 978-81-936820-6-7

Series: AIJR Proceedings
Proceedings DOI: 10.21467/proceedings.4

References

[1] R. Martin, "Highway Engineering," Blackwell Publishing, 2003.

[2] Australian Capital Territory, "Transport Canberra and City Services" Access online on April 2018 at https://www.tccs.act.gov.au/roads-paths/Road_Infrastucture_and_Maintenance/roadpavement.

[3] F. Onyango, Salim R. Wanjala, M. Ndege and L. Masu, "Effect of Rubber Tyre and Plastic Wastes Use in Asphalt Concrete Pavement" International Journal of Civil and Environmental Engineering, vol. 9, no. 11, pp. 1395-1399, sep, 2015. Access online on April 2018 at https://waset.org/publications/10002602/effect-of-rubber-tyre-and-plastic-wastes-use-in-asphalt-concrete-pavement.

[4] W.A. Zeiada, K.E. Kaloush, B.S. Underwood and M.S. Mamlouk, "Effect of Air Voids and Asphalt Content on Fatigue Damage Using the Viscoelastic Continuum Damage Analysis," *Conference: Airfield and Highway Pavement*, vol. pp. 1122-1133, 2013. Access online on 20 May 2018 at https://www.researchgate.net/publication/261635455_Effect_of_Air_Voids_and_Asphalt_Content_on_Fatigue_Damage_Using_the_Viscoelastic_Continuum_Damage_Analysis?enrichId=rgreq-66454f7fd59a7b9c6301de2f33375701-XXX&enrichSource=Y292ZXJQYWdlOzI2MTYzNTQ1NTtBUzozMjU3NjQ1NjMxMjgzMzlAMTQ1NDY3OTczMjg4Mg%3D%3D&el=1_x_2&_esc=publicationCoverPdf

[5] A. Papacostas and C. Simpson, "Air voids in asphalt," PAVERTREND, 2016. Access online on MaY 2018 at http://www.pavertrend.com.au/index.php/asphalt/air-voids-in-asphalt?showall=&limitstart=

[6] . Abdul Hassan, M. Mahmud, N. Adi, N. Rahmat, M. Hainin and R. P. Jaya, "Effects of Air Voids Content on The Performance of Porous Asphalt Mixture," Journal of Engineering and Applied Sciences, vol. 11, no. 20, pp. . 11884-11887, ARPN. October 2016.

[7] B. A. Chadbourn, E. L. Skok, B.L. Crow, D. E. Newcomb and S. Spindler "The Effect of Voids in Mineral Aggregate (VMA) on Hot-Mix Asphalt pavements," Final report, March, 2000. Minnesota Department of Transportation Office of Research Serices, Ireland, Boulevard.

[8] S. Badeli, A. Carter and G. Doré, "Importance of Asphalt Mixture Air Voids on the Damage Evolution During Freeze-Thaw Cycles," *Conference: Canadian Technical Asphalt Association*, November, 2016. Access online on March 2018 at https://www.researchgate.net/publication/308890481_The_Importance_of_Asphalt_Mixture_Air_Voids_on_the_Damage_Evolution_During_Freeze-Thaw_Cycles

[9] Pavement Interactive, "Compaction Importance," 2012. Access online on March 2018 at http://www.pavementinteractive.org/compaction-importance/

[10] F. N. Finn and J. A. Epps, "Compaction of Hot Mix Asphalt Concrete," Research Report 214-21, Texas Transportation Institute, The Texas A&M University System College Station, August 1980.

[11] A. Behl, and S. Chandra and , "Compaction Characteristics and Performance of Warm mix Asphalt"8th International Conference on maintenance and Rehabilitation of Pavements. July, 2016. Access online on 5 March 2018 at http://rpsonline.com.sg/proceedings/9789811104497/html/037.xml

[12] G. Ying , H. Xiaoming and Y. Wenbin, "The compaction characteristics of hot mixed asphalt mixtures," Journal of Wuhan University of Technology-Mater. Sci. Ed, vol. 29, no. 5, pp. 956-959, GAO. October, 2014. Access online on March 2018 at https://link.springer.com/article/10.1007/s11595-014-1027-z.

[13] J. A. Epps, B. M. Gallaway, W. J. Harper, W. W. Scott and J. W. Seay "Compaction of Asphalt Concrete Pavements," *Research Report 90-2F*, Texas Transportation Institute, Texas A&M University College Station, Texas. July 1969.

[14] F. Beainy, S. Commuri and M. Zaman, "Asphalt compaction quality control using Artificial Neural Network," 49th *IEEE Conference on Decision and Control*, CDC. 2010.

[15] AUSTROADS in conjunction with AAPA, "Pavement Work Tips," no. 17, pp. June, 1999. Access online on April 2018 at http://www.pavementengineering.com.au/wp-content/uploads/2015/12/Pavement-Work-Tips.pdf

[16] H. Jing, L. Pengfei and S. Bernhard "A study on fatigue damage of asphalt mixture under different compaction using 3D-microstructural characteristics," *Frontiers of Structural and Civil Engineerring*, vol. 11, no. 3, pp. 329-337. September, 2017. Access online on 5 March 2018 at https://link.springer.com/article/10.1007/s11709-017-0407-9

[17] N. Abdul Hassan, M. Z. H. Mahmud, N. Adi, N. Rahmat, M. R. Hainin and R. P. Jaya "Effects of Air Voids Content on the Performance of Porous Asphalt Mixtures," *Engineering and Applied Sciences*, vol. 11, no. 20, pp. 11884-

11887, ARPN. October, 2016. Access online on 5 March 2018 at http://www.arpnjournals.org/jeas/research_papers/rp_2016/jeas_1016_5163.pdf

[18] E. A. Igwe and K. I. Amadi-oparaeli "A Proof of Moisture Damage on Fatigue Life of Flexible Pavement Submerged in Water ," *Journal of Scientific and Engineering Research*, vol. 4, no. 9, pp. 210-216, JSERBR. 2017. Access online on 5 March 2018 at http://jsaer.com/download/vol-4-iss-9-2017/JSAER2017-04-09-210-216.pdf

[19] H. Y. Ahmed, "Methodology for Determining Most Suitable Compaction Temperatures for hot Mix Asphalt," *Journal of Engineering Sciences*, vol. 33, no. 4, pp. 1235-1253. July, 2005. Access online on 5 June 2018 at http://www.aun.edu.eg/journal_files/181_J_9085.pdf

[20] Transportation Research Circular, "Factors Affecting Compaction of Asphalt Pavements," General Issues in Asphalt Technology Committee, Number E-C105.Washington September, 2006. Access online on 5 May 2018 at http://onlinepubs.trb.org/onlinepubs/circulars/ec105.pdf

[21] L. N. Robert,M. P. Joe, and J. C. Newton "Effect of compaction on asphalt concrete performance," *Transportation Research Record*, no. 1217, pp. 20-28, Abbrev. March, 1990. Access online on March 2018 at http://onlinepubs.trb.org/Onlinepubs/trr/1989/1217/1217-003.pdf

[22] R. Neethu, A. Veeraragavan and J. M. Krishnan "Influence of Air Voids of Hot Mix Asphalt on Rutting Within the Framework of Mechanistic-Empirical Pavement Design," *2nd Conference of Transportation Research Group of India*, Procedia - Social and Behavioral Sciences 104, pp. 99-108, 2nd CTRG. 2013. Access online on May 2018 at https://www.sciencedirect.com/science/article/pii/S1877042813044935.

ISBN: 978-81-936820-6-7

Series: AIJR Proceedings
Proceedings DOI: 10.21467/proceedings.4

Modeling and Finite Element Analysis of Leaf Spring Using Pro-Engineer and ANSYS Softwares

Salem Elsheltat[1*], Abdulbaset Alshara [2] , Walid Elshara [3]

[1] Department of Mechanical Engineering, College of Engineering, Misurata University, Libya
[2,3] Department of Medical & Electromechanical Engineering, College of Medical Technology-Misurata, National Board for Technical and Vocational Education, Libya

DOI: https://doi.org/10.21467/proceedings.4.30
* Corresponding author email: salem.sheltat@eng.misuratau.edu.ly

ABSTRACT

Leaf spring is an important mechanism of suspension system in vehicles that is still widely used. In automotive industry, the motivation is to increase the capability to produce vehicles of inordinate quality at best prices. For saving the natural resources, reducing the weight of vehicle is constantly the priority of car manufacturing. While decreasing the weight of an automobile, engineering designers should consider the strength of materials and the size of components. This deigned leaf spring is built up of several plates with steel material, but the steel leaf spring has an excessive weight .The weight of leaf spring may perhaps be reduced by using strength materials, and reducing the thickness of leafs. The purpose of this paper is to study the deformations and stresses of the current design of leaf spring under static and dynamic loading conditions. The system of this leaf spring is designed to minimize the vibration forces that a vehicle confronts when moving on a surface. This leaf spring has been sketched via Pro-Engineer software, and analyzed through ANSYS. As a result of the conducted stress study, the deformations due to the static and dynamic loading are determined along the leaf spring. The main point of the analysis study is to improve the quality of this design for a leaf spring with a longer life, and achieve a big reduction in vibration forces; for the cost reduction, modification is carried out by varying the thickness of spring leaves; and an optimization study is accompanied to satisfy the allowable values of deformation and the factor of safety by changing the size of meshing elements. Altogether analytically calculated values of deformations and stresses are someway comparable to the values obtained from ANSYS.

Keywords: Leaf spring, Modeling, FEA, Deformation, Safety factor.

1 Introduction

When an engineering designer desires stiffness, negligible deflection is an adequate approach, as long as it does not destruct function. Elasticity is often required and is regularly provided by solid bodies with specific geometries. These bodies can give flexibility to the degree the designer strives for. This flexibility varies linearly or nonlinearly with applied loads. For the significance of machinery to engineering designers, springs have been comprehensively

 ISBN: 978-81-936820-6-7

investigated. Furthermore, there are world-wide rapid developments of mass-production techniques for making low cost ingenious springs .Mostly, springs are assorted as flat springs, wire springs, or special designed springs. Flat springs are compartmentalized into cantilever and elliptical shapes [1]. Leaf springs are widely used for the suspension system in cars and commercial vehicles to absorb vibrations and shocks. The spring is made of multi leaves with different lengths. The spring leaf is designed of an arc-shape. The inner leaf is the tallest blade and bent from both ends to form two holes where the spring should be attached to the frame of the vehicle. The outer blades are shorter than the inner blades, and those blades are all held up using bolts and rebound clips. The spring is attached from its centre to the axle of the vehicle. Importantly, the spring should be fixed from the front eye of the master blade to the vehicle's frame and freely in vertical motion from the rear [2]. For simplicity of the calculations, the bending stresses and deformations in laminated leaf springs are determined from formatted standard equations for simply supported beams. The main components (master leaf, graduated leaf, eye, camber, span, central clamp, rebound clips) of a semi-elliptic leaf spring are shown in figure 1.

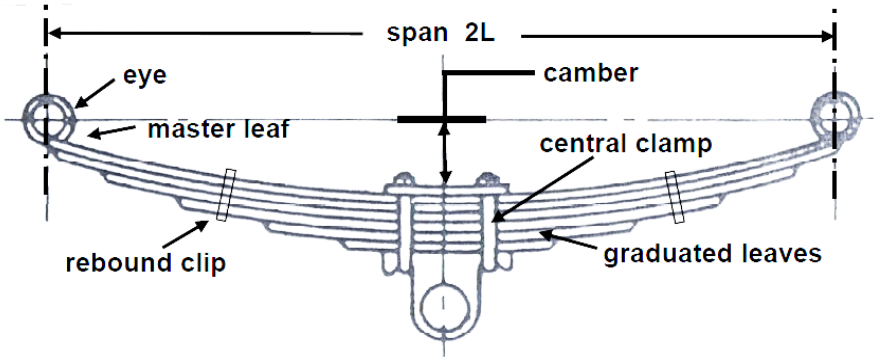

Figure 13 Semi-elliptic leaf spring [2].

1.1 Literature Survey

Some of the pervious studying papers that have done an excellent contribution are mentioned in this paragraph. Sarika Yede and Sheikh [3] modelled and finite element analysed a leaf spring made of different materials. The study concluded that from the comparison of different materials that glass fibre is better than composite material and EN-45 Steel. Amitkumar Magdum [4] analysed leaf springs using finite element methods considering the dynamic effect on stability of vehicle. The work concluded that the best harmonic response of a spring depends on the different materials and loads. The capacity to absorb energy is more in composite materials and less in steels. Shiva Shankar and Vijayarangan [5] designed and fabricated a composite mono leaf spring and tested it under loading conditions, and compared it to the steel spring. They concluded that more stresses are occurred in the steel spring than they are in the composite spring when subjected to the same loading condition. Also, they found out that the natural frequency is higher in the composite spring. Mahesh Khot and Sameer Shaikh [6] carried out a FEA analysis and did an experimental study on a leaf spring

ISBN: 978-81-936820-6-7

Series: AIJR Proceedings
Proceedings DOI: 10.21467/proceedings.4

made of a composite material and found out that this material can offer advantages in strength, light weight relative to conventional metallic materials. Trivedi Achyut and Bhoraniya [7] performed static and dynamic analysis on leaf Springs, the research concluded that with respect to conventional steel leaf spring composites having high strength to weight ration. Also, composites have less weight than conventional steel leaf spring. G Harinath Gowd and E Venugopal Goud [8] modelled a leaf spring and carried out a static analysis using ANSYS software and they concluded that the maximum stress is developed at the inner side of the eye sections. They recommended that the selected material must have good ductility, resilience and toughness to avoid sudden fracture for providing safety and comfort to the occupants. S. Karditsas, and others [9] have shown design process using finite element method (FEM) and simulation and tested a parabolic 2-leaf-spring for front axles of heavy duty under operating conditions. The stress limitations were exceeded and approximately uniform stress distribution was achieved along the length of the two leaves.

1.2 Problem Statement

This deigned leaf spring is built up of several plates with steel material, but the steel leaf spring has an excessive weight. The weight of leaf spring may perhaps be reduced by using strength materials, and reducing the leaf thickness. Another worry, due to the concentration of stresses at the sudden change of cross sections of the spring geometry, failure might occur at the eyes of the spring and at the portions around the central hole of the spring. Hence, stress analysis study is needed to be carried out on the entire geometry of the leaf spring.

1.3 Objectives of This Work

Firstly, a mathematical model will be developed for studying the deformations and stresses of the current design of leaf spring under loading conditions**.** Secondly, this leaf spring will be sketched via Pro-Engineer software, and analysed through ANSYS. The main point of the stress investigation is to improve the quality of this design for a leaf spring with a longer life, and achieve a big reduction in vibration forces. Thirdly, for the cost reduction, modifications will be carried out by varying the thickness of spring leaves. Fourthly, an optimization study will be accompanied to satisfy the allowable values of deformation and factor of safety by changing the size of meshing elements. Lastly, the results will be verified by comparison of the solution of analytical analysis and FEA.

2 Materials and Methods

The most common material that has been used widely in the world for the leaf spring industry is conventional steel. The advantages of using Steel are local availability, low cost, high strength. The selected material for the designed laminated leaf spring has mechanical properties such as Young's modulus of 200 GPa, tensile strength of 880 MPa, yield strength of 600 MPa, Fatigue of 275 MPa, and Poisson's ratio of 0.3 [10].

2.1 CAD Modelling via Pro/Engineer

Pro/E is a suite of programs that are used in the design, analysis, and manufacturing of a virtually unlimited range of products. Its field of application is generally mechanical engineering design, although recent additions to the program are targets at ship building and structural steel framework as well [11]. In this current paper, a computer model creation using the powerful design tool (Pro/Engineer) is to be carried out for a laminated leaf spring. The geometry of the spring has dimensions of (number of spring leaf (n=4), Length of span of the spring (2L=1000 mm), thickness of leaf (t = 10 mm), width of leaf (b = 220 mm)). Assuming that the total load of 140 KN is applied on the spring, and the material assigned to the leaf spring has an allowable deflection of (49.72 mm). Figure 2 shows the 3D solid model of the leaf spring that sketched via Pro/Engineer, this model is to be exported for a simulation via ANSYS software.

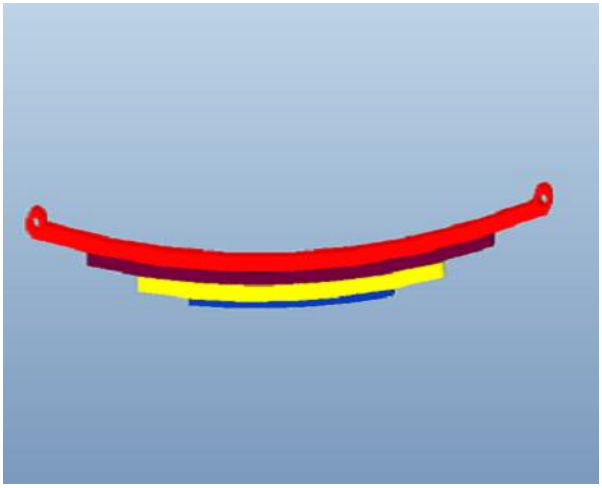

Figure 2: Pro-E model of the designed leaf spring

2.2 Finite Element Analysis via ANSYS

Finite element method (FEM) is a numerical method for solving differential equations that describe many engineering problems. One of the reasons for FEM's popularity is that the method results in computer programs versatile in nature that can solve many practical problems with a small amount of training .Capitalizing on an engineer knowledge of mechanics, reinforcing an engineer knowledge, and solving problems that can only be tackled numerically on the computer, using software tools like ANSYS, Pro/E, SolidWorks [12]. The goal of numerical simulation is to make predictions concerning the response of physical systems to various kinds of excitation and, based on those predictions, make informed decisions. To achieve this goal, mathematical models are defined and corresponding numerical solutions are computed. The main elements of numerical simulation and associated errors are summarized among these five stages: physical reality, mathematical model, numerical solutions, predictions and decision [13].

ISBN: 978-81-936820-6-7
Proceedings DOI: 10.21467/proceedings.4

Series: AIJR Proceedings

2.3 Simulation Steps in ANSYS

All real-life structures are three-dimensional. It is engineers who make the approximation as a one-dimensional (e.g., beam) or a two-dimensional (e.g., plane or plane solid) structure. When the stresses on a plane normal to one of the axes are approximately zero, then the solid is assumed in the state of plane stress. Similarly, when the corresponding strains are zero, the solid is in the state of plane strain [11].

In this current work, the leaf spring can be assumed to be solved as a beam element, using different sizes of elements. A static structure study is to be carried out using ANSYS 15 beginning with assigning the engineering data of the material used in this design, and going through the following steps.

2.4 Geometry and Boundary Conditions

When starting a static structure study in ANSYS, geometry has to be defined. The Pro-E model of a leaf spring is imported to ANSYS. The boundary conditions are to be specified. Figure 3 shows the static structure of the spring, where fixed supports are applied at both eyes and load (F= 7868.3 Ibf) is vertically applied as shown in figure 3.

2.5 Finite Element Discretization

We can discretize the geometry of the domain, depending on its shape, into a mesh of more than one type of element (by shape or order). For example, in the approximation of an irregular domain, we can use a combination of rectangles and triangles. However, the element interfaces must be compatible in the sense that solution is continuous [14]. For this case of study, the geometry of the leaf spring can be meshed by creating rectangle meshing type with element size of 0.3 in, 44950 elements, and 221503 nodes. . Figure 4 shows the finite element discretization of the laminated leaf spring.

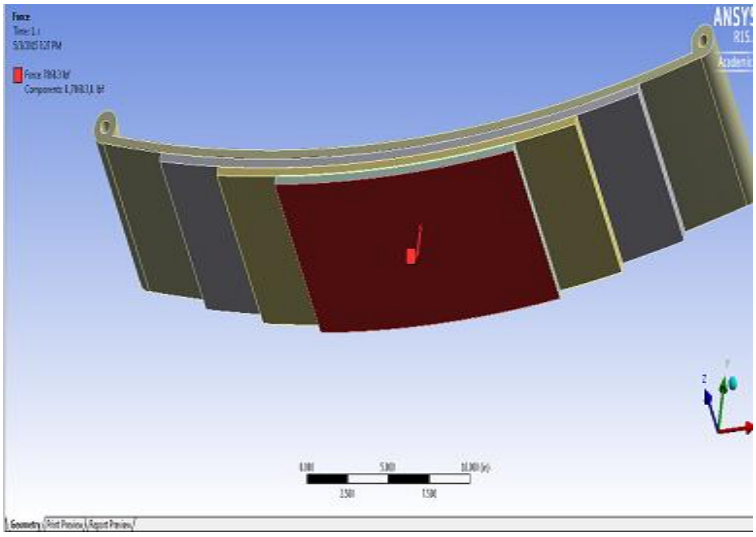

Figure 3: Static structure of laminated leaf spring

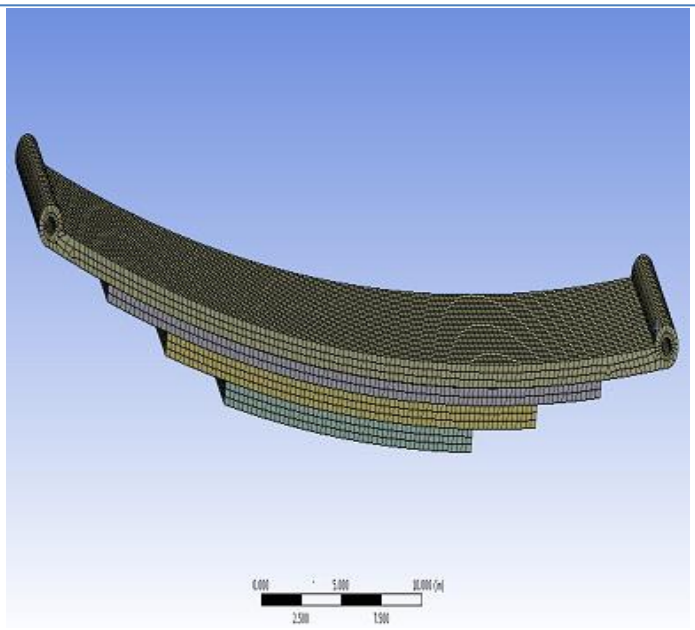

Figure 4: Finite element discretization of the leaf spring

3 Theory and Calculation

Laminated leaf spring can be assumed to be a beam of layers, which is fixed from one end and loaded from the other end. Figure 5 shows a simple cantilever type leaf spring. Considering a cantilever beam with the same length of span (2L), width (b), and thickness (t) of the designed leaf spring and subjected to the load (F) [2].

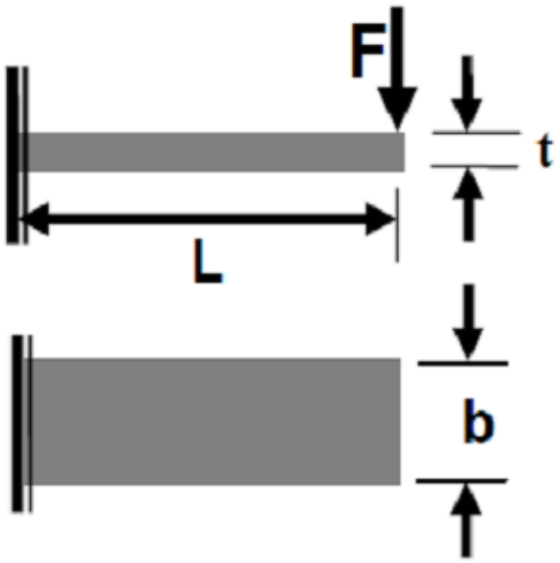

Figure 5: Simple cantilever type leaf spring [2]

ISBN: 978-81-936820-6-7
Proceedings DOI: 10.21467/proceedings.4

Series: AIJR Proceedings

3.1 Stresses and Deformation Equations

From the basic equations of bending stress and deflection of beam, the maximum bending stress(σ_{max}), maximum deflection (δ_{max}), Von Mises stress (σ_v), and factor of safety (F.S) can be calculated from the following formulas [1], [2].

$$\sigma_{max} = \frac{6\,F\,L}{n\,b\,t^2} \quad (1)$$

$$\delta_{max} = \frac{4\,F\,L^3}{n\,Y_a b\,t^3} \quad (2)$$

$$\sigma_v = \sqrt{{\sigma_{max}}^2 + 3\tau_{max}^2} \quad (3)$$

$$f.s = \frac{\sigma_y}{\sigma_v} \quad (4)$$

Where: maximum shear stress in the beam ($\tau_{max} = F/A$), A is the cross section of the beam (A= b*t), σ_y is the yield stress, and Y_a is Young's modulus for the material as previously specified.

4 Results and Discussion

From the beam equations that introduced in the previous section, the applied load is varied by an increment of 500 N, the corresponding maximum stresses, Von Misses Stresses and deformations are determined; the maximum load that this current leaf spring can bear without failing based on safety factor is 17500 N. Those equations are coded to the equations window of the Engineering Equation Solver (EES) software, and then solved. Table 1 shows the relations among the applied load (F), the maximum stress(σ_{max}), Von Mises stress (σ_v), maximum deflection (δ_{max}), and factor of safety o (F.S) for the leaf spring.

Table 1: Variation stresses and deformations with load

F (N)	σ_{max} (Pa)	δ_{max} (m)	σ_v (Pa)	F.S
7000	2.386E+08	0.01989	2.387E+08	2.514
9500	3.239E+08	0.02699	3.239E+08	1.852
10500	3.580E+08	0.02983	3.580E+08	1.676
11500	3.920E+08	0.03267	3.921E+08	1.53
12500	4.261E+08	0.03551	4.262E+08	1.408
13500	4.602E+08	0.03835	4.603E+08	1.303
14500	4.943E+08	0.04119	4.944E+08	1.213
15500	5.284E+08	0.04403	5.285E+08	1.135
16500	5.625E+08	0.04688	5.626E+08	1.066
17500	5.966E+08	0.04972	5.967E+08	1.005

4.1 ANSYS Simulation Solution

Based on the design parameters that have been specified for the leaf spring and from table 1 the critical applied load can be assumed to be 17500 N.

4.2 Distribution of Stresses, Deformations, and Factor of Safety

For thickness of 10 mm with mesh size of 0.3in, the stresses are calculated using the tool of beam results in ANSYS, all analysis results are illustrated in the following figures. Figure 6, shows the variation of Von Mises stresses caused to the leaf spring, and figure 7 is shown the corresponding total deformation in the leaves of the spring. For verification of this numerical results, firstly the maximum deformation and stress occurred at the areas around the force's applied point, which is the centre of the leaf, secondly the concentration of the stress accumulated at the eyes of the leaf spring.

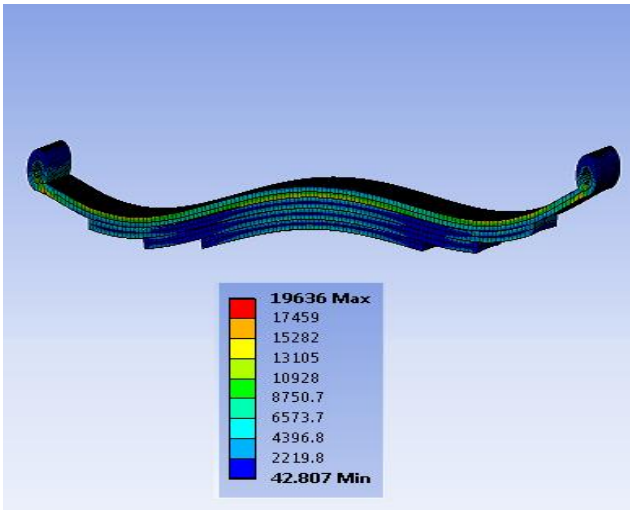

Figure 6: Von-Mises stress distribution (unites in psi)

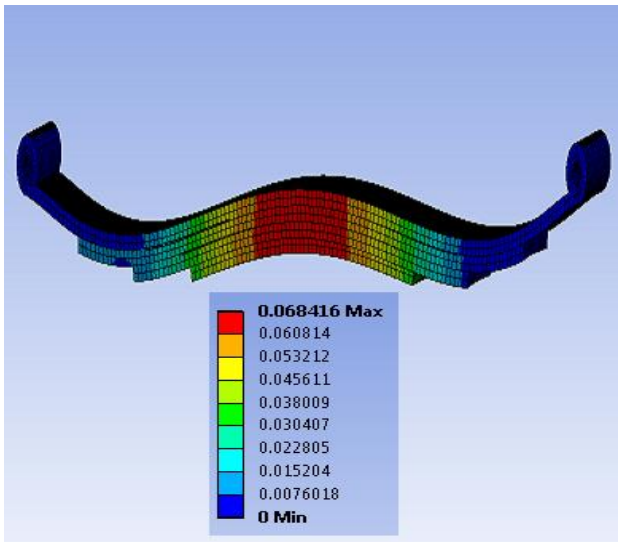

Figure 7: Total deformation distribution (unites in inches)

ISBN: 978-81-936820-6-7
Proceedings DOI: 10.21467/proceedings.4

Series: AIJR Proceedings

The safety factor for each element of this design is plotted in figure 8, since the safety factor is affected directly by the maximum stress, the minimum factor of safety occurred at the stress concentration areas of the spring. The numerical solution supports the design of the spring proposed in this work with safety factor of 1.8, which is good enough to be used in the car applications, with a convincing life span.

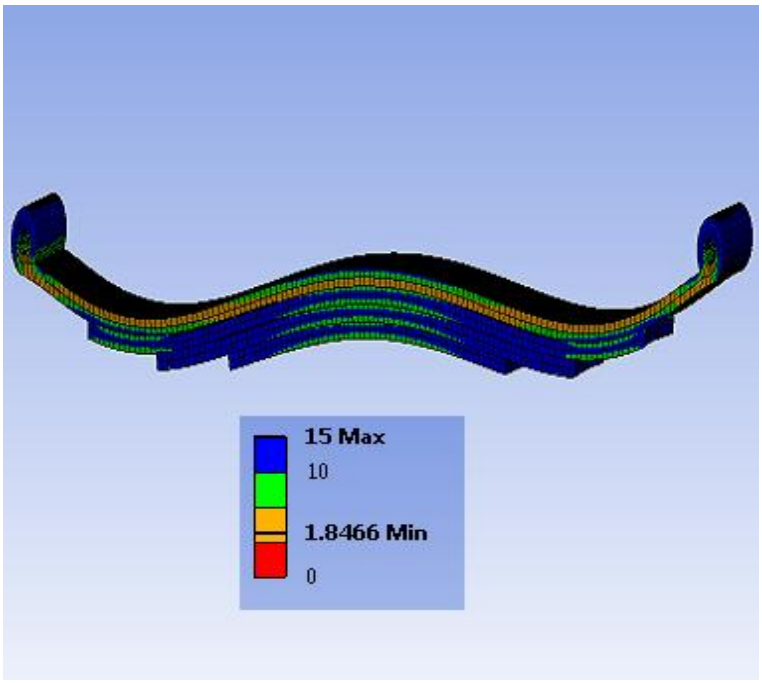

Figure 8: Safety factor distribution for the leaf spring

4.3 Design Parameter Variation

The leaf thickness is one of the important design parameter that should be varied in favour of reducing weight. ANSYS has a powerful simulation tool for changing the parameters, and the corresponding solutions can provide such a great visualization that helps the engineers for making their decisions. In this work as it's shown in table 2, stresses, deformations, safety factors are determined for each different value of the leaf thickness. From the table 2, its noticeable that as the thickness is increased, the better safety factor is achieved .However, engineers, should be worried about the weight and cost of the product.

Table 2: Variation thickness with stress, deformations, and Safety factors

Thickness (mm)	Mesh Element size (in)	Von-Mises Stress (psi)	Deformation (in)	Safety Factor
10	0.3	19636	0.068416	1.8466
15	0.3	9406	0.02281	3.8549
25	0.3	6876.6	0.015006	5.2729

4.4 Convergence Study

A convergence study is performed by varying the size of mesh element. Increasing the size of meshing element will reduce the number of equations that ANSYS solve. Therefore, the computer with higher specifications is required for less running waiting time. The disadvantage of increasing element meshing size is that it is not possible to create a mesh that precisely covers the entire area for a complicated geometry. This approximated solution will lead to deviations from the exact solutions. At the moment, the version of the simulator used in this work is academic and not able to perform a concise advanced study, but the principle of the converge study is applied by increasing the size of element for meshing the entire geometry of the leaf spring. The stresses and deformations are determined as it's shown in table 3. The mesh size of 0.3 with 44950 elements and 221503 nodes is the optimal meshing size among the options stated in this particular work in table 3.

In future studies, the mesh size should be reduced to its minimum to find the exact solutions, and to obtain a better decision for competitive design. The recommended analysis to complete this convergence study for obtaining more satisfying results is to reduce the element size of meshing by 0.1 in. This would increase the number of elements and nodes. In each step, run the solve tool to collect the results, and repeat this step until a no change in results is noticed. Consider the last mesh to be optical for your design and advanced studies. The numbers of elements and nodes might exceed millions, so keep in mind that high computer specifications are needed.

Table 3: Convergence study

Meshing Size (in)	Stress (Psi)	Deformation (in)
0.5	16146	0.0080364
1	14600	0.0079407
2	17108	0.0079639

5 Conclusions

In leaf spring world industry, reducing weight, and increasing strength are always the main matter in order to yield a competitive product. For that reason, the weight of leaf spring was reduced by using strength steal material, and reducing the thickness of leaves of the desired laminated spring. The geometry of spring was modelled using Pro/E and statically structurally analyzed using ANSYS. The Finite element analysis was the selected method for stress and deformation distributions. The thickness of the spring was varied with stresses and deformations. Based on a convergence study for the accuracy of the results obtained from FEM, the meshing element size is selected to be 0.3 inches for this current condition.

The theoretical results and finite element method solutions are somehow deviated, so an experimental solution is recommended for future studies. Finally, the optimal design steel leaf spring was made up of four plates with thickness of 10 mm, span of 1000 mm, and width of

ISBN: 978-81-936820-6-7
Proceedings DOI: 10.21467/proceedings.4

Series: AIJR Proceedings

220 mm. The steel material that is used in this spring should have a yield stress of 600Mpa and subjected to a load less than 17500 N. If heavier loads are desired, we recommend using a composite material that is lighter and has a better stiffness, though the cost reduction should be questioned.

6 References

[1] Richard Gordon, Keith Nisbett, "Shigly's Mechanical Engineering Design, " *The McGraw-Hill Companies*, Ninth Edition, ISBN. 978–0–07–352928–8, 2009.

[2]] R.S. Khurmi, J.K. Gupta,, "A textbook of Machine Design," *Eurasia Publishing*, year 2005.

[3] Sarika S. Yede, M. J. Sheikh, "Modeling and Finite Element Analysis of Leaf Spring," *International Journal of Computer Applications*, Proceedings on ICQUEST, no. 2, pp. 24-26, IJCA.2014,. Access online on 02 April 2018 at https://www.ijcaonline.org/proceedings/icquest/number2/18697-1548

[4] Amitkumar Magdum, "Dynamic Analysis of Leaf Spring Using ANSYS," *International Journal of modern Trends in Engineering and Research*, vol. 3, Issue. 10, pp. 51-59, IJMTER.. October, 2016. Access online on 10 April 2018 at https://www.ijmter.com/past-issues/

[5] G.S .Shiva Shankar, Sambagam Vijayarangan, "Mono Composite Leaf Spring for Light Weight Vehicle – Design, End Joint Analysis and Testing," *Materials Science (MEDŽIAGOTYRA)*, vol.12, No.3, pp. 220-225, MSM.. 2006. Received 20 June 2005; accepted 07 April 2006.

[6] Mahesh A. Khot , Sameer M. Shaikh, "Finite Element Analysis and Experimental Study of Composite Leaf Spring," *International Journal of Innovations in Engineering Research and Technology*, vol.3, Issue.1, pp. 01-09, IJIERT. January, 2016. Access online on 15 April 2018 at http://www.ijiert.org/vol_iss.php?id=17

[7] Trivedi Achyut V, R.M. Bhoraniya, "Static and Dynamic Analysis of Automobile Leaf Spring (TATA ACE)," *International Journal of Science Technology & Engineering*, vol.1, Issue.11, pp. 151-156, IJSTE. May, 2015. Access online on 10 May 2018 at http://ijste.org/index.php?p=Archieve&v=1&i=11.

[8] G Harinath Gowd, E Venugopal Goud, "Static Analysis of Leaf Spring," *International Journal of Engineering Science and Technology*, vol.4, No.8, pp. 3794-3803, IJEST. August, 2012.

[9] S. Karditsas, G. Savaidis, A. Mihailidis, "Leaf springs – Design, calculation and testing requirements," *35th International Conference on Mechanics and Materials, At Faliraki, Greece*, pp. 117-126, ICMMFG. June, 2014.

[10] SushilB.Chopade, Prof.K.M.Narkar, Pratik K Satav, "Design and Analysis of E-Glass/Epoxy Composite Monoleaf Spring for Light Vehicle," *International Journal of Innovative Research in Science Engineering and Technology*, vol..4, Issue.1, pp. 18801-18808, IJIRSET. January, 2015.

[11] Roger Toogood, "Pro/Engineer Wildfire 3.0 Tutorial and Multimedia CD," *SDC Publications Schroff Development Corporation*, ISBN.978-1-58503-307-2, 2006.

[12] Nam-Ho Kim, Bhavani V.Sankar, "Introduction to Finite Element Analysis and Design," *John Wiley and Sons,Inc*, ISBN.978-0-470-12539-7, 2009.

[13] Barna Szabo, Ivo Babuska, "Introduction to Finite Element Analysis Formulations, Verification and Validation ," *John Wiley and Sons,Inc* ,First Edition, ISBN.978-0-470-97728-6, 2011.

[14] J.N.Reddy, "An Introduction to the Finite Element Method Formulations, Verification and Validation ," *The McGraw-Hill Companies*, Third Edition, ISBN.13-978-0-07-060741-5.

Influence of Plastic Bottles Fibre on Self Compacting Concrete

Abdelhamed Ganaw*, Basel Meghari, Abdulnasir Alkoum , Mohammed Alawig

Department of Civil, College of Engineering, Elmergib University, Libya

DOI: https://doi.org/10.21467/proceedings.4.31

* Corresponding author email: engnaw12@gmail.com

ABSTRACT

It is well known to all of us that water plastic bottles waste has become a major problem to the environment. At the same time, incorporating the fibres in concrete like polypropylene is advantageous as they improve its properties. Nowadays self compacting concrete (SCC) has become very common in casting concrete due to its high flow properties and attained the required strength.

The aim of this research is to study the effect of addition of shredded waste water plastic bottles to the constituents of SCC and comparing the results with those resulted from employing polypropylene fibre available in the market to the mix.

In the study, SCC was produced at constant water content of 0.4 with the addition of constant super-plasticizer of 2% of cement weight, four fibre contents of 0.05, 0.075, 0.1 and 0.125 of the cement weight were employed to the mix, and then fresh and hardened properties of concrete were measured. From the results obtained, it was clearly observed that fresh and hardened properties of SCC can be obtained by using fibres produced from recycled water plastic bottles, and that off course will help in minimizing the pollution of environment.

Keywords: Self compacting concrete, polypropylene, plastic bottles and super-plasticizer

1 Introduction

Fibre has been used in concrete for many years because of their advantages; they increase concrete strength and sometimes prevent sudden failure in concrete. Natural and manufactured fibres are used in concrete to improve its properties [1]. Natural fibre of plants like Bamboo was added to concrete and resulted in little increase of its compressive strength and higher modulus of elasticity compared with reference concrete [2]. Manufactured fibres have been also used in concrete like, steel, glass, carbon, and Petrochemicals products fibres like polypropylene (PP), polyethylene (PET), polyester and nylon are also used in concrete production industry, and they improve its properties. Steel fibres are the most common fibres used in concrete they are available in the market with different lengths and shapes [3]. For instant, increase of steel fibres addition in concrete from 0.5% to 2% by volume resulted in an increase of concrete strength [4]. Moreover, flexure strength of concrete beams was increased by using steel fibres at percentages of 0.75 % and 1.5% by volume at 7, 14 and 28 days [5].

 ISBN: 978-81-936820-6-7

Fibre glass was also employed in concrete production at 0.03% by volume and resulted in an increase of concrete compressive and flexure strength up to 30% [6]. Polyethylene fibre was used in Indonesia in the production of self compacting concrete (SCC), percentages of up to 0.15 % of mix volume were used in concrete, however flow of concrete was decreased but still in the range and hardened concrete compressive and impact strength were good when fibre added in the range of 0.05 to 0.1%[7]. Polyethylene shredded fibres from water drinking bottles at slices of 2*10 mm are added to the concrete at 0.16 and 0.325 % of concrete volume, the results of hard concrete showed that compressive and flexure strength have been increased compared with reference concrete[8]. It is obviously that using fibres in concrete generally improves its properties which leads to the need to study both natural and manufactured fibres, moreover study of using of waste materials like drinking water bottles showed good results in concrete production but still a lack of such study on its effect on self compacting concrete, in this research the effect of such fibres on concrete will be done.

2 Materials Used

Portland cement used in concrete production was imported from Albourg Factory - Zliten, cement fineness of 3100 cm^2/g, soundness of 1.5mm and specific gravity of 3.15. Its properties were satisfied by British specifications [9]. Water used in this work was drinkable and satisfied by Libyan specifications [10]. Superplasticizer(SP)(Degasetpc7070) from (Yapichem) company was added to concrete mix at 2% of the cement weight, and its properties are accepted by European specification [11]. The used fine aggregate in the study was also imported From Zliten quarries, its gradation is accepted by the British standards BS 882:1992 [12], and has specific gravity of 2.65 and absorption of 0.0124. Coarse aggregate was imported from local quarry to produce SCC, it was passed from 20mm sieve and retained on 14, 10 and 5 mm sieves, and it was comply to the British standards BS 882:1992 [12]. Coarse aggregate has specific gravity of 2.67 and absorption of 0.0136. Aggregate gradations, specific gravity and absorption tests were carried out at the Alkhums School of engineering concrete lab. PP fibres (MonofilamentFibres, Sika) are available in the market were used in the study [13], PET fibres were produced from shredding of drinking water bottle, Figures 1 and compared with PP, Figure 2 (They are PET and PP from left to right).

3 Methodology of the research

Nine different mix proportions were designed in the study after defining the required water cement ratio (w/c=0.4) ratio and SP required to give high workability for SCC without segregation and that was obtained from experimental work of trial mixes in the lab. The first mix did not contain any fibre, and then PP and PET fibres were employed each at 0.05, 0.075, 0.1 and 0.125 %. Fresh concrete first produced by normal mixer in the concrete lab, slump flow test for SCC and J ring tests were carried out according to the British specifications [14, 15], all fresh concrete mixes were able to pass through the bars of J-Ring and gave the required

workability for Self compacting concrete. After that concrete was casted in three 100 mm cubes and three prisms of 400*100*100 mm and left in their moulds, no vibration was employed for SCC. After 24 hours concrete samples were extracted from their moulds and left merged in water. Finally, after 28 days, compressive and flexure strengths of SCC were measured.

4 Results and Discussion

4.1 Fresh properties of concrete

Table 1 shows fresh concrete spread diameter test results of reference and the highest fiber content mixes of 0.125%. It is clear that all mixes are in the range of SCC suggested by the specifications. A decrease of 7.38% in spread diameter was observed when PP fiber was added and just 4.7% decrease when PET employed, this result can be attributed to the high surface area of fiber when added to the mix. On the other hand, the increase of T_{500} value when fiber proves that the cohesion and viscosity of concrete is better which prevents concrete segregation. Table 2 shows the results of J-Ring test of fresh concrete. It is obviously that as the fiber added the passing resistance increases from 5.8 up to 9.2, and this is logic because of the effect of fiber which prevents the material from passing easily.

4.2 Hardened properties concrete

Figure 3 presents the relation between SCC compressive strength and fiber percentage in the mix. It is clear that as the fiber increases concrete compressive increases until percentage of 0.075%. The same results were obtained in the relation between flexure strength and fiber content as shown in Figure 4. However the trend in both tests started going down the percent of 0.1% still higher than the reference mix. However PP fiber resulted in higher concrete strength in both tests the difference is very small and can be neglected. These results agreed with other investigations presented in the introduction for normal concrete. Moreover, since this study was carried out on self compacting concrete, this can be considered a good result because SCC needs high flow which still available even the fiber content reached 0.125%.

4.3 Preparation of Figures and Tables

Table 1: *Slump test results of reference and higher fibre content mixes*

Mix	Fibre (%)	Diameter(mm)	Specification (mm)	Time T_{500} (sec)	Specification (mm)
Reference	0	745	650-800	1.9	2-5
PP	0.125	690	650-800	2.13	2-5
PET	0.125	710	650-800	2.02	2-5

ISBN: 978-81-936820-6-7
Proceedings DOI: 10.21467/proceedings.4

Series: AIJR Proceedings

Table 2: *J-Ring test results of reference and higher fibre content mixes*

Mix	Fibre (%)	Diameter (mm)	Specification (mm)	Time T_{500} (sec)	Specification (mm)	Value (mm)	Specification (mm)
Ref.	0	710	650-800	2.03	2-5	5.8	0-10
PP	0.125	665	650-800	2.36	2-5	9.2	0-10
PET	0.125	680	650-800	2.17	2-5	9.0	0-10

Figure 1: Preparing of PET from plastic bottles

Figure 2: Comparison between PET (left) and PP (right) fibres

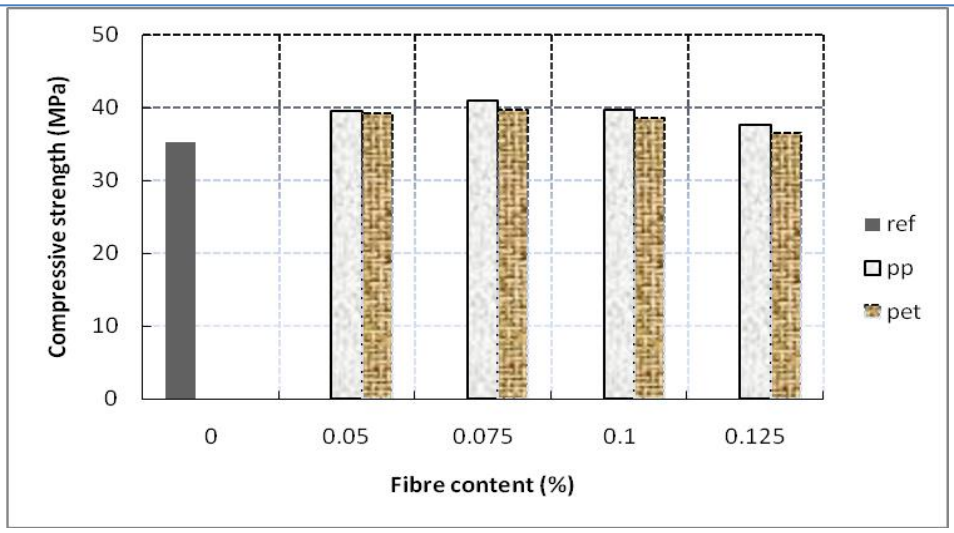

Figure 3: *Compressive strength vs. fibre content*

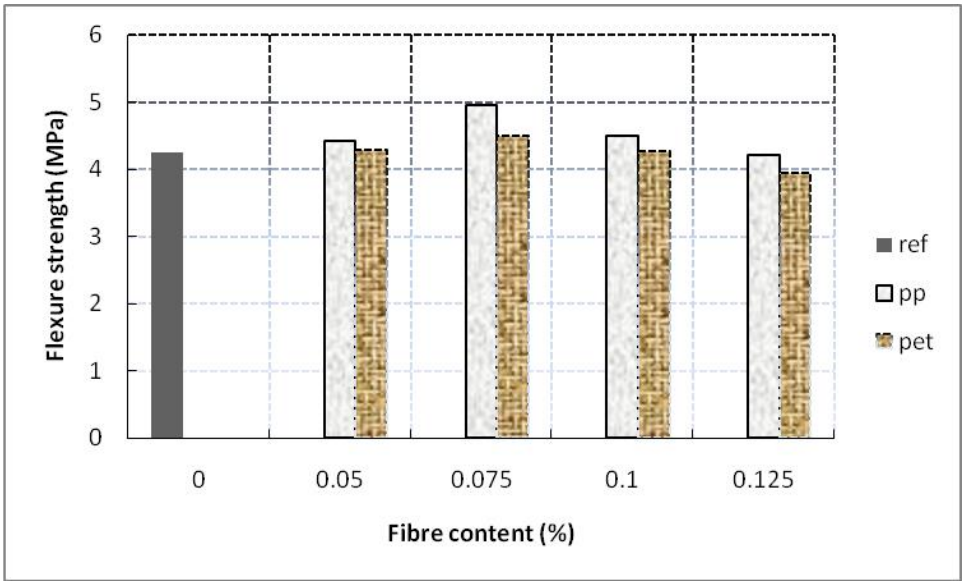

Figure 4: *Flexure strength vs. fibre content*

5 Conclusions

The main objective from the investigation was achieved, as the fibres excluded from waste drinking water bottles resulted in better concrete properties comparing with that of no fibre. Moreover, waste bottles fibres when compared with manufactured fibres available in the market for building objectives resulted in the same results without losing the advantages of self compacting behaviour of fresh concrete. Moreover, recycle of drinking water bottles will result in many advantages, minimizing concrete cost, land areas needed and pollution as this material is not degradable.

ISBN: 978-81-936820-6-7
Proceedings DOI: 10.21467/proceedings.4

References

[1] Neville, A. M., "*Properties of Concrete*," *Hand Book, Fifth Edition,* Pearson Education Limited, England, 2011.

[2] Ahmad, S. ؛Raza, A. ؛ Gupta, H, "*Mechanical Properties of Bamboo Fiber Reinforced Concrete*." 2nd international Conference on Research in Science, Engineering and Technology, Dubai-UAE, March, 2014

[3] Grunewald, S. "Performance-based design of self-compacting fiber reinforced concrete," *DUP Science*, Netherlands, 2004.

[4] Wang, C., "Experimental Investigation on Behavior of Steel Fiber Reinforced Concrete (SFRC)" *Master's Thesis in Civil Engineering, the University of Canterbury*, New Zealand, 2006

[5] Vairagade, L. N. ؛Bhedi, V. M, "Comparison of Strength between Steel Fiber Reinforced Concrete and Conventional Concrete," *International Journal on Recent and Innovation Trends in Computing and Communication*, vol. 3, no. 2, pp. 5-10, 2015

[6] Gornale, A. ؛ Quadri, S. I. ؛ Quadri, S. M. ؛ Ali, S. M. ؛ Hussaini, S. S. , "Strength Aspects of Glass Fibre Reinforced Concrete.," *International Journal of Scientific & Engineering Research*, vol. 3, no. 7, pp. 1-5, 2012.

[7] Widodo, S, "Fresh and Hardened Properties of Polypropylene Fiber Added Self-Consolidating Concrete," *International Journal of Civil and Structural Engineering*, vol. 3, no. 1, pp. 85-93, 2012

[8] Abdelgader A., Shailan D., "Mechanical properties of polymer concrete contain fibers of waste plastic," *Iraqi Journal of Mechanical and Material Engineering*, vol. D, no. 1, pp. 653-664. Iraq, 2009.

[9] British Standard Institute, BS EN 197-1 "*Cement - Part 1: Composition, specifications and conformity criteria for common cements*," London, UK, 2011

[10] Libyan Standard Specification, 294,"Used water in concrete," Tripoli, 1988

[11] British Standard Institute .BS EN 934-2:2009, "Admixtures for concrete, mortar and grout - Part 2: Concrete admixtures - Definitions, requirements, conformity, marking and labeling," London, UK, 2012.

[12] British Standard Institute .BS 882:1992, "Specification for aggregates from natural sources for concrete," London, UK, 2002.

[13] Sika Company, Polypropylene Fibers Data Sheet, 2015

[14] British Standard Institute .BS EN 12350-8:2010, "Testing fresh concrete - Part 8: Self-compacting concrete - Slump flow test," London, UK,2010.

[15] British Standard Institute .BS EN 12350-12:2010, "Testing fresh concrete - Part 12: Self-compacting concrete - J-Ring test," London, UK, 2010.

Prediction of Local Concretes Compressive Strength Using the Maturity Method

Mohammed Ali Abdalla Elsageer*, Wisam Elhmali Mansour, Hamad Suliman Abulaaj

Department of Civil Engineering, Faculty of Engineering, Sirte University, Libya

DOI: https://doi.org/10.21467/proceedings.4.32

* Corresponding author email: drmohammedalsger@gmail.com

ABSTRACT

This paper aims to study the maturity method to predict the compressive strength of a local concrete. This method is a non-destructive test of the concrete and can be used to know the time to remove concrete formwork. The method depends on time and the concrete temperature factor on the compressive strength of the concrete by using mathematical equations to predict the value of compressive strength. In the study two Portland Cement concrete mixtures were used, of grades C35 and C45, the compressive strength was tested at 6 hours and 1, 2, 4, 8, 16, 32, 64 days at different curing temperature 20, 30, 40 and 50 °C. The concrete strength was predicted by the maturity based on the Carino and Hansen equations, also the Datum temperatures for each mixture without which the concrete gained no strength was calculated. The laboratory results were compared with the theoretical results obtained from the equations of Carino and Hansen. The value of predicted compressive strength for concretes was accurate at early ages and highest or accurate in the later ages depending on the factors of the equations used.

KEYWORDS: Compressive strength, Maturity, Datum temperatures

1 Introduction

Increasing cost of construction has necessitated use of accelerated construction schedules to achieve economic benefits. Contractors need to know the strength of a structure or roadway in order to meet deadlines for formwork removal, a knowledge of in-situ concrete strength can reduce construction time and cost by efficient movement of forms. Furthermore it also establishes safe time for formwork removal to avoid catastrophic failure of structures with consequent danger to human life.

The strength development of concrete achieved in structural elements will be different from the strength of specimens that cured under standard curing condition, even though they are the same mixture for the following reasons [1]:

- Differences in maturity
- Differences in compaction and curing
- Water and cement migration within the cast element

 ISBN: 978-81-936820-6-7

The differences between the strength of concrete specimens cured under standard curing conditions and that of in-situ strength obtained even though they are the same mix make it difficult to decide whether the quality of concrete supplied to the site was of the required quality. Therefore, it is necessary to determine whether the structural element is adequately strong enough to withstand the intended loading, and allowing the contractor to remove the formwork. The methods listed below are some of the most popular and widely used methods of estimating the early-age concrete strength development during construction for formwork striking purposes [1]:

- Cured Specimens Alongside The Structure, Tables of Formwork Striking Times, Temperature Matching Curing Bath, Maturity Method, Penetration Tests, Break-Off Tests, Pull-Out Tests, Rebound-Hammer Test and Coring Test

1.1 The Maturity Methods

The term 'maturity or maturity index' can be defined as a 'temperature-time factor' that describes the combined effect of temperature and time on the development of concrete strength. The method developed is based on the principle that concretes cast from the same mix that have equal maturity will have equal strength regardless of their actual temperature-time history.

The maturity method is one of the most reliable methods of assessing early-age in-situ concrete strength, particularly for fast-track construction applications. Many methods have been proposed to determine the maturity of concrete empirically [2,3]. In recent years, however, many methods have been developed based on the concept of activation energy and the Arrhenius law[2] on the rate of reaction. This method has a wide variety of applications in the precast concrete industry that include the assessment of strength of prestressed heat accelerated concrete elements[2,3].

Maturity method in determining the time needed for the concrete to achieve adequate strength to permit the release of the pre-stressing force.

The in-situ concrete maturity can be determined using one of the following procedures:

1. Analyzing in-situ temperature recordings using maturity functions.
2. Using electronic maturity meters.
3. Using a commercial maturity probe, which is based on the evaporation of a volatile liquid.

The maturity index is determined from the temperature history of concrete by a maturity function; such as the Nurse-Saul or the Arrhenius formulation proposed by Freiesleben Hansen and Pedersen[2]. Once the maturity index or the equivalent age at a reference temperature, is determined the strength development of concrete cured at other than reference or standard curing temperature can be determined as well.

The index maturity of concrete at standard curing temperature; can then be used to determine the strength of concrete using the strength-maturity correlations of concrete cured at standard temperature. The strength-maturity correlations is developed by statistically analyzing the

strength data of cubes, which are cast from the same mix and cured isothermal at the reference temperature. The maturity testing procedure is described in Figure (1).

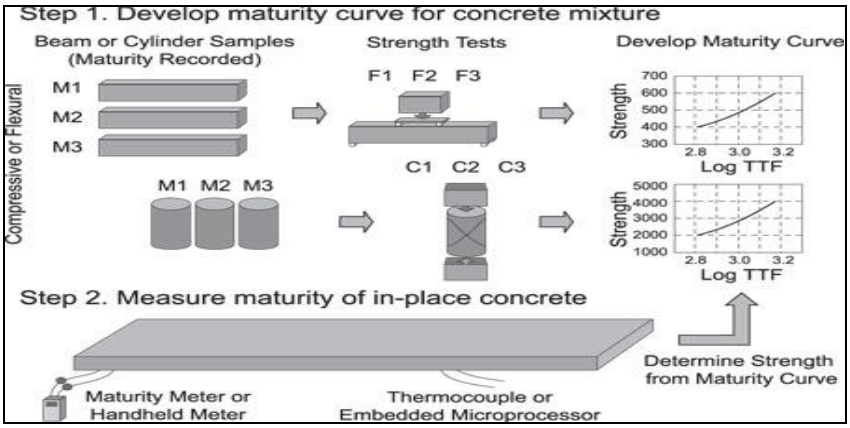

Figure (1): Maturity testing procedure [2]

The Maturity method saves time and money by the accurate prediction of concrete strength to remove formworks, cut and saw timing and open pavement to traffic. This method saves money by reducing the samples required to test. The strength of concrete estimation is also important to the new construction of buildings and roads. Maturity is useful for operating timing of pre-stressed concrete. The method can estimate the strength of concrete at any age. The negative side of the maturity method is that a complete hydration should continue without ceasing otherwise predictions will be incorrect. This method will not take into account some field actions, like inadequate vibration and insufficient curing. Every mixture has its own unique maturity. So strength maturity curve should be established for every individual mixture[2,3].

The equations used to predict the strength are based on **Nurse-Saul** maturity below:

$$M = \sum_0^t (T - T_0)\Delta t \quad (1)$$

Where:

M = Maturity index, °C-hours (or °C-days),

T = Average concrete temperature, °C, during the time interval Δt,

T_0 = Datum temperature (usually taken as -10 °C),

t = Elapsed time (concrete age in hours or days),

Δt = Time interval (hours or days).

The Strength-Maturity Relationship Proposed by Carino

Carino'S Strength- Time Relationship

$$S = S_\infty \frac{K_T(t-t_0)}{1+K_T(t-t_0)} \quad (2)$$

Where:

S_∞ = Limiting strength, N/mm²

t = Age, hours

K_T = Rate constant is equal to Arrhenius equation:

$$K_T = Ae^{\left[\frac{-E}{RT}\right]} \quad (3)$$

Where:

A = A constant

E = Activation energy, J/gmol

R = Universal gas constant, 8.3144 J/gmol-K

t^0 = Age when strength gain begins, hours

The parameters $S\infty$, K_T and t^0 in equation (2) are determined by best-fit curve fitting to strength vs. age data obtained by experiential tests to a concrete cured at different constant temperature. Moreover, the equation is used to determine concrete datum temperature and activation energy[5], which will be discussed in the activation energy section.

In 1982, Knudsen[6] , earlier than Carino, devised a similar equation to represent the degree of hydration of cement rather than concrete strength.

Carino's Strength- Maturity Relationship:

$$S = S_\infty \frac{K(M-M_0)}{1+K(M-M_0)} \quad (4)$$

Where:

S_∞ = Limiting strength, N/mm²

M = Maturity, °C-hours

K = A rate constant

M_0 = Maturity when strength gain begins, °C-hours

Freiesleben Hansen and Pedersen Strengh-Maturity Relationship[7, 8]

The equation is a Three Parameter Exponential (TPE) and was proposed in 1985[2], based on the assumption that the strength development should be similar to the curve and relationships of heat of hydration. The Freiesleben Hansen and Pedersen is as follows:

$$S = S_\infty e^{-\left(\frac{\tau}{M}\right)^\alpha} \quad (5)$$

Where:

S_∞ = Limiting strength, N/mm²

M = Maturity index, °C-hours

τ = Characteristic time constant

α = Shape parameter

Note that changing the value of the time constant preserves the same general shape of the curve while shifting it to the left or right. According to Carino changing the value of the shape parameter alters the shape of the curve in such a way that when α increases then the curve has a more pronounced S shape.

In 1977, Freiesleben Hansen and Pedersen[7] proposed an equivalent age function to compute a maturity index from the recorded temperature history of the concrete based on the well known Arrhenius equation. The earliest mention of the use of the Arrhenius equation, to describe the effects of temperature on the early rate of hydration of cement, was in 1962 by Copland et al[9].

The nonlinear proposed function is as follows:

$$t_e = \sum_0^t e^{\frac{-E}{R}\left[\frac{1}{273+T}-\frac{1}{273+T_r}\right]} \Delta t \qquad (6)$$

Where

t_e = The equivalent age at the reference temperature,

E = Apparent activation energy, J/mol,

R = Universal gas constant, 8.314 J/mol K,

T = Average absolute temperature of the concrete during interval Δt, Kelvin, and

T_r = Absolute reference temperature, Kelvin.

1.2 Aims and Objectives

The main aim of this paper is to estimate strength development of concrete using the maturity method.

2 Experimental Work

To obtain normal strength concrete of target mean strengths of C35 as classified by European standard BS EN 206-1:2000, the proportions were obtained using the BRE method (mix design of normal concrete)[10]. The mix percentage of the material are shown in Table1.

Table (1): Mix Percentage of The Material to be Used C 35

Cement	Water	sand	Coarse aggregate
1	0.549	1.346	2.617

The strength development under 20, 30, 40 and 50 °C, and were investigated.

3 Materials

All the materials used in all parts of this same study mentioned in detail and will respond as follows:

3.1 Cement

Portland cement type I class 42.5N was used in this study. The cement was supplied by Zliten Factory.

3.2 Aggregate

3.2.1 Coarse Aggregate:

The coarse aggregate used was graded aggregate comprise crushed dolerite stone with a nominal size ranging from 5 to 20 mm. Sieve analyses were carried out in accordance with BS 882:1992[11], in order to check whether the size distributions of the aggregate satisfy the limits

ISBN: 978-81-936820-6-7

Series: AIJR Proceedings
Proceedings DOI: 10.21467/proceedings.4

required in the standard. The sieve analysis test of aggregates was done on each size alone (20, 10) mm, both sizes of aggregate were mixed (The mixing ratio is 50% for each size) to improve the concrete mix, The sieve analysis test of the mixed aggregates was matching specifications.

3.2.2 Fine Aggregate

Natural sand from Sirte has been used. The sieve analysis test of fine aggregates was done on natural sand and fine aggregate up to 5mm, both sizes of aggregate were mixed to improve the mix although each of them was matching specifications. The mixing ratio is 30% size 5mm fine aggregate & 70% sand. the sieve analysis results was matching specifications.

4 Curing

After casting, the concrete specimens were wrapped in cling film then submerged in water tanks set at 30, 40 and 50 °C curing conditions. Except for 20 °C as the lab temperature was 20 ± 2 °C. The specimens were covered with damp hessian and plastic sheeting, the next day, i.e. 24 hours after casting, the specimens were demoulded and placed back in their initial curing conditions up till the time of testing.

5 Experimental Results and Data Analysis

5.1 Strength Development Concrete at Different Curing Temperatures

The strength development under 20, 30, 40 and 50 °C curing regimes for concretes, with strength error bars based on three replicate samples is shown in Figure (2). At an early age the strength development of the concrete at high curing temperatures is greater than at low curing temperatures. This is attributed to an increase in the hydration reaction rate. However, at a later age, the strength achieved at high curing temperatures was reduced. The strength development under 20, 30, 40 and 50 °C curing regimes will be used to determine the activation energy and datum temperature of the concrete under investigation according to the ASTM C1074.

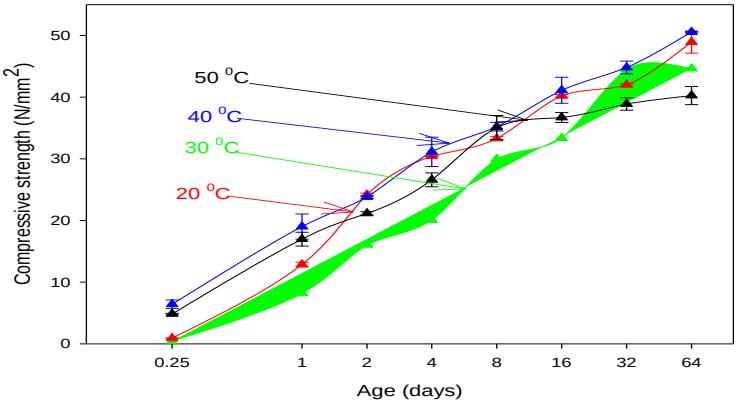

Figure (2): Compressive Strength for C35 Concrete

5.2 Estimation Compressive Strength by The Maturity Method

The maturity method can be used to predict compressive strength of any concrete structural element. In this study slab of grade C35 was cast, the slab size was 35 x 35 x 25 cm and cured outdoors in order to simulate behavior of concrete in-site. The temperature history of the slabs was recorded in order to use to predict the compressive strength by the maturity method. Beside that the actual compressive strength was measured using concrete cubes cured close to slabs, the compressive strength measured from the age of 6 hours up to 64 days.

5.3 Recording The Concrete Temperature

The temperature history of the concrete slab was measured and recorded by a digital thermometer UT321, thermocouple were put inside the concrete in the time of casting and the device was connected to the computer to record the temperature automatically. The recording was to the duration until the slab temperature become the same as the air temperature. Figure (3) shows the temperature history of the slab.

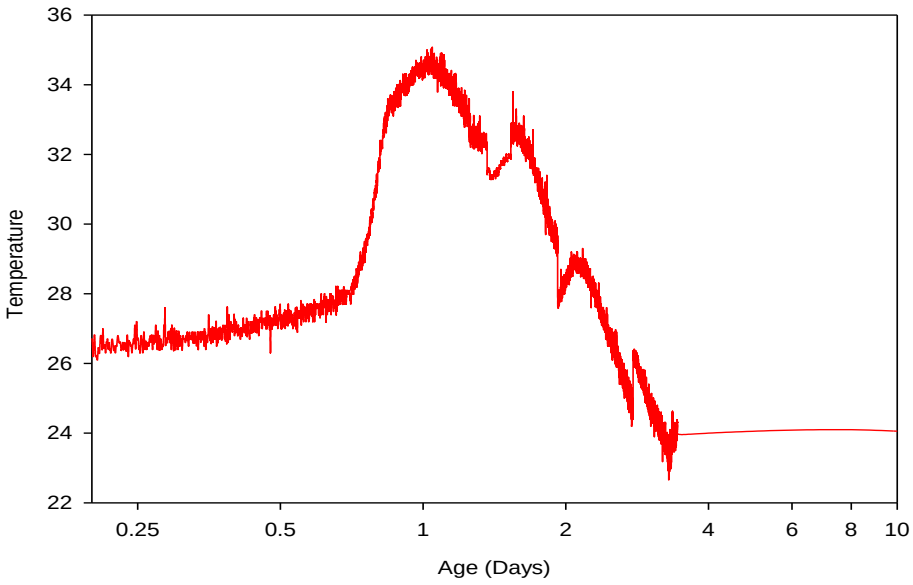

Figure (3): Temperature History of The Slab

5.4 The Use of Maturity Functions to Predict Concrete Strength Development

The temperatures histories were converted into predicted strength development, using Carino equation and the Three Parameter Equation (TPE) suggested by Freiesleben Hansen and Pedersen equation. Predicted strengths were then compared with the actual strength of cubes cured in order to investigate the accuracy of the equations.

A summary of the stages used to predict the strength of the concretes:

o Determine the activation energy and the datum temperature.

ISBN: 978-81-936820-6-7
Proceedings DOI: 10.21467/proceedings.4

Series: AIJR Proceedings

o Determination of model parameters for maturity functions, Strength-age parameters based on the Carino's equation and the Freiesleben Hansen and Pedersen equation for concrete cured under standard 20 oC conditions.

The parameters $S\infty$, k and t_0 of Carino's equation and $S\infty$, τ and α of the Three Parameter Equation suggested by Freiesleben Hansen and Pedersen for the Arrhenius equivalent age function, producing the best fit for the experimental data at standard 20 °C, have been calculated. The regression analysis values are listed in Tables (2), and (3) for the concrete grades of 35.

- **Carino Equation :**

Table (2): Parameters Based on Carino Equation (Strength-Age Relationships)

Parameters	20 ^{0}C
S^∞ (N/mm2)	44.6443
k (days-1)	0.2000
t^0 (days)	1.4832E-016
R^2	0.9819

- **Hansen Equation :**

Table (3): Parameters Based on Hansen Equation (Strength-Age Relationships)

Parameters	20 ^{0}C
S∞ (N/mm2)	55.5283
τ (days)	3.4769
a	0.5500
R2	0.9931

Note:

o Carino (NS) means that the strength-maturity relationship that has been described by Carino with maturity calculated according to the Nurse-Saul equation is used.

o Carino (Arh) means that the strength-age relationship that has been described by Carino with equivalent age calculated according to expression suggested by Freiesleben Hansen and Pederson using the Arrhenius equation is used.

o Hansen (NS) means that the strength-maturity relationship that has been described by Freiesleben Hansen and Pederson with maturity calculated according to the Nurse-Saul equation is used.

o Hansen (Arh) means that the strength-age relationship that has been described by Freiesleben Hansen and Pederson with equivalent age calculated according to expression suggested by Freiesleben Hansen and Pederson using the Arrhenius equation is used.

The activation energy and datum temperature determined according to the ASTM C1074, the datum temperature value is 5.5 °C and the activation energy values determined from the two methods (ASTM standard and TPE) as in Table 4.

Table (4): Apparent Activation Energy Based on Carino and TPE Methods

Activation energy (kJ/mol) based on	
Carino method	TPE method
15.84	30.06

Figure (4) shows that the only function predict the strength quit well up to age of 8 days is Carino (Arh), at later ages the strength over estimated. The other function predict the strength well up to the age of 1 day only and overestimated the strength for the other ages.

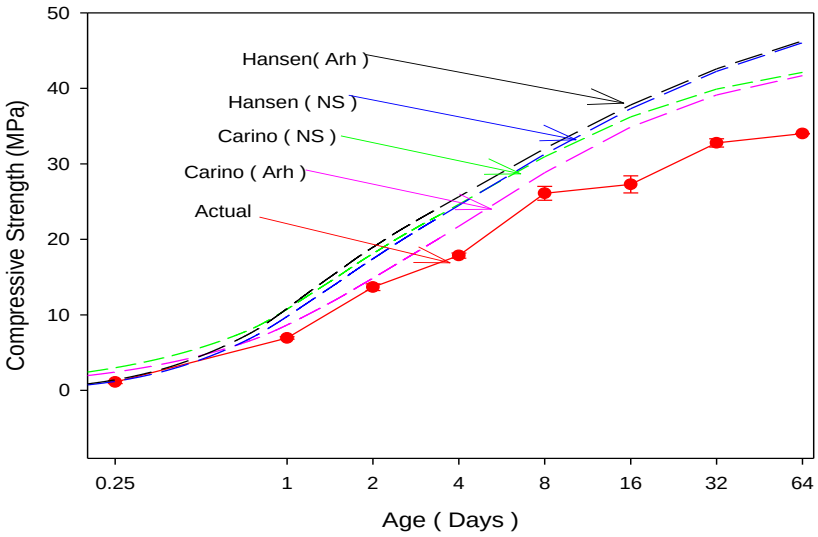

Figure (4): Predicted Compressive Strength Based on The Carino and TPE Equation.

Changing the values of datum temperature in the maturity equation between the determined values 5.5 ^{O}C and recommended values by the standard that -11 ^{O}C, shows that Hansen (NS) function accurately predict the strength up to 8 days. The other equation overestimated the strength at all ages as shown in figure (5).

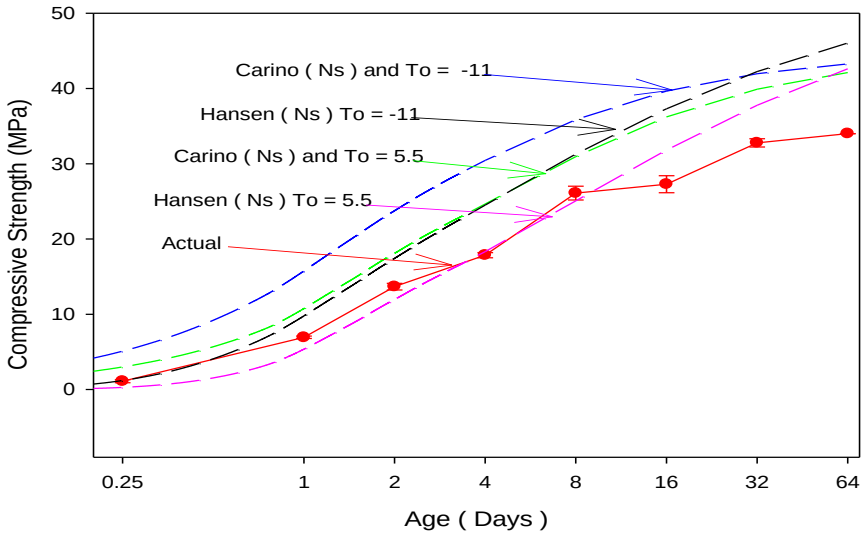

Figure (5): Predicted Compressive Strength Based on The Carino and TPE Equation.

ISBN: 978-81-936820-6-7
Proceedings DOI: 10.21467/proceedings.4

Series: AIJR Proceedings

6 Conclusions

Based on the results of this study, the following conclusions are drawn:

- At early age (1- 4 days) the strength development under 20, 30, 40 and 50°C curing regimes for the concrete cubes increases as the temperature increase. From the age of 8 to 64 days the strength development the strength development decreases as the temperature increase
- The study has shown that Carino (Arh) function is able to predict the compressive strength with sufficient accuracy up to the age of 8 days.
- The study has shown that equation Hansen (NS) considered very accurate to predict the compressive strength using determined datum temperature up to the age of 8 days.

Acknowledgment

First and foremost, we thank Allah. This paper based on undergraduate project during the Academic year 2013/2014 done by the students, Ahmed Mohammed Emsilkh, Ali Nurie Emhlhel, Abdullah Mansour Emhemed and Wisam Elhmali Mansour under the supervision of Dr. Mohammed Ali Abdalla Elsageer

The authors are gratefully and sincerely thank the students for their hard work on the experimental and theoretical parts of the project.

Special thanks are due to Mr. Ahmed and Mrs. Haw the technicians in the concrete lab for their assistance with the laboratory work.

References

[1] Newman, J. B. and Choo, B. S., Advanced Concrete Technology, Volume 2: Concrete Properties 2003: Elsevier Science & Technology.

[2] Malhotra, V. M. and Carino, N. J., Handbook on nondestructive testing of concrete 2004: ASTM International.

[3] Carino, N. J. and Lew, H. S., The maturity method: From theory to application. Cement, Concrete, and Aggregates, 1984. 6(2): p. 61-73.

[4] Association, American Concrete Pavement, Maturity testing of concrete pavements: Applications and benefits. Publication IS257P, 2002.

[5] ASTM C 1074, Standard Practice for Estimating Concrete Strength by the Maturity Method," Annual Book of ASTM Standards, 2004.

[6] Geiker M. and Knudsen T., Chemical Shrinkage of Portland cement Pastes. Cement and Concrete Research, 1982. 12(5): p. 603-610.

[7] Hansen, P. F. and Pedersen, E. J., Maturity computer for controlled curing and hardening of concrete, 1977.

[8] Hansen, P. F. and Pedersen, E. J., Curing of concrete structures 1984.

[9] Copeland, L. E., Kantro, D. L., and Verbeck, G. J., Chemistry of hydration of Portland cement 1960: Portland Cement Association, Research and Development Laboratories.

[10] Teychenne, D., R. Franklin, and H. Erntroy, Design of normal concrete mixes, Vol. 2.1997: BRE (Building Research Establishment UK). 46.

[11] BSI, BS 882:1992 specification for aggregate from natural sources for concrete 1992, BSI-British Standards Institution.

Design of Vertical Pressure Vessel Using ASME Codes

Najeeb A. Yahya[1]*, Othman M. Daas[2] , Nureddin O. Fahel Alboum[3], Ahmed H. Khalile[4]

Department of Mechanical & Industrial, College of Engineering, Zawia University, Libya

DOI: https://doi.org/10.21467/proceedings.4.33

* Corresponding author email: nyahya@zu.edu.ly

ABSTRACT

While preparing this paper many of companies are subjecting to the hazards resulted from the incorrect design and manufacturing of pressure vessels (leakage or Explosion), those used in the storage of dangerous liquids or pressurized fluids. The main objective of using the pressure vessels are used as containers to contain many of materials such as: liquids, air, gases, chemical compounds and fuel, moreover pressure vessels considered as important prop in petroleum and chemical industries especially as storages for oil and chemical components. The main goal of this paper to shed light on the importance processes of the Mechanical Design and Analysis of Vertical Pressure Vessels, also to give scratch to prevent this hazard using. The used model is very close shape to the used vessels in such companies. The design of vertical pressure vessel is carried out using the American Society of Mechanical Engineers (ASME) Codes. ASME section VIII and Division 1 are normally used in design. Various components of the pressure vessel are designed by calculating the appropriate design factors like thickness of the shell, head, stress analysis etc. to validate the design result the pressure vessel is modelled and analyses in Solid works software. The engineering geometrical drawings and Finite Element Analysis (FEA) have been achieved on the targeted model of Vertical Pressure Vessel by using very moderate computer programs to give results agreed and compatible with correct choose of ASME codes. Throughout this paper, the permissible pressures are very considered as well as determination the wall thickness of the vessel is firmed to reach the acceptable maximum stresses. Furthermore, the design of targeted pressure vessel has been achieved under the range of ASME codes and engineering standards to reach the allowable designing boundaries.

Keywords: Pressure vessels; ASME codes; Standards; Maximum stresses; Solid works software.

1 Introduction

Pressure vessels are one of the main equipment those widely used in industrial facilities. The pressure vessels defined as cylindrical or spherical vessels those designed to store or hold pressurized liquids, gases or fluids with a differential pressure between inside and outside. Usually, the inner pressure is higher than the external pressure, except in some cases. The fluid inside these vessels may undergo a change in state as in the case of steam boiler or may

 ISBN: 978-81-936820-6-7

combine with other reagent as in the case of chemical reactor. The reservoirs designed such that no leakage can occur, also deal with operational levels of high pressure and high temperatures[1]. The pressure vessels are differ in terms of capacity, heat and pressure, some of these vessels may contain more the half million barrels of crude oil, the temperatures sometimes more than 200 ^{o}C specially in asphalt tanks and high viscosity products, the temperatures may slope down to 14^{o}C especially in tanks store hydrocarbons materials such as propane, butane and others, so it is necessary to understand the types of reservoirs and their components as well as the appropriate storage methods[2]. Pressure vessels usually are cylindrical or spherical with semi-spherical covers (domes) and cylindrical tanks. Cylindrical vessels very wide in use and very simple to manufacture and ease in use such as boilers, heat exchangers, refineries …etc. According to the importance of pressure vessels, many of published researches achieved especially in Designing and Analysis of Stresses on the reservoirs as well as the exact use of designing standards, methods of numerical analysis and the mathematical simulation models to identify different collapse occur on reservoirs.

(Apurva R)[3] and friends have used ASME codes to design and analysis of pressure vessel by using maximum permissible pressure to find the factor of safety to obtain the finest design, furthermore, the Finite method element used to study the stresses distribution those deal to reservoir failure. (B. Thakkar and S. Thakka)[4] are designed and constructed in accordance with ASME codes Section VIII, Division 1 by changing internal pressure values of the vessel to obtain the premium design and determination of critical points of collapse in vessel's body. (V. Kumar)[5] used the ANSYS program to design and analyze the loads on the installation fits of horizontal pressure vessel to determine the high stresses concentration between the stiffeners and the wall of the tank, the results were compared with permissible strain of design. (Maharishi J. Bhatt)[6] Studied the design of connecting the nozzle with the tank wall, also to connect this nozzle with upper or lower cover according to ASME codes Section VIII, Division 1. Generally speaking, this paper includes the steps designing calculations to support the nozzle with the tank body and connecting regions.

2 History of ASME Codes for Pressure Vessel

Pressure vessels store energy and as such, have inherent safety risks. Many states began to enact rule and regulations regarding the construction of steam boilers and pressure vessels following several catastrophic accidents that occurred at the turn of the twentieth century that resulted in large Loss of life. By 1911 it was apparent to manufacturers and users of boilers and pressure vessels that the lack of uniformity in these regulations between states made it difficult to construct vessels for Interstate commerce. A group of these interested parties appealed to the Council of the American Society of Mechanical Engineers to assist in the formulation of standard specifications for steam boilers and pressure vessels. (The American Society of Mechanical Engineers was organized in 1880. As an educational and technical society of mechanical engineers.) After years of development and Public comment, the first

edition of the Code, ASME Rules of Construction of Stationary Boilers and for Allowable Working Pressures, was published in 1914 and formally adopted in the Spring of 1915. The first Code rules for pressure vessels, entitled Rules for the Construction of Unfired Pressure Vessels, followed in 1925. From this simple beginning the Code has now evolved into the present eleven Section document, with multiple subdivisions, parts, subsections, and Mandatory and non-mandatory appendices.

Almost all pressure vessels used in the process industry in the United States are designed and constructed in accordance with Section VIII, Division 1. A pressure vessel is a closed container designed to hold gases or Liquids at a pressure different from the ambient pressure. The end caps fitted to the cylindrical body is called heads. Pressure vessels are used in a variety of applications. These include the industry and the private sector. Steel pressure vessel in the industrial sector, pressure vessels are designed to operate safely at a specific pressure and temperature, technically referred to as the "Design Pressure" and "Design Temperature". A vessel that is inadequately designed to handle a high pressure constitutes a very significant safety hazard. Because of that, the design and Certification of pressure vessels is governed by design codes such as The ASME Boiler and Pressure Vessel Code in North America, the Pressure Equipment Directive of the EU (PED), Japanese Industrial Standard (JIS), CSA B51 in Canada, AS1210 in Australia and other international standards like Lloyd's, Germanischer Lloyd, Det Norske Veritas, Stoomwezen etc. Pressure vessels can theoretically be almost any shape, but shapes made of sections of spheres, cylinders and cones are usually employed. More complicated shapes have historically been much harder to analyse for safe operation and are usually far harder to construct. Theoretically a sphere would be the optimal shape of a pressure vessel.

Unfortunately the sphere shape is difficult to manufacture, therefore more expensive, so most of the pressure vessels are cylindrical shape with 2:1 semi elliptical heads or end caps on each end. Smaller pressure vessels are arranged from a pipe and two covers. Disadvantage of these vessels is the fact that larger diameters make them relatively more expensive. Generally, almost any material with good tensile properties that is chemically stable in the chosen application can be employed. Many pressure vessels are made of steel.

3 Using Method of (ASME Section II & VIII, Div1) Calculation

3.1 Selection of Materials by using (ASME Section II: A,D)

The (Section II: A, D) is used to determine selected materials with full description, it permits to use codes for components with different constructions[3].

The main component of any vessel is metal shells with different dimensions on bottom, top and wall. All these dimensions should be suitable with codes under the authority of the designer himself.

ISBN: 978-81-936820-6-7
Proceedings DOI: 10.21467/proceedings.4

Series: AIJR Proceedings

3.2 Design of Vessels by using (ASME Section VIII, Div1)

This code (standard) is used for designing vertical tanks (vessels), according to minimum requirements of design without any failure of tank parts. The specialized code for the vessels those used within range of (0.1 MPa to 20 MPa) and for this range most of vertical vessels are selected [9]. The cylindrical pressure vessel composed of: (Shell – Head – Nozzles – Base support).

3.2.1 Shell Design

The ASME codes presents basic rules while designing shells. It is clear that the thickness of these shells is main consideration, the welding operation on vessels is necessary too. The used thickness equations are:

- In case of circumference stresses (longitudinal welding)

Where: $(p < 0.385\ SE)$ $\quad t_s = \frac{PR}{SE-0.6P}$, $\quad P_s = \frac{SEt_s}{R+0.6t_s}$

- In case of longitudinal stresses (circumference welding)

Where: $(p < 1.25\ SE)$ $\quad t_s = \frac{PR}{2SE+0.4P}$, $\quad P_s = \frac{2SEt_s}{R-0.4t_s}$

Where:

t_s = Shell thickness.

P = Designing pressure.

P_s = Maximum pressure.

R = Internal Radius.

S = Maximum allowable stress.

E = Coefficient of connection of welding.

Note that: E = 1.0 if radiated test is used, meanwhile E = 0.7 is used if non-radiated tests are used

3.2.2 Heads Design

Most of used closing heads are curved to resist pressure, reduce thickness and cost reduction. There are many types of closing heads and mostly used is semi-elliptical head. In this type the base diameter to the high = $\frac{D}{h} = \frac{4}{1}$

The head cover will consist of two main parts are shown in Figure 1:

Spherical radius = (L = 0.9D)

Radius of the neck = (ri = 0.17D)

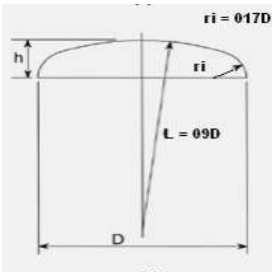

$t_h = \frac{PD}{2SE-0.2P}$, $\quad P_h = \frac{2SEt}{D+0.2t_h}$

Where:

t_h = head thickness.

P = Designing pressure.

P_h = Maximum pressure.

S = Maximum allowable stress.

D = Internal diameter of tank body.

E = Coefficient of connection of welding.

3.2.3 Nozzles Design

During providing the pressure vessels with nozzles, it is important to support these nozzles to avoid or prevent any failure. The type of nozzle is shown in Figure 2

$$t_n = \frac{PR}{(SE-0.6P)}$$

$$A_r = d_n * t_s * f$$

$$A_s = D_n(T_s - t_s) - 2T_n(T_s - t_s)$$

$$A_n = 2[\,2.5(T_s)*(T_n - t_n)\,]$$

$$A_r < (A_s + A_n)$$

$$d_s = d_n + 2(t_n)$$

$$x = r_n + T_n \;,\; y = 2.5*T_s$$

$$d_n = D_n - 2\,(T_n + \text{Corrosion Allowance})$$

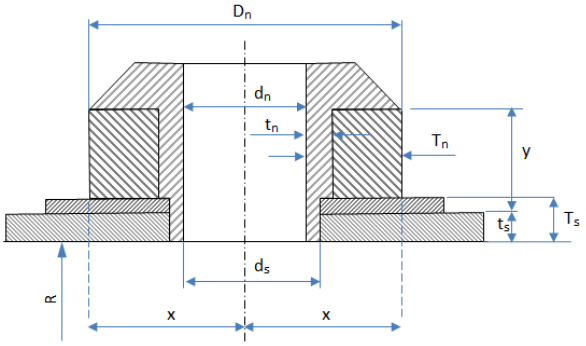

where:

D_n = External nozzle diameter

d_n = Internal nozzle diameter

d_s = Diameter of nozzle on tank wall

f = correction coefficient = 1

t_s = Required thickness of tank

T_s = Actual body thickness

t_n = Required nozzle thickness

T_n = Actual nozzle thickness

r_n = Radius of internal hole

A_r = Area of nozzle hole

A_s = Area of connecting region

A_n = Area of nozzle wall

3.2.4 Support Base Design

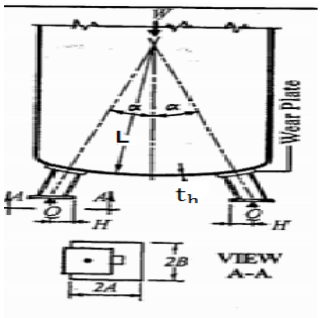

During designing of high vessels, the support bases, size, volume, weight, wind and earthquake should be taken into consideration. In this work the legs support were used. The support legs are shown in Figure 3. The number of legs depends on the size of the tank and the size of stored material in the tank. The dimensions of the legs and stresses can be calculated as:

- Longitudinal stresses

ISBN: 978-81-936820-6-7
Proceedings DOI: 10.21467/proceedings.4

$$S_L = \frac{Q}{{t_h}^2}\left[\cos\alpha\,(k_1+6k_2) + \frac{H}{L}\sqrt{\frac{L}{t_h}}\,(K_3+6K_4)\right]$$

- Circumference stresses

$$S_c = \frac{Q}{{t_h}^2}\left[\cos\alpha\,(k_5+6k_6) + \frac{H}{L}\sqrt{\frac{L}{t_h}}\,(K_5+6K_6)\right]$$

Note that the longitudinal Stress always positive values (k2, k4, k6, k8) mean while the compressional strain (k1, k3, k5, k7) negative values [11].

3.3 Design Calculations and Results

The studied vessel with internal pressure not exceeding (1.55 MPa) and internal temperature not exceeding (100 °C). Table 1 shows the initial material used in vessel.

Table 1: *Initial material used in vessel*

Part	Material
Tank Shell	SA 515 – Gr 70
Head Cover	SA 515 – Gr 70
Tank Nozzle	SA 106 Gr (B)
Support Base	SA 515 – Gr 70
Support Legs	SA 106 Gr (B)

3.4 Vessel Shell Calculations

Table 2: *Properties and dimensions of vessel shell*

Internal Pressure	1.55 MPa
Internal Temperature	100 °C
External Pressure	0.103 MPa
Shell Length (L)	4000 mm
Internal Tank Diameter (Di)	1500 mm
Material Type	SA 515 – Gr 70
Permissible Material Stress	137.9 MPa
Link Efficiency	1.0
Corrosion Permeability	3 mm
Density of Material	7.73 g/cm^3

3.4.1 Vessel Shell Thickness

Where:

$$P < 0.385 * S * E = 1.55 < 0.385 * 137.9 * 1$$

$$t_s = \frac{PR}{SE - 0.6P} + c.a$$

$$t_s = \frac{1.55 * \left(\frac{1500}{2}\right)}{(137.9 * 1) - (0.6 * 1.55)} + 3 = 11.48\, mm$$
$$(use\ t_s = 12\ mm)$$

3.4.2 Maximum Pressure on Vessel Shell

$$p_s = \frac{SEt}{R + 0.6t_s}$$
$$p_s = \frac{137.9 * 1 * 12}{\left(\frac{1500}{2}\right) + 0.6 * 12} = 2.19\, MPa$$

3.4.3 Vessel Shell Mass

$$Volume = \frac{\pi * \left(D_0^2 - D_i^2\right)}{4} * L$$
$$Volume = 228004.22\ cm^3$$
$$Mass = Volume * Density$$
$$Mass = 228004.22 * 7.73 = 1762.472\ Kg$$

3.4.4 Liquid Mass at Vessel Shell

$$Volume = \frac{\pi * \left(D_i^2\right)}{4} * L$$
$$Volume = 7068583.47\ cm^3$$
$$Mass = Volume * Density$$

Liquid Density=1.00 g/cm^3

$$Mass = 7068.58\, Kg$$

3.5 Head Calculations

Table 3: *Properties and dimensions of head cover*

Head cover type	Semi-Elliptic
Internal Tank Diameter	1500 mm
Material Type	SA 515 – Gr 70
Permissible Material Stress	137.9 MPa
Link Efficiency	1.0
Corrosion Permeability	3 mm
Internal Spherical Radius	1350 mm
Head High	375 mm

3.5.1 Required Head Thickness

$$t_h = \frac{PD}{2SE - 0.2P} + c.a$$

ISBN: 978-81-936820-6-7
Proceedings DOI: 10.21467/proceedings.4

Series: AIJR Proceedings

$$(use\ t_h = 12\ mm) \qquad t_h = 11.44\ mm$$

3.5.2 Maximum Pressure at the Head

$$P_h = \frac{2SEt}{D + 0.2t_h}$$

$$P_h = \frac{2 * 137.9 * 1 * 12}{1500 + 0.2 * 12} = 2.2\ MPa$$

3.5.3 Mass of Head

$$Volume = \frac{2}{3} * \pi(Lo^2 - Li^2) * h$$

$$Volume = 25559.99\ cm^3$$

$$Mass\ =\ Volume\ * Density$$

$$Mass\ =\ 25559.99 *\ 7.73$$

$$Mass\ =\ 197.58\ kg$$

$$Mass\ of\ two\ heads\ =\ 197.58 * 2 = 395.16\ kg$$

3.5.4 Liquid Mass at Head

$$Volume = \frac{2}{3} * \pi(Li^2) * h$$

$$Volume = \frac{2}{3} * \pi(135^2) * 37.5 = 1431388.153\ cm^3$$

$$Mass\ =\ Volume\ * Density$$

Liquid Density=1.00 g/cm^3

$$Mass\ =\ 1431.388\ Kg$$

$$Liqud\ Mass\ of\ two\ heads\ = 2862.776\ kg$$

3.6 Nozzle Calculations

Table 4*: Properties and dimensions of tank nozzle*

Nozzle Length	200 mm
External Nozzle Diameter	203 mm
Material Type	SA 106 Gr (B)
Permissible Material Stress	117.9 MPa
Link Efficiency	1.0
Corrosion Permeability	3 mm

3.6.1 Required Nozzle Thickness

$$t_n\ = \frac{PR}{(SE - 0.6P)}$$

$$t_n = \frac{1.55 * (\frac{203}{2})}{(117.9 * 1 - 0.6 * 1.55)} = 1.5\ mm$$

$$(use\ T_n = 10\ mm, ts = 12\ mm\ and\ Ts = 22\ mm$$

3.6.2 Nozzle Reinforcement

$d_n = D_n - 2\ (T_n + Corrosion\ Allowance)$

$d_n = 203 - 2(10+3)$, $d_n = 177\ mm$

$d_s = d_n + 2(t_n)$

$d_s = 177+2(1.5)$, $d_s = 180\ mm$

$A_r = d_n * t_s * f$

$A_r = 177*12*1$, $A_r = 2124\ mm2$

$A_s = D_n\ (T_s-t_s)-2T_n(T_s-t_s)$

$A_s = 203*(22-12)-2*10*(22-12)$, $A_s = 1830\ mm2$

$A_n = 2[\ 2*1/2(Ts).(T_n - t_n)\ ]$

$A_n = 2[\ 2.5(22).(10 - 1.5)\ ]$, $A_n = 935\ mm2$

$A_r < (A_s+A_n)$

$2124 < (1830+935)$

$x = R_n + T_n$

$x = (177/2) +10$, $x = 98.5\ mm$

$y = 2.5*T_s$

$y = 2.5*22$, $y = 55\ mm$

3.6.3 Mass of Nozzle

$$Volume = \frac{\pi * (D_n^2 - d_n^2)}{4} * L$$

$$Volume = \frac{\pi * (20.3^{\ 2} - 17.7^2)}{4} * 20 = 1551.95\ cm^3$$

$$Mass\ =\ Volume\ *Density$$

$$Mass\ =\ 11.99\ kg$$

$$Mass\ of\ two\ nozzles\ =\ 11.99 * 2 = 23.99\ kg$$

3.6.4 Total Mass of Pressure Vessel

Total mass of vessel parts = 130.9+23.99 + 395.16 + 1762.472 = 2312.5 kg

Total liquid mass = 2862.7763+7068.58 = 9931.36 kg

Total mass (T_m)= 9931.36+2312.5 = 12243.9 kg

ISBN: 978-81-936820-6-7
Proceedings DOI: 10.21467/proceedings.4

Series: AIJR Proceedings

3.7 Design of Pressure Vessel Support

Table 5: *Properties and dimensions of vessel support*

Material Type	SA 106 – Gr (B)
Permissible Material Stress on installation sheet	137.9 MPa
Permissible Material Stress on support	117.9 MPa
Link Efficiency (E)	0.6
Number of supporting Legs (n)	4
Spherical Radius (L)	1350 mm
Designed Pressure (P)	55.1 MPa
Lower cover Thickness (th)	12 mm

Total mass $= T_m = 12243.9\ kg$

$T_{wf} = 12243.9 * 9.81 = 120112.3$ N

$$Q = \frac{T_{wf}}{n} = \frac{120112.3}{4}$$

$$Q = 30028.1\text{N}$$

$H = 155$ mm , $2A = 2B = 300$ mm

$\cos\alpha = 0.95$, $c = \sqrt{AB} = 150$

$$D_L = 1.8\frac{C}{L}\sqrt{\frac{L}{t_h}} = 1.8*\frac{150}{1350}*\sqrt{\frac{1350}{12}} = 2.12 \text{ mm}$$

From charts 1,2,3,4 values of K_1 to K_8 can be defined [11].

K_1=0.055 K_2=0.02 K_3= 0.06 K_4=0.02

K_5=0.015 K_6=0.01 K_7=0.02 K_8=0.01

1.1.1 Calculations of supporting leg dimensions

$$Q = 30028.1\ N$$

$$E * S = \frac{Q}{A} = \frac{Q}{\frac{\pi}{4}({D_o}^2 - {D_i}^2)}$$

$$0.6 * 117.9 = \frac{30028.1}{\frac{\pi}{4}({D_o}^2 - 75^2)}$$

$$D_o = 79\ mm$$

4 Finite Element Analyses

The FE analysis starts with an axisymmetric analysis of pressure vessel. Solid works software is used for the three dimensional modeling of solid structures. The element is defined by eight nodes having three degrees of freedom at each node i.e. translations in the nodal x, y, and z directions. The finite element model consists of hemispherical heads, cylindrical shell and legs support. In boundary condition, the vessel is supported at the end corners and internal pressure of 1.55 MPa is applied at the inner surface. The boundary condition for hemispherical

and end connection pressure vessels are shown in the figure. All parts of vessel have been drawn after finishing all designing calculations. All the drawings drawn by SolidWorks Program. The vertical pressure vessel assembly are shown in Figure 4.

The main purpose of simulation is to determine critical points, stresses concentrations resulted by internal pressure and the distributions of stresses at different regions on vertical pressure vessel with four legs support. The results are shown in Figure 5,6 and 7.

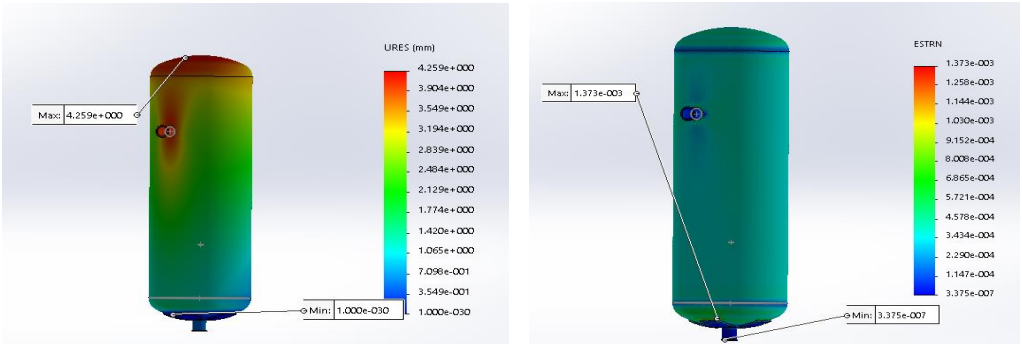

5 Conclusions

It is very clear that the pressure vessels are integrated system in terms of parts and competence. Mechanical design of pressure vessel had been done using SolidWorks software. During the designing of Pressure vessels, it is very important to design each part of these vessels individually to obtain more accurate design. All the pressure vessel components are selected on basis of available ASME standards and the manufactures also follow the ASME standards while manufacturing the components. The designing simulation concludes that the stresses concentration regions concentrated on the regions that connect between the bottom of the tank and the fixing base as well as the regions of fixing of the nozzle on the tank body. Also the designing simulation concludes that the most affected regions to displacement by internal

ISBN: 978-81-936820-6-7
Proceedings DOI: 10.21467/proceedings.4

pressure are the away regions from fixing points (i.e., farther away from installation points the higher displacement value.)

References

[1] A. Eljondi, "Tanks for Petroleum and Control," Books, 2015.

[2] M. Hassn and A. Eljondi, "Study of allowances External loads at nozzle/shell junctions of petroleum tanks," Journal of Engineering Sciences, First edition, Damusq 2006.

[3] P. Apurva, "Design and Analysis of Pressure Vessel," International Journal of Innovative Research in Technology & Science, Mumbai 2011.

[4] B. Thakkar and S. Thakkar, "Design of Pressure Vessel Using ASME Code, SECTION VIII, DIVISION 1," International Journal of Advanced Engineering Research and Studies, India 2012.

[5] V. Kumar, N. Kumar, S. Angra and P. Sharma, "Design of Saddle Support for Horizontal Pressure Vessel," International Journal of Mechanical, Aerospace, Industrial, Mechatronic and Manufacturing Engineering, 2014.

[6] M. Bhatt, A. Gohil, H. Shah and N. Patel. "Design Calculation Of Nozzle Junction Based On ASME Pressure Vessel Design Code," International Journal of Advance Engineering and Research Development, India 2014.

[7] ASME COMPANY. "ASME Boiler and Pressure Vessel Code, VIII Division 1 ," New York , 2010.

[8] E. Kaynejad. "Pressure Vessel Design,fabrication and test ASME section VIII, div. 1 ,"

[9] M. DENNIS, "PRESSURE VESSEL DESIGN MANUAL," Third edition, USA, 2004.

[10] V. Patil, "Determination of Safety of Inclined Leg Support for Pressure Vessel Subjected to Arbitrary Wind Load Using FEA," International Journal of Innovations in Engineering and Technology, Vol. 2, 2013

[11] E. Megyesy "Pressure vessel hand book," , Oklahoma 2001.

Design Methodology for Supply Water Distribution Network; Case Study: Al-Hadeka District, Garaboulli-Libya

Khairi Algrad, Abdulghani Ramadan*

Department of Mechanical Engineering, Faculty of Engineering, Elmergib University, Libya

DOI: https://doi.org/10.21467/proceedings.4.34

* Corresponding author email: amramadan@elmergib.edu.ly

ABSTRACT

Pipe network is a hydraulic network containing several or many inter-connected branches where fluid (water) flows through it. This paper presents a design methodology for a supply water pipe network for Al-Hadeka district at Garaboulli-Libya. The proposed network provides water to 150 residential units with an average occupation density of 7 persons per unit. The main objective is to determine the flow rate and pressure head at each individual section of the network in addition to water demand of the region. The governing differential equations were formulated based on the continuity and the energy equations. Hardy Cross Method and EPANET Software were implemented to perform the calculations. Two cases were analyzed and investigated, namely, gravity flow and forced flow. Results of both cases were interpreted and compared. There is a good agreement between the results of both methods, in terms of flow velocities in pipes and pressure heads. These values lie in the allowable range in accordance with the known standards and specifications for water distribution networks. The use of the available software, EPANET, for analysis saves time and effort and gives acceptable results of appropriate precision.

Keywords: Pipe network**,** Hardy Cross, EPANET, Gravity flow, Forced flow.

1 Introduction

Water distribution networks serve many purposes in addition to the provision of water for human consumption. Piped water is used for washing, sanitation, irrigation and fire fighting. Networks are designed to meet peak demands; in parts of the network this creates low-flow conditions that can contribute to the deterioration of microbial and chemical water quality. The purpose of a system of pipes is to supply water at adequate pressure and flow. However, pressure is lost by the action of friction at the pipe wall and pipe accessories and fittings such as valves, elbows…etc. The pressure loss is also dependent on the water demand, pipe length, gradient and diameter. Several established empirical equations describe the pressure–flow relationship and these have been incorporated into network modelling software packages to facilitate their solution and use. Traditionally, a water distribution network design is based on the proposed street plan and the topography. Various equations have been used in this study

 ISBN: 978-81-936820-6-7

as the continuity equation and the energy equation. Hardy Cross Method and EPANET Software was used to perform the calculations required. The hydraulic analysis for the network is applied to two cases, gravity flow and forced flow. Extensive research work on supply water networks has been carried out in literature. For example, studies as shown in references [1], [2], [3], [4] & [5]. Generally, they focused on designing and analyzing supply water pipe networks by Hardy Cross method and EPANET software. Flow rates and pressure heads at each node and junction in the network are calculated and determined. Comparison of results were also interpreted and discussed.

2 Site Overview

The site is located in Al-Hadeka district at Al-Garaboulli city, with an area of 31125 m^2 and 150 housing utilities as shown in Figure 1.

Figure 1: Site Overview for Al-Hadeka district at Al-Garaboulli city.

According to population surveys in Libya , in the year 2014 , it was found that the family member average is 7 persons , this was done with the help of population private data of the previous years , this comprehensive population scanning is done regularly every 10 years, amongst the methods used for future population scanning is the Geometric Method. Accordingly, population of this area is approximated to be 1050 persons and Water consumption rate is 270 Litre/day/person, so that the total water demand is about 284 m^3/day [6].

3 Design Methodology

3.1 Hardy Cross Method

Hardy Cross method is an effective method in pipe networks analysis. The Hardy Cross method of analysis is a simplified version of the iteration linear analysis. This method is mainly based on assuming reasonable starting values for water flow rates inside network pipes and their directions according to the proposed loops. Then, the values of flow rates should be adjusted iteratively in order to reach to an optimum and precise approximation. Moreover, the head loss in pipes is evaluated simultaneously. In order to apply this method, the site is divided into many subdivisions and loops as shown in Figure 2.

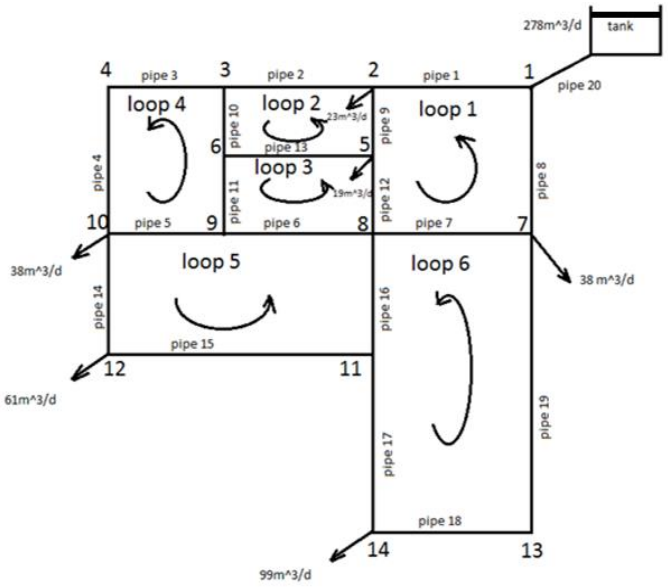

Figure 2: Schematic drawing for pipe network nodes, junctions and loops.

3.2 EPANET Software

EPANET Software, as shown in Figure 3, performs extended period simulation of hydraulics and pipe network analysis. Moreover, it is designed to be applicable also to pressurized pipe networkers. A pipe network consists of pipe, nodes (pipe junctions), pumps, valves and storage tanks or reservoirs. EPANET evaluates the flow rates of the water in each pipe, the pressure at each node. EPANET provides an integration environment for editing network input data, performing hydraulic analysis, and viewing the result in a variety of formats, these include colour- coded network maps, data tables, time series graphs, and contour plots. EPANET was developed by the Water Supply and Water Resources Division of the U.S. Environmental Protection Agency.

ISBN: 978-81-936820-6-7
Proceedings DOI: 10.21467/proceedings.4

Series: AIJR Proceedings

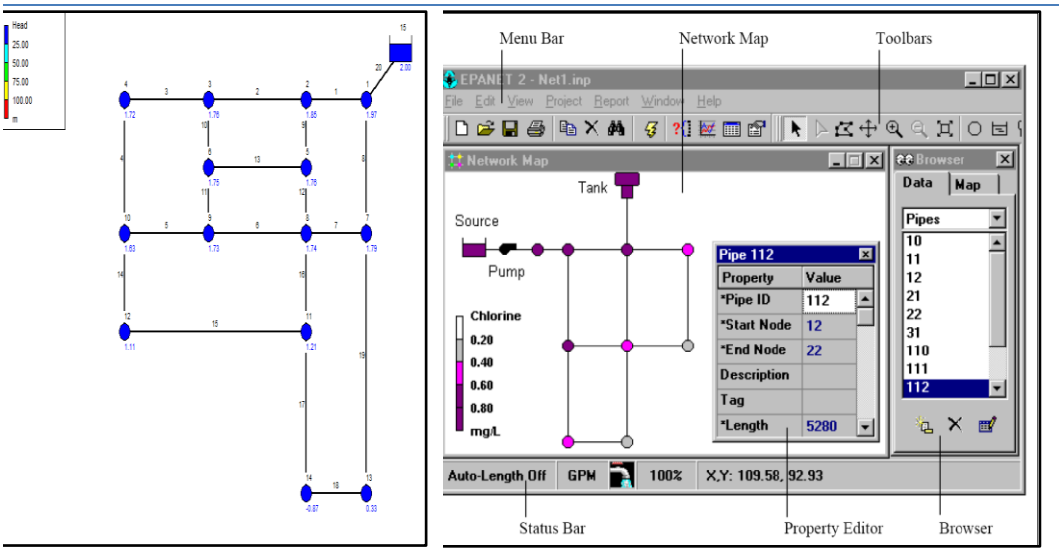

(a) (b)

Figure 3: Pipe network analysis by EPANET

(a) Present study pipe network. (b) EPANET software interface.

3.3 Solution Procedure

Following are the steps carried out to model water distribution network using Hardy Cross method and EPANET;

Step 1: Draw a network representation of distribution system.

Step 2: Edit the properties of the objects that make up the system. It includes editing the properties and entering required data in various objects like reservoir, pipes, nodes and junctions.

Step 3: Describe how the system is operated.

Step 4: Select a set of analysis option.

Step 5: Run a hydraulic analysis program/software.

Step 6: View the results of the analysis which can be viewed in various forms i.e. in the form of tables or graphs.

In addition, the pipe network design and operating conditions for this study according to known standards and specifications, [6] are as follows;

- Flow velocity inside pipes ranges from (0.1 to 1.5) m/s.
- The allowable pressure at nodes ranges from (1.5 to 3) bar.
- Pipe diameters range from (32 to 110) mm.
- Pipe material is HDPE can withstand pressure up to 6 bar.

In order to simplify the analysis, some assumptions are also considered as follows;

- Secondary losses inside pipe network fittings and other accessories are assumed to be negligible.

- Pipes are located at the same level inside the study area.

Storage tank capacity of 900 m^3 provides water to site at least for 3 days in case of emergency.

4 Results and Discussion

The hydraulic analysis for the pipe distribution network is applied to two design scenarios, namely, gravity flow case and forced flow case (using a pump).

4.1 Case I: (Gravity Flow)

In the first case the water level on the reservoir is located just 2 meters above ground surface. Results of Hardy Cross method are shown in Table 1 and Table 2.

Table 1: Output results of water flow rates in pipes.

Link ID	Q (m^3/s)	Q (L/s)	Q (m^3/day)
Pipe 1	0.001808	1.808	156.2112
Pipe 2	0.000726	0.726	62.7264
Pipe 3	0.000572	0.572	49.4208
Pipe 4	0.000572	0.572	49.4208
Pipe 5	0.000483	0.483	41.7312
Pipe 6	0.00011	0.11	9.504
Pipe 7	0.000351	0.351	30.3264
Pipe 8	0.00141	1.41	121.824
Pipe 9	0.000816	0.816	70.5024
Pipe 10	0.000154	0.154	13.3056
Pipe 11	0.000377	0.377	32.5728
Pipe 12	0.000373	0.373	32.2272
Pipe 13	0.000223	0.223	19.2672
Pipe 14	0.000615	0.615	53.136
Pipe 15	9.1E-05	0.091	7.8624
Pipe 16	0.000619	0.619	53.4816
Pipe 17	0.000528	0.528	45.6192
Pipe 18	0.00062	0.62	53.568
Pipe 19	0.00062	0.62	53.568
Pipe 20	0.00322	3.22	278.208

Table 2: Head values at each node.

Node ID.	Head (m)
1	1.97
2	1.85
3	1.76
4	1.72
5	1.76
6	1.75
7	1.79
8	1.74
9	1.73
10	1.63
11	1.21
12	1.11
13	0.33
14	-0.87

Results from EPANET software are shown in Table 3. Flow rates at each pipe, flow velocity, unit head loss and friction factor are determined.

ISBN: 978-81-936820-6-7
Proceedings DOI: 10.21467/proceedings.4

Series: AIJR Proceedings

Table 3: EPANET output results for case I.

Link ID	Flow rate (m^3/day)	Velocity (m/s)	Unit Head loss (m/km)	Friction factor
Pipe 1	1.2615	0.40	72.8	0.025
Pipe 2	95.16	0.22	71.2	0.030
Pipe 3	44.48	0.27	820.	0.031
Pipe 4	44.48	0.17	820.	0.031
Pipe 5	61.42	0.27	2	10.03
Pipe 6	9.401	20.1	130.	40.03
Pipe 7	23.03	0.19	01.1	0.034
Pipe 8	9.7112	0.32	31.8	0.026
Pipe 9	26.17	0.27	631.	0.029
Pipe 10	51.31	20.1	070.	340.0
Pipe 11	13.32	0.14	400.	50.03
Pipe 12	64.33	0.16	430.	40.03
Pipe13	26.81	0.10	160.	10.04
Pipe 14	05.35	0.48	58.7	0.029
Pipe 15	95.7	0.12	50.8	0.041
Pipe 16	7453.	0.50	888.	0.029
Pipe 17	5245.	0.65	219.8	0.029
Pipe 18	4853.	0.77	6326.	0.028
Pipe 19	4853.	0.49	888.	0.029
Pipe 20	278.00	0.34	1.26	0.024

From above results, Table 2 clearly shows that at node no. 14, the value of pressure head is negative. This means that the pressure at this node is less than atmospheric pressure which in turn implies that water will not reach the node and hence it is clear that the height of the elevated reservoir in case I, is undersized. Therefore, the water reservoir should be located at higher elevation. For this purpose, the tank is elevated at 20 m above ground surface level, this is considered as case II.

4.2 Case II: Gravity Flow using Elevated Tank

Because of the negative pressure in the case I, the tank height will be change to 20 m above ground. The obtained results of both Hardy Cross and EPANET are shown and compared in Table 4 and Table 5.

Table 4: Comparison of results for pressure head in case II.

Node ID	Head, H-C (m)	Head, Epanet (m)	Error, %
1	19.98278	19.97	0.06397
2	19.89224	19.85	0.212357
3	19.83574	19.76	0.381859
4	19.81069	219.7	0.457766
5	19.84119	619.7	0.409176
6	19.8304	519.7	0.405418
7	19.86057	19.79	0.355338
8	19.83201	19.74	0.463942
9	19.82799	319.7	0.494182
10	19.76803	319.6	0.698249
11	19.45122	119.2	1.240142
12	19.50449	1119.	2.022568
13	18.81528	318.3	2.579171
14	17.88649	317.1	4.22941

Table 5: Comparison of results for flow rates in case II.

Link ID	Q(m^3/day) H-C	Q(m^3/day) Epanet	Error, %
Pipe 1	156.2112	1.2615	0.000768
Pipe 2	62.7264	95.16	1.237756
Pipe 3	49.4208	44.48	1.984589
Pipe 4	49.4208	44.48	1.984589
Pipe 5	41.7312	61.42	2.10586
Pipe 6	9.504	9.410	10.5397
Pipe 7	30.3264	23.30	0.021104
Pipe 8	121.824	9.7112	0.027909
Pipe 9	70.5024	26.17	1.07457
Pipe 10	13.3056	51.31	1.5362
Pipe 11	32.5728	13.32	1.359416
Pipe 12	32.2272	64.33	4.38387
Pipe13	19.2672	26.81	3.359077
Pipe 14	53.136	05.35	0.161849
Pipe 15	7.8624	95.7	1.11416
Pipe 16	53.4816	7453.	0.02169
Pipe 17	45.6192	5245.	0.217452
Pipe 18	53.568	4853.	0.164277
Pipe 19	53.568	4853.	0.164277

ISBN: 978-81-936820-6-7
Proceedings DOI: 10.21467/proceedings.4

Series: AIJR Proceedings

It should be noted that no negative pressure head values are noticed. The assumption of elevating the water tank to a height of 20 m is reasonable and logic. Moreover, the comparison between the results from Hardy Cross method and EPANET shows a good agreement between results of both methods.

4.3 Case III: Forced flow Using Pump

Another alternative for solving the problem of negative pressure in case I, is based on using a ground water tank equipped with a pump station. In this case, water is forced to flow into the pipe distribution network ensuring suitable water demands and pressure heads values at pipes' nodes. Figure 4 shows the characteristics curve for the chosen pump to be used in the system and analyzed by EPANET Software simulation.

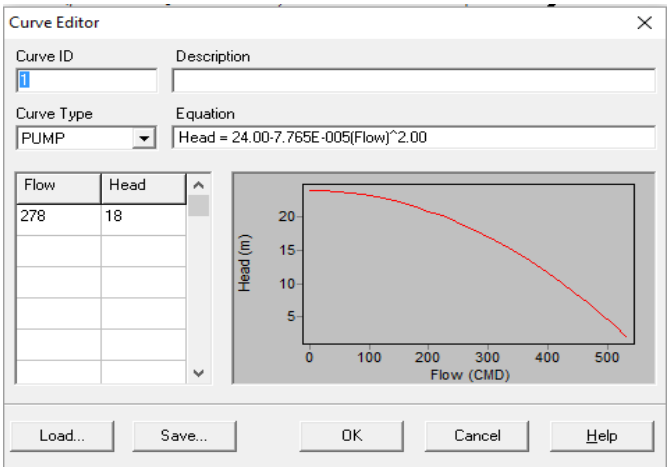

Figure 4: Characteristic curve of the chosen pump.

Table 6 and Table 7 show the results for case III when a pump is considered in the pipeline.

Table 6: Results for demand and pressure head at each node for case III.

Node ID	Demand (m^3/day)	Head (m)
1	0	20
2	23	19.87
3	0	19.78
4	0	19.74
5	19	19.79
6	0	19.78
7	38	19.82
8	0	19.77
9	0	19.76
10	38	19.66
11	0	19.24
12	61	19.13
13	0	18.35
14	99	17.15

Table 7: Results for flow rate, velocity, unit head loss and friction factor for case III.

Link ID	Flow rate (m^3/day)	Velocity m/s	Unit Head loss m/km	Friction factor
Pipe 1	156.21	0.40	2.84	0.025
Pipe 2	61.95	0.22	1.28	0.030
Pipe 3	48.44	0.27	0.93	0.031
Pipe 4	48.44	0.17	0.93	0.031
Pipe 5	42.61	0.27	1.73	0.032
Pipe 6	10.49	0.12	0.46	0.038
Pipe 7	30.32	0.19	1.16	0.034
Pipe 8	121.79	0.32	1.86	0.026
Pipe 9	71.26	0.27	1.59	0.029
Pipe 10	13.51	0.12	0.48	0.042
Pipe 11	32.13	0.14	0.57	0.037
Pipe 12	33.64	0.16	0.61	0.033
Pipe13	18.62	0.10	0.49	0.042
Pipe 14	53.05	0.48	8.74	0.029
Pipe 15	7.95	0.12	0.89	0.041
Pipe 16	53.47	0.50	8.94	0.029
Pipe 17	45.52	0.65	19.89	0.029
Pipe 18	53.48	0.77	26.78	0.028
Pipe 19	53.48	0.49	8.92	0.029

In the case of water supply from ground tank using a pump, case III, it is found that the pressure head at the end of each junction (node) and corresponding value of flow rate are acceptable and ensure providing water to consumers. Furthermore, it can be noticed that the velocities at each pipe in Table 7 are within the recommended range stated in the relevant standards.

5 Conclusions

In this paper, Hardy Cross Method and EPANET software were used to perform the required calculations and the hydraulic analysis for the network under study, Al-Hadeka district at Garaboulli city –Libya. Two Scenarios were proposed, gravity flow and forced flow. For gravity flow, Case I, water level in the storage tank is assumed to be 2 meters above the ground. Results show that there is a deficiency in providing the required water quantities at some nodes in the network. In order to correct the situation, storage tank elevation is adjusted to 20 meters above ground, case II. Results indicate that the flow rates and pressure heads among the junctions of the pipe networks are acceptable and lie in the allowable values.

Another alternative is to apply a pump in the network, case III, forced flow. As expected, there is a better output results in terms of flow rates, velocities in pipes and pressure heads at the required points of demand. The obtained values were found to be within the allowed ranges

ISBN: 978-81-936820-6-7

Series: AIJR Proceedings
Proceedings DOI: 10.21467/proceedings.4

in accordance with the specifications and standards for water distribution networks. Finally, the use of available software for analysis saves time and effort and gives results of appropriate precision.

References

[1] I.I. Nwajuaku, Y.M. Wakawa, O.J. Adibeli**, "**Analysis of Head-loss Equations under EPANET and Hardy Cross Method," *Saudi Journal of Engineering and Technology*, vol.2, issue 3, pp. 125-134, Mar, 2017.doi: 10.21276/sjeat.2017.2.3.1.

[2] A. E. Adeniran and M. A. Oyelowo, "An EPANET Analysis of Water Distribution Network of the University of Lagos, Nigeria," *Journal of Engineering Research*, Volume 18, No. 2, June 2013.

[3] N. Moosavian, M. R. Jaefarzadeh, "Hydraulic Analysis of Water Supply Networks Using a Modified Hardy Cross Method," *International Journal of Engineering Transactions*, Vol. 27, No. 9, pp 1331-1338, Sep. 2014.

[4] G. Venkata Ramanaa , V. S. S. Sudheer , B.Rajasekhar, "Network analysis of water distribution system in rural areas using EPANET," *Procedia Engineering*, vol. 119, pp 496-505, 2015.

[5] R.K.Rai, N.G. Sanap, "Analysis of Hydraulic Network using Hardy Cross Method and EPANET," *International Journal of Innovative Research in Science and Engineering*, vol3, issue 3, pp 516-522, Mar. 2017.

[6] "Design Standard", *Housing and Infrastructure Board, HIB*, Tajoura, Libya, Aug. 2008.

ESTIMATION OF EMPENNAGE DESIGN WEIGHT IN CONCEPTUAL DESIGN PHASE FOR TACTICAL UAVs

Abdulhakim Muhammad Essari

Department of Mechanical and Industrial Engineering, Elmergib University, Alkhoms – Libya

DOI: https://doi.org/10.21467/proceedings.4.35
* Corresponding author email: hakimsari@yahoo.com

ABSTRACT

New formulas for empennage weight estimation and for takeoff weight estimation, in conceptual design phase are derived for a tactical unmanned aerial vehicle (TUAV). Formulas are derived by analyzing existing UAVs of the weighs from 100 to 500 kg, and which have similar characteristics. Based on statistical trends, obtained from analyzed existing UAVs, takeoff weight is estimated from mission specification, and given payload weight. Software tools are developed in Matlab to facilitate takeoff and component weight calculations. The least square method is applied to analyze statistical data in order to develop trend functions which correlate TUAVs empty weight and takeoff weight. Existing formulas, developed for general aviation, for empennage and takeoff weight estimations are applied to TUAV and promising one are selected and adjusted to TUAV conceptual design phase. Empennage weight is related to geometrical parameters, maximum speed, and takeoff weight of the TUAVs

KEYWORDS: TUAV, Empennage, takeoff weight, conceptual design phase.

1 Introduction

The dependence on Unmanned Aerial Vehicles (UAV's) in last decade grow significantly especially for combat missions, and the demand for UAV's is greatly increased. UAV's play an important role in fields like, information superiority, collateral damage, urban area fighting and precision strikes against high payoff targets. UAV's evolved to include size growth of strategic UAV's for carrying more payload weight, and longtime endurance, and minimize tactical UAV's size. The most important parameter which dictates all other design parameter is estimation of the UAV's weight. Since there are no enough reliable sources for such estimation, the main goal of this paper is to establish empirical relationships which will lead to reliable empennage weight estimation of the UAV's, with emphasis on tactical UAV's. Only

 ISBN: 978-81-936820-6-7

conceptual design phase is considered to be effort of relatively small group of engineers and specialists. This phase is also the cheapest it should provide the answer if the vehicle is possible to design and what characteristics will it have. It is also only paper phase requiring no special equipment and research. Outer geometry of the vehicle is also defined in this phase.[1]

Since conceptual design phase cost least, it is wise to perform it thoroughly and to postpone crucial decisions as late as possible since all subsequent phases are continuation of this phase. This research will contribute to this problem by deriving equations for empennage weight estimation.

2 Materials and Methods

Models of conventional tactical UAVs weights between 100 to 450 kgs are chosen for empennage weight estimation.[2] The parameters values of these UAVs are input into Matlab program to get the results on charts, the results are evaluated for UAV weights 220 kg as takeoff weight to find out the suitable empennage weight.

2.1 Jay Gundlach Method: [1]

The formula used by Gundlach is established for both small and big aircrafts by changing w_a value according to the aircraft type. W_a ranges between 3.5–8 lb/ft2 for supersonic fighters and between 0.8 – 1.2 for small aircrafts. As shown in figure (1).

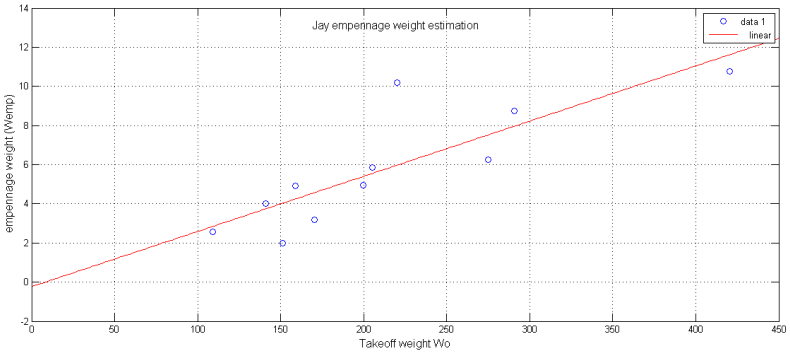

Figure (1) Jay Gundlach empennage weight estimation

, $w_a = 0.8\text{:}\ 1.2$ lb/ft2 $Wemp = w_a \times (S_h + S_v)$ (1)

W_{emp}, empennage weight, S_H and S_V, surface areas of horizontal and vertical stabilizer.

2.2 Usaf Method: [3]

The equations suggested by United States air force (Usaf) for finding empennage weight estimation should be applied to aircrafts with performance doesn't exceed 300 knots speed.

2.2.1 Horizontal Tail:

$$W_h = 127 \times \left(\left(\frac{w_o N_z}{10^5} \right)^{0.87} \times \left(\frac{S_h}{100} \right)^{1.2} \times 0.289 \times \left(\frac{l_h}{10} \right)^{0.483} \times \left(\frac{b_h}{t_h} \right)^{0.5} \right)^{0.458} \quad (2)$$

Where, W_o, takeoff weight of UAV, S_H and S_V, surface areas of horizontal and vertical stabilizer, L_H and L_V, horizontal and vertical stabilizer arm (distance between center of gravity and aerodynamic center), b, the wing span, t, tail thickness, N_z, ultimate load factor,

Figure (2) explain the relationship between takeoff weight and horizontal tail weight

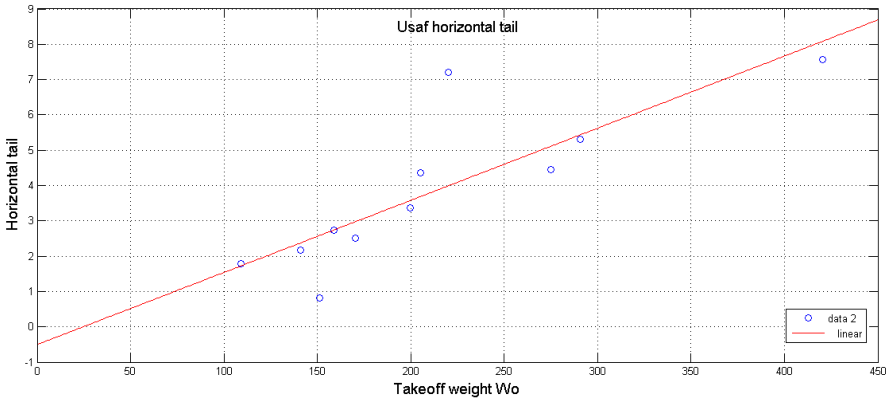

Figure (2) Usaf horizontal tail weight estimation

2.2.2 Vertical Tail:

$$W_v = 98.5 \times \left(\left(\frac{w_o N_z}{10^5} \right)^{0.87} \times \left(\frac{S_v}{100} \right)^{1.2} \times 0.289 \times \left(\frac{b_v}{t_v} \right)^{0.5} \right)^{0.458} \quad (3)$$

By substitution in equation (3) for V-tail weight estimation we get the results shown in figure (3), figure (4) show the results got for equation (4).

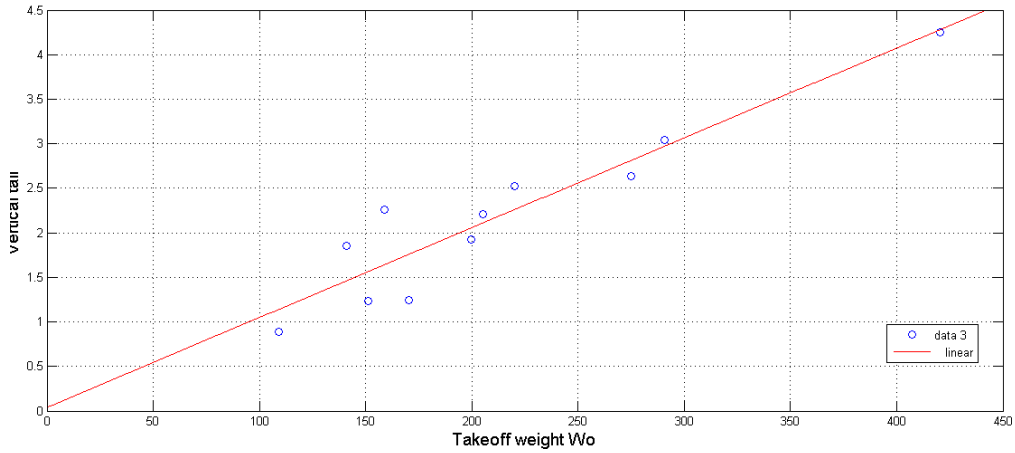

Figure (3) Usaf vertical tail weight estimation

ISBN: 978-81-936820-6-7
Proceedings DOI: 10.21467/proceedings.4

Series: AIJR Proceedings

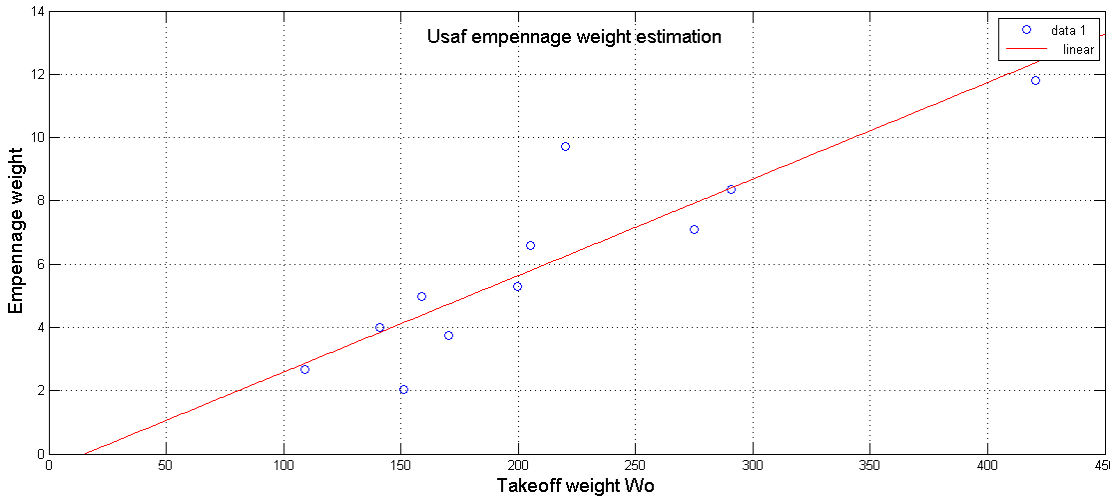

Figure (4) Usaf empennage weight estimation

2.3 Torenbeek Method: [4]

The following equation is applied to light transport aircrafts which has dive speed less than 200 knots.

$$W_{emp} = 0.04 \times (N_z \times (S_v + S_h)^2)^{0.75} \quad (4)$$

Where, W_{emp} is empennage weight. S_H and S_V are surface areas of horizontal and vertical stabilizer, and Nz is ultimate load factor.

Torenbeek equation (4), is a simple equation and it is completely depends upon the areas of both horizontal and vertical tails and ultimate load factor.

By substitution in Torenbeek equation (4) we get the results shown in figure (5):

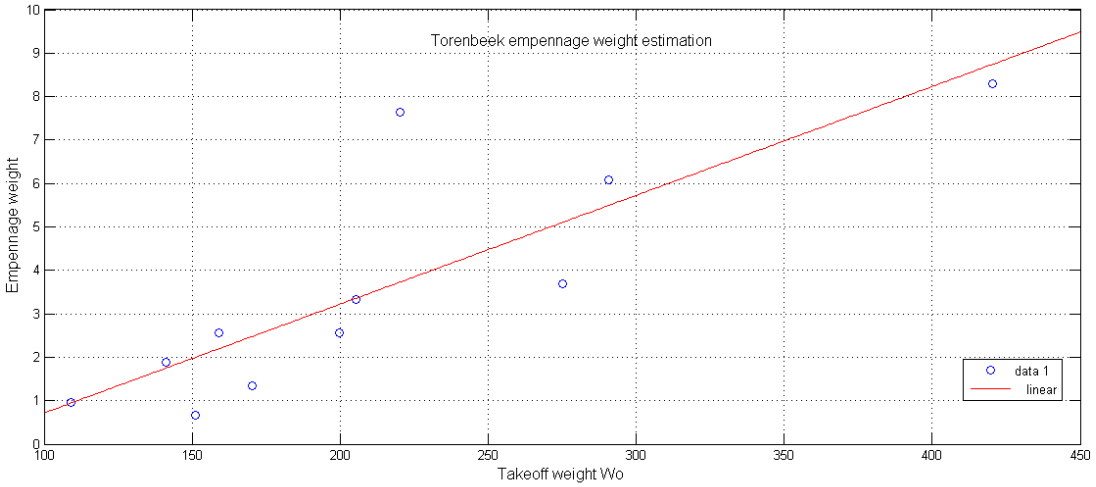

Figure (5) Torenbeek empennage weight estimation

2.4 Raymer Method: [3]

The following equations from Raymer are established for general aviation aircrafts.

2.4.1 Horizontal Tail:

Raymer equation for horizontal tail weight estimation is:

$$W_h = 0.016 \times (N_z \times W_{dg})^{0.414} \times q^{0.168} \times S_h^{0.896} \times \left(\frac{100 \times t/c}{cos\Lambda}\right)^{-0.12} \times \left(\frac{A}{cos^2 \Lambda_h}\right)^{0.043} \times \lambda_h^{-0.02} \quad (5)$$

Where, S_H and S_V, surface areas of horizontal and vertical stabilizer, b, the wing span, C is mean aerodynamic chord, V_H, Tail volume coefficient, V_V, Vertical Tail volume coefficient, t, tail thickness, N_z, ultimate load factor, A, aspect ratio, q, dynamic pressure, Λ, sweep angle at 25% MAC, λ, taper ratio.

Figure (6) show the relationship between takeoff weight and horizontal tail weight according to equation (5).

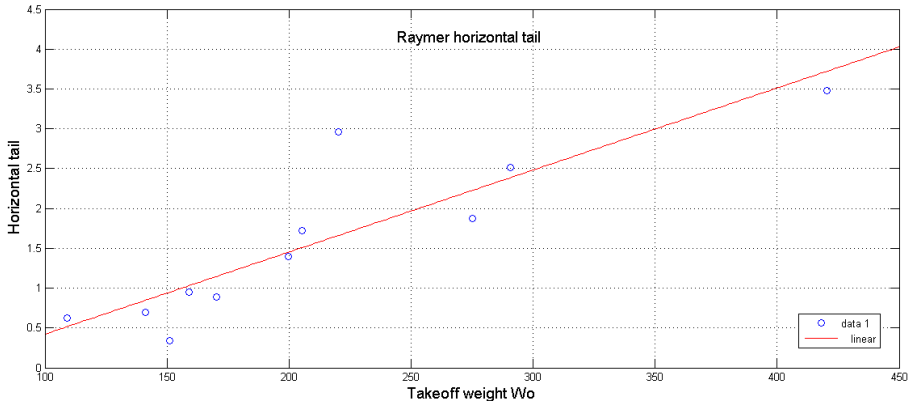

Figure (6) Raymer horizontal tail weight estimation

2.4.2 Vertical Tail:

$$W_h = 0.073 \times \left(1 + 0.2 \times \frac{H_t}{H_v}\right) \times (N_z \times W_{dg})^{0.376} \times q^{0.122} \times S_h^{0.873} \times \left(\frac{100 \times t/c}{cos\Lambda}\right)^{-0.49} \times \left(\frac{A}{cos^2 \Lambda_h}\right)^{0.357} \times \lambda_h^{0.039} \quad (6)$$

From equation (6) we got the results shown in figure (7),

ISBN: 978-81-936820-6-7
Proceedings DOI: 10.21467/proceedings.4

Series: AIJR Proceedings

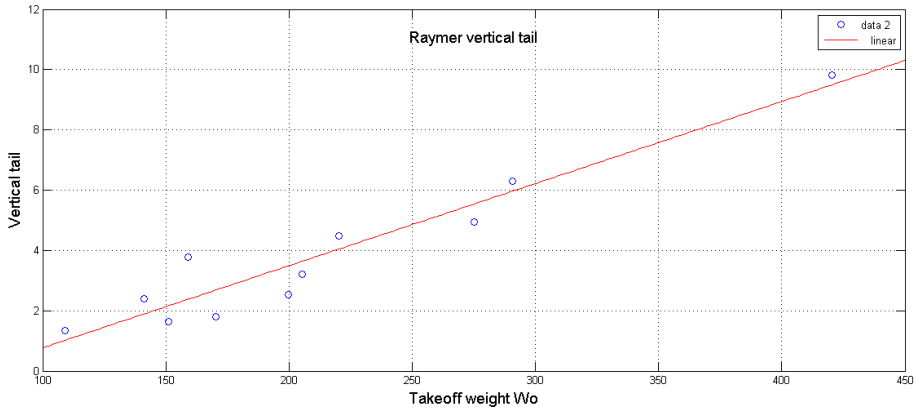

Figure (7) Raymer vertical tail weight estimation

Figure (8) explain the results for empennage group, (horizontal and vertical), weight estimation from Raymer.

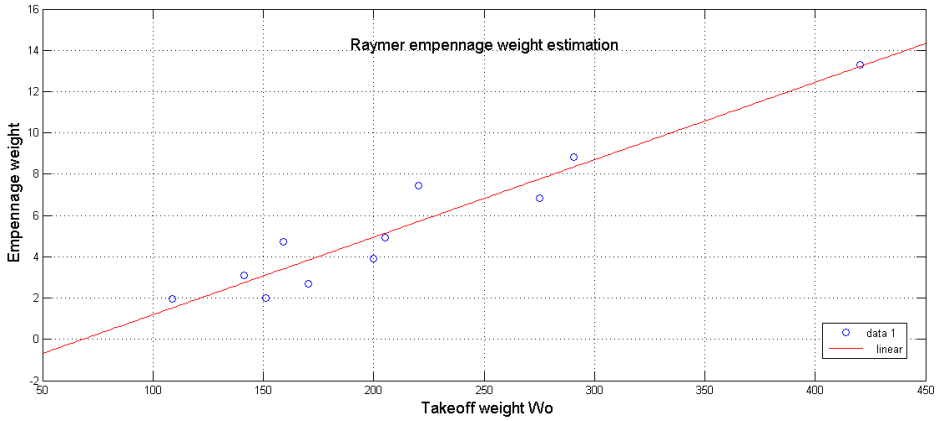

Figure (8) Raymer empennage weight estimation

2.5 Kundu Method: [5]

Horizontal and vertical tails are lifting surfaces. The empennage does not have an engine or undercarriage installation.

Both the horizontal and vertical tails plane mass estimations have a similar form but they differ in the values of constants used.

The equation used here is established for Civil Aircraft.

$$M_{emp} = 0.0213 \times (M_{to} \times N_z)^{0.48} \times S_w^{0.78} \times A \times (1+\lambda)^{0.4}/(cos\Lambda \times t/c^{0.4}) \qquad (7)$$

M_{emp}- empennage mass,M_{to} - takeoff weight mass

For nonmetals are used, if there is reduction in mass due to lighter material, then the mass is reduced by that factor. If there is a 10% mass saving, then:

M_E *nonmetal* $= 0.9 \times M_E$ *all metal*

Figure (9) show the results got from equations (7) and (8) for empennage weight estimation.

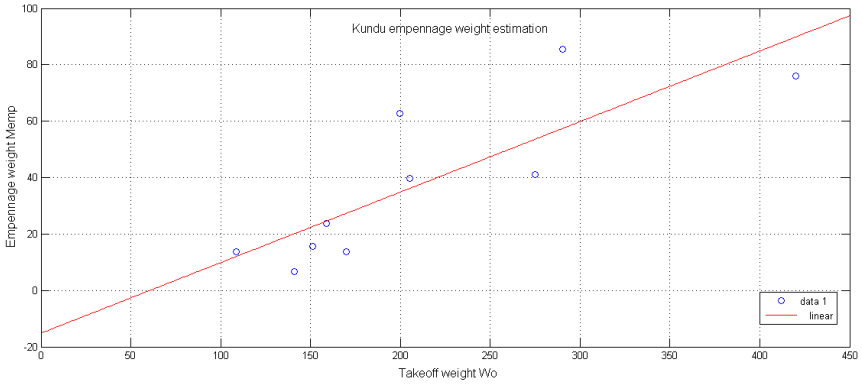

Figure (9) Kundu empennage weight estimation

2.5.1 Horizontal Tail:

$$M_H = 0.02 \times kconf \times (M_{to} \times N_z)^{0.48} \times S_w^{0.78} \times A \times (1+\lambda)^{0.4} / (cos\Lambda \times t/c^{0.4}) \quad (8)$$

2.5.2 Vertical Tail:

$$M_v = 0.0215 \times kconf \times (M_{to} \times N_z)^{0.48} \times S_w^{0.78} \times A \times (1+\lambda)^{0.4} / (cos\Lambda \times t/c^{0.4}) \quad (9)$$

For V-tail configurations, use k_{conf} = 1.1 for a T-tail, 1.05 for a midtail, and 1.0 for a low tail.

Where, W_o, takeoff weight of UAV, W_{emp}, empennage weight, S_H and S_V, surface areas of horizontal and vertical stabilizer, S, wing reference area, L_H and L_V, horizontal and vertical stabilizer arm (distance between center of gravity and aerodynamic center), b, the wing span, C is mean aerodynamic chord, V_H, Tail volume coefficient, V_V, Vertical Tail volume coefficient, t, tail thickness, N_z, ultimate load factor, A, aspect ratio, q, dynamic pressure, Λ, sweep angle at 25% MAC, λ, taper ratio.

2.6 Kroo Method: [6]

Kroo introduces two formulas for both horizontal and vertical tails.

2.6.1 Horizontal Tail:

The horizontal tail weight, including elevator, is determined similarly, but the weight index introduces both exposed and gross horizontal tail areas as well as the tail length (distance from airplane c.g. to aerodynamic center of the horizontal tail). The method assumes that the elevator is about 25% of the horizontal tail area.

$$W_h = 5.25 \times S_h + 0.8 \times 10^{-6} \times \frac{(N_z \times {b_h}^3 \times W_o \times mac \times S_h^{0.5})}{\left(\left(\frac{t_h}{c_h}\right) \times (\cos)^2 y_h \times l_h \times S_h^{1.5}\right)} \quad (10)$$

ISBN: 978-81-936820-6-7
Proceedings DOI: 10.21467/proceedings.4

Series: AIJR Proceedings

Figures (10),(11), and (12) explain the results of equations (10) and (11) for horizontal, vertical, and empennage weight estimation by Kroo method.

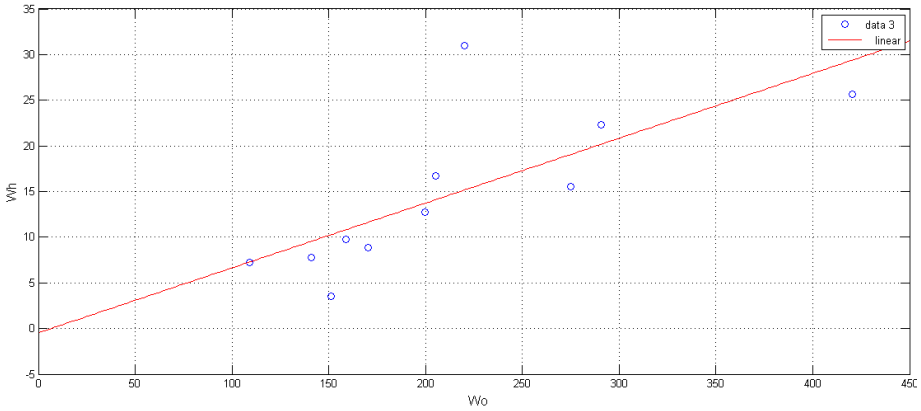

Figure (10) Kroo horizontal tail weight estimation

2.6.2 Vertical Tail:

The rudder itself may be assumed to occupy about 25% of S_V and weighs 60% more per area. The weight of the vertical portion of a T-tail is about 25% greater than that of a conventional tail; a penalty of 5% to 35% is assessed for vertical tails with center engines.

$$W_V = 2.62 \times S_v + 15 \times 10^{-6} \times \frac{\left(N_z \times {b_v}^3 \left(0.8 + 0.44 \times \left(W_o/S_{ref}\right)\right)\right)}{\left(\left(\frac{t_h}{c_h}\right) \times (\cos y_h)^2\right)} \quad (11)$$

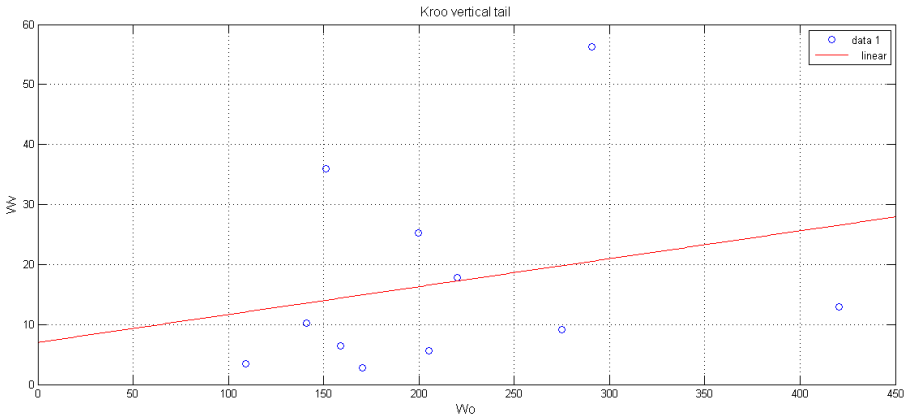

Figure (11) Kroo vertical tail weight estimation

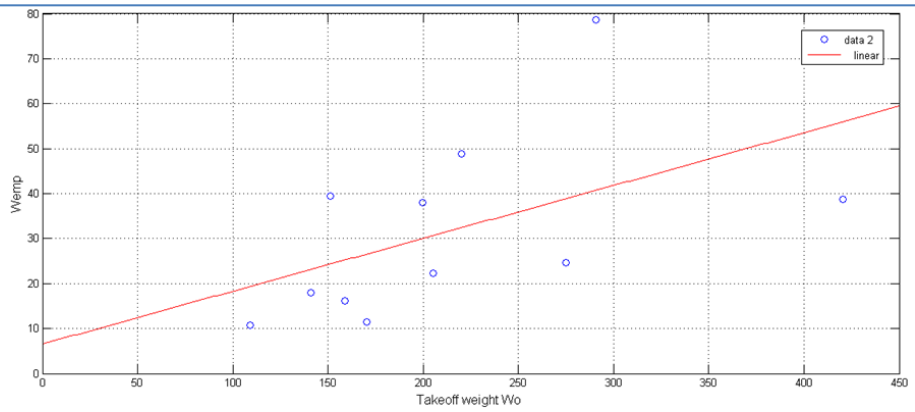

Figure (12) Kroo empennage weight estimation

3 Results and Discussion:

3.1 Empennage Weight Formulas Selection:

For empennage weight estimation many formulas were used for finding the estimated empennage weight, and the results were explained on charts to get the best one. The formulas used for empennage weight mostly were founded for general aviation aircrafts and because of presence a lot of tail group shapes and designs. So in some cases we see unreasonable and extreme results for empennage weight estimation, but in some few cases we got acceptable results such as in Jay Gundlach, Torenbeek and Usaf formulas.

Empennage group has no specific design criteria, because some UAVs have special empennage shapes, some of them have no horizontal tail instead they have delta wing, in some cases the vertical tail is much bigger than the horizontal tail and in some case there are two vertical tails.

3.2 New Formula for Empennage Weight Estimation:

These equations of our work for horizontal and vertical tails weight estimation are modified of Cessna equations. They should be applied to small size and low performance aircrafts which has maximum speed less than 350 km/hr. [7], [8].

3.2.1 Horizontal Tail:

The equation from Cessna for horizontal tail weight estimation, originally established for general aviation aircrafts. The new equation (12) now is valid for UAV's.

$$W_h = \frac{1.46 \times (Wo)^{0.887} \times (S_h)^{0.101} \times A_h^{0.138}}{57.5 \times t_r^{0.223}}\ lb \qquad (12)$$

Where, W_o is takeoff weight, S_H and S_V, surface areas of horizontal and vertical stabilizer, b, the wing span, C is mean aerodynamic chord, V_H, Tail volume coefficient, V_V, Vertical Tail

ISBN: 978-81-936820-6-7
Proceedings DOI: 10.21467/proceedings.4

Series: AIJR Proceedings

volume coefficient, t, tail thickness, N_z, ultimate load factor, A, aspect ratio, q, dynamic pressure, Λ, sweep angle at 25% MAC, λ, taper ratio.

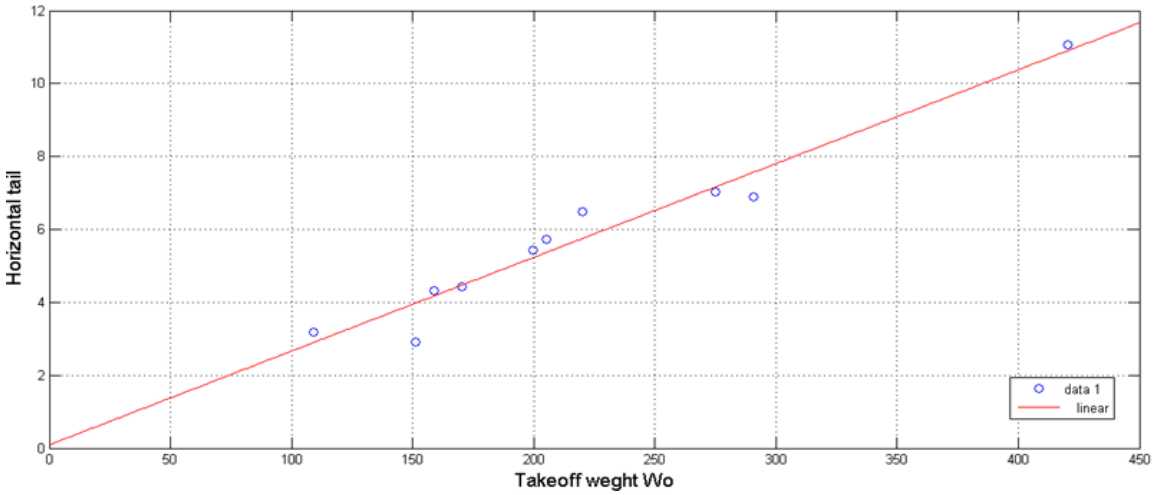

Figure (13) chart for the new equation for horizontal tail weight estimation

3.2.2 Vertical Tail:

The equation from Cessna for vertical tail weight estimation, originally established for general aviation aircrafts. My equation (13) now is valid for UAV's.

$$W_v = \frac{0.039 \times W_o^{0.567} \times S_v^{1.249} \times A_v^{0.482}}{15.6 \times t_r^{0.747} \times \left(cos\Lambda_{1/4}\right)^{0.882}}\ lb \qquad (13)$$

Figure (14) show the results from equation (13) for vertical tail weight estimation by the new equation.

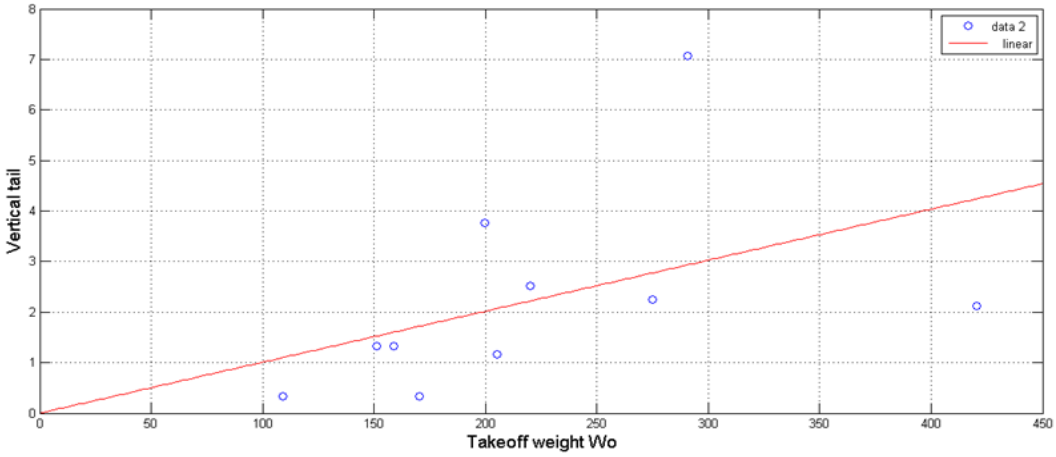

Figure (14) chart for the new equation for vertical tail weight estimation

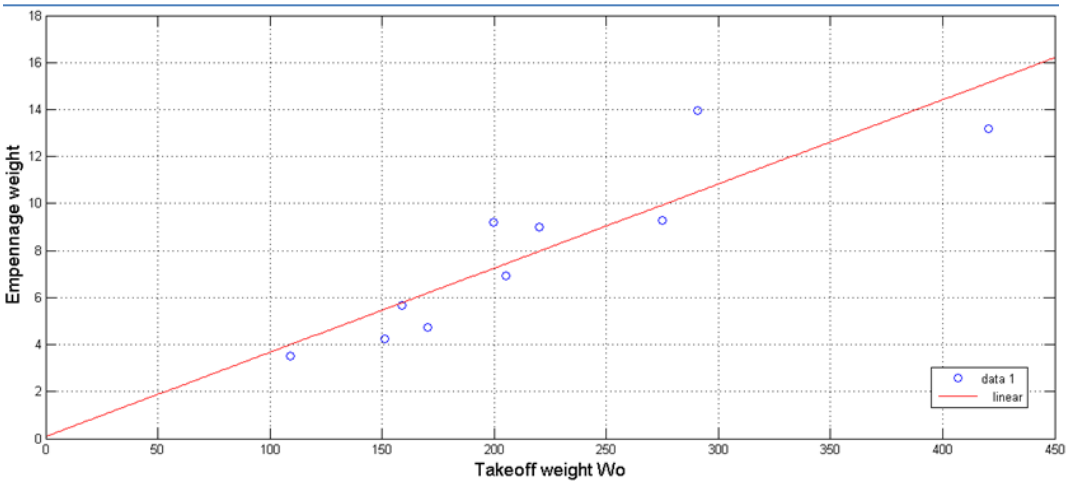

Figure (15) Empennage group

4 Conclusions

Various weight design formulas are applied to estimate empennage weights of UAVs. Since these formulas are developed for manned aircrafts (which are much heavier than tactical UAVs) they sometimes give unacceptable estimations (to high values or to small values than it could be expected by common sense). Modification in coefficients of the available formulas is done in order to get better fit UAV design process. These modified formulas are the main contribution of this paper. Application of these formulas estimates more accurately empennage weight of the UAVs. Two suggested formulas for empennage weight estimation including horizontal and vertical tails are introduced.

References:

[1] Jay Gundlach. Designing Unmanned Aircraft Systems: A Comprehensive Approach. Published by the American Institute of Aeronautics and Astronautics, Inc. 2012.

[2] Paul Jackson. Jane's All the World's Aircraft. 2004-2005.

[3] Daniel P. Raymer. Aircraft Design: A conceptual Approach. Published by the American Institute of Aeronautics and Astronautics, Inc. Second Edition 1992.

[4] Egbert Torenbeek. Synthesis of subsonic airplane design. Torenbeek1976

[5] Ajoy Kumar Kundu. Aircraft Design. Published in the United States of America by Cambridge University Press, New York. 2010.

[6] Ilan Kroo. Aircraft Design: Synthesis and Analysis. This textbook is copyright by Desktop Aeronautics, Inc. 2001.

[7] Jan Roskam. Aircraft Design. Part 5. Component Weight Estimation. 1989.

[8] Mohammad H. Sadraey. Aircraft Design: A system Engineering Approach. A john Wiley & Sons, Ltd Publications. 2012.

ISBN: 978-81-936820-6-7
Proceedings DOI: 10.21467/proceedings.4

Series: AIJR Proceedings

Track 5

Engineering Systems and Sustainable Development

 ISBN: 978-81-936820-6-7

Exergy Analysis of a Brine Mixing Once – Through MSF-BM Distillation Plant

Usama Ahmed Ezzeghni[1*], Mohamed Abduljawad[2]

[1]Department of Desalination Researches, Nuclear Research Center, Libya
[2]Department of Scientific Publications Authority of Natural Sciences, Research and Technology, Libya

DOI: https://doi.org/10.21467/proceedings.4.36
* Corresponding author email: elzoghni@gmail.com

ABSTRACT

Exergy analysis is a tool that can be used to detect the sites and causes of thermodynamic inefficiencies in a thermal process, as well as to prospect the design performance of any industry plants. The practice of such an analysis in seawater desalination plants is of increasing importance to discover the sites of the biggest irreversible losses. In this paper a full exergy analysis of a brine mixing once through multi stage flash MSF-BM desalination plant was carried out to identify the component that has the largest exergy destruction. The MSF-BM desalination plant is located at 30 km north-west of Tripoli the capital of Libya.

Exergy flow rates are estimated all over the plant and exergy flow diagram is prepared. The results of the exergy analysis show that the multi-stage flash unit, pumps and motors are the major sites of highest exergy destruction, where 61.48 % of the entire input exergy took place in the MSF unit, and 19.8 % happens in the pumps and motors. The second law of efficiency was estimated to be 6.24 %, which seems to be low that mean some improvements should be made to improve the plant efficiency and reduce exergy destruction, the improvement can be made to the MSF unit by increasing the number of flashing stages and to the pumps and motors by installing modern pumps with high efficiency.

Keywords: seawater desalination; exergy; exergy flow rates, exergy analysis.

1 Introduction

The leading desalination approaches used are multi-stage flash distillation (MSF), which establishes 44% of installed world capacity, and reverse osmosis (RO) with constitutes 42% that also comprises nanofiltration (NF). Consequently, these two approaches create about 86% of total world capacity. The outstanding 14% is made up of electrodialysis (EDR) (6%), vapor compression (VC) (4%), and multiple-effect distillation (ME) (4%) [1]. Even if these techniques are well established, there is a necessity to push the state of the art forward to make the operation of these plants more effective. An evaluation of the idealized and actual

 ISBN: 978-81-936820-6-7

desalination technologies displays that the actual energy cost of desalination is around 5–10 times the cost under ideal operation. This matches to a second law efficiency of under 20% and points out that there are good chances in the MSF plants for improvements. The initial step in any upgrading or development project is diagnostics, and the dominant diagnostics tool in thermodynamics is second law analysis. Such an analysis aids to discover the locations of maximum entropy generation and, thus, exergy destruction then to recognize the components that are responsible for the highest losses in the system [2].

All studies approved that desalination technologies have a total exergy efficiency less than 30 %, multi-stage flash desalination type is considered the lowest exergy efficiency amongst the desalination technologies, its energy efficiency fluctuates between 1.8% - 7.73 %. Papers available in exergy desalination field are not much due to the shortage of the data and complexity of exergy estimation of the seawater streams [3]. Osman A. Hamed et al. showed that second law simulation papers revealed that exergy destruction of the MSF distillers varied between 16.7 to 23.6 kWh/m^3 compared to the others of only 2 kWh/m^3 of an ideal reversible process. So, it has been recommended that hard work researches are to be done to decrease the energy consumption of the MSF distiller.

The second law of thermodynamics (exergy analysis) becomes further appreciated to measure the performance of the desalination systems. Exergy analysis interprets for the obtainable forms of energy in the system streams and energy supply with a reference environment and recognizes the major losses of energy/exergy destruction. This helps in evolving an effective desalination processes by reducing the hidden losses [4].

The exergy analysis is principally derived from second law of thermodynamics and provides a perfect basis of the inefficiencies of a MSF desalination plant. The aim of this paper is to make an exergy analysis, exergetic efficiency, and exergy destruction of MSF-BM desalination plant. The analysis is performed for the plant based on the available operating data.

2 Plant Description

The MSF desalination plant has been erected in Tajoura 30 km north-west of Tripoli the capital of Libya. The plant contains 12 stages and designed to produce 1200 m^3/day of distillate water [2]. Figure 1 shows the schematic diagram of the plant. The feed seawater is pretreated with antiscalant, antifoam chemicals and sodium-bisulfite to remove residual chlorine, then, it passes through the tube bundle of the stage 12, to increase the feed seawater temperature further until it reaches the brine heater inlet temperature (98.6 °C), after passing through the brine heater, the feed water reaches the top brine temperature (108 °C) using outside heating steam supplied by an external boiler at a temperature of 115 °C. The heated feed seawater goes into the first distilling chamber and flashes to a vapor pass through a wire mesh called a demister to trap the entrained droplets and the vapor condenses over the tube bundle and collected on trays as a distilled water, the same thing happens in each stage. The

produced distillates in each stage are collected in an external distillate pipe and then discharged out of the plant using a distillate pump. The outstanding concentrated feed seawater is discharged out of the plant through the blow down pump. Due to the summer/winter fluctuations of the seawater temperature (min 15 °C/max 28 °C), the plant is provided with an automatic remixing device, which saves the inlet temperature of the feed seawater at 28 °C [5].

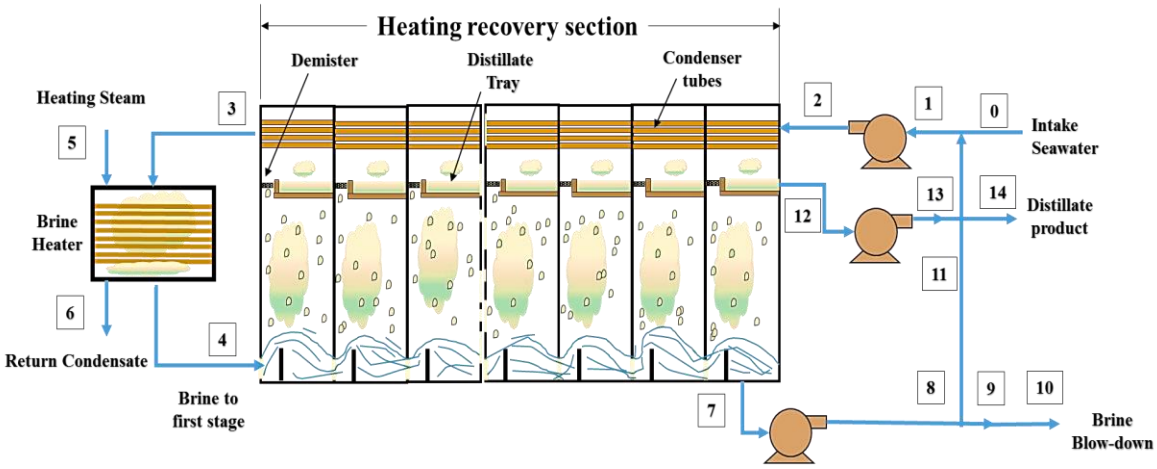

Figure 1: *Schematic of the MSF-BM distillation plant.*

3 Exergy Analysis

This once through MSF desalination plant was analysed under the following assumptions without losing accuracy, to simplify the model and make the distillation process shown in Figure 1 an idealized distillation process:

- All components of the system are assumed time-invariant (steady state) with negligible potential and kinetic energy effects.
- The reference state temperature and pressure are the temperature of the feed seawater and 1 atm, respectively.
- The salinity of the incoming raw water is constant.
- Distillate product is salt free.
- The saline water or the mixture of salt and water is an ideal solution so the mixture properties are the average of component properties.
- Saline water, which consists of salt and water, is incompressible constituents.
- Thermodynamic properties of seawater are taken as that for sodium chloride solutions, since the latter is the primary constituent (80- 90%) in seawater.
- The impact of chemical exergy to total exergy is minor and insignificant.
- The flashing chambers and other system components are assumed to have negligible heat losses.

ISBN: 978-81-936820-6-7
Proceedings DOI: 10.21467/proceedings.4

Series: AIJR Proceedings

The properties of seawater depend on its pressure, temperature and salinity. The later can be defined as ppm (parts per million on a mass basis), percentage (sal), salt mass fraction (mf_s) or a salt mole fraction (x_s). mf_s and x_s are described as [4, 5]:

$$mf_s = \frac{m_s}{M_m} = \frac{N_s M_s}{N_m M_m} = x_s \frac{M_s}{M_m} \quad and \; Mf_w = \frac{M_w}{M_m} = x_w \tag{1}$$

where m is mass, M is the molar mass, N is the number of moles, and x is the mole fraction. The letters s, w, and m stands for salt, water, and seawater, respectively [6].

The molar mass of the seawater is

$$\boldsymbol{M_m = \frac{m_m}{N_m} = \frac{N_s M_s + N_w M_w}{N_m} = x_s M_s + x_w M_w} \tag{2}$$

The molar masses of NaCl and water are 58.5 kg/kmol and 18.0 kg/kmol, respectively [6].

Mass fractions are used for salinity calculations, where mole fraction used for the minimum work calculations. Combining equations 1 and 2 and noting that $x_s + x_w = 1$ gives the following relations:

$$x_s = \frac{M_w}{M_s\left(1/mf_s - 1`\right) + M} \; and \; x_w = \frac{M_s}{M_w\left(1/mf_w - 1\right) + M_s} \tag{3}$$

Solutions that have a concentration less than 5 % are considered dilute solutions that behave as an ideal solution, so the effect of unlike molecules are neglected. Seawaters and saline underground waters are all ideal solutions since they have about a 4% salinity [4, 5].

The enthalpy and entropy of a mixture are determined from

$$H = \sum m_i h_i = m_s h_s + m_w h_w \quad \text{and} \quad S = \sum m_i s_i = m_s s_s + m_w s_w \tag{4}$$

Dividing by the total mass of the mixture gives the quantities per unit mass of mixture

$$H = \sum m_i h_i = m_s h_s + mf_w h_w \quad \text{and} \quad S = \sum mf_i s_i = mf_s s_s + mf_w s_w \tag{5}$$

During mixing, no heat is released or absorbed that means the enthalpy of mixing and the mixture of an ideal gas is zero (and thus the enthalpies of its single constituents). Consequently, the enthalpy of an ideal mixture at a defined temperature and pressure is the summation of the enthalpies of its single constituents at the same temperature and pressure [7], then, it follows that the enthalpy of a seawater which can be determined from the relation above by evaluating the enthalpies of individual components at the mixture temperature and pressure.

The feed seawater to the desalination plant is at about 15 °C, 1 bar, and a salinity of 40,000 ppm, these condition can be taken as a conditions of the environment, then the properties at the dead state become T_0 = 298.15 °K, P_0 = 1 bar = 101.325 kPa; salinity = 40,000 ppm = 4 %.

4 Enthalpy and Entropy of Pure Water and Salt

Properties of pure water are available in arranged tables or computer programs. Water properties expected by the built-in functions of the Engineering Equation Solver (EES) software at temperature and pressure were used [6]. Furthermore, the equations 6 and 7 can be used for calculating enthalpy and entropy, respectively for pure water properties and provide a very close values to that achieved by EES software [6].

$$h_w = 141.355+4202.07*t-0.535*t^2+0.004*t^3 \quad (6)$$

$$s_w = 0.1543+15.383*t-2.996*t^2+8.193*t^3-1.370*10^{-7}*t^4 \quad (7)$$

The reference state of salt is taken at 0°C, so the enthalpy and entropy of salt at temperature T can be estimated by following equation

$$h_s = h_{so} + C_{ps}(T - T_o) \quad \text{and} \quad h_s = h_{so} + C_{ps}\, ln(T/T_o) \quad (8)$$

The specific heat of salt C_{ps}=0.8368 kJ/kg.°K. The enthalpy and entropy of salt at T_o = 15°C h_{so} = 12.552 kJ/kg and s_{so}= 0.04473 kJ/kg.°K, respectively (The enthalpy and entropy of incompressible constituents are independent of pressure) [4].

The entropy of each constituent in an ideal solution at a defined temperature T and pressure P is

$$\bar{S}_i = S_{i,pure}(T,\bar{P}) - R_u \ln x_i \quad (9)$$

Then the entropy of a saline solution (salt and water) is

$$\bar{S} = x_s\bar{s}_s + x_w\bar{s}_w = x_s\left[\bar{S}_{s,pure}(T,P) - R_u \ln x_s\right] + x_w\left[\bar{S}_{w,pure}(T,P) - R_u \ln x_w\right] = x_x\bar{S}_{s,pure}(T,P) - R_u(x_s ln x_s + x_w ln x_w) \quad (10)$$

The entropy of saline water per unit mass is estimated by dividing by the molar mass of saline water. So the equation 10 can be written as:

$$S = mf_s s_{s,pure}(T,P) + mf_w s_{w,pure}(T,P) - R_m\,(x_s \ln x_s + x_w \ln x_w)\ (kJ/kg.°K) \quad (11)$$

The specific exergy of each stream is given by

$$\Psi = h - h_o + T_o(S - S_o) \quad (12)$$

Then the exergy flow rate related becomes

$$\dot{X} = \dot{m}\Psi = \dot{m}\,[h - h_o + T_o(S - S_o)] \quad (13)$$

By means of the previous equations, the specific exergy and exergy flow rates at different locations shown in Figure 1 are estimated.

ISBN: 978-81-936820-6-7
Proceedings DOI: 10.21467/proceedings.4

Series: AIJR Proceedings

The overall exergy balance for any system can be expressed as [8].

$$X_{in} = X_{out} - X_{destroyed} = \Delta X_{system} \quad (14)$$

If there is no work interaction (adiabatic steady sate system), the earlier equation can be simplified to

$$X_{destroyed} = X_{in} - X_{out} \quad (15)$$

The exergy efficiency of all constituents can be estimated by

$$\eta_c = 1 - X_{destroyed}/X_{out} \quad (16)$$

5 Results and Discussion

Tajoura desalination plant was analysed using the relations prescribed above, where the specific exergy, the exergy flow rates and the rate of exergy change at different locations are calculated, and the results are tabulated in Table 1. The locations of the states are illustrated in the diagram of Tajoura plant shown in Figure 1. The feed seawater enters the plant and the final permeate and concentrate leaving the plant are at the same dead state temperature and pressure, but at different salinities. Thus, the exergies of the concentrate line differ only due to the change in salinities, as it can be seen from Table 1 the raw feed seawater at state 0 has zero exergy since it is at the dead state. The brine at state 10 leaves the system at a high salinity of 58,700 ppm.

The results of the analysis are obtained using the EES software and are given in Table 1. Saline water is heated from (98.61°C) 371.76 °K to (108 °C) 381.15 °K at a rate of 3621 kg/s by super-heated steam at 179.91 °C in a heat exchanger. Steam leaves the heat exchanger at the same temperature as saturated liquid. An energy balance on the heat exchanger gives the condensation rate of steam to be 2.06 kg/s, where the heat transfer rate to the saline water from steam is

$$\dot{Q}_{in,steam} = \dot{m}_{steam}\, h_{fg} = 4142.36\ kJ/s$$

Taking the dead state temperature to be To 288.15 °K, the rate of exergy supply by the steam is

$$\dot{X}_{in,steam} = \dot{m}_{steam}(\Delta h - T_o \Delta s)\ or\ \dot{m}_{steam}\left(h_{fg} - T_o Ts_{fg}\right)$$

$$\dot{X}_{in,steam} = 1508.36\ kJ/s$$

The total exergy rate is the sum of the exergy variations through the pumps and can be expressed as

$$\Delta\dot{X}_{pumps} = \Delta\dot{X}_{seawater\ pump} + \Delta\dot{X}_{distillate\ \ pump} + \Delta\dot{X}_{brine\ blowdown\ pump}$$

$$= \left(\dot{X}_2 - \dot{X}_1\right) + \left(\dot{X}_8 - \dot{X}_7\right) + \left(\dot{X}_{13} - \dot{X}_{12}\right) = 9085.24\ kW$$

For a combined pump-motor efficiency of 79%, the exergy supplied in the form of electric power is

$$\dot{X}_{in,pumps} = \frac{\Delta \dot{X}_{pumps}}{\eta_{ump-motor}} = 11500.30\ kW$$

Where, a combined pump-motor efficiency can be expressed as the ratio of the mechanical energy transferred to the fluid over the electrical energy consumed [7].

$$\dot{X}_{in,\ total} = \dot{X}_{in,\ steam} + \dot{X}_{in,\ pumps} = 13008.67\ kW$$

Table 1: *Properties and exergy flow rates at various locations all over the plant.*

Location	Temperature, T, °K	Pressure P, kPa	Salinity, ppm	Mass flow rate, kg/s	Specific exergy ψ, kJ/kg	Exergy flow rate, $\dot{X}$, kW
0	288.15	101.325	40,000	52.58	0.00	0.00
1	301.15	281.325	52,100	123.12	25.4365	3131.801
2	301.15	700	52,100	123.12	4.291	7915.647
3	371.73	700	52,100	123.12	102.929	12672.882
4	381.15	700	52,100	123.12	111.66	13747.794
5	453.06	1000	-	2.06	733.797	1508.360
6	453.06	1000	-	2.06	0.000	0.000
7	310.57	101.325	58,700	123.12	9.60737	1182.881
8	310.57	180	58,700	123.12	16.8889	2079.402
9	310.57	180	58,700	52.58	16.8889	888.076
10	288.15	101.325	58,700	52.58	9.56663	503.045
11	310.57	180	58,700	70.54	16.8889	1191.326
12	310.57	101.325	1	13.89	22.2146	308.537
13	310.57	300	1	13.89	41.8758	581.608

The minimum work requirement to extract product water with a mass flow rate of 51.25 kg/s from the incoming seawater with a salinity of 40,000 ppm at 15 °C, 1 atm into 13.89 kg/s of fresh water with zero salinity and 29.67 kg/s of concentrate water with a salinity of 58,700 ppm at the same temperature and pressure. The minimum work input for a steady flow adiabatic process is the work input required for a reversible adiabatic process and is equivalent to the variance between the leaving exergy streams and the entering exergy streams, plus the salinity exergy [8]. Where, the inlet and exit streams are at the same temperature and pressure,

ISBN: 978-81-936820-6-7
Proceedings DOI: 10.21467/proceedings.4

Series: AIJR Proceedings

and thus, this work is totally due to the composition of the entering and leaving streams. Therefore

$$\dot{W}_{min} = \dot{X}_{outgoing\ brine\ and\ product\ water} - \dot{X}_{incoming\ seawater} = \dot{X}_{14} + \dot{X}_{10} - \dot{X}_0 = 811.58\ kW$$

The second-law efficiency is a degree of the process approximation to a reversible process, and it specifies the range accessible for potential improvements, noting that the second-law efficiency ranges from 0 for a totally irreversible process to 100 percent for a totally reversible process [9], the second law efficiency of the plant is the ratio of the minimum required inlet exergy to the total actual exergy, which can be expressed as

$$\dot{X}_{II} = \frac{\dot{X}_{in,min}}{\dot{X}_{in,total}} = 6.36\ \%$$

This value indicates that this MSF plant at the specified rates could be accomplished using only 811.58 kW of exergy (or work input) instead of 13008.67 kW. Then, the total exergy destruction becomes

$$\dot{X}_{destroyed,total} = \dot{X}_{in,total} - \dot{X}_{in,min} = \dot{X}_{in,total} - \dot{W}_{min} = 12197.08\ kW$$

The real value of second law analysis becomes more evident when the analysis is performed at the component level, and the sites of maximum exergy destruction upto the smallest exergy destruction are calculated according to following exergy balance equations:

$$\dot{X}_{destroyed,pumps} = \dot{X}_{in,pumps} - \Delta\dot{X}_{pumps} = 2415.06\ kW\ (19.8\ \%\ of\ total)$$

The exergy balance for any system undergoing any process is expressed as:

$$X_{in} - X_{out} - X_{destroyed} = \Delta X_{system}$$

For adiabatic steady state system, which has no energy transfer by work and no change in exergy, the relation above can be simplified to

$$\dot{X}_{destroyed} = X_{in,\ by\ mass} - \dot{X}_{out,\ by\ mass}$$

The exergy destruction fraction within a component is determined from

$$f_{Destroyed}\ \frac{\dot{X}_{destroyed,component}}{\dot{X}_{destroyed,\ total}} = \frac{\dot{X}_{destroyed,component}}{12197.08\ kW}$$

The amounts and fractions of exergy destroyed in the various components are determined to be as follows:

For the MSF unit:

$$\dot{X}_{destroyed,MSF} = (\dot{X}_2 + \dot{X}_4) - (\dot{X}_3 + \dot{X}_7 + \dot{X}_{12})$$

$$\dot{X}_{destroyed,MSF} = 7499.14\ kW\ (61.48\%)$$

For the steam-brine HX:

$$\dot{X}_{brine\ HX} = (\dot{X}_3 + \dot{X}_5) - (\dot{X}_4 + \dot{X}_6) = 433.45\ (3.56\%)$$

For the mixing point:

$$\dot{X}_{destroyed,\ mixer} = \dot{X}_0 + \dot{X}_{11} - \dot{X}_1 = -1940.47\ kW\ \ (15.9\ \%)$$

For the discharged brine:

$$\dot{X}_{destroyed,\ brine} = \dot{X}_9 - \dot{X}_{10} = 385.03\ kW\ (3.16\ \%)$$

For the product water:

$$\dot{X}_{destroyed,\ product} = \dot{X}_{13} - \dot{X}_{14} = 273.07\ kW\ (2.24\ \%)$$

The exergy analyses were conducted to obtain that the largest exergy destruction about 61.48 % of the total exergy input occurs within the MSF unit, followed by the next largest exergy destructions occur in the pumps and their motors 19.8 %, and the heat exchanger 3.56 %. The remaining exergy destruction are 3.16% and 2.24% of total exergy happens at the brine and product streams, respectively. The locations of the above stated amounts and percentages are shown in Figure 2.

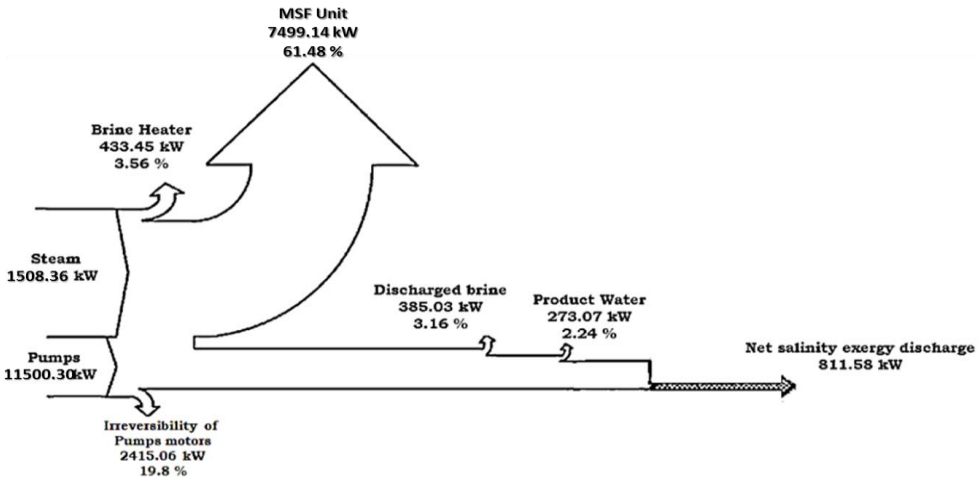

Figure 2: *Exergy flow diagram with exergy destruction amount and percentages.*

6 Conclusion

In conclusion, exergy analysis was found cooperative and significant tool for investigating the MSF-BM desalination plant from the vision of optimum usage of energy and must be taken into consideration at preliminary steps of design. Furthermore, it is shown that second-law efficiency (exergetic efficiency) is a valuable tool for a decision-maker to optimize the performance of different designs, where the second law efficiency was evaluated to be 6.24%, which is very low, in reality the second law efficiency of a modern power plant is over 50%. Therefore, it offers a potential for performance improvement. The exergy analysis shows that,

ISBN: 978-81-936820-6-7
Proceedings DOI: 10.21467/proceedings.4

Series: AIJR Proceedings

the highest exergy destruction was 61.48 % that occurs in MSF chambers followed by the pumping motor with 19.8 % of the total input exergy that means some modifications for performance improvement can be considered according to the modern designs, as well as high efficient motors can be used to increase the second law efficiency. Moreover, an important exergy savings can be achieved by using hybrid designs. Additionally, the heat loss by the power plants can be used as heat source for generating the steam for the brine heater to enhance the performance of the desalination plants.

References

[1] K. Wangnick, 1998 IDA Worldwide Desalination Plants Inventory, Wangnick Consulting, in cooperation with IDA, IDA Report No. 16, 2000.

[2] O. Hamed, Thermal performance of multi stage flash distillation plants in Saudi Arabia, Al Jubail plant and others. Desalination 2000; 128:281–92.

[3] M. Al-Weshahi, A. Anderson, G. Tian, Exergy Efficiency Enhancement of MSF Desalination by Heat Recovery from Hot Distillate Water Stages.

[4] U. Ezzeghni, M. El-bourawi, Exergy analysis of a 10,000 m^3/day Tajoura SWRO desalination plant, The 1st International Conference on Chemical, Petroleum, and Gas Engineering (ICCPGE 2016) 20th – 22th December 2016, Alkhoms-Libya.

[5] G. Gude, N. Nirmalakhandan, S. Deng, A. Maganti, Desalination at low temperatures: An exergy analysis. Desalin. Water Treat. 2012, 40, 272–281.

[6] M. Abduljawad, U. Ezzeghni, Optimization of Tajoura MSF desalination plant, Desalination 254 (2010) 23–28.

[7] N. Kahraman and Y.A. Cengel, Exergy analysis of a MSF distillation plant, Energy Conv. Mgmt., 46 (2005) 2625–2636.

[8] N. Kahraman, Y. Cengel, B. Wood and Y. Cerci, a combined RO, NF, and EDR desalination plant. Desalination, 171 (2004) 217–232.

[9] Improving the thermodynamic and economic efficiencies of desalination plants: Minimum work required for desalination and case studies of four working plants. Desalination and water purification research and development program final report No. 78, U.S. Department of the interior, November 2003.

The Optimal Membrane Type for the Next Membrane Replacement of Tajoura SWRO Desalination Plant

Usama Ahmed Ezzeghni*

Department of Desalination Researches, Nuclear Research Center, Libya

DOI: https://doi.org/10.21467/proceedings.4.37

* Corresponding author email: elzoghni@gmail.com

ABSTRACT

Desalination of seawater in Libya has the capability to increase the accessible resources for producing drinkable water. Desalination of seawater with reverse osmosis membrane technology is one of the most significant techniques in the field of seawater desalination, for the latter technique the membrane manufacturers had created a new advanced membranes that deliver a high output fresh water and high salt refusal that cause a decline in operating cost through lower energy consumption compared to the other thermal desalination technologies .This paper aims to compare between several membrane products developed by different companies to improve the productivity of Tajoura Seawater Reverse Osmosis (SWRO) Desalination plant with high quality fresh water. The membrane type SW30HRLE-440i was selected for the next membrane replacement, which increases the plant productivity from 12,000 to 14,300 m^3/d with decreasing the number of membrane elements from 1080 to 900 membrane elements. In addition, the suggested membrane provides a high rejection, which results in an improved water quality with a salinity of less than 100 ppm where it was almost 200 ppm, as well as it allows the plant to be designed and operated at a lower operating cost through a reduced specific energy consumption, which was 8.492 to 5.48 kWh/m^3 and can be less than 2 kWh/m^3 if a modern energy recovery device (ERD) is used with a significant modification to the plant.

Keywords: reverse osmosis; advanced membranes; low energy; high rejection, high quality.

1 Introduction

Reverse osmosis (RO) desalination technology has been well-known for more than three decades. Progressive advances in membrane materials and high energy saving through energy recovery devices have made modern RO process more attractive and economically competitive than other desalination technologies [1]. Due to increased consumption of fresh water in Libya and the noticed improvements of a reverse osmosis technology, it has led to increased demand of this technology locally and globally. Furthermore, identifying the future needs for desalination technology development, as well as a research and development activities that will result in cost-effective and more efficient desalination technologies that can

 ISBN: 978-81-936820-6-7

meet the upcoming requirements [2]. In this paper Tajoura (SWRO) plant will be developed in parallel with the occurred developments of spiral wound membrane elements that permits desalination plants to be designed and operated to either lower operating cost through reduced energy consumption, or to decrease membrane replacement cost by increasing plant productivity at lower operating flux.

2 Tajoura reverse osmosis plant

The seawater desalination plant illustrated in figure 1 located at Tajoura on the Mediterranean coastline about 30 km east of Tripoli. The plant was planned to yield about 10,000 m^3/day of fresh water with a total dissolved solid of less than 200 milligrams per liter (ppm). The main purpose of the plant is to provide Nuclear Research Center (NRC) with an industrial and drinking water and to substitute the deficiency of drinking water at Tajoura city. It is consisting of a two passes. The first pass uses polyamide membranes to desalt seawater and the second pass is used to desalt the product of the first pass.

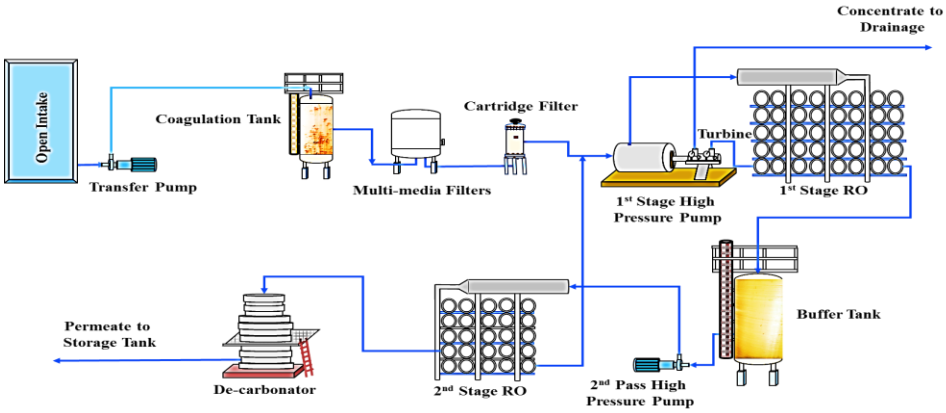

Figugre 1: *Schematic diagram of the SWRO desalination plant.*

Tajoura SWRO desalination plant with design parameters shown in table 1 [3], where seawater intake head is fitted at a distance of 1,300 m into the sea 7 m underneath the sea level and 6 m overhead the sea bottom. The feed water collected by gravity into a basin with a capacity of 5,580 m^3 through two 760 mm diameter plastic pipes at the seashore, then 750 m^3/hr (1,500 m^3/hr for 100% operation) are pumped to the pre-treatment side.

Table 1: *The major design parameters of Tajoura desalination plant.*

Item	First stage	Second pass*
Number of RO racks	4	2
Pressure vessels (PVs) configuration	1 stage	3 stages (24-12-6)
No. of PVs	180	84
No. of membranes	1080	504

No. of membranes per PV	6	6
Nominal diameter, inch	8	8
Membrane model	TFC 2822SS-360	TFC 8600 PA
Design pressure, bar	82.8	41
Working pressure, bar	54	31
pH	5–6	5–6
Maximum temperature, ^{o}C	45	45
Feed flow, m^3/d	34,285	552
Permeate flow, m^3/d	12,000	426
Concentrate flow, m^3/d	22,285	84
Design salt rejection, %	99.6	98
Recovery, %	35	85
Permeate salinity, mg/L	> 200	170

*The second pass of the plant was not included in this study because the drinking water specifications can be achieved by the first stage only.

The pre-treatment contains an online coagulation-flocculation tank, 8-media filters and 5 μm cartridge filters. Some chemicals are added before the feed water reaches the coagulation flocculation tanks. The chemicals are anti-scalants, which are injected to decrease scales accumulation, sulphuric acid used for pH adjustment, Copper sulphate as a disinfectant, sodium hydrogen sulphite for removing chlorine residue if added and ferric chloride sulphate for flocculation.

The pre-treated feed water then is fed to the RO assembly. The RO assembly consists of two passes. The first stage or pass contains four racks with a high-pressure pump for each. The pre-treated water exit from the cartridge filters is fed to first stage by means of four high pressure pumps coupled to a recovery turbine to recover about 30% of its energy requirement. The permeate of the first pass is collected in two inter-connected buffer tanks, and then it is fed to two racks of a second pass by mean of two other high-pressure pumps.

The product of the first stage is recovered by 85% using the second pass and collected in an intermediate tank for further post treatment. The brine stream from the second pass is recycled back and combined with the feed water of the first stage after the cartridge filter. The product will be sent through a degasifier for removing carbon dioxide and the final product treated by sodium hydroxide for pH adjustment and chlorinated by calcium hypochlorite before reaching the final storage tank [4].

3 A comparison between suggested membrane elements

Several membrane types developed by different manufacturers were evaluated based on commercially available RO process design softwares to predict the performance of Tajoura SWRO plant, optimizing membrane selection and operating conditions. Additionally, an estimation of water production quantity and quality from a given input parameters. Such of

ISBN: 978-81-936820-6-7
Proceedings DOI: 10.21467/proceedings.4

Series: AIJR Proceedings

these programs are FilmTec (ROSA), Hydranautics (IMSDesign) and Toray Industries (TorayDS).

Table 2: *Comparison between suggested and installed membranes.*

Company Name	Koch	Toray	Hydranautics	DOW Filmtec
Design software		TorayDS	IMS design	ROSA
Configuration	1 stage	1 stage	1 stage	1 stage
No. of PVs	180	150	150	150
No. of membranes	1,080	900	900	900
No. of membranes per PV	6	6	6	6
Nominal diameter, inch	8	8	8	8
Membrane model	TFC 2822SS-360	TM820V-440	SWC6 MAX	SW30HRLE-440i
Max. operating pressure, bar	82.8	83	83	83
Working pressure, bar	55	53	50.8	54.92
pH	8	8	8	8
Maximum temperature,oC	45	45	45	45
Feed flow, m^3/d	34,285	34,285.7	34,285.7	34,285.71
Permeate flow, m^3/d	12,000	12,000	12,000	12,000.12
Design salt rejection, %	99.6	99.8	99.6	99.7
Recovery, %	35	35	35	35
Permeate salinity, mg/L	> 200	164.6	276.1	98.92
Feed salinity, mg/L	36,204	37,978.26	37,980.65	37,993.95

A permeate salinity goal of less than 300 mg/L was achieved for all the suggested membranes. Table 2 shows a performance comparison of different membranes to validate high productivity, less salt passage, lower energy consumption that will contribute in reduction of the unit water cost of Tajoura SWRO plant. The membranes and the suppliers related to are listed below:

- DOW Filmtec (SW30HRLE-440i);
- Toray and (TM820V-440), and
- Hydranautics (SWC6 MAX).

4 Unit product cost

The unit product cost decreased continuously over the years due to developments occurred in membrane productivity with less energy consumption. An economic evaluation analysis was achieved based on the calculation done by Element Value Analysis (EVA) tool that has been added to ROSA 9.1 program. The attained results are shown in table 3, which show very close values of the capital estimation of membrane elements, energy expenses, membrane

replacement expense, operating expense and the water cost net present value (NPV). The earlier expenses were calculated in parallel with optimization of Tajoura SWRO plant. The following parameters should be taken into considerations:

- Production capacity (m^3/h) = 500 (12,000 m^3/d)
- Permeate recovery (%) = 35
- Interest rate (%) = 8
- Power cost (L.D. kWh)= 0.068

The plant lifetime expected to be 25 years according to the latest refurbishment done by a Canadian company Jadmedic in 1998 [3], an interest rate of 8 % and unit power costs of 0.068 L.D./kWh. All estimations based on common market prices in early 2016.

Table 3: *Estimated water cost.*

Projection Results			
Permeate production (m^3/h)	500	500	500
Feed pressure (bar)	53	50.8	54.92
Concentrate pressure (bar)	52	49.3	53.37
Recovery (%)	35.00	35.00	35.00
Capital Expense			
Membrane Model	TM820V-440	SWC6 MAX	SW30HRLE-440i
Company Name	Forever Pure Place	Forever Pure Place	Watersurplus
Total elements	900	900	900
Element cost ($/element)	975.00	846.40	754.00
Capital for elements ($)	877500.00	761760.00	678600.00
Capital ($/$m^3$)	0.01	0.01	0.01
Operating Expense			
Pumping power (kW)	2703.20	2639.7	2741.6
Pump specific energy (kWh/m^3)	5.47	5.28	5.48
Brine energy recovery (kWh/m^3)	-122.41	-122.41	-122.41
Net energy consumption (KWh/m^3)	127.88	127.69	127.89
Net energy cost ($/yr)	22851893.03	22816832.14	22851893.03
Energy expense NPV (Net Present Value) ($)	203288847.88	243564576.44	243938843.61
Energy expense ($/$m^3$)	86.96	86.82	86.96
Membrane replacement cost			
Replacement rate (%/yr)	15	15	15
Replacement price ($/element)	975.00	846.40	754.00
Replacement cost for elements ($/yr)	131625.00	114264.00	101790.00
replacement membrane NPV ($)	1405067.42	1219742.63	1086585.47
Membrane replacement expense ($/$m^3$)	0.32	0.28	0.25

ISBN: 978-81-936820-6-7
Proceedings DOI: 10.21467/proceedings.4

Series: AIJR Proceedings

Operating expense subtotal			
Operating expense NPV ($)	245343911.02	244784319.07	245025429.08
Operating expense per m^3	87.28	87.10	87.20
Total			
Cost NPV ($)	877500.00	761760.00	678600.00
Life Cycle Cost ($/$m^3$)	0.01	0.01	0.01
Total System			
Operating expense NPV ($)	245343911.02	244784319.07	245025429.08
Cost of water NPV ($/$m^3$)	2.25	2.24	2.24

5 Results and discussion

DOW Filmtec (SW30HRLE-440i) was selected as a candidate membrane for the next membrane replacement because the permeate salinity is 98.92 ppm, which was the lowest permeate salinity achieved compared by the other membranes. Furthermore, the number of membrane elements of the first stage were decreased from 1080 to 900 elements, thus, decreasing the next membrane replacement cost and /the number of throwing away membranes. Consequently, the number of pressure vessels of the first stage can be decreased from 180 to 150 (30 PVs extra), as well as the first stage racks are decreased from four racks to three racks. The earlier results don't include the second pass of the plant. Therefore, the second pass can be used for any other purposes.

If the extra 30 pressure vessels are comprised, the product capacity can be increased from 12,000 m^3/d to 14,300.15 m^3/d with a salinity of 99.59 mg/L, which is still smaller than the salinity achieved by the first stage of the current installed membranes taken into consideration the feed pressure within 54-55 bar, see detailed design results in table 4. Finally, the specific energy consumption decreased from 8.492 to 5.48, then to 5.47 kWh/m^3 , if the extra PVs are used, the earlier results are not including ERD and can be less than 2 kWh/m^3 if modern ERDs are used.

Table 4: Detailed design results of using all the extra pressure vessels of the 1st stage

Company Name	Koch	DOW Filmtec	DOW Filmtec
Design software used		ROSA	ROSA
Configuration of PVs	1 stage	1 stage	1 stage
No. of PVs	180	150	180
No. of membranes	1,080	900	1,080
No. of membranes per PV	6	6	6
Nominal diameter, inch	8	8	8
Membrane model	TFC 2822SS-360	SW30HRLE-440i	SW30HRLE-440i

Max. operating pressure, bar	82.8	83	83
Working pressure, bar	55	54.92	54.77
Feed flow, m^3/d	34,285	34,285.71	40,857.14
Permeate flow, m^3/d	12,000	12,000.12	14,000.15
Concentrate flow, m^3/d	22,285	22,285.59	26,556.99
Design salt rejection, %	99.6	99.7	99.7
Recovery, %	35	35	35
Permeate salinity, mg/L	> 200	98.92	99.59
Feed salinity, mg/L	36,204	37,993.95	37,993.95
Specific energy consumption (kWh/m^3)	8.492	5.48	5.47

6 Conclusions

The productivity of the plant was increased with lower energy consumption and less number of membrane elements and pressure vessels (PVs) with insignificant modification to the piping system of the plant if needed. For reasonable comparison, the recovery of the plant was not increased to avoid massive modification to the plant. Additionally, the plant can be optimized to decrease the unit product cost to less than 2 kWh/m^3 by replacing a conventional pretreatment and the energy recovery device with up-to-date techniques. In conclusion, latest improvements in membrane technology have made SWRO desalination more attractive because they had demonstrated significant enhancements in the rejection performance and the productivity of seawater reverse osmosis at lower feed pressure and less number of elements and pressure vessels, which will contribute in reduction of desalted water price, consequently, resulting in great improvement of the plant performance.

References

[1] H. Iskandar, M. Zhang, and J. Steven, "Simulation and Economic Optimization for a Brackish-Seawater Mixed Feed Reverse Osmosis Process Iskandar", Singapore.

[2] U. Ezzeghni, and M. El-Bourawi, "Exergy analysis of a 10,000 m^3/day Tajoura SWRO desalination plant", The 1st International Conference on Chemical, Petroleum, and Gas Engineering (ICCPGE 2016) 20th – 22th December 2016, Alkhoms-Libya.

[3] I. El-Azizi, and A. Omran, "Design criteria of 10,000 m^3/d SWRO desalination plant of Tajura, Libya", Desalination, vol. 153, pp. 273-270, 2002.

[4] M. Aboabboud, S. Elmasallati, and Y. Albriki., "Tajoura reverse osmosis seawater desalination plant operating and maintenance experience", Desalination, vol. 203, pp. 119-133, 2007.

[5] M. Ashour, and S. Ghurbal, "Economics of seawater desalination in Libya", Desalination, vol 165, pp. 215–218, 2004.

ISBN: 978-81-936820-6-7
Proceedings DOI: 10.21467/proceedings.4

Series: AIJR Proceedings

Feasibility Study of Cardboard Waste Recycling

Mahdi Esmieo*, Moad Shaklawon, Omar Shaneb

Department of Industrial engineering, College of Industrial Technology - misurata, Libya

DOI: https://doi.org/10.21467/proceedings.4.38

* Corresponding author email: mahdi.esmieo@gmail.com

ABSTRACT

Waste management and utilization strategies are major concerns in several countries. Cardboard recycling is a common technique for treating Paper waste, as production recipe contains waste mass by 80%, printed paper contains toxic substances that are used in the manufacture of inks and colors, and their disposal by incineration produces toxic fumes as well as carbon in the form of small grains attached to the air and attack the human respiratory system. In most developed countries where land is scarce and the environmental controls are strict, environmental policies tend to reduce landfill disposals as much as possible. In this paper a feasibility study of cardboard waste recycling in Misurata has been conducted. The paper explores the technical options available for a such recycling. Determine the factors that are considered important for the economic success of the project. In addition, a feasibility study has been conducted. Several economic indicators such as payback period, internal rate of return have been estimated. The results have shown that cardboard recycling is economically feasible. Furthermore, a sensitivity analysis for the important factors have been conducted in order to show their effect on the feasibility that system.

Keywords: Cardboard, economic, recycling, feasibility study, waste.

1 Introduction

Rapid expansion of industry, urbanization and increasing of population, especially in large cities like Misurata, has dramatically increased the amount of solid waste generated in Libya. However, issues related to sound municipal solid waste management – including waste reduction and disposal – have not been addressed adequately. In addition, the collection and the separation treatment of solid waste are still neglected. In the last few years, the Environmental General Authority in Libya has worked to create regulations and instructions for waste management, but up to now they are still under development [6]. This belongs to the fact that there is only little information available regarding recycling, handling and disposal of waste. Therefore, an appraisal of the current situation regarding solid waste management in Libya is required [1]. Cardboard recycling is a common practice of solid waste management in European countries, for it renders the economic success of the project. On the contrary, most

of the solid waste in Libya is still dumped. Municipal solid waste contains valuable cardboard that could be recycled.

Solid waste management and cardboard waste recycling (CWR) have attracted significant attention and great deal of research in several countries such as Denmark [8], America [7], Australia [4], South Africa [5], and India [2]. Rare studies on solid waste have been conducted in Libya indicating that no proper management is existing yet [3, 6]. Thus, work is still required to establish a database, information and statistics on CWR, collection, transportation and treatment. In this paper, economic indicators was investigated and its factors that are considered important for the economic success of the project was determined.

2 Cardboard Recycling.

Cardboard is one of the most commonly used materials for packaging and comes in a variety of forms. Also referred to as corrugated cardboard. It is a recyclable material that could be recycled by cardboard factories to save money. It is a recyclable material that could be recycled by cardboard factories to save money Instead of being disposed as landfill or burn them. Cardboard recycling is the reprocessing and reuse of thick sheets or stiff multi-layered papers that have been used, discarded or regarded as waste. Products that are made from recycled cardboard include more cardboard boxes, egg cartons and even kitty litter.

3 Study area

Misurata is the third largest city in Libya. It serves a community of about 400,000 people. The study has been conducted in the city of Misurata, which situated in the western north part of Libya as a case study. In this paper, CWR feasibility study in the city of Misurata has been investigated through an extensive survey contained information on collection, internal transport and treatment.

3.1 Waste collection, transportation and final treatment

Solid wastes generated at all zones are collected by municipal companies, and then transported to the final dumping site. There are three trans-shipment points in the city. The municipality has the responsibility for offsite transportation of the waste to the final disposal site. From daily to three times a week [6], the municipality labor collect the solid wastes from the on-site storage containers and transport them along with general domestic waste to open dumping sites outside the city. Generally, simple trucks and in some cases uncovered tractors are used for waste transportation [6]. These open tractors are passing within residential areas which increases the potential risk to the public and the environment. All domestic waste dispose, are in open dumping sites outside of the city [6]. In these open dumping sites, the waste is buried and sometimes combusted. Figure 1 shows the quantity of CW in one of the zones.

ISBN: 978-81-936820-6-7

Series: AIJR Proceedings
Proceedings DOI: 10.21467/proceedings.4

Figure 2 depicts the qualitative analysis of solid waste in Misurata identifies organics as the major component (56%), followed by plastics (26.5%). This high plastic rate is due to the widespread use of disposables rather than the reusable for different purposes (e.g. bottles, packing materials and food bags). Whereas paper had the third highest percentage (8%) [6].

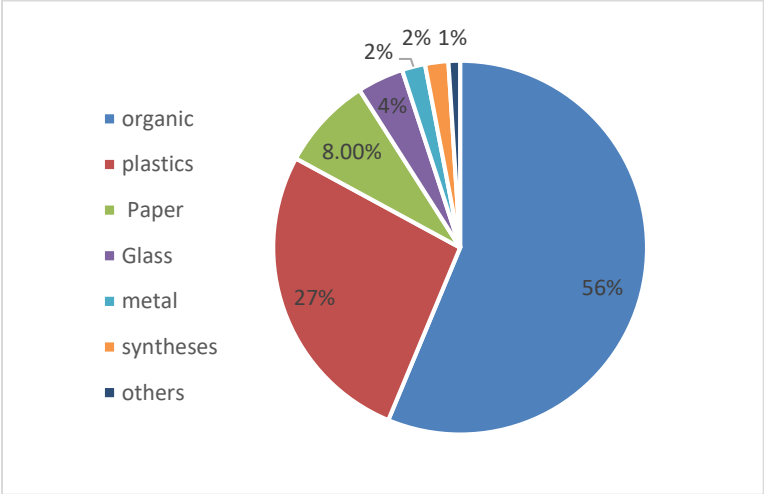

4 Feasibility Study

The present study was conducted through various field visits to several areas within the city of Misurata as well as cardboard factories in the city. This study is concerned with the feasibility study of establishing a CR plant to produce egg dishes. The assumed plant capacity is 20 ton per month to produce 250,000 dishes (i.e. 1200 dishes per hour).

4.1 Raw materials

The raw material used in the recycling of cardboard depends heavily on the waste of paper and cardboard by up to 80%. To produce one ton of carton roll, the following quantities and materials shown in table 1 are required: This industry needs a large amounts of water for the

cleaning and forming process, and then the paper is re-dried until the percentage of water reaches only 6%, which is the percentage allowed in the carton. Thus, the weight of the egg dish is 80 g.

Material description	%
Corrugated Cardboard (Mixed Cardboard)	80 %
paper-making additives (pulp)	18 %
Chemicals & reagents	0.2 %
Abiatic acid	1.8 %

4.2 Cardboard Recycling Process

The cardboard recycling process involves a number of steps, including collection, transportation, sorting, processing into usable raw materials and finally using that raw material to produce new egg dishes products. At the reprocessing plant, cardboard and water are mixed together at high speed in a 'Turboflex Pulp Maker' to break up the cardboard into separate fibres. Contaminants such as staples, wires, plastics and strings are removed by passing the pulp through a cleaning and screening equipment. The pulp is then treated with chemicals and heated to loosen ink and glue so they can be washed out. The cleaned pulp is diluted with water and mixed with small amounts of paper-making additives. The paper is then turned into new Egg dishes products, using the same pressing and drying process used to make paper and cardboard from virgin materials.

In the refining stage, the pulp is beaten to make the paper fibers swell. In this process, egg dishes are obtained. When the goal is to produce white recycled paper, the pulp is bleached with oxygen or chlorine dioxide to make them brighter or whiter or coloring using other artificial colors.

4.3 Costs

4.3.1 Materials Cost

Table 2 shows the first year total materials cost. The total cost equals to the summation of materials fee aaccording to annual production capacity.

Material description	Quantity	Unit Cost, $	Contribution, $/20 ton
Mixed Cardboard	16 ton	70	1120
paper-making additives (pulp)	3.6 ton	272	979.2
Chemicals & reagents	40 kg	0.83	33.2
Abiatic acid	0.360 ton	363	130.68
Grand total per year			2263.08

ISBN: 978-81-936820-6-7
Proceedings DOI: 10.21467/proceedings.4

Series: AIJR Proceedings

4.3.2 Assumptions

- Recycling equipment's & installation cost= 99,000 $.
- Waste input to incinerator = 75% of the total waste.
- Depreciation rate = 5%.
- The yearly operational cost of the recycling plant includes utility costs water 28,500$ at a rate of 44 m^3 per month, electricity 12,000 Kw monthly, human resource costs shown in table 3, and other administrative costs, excluding equipment maintenance cost equal to 40,000 $.
- The average population growth (for the last 30 years) equal to 2% [9].

job description	Job Requirements	number	Salary $	Total salary $
Production Manager	project management	1	1500	1500
Production Supervisor	Supervision and control	1	1100	1100
Labor operation	Production & processing	5	800	4000
Grand total per				6600 /month

5 Calculation and Results

The indices calculated are the yearly profit, net present value, and break-even point. Tables 4 and (5) explain the calculations for the first year. Table 2 illustrates the total quantity of waste collected each year.

Table 4: Waste generated

• **Possible waste per year**	
Cardboard waste per year	1500
Waste incinerated (75%)	1125
• **Ability**	
Time	8 hr/day
Capacity line	1200 pc /hr
Capacity	3,000,000 pc/year

Table 5 shows the first year total revenue. The total revenue equals to the summation of egg dishes selling revenue. The average price for dish equal to 0.30 $.

Table 5: shows the first year total revenue

Description	**Quantity**
	costs
Fixed Costs	36,000 $
• Variable Costs	
Operational Costs	427,800 $

Maintenance	40,000 $
Raw materials	27,156.9 $
Total Variable costs	494,956 $
Total costs	530,956 $
• **Revenue**	
Egg dishes (average price =0.30 $)	3,000,000*0.30
Total Revenue	900,000 $
Net Profit	306,190.1

Whereas: Contribution= unit price- unit variable cost.
Breakeven point= Fixed cost/contribution

- Breakeven point= $\frac{36000}{0.30-0.20} = 360{,}000$

Figure (3) depicts the yearly profit of the plant. It is clear that the project loses only during the first 2 years under the given conditions.

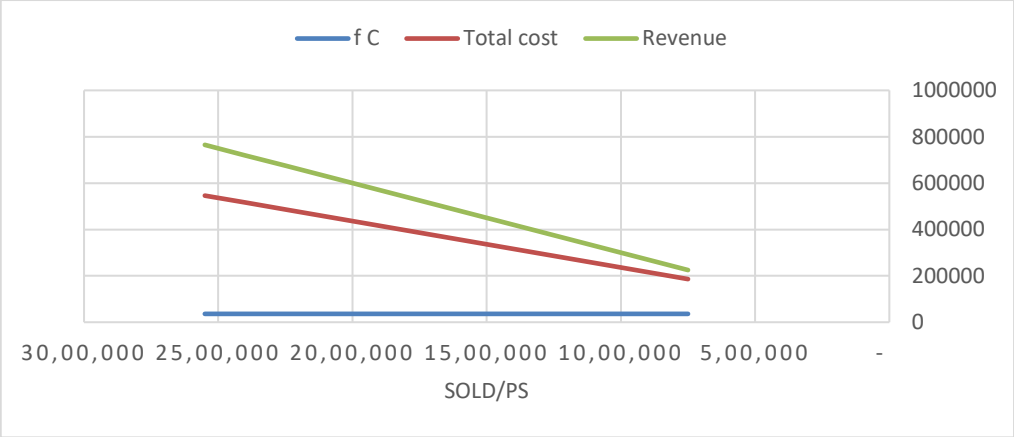

6 Conclusions

In light of the increasing importance for environmentally waste recycling while maintaining the proper stewardship of pollution and solid waste, CWR plants have the ability to become a vital part of the Libya industry. The result of the cost analysis indicates potential economic savings for the Recycling system in Misrata. It is suggested that a similar study should be undertaken focusing on other waste types so as to further underpin future waste management objectives in Libya.

References

[1] A. Omran, A.Gebril, A. Pakir, Municipal Solid Waste Management in BENGHAZI (LIBYA): Current Practices and Challenges, *Environmental Engineering and Management Journal*, Vol.9, No. 9, 1289-1296, 2010.

ISBN: 978-81-936820-6-7
Proceedings DOI: 10.21467/proceedings.4

[2] Amitava Bandyopadhyay , "A regulatory approach for e-waste management: a cross-national review of current practice and policy with an assessment and policy recommendation for the Indian perspective", Int. J. of Environment and Waste Management , Vol. 2, No.1/2 pp. 139 - 186,2008.

[3] Population in The city of Misurata 2014, Municipility of Misurata Report, 2014.

[4] Joe Pickin, Paul Randell, "Australian National Waste Report 2016," Department of the Environment and Energy, june, 2017.

[5] Packaging Council of South Africa, "Design for Recycling for packaging and paper in South Africa," March, 2014.

[6] Mohamed Sawalem, Ibrahim Badi, Suleman Aljamel, Evaluation of Solid Wastes for Utilisation in Biogas Plant in Libya – a Case Study, *IJESRT*, November, 2015.

[7] Scott M. Kaufman, "ANALYSIS OF TECHNOLOGY AND INFRASTRUCTURE OF THE PAPER RECYCLING INDUSTRY IN NEW YORK CITY," Columbia University. May, 2004.

[8] Hazel Fargher, Perry Franklin, Rachel Komara, "Increasing Paper and Cardboard Collection for Recycling in Denmark. May, 2015.

[9] http://www.tradingeconomics.com/libya/population-growth-annual-percent-wb-data.html

Designing and optimizing 10,000 m^3/day conventional SWRO desalination plant

Usama Ahmed Ezzeghni*

Department of Desalination Researches, Nuclear Research Center, Libya

DOI: https://doi.org/10.21467/proceedings.4.39

* Corresponding author email: elzoghni@gmail.com

ABSTRACT

Desalination of seawater has been considered as one of the most promising techniques for supplying a fresh water in Libya. Reverse osmosis (RO) is one of the main technologies for big size desalination plants for the reason that it offers an ability of producing a high quality and quantity of fresh water from seawater with a minor specific energy consumption compared to the other thermal evaporation processes. This paper aims to collect and apply the most useful mathematical equations and software of designing a seawater RO desalination plant with a capacity of 10,000 m^3/day. Moreover, its pretreatment equipment such as sedimentation tank, high-pressure pump, multimedia and cartridge filters.

IMSdesign software developed by Nitto Hydranuatics Company used for designing and optimizing the membrane assembly of the suggested plant. Additionally, the energy recovery device (ERD) specification accomplished by the same earlier software. In addition, the recommended antiscalant dose predicted by PWT ProDose software.

The recovery of the plant increased to more than 40% with less number of membrane elements due to installing new advanced membranes (SWC6 MAX) developed by Nitto Hydranuatics Company. Moreover, pressure exchanger device recommended for the designed plant to decrease the specific pumping energy from 4.81 kWh/m^3 to 2.09 kWh/m^3, which saves more energy, thus, decreases the unit product cost of the plant.

Keywords: seawater desalination; reverse osmosis technique, plant design.

1 Introduction

The seawater desalination option is one of the most important strategic decisions for drinking water source in Libya, especially after growing the population and its gathering at the Libyan coast regions, which exceeds 1,900 kms. The option of using RO desalination technology is one of the most recommended technique, because of the efforts of the membrane's manufacturers in developing new membranes with high productivity and quality as well as, the efforts of ERDs manufacturers in reducing the specific energy consumption, by getting benefit of the wasted pressure of concentrated water. Additionally, advantages that make RO desalination as a competitor option compared to the other thermal desalination methods it can be operated and maintained easily with lower operating cost. Furthermore, design

 ISBN: 978-81-936820-6-7

flexibility of the plant according to the available space. It should be noticed that the world's largest RO plant was built in Israel at a capacity of 333,000 m^3/d [1].

From the vision of the developments in RO technology and its selection by many countries as a challenging option, this paper aims to design a reverse osmosis desalination plant with a production capacity of 10,000 m^3 / day based on seawater analysis sample of a Libyan coast (Tripoli city), the design includes selecting membrane type, calculation the number of membranes, pressure vessels and several pre-treatment equipment such as sedimentation tank, multi-media and cartridge filters, as well as, high pressure pump and energy recovery device.

2 Proposed Plant Description

The feed water is collected into a sedimentation tank for removing the largest particles and then pumped by transfer pumps through a multimedia filters containing three types of media layers (anthracite, sand and garnet) to reduce the Silt Density Index (SDI) and turbidity to less than 3% and one NTU, respectively. Then a filtered water to be passed through a cartridge filters containing filters with pore size not exceeding 5 microns. The filtered feed water is ready to be pumped through the membrane assembly by means of high-pressure pumps. The desalinated water is then delivered to the product storage tanks and the concentrated water is returned to seawater in some different discharge ways to avoid any environmental problems. Energy recovery devices will be installed in the concentrated stream to reduce the rate of specific energy consumption and thus, reduce the cost of fresh water production. Figure 1 shows the overall schematic diagram of the projected plant.

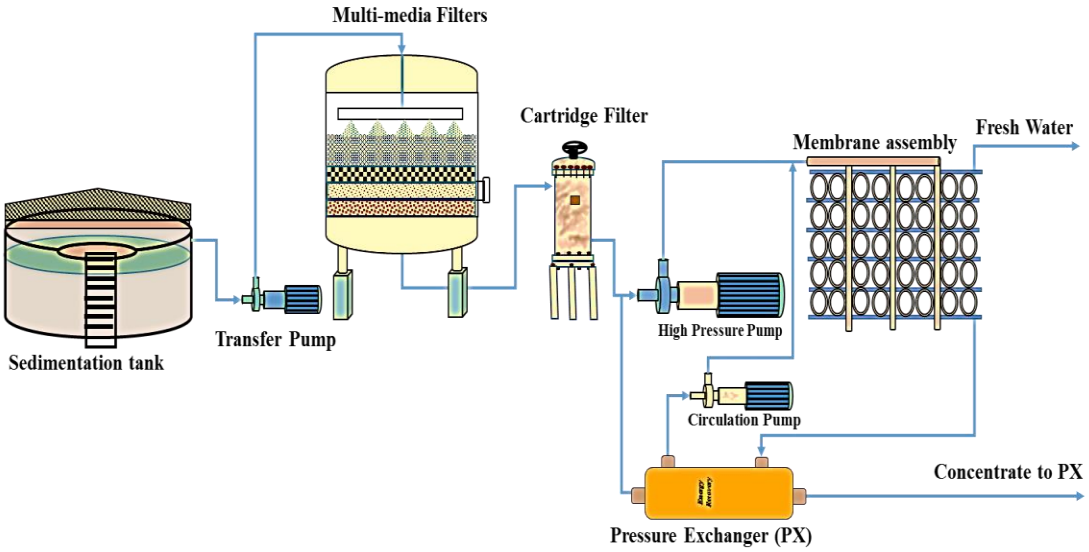

Figure 1: Ggeneral schematic diagram of the proposed plant.

3 Design Calculations

In this section a detailed calculation for all the equipment shown in Figure 1 will be covered in the next subsections, it should be noticed that, the design calculations presented down here are based on seawater analysis of Libyan offshore. The most important required chemical components for plant design are shown on Table 4.

3.1 Clarification (Sedimentation) Tank

The clarification is the first step in feed water pre-treatment section, it is used to give the opportunity for removing the particles that may block the filtration system as well as, to add some chemicals such as disinfectants, coagulants and flocculants if needed.

Sedimentation chamber rise rate and slow mix chamber detention time are the most important factors utilized in sizing clarification tanks.

- Detention Time

Detention time is the theoretical average length of time the water is in the clarifier tank. Detention time depends on two following parameters:

- Volume of the clarifier, and
- Water flow rate.

The detention time can be attained as follows:

$$D_t = \frac{V_c}{F} \quad (1)$$

where

D_t= Detention time

V_c= Volume of clarifier

F= Flow rate

Where the typical detention time of most clarifiers varies between 20 to 30 minutes [2], therefore, the volume of slow mix chamber can be calculated as follows:

$$V_{smc} = F \text{ x } D_t \quad (2)$$

where

V_{smc} = Volume of slow mix chamber

V_{smc} = 535.465 m³ (Based on 30 minutes detention time).

$$A_{smc} = \frac{\mathrm{V_{smc}}}{\mathrm{h_{smc}}} \quad (3)$$

where

A_{smc} = Slow Mix Chamber Area

h_{smc} = Slow Mix Chamber Height

Where typical height recommended by different companies are between 3 and 6 m.

A_{smc} =146.39 m²

$$(d_{smc})^2 = \frac{(4) * (A_{smc})}{3.14} \quad (4)$$

where

ISBN: 978-81-936820-6-7
Proceedings DOI: 10.21467/proceedings.4

Series: AIJR Proceedings

d_{smc} = Slow Mix Chamber Diameter

$(d_{smc})^2$ =186.48 m²

d_{smc} =13.66 ~ 14 m

- Rise rate

Rise rate is a main parameter in defining the clarifier efficiency. It is also well-known as the surface loading rate, surface settling rate, or overflow rate. Rise rate is defined as the flow per unit surface area of the clarifier, and it varies between 25 to 75 m³/d per m² [2].

$$A_{TWS} = \frac{F_C}{R_R} \quad (5)$$

where

A_{TWS} = Treated Water Surface Area.

F_C = Clarifier Flow rate

R_R = Rise rate

A_{TWS} = 438 m²

Therefore, the area of the total clarifier can be calculated as follows:

$$A_{TC} = A_{TWS} + A_{smc} \quad (6)$$

where

A_{TC} = Total Clarifier Area

A_{TC} = 584.41 m²

$$(d_c)^2 = \frac{(4)*(A_{TC})}{3.14} \quad (7)$$

where

d_c = Clarifier diameter

$(d_c)^2$ = 744.47 m²

d_c ~ 27 m

3.2 Transfer Pumps

Transfer pumps are used to pump the clarified seawater to the pressure required by multimedia filters, which can be calculated as follows:

Outlet pressure = Required pressure at the top outlet (4.5 bar)

Gross feed flow to filtration plant = 1070.93 m³/hr

Four pumps are recommended to pump the raw water to filtration system, three in operation and one standby, to avoid plant shutdown during maintenance duties.

Feed flow per pump = 356.97 ~ 360 m³/hr

Where the pressure and feed flow to filtration plant are known, the transfer pumps can be chosen using a coverage chart, which makes it possible to make a preliminary selection through a group of pump sizes based on a specific impeller speed.

3.3 Multi-Media Filters

The dimensions of the multi-media vessels are calculated as follows:

- Filter Dimensions and Media Quantities
- Diameter

The vessel diameter is based on the normal service flow rate, the service water requirement and the relationship between area and diameter.

$$F_f = \frac{F_{fp}}{N_f} \quad (8)$$

where

F_f = Feed flow per filter

F_{fp} = Feed flow to filtration plant

N_f = Number of filter units

$F_f = 133.87 \frac{m^3}{hr}$

$$A_f = \frac{F_f}{F_{sd}} \quad (9)$$

where

A_f = Required cross sectional filtration area per filter

F_f = Feed flow per filter

F_{sd} = Service down-flow rate

A_f =7.44 m²

$$ID \left(\frac{Af*4}{\pi}\right)^{\frac{1}{2}} \quad (10)$$

where

ID = Required internal diameter

= 3.08 m

- Media Quantities

Table 1 shows the filtering material layers for each media for the designed plant. A typical multi-media filter has the following top to bottom layer configuration (media bed depths shown are the minimum allowed).

- (0.45 - 0.60 m) of anthracite;
- (0.2 – 0.3 m) of sand, and
- (0.10 – 0.15 m) of garnet [3].

Table 1: *Filtering material*

Filtering material layer	Grain size, mm	Layer depth, m (in)	Media quantity (m³)
Anthracite	0.85–0.95	0.6 (23.6)	4.5
Sand	0.45–0.55	0.3 (11.8)	2.2
Supporting layer (Garnet)	0.3	0.15 (5.9)	1.1

ISBN: 978-81-936820-6-7
Proceedings DOI: 10.21467/proceedings.4

Series: AIJR Proceedings

$$Q_M = L_T * \frac{(ID)^2 * \pi}{4} \quad (11)$$

where

Q_M = Media Quantity

L_T = Layer Thickness

Straight Shell Height

A multi-media filter requires 50% minimum freeboard to allow bed expansion during the backwash cycle.

$$\text{Straight}_{\text{Shell Height}} = (\text{Depth}_{\text{Anthracite}} + \text{Depth}_{\text{Sand}} + \text{Depth}_{\text{Garnet}}) \text{x } (1 + 50\% \text{ Freeboard}) \quad (12)$$

$\text{Straight}_{\text{Shell Height}}$ = 1.58 m

- Service and Backwash Performance per Filter
- Service Flow Rate

The allowable flow rate through a multi-media filter is 290 - 530 $m^3.d^{-1}/m^2$. Normal service flow is 290 - 350 $m^3.d^{-1}/m^2$. Flow rates of 470 - 530 $m^3.d^{-1}/m^2$ should only be used for short periods of time, when one filter is being cleaned and the other filters must temporarily process the higher flow rate. Flow rates above 530 m^3.d-1/m^2 must not be used, as impurities will be driven through the media bed.

Gross water throughput per filter unit per cycle = Feed flow per filter * Backwash frequency (13)

Gross water throughput per filter unit per cycle= 3212.79 m^3

- Backwash Flow Rate

The backwash flow rate is an essential parameter to expand the filter media depth via 30%, it depends on temperature, because the pressure pushing up the filter media is a function of the water viscosity, which decreases with increasing temperature.

Backwash flow rate (without air)=Required cross-sectional filtration area per filter x Water up flow during backwash (without air) (14)

$$\text{Backwash water flow rate (without air)} = 260.4 \ \frac{m^3}{hr}$$

Backwash time (without air) = 10 min

$$\text{Backwash water volume (without air)} = \frac{\text{Backwash water flow (without air) x Backwash time without air}}{60} \quad (15)$$

Backwash water volume (without air)= 43.38 m^3

$$\text{Raw water volume used to rinse} = \frac{\text{Feed flow per filter x Rinse time (at service flow)}}{60} \quad (16)$$

Rinse time (at service flow) = 5 min

Raw water volume used to rinse = 11.16 m^3

Water up-flow during backwash - together with air = Air up-flow during backwash + Water up-flow during backwash - without air (17)

Water up-flow during backwash - together with air = 85 m/h

Backwash water flow rate (with air) = required cross sectional filtration area per filter ∗ Water up-flow during backwash - together with air (18)

Backwash water flow rate (with air) = 632.4 m^3/hr

$$\text{Backwash water volume (with air)} = \frac{\text{Backwash water flow (with air)} * \text{Backwash time with air}}{60 \text{ min}} \quad (19)$$

Backwash time with air = 5 min

Backwash water volume (with air) = 52.68 m^3

Total filtered water volume required for backwash = Backwash water volume (without air) + Backwash water volume (with air) (20)

Total filtered water volume required for backwash = 96.06 m^3

Total filtered and raw water required for backwash = Raw water volume used to rinse + Total filtered water volume required for backwash (21)

Total filtered and raw water required for backwash = 107.22 m^3

- Rinse Flow Rate

To adequately rinse the media bed, the flow rate must be at least 350 $m^3.d^{-1}/m^2$ for 1 bed volume.

Rinse Flow = Rinse Flow Rate $*$ $(\text{Diameter})^2 * \pi/4$ (22)

Rinse Flow = 2607.71 m^3/d

- Air Scour Flow

For an effective air scour, the air flow rate of the recommended design blower must be at least 50 $m^3.hr\ -1/m^2$ (3 $SCFM/ft^2$) at 0.5 bar.

Air flow-rate requirement = Required cross-sectional filtration area per filter ∗Air up-flow during backwash (23)

Air flow-rate requirement = 371.85 m^3/hr

- Net Production per Filter

Net production of filtered water = Gross water throughput per filter unit per cycle- Total filtered water volume required for backwash (24)

Net production of filtered water = 3116.73 m^3

Time of production of net volume filtered water = Backwash frequency-(Backwash time with air + Backwash time without air+ Rinse time (at service flow))/60 (25)

Time of production of net volume filtered water = 23.67 hr

Net production rate of filtered water = Net production of filtered water/ Time of production of net volume filtered water (26)

Net production rate of filtered water =131.69 m^3/hr

Net production rate = Net production rate of filtered water ∗ Number of filter units (27)

Net production rate = 1053.54 m^3/hr

3.4 Cartridge Filters

The filter elements of a cartridge filter are selected based on two measures, the nominal micron rating and the service water flow rate. The standard diameter of the filter elements is 2.5 inches.

ISBN: 978-81-936820-6-7

Series: AIJR Proceedings
Proceedings DOI: 10.21467/proceedings.4

The standard length of the filter elements can be either 30 or 40 inches. The choice of 30-inch or 40-inch cartridges often depends on the availability of standard filter housings. In general, there is not much cost difference between housings for 30-inch or 40-inch cartridges, so if there are no other constraints a 40-inch cartridge system generally is the most economical.

- Filter Element Quantity and Height

The number of 10" lengths of cartridge required for a system can be calculated as follows:

Quantity = Service water requirement / Flow per 10-inch length (28)

(10-inch lengths) (at available pressure drop)= 1170.6 ~1171 element

Using a filter element that can support 0.9 m^3/h per psid per 10-inch length, the quantity of filter elements for the entire system can be calculated as follows:

$$\text{Quantity (40-inch lengths)} = \frac{\text{Quantity (10-inch lengths)}}{\text{Quantity (10-inch elements per element)}} \quad (29)$$

= 292.75 ~ 293 element

No. of cartridge vessels = Quantity (40-inch lengths) / Quantity per vessel (30)

= 5.86 ~ 6 cartridge vessels

Feed flow per filter = Service water requirement / No. of cartridge vessels (31)

Feed flow per filter = 175.59 $\frac{m^3}{hr}$

3.5 High Pressure Feed Pump

Selection of the high pressure pump (HPP) depends on the minimum and maximum flow rates, discharge pressure required, suction pressure available and the maximum temperature, where these parameters can be obtained from IMSDesign detailed report. Table 2 shows design parameters of the high pressure feed pumps.

- Variable Speed Pumps

Variable speed motors are used to control motor operating speed. This allows a pump to operate at different speeds and thus reduce pump size and/or number of stages and eliminate the need for a speed-increasing gearbox in some applications. High-speed pumps are especially useful for high head, low-flow applications and the ability to alter pump speed allows operation over a wide range of conditions. Variable speed drives also provide a pump system with a built-in soft start and stop to prevent shocks to the system and water hammering to the membranes.

Table 2: *High pressure pump design parameters*

Power Calculation (without ERD)	
Pump pressure (bar)	52.9
Product flow m^3/d	10000
Pump flow m^3/d	25000
Pump efficiency %	83
Motor efficiency %	93

VFD efficiency %	97
Power/stage/pass Kw	2004.4
Brake horse power BHP	2686.8
Total pumping power kW	2004.4
Pumping specific energy kwh/m³	4.81

3.6 Reverse Osmosis Membrane System

The following steps were used to design the membrane assembly of the SWRO desalination plant.

- Selection of Membrane Element Type

Elements are selected according to feed water salinity, feed water fouling tendency, required productivity and salt rejection, as well as energy requirements, where the membrane selected for the designed plant is SWC6 and IMSDesign software were used to give the information required for the designed system. This software is available on the Website of Hydranautics Company. Table 3 lists all the specifications of SWC6 MAX membranes.

Table 3: *Membrane specifications (*SWC6 MAX)

Performance	
Permeate Flow	50 m³/d
Salt Rejection	99.8% (99.7% min)
Applied Pressure	55 bar
Type	
Configuration	Spiral Wound
Membrane Polymer	Composite Polyamide
Membrane Active Area	40.8 m²
Application Data	
Maximum Applied Pressure	83 bar
Maximum Chlorine Concentration	< 0.1 ppm
Maximum Operating Temperature	45 °C
pH Range, Continuous (Cleaning)	2-11
Maximum Feed water Turbidity	1.0 NTU
Maximum Feed water SDI (15 mints)	5
Maximum Feed Flow	17.0 m³/h
Minimum Ratio of Concentrate to Permeate Flow for any Element	5:1
Maximum Pressure Drop for Each Element	15 psi

- Selection of Average Membrane Flux

The flux design selection depends on an experimental data, experience where the typical membrane design fluxes based on the feed supply. The recommended design flux for this plant is 13.5 l/m²-h.

ISBN: 978-81-936820-6-7

Series: AIJR Proceedings
Proceedings DOI: 10.21467/proceedings.4

- Number of Elements Needed

The number of elements N_E can be calculated using equation (32) by dividing the design permeate flow rate Q_P by the design flux f and by the membrane active area of the chosen element S_E (ft² or m²).

$$N_E = \frac{Q_P}{f.S_E} \quad (32)$$

where

N_E = Total number of elements.

Q_P =required permeate flow.

S_E = Membrane active area, and

f = Average flux.

N_E = 756 membrane elements

- Number of Pressure Vessels Needed

For this plant, 6-element vessels will be used, so, the number of pressure vessels will be:

$$N_V = \frac{N_E}{N_{EpV}} \quad (33)$$

where

N_V = Total number of pressure vessels.

N_E = Total number of elements; and

N_{EpV} = No. membrane element per PV.

N_{EpV} = 756 / 6 = 126 PVs

- Number of stages selection

The stage number of the RO planta describes the number of pressure vessels in series, where the inlet feed water will goes through till it leaves the desalination plant as brine. Typically, the number of serial element positions is linked with the system recovery and the number of stages, for the designed SWRO plant the recovery is 40% and one stage plant will be selected to avoid the expected scaling problems and the uncaring in operation and monitoring of the plant. The RO stage consist of two parallel RO racks with 126 pressure vessels. Each pressure vessel contains six spiral wound RO membranes.

Table 4: *Seawater analysis (Libyan offshore sample)*

PH	8	CO_3	12.653	mg/l
Cations	mg/l		Anions	mg/l
Ca	455		HCO_3	163
Mg	1427		SO_4	2915
Na	11600		Cl	20987
K	419		F	0
NH_4	0		NO_3	0

Ba	0	PO_4	0
Sr	0	SiO_2	2
Cal. TDS	37981	B	0

- Membrane Systems Report

Integrated Membrane Solutions Design (IMSDesign) software was used to design, optimize and analyze the performance of the designed plant and testing the configuration according to seawater analysis shown in Table 4. The design parameters of the designed desalination plant are presented in Table 5.

Table 5: *Design parameters of the plant*

Company Name	Hydranautics
Design software used	IMS design
Pressure vessels (PVs) configuration	1 stage
Permeate recovery %	40
Average flux, lmh	13.5
No. of pressure vessels (PVs)	126
No. of membranes	756
No. of membranes per (PV)	6
Nominal diameter, inch	8
Membrane model	SWC6 MAX
Max. operating pressure, bar	83
Working pressure, bar	52.9
Ph	8
Maximum temperature, °C	45
Feed flow, m^3/d	25000
Permeate flow, m^3/d	10000
Concentrate flow, m^3/d	15000
Design salt rejection, %	99.6
Concentrate salinity, mg/l	63119.2
Permeate salinity, mg/l	295.51
Feed salinity, mg/l	37981

ISBN: 978-81-936820-6-7
Proceedings DOI: 10.21467/proceedings.4

Series: AIJR Proceedings

3.7 Energy Recovery Devices (ERD)

In SWRO desalination plants, about 55 to 60% of the feed pressure leaves the plant with approximately 870 psi (60 bar) through the brine stream. This energy can be recovered to decrease the specific energy consumption of the plant using turbocharger, pelton wheel and pressure exchanger.

Table 6: *Pressure exchanger parameters*

Parameter	Power Calculation (without PX)	Power Calculation (with PX)	
	Pass 1	Pass 1	ERD boost
Pump pressure (bar)	52.9	54.1	1.7
Product flow m^3/d	10000	10000	-
Pump flow m^3/d	25000	10153.9	14846.1
Pump efficiency %	83	83	83
Motor efficiency %	93	93	93
VFD efficiency %	97	97	97
Power/stage/pass Kw	2004.4	832.6	37.2
Brake horse power BHP	2668.8	1116	49.9
Total pumping power kW	2004.4	869.8	
Pumping specific energy kwh/m^3	4.81	2.09	

The high-pressure concentrate is fed into the energy recovery device, where a pressure exchanger (PX) will be suggested for this plant. This PX supplies about 94 % of the high-pressure pump's energy requirement. Table 6 shows power calculation of the designed plant with and without pressure exchanger, which is achieved by IMSDesign software.

3.8 Chemical Requirements

Most of SWRO desalination plants need some chemicals to be added to the feed water before passing through the membrane assembly. The chemicals are dosed based on the feed water analysis, there are several chemicals added to the feed water such as disinfectant, coagulant and flocculants, sodium meta-bisulfide if chlorine is injected to the feed water. In this design the feed water needs to be treated with antiscalant to prevent the scales accumulation on the membranes surface. A detailed information will be described in the following subsection.

- Antiscalant

For dosage rate calculation of antiscalants, the manufacturers should be contacted. Overdosing should be avoided. Attention must be taken that no significant amounts of cationic polymers are existing once dosing an anionic scale inhibitor, because precipitation reactions may happen, similarly may occur, by dosing a negatively charged antiscalant and cationic polyelectrolytes or multivalent cations (e.g., aluminum or iron). In SWRO plants working with total dissolved solids of more than 35,000 mg/L, scaling is not that problematic

as in brackish water desalination plants BWRO since the permeate recovery of the SWRO plants is limited to 30-45%, but still, an antiscalant is recommended if operating the SWRO plants with a permeate recovery of 35% or more [4].

A computer model developed by Professional Water Technologies, Inc. was used to determine the performance of an antiscalant (TITAN ASD 200 SC LIQUID SUPER CONC) supplied by the same antiscalant manufacturer. Table 7 shows the results of the computer model indicate that an antiscalant dose of 0.2 mg/l at the feed side and 0.3 mg/l at the concentrate side would effectively control membrane scaling based on the input feed water chemistry and a design recovery of 40 percent.

Table 7: The suggested antisclant dosage rate

Product Selection	
TITAN ASD 200 SC LIQUID SUPER CONC	
Recommended Dose Rates	
Feed (mg/l)	Concentrate (mg/l)
0.2	0.3
Est. Product usage (100%)	
kgs/day	mt/yr

4 Results and Discussion

The plant designed with advanced SWC6 MAX membranes increases the productivity of the plant with less number of membrane elements and pressure vessels, this design was compared with an existing SWRO plant in Tajoura, with the same capacity, it is found that the number of elements, as well as the number of pressure vessels were decreased from 1080 element to 756, which will decrease the cost of the next membrane replacement as well [5]. Furthermore, the pumping specific energy of the HPPs were decreased due to installation of PX with a hydraulic efficiency in the range of 94-96%, in addition to that the overall recovery were increased from 35% to 40% and it can be increased to more than 50%, but the researchers suggested 40% recovery to avoid scaling, fouling problems and decreasing chemicals consumptions. As far as the pressure exchanger was selected as ERD for designed SWRO plant, the pressure exchanger conversion efficiency of more than 94%, and therefore, the unit designed saves more than 60 % of the destroyed power, which will decrease the unit product cost.

5 Conclusion

In conclusion, the SWRO desalination plant were designed and optimized using IMSDesign software. Furthermore, some mathematical equations were collected and applied for designing several pretreatment equipment. Therefore, the design was prepared and ready for development by other researchers or students; whatever other ideas of SWRO plant design are becomes recognizable.

ISBN: 978-81-936820-6-7

Series: AIJR Proceedings
Proceedings DOI: 10.21467/proceedings.4

The optimal design of SWRO process has been addressed in this work using an advanced membrane (SWC6 MAX) developed by Hydranautics Company. The design of plant with a new SWRO element had improved permeability and quality; these features provide system designers with new options to reduce the capital cost of the system as well as, the operating cost. Although the new low energy membranes run at lower pressure.

The greatest sensible and applied way to rise efficiency or decrease the power input of the designed plant meaningfully seems to be replacing the throttling valve and old turbine or reverse running pumps on the brine stream by modern pressure exchanger, the use of a pressure exchanger as energy recovery system enables decreasing the total pumping power of the reverse osmosis desalination plants.

References

[1] N. Voutchkov, Desalination engineering: planning and design. New York: McGraw-Hill, 2013.

[2] FSC Architects & Engineers, Class II Water Treatment Plant Operator Program Manual, (2003).

[3] N. Voutchkov, Considerations for selection of seawater filtration pretreatment system, Desalination 261 (2010) 354–364.

[4] Technical Manual, Dow Water & Process Solutions, FILMTEC Reverse Osmosis Membranes, June, (2004).

[5] I.M. El-Azizi and A.A. Mohamed Omran, Design criteria of 10,000 m3/d SWRO desalination plant of Tajura, Libya. Desalination, 153 (2003) 273–279.

Finite element modeling and simulation of a microstructure silicon beam resonant

Mohamed Shaglouf*, ElJaroshi Diryak ,Ahmed Abugalia

Department of Electrical and Electronics, College of Engineering, Sirte University, Libya

DOI: https://doi.org/10.21467/proceedings.4.40
* Corresponding author email: shaglouf@SU.edu.ly

ABSTRACT

This paper establishes the Finite Element Method (FEM) model of a practical silicon beam resonator attached to a diaphragm used for measuring pressure. In this paper presents two location error models. Analyze, calculate, and investigate the relationship between the basic natural frequency of the beam resonator and the measured pressure for two error models are discussed.

Key Words: Finite Element Method, Beam, Pressure.

1 Introduction

During the past decade, many experts in sensor technology have noticed the rapid development in silicon resonant sensors. The silicon microstructure resonant sensors are noted for the advantages of a generalized resonant sensor, such as direct digital output (without A/D conversion), long-term stability, low hysteretic and high repeatability. Other advantages of silicon material are excellent mechanical properties; high strength; free from mechanical hysteretic; suit ability to batch processing at low cost; and the compatibility of mechanical and electrical properties. Meanwhile, the dynamic characteristics of silicon resonant sensors are much better than those of conventional ones, due to their high working frequency [1]. In addition, the temperature characteristics of silicon resonant sensors are much better than those of another important silicon sensors such as the piezoresistive sensor. It is much easier to interface them with a microprocessor to develop smart or 'intelligent' sensors or sensor systems due to their unique operating principle based on the relationship between the natural frequency and measured signal instead of the silicon piezoresistive effect. Recently, it has been reported that some prototypes, with different structure and configurations, and even few batch products of silicon resonant sensors have come into being for measuring pressure, differential pressure or force. They have been developed and manufactured in Japan, USA, Netherlands and Britain. Although the properties of these silicon resonant sensors have not reached the designed criteria, they could be used widely in many technical fields in the near future.

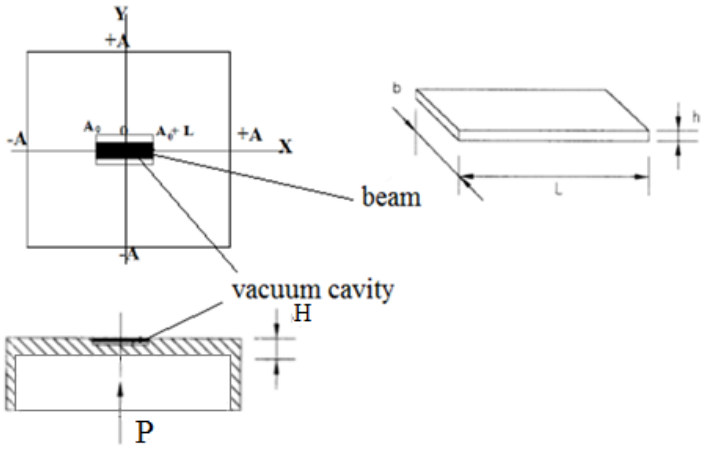

Figure 1: *Sensing structure of the sensor*.

Figure 1 shows the structure of a silicon resonant sensor for measuring pressure. The preliminary sensing unit is a square diaphragm. The measured pressure acts perpendicularly to the lower surface of the diaphragm and yields the stress. T]he final sensing unit is a beam, which is attached to the upper surface of the diaphragm. Moreover, the thickness of the beam h should be less than the thickness of the diaphragm H, and the width of the beam L should be less than the half length of the diaphragm A. Based on the above structural feature, an appropriate initial stress is applied along the axial direction of the beam, which is almost identical with the stress of the square diaphragm at the same position. Thus the natural frequency of the beam is varied with the applied pressure which acts on the square diaphragm. Therefore, the pressure will be measured by the natural frequency changes of the beam. In addition, the beam resonator has a very high Q factor because it can be packaged within a vacuum housing.

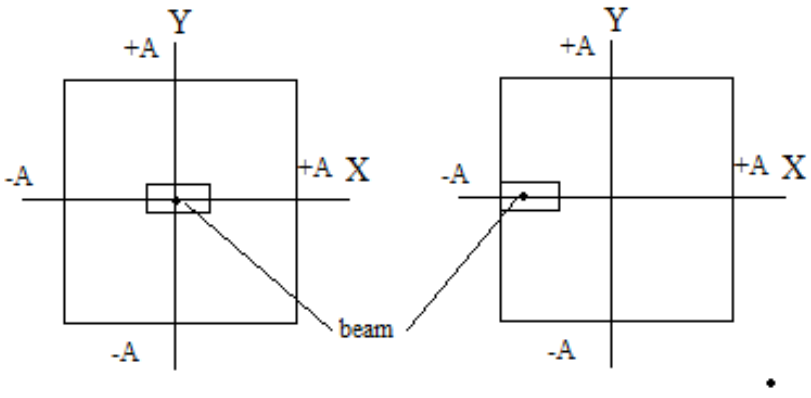

Figure 2: *Ideal locations of the beam at the diaphragm.*

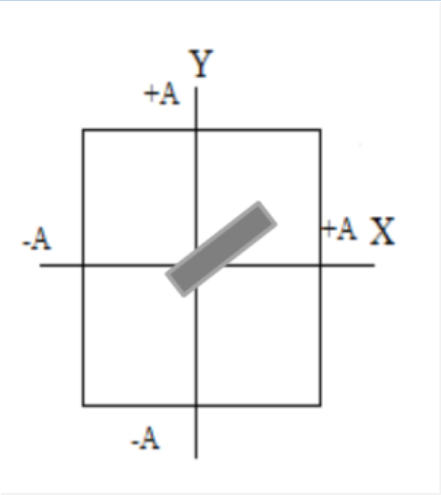

Figure 3: *Error model 1 of beam's location at the diaphragm*

Figure 2 shows the ideal location scheme of the beam. Figure 3 shows the location error model 1 within the positive stress range, while Figure 4 shows the location error model 2 within the negative stress range. It is certain that the frequency-pressure relationship varies with the deviation B in the x-axis, deviation D in the y-axis and the angular deviation a relative to its ideal location for the above error cases. In order to improve the exchangeability of the sensor, it is necessary to investigate the influence laws of the above deviations on the frequency-pressure relationship of the beam resonator. The objective of this paper is to study the above problems in order to obtain some directions during developing the silicon resonator sensors by using of a finite element model (FEM).

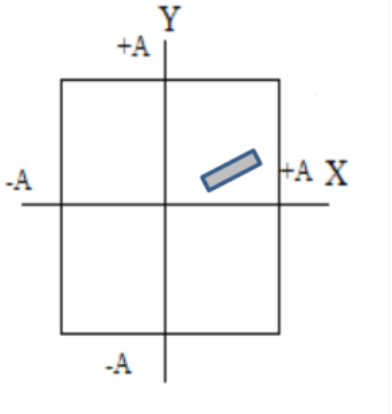

Figure 4: *Error model 2 of beam's location at the diaphragm*

2 Stresses on the upper surface of the square diaphragm

According to the structural feature and the design demands for the sensor, the square diaphragm is within the range of a small deflection. Then the differential equation can be written as follows:

ISBN: 978-81-936820-6-7
Proceedings DOI: 10.21467/proceedings.4

$$\frac{\partial^4 W(x,y)}{\partial x^4}+2\frac{\partial^4 W(x,y)}{\partial x^2\partial y^2}+\frac{\partial^4 W(x,y)}{\partial y^4}=\frac{P}{D_s} \quad (1)$$

$$\text{Where } D_s=\frac{EH^3}{12(1-\mu^2)}$$

Where W (x,y) is the displacement of the square diaphragm under the applied pressure P, and Ds is the flexural rigidity of the square diaphragm.

And according to the built-in edge of the square diaphragm, its displacement can be assumed as follows:

$$W(x,y)=W_{\max}H\left(\frac{x^2}{A^2}-1\right)^2\left(\frac{y^2}{A^2}-1\right)^2 \quad (2)$$

Where Wmax is the ratio between the maximum normal displacement and the thickness of the square diaphragm, and A, H are the half-length and thickness of the square diaphragm.

By substituting Eq. (2) into Eq. (1), the displacement, W(x,y) can be obtained. Then stresses on the upper surface of the square diaphragm can be also obtained.

$$\rho_x(x,y)=-\frac{49p}{96}\left(\frac{A}{H}\right)^2\left[\left(\frac{3x^2}{A^2}-1\right)\left(\frac{y^2}{A^2}-1\right)^2+\mu\left(\frac{x^2}{A^2}-1\right)^2\left(\frac{3y^2}{A^2}-1\right)\right]$$

$$\rho_y(x,y)=-\frac{49p}{96}\left(\frac{A}{H}\right)^2\left[\left(\frac{3y^2}{A^2}-1\right)\left(\frac{y^2}{A^2}-1\right)^2+\mu\left(\frac{y^2}{A^2}-1\right)^2\left(\frac{3x^2}{A^2}-1\right)\right] \quad (3)$$

Where σx(x,y),σy(x,y) Stresses of the square diaphragm.

3 Finite element model of the beam

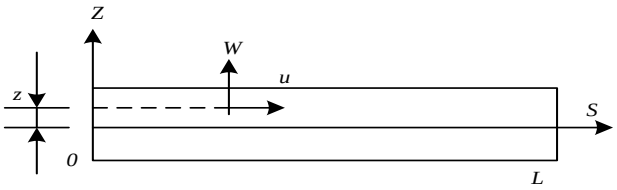

Figure 5: *Mathematical model of the beam*

Figure 5 shows the mathematical model of the beam. The vibrating displacements of the beam at an arbitrary point are as follows:

$$\begin{cases} u(s,z,t)=-z\dfrac{dw(s)}{ds}\cos\omega t \\ w(s,t)=w(s)\cos\omega t \end{cases} \quad (4)$$

Where u (s,z,t)-w (s,t) are axial and normal vibrating displacements of the beam in Cartesian coordinate of the beam, and s ,z are axial and normal coordinates of the beam in Cartesian coordinate of the beam.

The energy expressions of the beam resonator can be written as follows:

The potential energy

$$U = \frac{Ebh^3 \cos^2 \omega t}{24} \int_S \left[\frac{d^2 w(s)}{ds^2} \right]^2 ds \tag{5}$$

Where, U is the potential energy of the beam ,and S is the integrated length of the beam.

The kinetic energy

$$T = \frac{\rho bh\omega^2 \sin^2 \omega t}{2} \int_S \left[w(s) \right]^2 ds \tag{6}$$

Where, T is the kinetic energy of the beam, and ρ is the density of the sensing structure.

In addition, the initial potential energy of the beam, which is caused by $\sigma_s^0(s)$, is

$$U_0 = -\frac{bh \cos^2 \omega t}{2} \int_S \sigma_s^0(s) \left[\frac{dw(s)}{ds} \right]^2 ds \tag{7}$$

From Fig(1) and equation (3), according to the above analyses,

$$\sigma_s^0(s) = \sigma_x(x,0) = \frac{49P}{96} \left(\frac{A}{H} \right)^2 \left[\left(\frac{3x^2}{A^2} - 1 \right) - \mu \left(\frac{x^2}{A^2} - 1 \right)^2 \right] \tag{8}$$

Where σ_s^0 (s) is the initial axial stress of the beam.

The following relation for the error cases yields:

$$\sigma_s^0(s) = \sin^2 \beta(s) \sigma_x(x,y) + \cos^2 \beta(s) \sigma_y(x,y) \tag{9}$$

Then the total potential energy of the beam is:

$$U_T = U - U_0 \tag{10}$$

Where U0 is the initial potential energy of the beam, which is caused by σ_s^0 (s) ,and UT is the total potential energy of the beam.

In Eq. (7), if σ_s^0 (s) is a constant σ_s^0 the analytic relationship between the basic natural frequency and the initial axial stress can be directly obtained:

$$\omega = \frac{22.38h}{L^2} \sqrt{\frac{E}{12\sigma}} \sqrt{1 + 0.295 \frac{\sigma_s^0 L^2}{Eh^2}} \tag{11}$$

Where ω[rad/s],w(s) Natural frequency and its corresponding vibrating shape along the axial direction of the beam.

However, from Eqs. (3), (8) and (9), $\sigma_s^0(s)$ is varying. Therefore, The finite element equation of the beam resonator can be written as follows:

ISBN: 978-81-936820-6-7

Series: AIJR Proceedings
Proceedings DOI: 10.21467/proceedings.4

$$\left(\boldsymbol{K}-\omega^2\boldsymbol{M}\right)\boldsymbol{a}=0 \qquad (12)$$

Where K is assembly stiffness Matrix, M-assembly is Mass Matrix, and a is the assembly nodal vector, consisting of all aj.

For the actual structural features of Fig. 1, the boundary conditions of the beam are as follows

$$\begin{cases} s=-a: & w(s)=w^{©}(s)=0 \\ s=+a: & w(s)=w^{©}(s)=0 \end{cases} \qquad (13)$$

From Eqs. (12), (13), natural frequencies and the corresponding vibrating shapes of the beam resonator can be obtained.

4 Calculations and Simulations

In this work, the main investigation is the detailed vibration shape of the beam resonator simultaneously. The sensor is made of silicon, thus E $=1.3\text{x}\,10^{11}$ Pa, $\rho = 2.33\,\text{x}\,10^{3}$ kg/m3, and $\mu = 0.17$. Moreover, the total element number of the beam N is 19 for FEM calculations.

The half-length and thickness of the square diaphragm are A=1mm and H=0.1 mm, respectively. In addition, the width and thickness of the beam are b=50 μm and h=5μm.

Define, Δf(B, D, a) [hz] = Δf (P, B, D, a) –f (0, 0, 0, 0) as the variation of the basic natural frequency of the beam within (0, ρ), with the x-axis deviation B. y-axis deviation D and the angular deviation a relative to its ideal location.

Define β(B, D, a)=[Δf(B, D, a,) -Δf(0, 0, 0)]/Δf(0, 0, 0)] as the relative variation of the basic natural frequency variation of the beam within (0, P), with the x-axis deviation B. y-axis deviation D and the angular deviation a relative to its ideal location.

Table 1: *The relative variation β(B, D, 0) of the frequency variation of the beam.*

D μm	*B μm*			
	0	*2*	*4*	*6*
0	*0.001*	*0.001*	*0.001*	*0.001*
2	*0.002*	*0.001*	*0.001*	*0.001*
4	*0*	*0.001*	*0.001*	*0.001*
6	*0.001*	*0.001*	*0.001*	*0.001*

Table 2: *The relative variation β(B, D, 3) of the frequency variation of the beam.*

D μm	*B μm*			
	0	*2*	*4*	*6*
0	*0.002*	*0.002*	*0.001*	*0.001*
2	*0.001*	*0.001*	*0.002*	*0.002*
4	*0.001*	*0.001*	*0.001*	*0*
6	*0.001*	*0.001*	*0.001*	*0.001*

Table 3: *The relative variation β(B, D, -3) of the frequency variation of the beam.*

D μm	*B μm*			
	0	*2*	*4*	*6*
0	*0.001*	*0.002*	*0.001*	*0.001*
2	*0*	*0.002*	*0.001*	*0.001*
4	*0.001*	*0.002*	*0*	*0.001*
6	*0.002*	*0.001*	*0.002*	*0.001*

Table's 1~3 shows β(B, D, 0), (a= 0deg), β(B, D, 3) (a=+3deg) and β(B, D, -3) (a =-3deg.), within (0, 106)pa. as the beam is located at different positions, i. e., with different ,x-axis deviation B, y-axis deviation D and the angular deviation a relative to its ideal location on the square diaphragm. The design ideal location is (-300, +300) μm (or L=600μm) within the positive stress range of the beam, and the beam's axial direction is along the x- axis of the square diaphragm, which corresponds to B = 0, D=0, a=0. In addition, f(0, 0, 0)= 106648Hz. Δf(0, 0, 0)=9924Hz.

From Table's 1~3, the variation of the basic natural frequency of the beam, which is influenced by the deviation D, the deviation B, and the angular deviation a of the beam relative to its ideal location, are almost the same within the positive stress range.

Table's 4~6 shows β(B, D, 0), (a= 0deg), β(B, D, 3) (a=+3deg) and β(B, D, -3) (a =3deg.), within (0, 106)pa. as the beam is located at different positions, i. e., with different ,x-axis deviation B, y-axis deviation D and the angular deviation a relative to its ideal location on the square diaphragm. The design ideal location is (+700, +1000) μm (or L=200μm) within the negative stress range of the beam, and the beam's axial direction is along the x- axis of the square diaphragm, which corresponds to B = 0, D=0, a=0. In addition, f(0, 0, 0)= 426564Hz. Δf(0, 0, 0)=10475Hz.

Table 4: *The relative variation β(B, D, 0) of the frequency variation of the beam.*

D μm	*B μm*			
	0	*-2*	*-4*	*-6*
0	*0*	*-0.005*	*-0.019*	*-0.025*
2	*0*	*-0.006*	*-0.021*	*-0.025*
4	*0.001*	*-0.006*	*-0.018*	*-0.026*
6	*0.002*	*-0.005*	*-0.018*	*-0.025*

ISBN: 978-81-936820-6-7
Proceedings DOI: 10.21467/proceedings.4

Series: AIJR Proceedings

Table 5: *The relative variation β(B, D, 3) of the frequency variation of the beam.*

D μm	*B μm*			
	0	*-2*	*-4*	*-6*
0	*-0.001*	*-0.008*	*-0.021*	*-0.026*
2	*-0.001*	*-0.011*	*-0.021*	*-0.026*
4	*-0.001*	*-0.012*	*-0.017*	*-0.031*
6	*-0.002*	*-0.013*	*-0.023*	*-0.029*

Table 6: *The relative variation β(B, D, -3) of the frequency variation of the beam.*

D μm	*B μm*			
	0	*-2*	*-4*	*-6*
0	*-0.001*	*-0.008*	*-0.025*	*-0.030*
2	*-0.001*	*-0.012*	*-0.025*	*-0.030*
4	*-0.001*	*-0.012*	*-0.026*	*-0.030*
6	*-0.002*	*-0.010*	*-0.025*	*-0.033*

From Table's 1~3, the variation of the basic natural frequency of the beam, which is influenced by the deviation D, the deviation B, and the angular deviation a of the beam relative to its ideal location, within the negative stress range. Therefore, the y-axis deviation B should be reduced as much as possible. Comparing the above tables, it is obvious that locating the beam in the middle of the square diaphragm is much better than at the edge.

5 Conclusion

Based on the Finite Element Method model and analyses of the initial stresses applied to the beam resonator attached to a square diaphragm, this paper first calculates, analyses and investigates the relationship between the basic natural frequency of the beam resonator and the measured pressure for two error models. An important result is obtained it is necessary to monitor the processing accuracy in the x-axis, y-axis and the reference angle a relative to the ideal coordinate, within the positive stress range, while only in the x-axis within the negative stress range as the beam axial direction is along the x-axis of the square diaphragm. In addition, locating the beam in the middle of the square diaphragm is much better than at the edge.

References

[1] Masayoshi Esashi. Resonant Sensors by Silicon Micromachining [C]. Proceedings of the Annual IEEE International Frequency Control Symposium, 1996: 609-614.

[2] M. P. Henry, D. W. Clarke, N. Archer, etc. A self-validating digital Coriolis mass_flow meter: an overview [J]. Control Engineering Practice 8, 2000: 487-506.

[3] M.V Shutov, D L Howard, E E Sandoz, Electrostatic actuators with long range translation,, the 12th International

Conference on Solid-State Sensors, Actuators and Microsystems, 1: 356-359(2003).

[4] Brian D Jensen, Senol Mutlu, Sam Miller, Shaped comb fingers for tailored electromechanical restoring force, Journal of Microelectromechanical Systems, 12（3）: 373-383(2003).

[5] Middelhock S. Quo vadis silicon sensor[J]. Sensor and Actuators, 1994, A41/42: 1-8.

[6] Luo R C. Sensor technologies and microsensor issues for mechatronics systems (Invited Paper)[J]. IEEE/ASME Transactions on Mechatronics, 1996, 1(1): 39-49.

[7] Parsons P, Glendinning A, Angelidis D. Resonator sensor for high accuracy pressure measurement using silicon technology[M]. IEEE Aerospace Electronic Systems, 1992, 7(7): 45-48.

[8] Buser R A, Derooij N F. Resonant silicon structures[J]. Sensors and Actuators, 1989, A17, 145-154.

[9] Zook J D, Burns D W. Characteristics of polysilicon resonant microbeams[J].Sensors & Actuators, 1992, A 35: 51-59.

[10] Zhang L M, Uttamchandani D, Culshaw B. Measurement of the mechanical properties of silicon microresonantors[J]. Sensors & Actuators, 1991, A 29: 79-84.

[11] Buser Rudolf A, de Rooij Nicolaas F, Silicon pressure sensor based on a resonating element[J]. Sensors & Actuators, 1991, A 25-27 : 717-722.

ISBN: 978-81-936820-6-7

Series: AIJR Proceedings
Proceedings DOI: 10.21467/proceedings.4

Wind Energy Reliability Analysis based on Monte Carlo Simulation Method

Khaled Abdusamad*

Mechanical Engineering Department, Garaboulli Engineering Faculty, Elmergib University, Libya

DOI: https://doi.org/10.21467/proceedings.4.41

* Corresponding author email: kmatok70@gmail.com

ABSTRACT

Reliability is defined as the probability that an item will continue to achieve its intended function without failure for a specified period of time under operation conditions. The challenges of addressing energy supply and climate change are expected to drive the growth of renewable-based electrical generation such as from wind. Consequently, worldwide growth in wind energy is expected to increase as more wind turbines are installed to meet clean electricity demand and decrease the usage of fossil fuel. However, wind has risks and uncertainties that need to be addressed, perhaps the most significant challenge wind speed variability, which emphasizes that it cannot be considered as a reliable means of meeting the electrical loads. This paper suggests a Monte Carlo summation method, which can be utilized to apply reliability analysis in order to obtain the most-likely resistance-load relationship and the system probability of failure. A case study, which is based upon collected data from actual measurements, is presented in order to study the performance of a group of wind-turbines that deliver electricity to satisfy the demand of a certain load in a suggested area.

Keywords: Reliability, Wind energy, Probability of failure, Monte Carlo summation, Weibull distribution

1 Introduction

Due to the increase in the demand of electric power and great trend to integrate the wind energy with different renewable sources, the concept of reliability has become a very important factor in the overall wind energy systems. In the recent years, the production of electric power based on wind energy is developing remarkably, which results great development in the performance of wind turbines in general. The main factor in making wind energy industry more efficient is improvement the reliability of wind turbine performance. This has led to many wind turbine reliability models being developed. Therefore, it is very significant to continue developing new and accurate reliability models. Researchers have recognized the advantages of integrating both reliability and performance in a consolidated mathematical model. For instance, a reliability evaluation of a laboratory-based Micro Grid system consisting

 ISBN: 978-81-936820-6-7

of wind, is proposed using a Monte Carlo Simulation method for the system well-being analysis [1]. The study showed the system well-being computation index provided a bridge between the deterministic and probabilistic methods and defined indices that can be useful in a practical Micro Grid reliability evaluation. In another study conducted by Sameer Vittal et. al, the system performance and reliability analysis of wind turbines using Monte Carlo methods based on system transport theory was utilized to develop a performability model of extreme-weather wind turbines [2]. An enhanced model for calculation of reliability indices for different wind power plants configuration concepts was studied [3]. The autoregressive moving average model was used combined with the sequential Monte Carlo simulation in order to predict the expected energy not served more accurately during the failure. K. Hagkwen, and C. Singh suggested a reliability simulation in wind farm with different wind turbines at different heights, and it was found that as the height of some wind turbines is higher, energy loss by wake effect drops due to shear effect [4]. A new Monte Carlo simulation procedure and nearby regional weather station data are used to predict wind speed and turbine energy. The results indicated that the replacement of on-site wind data can replace provide accurate predictions of proposed nearby wind turbine [5]. Another computational model using one year of wind speed data of a weather station located downwind of the wind turbine site resulted in the greatest match of simulation results to the measured values. A forecasting method that applies Resistance–Load technique to estimate the reliability of a wind-energy system is studied in. The method is a combination of a prediction and risk-based approach, whereas the prediction technique models the power generation and demand scenarios, while the Resistance–Load technique, estimates reliability of the system [6].

The current work presents an application of Monte Carlo summation method, which can be utilized to estimate the reliability of the wind energy system. In this study, probability of failure is a significant parameter to determine the proposed target through obtaining the most-likely resistance-load and performance relationship. The following sections of the current paper is arranged as follows: Section 2 presents background about Monte Carlo simulation method procedure. Section 3 explains the methodology of the proposed model and the utilization of Resistance–Load technique to estimate the system performance based on its requirements. In order to demonstrate the use of the proposed method and its capability, case study is provided in Section 4. The obtained results and discussion regarding the proposed model are showed in Section 5. Finally, conclusions and suggestions for further research are presented in Section 6.

2 Monte Carlo Simulation

Monte Carlo simulation is a powerful statistical analysis tool, which widely used in engineering fields to evaluate the probability of failure of the energy systems. This simulation performs random sampling and conducts a large number of experiments on computer, which displays the statistical characteristics of the model outputs to their distributions. The outline of Monte Carlo simulation consists of three steps, which is illustrated in Figure 1. In step 1, the

ISBN: 978-81-936820-6-7

Series: AIJR Proceedings
Proceedings DOI: 10.21467/proceedings.4

cumulative distribution functions (CDF) of the random variable is equated to the generated random number u_i, that is, $F_X(x_i) = u_i$, and the equation is solved for x_i as follows [7,8]:

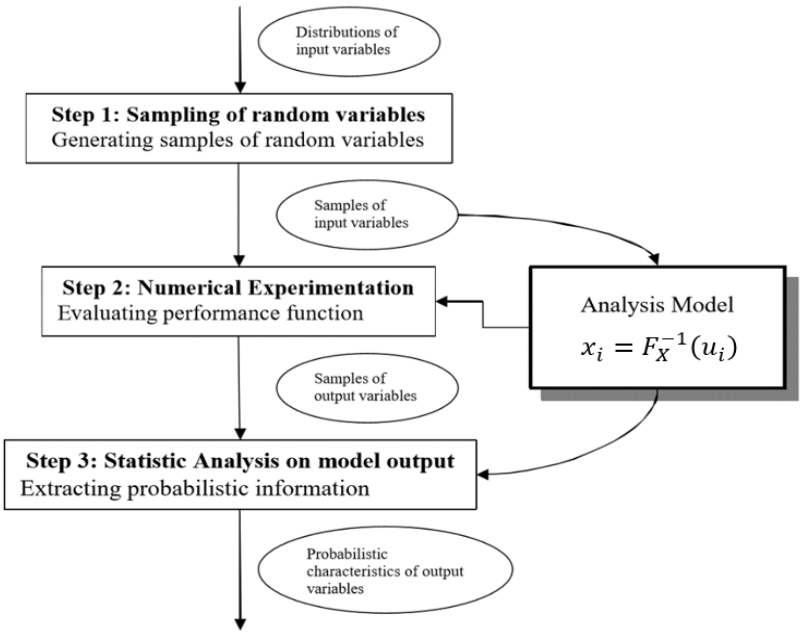

Figure 1: Monte Carlo Simulation Technique [7-10]

$$x_i = F_X^{-1}(u_i) \quad (1)$$

Evaluating the performance function represented in step 2. If the random variable X with parameters λ_X and ζ_X is lognormally distributed , the ith random number x_i according to the lognormal distribution can be generated.

$$\ln(x_i) = \lambda_X + \zeta_X \phi^{-1}(u_i) \quad (2)$$

$$u_i = \phi\left(\frac{\ln(x_i) - \lambda_X}{\zeta_X}\right) \quad (3)$$

$$x_i = \exp\left(\lambda_X + \zeta_X \phi^{-1}(u_i)\right) \quad (4)$$

where u_i is random number ($0\ and\ 1$), and where λ_X and ζ_X are the two parameters of the lognormal distribution. A computer program can be written to generate random numbers according to any distribution. In fact, many available computer programs can generate random numbers for commonly used distributions. If the computer cannot generate a specific distribution, Eq. (1) can be used to obtain it. In step 3, statistical analysis on the proposed model are applied in order to extracting probabilistic information through multiple tries [9-11]. Resistance–Load is an application of Monte Carlo technique, which widely used for the reliability assessment of systems having a certain "resistance", R, against an applied "load", L. The technique is utilized for an energy system considers the random nature of electrical generation and load simultaneously. The basic concept of Resistance–Load technique is that

energy systems are considered reliable when power generation i.e. R, exceeds L value. Consequently, the probability of R > L can be determined by employing this method, which submits an expectation about the energy reliability of the selected wind farm. Forecasting reliability using R–L technique consists of several steps, which are summarized in the next section [6].

3 Methodology

In order to define the reliability of an existing wind energy system based on R–L technique, several steps must be considered. First, identifying of the random and deterministic variables of the proposed model should be taken into consideration to analyse the probability distribution of both variables. Then, determine the respective probability distribution parameters is required before modelling the R–L values. Finally, Monte Carlo simulation is applied to estimate the probability of failure of the entire system [6].

3.1 Identifying the Random and Deterministic Variables of the System

Forecasting reliability using Monte Carlo simulation based Resistance–Load technique requires identifying the random and deterministic variables of the proposed model. In this work, R represents the total energy output generated by the selected wind farm over several years; modeling its value requires simulated wind speeds (v) and system losses (loss). The generated power by a single wind turbine rotor is determined according to the following relation [12-14] :

$$P_W = \frac{1}{2} A \rho_a C_P v^3 \quad (5)$$

where, P_w represents the generated or produced power by the rotor of a wind turbine, ρ_a is the air density, v is the wind speed, A is the rotor swept area of a wind turbine, and Cp is the performance coefficient of a wind turbine. System losses for a known probability distribution are simulated using distribution parameters, such as, mean and variance through Monte-Carlo simulation technique. The model of the system is described as follows:

$$Performance = (\frac{1}{2} A \rho_a C_P v^3 - losses) - Load \quad (6)$$

The random variables of the proposed model are:

1-The air density ρ_a $(\frac{m^3}{kg})$ 2-The wind speed v (m/s) 3-The demeaned load L (Watt)

The deterministic variables of the system are:

1- The swept area of the wind turbine rotor A (m^2) refers to the area of the circle created by the blades as they sweep through the air.
2- Wind turbine power coefficient C_p, which is defined as the proration of the produced power by the wind turbine's generator to the power in the wind. The system losses is determined according to listed in Table 1:

ISBN: 978-81-936820-6-7
Proceedings DOI: 10.21467/proceedings.4

Series: AIJR Proceedings

Table 1: *Summary Losses value is the wind turbines* [6]

Type of Loss	Value (%)
WTG Unavailability ($loss_1$)	3
Collection and Substation Unavailability ($loss_2$)	0.5
Electrical and Transmission Loss ($loss_3$)	2
Utility/Grid Unavailability ($loss_4$)	0.5
King and Blade Degradation ($loss_5$)	3
Wake Induced Turbulence Loss ($loss_6$)	5

The total system losses can be calculated from the next formula:

$$P_{loss} = (loss_1 + loss_1 \dots\dots + loss_1)/100 * N_T * P_{out} \quad (7)$$

where N_T is the number of wind turbines in a wind farm.

3.2 Probability Distribution Analysis

In order to analyse the probability distributions for the wind speed, losses and load, graphical techniques, such as histogram and probability plot are required. Furthermore, modelling R and L values is based on distribution parameters and simulation techniques. By using EasyFit software, the best wind speed distribution can be obtained. The software allows using different types of distributions and compare then in terms of some tests such as K-S test, Chi square test, and Anderson darling test. To obtain simulated wind speeds, probability distribution identification is required based on historical wind speed data. In line with pervious work, the current study's wind speed distribution can be described using Weibull distribution when Chi square test considered [9,10] The Weibull distribution is represented by two-parameter; Weibull shape parameter (K), and Weibull scale parameter C, which are determined based on the mean ($\bar{v}$) and standard deviation (σ_v)of wind data [15-17].

$$K = \left(\frac{\sigma_v}{\overline{v}.}\right)^{-1.086} \quad (8)$$

$$\frac{C}{\bar{v}} = \left(0.568 + \frac{0.433}{K}\right)^{-1/K} \quad (9)$$

Weibull shape parameter, k, generally ranges from 1.5 to 4 for most wind conditions. In addition, Weibull distribution whose cumulative distribution function (CDF) is given as follows [15-17]:

$$F(v) = P[V \leq v) = \int_0^v f(v)dv = 1 - exp\left\{-\left(\frac{v}{C}\right)^K\right\} \quad (10)$$

where $P(\leq v)$ is the probability of the measured wind speed is less than or equal v. Figure 2 illustrates the effect of the shape parameter on the cumulative distribution function. Equation 11 presents the definition of the Weibull probability density function. Figure 3 displays the effect of the shape parameter on the probability density function [15-17].

$$f(v) = (v) = \left(\frac{k}{c}\right)\left(\frac{v}{c}\right)^{k-1} \exp[-\left(\frac{v}{c}\right)^{k}] \quad (11)$$

When the shape parameter K is equal to 2, the P.D.F. is given its own name, the Rayleigh probability density function, which is defined as follows [15-17]:

$$f(v) = \frac{2V}{c^2} * \exp\left[-\left(\frac{v}{c}\right)^2\right] \quad (12)$$

The equation of the cumulative Rayleigh function is defined as follows [15-17]:

$$F(v) = 1 - \exp\left[-\frac{\pi}{4} * \left(\frac{v_i}{\bar{v}}\right)^2\right] \quad (13)$$

3.3 Modelling the Resistance (R) and Load (L) Values.

An energy system's load is considered independent of wind speed, and the resistance represents the total electrical output generated by the wind turbines over several years. Modelling R-L values requires first simulated wind speeds (v), air density (ρ_a), and system losses (loss).

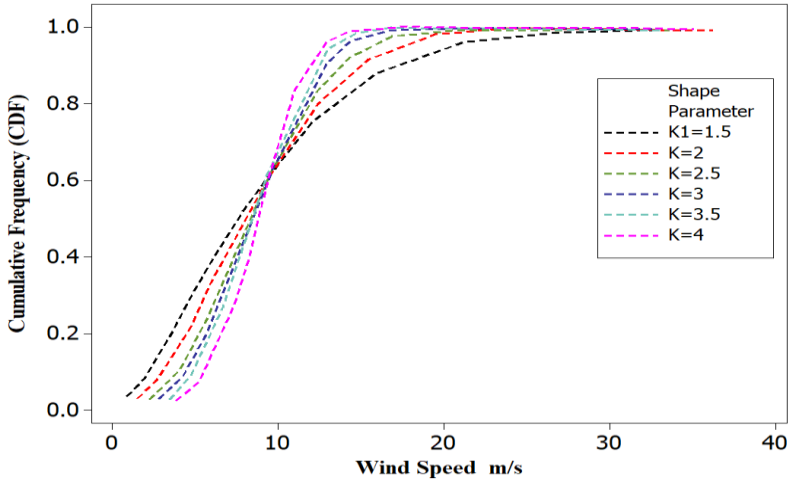

Figure 2: The Effect of the Shape Parameter on the Cumulative Distribution Function

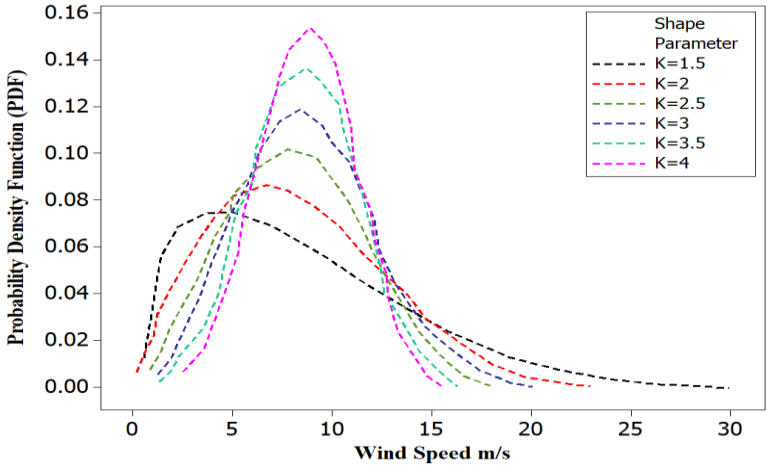

Figure 3: The Effect of the Shape Parameter on the Probability Density Function

ISBN: 978-81-936820-6-7
Proceedings DOI: 10.21467/proceedings.4

Using the simulated losses and wind speeds, the net generated P_{NET} from each wind turbine is calculated from the following equation:

$$P_{NET} = P_w - P_{LOSS} \quad (14)$$

The reliability of the proposed system is carried out to study the probability of failure to satisfy the load power demand and calculate P(R<L). The total net power (resistance) is determined as follows:

$$The\ total\ net\ power\ (R) = N_T * P_{NET} \quad (15)$$

3.4 Determine the Probability of Failure

The probability of failure represents the probability of failure, which requires a knowledge about the wind turbine specification. In this issue, the power curve of each single wind turbine displays the required specification to apply Monte Carlo simulation.

4 Case Study

In order to utilize the proposed model to determine the reliability of the wind energy systems, collected data, which are related to an area in Tripoli -Libya is selected [18]. The specifications that are selected to be set up in the area are illustrated in Table 2 [19]. In of the wind turbines addition, Fig, 4, which shows the dependence between wind speed and produced electrical power of the selected wind turbine. It can be realized that there are three stages should be explained. Stage 1 occurs when the wind speed between (3m/s) to the rated speed (11m/s). Then, stage 2 occurs when the wind speed between the rated speed (11m/s) to the cut off speed (20m/s). Finally, stage 3 occurs when the wind speed more than or equal the cut off speed at (20m/s). Therefore, there is a need to find the produced power at each stage for each turbine in the proposed wind farm, which can be determined as follows:

- Stage 1: $\mathrm{P_{produced}} = \frac{1}{2}\,\mathrm{A}\,\rho_a\,\mathrm{C_P}\,\mathrm{v}^3 - \mathrm{Losses}$ - Stage 2: $\mathrm{P_{poduced}} = 1057\ \mathrm{KW} - \mathrm{losses}$

-Stage 3: $\mathrm{P_{out}} = 0\ \mathrm{W}$

Table 2: *1057kW Wind Turbine General Specification* [19]

Category	Specification
Rated Power	1057 1057
Number of Blades	3 blades
Rotor Diameter	60 m
Cut-In Wind Speed	3 m/s
Rated Wind Speed	11/m/s
Hub Height	66 m
Cut-Out Wind Speed	20 m/s
Coefficient of Power	40%

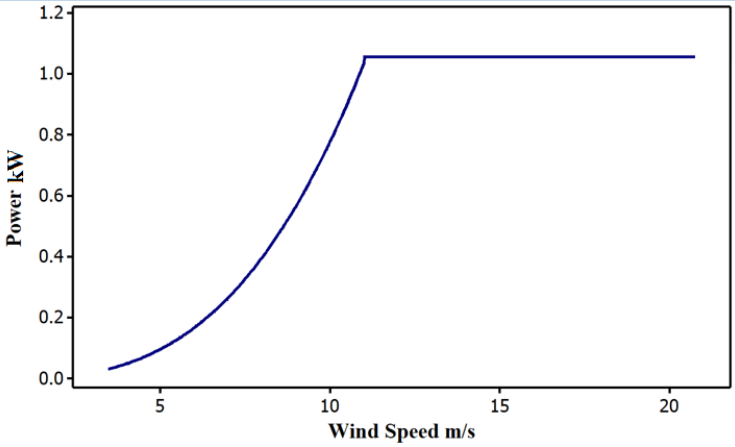

Figure 4: 1057kW Wind Turbine power curve

The obtained data is representing in the average of wind speeds, air pressures, and temperatures for every day in the year during the study period of the selected area. Figure 5 displays the fluctuations of the average wind speed throughout the study for the same location [18]. Since, the obtained wind speed data are measured at 10 m, an adjustment must be made to obtain wind speeds at the turbine hub height. Several common functions that describe the change in mean wind speed with height are utilized. With the aid of Eq. 15, the average wind speed at the turbine hub height is determined.

$$v_z = v_R * \left(\frac{Z}{Z_R}\right)^{\alpha} \quad (16)$$

where α is the friction coefficient for various terrain characteristics, which is determined from Table 3. Finally, the suggested wind farm consists of twenty-wind turbine to cover the load in the selected area. Section 5 presents the results that obtained from applying the proposed model.

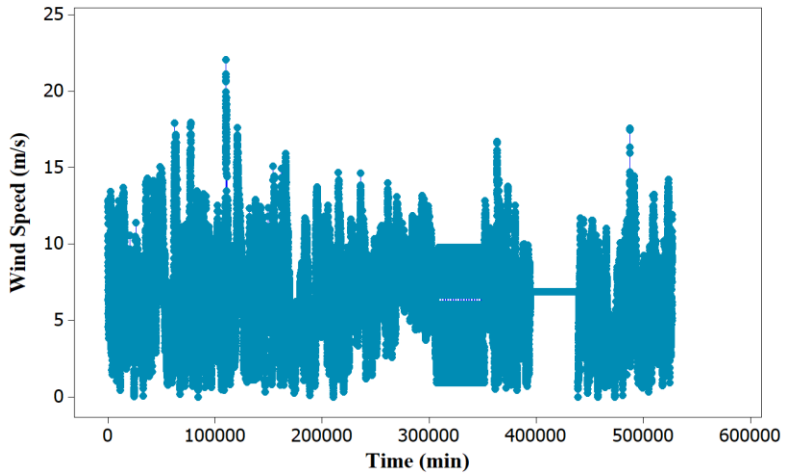

Figure 5: The fluctuations of the average wind speed during the duration of the study [18]

ISBN: 978-81-936820-6-7
Proceedings DOI: 10.21467/proceedings.4

Table 3: *The friction coefficient for various terrain characteristics* [12,13]

Type of terrain	Roughness class	β
Water areas	0	0.01
Open country, few surface Features	1	0.12
Farm land with building and hedges	2	0.16
Farm land with many trees, Forests, villages	3	0.28

5 Results and Discussion

The obtained results indicate that there is dramatic changes in the wind speed when it reaches 9m/s. The performance before this value is negative, which means the demand power of the selected area is greater than the produced power by the proposed wind farm. Figure 6 displays wind speed time series with respect to its frequency. The diagram shows that most available wind speeds range from 9 m/s to 10 m/s. Figure 7 shows the Weibull probability density function and cumulative distribution function of the wind speed. Weibull probability density function curve displays the wind speed probability distribution of the obtained wind speed data. Furthermore, Weibull cumulative distribution curve describes the probability that every single value of the obtained wind speed data takes a value less than or equal to the wind speed variable. The curve shows that the likelihood of the selected wind turbines operating at the rated speed is approximately 25%. The behaviour of the performance of the proposed system with respect to the wind speeds is illustrated in Fig 8. It is obvious that the performance reaches 129 MW at 20 m/s but the frequency of this value is low. However, when wind speed is between (3-8) m/s, the system performance is negative, which submits an indication that the probability of failure of the proposed system in this range is significant value. Table 4 presents details regarding the system generated power against the load of the selected area. The Monte Carlo simulation results are illustrated in Table 5 with several trails. It is noted that as the number of simulations is increase the probability of failure converges, computation error decreases and run time increases significantly.

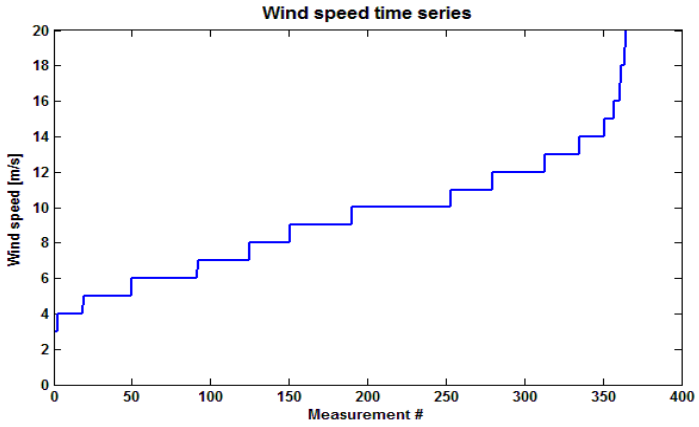

Figure 6: Wind speed time series

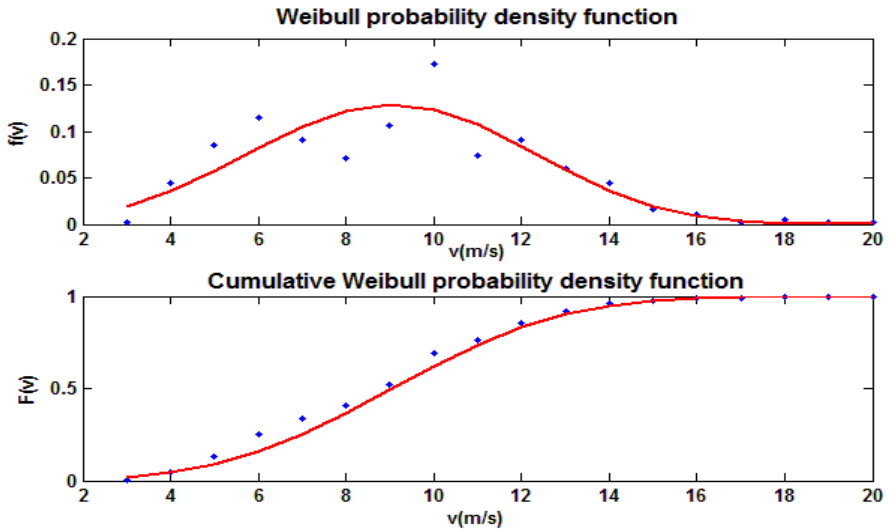

Figure 7: Weibull probability density function and cumulative distribution function

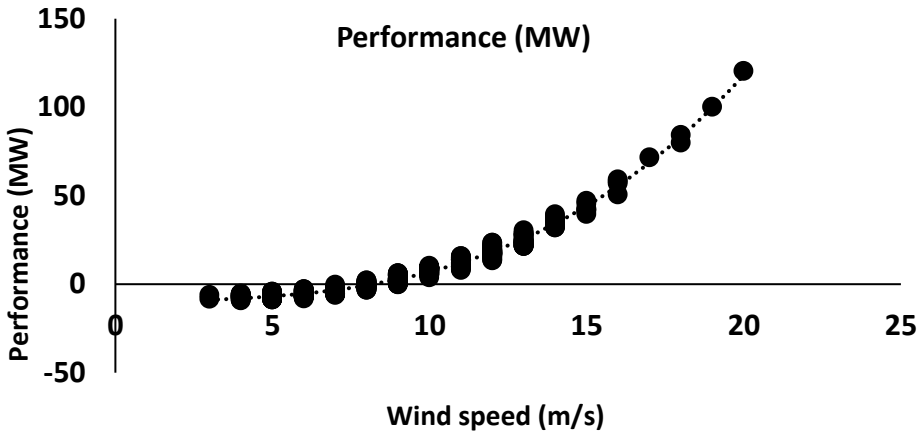

Figure 8: The trend of the system performance with respect to the wind speed

Table 4: *The system simulation results*

Wind speed m/s	Resistance MW	Load MW	Performance MW	Wind speed m/s	Resistance MW	Load MW	Performance MW
3	0.7	7.9	7.3-	12	27.1	9.0	18.0
4	1.1	8.2	7.1-	13	33.8	9.2	24.6
5	2.1	9.1	7.0-	14	43.3	8.4	34.9
6	3.4	9.3	5.9-	15	52.1	9.1	43.0
7	5.2	8.8	3.6-	16	65.0	8.9	56.2
8	7.7	8.4	0.7-	17	76.9	8.0	68.9
9	11.3	8.5	2.7	18	88.8	7.2	81.7
10	15.5	7.6	7.9	19	114.1	8.6	105.5
11	20.6	8.4	12.2	20	139.3	10.0	129.3

ISBN: 978-81-936820-6-7
Proceedings DOI: 10.21467/proceedings.4

Series: AIJR Proceedings

Table 5: *System probability of failure and error with several trails numbers*

Number of trails	Number of failures	Pf (%)	Error (%)	Simulation time(sec)
10000	2530	25.3	8.6946	2.1359
100000	25174	25.17	2.7449	19.979
1000000	252880	25.29	0.86933	2522.8

6 Conclusions

In this study, an effective method based on Monte Carlo simulation is performed to determine the reliability of wind energy systems. The proposed technique is represented to obtain the most-likely generated power-power demand and performance relationship to estimate the system probability of failure in the selected area. It is found that as the number of simulations is increase the probability of failure slightly decreases; computation error reduces significantly and run time increases remarkably. Further, it can be summarized that the wind speed has the most influence on the performance of the wind energy systems, then the demanded power. To obtain simulated wind speeds, it was found that wind speed distribution can be described using Weibull distribution when Chi square test considered. This model may be considered as platform and can be used for other locations in Libya. Future work should be focused on different types of wind turbines and several areas in Libya in order to estimate the most proper locations that represent high the reliability of wind energy systems.

References

[1] Youli, Su, and Ken Nagasaka, "Monte Carlo simulation method used in reliability evaluation of a laboratory-based micro grid," *Proceedings of the international multi conference of engineers and computer scientists*, Vol 2. 2010..https://pdfs.semanticscholar.org/f26e/969fffc5f035281927cb9670eb25abf8e3f3.pdf

[2] Vittal, Sameer, and Michel Teboul, "Performance and reliability analysis of wind turbines using Monte Carlo methods based on system transport theory," *46th AIAA/ASME/ASCE/AHS/ASC Structures, Structural Dynamics and Materials Conference*, p. 2218. 2014. https://arc.aiaa.org/doi/abs/10.2514/6.2005-2218

[3] Topić, Danijel, Damir ŠljivAc, and Marinko STojkov, "Reliability model of different wind power plant configuration using sequential Monte Carlo simulation," *Eksploatacja i Niezawodnosc-Maintenance and Reliability*, p. 237. Jan, 2016. http://bib.irb.hr/datoteka/632590.EiN_2016-2_article_11.pdf

[4] Kim, Hagkwen, and Chanan Singh, "Reliability Simulation in Wind Farm with Different Wind Turbines," *Proceedings of National Power Systems Conference*, 2012. http://www.iitk.ac.in/npsc/Papers/NPSC2012/papers/12170.pdf

[5] Gallagher, Ron, and Andrew Curtis Elmore, "Monte Carlo simulations of wind speed data," *Wind Engineering 33(6)*, p. 661-673. Dec, 2009. http://journals.sagepub.com/doi/abs/10.1260/0309-524x.33.6.661

[6] Chaudhry, Nikhil, and Larry Hughes, "Forecasting the reliability of wind-energy systems: A new approach using the RL technique," *Applied energy 96*, p. 422-430. Aug, 2012. https://www.sciencedirect.com/science/article/pii/S0306261912001778

[7] Mooney, Christopher Z, "*Monte carlo simulation*," Vol. 116. Sage Publications, Apr, 1997.

[8] Christopher, W, "Wind Turbine Reliability: Understanding and Minimizing Wind Turbine Operation and Maintenance Costs," Department of Energy. 2006.

[9] Rao, Singiresu S., Singiresu S. Rao, and S. S. Rao, "*Reliability-based design*," 1992. https://prkwrhnfx07.storage.googleapis.com/MDA3MDUxMTkyNg==07.pdf

[10] Haldar, Achintya, and Sankaran Mahadevan, "*Probability, reliability, and statistical methods in engineering design*," New York: Wiley. Vol. 1.2000. https://prkwrhnfx07.storage.googleapis.com/MDQ3MTMzMTE5OA==07.pdf

[11] Hall, P. L., and J. E. Strutt, "Probabilistic physics-of-failure models for component reliabilities using Monte Carlo simulation and Weibull analysis: a Parametric Study a parametric study," *Reliability Engineering & System Safety*. V0l 3. p. 233-242. Jun, 2003. https://www.sciencedirect.com/science/article/pii/S0951832003000322

[12] Manwell, James F., Jon G. McGowan, and Anthony L. Rogers, "*Wind energy explained: theory, design and application*," John Wiley & Sons. Sep, 2010.

[13] Jain, Pramod, "*Wind energy engineering*," McGraw-Hill Education. Jan, 2016.

[14] Gipe, Paul, "*Wind energy basics: A guide to small and micro wind system*," White River Junction, VT: Chelsea Green publishing company. Mar, 1999.

[15] Murthy, DN Prabhakar, Michael Bulmer, and John A, "Weibull model selection for reliability modelling," *Reliability Engineering & System Safety 86*. V0l 3. p. 257-267. Dec, 2004. https://www.sciencedirect.com/science/article/pii/S0951832004000237

[16] Xie, M., and Lai, C.D, "Reliability Analysis Using an Additive Weibull Model with Bathtub-shaped Failure Rate Function," *Reliability Engineering & System Safety 52*. V0l 1. p. 87-93. Apr, 1996. https://www.sciencedirect.com/science/article/pii/0951832095001492

[17] Lai, C. D., Min Xie, and D. N. P. Murthy, "A modified Weibull distribution," *IEEE Transactions on reliability* 52. V0l 1. p. 33-37. Mar, 2003. https://ieeexplore.ieee.org/abstract/document/1179794/

[18] Data. Provided by Center of Solar Energy Research and Studies, 2015

[19] Data of a Variable Speed Wind Turbine, 1057 KW rated power, three phase permanent magnetic type 440/660 V 60 Hz. Provided by Dr. Kathryn Johnson, Colorado School of Mines, 2013

ISBN: 978-81-936820-6-7

Series: AIJR Proceedings
Proceedings DOI: 10.21467/proceedings.4

Zero Energy and Low Water Schools: Case Study-Building of Garaboulli Engineering Faculty-Libya

Salhin M. Alaud [1*], Khalid M. H. Jaballa[2], Abdulghani M. Ramadan[3]

[1] Civil Department, Garaboulli Engineering Faculty, Elmergib University, Libya

[2, 3] Mechanical Department, Garaboulli Engineering Faculty, Elmergib University, Libya

DOI: https://doi.org/10.21467/proceedings.4.42

* Corresponding author email: s.alaud@elmergib.edu.ly

ABSTRACT

The current paper presents the design methodology for reducing the water consumption to reach a zero energy building. The building of the Garaboulli Engineering Faculty (GEF), Libya was chosen as a case study. The required energy will be supplied by renewable energy. In order to meet the required loads, solar energy is used in the design to generate heating, cooling, and electric power by using different techniques such as solar thermal collectors and photovoltaic panels. Moreover, rain water is used as a source of water supply for the building. To reach the low water and Zero Energy aims, different techniques such as recycling of greywater and solar cooling were adopted. Finally, the proposed system will be feasible for a long term of operation.

Keywords: Zero energy, Low water, Renewable energy, Rain water.

1 Introduction

The daily required of energy used increases continuously with a growing population. New buildings are constructed faster than old ones and thus increase the consumption of energy. On the other hand, the load on government supply of electricity or water increases over time. In the educational buildings, the increasing of consumption is depends on increase of student number.

Recently, water and power outages have increased as a result of increased demand of energy and water, and poor production capacity. From this perspective, alternatives ways are needed to find water and energy and ensure constant supply without interruption. Introducing of zero energy principle with rationing the water and energy uses into school buildings are particularly necessary when the supply of energy and water are intermittent. The zero energy is defined by the annual of the total energy amount used by the building that renewable energy sources. In general, a net zero energy is a building with highly reduced energy needs through efficiency gains such that the renewable technologies can supply the energy needs. In this paper, Garaboulli Engineering faculty building has designed to be low water consumption and zero energy building. Solar panels can generate the required amount of electricity that consumed by the faculty building every year.

 ISBN: 978-81-936820-6-7

The large area of the building's roof allows collecting an ample amount of rainwater. Reuse of greywater for some purposes throughout the building will also save extra water.

2 Description and Aims of the Project

The building of Garaboulli Engineering Faculty is located at the north of the Garaboulli city on total area 17000 m². The surface area of the main and attachment buildings is about 2100 m². The green area is more than 2000 m². The main building has four toilets with four sinks in each of six parts in two stories with total of 24 toilets and 24 sinks. A small kitchen is also including in the building. There are another toilet and kitchen in the gate building. The construction has 15 class rooms, 1 theatre, 2 electronic labs and 16 offices. Figure 1 illustrates the plan of the building and surrounded garden area. The project aims to benefit of the large surface area to generate the energy (electric, heating and cooling) from the solar and to collect the rain water to reduce the dependency on the general city network.

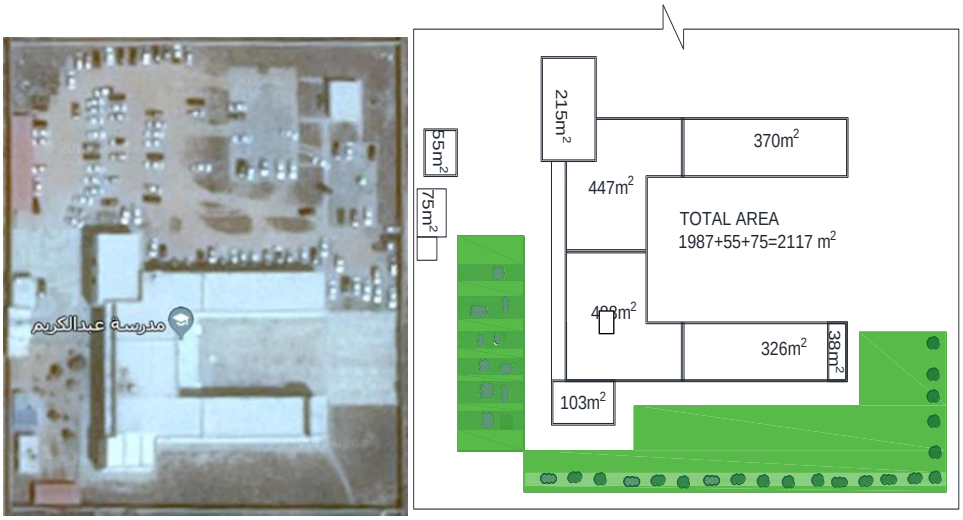

Figure 1: *Garaboulli Engineering Building, Plan (left) and air photo (right)*

3 Design Methodology

The current research attempts to find a suitable design to minimize the usage of water consumption from the city network by collecting the rain water and recycle the grey water or dispense on the network electricity by designing solar panels and heaters to generate the energy.

3.1 Low Water

Rainwater exploitation may not be sufficient to cover the total consumption of water, as this requires a very large area of water storage. Annual rainfall in some areas is also insufficient. The best ways are: rainwater exploitation to relieve the consumption from the public network, rationalize the consumption of water and recycling the grey water.

ISBN: 978-81-936820-6-7
Proceedings DOI: 10.21467/proceedings.4

Series: AIJR Proceedings

3.1.1 Rain Water Collection

In general, Libya has a dry climate with intense rain storms and short in duration. Along the north of Libya, the rainfall months are from September to May, with most severe from October to January. The annual rainfall for Garaboulli city is taken a similar of the average of annual rainfall of the two nearest cities, Tajura and Tripoli, which have recorded data. The average of annual rainfall of these cities were similar in two different studies, 288 mm/year, where the results of Tajura was based on 40 years [1] and in Tripoli was based on 30 years of data [2]. The catchment area of the main building of the college (2000 m²) has considered. For the runoff, it is estimated that 15% of the rain water volume is released during the time required to fill the detention facility [1]. This is due to unavoidable any leakages or a possible overflow in the gutter downpipe system, or in the case of the downpour is too light to produce sufficient runoff. However, the total volume of detention facility is designed on 85 % of the total rainwater collected as in Equation 1.

$$q = 0.85 \times 288 \times 2000 = 489.6 \times 10^3 l/year = 489.6\, m^3/year \quad (1)$$

3.1.2 Water Consumption

There are many studies and standards determine the varying amount of consumption in the universities and schools, such as 4.86 -6.3 litters / student / day for secondary schools [3] and 125 - 180 *l/capita/day* for Universities [4]. The large amount of the consumption at universities is due to use of larger this amount in laboratories, gardens and other facilities, while in the school case, the consumption only for drinking, washing and toilet flushing. The water consumption can be divided into:

1. Toilet flushing which make up about 30% of overall water consumption which produce the black water.
2. Wash basins, and floor cleaning that produces grey water as well as bidet faucets which mix with toilet sludge.
3. Water used to irrigate the garden.
4. Laboratory consumption such as concrete labs

Gray water can be recycled to use in the toilet flushing and irrigate the garden after a filtration and treatment process. Figure 2 illustrates the cycle of rain and city network water.

There are no reliable data for the water consumption in the target Faculty. Since the water consumption in the Faculty is limited to: *i.* washing; *ii.* toilet flushing; and *iii.* a small Garden, the consumption in our study for i and ii is estimated to be *6 l/capita/day*. If we consider that the consumption rate is limited to school days only and the number of annual school days is 280, the quantity required for annual consumption of water is 280 x 6 = 1680 *l*/capita/year.

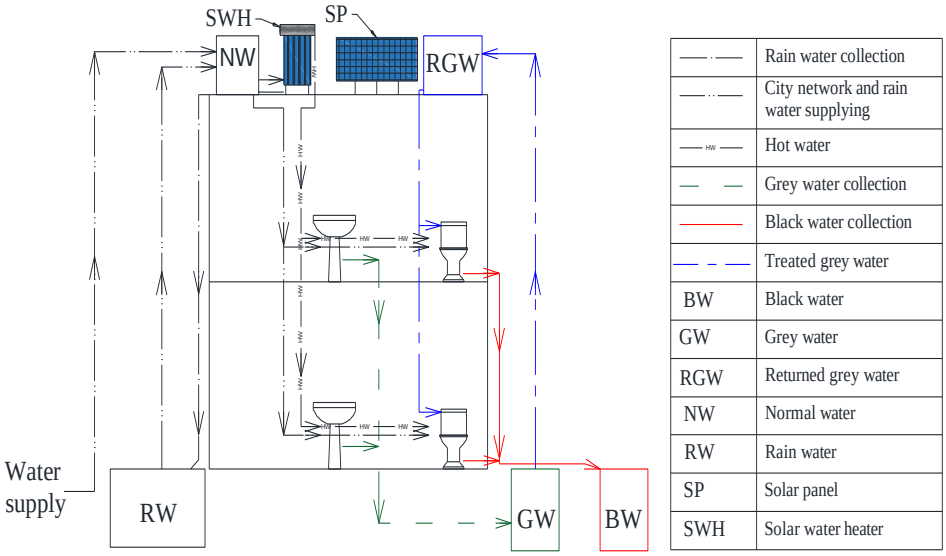

Figure 2: *General section of water cycle*

Assuming that the total daily number that can be presence in the college is a maximum of 700 people, thus, the annual consumption required is 700 x 1680 = 1176 x10^3*l/capita/year* or 98 *m^3/month*. The use of grey water in the flushing will save about 30% of the consumption amount, thus, the needed consumption will be 68.6 *m^3/month*. The garden consumption (iii) is estimated to be 30 *m^3/month,* therefore, the monthly amount of water consumption is 98.6 *m^3/month* or say 100 *m^3/month*. Figure 3 illustrates the monthly average collected from rainwater [2] compared to the total monthly consumption as a percentage. The total rain water collected is 489 *m^3/year* and the total consumption requirement 1200 *m^3/year,* thus, the needed water from the city network is 711 *m^3/year* with save more than 40% of the consumption.

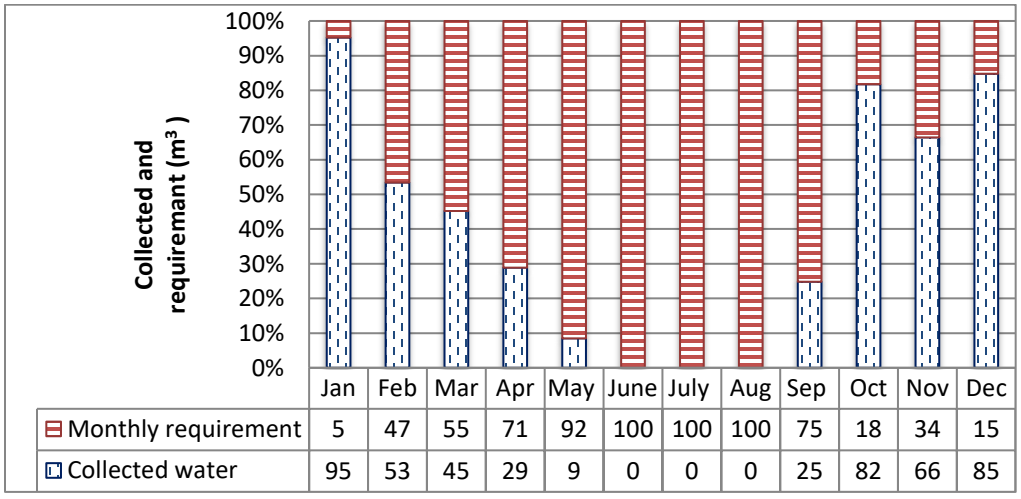

	Jan	Feb	Mar	Apr	May	June	July	Aug	Sep	Oct	Nov	Dec
Monthly requirement	5	47	55	71	92	100	100	100	75	18	34	15
Collected water	95	53	45	29	9	0	0	0	25	82	66	85

Figure 3: *Collected water and monthly requirement*

ISBN: 978-81-936820-6-7
Proceedings DOI: 10.21467/proceedings.4

Series: AIJR Proceedings

3.2 Cooling, Space Heating and SHW Loads

In order to a achieve Net Zero Energy (NZE), Combi-system is the highest prospective technology which can offer that. A solar Combi-system is providing space heating, Service Hot Water (SHW) and cooling stock by solar collectors and an absorption cooling cycle. In this paper, for the purpose of designing a solar heating system, f-chart method and ϕ-utilizability method are integrated together to merge the advantages and merits of the two methods to get more accurate and precise results[5],[6]. In order to start design process, relevant weather data required are shown in RetScreen software including local weather data, air temperature, latitude, tilt angle, daily solar radiation on horizontal surface...etc[8]. Moreover, Table 1 shows the input and design data for faculty of engineering at Garaboulli, includes the number of occupants, average daily service hot water consumption per capita in addition to other related data. In addition, Table 2 shows the proposed solar collector specifications. The first step in the design of solar thermal system is to determine the energy demand of the building by using RetScreen software, and assumption a faculty operation whole the year. Table 3 summarizes the different energy demands for the space heating, cooling, service hot water, and electric devises (Baseline energy) such as computers, lighting, surface pumps that calculated according to annual consumption of the faculty building. It should be noted that the total heating load requirement which covered by solar thermal system is calculated as following in Equation 2;

$$Total\ heating\ load\ =\ heating\ for\ cooling\ +space\ heating\ load\ +SHW\ load \quad (2)$$

Total heating load = 3.65×10^{12} (J)

Table 4: *Input and design data for the faculty building*

S. No.	Item	Value	unit
1	Latitude	32	^{o}N
2	Tilt Angle	42	degree
3	Number of Students	700	
4	Average Service Hot Water Consumption	2.3	L/day/student
5	Water Service Temperature	60	^{o}C
6	Water Density	1000	kg/m^3

Table 5: *The proposed Solar Collector Specifications*

S. No.	Item	Value	unit
1	Type of Collector	Tubular	
2	Gross Area of collector	4.619	m^2
3	(F_RU_L)	-1.26	W m^{-2} ^{o}C^{-1}
4	$F_R(\tau\alpha)_n$	0.51	
5	Collector Flow Rate	0.566	L/s
6	Collector Fluid Specific Heat	3600	J kg^{-1} ^{o}C^{-1}
7	Collector Fluid Density	1034	kg m^{-3}
8	Heat Exchanger Effectiveness	0.8	
9	Storage Tank Capacity	1610	Litre

Table 6: *Energy demands for the faculty building*

Month	Cooling load demand (J)	Heating load for cooling demand (J)	Heating load (J)	SHW (J)	Total heating load (J)	Electric devices load (kWh)
Jan	0.00	0.00	2.15 x10^{11}	8.95 x10^{09}	2.23 x10^{11}	10,477.3
Feb	2.69 x10^{09}	4.21 x10^{09}	1.91 x10^{11}	8.37 x10^{09}	2.04 x10^{11}	9,463.4
Mar	3.32 x10^{10}	5.19 x10^{10}	1.85 x10^{11}	9.22 x10^{09}	2.47 x10^{11}	10,477.3
Apr	4.67 x10^{10}	7.30 x10^{10}	1.67 x10^{11}	8.53 x10^{09}	2.49 x10^{11}	9,225.6
May	1.57 x10^{11}	2.46 x10^{11}	9.00 x10^{10}	8.18 x10^{09}	3.44 x10^{11}	9,533.1
Jun	2.22 x10^{11}	3.47 x10^{11}	3.39 x10^{10}	7.21 x10^{09}	3.88 x10^{11}	9,225.6
Jul	2.48 x10^{11}	3.87 x10^{11}	2.08 x10^{10}	6.86 x10^{09}	4.15 x10^{11}	6,308.8
Aug	2.49 x10^{11}	3.89 x10^{11}	2.08 x10^{11}	6.53 x10^{09}	4.16 x10^{11}	6,308.8
Sep	2.26 x10^{11}	3.54 x10^{11}	3.11 x10^{11}	6.37 x10^{09}	3.91 x10^{11}	6,105.3
Oct	1.27 x10^{11}	1.98 x10^{11}	9.62 x10^{10}	6.98 x10^{09}	3.01 x10^{11}	9,185.6
Nov	4.04 x10^{10}	6.32 x10^{10}	1.75 x10^{11}	7.39 x10^{09}	2.46 x10^{11}	8,889.3
Dec	0.00	0.00	2.15 x10^{11}	8.35 x10^{09}	2.23 x10^{11}	9,185.6
Annual demand		2.11 x1012	1.44 x10^{11}	9.29 x10^{10}	3.65 x10^{12}	104,386.40

Heating for cooling is defined as the heating energy which is required for absorption cooling system. It can be calculated as follows;

Heating for cooling = cooling load demand x COP

In this study, the absorption cooling system COP is equal to 0.64.

Next step, by using ϕ-chart method, the number of collectors and the solar monthly energy collected by collectors can be estimated with following Equation 3;

$$Q = F_R(\overline{\tau\alpha})\overline{H_T}\,\overline{\emptyset} \tag{3}$$

Where is:

Q, the monthly energy collected by collectors (J/m^2).

$F_R(\tau\alpha)_n$, is readily determined from collector specifications.

H_T, is the monthly average daily radiation on tilted surface on the collector.

ϕ , is the monthly average daily utilizability.

In order to calculate the required collectors' area in square meters and the available total annual solar energy (J/m^2) in site. First, the solar radiation on tilted surface on collector in (Kwh/m^2) should be calculated. Table 4 summarizes the estimated average monthly solar radiation on tilted surface on collectors. Furthermore, the monthly and annual solar thermal energy collected by collectors is also shown in Table 5. In view of the data shown in Tables 4 and 5, total annual solar thermal energy available $=3.49 \times 10^{09}$ (J/m^2), and total annual thermal energy demand $=3.65 \times 10^{12}$ (J) , taken from Table 4. Then, total collector area required is determined by Equation 4;

$$Total\ Collector\ Area\ Required = \frac{Total\ Annual\ thermal\ energy\ demand}{total\ annual\ solar\ thermal\ energy\ available} \tag{4}$$

ISBN: 978-81-936820-6-7
Proceedings DOI: 10.21467/proceedings.4

Series: AIJR Proceedings

Table 7: *The average monthly solar radiation on tilted surface on collectors*

Month	$\overline{H_o}$	$\overline{H}$	K_T	H_d	H_b	R_b	ϱ_g	$\overline{H_T}$	$\overline{H_T}$
	J/m^2) x10^7	(kWh/m^2)	(-)	(J/m^2) x10^6	(J/m^2) x10^7	(-)	(-)	(kWh/m^2)	(J/m^2) x10^7
Jan	1.99	2.9	0.53	3.83	0.661	1.90	0.2	4.50	1.62
Feb	2.42	4	0.60	4.39	1.00	1.60	0.2	5.61	2.02
Mar	3.06	5	0.59	6.28	1.17	1.24	0.2	5.67	2.04
Apr	3.63	6	0.60	7.40	1.42	0.96	0.2	5.72	2.06
May	4.00	6.5	0.58	8.23	1.52	0.78	0.2	5.43	1.96
Jun	4.14	7	0.61	8.32	1.69	0.70	0.2	5.49	1.98
Jul	4.07	7.1	0.63	8.02	1.75	0.73	0.2	5.69	2.05
Aug	3.79	6.5	0.62	7.54	1.59	0.86	0.2	5.80	2.09
Sep	3.30	5.5	0.60	6.69	1.31	1.10	0.2	5.76	2.07
Oct	2.66	4	0.54	5.62	0.878	1.44	0.2	4.96	1.79
Nov	2.12	3.1	0.53	4.08	0.708	1.79	0.2	4.59	1.65
Dec	1.85	2.3	0.45	3.69	0.459	2.01	0.2	3.52	1.27

Table 8: *The monthly and annual solar thermal energy collected by collectors*

Month	H_T (kWh/m^2)	R	a	B	$r_{t,n}$	$r_{d,n}$	R_n	a	b	c	Ø	Q (J/m^2) x10^8
Jan	4.50	1.55	0.55	0.53	0.16	0.15	1.58	-0.82	-0.69	0.48	1	2.5
Feb	5.61	1.40	0.59	0.49	0.16	0.14	1.42	-1.15	-0.35	0.69	1	2.8
Mar	5.67	1.13	0.65	0.44	0.14	0.13	1.14	-1.11	-0.38	0.67	1	3.2
Apr	5.72	0.95	0.70	0.38	0.13	0.12	0.96	-1.15	-0.35	0.69	1	3.14
May	5.43	0.84	0.75	0.34	0.13	0.12	0.83	-1.10	-0.40	0.65	1	3.08
Jun	5.49	0.78	0.77	0.32	0.12	0.11	0.78	-1.21	-0.29	0.73	1	3.01
Jul	5.69	0.80	0.76	0.33	0.13	0.12	0.80	-1.29	-0.21	0.80	1	3.23
Aug	5.80	0.89	0.72	0.36	0.13	0.12	0.89	-1.25	-0.25	0.76	1	3.29
Sep	5.76	1.05	0.67	0.41	0.14	0.13	1.05	-1.17	-0.33	0.70	1	3.16
Oct	4.96	1.24	0.61	0.47	0.15	0.14	1.26	-0.89	-0.61	0.52	1	2.81
Nov	4.59	1.48	0.56	0.52	0.16	0.15	1.50	-0.82	-0.68	0.48	1	2.52
Dec	3.52	1.53	0.53	0.54	0.17	0.16	1.56	-0.40	-1.11	0.28	1	1.99
Total Annual solar thermal energy available												34.9

Total Collector Area Required = $3.65 \times 10^{12}\,(J) / 3.49 \times 10^{09}\,(J/m^2)$= 1046 ($m^2$)

The number of collectors required is calculated by Equation 5;

$$Number\ of\ collectors\ needed\ = \frac{Total\ Collector\ Area\ required}{Area\ of\ single\ collector} \quad (5)$$

Number of collectors needed = (1046/4.619) = 226.4 collectors approx. **227** collectors.

After that, the estimated solar fraction which is defined as the percentage of the energy requirements that can be met by a solar energy system. It is calculated by f-Chart method. Table 6 shows the energy met by the solar system and solar fraction. The solar collector combi-system proposed is collector type Tubular – with model SEIDO5-16 AS/AB and tilt angle of 42° with horizontal surface. The working fluid used in this collector is anti-freezing with water solution. For cooling, the absorption cycle is used to cover the cooling load with COP 0.64. All the process of working fluid inside the system between the hot region and cold region are controlled by sophisticated computerized system [7].

Table 9: *Energy met by the solar collector and the value of solar fraction*

Month	Total Heating Energy demand (J/month) x10^{11}	second per month	$\frac{(\overline{\tau\alpha})}{(\overline{\tau\alpha})_n}$	X (-)	Y (-)	f (-)	f actual (-)	Energy met by collector (J) x10^{11}
Jan.	2.23	2678400	0.96	-3.686	1.145	1.154	1.00	2.23
Feb.	2.03	2419200	0.96	-3.618	1.418	1.286	1.00	2.03
Mar.	2.46	2678400	0.96	-3.200	1.310	1.202	1.00	2.46
Apr.	2.48	2592000	0.9	-2.941	1.187	1.119	1.00	2.48
May	3.43	2678400	0.9	-2.087	0.844	0.850	0.85	2.92
Jun.	3.87	2592000	0.9	-1.709	0.732	0.747	0.75	2.89
Jul.	4.14	2678400	0.9	-1.614	0.732	0.740	0.74	3.07
Aug.	4.16	2678400	0.9	-1.597	0.745	0.748	0.75	3.11
Sep.	3.91	2592000	0.9	-1.687	0.760	0.765	0.76	2.99
Oct.	3.01	2678400	0.96	-2.380	0.939	0.933	0.93	2.80
Nov.	2.45	2592000	0.96	-3.029	1.029	1.036	1.00	2.45
Dec.	2.22	2678400	0.96	-3.642	0.898	1.003	1.00	2.22
Total	36.5	Annual solar fraction					0.87	31.7

3.3 Photovoltaic System Design

The Photovoltaic system is used to cover the electrical power demand for the faculty building. Two cases are considered; On-Grid design and off-Grid design. Table 7 shows the specification of module used to produce the electric power (kWh) [8].

By using PVwatts program, the monthly power production output (kWh/month) can be estimated as shown in Table 8. It gives the monthly power production under the conditions; tilt angle 42°, the module face on south direction, and assuming 15% losses due to shadow, wiring and dust. It should be noted that the net total electric energy needed and sent to Grid is zero. In this sense, the electric design is net zero energy class.

ISBN: 978-81-936820-6-7
Proceedings DOI: 10.21467/proceedings.4

Series: AIJR Proceedings

Table 10: *Energy met by the PV system with* specifications of PV module used

Design PV System		
Efficiency of the inverter	0.9	AC to DC
Voltage DC system	49	volte
Peak Amp for module	7.86	
Peak sun hours	4	hr/day
Design module system	Mono-silicon module	
Type of Module	Grape Solar	Gs-S-385-TS
Power of module (W)	385	Watt
Area of a module m^2	2.56	m^2
Nominal voltage for module	49	Volte

Table 11: *Electric energy demand and PV power production On –Grid output data*

Month	Heating demand still not covered kWh	Electric device demand kWh	electric demand from PV system kWh	PV system Production kWh	Need from grid kWh	Send to grid kWh
Jan.	0.0	10,477.38	10,477.38	9,335	-1142.38	0
Feb.	0.0	9,463.44	9,463.44	9,385	-78.44	0
Mar.	0.0	10,477.38	10,477.38	11,716	0	1238.62
Apr.	0.0	9,225.6	9,225.6	11,985	0	2759.4
May	4,434.8	9,533.12	13,967.87	11,872	-2095.87	0
Jun.	5,415.7	9,225.6	14,641.29	11,894	-2747.29	0
Jul.	5,950.1	6,308.88	12,258.97	12,878	0	619.02
Aug.	5,789.0	6,308.88	12,097.87	13,284	0	1186.12
Sep.	5,071.5	6,105.37	11,176.84	11,968	0	791.15
Oct.	1,112.5	9,185.68	10,298.22	10,698	0	399.77
Nov.	0.0	8,889.37	8,889.37	8,922	0	32.628
Dec.	0.0	9,185.68	9,185.68	8,223	-962.68	0
Total			132,159.95	132,160.00	-7027	7027

In order to calculate the number of modules and total area meter square needed to cover the electric load, PVwatts program is used. The size of capacity for PV modules is (87.5 kW). Then, total number of PV modules can be calculated from Equations 6 and 7;

$$Size\ DC\ (KW) = Module\ Capacity \times No.of\ Modules \quad (6)$$

Thus, $No.of\ Modules = \frac{87.5 \times 1000}{385} = 227.27 = approx\ 228\ module$

$$The\ total\ area\ for\ PV\ modules\ =\ No.of\ modules\ x\ Area\ of\ module \quad (7)$$

$$= 228\ x\ 2.56 = 583.68\ m^2$$

Another method for design PV system called stand-alone system (off-grid system) in which the system is working without any auxiliary source or supply for electricity such as grid [9]. Stand–alone system use batteries to store a power replacing the grid, Table 9 show the specification of batteries. It should be noted that the total number of batteries used for the PV system in this study is 715 batteries with number of modules 426 covered $1091.61\ m^2$.

Table 12: *Specifications of the batteries for the stand-alone PV system*

PV system for Stand-alone system		Unit
Discharge limit	0.75	
Battery current Amp.hours	300	Ah/day
Battery Voltage	12	Volt
Efficiency of battery	0.8	
Anatomy days	3	Days

4 Conclusions

In this paper, the low and zero energy building design principles are applied to the faculty of engineering building at Garaboulli-Libya. Collected rain water and recycled grey water quantities are designed to be used for drinking, washing and toilet flushing or irrigation. The cooling, space heating and service hot water demand is determined. In addition, the total number and the area of the solar collectors are also evaluated. The electric demand for the building is also determined. Two design scenarios for covering electrical demands are adopted; Off-Grid and On-Grid. Total number of PV modules and total area are also calculated. Results show that the net zero energy design could be applicable for space heating, cooling and electricity demand. However, low energy design principle could be the case of rain water and grey water demand since the quantities are not sufficient to meet the required water demand.

Finally, the issue of insulation, walls material, shading and other architectural measures are not taken into considerations in this study.

References

[1] Housing and Infrastructure Board, "Guidance Document," Program Management Department, Tajura, Libya, 2008.

[2] A. M. Ramadan, "Design Methodology and Maintenance Strategy of a Solar Gradient Solar Pond Coupled with an Evaporation Pond," M.Sc thesis, Tripoli University, Tripoli, Libya, 1999.

[3] A. M. Shuraideh, "Water consumption Practices in Schools of Nablus directorate of Education," M.Sc theses, Nablus: An-najah National University, 2015.

[4] J. Zhang, "University of California Berkeley Water Usage and Conservation," Study Report, Chancellor's Advisory Committee on Sustainability, California, 2010.

[5] F-Chart Active and Passive Solar Systems Analysis, online in 2008 at https:// www.fchart.com/fchart/fchart.shtm

[6] I. F. Okafor and G. Akubue, "F-Chart Method for Designing Solar Thermal Water Heating Systems," International Journal of Scientific & Engineering Research, Volume 3, Issue 9, September 2012 , ISSN 2229-5518

[7] C. Webera, M. Bergerb, F. Mehlinga, A. Heinricha, T. Núñeza1, "Solar Cooling with Water–ammonia Absorption Chillers and Concentrating Solar Collector – Operational Experience," International Journal of Refrigeration ,Volume 39, Pages 57-76, March 2014

RET Screen International webpage, online in 2018 at http://www.retscreen.net

[8] Jin-Hee Kim , Ha-Ryeon Kim , and Jun-Tae Kim , "Analysis of Photovoltaic Applications in Zero Energy Building Cases of IEA SHC/EBC

[9] Task 40/Annex 52," Sustainability 2015, 7, 8782-8800; doi:10.3390/su7078782, 2015

Synthesis and Characterization of Magnetic $CoFe_{1.9}Cr_{0.1}O_4$ Nanoparticles by Sol-gel Method and Their Applications as an Adsorbent for Water Treatment

Ibrahim A. Amar*, Abubaker Sharif , Najat A. Omer, Naght E. Akale, Fatima Altohami[5] Mabroukah A. AbdulQadir

Department of Chemistry, Faculty of Sciences, Sebha University, Sebha/Libya

DOI: https://doi.org/10.21467/proceedings.4.43

* Corresponding author email: ibr.amar@sebhau.edu.ly

ABSTRACT

Water contamination by synthetic dyes is considered as a serious environmental issue, globally. In this study, the adsorptive removal of a very toxic cationic dye, methylene blue (MB), from aqueous solution was investigated using spinel ferrite, $CoFe_{1.9}Cr_{0.1}O_4$ (CFC), magnetic nanoparticles as an adsorbent. $CoFe_{1.9}Cr_{0.1}O_4$ powder was successfully synthesized via a sol-gel process and characterized by X-ray powder diffraction (XRD), Fourier transform infrared spectroscopy (FTIR) and scanning electron microscope (SEM) techniques. The effect of various experimental parameters on MB removal including; contact time, initial dye concentration, adsorbent dosage, solution pH and temperature were investigated. The results revealed that about 94 % of MB was removed under the optimal operational conditions. The adsorption kinetics showed that adsorption data were better described by pseudo-second-order model (PSO). In addition, the adsorption isotherms follow Langmuir isotherm model and the maximum monolayer adsorption capacity was found to be 11.41 mg/g. The calculated thermodynamic parameters (i.e., ΔG^o, ΔH^o, ΔS^o) indicate that the proposed adsorption process of methylene blue onto $CoFe_{1.9}Cr_{0.1}O_4$ nanoparticles is exothermic and spontaneous in nature. The results suggest that the synthesized magnetic nanoparticles (CFC) can be employed for the removal of toxic cationic synthetic dyes from wastewater.

Keywords: Spinel ferrites, adsorption, magnetic nanomaterials, methylene blue removal, nanotechnology, water purification.

1 Introduction

Water contamination by synthetic dyes has become a serious worldwide environmental issue owing to their adverse effect to human beings and aquatic life [1]. Dyes are important class of materials that have been widely used as coloring agents in many industries (e.g., paper, textile, cosmetics, etc.) [2]. Most of organic dyes which are discharged into the environment are toxic, mutagenic and carcinogenic in nature [3, 4]. Methylene blue (MB), a cationic dye, has found widespread use in textile industry [2]. The exposure to MB can cause a various type of health

 ISBN: 978-81-936820-6-7

problems including; vomiting, nausea, profuse sweating, increased heart rate, mental confusion, quadriplegia, jaundice and cyanosis, etc. [2, 5]. Thus removal of this very toxic dye before getting discharged into water body is of crucial importance.

Adsorption is among different techniques (e.g., coagulation-flocculation, oxidation, membrane filtration, ion-exchange, photocatalytic degradation and biological treatment) that have been developed with the aim of treating dye-contaminated water. Adsorption is preferred due to its remarkable advantages such as; availability of various adsorbent types, ease of operation, low cost, simplicity of design, high removal efficiency and insensitivity to toxic pollutants, etc. [5-8].

Recently, magnetic nanoparticles (MNPs) have attracted considerable attention as adsorbent materials for the devolvement of next generation water treatment technology [9, 10]. Nanotechnology offers a great potential not only in advancing the current water treatment technologies, but also in providing a secure and sustainable water supply approach [11]. Among MNPs adsorbents, spinel ferrites (MFe_2O_4, M = Co, Mg, Mn, Zn, etc.) are considered as promising adsorbent materials owing to their large specific surface area, fast kinetics, ease of functionalization, moderate saturation magnetization, ease of separation from water in the presence of external magnetic field, and thermal, chemical and mechanical stabilities, etc. [9, 10, 12]. Therefore, various spinel ferrites and their composites including; $MnFe_2O_4$ [13], $NiFe_2O_4$ [14], $Mn_{0.2}Zn_{0.8}Fe_2O_4$ [15], XFe_2O_4/GO (X = Co, Mn, Ni) [16] and AC/$Mn_{0.6}Zn_{0.4}Fe_2O_4$ [8] have been used as nano-adsorbents for MB removal from aqueous solutions. Recently, Reddy et al. [9] and Kefeni et al. [4] have reviewed the recent advances in the application of spinel ferrites nanoparticles (SFNPs) in the field of water purification. To the best of our knowledge, there is no report on using $CoFe_{1.9}Cr_{0.1}O_4$ (CFC) nanoparticles as adsorbent for the adsorptive removal of MB. Thus, the aim of the present work is to synthesise CFC nanoparticle and investigating its adsorption properties for MB removal from aqueous solutions.

2 Materials and Methods

2.1 Materials

Methylene blue dye (319.85 g/mol) was purchased from ScP (Surechem products). Cobalt nitrate ($Co(NO_3)_2{\cdot}6H_2O$) was purchased from Analyticals, Iron nitrate nonahydrate ($Fe(NO_3)_3{\cdot}9H_2O$) was purchased from Berck and Scientific Supplies. Chromium nitrate ($Cr(NO_2)_3.9H_2O$) was purchased from Farmitalia Carloerba-SPA. Citric acid ($C_6H_8O_7$) was purchased from Labkem. Ethylenediaminetetraacetic acid, EDTA, ($C_{10}H_{18}N_2O_8$) was purchased from Serva. Hydrochloric acid (HCl) was purchased from BDH Chemicals. Sodium hydroxide (NaCl) was purchased from Fluka. Amonia was purchased from Scharlau. All chemical were used as received without further purification.

ISBN: 978-81-936820-6-7

Series: AIJR Proceedings
Proceedings DOI: 10.21467/proceedings.4

2.2 Synthesis of $CoFe_{1.9}Cr_{0.1}O_4$ Nanoparticles

$CoFe_{1.9}Cr_{0.1}O_4$ (CFC) magnetic nanoparticles were synthesized using sol-gel method [17]. Briefly, $Co(NO_3)_2{\cdot}6H_2O$, $Fe(NO_3)_3{\cdot}9H_2O$ and $Cr(NO_2)_3.9H_2O$ were used as starting materials. Calculated amounts of these materials were dissolved in deionized water. Then, citric acid and EDTA were added to the mixed solution before adjusting its pH value to around 6 using ammonia solution. The mixed solution was evaporated to dryness and the resulted solid product was calcined in air at 600 °C for 3 h to obtain CFC powder.

2.3 Characterization of $CoFe_{1.9}Mo_{0.1}O_4$ Nanoparticles

XRD analysis was carried out using a Philips – PW 1800 diffractometer with CuKα radiation (λ=1.54186 Å). The sample was scanned over 2θ ranging from 1.4 to 79.4°, with a step size of 0.02°. Equations (1) and (2) were used to estimate the average particle size (D) and lattice parameters (a) of CFC nanoparticles [18].

$$D = \frac{0.9\,\lambda}{(\beta\cos\theta)} \tag{1}$$

$$d_{hkl} = \frac{\lambda}{2sin\theta} \quad ; \quad a = d_{hkl}\sqrt{h^2 + k^2 + l^2} \tag{2}$$

Where λ is the wavelength of the X-ray, θ is the Bragg angle, β is the full width at half maximum (FWHM) of the peak in radiance, d is the interplanar distance and hkl are the Miller indices.

Fourier transform infrared spectrum (FTIR) was collected in the region of 400 to 4000 cm-1, in KBr pellets, using a Bruker Tensor 27 spectrophotometer. The surface morphology of CFC nanoparticles was investigated by scanning electron microscopy (SEM) using a LEO 1430PV instrument. Typical "drift method" was used to determine the pH of CFC nanoparticles at the point of zero charge (pH_{PZC}) using NaCl solution (0.1 mol/L) [19]. Then, 25 mL of NaCl was transferred to a series flasks and the initial pH value (pH_i) was adjusted to 3, 5, 7, 9 and 11 by adding either a 0.1 mol/L solution of HCl or NaOH. To each flask, 0.1 g of CFC nanoparticles was added and the flasks were closed tightly. After a shaking of 24 h, the final pH value (pH_f) was measured. The pH_{PZC} was obtained from the plot of ΔpH (pH_i -pH_f) against the pH_i [20]. All experiments were carried out at room temperature (~ 25 °C), otherwise stated.

2.4 Adsorption Experiments

A stock solution of MB (500 mg/L) was prepared by dissolving the accurate amount of MB into deionized water. The desired concentration of MB was obtained by diluting the stock solution. The adsorption experiments were performed in batch mode by shaking the adsorbent (CFC) and 20 mL of MB solution in a closed 25 mL Erlenmeyer flask for a certain agitation

time at speed of 320 rpm using an orbital shaker (IKA-Werke). The MB adsorption into CFC surface was investigated under different experimental conditions including; contact time (0-120 min), initial dye concentration (25-55 mg/L), adsorbent dosage (0.01-0.20 g/20 mL), initial pH (3-11), and solution temperature (25-55 ºC). A diluted solution of either HCl or NaOH at a concentration of 0.1 mol/L was used to adjust the pH of dye solution using a pH meter (Jenway model 3505). A single beam UV-vis spectrophotometer (Jenway model 6305) was used to determine the MB concentration before and after adsorption experiments at λ_{ma} of 662 nm [2]. The percentage of MB removal (%*R*), the amount of MB adsorbed at any time t (q_t, mg/g) and the amount of MB adsorbed at equilibrium (q_e, mg/g), are calculated using the following equations [3, 21]:

$$\%R = \frac{C_o - C_t}{C_o} \times 100 \tag{3}$$

$$q_t = \frac{V(C_o - C_t)}{m} \tag{4}$$

$$q_e = \frac{V(C_o - C_e)}{m} \tag{5}$$

where C_o is the initial dye concentrations (mg/L), C_t and C_e are the final dye concentration (mg/L) at any time t and at equilibrium, respectively. m is the adsorbent dosage (g) and V is the volume of dye solution (L). To minimize the experimental errors, the adsorption experiments were performed in triplicate and the data were reported as the mean ± SD.

3 Theory and Calculation

3.1 Adsorption Kinetics

In this study, two common kinetic models including; pseudo-first-order (PFO) [22] and pseudo-second-order (PSO) [23] were applied for better understanding the adsorption process kinetics. For this purpose, the experimental data were fitted to the linear forms of PFO (Equation (6)) and PSO (Equation (7)), as expressed below [24];

$$\ln(q_e - q_t) = \ln q_e - k_1 t \tag{6}$$

$$\frac{t}{q_t} = \frac{1}{k_2 q_e^2} + \frac{1}{q_e} t \tag{7}$$

where q_e and q_t are as stated above, k_1 is PFO constant (min^{-1}) and k_2 is PSO (g/mg min). The values of q_e and k_1 were calculated from the intercept and slope of the plot of $\ln(q_e - q_t)$ versus t, respectively. The values of k_2 and q_e and were calculated from the intercept and the slop of plot of t/q_t versus t.

ISBN: 978-81-936820-6-7

Series: AIJR Proceedings
Proceedings DOI: 10.21467/proceedings.4

3.2 Adsorption Isotherms

To describe the nature of adsorbate-adsorbent interaction, the two most widely used isotherm models namely Langmuir [25] and Freundlich [26] were employed. Therefore, the experimental data at varying initial dye concentrations (25-55 mg/L) were fitted using these isotherm models. Langmuir and Freundlich isotherm models are suitable for describing the adsorption on homogenous and heterogeneous surfaces, respectively. The linearized forms of Langmuir and Freundlich isotherms can be expressed using Equations (8) and (9), respectively, as described below [24];

$$\frac{C_e}{q_e} = \frac{1}{q_{\max} K_L} + \frac{1}{q_{\max}} \tag{8}$$

$$\ln q_e = \ln K_F + \frac{1}{n} \ln C_e \tag{9}$$

where $q_{\max}$ is the maximum amount of MB adsorbed (mg/g), K_L and K_F are Langmuir (L/mg) and Freundlich ((mg/g)/(mg/L)^n) constants, respectively. n is Freundlich intensity parameter (dimensionless), which indicates the surface heterogeneity or the adsorption driving force. The adsorption isotherm is favourable $(n < 1)$, unfavourable $(n > 1)$, irreversible $(n = 0)$ and linear $(n = 1)$. The values of $q_{\max}$ and K_L, respectively, were calculated from the slope $(1/q_{\max})$ and the intercept $(1/q_{\max} K_L)$ of the linear plot of C_e against $C_e/q_{\max}$. The values of n and K_F, respectively, were calculated from the slope $(1/n)$ and the intercept $(\ln K_F)$ of the linear plot of $\ln C_e$ against $\ln q_e$. The feasibility of adsorption process can be evaluated using a dimensionless constant related to Langmuir isotherm called separation factor (R_L). The R_L value can be determined using the following equation [24].

$$R_L = \frac{1}{1 + K_L C_e} \tag{10}$$

The value of R_L suggests the type of the isotherm as follows; unfavourable $(R_L > 1)$, favourable $(0 < R_L < 1)$, irreversible $(R_L = 0)$ and linear $(R_L = 1)$.

3.3 Adsorption Thermodynamics

The thermodynamic parameters including Gibb's free energy change (ΔG^o), enthalpy change (ΔH^o) and entropy change (ΔS^o) were calculated using the following equations [24, 27];

$$\Delta G^o = \Delta H^o - T\Delta S^o \tag{11}$$

$$\ln K_c = \frac{-\Delta H^o}{R}\frac{1}{T} + \frac{\Delta S^o}{R} \tag{12}$$

$$K_c = \frac{C_s}{C_e} \tag{13}$$

where K_c is the distribution coefficient which calculated using Equation (13), C_s is the dye concentration on the adsorbent surface (mg/L), R is the gas constant (8.314 J/mol/K) and T is absolute temperature (K). The values of ΔH^o (kJ/mol) and ΔS^o (kJ/mol) were determined from the slope and the intercept of the plot of $\ln K_c$ versus $(1/T)$, respectively.

4 Results and Discussion

4.1 Characterization of $CoFe_{1.9}Cr_{0.1}O_4$ Adsorbent

Figure 1 shows the characteristic of $CoFe_{1.9}Cr_{0.1}O_4$ (CFC) magnetic nanoparticles. The XRD patterns of CFC calcined in air at 600 °C for 3 h are shown in Figure 1(a). The result indicates that a single phase of spinel ferrite (CFC) was obtained and all the diffraction peaks in XRD pattern are well indexed to the cubic structure of magnetite (JCPDS card No. 19-0629). The average crystallite size (*D*), lattice parameters (*a*) and the unit cell volume (a^3) of CFC adsorbent were found to be 38.63 nm, 8.3160 ± 0.0996 Å and 575.29 $(Å)^3$, respectively. The FTIR spectrum of CFC nanoparticles is presented in Figure 1(b). As shown, the typical characteristic peak for all spinel oxides which corresponds to metal-oxygen vibration (Fe-O) was observed at 586 cm^{-1}. The absorption peaks within the range of 874 to 1129 cm^{-1} are assigned to NO_3^- group that trapped during the synthesis of CFC nanoparticles. The observed peaks at approximately 1626 and 3402 cm^{-1} were attributed to O-H bending vibrations and O-H stretching vibrations, respectively [21, 28, 29]. Figure 1 (c) represents the SEM image of CFC magnetic nanoparticles which shows a heterogeneous structure with many pores. These pores are expected to enhance the adsorption properties of CFC nanoparticles. Figure 1(d) shows the pH at the point of zero charge (pH_{PZC}) of CFC nanoparticles. As can be seen, the pH_{PZC} value of CFC nanoparticles was equal to 6.33.

4.2 Adsorption Study

4.2.1 Effect of Contact Time

Figure 2 shows the effect of the contact time on the removal percentage (%R) of MB. In this experiment, 25 mg/L, 60 min and 0.01 g/20 mL were used as the initial MB concentration, contact time and adsorbent dosage, respectively. As can be seen, the %R increased significantly with increasing the contact time. In addition, a value of about 69.79% was attained when the contact time reached a 60 min after which no significant change in the %R was observed. This could be due to the saturation of the available active sites onto the adsorbent [30]. Thus, 60 min seems to be the optimum contact time.

ISBN: 978-81-936820-6-7
Proceedings DOI: 10.21467/proceedings.4

Series: AIJR Proceedings

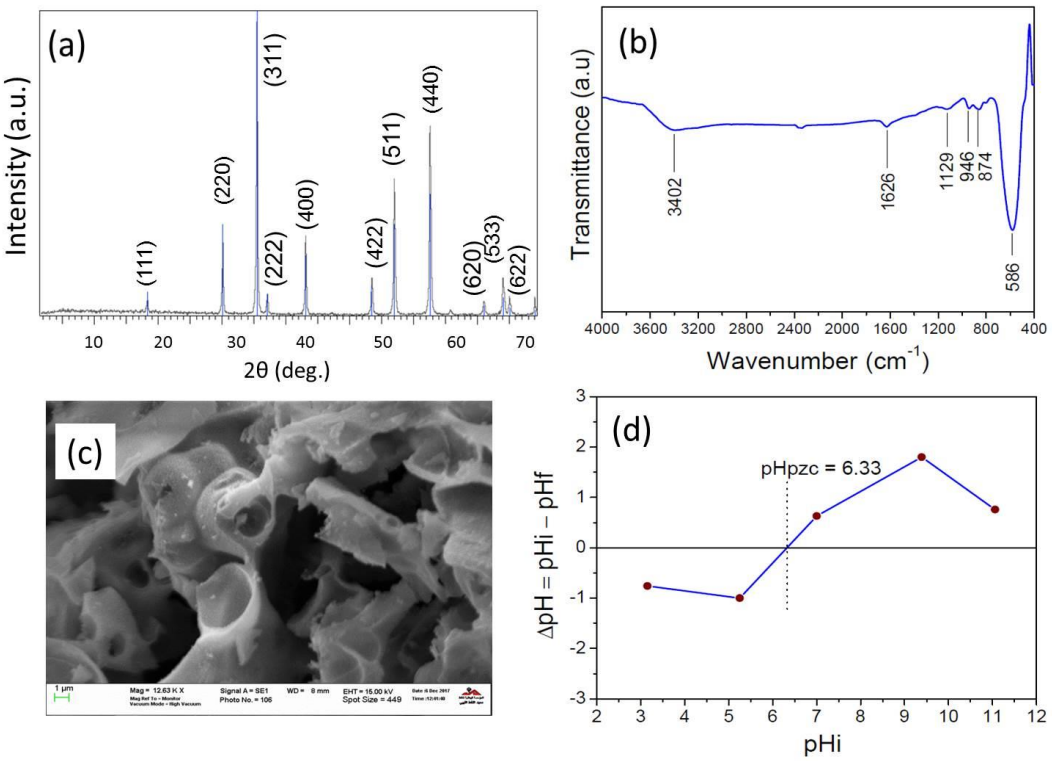

Figure 1: (a) XRD pattern, (b) FTIR spectrum, (C) SEM and (d) the point of zero charge of CFC magnetic nanoparticle

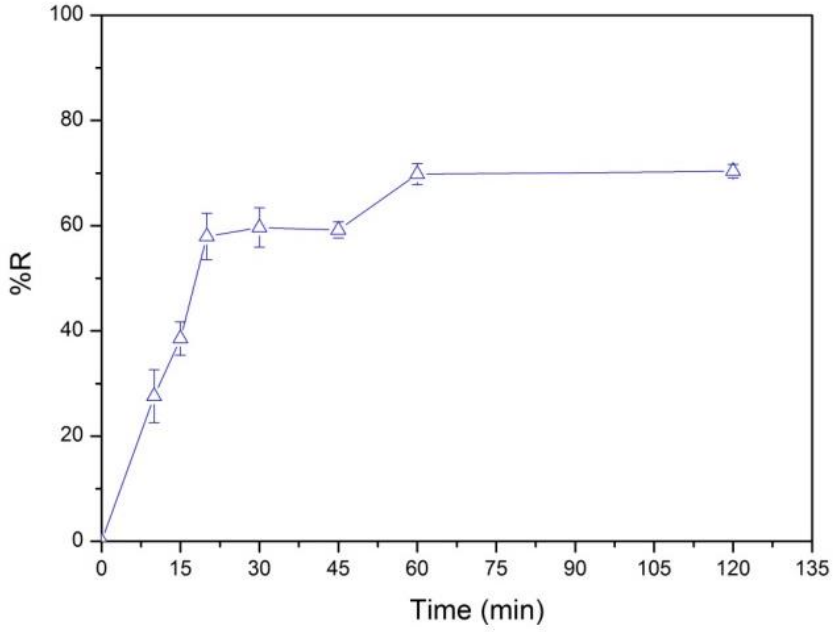

Figure 2: *Effect of the contact time on the percent removal of MB*

4.2.2 Effect of the initial dye concentration

The effect of MB dye concentration on the %R was investigated by varying the initial MB concentration from 25 to 55 mg/L and keeping the other operational condition at constant values (contact time of 60 min, adsorbent dosage of 0.01g/20 mL and room temperature. As shown from Figure 3, there is significant decrease in the %R value from 69.79% to 22.85% with increasing the MB concentration from 25 to 55 mg/L. This decrease in the percentage removal of MB could be due to the saturation the active adsorption sites of the adsorbent nanoparticles (CFC) after adsorbing a certain amount of MB dye molecules [31]. Therefore 25 mg/L was chosen as an optimum concentration for further studies.

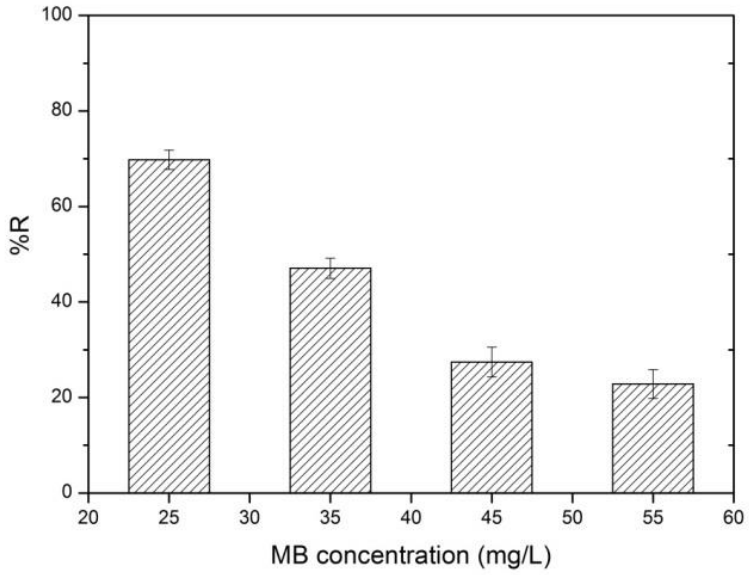

Figure 3: *Effect of the initial dye concentration on the MB removal percentage*

4.2.3 Effect of Adsorbent Dosage

The adsorption of MB (25 mg/L) using different adsorbent dosages (0.01-0.20 g/20 mL) is shown in Figure 4. The results reveal that the %R of MB increased from 45.92 to 69.97% by increasing the adsorbent dosage from 0.01 to 0.02 g/20 mL. This could be due to the increase in the number of active sites on the adsorbent surface [3]. However, no significant change in the %R was observed by future increasing the adsorbent dosage from 0.02 to 0.2 g/20 mL. Thus, 0.02 g/20 mL was chosen as the optimum adsorbent dosage. Figure 4 also shows that the amount of MB adsorbed at the equilibrium (q_e, mg/g) decreased significantly as the adsorbent dosage was increased 0.01 to 0.2 g/20 mL (22.96 to 1.83 mg/g). This may be due to the decrease in adsorbent total surface area as a result of aggregation or overlapping of the available active sites [2].

ISBN: 978-81-936820-6-7
Proceedings DOI: 10.21467/proceedings.4

Series: AIJR Proceedings

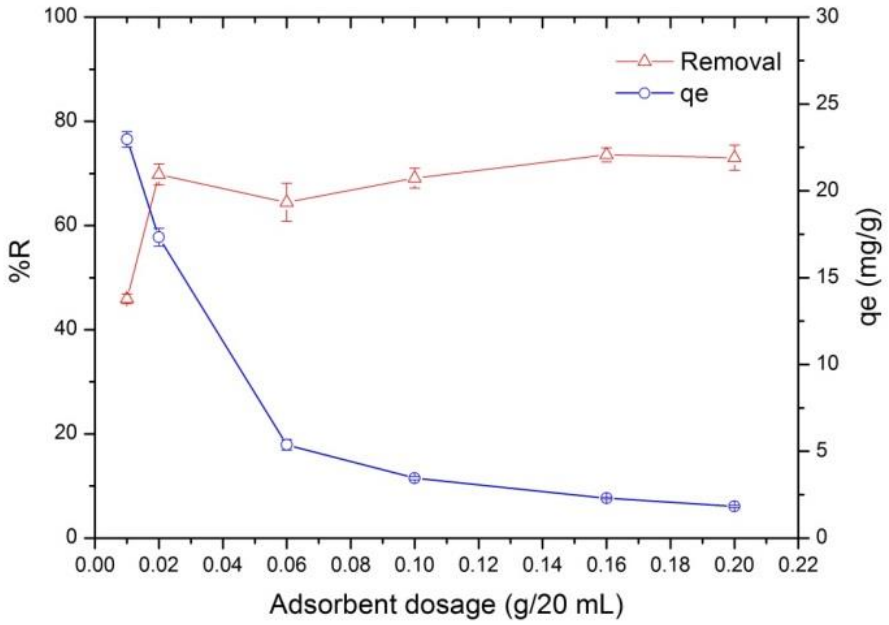

Figure 4: *Effect of the adsorbent dosage on the MB removal percentage and the amount of MB adsorbed at the equilibrium*

4.2.4 Effect of Solution pH

Figure 5 shows the effect of initial solution pH on the %R MB onto CFC nanoparticles. This effect was investigated by varying the initial pH of MB solution from 3 to 11 and keeping the other experimental condition at the optimized values. As shown, there is an increase in the %R value by increasing the solution pH from 3 to 5 (81.84 to 93.54%). However, the %R value decreased as the solution pH was further increased. Therefore, a pH value of 5 was chosen as the optimum value. As mention above, the pH_{PZC} of CFC was found to be 6.33, suggesting that its surface will be positively charged below the pH_{PZC} and negatively charged above the pH_{PZC} [9]. MB is a cationic dye and gives positively charged ions in the aqueous solutions [32]. This means that the %R value should be high above 6.33 as the surface of CFC is negatively charged. In addition, MB molecules that contain Cl^- and NaOH that used for adjusting the pH values will undergo to replacement reaction and resulting in NaCl formation. Hence, the decreased %R values at high pH values (> 5) might be due to in the increase in the solution ionic strength that resulted from NaCl formation [33].

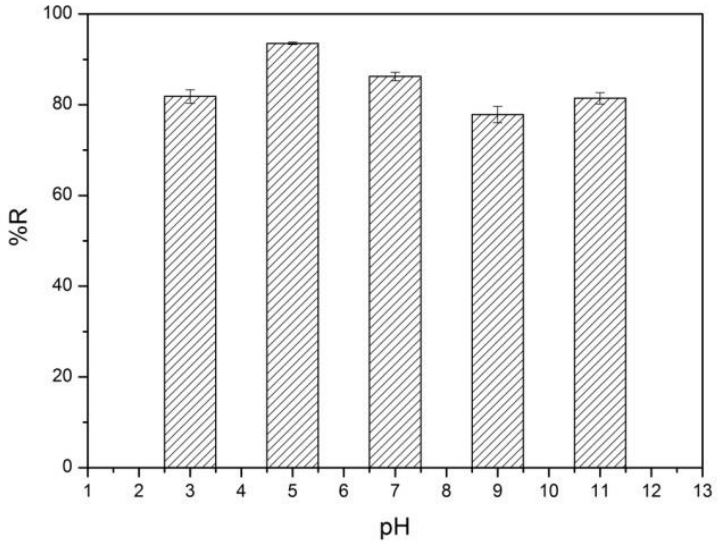

Figure 5: *Effect of initial pH on the MB removal percentage*

4.2.5 Effect of Solution Temperature

To investigate the effect of solution temperature on the %R of MB onto CFC nanoparticles, the experiment was carried out at different temperatures (25 to 55 °C) under the optimum operational conditions (contact time of 60 min, initial MB concentration of 25 mg/L and adsorbent dosage of 0.02 g/20 mL and pH value of 5). The results revealed that the %R decreased from 91.06 to 59.11% with increasing the solution temperature from 25 to 55 °C, as presented in Figure 6. This indicates that the proposed adsorption process is exothermic in nature. This decrease in the %R of MB with increasing solution temperature can be attributed the increase in the mobility of dye molecule. Consequently, less MB molecules were adsorbed onto CFC nanoparticles at high temperature [6].

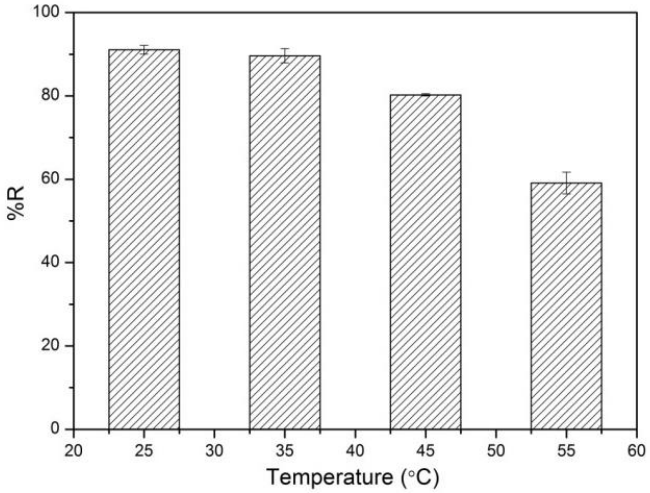

Figure 6: *Effect of solution temperature on the MB removal percentage*

ISBN: 978-81-936820-6-7
Proceedings DOI: 10.21467/proceedings.4

Series: AIJR Proceedings

4.3 Adsorption Kinetics

In the present study, pseudo-first-order (PFO) and pseudo-second-order (PSO) kinetic models were employed to evaluate the adsorption data using linear regression method. Table 1 lists the fitting parameters of these two models. As listed in the table, the calculated $q_{e,cal}$ value that obtained from PSO is close to the experimental $q_{e,exp}$ value, in contrast to the value obtained from PFO. In addition, the correlation coefficient (R^2) value of PSO was found to be 0.9759 which is higher than that of PFO (0.8208). This indicates that the pseudo-second-order model is more applicable for describing the adsorption kinetics of MB onto CFC nanoparticle.

Table 1: *Kinetic parameters for the adsorption of MB onto CFC nanoparticles*

$q_{e,exp}$ (mg/g)	Pseudo-first-order		
	$q_{e,cal}$ (mg/g)	k_1 (min^{-1})	R^2
17.73	20.63	7.01×10^{-2}	0.8208
	Pseudo-second-order		
	$q_{e,cal}$ (mg/g)	k_2 (g/mg.min)	R^2
	19.25	6.69×10^{-3}	0.9759

4.4 Adsorption Isotherms

Langmuir and Freundlich isotherm parameters such as $q_{\max}$, K_L, K_F, n and R^2 are listed in Table 2. According to the tabulated values, Langmuir isotherm model exhibits the highest correlation coefficient value $(R^2 = 0.9859)$. This means that the proposed adsorption process is better described by Langmuir isotherm. Furthermore, the maximum adsorbed amount of MB $(q_{\max})$ is found to be 11.41 mg/g. This value is higher than the value (3.31 mg/g) that reported by Patil et al. [34] for MB adsorption using an adsorbent composed of polyaniline-spinel ferrite (PANI-$NiFe_2O_4$) and lower than the value (40.97 mg/g) obtained using $Mn_{0.2}Zn_{0.8}Fe_2O_4$ as an adsorbent as reported by Hou et al. [15]. In addition, the calculated R_L values within the initial concentration range of 25-55 mg/L were less than unity (0.59-0.39), indicating the favourability of the adsorption of MB onto CFC nanoparticles [24].

Table 2: *Adsorption isotherm parameters for adsorption of MB onto CFC nanoparticles*

Langmuir isotherm		
$q_{\max}$ (mg/g)	K_L (L/mg)	R^2
11.41	0.109	0.9859
Freundlish isotherm		
K_F (mg/g)/(mg/L)^n	n	R^2
27.8	4.69	0.7455

4.5 Adsorption Thermodynamics

Table 3 summarizes the calculated thermodynamic parameters of MB adsorption on CFC nanoparticles. The negative values of ΔG^o at different solution temperatures (298-328 K) indicate the proposed adsorption process is feasible and spontaneous in nature. In addition, as the solution temperature increased, the negative ΔG^o values decreased, indicating that low temperature is favourable for MB adsorption. The negative ΔH^o value implies that MB adsorption is exothermic process in nature. Furthermore, the value of ΔS^o was negative, indicating the decreased randomness at the solid/liquid interface during the proposed process.

Table 3: *Thermodynamic parameters for adsorption of MB onto CFC nanoparticles*

ΔH^o (kJ/mol)	ΔS^o (J/mol.K)	ΔG^o (kJ/mol)			
		298 K	308 K	318 K	328 K
- 53.26	- 157.38	-6.36	-4.79	-3.21	-1.64

5 Conclusions

In summary, spinel ferrite, $CoFe_{1.9}Cr_{0.1}O_4$ (CFC), magnetic nanoparticles were successfully synthesized and employed as adsorbent for the removal of MB from aqueous solutions. The adsorption process was highly dependent on the operational conditions. More than 90% of MB was removed at the optimum conditions (i.e., contact time of 60 min, initial dye concentration of 25 mg/L, adsorbent dosage of 0.02 g/20 mL, initial solution pH of 5 and solution temperature of 25 °C. The kinetic study indicated the applicability of pseudo-second-order for describing the adsorption data. The isotherm study revealed that Langmuir isotherm better described the adsorption of MB onto CFC nanoparticles. The maximum adsorbed amount of MB was found to be 11.41 mg/g. The calculated thermodynamic parameters demonstrated that the proposed adsorption process was feasible, spontaneous and exothermic in nature. The results revealed that the prepared magnetic adsorbent (CFC) is a promising and can be employed for the removal of very toxic organic materials from wastewater.

6 Acknowledgment

The authors are thankful to the Department of Chemistry, Sebha University, Sebha, Libya for the financial support of this work. The authors also thank the Central Laboratory at Sebha University, Sebha Libya for providing the furnace for material calcination. The authors thank the Libyan Petroleum Institute, Tripoli, Libya for performing XRD and SEM analysis. The authors also thank Mr. Fathi Elsharif and Mr. Khaled Azzabi from the Nuclear Research Centre, Tajoura, Libya for performing FTIR analysis.

References

[1] C. Santhosh, V. Velmurugan, G. Jacob, S. K. Jeong, A. N. Grace and A. Bhatnagar "Role of nanomaterials in water treatment applications: A review," *Chemical Engineering Journal*, vol. 306, pp. 1116-1137, 2016.

[2] H. Singh, G. Chauhan, A. K. Jain and S. K. Sharma, "Adsorptive potential of agricultural wastes for removal of dyes from aqueous solutions," *Journal of Environmental Chemical Engineering*, vol. 5, pp. 122-135, 2017.

[3] F. Moeinpour, A. Alimoradi, and M. Kazemi, "Efficient removal of Eriochrome black-T from aqueous solution using $NiFe_2O_4$ magnetic nanoparticles," *Journal of Environmental Health Science and Engineering*, vol. 12, pp. 112, 2014.

[4] K. K. Kefeni, B. B. Mamba, and T. A. M. Msagati, "Application of spinel ferrite nanoparticles in water and wastewater treatment: A review," *Separation and Purification Technology*, vol. 188, pp. 399-422, 2017.

[5] M. Rafatullah, O. Sulaiman, R. Hashim and A. Ahmad, "Adsorption of methylene blue on low-cost adsorbents: A review," *Journal of Hazardous Materials*, vol. 177, no. 1-3, pp. 70-80, 2010.

[6] T. K. Mahto, A. R. Chowdhuri, and S. K. Sahu, "Polyaniline-functionalized magnetic nanoparticles for the removal of toxic dye from wastewater," *Journal of Applied Polymer Science*, vol. 131, pp. 40840, 2014.

[7] A. Ahmed, S. H. Mohd-Setapar, C. S. Chuon, A. Khatoon, W. A. Wani, R. Kumar and M. Rafatullah, "Recent advances in new generation dye removal technologies: noval search for approaches to repocess wastewater," *RSC Advances*, vol. 5, pp. 30801-30818, 2015.

[8] R. Wang, J. Yu, and Q. Hao, "Activated carbon/$Mn_{0.6}Zn_{0.4}Fe_2O_4$ composites: Facile synthesis, magnetic performance and their potential application for the removal of methylene blue from water," *Chemical Engineering Research and Design*, vol. 132, pp. 215-225, 2018.

[9] D. H. K. Reddy, and Y. S. Yun, "Spinel ferrite magnetic adsorbents: alternative future materials for water purification?," *Coordination Chemistry Reviews*, vol. 315, pp. 90-111, 2016.

[10] D. Mehta, S. Mazumdar, and S. K. Singh, "Magnetic adsorbents for the treatment of water/wastewater-A review," *Journal of Water Process Engineering*, vol. 7, pp. 244-265, 2015.

[11] Y. Zhang, B. Wu, H. Xu, H. Liu, Hui, M. Wang, Y. He and B. Pan, "Nanomaterials-enabled water and wastewater treatment," *NanoImpact*, vol. 3–4, pp. 22-39, 2016.

[12] J. Gomez-Pastora, E. Bringas, and I. Ortiz, "Recent progress and future challenges of high performance magnetic nano-adsorbent in environmental applications," *Chemical Engineering Journal*, vol. 256, pp. 187-204, 2014.

[13] X. Hou, J. Feng, Y. Ren, Z. Fan and M. Zhang, "Synthesis and adsorption properties of spongelike porous $MnFe_2O_4$," Colloids and Surfaces A: *Physicochemical and Engineering Aspects*, vol. 363, pp. 1-7, 2010.

[14] X. Hou, J. Feng, X. Liu, Y. Ren, Z. Fan, T. Wei, J. Meng and M. Zhang, "Synthesis of 3D porous ferromagnetic $NiFe_2O_4$ and using as novel adsorbent to treat wastewater," *Journal of colloid and interface science*, vol. 362, pp. 477-485, 2011.

[15] X. Hou, J. Feng, X. Liu, Y. Ren, Z. Fan and M. Zhang, "Magnetic and high rate adsorption properties of porous $Mn_{1-x}Zn_xFe_2O_4$ ($0 \leqslant x \leqslant 0.8$) adsorbents," *Journal of colloid and interface science*, vol. 353, pp. 524-529, 2011.

[16] L. G. Bach, T. V. Tran, T. D. Nguyen, T. V. Pham and S. T. Do, "Enhanced adsorption of methylene blue onto graphene oxide-doped XFe_2O_4 (X = Co, Mn, Ni) nanocomposites: kinetic, isothermal, thermodynamic and recyclability studies," *Research on Chemical Intermediates*, vol. 44, pp. 1661-1687, 2018.

[17] Y. Ling, J. Yu, B. Lin, X. Zhang, L. Zhao and X. Liu, "A cobalt-free $Sm_{0.5}Sr_{0.5}Fe_{0.8}Cu_{0.2}O_{3-\delta}$-$Ce_{0.8}Sm_{0.2}O_{2-\delta}$ composite cathode for proton-conducting solid oxide fuel cells," *Journal of Power Sources*, vol. 196, pp. 2631-2634, 2011.

[18] Y. P. Fu, S. H. Chen, and J. J. Huang, "Preparation and characterization of $Ce_{0.8}M_{0.2}O_{2-\delta}$ (M = Y, Gd, Sm, Nd, La) solid electrolyte materials for solid oxide fuel cells," *International Journal of Hydrogen Energy*, vol. 35, pp. 745-752, 2010.

[19] M. Kosmulski, Surface charging and points of zero charge: CRC press, 2009.

[20] H. N. Tran, Y. F. Wang, S. J. You and H. P. Chao, "Insights into the mechanism of cationic dye adsorption on activated charcoal: The importance of π–π interactions," *Process Safety and Environmental Protection*, vol. 107, pp. 168-180, 2017/04/01/, 2017.

[21] W. Konicki, D. Sibera, E. Mijowska, Z. Lendzion-Bieluń and U. Narkiewicz, "Equilibrium and kinetic studies on acid dye Acid Red 88 adsorption by magnetic $ZnFe_2O_4$ spinel ferrite nanoparticles," *Journal of colloid and interface science*, vol. 398, pp. 152-160, 2013.

[22] S. Lagergren, "About the Theory of so-called Adsorption of Soluble Substances," *Kungliga Sevenska Vetenskapasakademiens Handlingar*, vol. 24, pp. 1-39, 1898.

[23] Y. S. Ho, and G. McKay, "Pseudo-second order model for sorption processes," *Process Biochemistry*, vol. 34, pp. 451-465, 1999.

[24] H. N. Tran, S. J. You, A. Hosseini-Bandegharaei and H. P. Chao, "Mistakes and inconsistencies regarding adsorption of contaminants from aqueous solutions: A critical review," *Water Research*, vol. 120, pp. 88-116, 2017.

[25] I. Langmuir, "The constitution and fundamental properties of solids and liquids. Part I. Solids. ," *The Journal of the American Chemical Society*, vol. 38, pp. 2221-2295, 1916.

[26] H. M. F. Freundlich, "Over the adsorption in solution," *The Journal of Physical Chemistry*, vol. 57, pp. 385-470, 1906.

[27] L. R. Bonetto, F. Ferrarini, C. D. Marco, J. S. Crespo, R. Guégan and M. Giovanela, "Removal of methyl violet 2B dye from aqueous solution using a magnetic composite as an adsorbent," *Journal of Water Process Engineering*, vol. 6, pp. 11-20, 2015.

[28] M. Stoia, and C. Muntean, "Preparation, Characterization and Adsorption Properties of MFe_2O_4 (M = Ni, Co, Cu) Nanopowders," *Environmental Engineering and Managment Journal*, vol. 14, pp. 1247-1259, 2015.

[29] W. Wang, Z. Ding, M. Cai, H. Jian, Z. Zeng, F. Li and J. P. Liu, "Synthesis and high-efficiency methylene blue adsorption of magnetic PAA/$MnFe_2O_4$ nanocomposites," *Applied Surface Science*, vol. 346, pp. 348-353, 2015.

[30] K. Erol, K. Köse, D. A. Köse, U. Sızır, S. İ. Tosun and L. Uzun, "Adsorption of Victoria Blue R (VBR) dye on magnetic microparticles containing Fe (II)–Co (II) double salt," *Desalination and Water Treatment*, vol. 57, pp. 9307-9317, 2016.

[31] S. Chawla, H. Uppal, M. Yadav, N. Bahadur and N. Singh, "Zinc peroxide nanomaterial as an adsorbent for removal of Congo red dye from waste water," *Ecotoxicology and Environmental Safety*, vol. 135, pp. 68-74, 2017.

[32] M. F. Zayed, W. H. Eisa, and B. Anis, "Removal of methylene blue using Phoenix dactylifera/PVA composite; an eco-friendly adsorbent," *Desalination and Water Treatment*, vol. 57, pp. 18861-18867, 2016.

[33] Z. A. Al-Anber, M. A. Al-Anber, M. Matouq, O. Al-Ayed and N. M. Omari, "Defatted Jojoba for the removal of methylene blue from aqueous solution: Thermodynamic and kinetic studies," *Desalination*, vol. 276, pp. 169-174, 2011.

[34] M. R. Patil, and V. Shrivastava, "Adsorptive removal of methylene blue from aqueous solution by polyaniline-nickel ferrite nanocomposite: a kinetic approach," *Desalination and Water Treatment*, vol. 57, pp. 5879-5887, 2016.

ISBN: 978-81-936820-6-7

Series: AIJR Proceedings
Proceedings DOI: 10.21467/proceedings.4

To What Extent Do Preschool Classrooms Match With The Architectural Design Considerations? Al-Khums City Centre, Libya as Case Study

Mustafa Zarigan*, Lutfi Senan , Muftah Omeman

Department of Architecture and Planning Engineering, College of Engineering, Elmergib University, Libya

DOI: https://doi.org/10.21467/proceedings.4.44
* Corresponding author email: mazarigan@elmergib.edu.ly

ABSTRACT

In the recent few years, there has been a continued increase in the number of preschools in Libya in general and in AL-Khums city in particular. The classrooms are crucially important in terms of child development during preschool education. There is a lack of prior local studies that deal with the architectural design standards of preschools. Indeed, most preschools in Al-Khums city were not standard and appropriately designed for children as preschools. They are originally residential buildings with switched usage. The main aim of this research is to investigate to what extent the classrooms match with the principles and design standards that specific to the Libyan context in the field of preschools design. These principles and criteria for the design of preschools in Al-Khums city will help decision-makers, architects, educational institutions, teachers, supervisors to ensure quality education that provided to children in a perfect indoor environment. To achieve the aim of this research, three preschools in the city centre has been selected. The results let to the conclusion that all of the classrooms are not enough for indoor children's activities. Hence, it is obvious from this small-scale study that the preschools in Libya do not respond to the needs of preschoolers. Thereby, the successful architectural design of preschools is the process that meets all the functional and educational requirements. This is done by taking into account the architectural design principles for the classrooms during the design process.

Keywords: Preschools, Classrooms, Spaces, Architectural Design Principles and Considerations.

1 Introduction

In the recent years, the outcomes of the early education and its role in improving a child's future academic performance have been understood. However, the quality of classrooms spaces was ignored. We have a long understanding that, more than any other building type, early childhood educational facilities have a profound impact on their occupants[1]. The children are greatly influenced by the spaces and facilities of the preschools [1]. Hence, the

 ISBN: 978-81-936820-6-7

design of these facilities, cannot be understated as children in this country spend more than 1000 hours in preschool in two years.

Several developed countries including Canada, USA, UK, France, Belgium and Australia had detailed guidelines for architectural design principles and considerations in terms of preschool design. Nevertheless, Libya has few architectural design considerations that are insufficient to be a guide for architects. The main scope of this research is to study indoor spaces in general and their status in classrooms in particular which appears to be more complex and raises some interesting architectural questions of significance to this research. Outdoor spaces, activities and environmental aspects are beyond this study.

There are no official statistics showing the number of children aged five and six years, but some academic sources suggest that the number of children under the age of six is up to 7 per cent (470,000).

This research demonstrates how the design of the tangible indoor environment should evolve to respond to the developmental needs of preschool in terms of classrooms. Both literature and analysis on preschool environments have been used to inform architects of particular design implications used to create a physical space successful in fostering and enhancing positive child development and effective learning.

2 Definitions

Terminology varies from country to country. A preschool, also known as nursery school, pre-primary school and kindergarten. It is an early childhood program in which children combine learning with the play before they begin compulsory education at primary school [2]. The term preschool which used in this paper is to address the educational settings visited, which are preparatory classes starting two years before primary schools. In addition, class size in this paper mentions the number of children learning in one space at one time, and how many square meters get every child.

3 Development of Preschools in Libya

In Libya, the first preschool - in its current form – was existed in 1910 and followed the method of Madame *Montessori* because the children had Italian nationality. In 1921, there were 3 preschools in Tripoli with 386 children of both sexes as well as one preschool in Benghazi and another one in Derna city. Later, in 1939, the number of preschools reached 8. After independence (1953), despite poverty and illiteracy, the Ministry of Social Security has incorporated the preschool phase into the learning system. In 1963, for the first time was referred to preschool (age 4-6 years). The following table shows the expansion of public preschools and the increase in the number of their children from 1960 to 1970[3].

ISBN: 978-81-936820-6-7

Series: AIJR Proceedings
Proceedings DOI: 10.21467/proceedings.4

Table 1: *Development of preschools in Libya*[3]

No	Academic Year	Number of Preschools	Number of Children
1.	1960-1961	18	1830
2.	1961-1962	17	1717
3.	1962-1963	14	1414
4.	1963-1964	21	1404
5.	1964-1965	18	1697
6.	1965-1966	21	1760
7.	1966-1967	21	1623
8.	1967-1968	24	1623
9.	1968-1969	18	1418
10.	1969-1970	19	1261
11.	1980-1981	40	-
12.	1981-1982	45	-
13.	1982-1983	56	-
14.	2006-2007	341	22731
15.	2008-2009	320	49929

After the revolution (2011), the preschool stage became part of the educational system of the Libyan Ministry of Education. In view of the continuous encouragement and interest of the Ministry, the number of preschools increased significantly in various cities including Al-Khums city. As a result, in 2015 the number of children in preschools increased by 50%. For this reason, the ministry established a special management for preschools and its functions are to prepare plans, programs, organise the laws and regulations as well as develop standards, conditions, specifications for buildings and equipment for preschools, including:

1. Adherence to international standards in selecting the site in proportion to the child at this stage.
2. Adhering to international standards in the design of kindergartens buildings in conformity with international quality standards.
3. Compliance with international safety and security standards in kindergartens.
4. The beautiful and exciting entrance to the child and the beloved he has who loves him in the kindergarten.
5. Floors, columns and stairs are equipped so as to reduce the injury of the child in case of falling.
6. The existence of emergency exits in sufficient numbers and to be in children's sites, and easy to reach.
7. The presence of fire extinguishers.

Today, preschool education is lasting two years and is for children aged four and five in order to prepare them for primary school at age of six. At the age of 4 children called the first year of foundation and 5 years of age called the second year of foundation before they go into primary school. This stage is optional. It can be publicly which funded by the education ministry or privately operated. Although, pre-schools do not have specific curricula or educational programs, the present curriculum is similar to the first year of primary school. Early years education in Libya is provided half-time for children which lasts three hours from 8:00 am to 11 am in public preschools. Meanwhile, the private is diversity[3].

4 Study area

Al Khums (Khoms - Homs) is a city in north-western Libya. It is located on the Mediterranean coast about 120 Km east of Tripoli, the capital of the country. It has a population of around 220,000 people. Figure 1 shows the selected preschools in the study area.

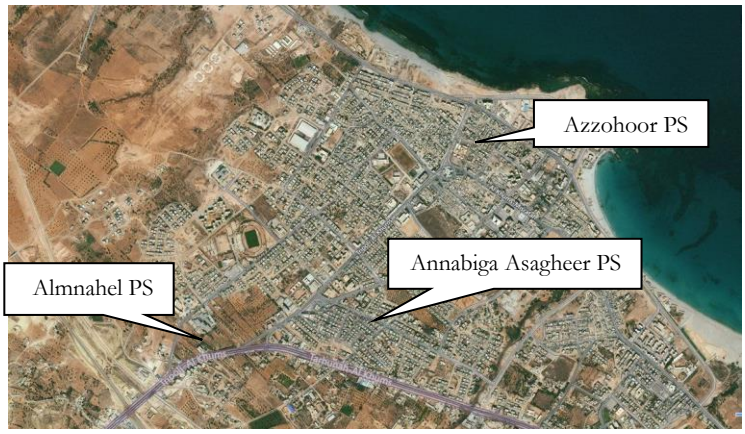

Figure 1: *Alkums City- Study area*

5 Results and Discussion

In preschool, classroom spaces are an important aspect of the learning environment for young children. The findings emphasize that not only the classrooms spaces but also the shape, furnishings and natural and artificial light and others.

5.1 Classrooms Spaces

Classrooms can vary in size and serve different functions, with children moving from one to another for different purposes. Instead of being single-purpose spaces, they can allow for a number of different activities, such as reading, research, group work and art. Olds (2001) stated that each child needs a space to place his/her own belongings which, in turn, give him a sense of ownership[4]. The classroom should well-equipped, with sufficient materials and toys. Planning considerations and design principles of preschools have been categorized and defined by the Libyan Urban Planning Department[5] as follows:

ISBN: 978-81-936820-6-7
Proceedings DOI: 10.21467/proceedings.4

Series: AIJR Proceedings

- One preschool for every 4000 inhabitants and 2 preschools per primary school
- The total area of the site is 25 - 30 square meters per child
- The size of the classroom is 15-20 children
- The walking distance from the residence to school by feet is no more than 500 m
- Some academic The roofed area is 2.5 - 3 square meters per child

Despite the fact that preschooler needs space where he/she can play with his/her peers, smaller and quiet areas are essential for his/her own solitary activity (ergonomic) [1]. In a similar vein, classroom space should be large enough to accommodate a desired number of preschoolers. Jaclynn Shaw stated that "children are exceedingly sensitive to space; they respond to many kinds: big and small spaces, open spaces, cozy spaces, and especially hidden private spaces"[6]. Thus, the zoning of activity areas is very important. Recently, moving towards a classroom flexible in its design is a current trend within the design of preschool facilities. Therefore, designating spaces for classroom work such as reading and writing should be implemented. Besides the functional demands of the classroom, the question for design should be how the children feel inside it and how they are going to experience the space.

5.2 Case Studies

Three preschools has been selected (Figure 1). Two of them are basically residential buildings and the third one is designed as preschool (only one in the study area). However, its design similar to a residential building because there are no architectural design considerations have been applied in its design as preeschool. The selected case studies are:

- Azzohoor Preschool (Public Preschool)
- Almnahel Preschool (Private Preschool)
- Annabega Assageer Preschool (Private Preschool)

Azzohoor Preschool (Public Preschool)

Figure 2: *A classroom in Azzohoor Preschool*

Table 2: *Main information about Azzohoor Preschool* [7]

No	No of Preschoolers	Classrooms Size (m)				No of Windows			Size m² / child
		Area m²	Length	width	height	units	Size≈m²	Direction	
1.	45	32	8	4	3	2	2	East - West	**0.71**
2.	44	32	8	4	3	2	2	West	**0.72**
3.	43	32	8	4	3	2	2	East - West	**0.74**
4.	45	32	8	4	3	2	2	East	**0.71**

5.2.1 Almnahel Preschool (Private Preschool)

Table 3: *Main information about Almnahel Preschool* [7]

No	No of Preschoolers	Classrooms Size (m)				No of Windows			Size m² / child
		Area m²	Length	width	height	units	Size≈m²	Direction	
1.	18	24	6	4	3	2	1.5	West	**1.33**
2.	18	18	4.5	4	3	4	1.6	East	**1.00**
3.	12	9	3	3	3	3	1.6	North	**0.75**

Annabega Assageer Preschool (Private Preschool)

Figure 3: *A classroom in Annabega Assageer*

ISBN: 978-81-936820-6-7
Proceedings DOI: 10.21467/proceedings.4

Series: AIJR Proceedings

Table 4: *Main information about Annabega Assageer Preschool* [7]

No	No of Preschoolers	Classrooms Size (m)				No of Windows			Size m² / child
		Area m²	Length	width	height	units	Size≈m²	Direction	
1.	10	12.25	3.5	3.5	3	1	0.80	North	**1.22**
2.	10	9	3	3	3	1	0.80	South	**1.11**
3.	18	12.25	3.5	3.5	3	1	0.80	North	**1.22**

The three preschools that were part of this research their classes are small and did not have appropriate facilities. In public preschool, for instance, space was inadequate because classrooms were overcrowded. Approximately 44 preschoolers were enrolled per classroom. The tables in three of them were arranged in lines. In addition, there are no any materials, toys, bookcases, art activities, blocks and manipulatives/fine motor. It was very poor and space generally lacked adequate lighting. Very limited attention was paid to safety issues. In the three cases, there are no bathrooms or kitchen were located near the class. Even water source not existed. In general, there is lack in numbers of toilets.

5.3 Shape and Furnishings

In Libya, classrooms designs are usually rectangular or square shape. For example, in one of the selected preschools, all its classrooms are rectangles 8 * 3 m (table 1) and some classes are only 3 * 3 m (as shown in tables 2 & 3 and figure number 3 & 4).

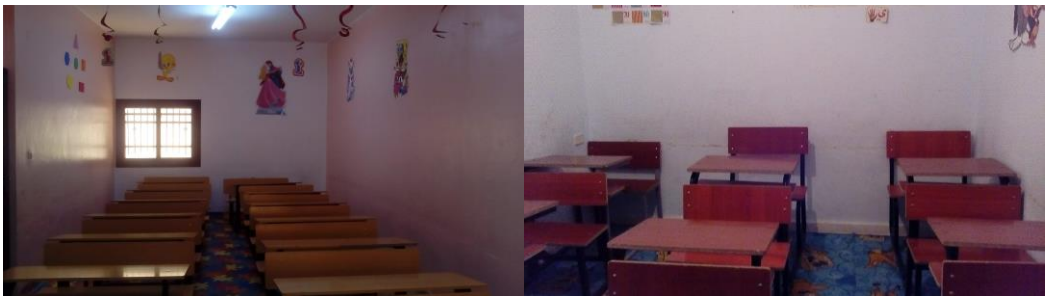

Figures 3 & 4: *classrooms are rectangular and square shape*

In terms of classroom furniture, the classroom style seating is often rectangular desks that are arranged in horizontal rows which, in fact, were used in the middle of the last century. Whereas, an open classroom was implemented during the 1970s in the developed countries. This classroom type still used today [3]. Rearranging furniture in preschool classrooms may encourage classroom activities. In addition, in three examples, often only one style of furniture is used for all children. Desks and chairs in two of three preschools are the same sizes as primary schools. Moreover, the furniture characteristics are heavyweight and oversized for

preschoolers. From previous tables, the size of the classrooms are not enough for carrying, lifting and turning desks.

5.4 Natural and artificial Light

There is no doubt that daylight and/or artificial light play a crucial role in the learning environment. The quality and quantity of light affect preschoolers' ability to see clearly, concentrate and learn effectively in the classroom. The light in all visited classrooms are very poor in both natural and artificial lighting (Figure5,6 & 7). In addition, windows orientations are not applicable to the standards, for instance, some classes windows are placing in the front and in the back of the classroom which could make glare. Furthermore, their number in each classroom are very few, for example, some classrooms have only one window and its area is only 0.70 m^2. Moreover, halogen and fluorescent bulbs (lamps) are only one or two in each classroom.

Figures 5, 6 & 7: *Natural and artificial lighting in different classrooms*

6 Conclusions

It is notable that most preschools in the study area are not standard and appropriately designed for children. They are mostly located in residential areas and apartment buildings that are painted to suit children. Recently, the Ministry of Education has focused on the educational progress of children in preschools. We hope that running the functional ideas of this study and considering the conditions, climate, and environment lead to a guideline for designing a standard preschool where children can learn, play, and grow up. This research can be generalized to other educational spaces such as elementary schools, training centres, and centres for Intellectual Development of Children and Adolescents. More studies in larger research fields are recommended for designing preschools environment, with a focus on indoor and outdoor elements, to improve children's learning.

References

[1] Day, D. E. (1983). Early childhood education: A human ecological approach (T.W. Hipple, Ed.). Glenview, Illinois: Scott, Foresman and Company

[2] B. E Şahin & N. Dostoğlu, "*Evaluation of Kindergarten Group Rooms in the Context of Size: Children and Teacher's Perspective in Turkey*. European Journal of Contemporary Education, 2014, Vol.(10), № 4

[3] Amer, F. O (2018). Education in Libya and some other countries: A comparative study Access online on 19 August 2018 at www.bing.com

[4] Olds, 2001, The Libyan Urban Planning Department

[5] Jaclynn, S, The Ministry of Education. Preschool management, Alkhums branch.

Solar Hydrogen Production System Simulation Using PSCAD

Matouk M. Elamari

Electronic department Engineering Academy Tajoura Libya

DOI: https://doi.org/10.21467/proceedings.4.45

* Corresponding author email: matoukelamari@yahoo.com

ABSTRACT

Hydrogen is a potential future energy storage medium to supplement a variety of renewable energy sources. It can be regarded as an environmentally-friendly fuel, especially when it is extracted from water using electricity obtained from solar panels or wind turbines. One of the challenges in producing hydrogen by using solar energy is to reduce the overall costs. It is therefore important that the system operates at maximum power. In this paper a PSCAD computer simulation based on a water-splitting, hydrogen-production system is presented. The hydrogen production system was powered by a photovoltaic (PV) array using a proton exchange membrane (PEM) electrolyser. Optimal matching between the PV system and the electrolyser is essential to maximise the transfer of electrical energy and the rate of hydrogen production. A DC/DC buck converter is used for power matching by shifting the PEM electrolyser I-V curve as closely as possible toward the maximum power the PV can deliver. The simulation shows that the hydrogen production of the PV-electrolyser system can be optimised by adjusting the converter duty cycle generated by PWM circuit.

Keywords – Renewable - photovoltaic- solar hydrogen- PEM electrolyser.

1 Introduction

In recent years, the central aim of world energy policy has been to develop renewable energy sources and share the energy they produce to reduce dependence on fossil fuels and to reduce the harmful emissions that result when they are burned. To fully take advantage of the environmental benefits of hydrogen, it must be produced from a renewable feedstock (renewable energy), but most of the hydrogen that is currently produced is derived from natural gas, which is a non-renewable fossil fuel.

Hydrogen produced from renewable energy sources offers the promise of a clean, sustainable energy carrier that can be produced from domestic energy resources around the globe. One method of hydrogen production using a renewable energy source is the electrolysis of water using renewable electricity, i.e., electricity generated from photovoltaic cells, wind turbines, hydroelectric turbines, or generators fuelled by biomass.

 ISBN: 978-81-936820-6-7

Several potential applications for electrolysis use solar- and wind-produced electricity. Solar PV cells and wind turbines convert solar energy and wind power, respectively, into electricity that can be used to produce hydrogen from water by electrolysis. Electrolysis using solar energy is a very attractive process to produce hydrogen .The exploitation of this important potential comes through the conversion of the solar energy to an energy vector that is versatile, storable, transportable and ecologically acceptable. Today, hydrogen seems to be the best candidate

2 Components of the solar hydrogen production system

Hydrogen production through water electrolysis using solar photovoltaic cells to provide the required electricity is highly feasible. Both water and solar energy are available in huge amounts, and hydrogen provides an ideal means for storing and transporting electricity from solar energy. The PV uses light to generate DC electrical energy. The PV cell consists of one or two layers of a semi-conducting material (p-n junctions), usually silicon. When light shines on the cell, an electric field is created across the layers, which causes electricity to flow. The greater the intensity of the light, the greater the more power the PV cell delivers. The electric current produced by the PV cell is passed through water in an electrolyser, and the water molecules separate into hydrogen and oxygen. The most common electrolyser uses a proton exchange membrane (PEM) as a catalyst in the electrolysis process. In comparison to electrolysers that use a liquid electrolyte that must be replenished frequently, the PEM electrolyser has the advantages of producing very pure hydrogen, and requiring much less maintenance. In addition, it has easily scalable cells, and it can operate at much higher current densities than other types of electrolysers (1-2 A/cm2), with conversion efficiencies ranging from 50-90%. As mentioned earlier, electrolysers are thought to be a potentially cost-effective way of producing hydrogen locally. Electrolysers are compact and can realistically be located at existing fuelling places. Also, they offer a way to produce hydrogen with electrical power generated from renewable sources. Currently, renewable sources, such as solar, wind, and hydropower, produce only electricity, but the electricity they generate can also be used to produce hydrogen fuel through the use of electrolysers.

Figure 1 shows a PV hydrogen production system, which usually consists of the following main components: a PV array to supply the DC power to the system and PEM electrolyser; and DC-DC converter that consists of a control unit for power matching between the PV material and the PEM electrolyser and for providing the delivery of maximum power by PV material to maximize the hydrogen production rate.

Studies have been conducted on connecting solar PVs directly to an electrolyser (shown by the dotted path), thereby avoiding the need for a DC-DC converter. However, in this case, PV modules are not optimized to supply the most power the PV modules can deliver.

ISBN: 978-81-936820-6-7

Series: AIJR Proceedings
Proceedings DOI: 10.21467/proceedings.4

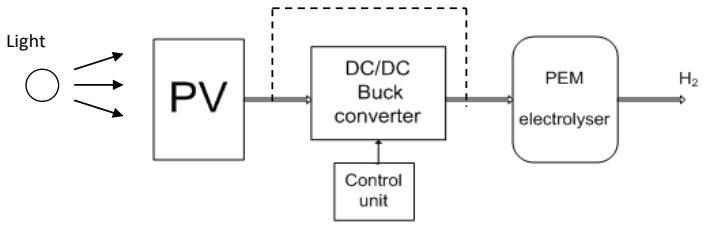

Figure 1: *Block diagram of a PV hydrogen production system*

One of the challenges in producing hydrogen by using solar energy (PV-Hydrogen system) is to reduce the cost. Therefore, it is important that the system operate at maximum power. This operation is usually achieved by matching the power generated by the PV cell with the power required to produce hydrogen.

3 PSCAD simulation

This part describes the use of PSCAD/EMTDC software to simulate the performance of a solar PV-PEM hydrogen production system.

System components:

Only the essential solar hydrogen production system components are included in this simulation programme. These components are the photovoltaic module, the DC-DC buck converter and the proton exchange membrane electrolyser.

The input data to the simulation programme are the solar irradiance hits the photovoltaic module, and the ambient temperature. The output results of the simulation are:

- Characteristics of the photovoltaic current, voltage, and power at standard test conditions ($1000\ W/m^2$ and $25\ ^oC$).
- Current and voltage readings at the input and output of the DC-DC buck converter
- Characteristics of the electrolyser's current and voltage
- Characteristics matching of the photovoltaic source and the electrolyser
- The operating current of the system
- Hydrogen production rate

4 PV Model

The PV solar cell was modelled in PSCAD/EMTDC, as shown in Figure 2 There are two inputs and two outputs in this block. The inputs are terminal voltage and irradiance. The

voltage varies from zero up to the open circuit voltage of the solar cell. The irradiance is assumed to be fixed at the standard test condition of 1000 W/m^2.

The two outputs are the current and power delivered by the solar cell. The maximum current is controlled by the irradiance. (More irradiance gives more current.) The power is the result of multiplying the voltage and the current.

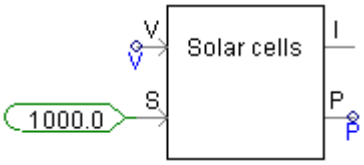

Figure 2: *Solar cell PSCAD block*

Table 1: *provides the parameters used in modelling a crystalline silicon solar cell [2] ,[7].*

Symbol/Value	Description	Unit
$q = \square 1.602 \times 10^{-19}$	Electron charge	C
$k = 1.38 \times 10^{-23}$	Boltzmann constant	J/□K
$n = 1.792$	Non-ideality factor	
$Ta = \square 293$	Ambient temperature	°K
$T_{ref} = \square 293$	Reference temperature	°K
$I\,sc = \square 2.0$	Short circuit current at reference state	A
$NOCT = \square 49$	Nominal Operating Cell Temperature	°C
$J\,o = 1.6 \times 10^{-3}$	Temperature coefficient	A/°K
$S = 1000$	Irradiance	W/m^2
$I_{do}\,do = \square 71.1 \times 10^{-9}$	Diode reversal current	A

Table 1 Parameters used in modelling a solar cell based on a crystalline Silicon solar cell

The following equations were implemented in FORTRAN codes inside the block model:

$$T = T_a + S\frac{(NOCT - 20)}{800} \quad (1)$$

$$E_g = 1.16 - 7.02 \times 10^{-4} T^2 (T + 1108) \quad (2)$$

$$I_0 = I_{do}\left(\frac{T}{T_{ref}}\right)^3 \exp\left(\frac{qE_g}{nK}\left(\frac{!}{T_{ref}} - \frac{1}{T}\right)\right) \quad (3)$$

$$I_{ph} = I_{sc}\frac{s}{1000} + J_o(T - T_{ref})\,.. \quad (4)$$

ISBN: 978-81-936820-6-7
Proceedings DOI: 10.21467/proceedings.4

Series: AIJR Proceedings

$$I_d = I_0 \exp(\frac{qV}{nkt} - 1)... \quad (5)$$

$$I = I_{ph} - I_d ... \quad (6)$$

Where:

T = cell temperature.

T_a = ambient temperature.

I_0 = dark saturation current.

E_g = energy gap of cell semiconductor.

Id = diode current.

I_{ph} = photo current or light generated current.

V = cell output voltage.

4.1 Response of the solar cell to changes in irradiance

The characteristics of the solar cell at different levels of irradiance are shown below in Figure 3. The irradiance has a large effect on short-circuit current (the horizontal part of the I–V curves), while the effect on open-circuit voltage (the vertical part of the curve) is rather weak.

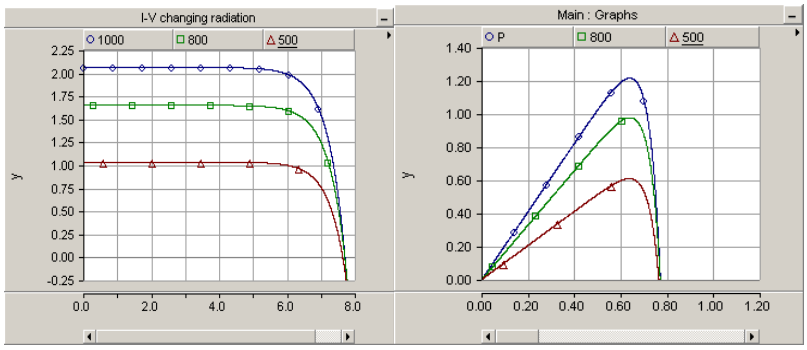

(a) *I-V characteristics* **(b)** *V-P characteristics*

Figure 3: *the effect of irradiance on current and power in the solar cell*

According to the voltage and power curves, the maximum output power of a photovoltaic cell changes with irradiance. When the irradiance is greater, the cell generates more power.

4.2 Response of the model PV solar cell to changes in temperature

As seen in Figure 4 as the cell temperature increases, the open circuit voltage decreases, whereas the short circuit current increases slightly. Increasing the temperature causes the voltage to decrease. This is a particularly severe problem, since the cell is often operated at the maximum power point, which is within the region.

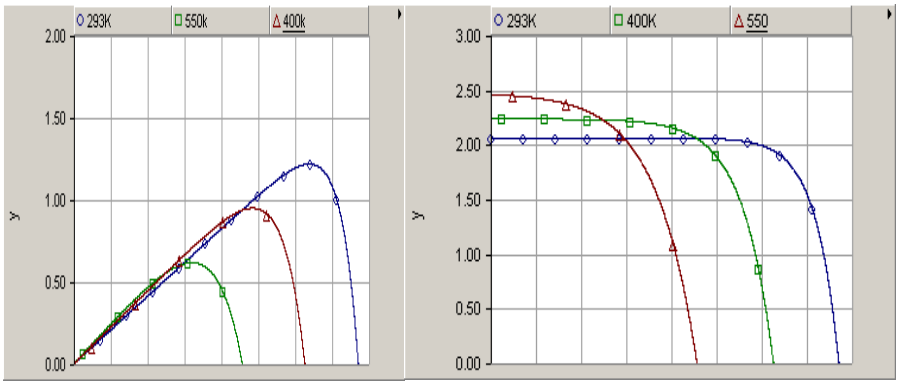

(a) *I-V characteristics* **(b)** *V-P characteristics*

Figure 4: *the effect of temperature on current and voltage*

The cell temperature varies because of changes in the ambient temperatures and because of changes in the levels of irradiance. Since only a small fraction of the irradiance on a cell is converted to electricity, most of that incident energy is absorbed and converted into heat.

From the simulation curve for the solar cell's I-V characteristics, we can see that the two values used to characterise the output of solar cells for a given irradiance level and operating temperature are:

1. Short circuit current, Isc, is the maximum current when the voltage is zero, i.e., the terminal points of the photovoltaic module are short circuited. The short circuit current is directly proportional to the available sunlight.
2. Open circuit voltage, Voc, is the maximum voltage when the current is zero, i.e., terminal points of the photovoltaic module are open circuited. The open circuit voltage increases logarithmically with increasing sunlight.

These two parameters are usually provided in the data sheets of PV modules. These parameters establish the operating point of the PV module along the I-V curve, i.e., the operating point moves along the I-V curve. It is desirable for the operating point to be at the point where maximum power from the PV module is generated. This is known as the maximum power

ISBN: 978-81-936820-6-7
Proceedings DOI: 10.21467/proceedings.4

point (MPP; $P_{mp} = V_{mp} \times I_{mp}$). V_{mp} and I_{mp} are the operating voltage and operating current at the maximum power point.

In practical applications, solar cells do not operate under standard conditions, because they are affected irradiance and temperature. Often, manufacturers provide plots that show the I-V curves shifting with irradiance and cell temperature changes.

4.3 Model of the PEM electrolyser

PEM water electrolysis is one of the most popular ways of producing pure hydrogen with compact equipment at a comparatively high level of efficiency. PEM is composed of a membrane, cathode, and anode, which produce hydrogen by providing pure water to one side of the polymer ion exchange film, which is placed between the anode and cathode.

The PEM cell is capable of high efficiency electrolysis under high current density conditions. The power consumption is proportional to the instantaneous current density, so the main consideration is the amount of current that can flow to the PEM cell from the DC-DC converter.

A unit PEM cell for water electrolysis was modelled by PSCAD/EMTDC block, as shown in Figure 5 the specifications for the cell are as follows:

- the operating temperature is 294 ^{o}K
- the effective area is 50 cm^2
- the maximum electrolyte current is 50 A
- the electrolyte voltage is 2 V

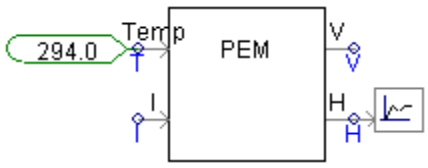

Figure 5: *PSCAD PEM electrolyser block*

The PEM model has two inputs and two outputs. The two inputs are current and temperature and the two outputs are voltage and the volume of hydrogen. The equations below govern the relationships between input and output variables.

The V-I relationship of a PEM cell is given by the following equations from [3],[4].

$$V = V_0 + \eta_c + \eta_a + IR, \tag{7}$$

where V is PEM cell voltage, V_0 is the theoretical dissociation voltage, which depends on absolute temperature T (ºK), as shown:

$$V_0 = 1.5 - 1.5e^{-3}T + 9.5e^{-5}T\ln(T) + 9.8e^{-8}T^2 \quad (8)$$

The term η^0 is an excess voltage on the cathode side, and its value varies from 0.05 to 1 V.

The term η^a is an excess voltage on the anode side, with a maximum value of 0.3 V.
R is the electrical resistance of PEM. In the simulation, the value of R is set to 0.037 ohm. The current (I) represents the current that flows through the PEM electrolyser.
Figure 6 shows the V-P characteristics of the PEM cell electrolyser model. The voltage-current graph shows that, for the PEM (Proton Exchange Membrane) electrolyser, the current only starts to flow at a certain voltage, after which it rises continuously. The slope of the curve is dependent on its equivalent ohmic resistance.
The applied voltage must be at least as large as the theoretical cell voltage in order for current to flow, which leads to a release of hydrogen at the cathode and oxygen at the anode.

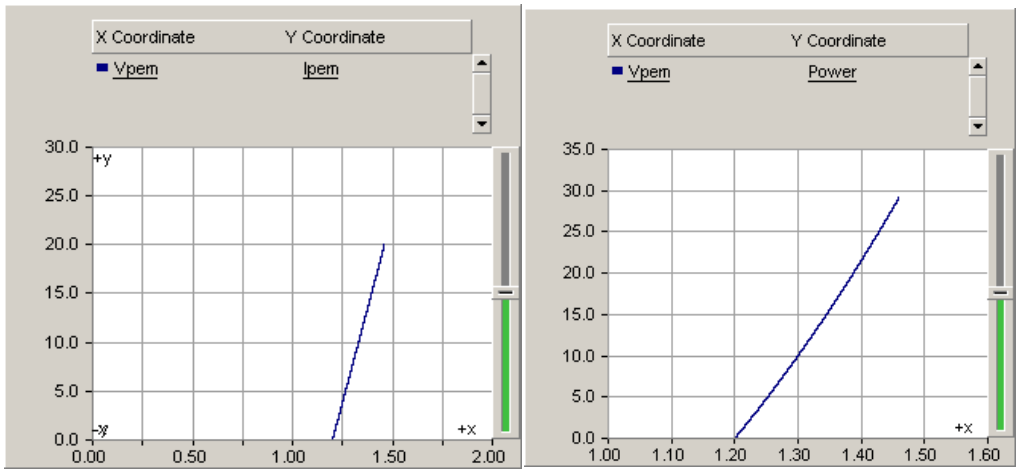

Figure 6: *I-V and V-P Curves for the PEM electrolyser PSCAD model*

5 PV–PEM electrolyser power matching using a DC-DC buck converter

The need for optimal power matching in the PV–PEM hydrogen production system is essential for maximum power transfer between the PV generator and the PEM electrolyser. The DC-DC buck converter is used for matching the power characteristics of both components.

ISBN: 978-81-936820-6-7
Proceedings DOI: 10.21467/proceedings.4

Figure 7 shows the PSCAD/EMTDC simulation for the PV-PEM hydrogen production system using a DC-DC buck converter. The PV generator generates the DC power at standard conditions (1000 W/m^2 and 25 ^{0}C).

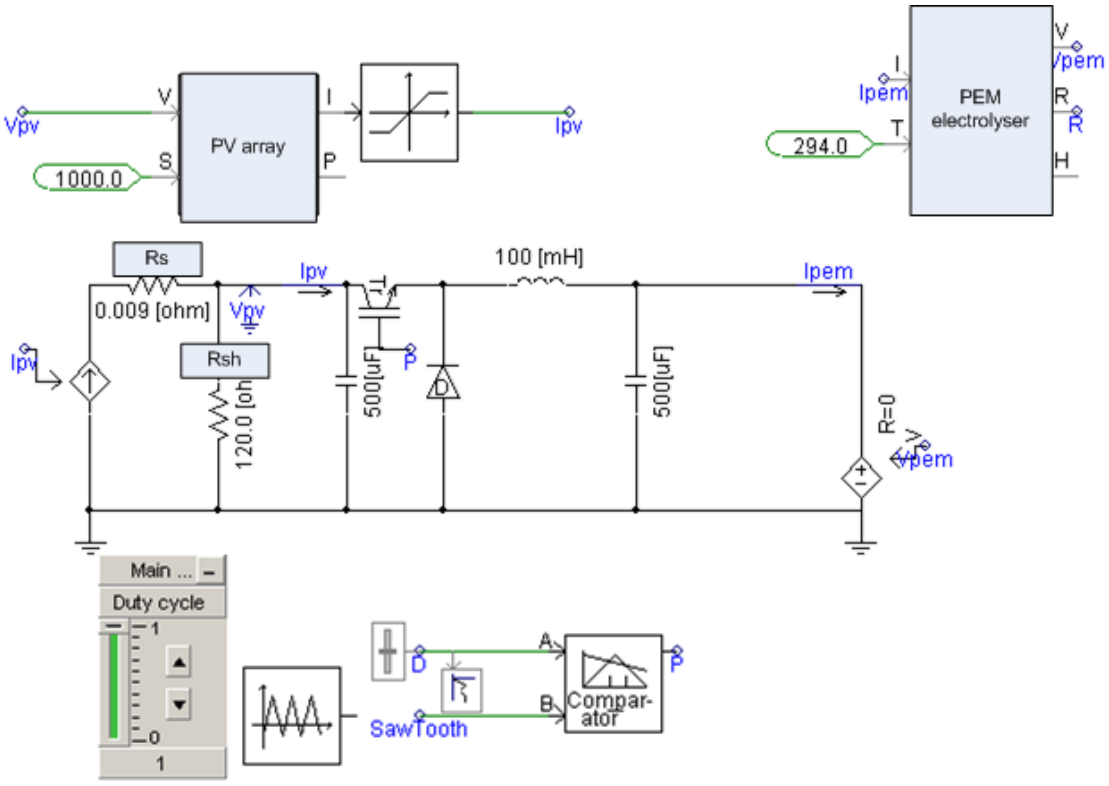

Figure 7: *PSCAD simulation of the PV-PEM electrolyser hydrogen production system using a buck converter*

The series resistance Rs and shunt resistance Rsh are calculated as follows:

$$Rs\langle\frac{0.01V_{oc}}{I_{sc}} \text{ and } Rsh\rangle\frac{100V_{oc}}{I_{sc}}$$

To generate different duty cycle values, a fixed-amplitude, saw tooth signal is compared with a changeable voltage level. A comparator produces pulses with different duty cycles. The pulses switch the buck converter switch on and off , and the durations of the on and off states control the relationships between the PV voltage Vpv and current Ipv and the PEM electrolyser voltage Vpem and current Ipem, as follows:

$$D = \frac{Ton}{Ton + Toff} = \frac{Vpem}{Vpv} = \frac{Ipv}{Ipem} \tag{9}$$

From equation (9), it is apparent that there is a different operating point for every duty cycle of the switch of the DC-DC converter.

The following PSCAD simulation results were obtained under standard irradiance (1000 W/m^2) and standard temperature (25 ^{0}C), and the measured values are volts for voltage readings and amperes for current values.

The power supply of the circuit is a PV module, and its characteristics are shown in Figure 8. The short-circuit current is 0.7 A, and the open-circuit voltage is 20 V; the operating voltage of the two-cell PEM electrolyser is approximately 5.8 V.

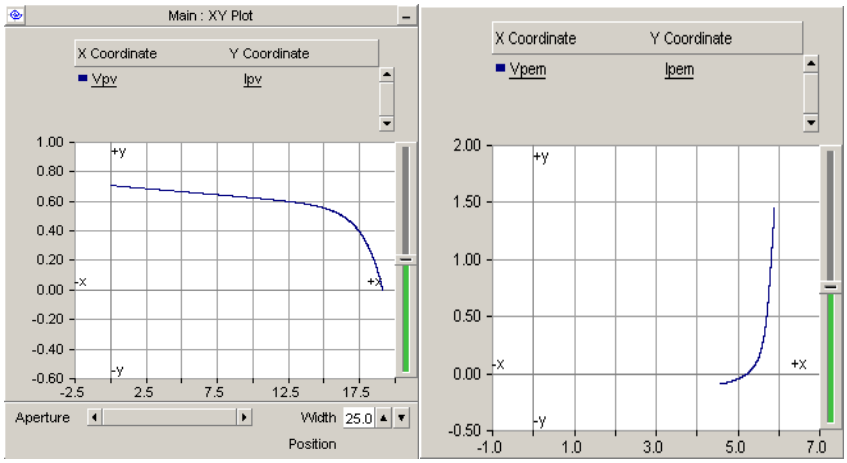

Figure 8: *I-V characteristics of (a) PSCAD model of the PV module and (b) PSCAD model of the PEM electrolyser*

Voltage, current, and power readings were taken at the terminals of the buck converter by varying the duty cycle value from 0.05 to 1 with scale of 0.5. As shown in Figure 9 , the operating voltage of the PEM electrolyser is considered to have an exponential shape with a maximum value of 5.8 V. The graphs show the power matching between the PV generator and the PEM electrolyser,

Voltage, current, and power readings were taken at the terminals of the buck converter by varying the duty cycle value from 0.05 to 1 with scale of 0.5. As shown in Figure , the operating voltage of the PEM electrolyser is considered to have an exponential shape with a maximum value of 5.8 V. The graphs show the power matching between the PV generator and the PEM electrolyser,

ISBN: 978-81-936820-6-7
Proceedings DOI: 10.21467/proceedings.4

Series: AIJR Proceedings

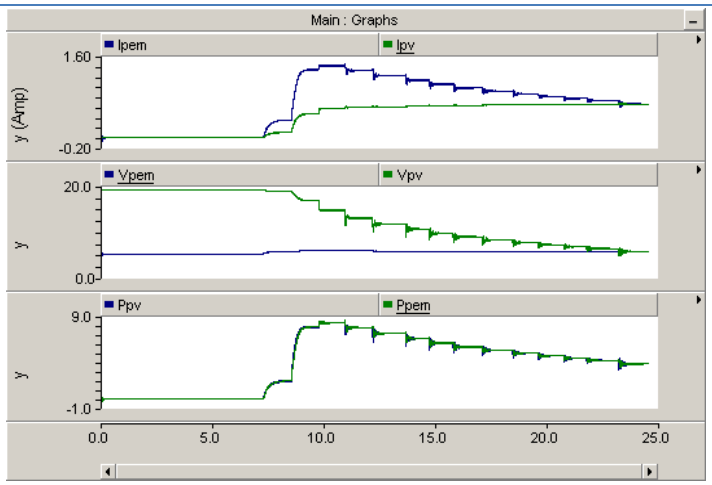

Figure 9: *PSCAD simulation results for the PV-PEM electrolyser*

where:

Ipem and Ipv are the PEM electrolyser and PV current values in (A), respectively

Vpem and Vpv are PEM electrolyser and PV voltage values in (V), respectively

Ppem and Ppv are yjhe PEM electrolyser and PV power in (W), respectively

From the previous results, it is apparent that the duty cycle governs the voltage and current on both sides of the buck converter, keeping the output voltage fixed at the PEM operating voltage. Current measurements at the power matching duty cycle (D = 4) show that the electrolyser current will be increased by about 2.5 times the PV operating current. This will increase the hydrogen production rate of the system while minimizing the solar PV area and decreasing the hydrogen production cost.

The power matching duty cycle D can be calculated, by using voltage and current values as follows:

$$dutycycleD = \frac{Vpem(V)}{Vpv(V)} = \frac{5.88}{14.71} = \frac{Ipv(A)}{Ipem(A)} = \frac{0.56}{1.40} = 0.4$$

The duty cycle needed to achieve maximum power point operation is equal to the ratio between the voltage of the PEM electrolyser and the PV array voltage at its maximum power point.

$$Dutycycle = \frac{V_{PEM}}{V_{mpp}}. \qquad (10)$$

The observation that the PV maximum power point voltage (Vmpp) has an almost linear relationship with the open-circuit voltage (Voc) of the solar photovoltaic module is apparent in the equation:

$$V_{mpp} = KV_{oc}.. \tag{11}$$

Where K is a constant that has different values for different solar panels, and V_{oc} is the open-circuit voltage. The open-circuit voltage (Voc) can be measured by disconnecting the PV at regular intervals.

AQ

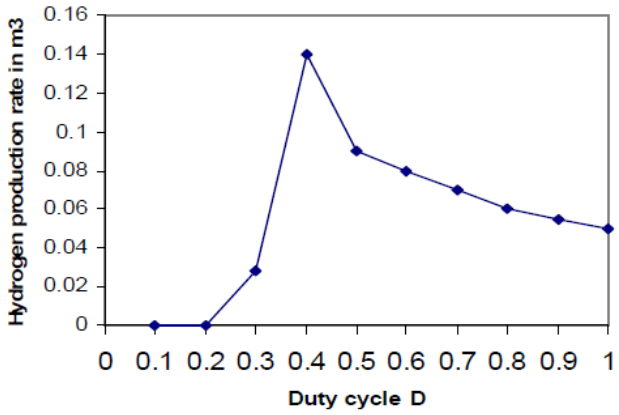

Figure 10: *Hydrogen production rate at different converter duty cycle*

The simulation shows that the hydrogen production of the PV-electrolyser system can be optimised by adjusting the converter duty cycle generated by PWM circuit. The strategy used was to fix the duty cycle at the ratio of the PV maximum power voltage to the electrolyser operating voltage.

6 Conclusion

A PSCAD software computer model was developed that was capable of exploring modelling for a photovoltaic-hydrogen production system with power matching using a DC/DC Buck converter. The evaluation took into account the different factors that affect the I-V characteristics of a PV array. The simulation proved that the operating voltage of the electrolyser and the PV voltage at maximum power were the key elements in power matching. The results show that the hydrogen production of the PV-electrolyser system can be optimised by adjusting the switch converter duty cycle generated by PWM circuit, the strategy used was to fix the duty cycle at the ratio of the PV maximum power voltage to the electrolyser operating voltage.

References

[1]. The International Energy Agency, World Energy Outlook 2007, http://www.iea.org/weo/2007.asp

[2]. B. S. Borowy, Z. M. Salameh; "Methodology for Optimally Sizing Combination of Battery Bank and PV Array

in a Wind/PV Hybrid System", IEEE Transactions on Energy Conversion 11(2), pp. 366 – 373, 1996

[3]. M. Park, D. Lee, and I. Yu; "PSCAD modelling and simulation of solar powered hydrogen production system", Renewable Energy 3, pp. 2342-2355, 2006.

[4]. R. Muhida, M. Park, and M. Dakkak; "A maximum power point tracking for photovoltaic-SPE systems using a maximum current controller", Solar Energy Materials and Solar Cells 75, pp. 697-706, 2003.

[5]. G. E. Ahmed, E.T. El Shenawy; "Optimal photovoltaic system for hydrogen production", Renewable Energy 31, 2006.

[6]. J. Bockr isHogbin; "The solar hydrogen alternative", Pool Pty Ltd., Redfern NSW Australia, 1976.

[7]. Abd El-Shafy A. Nafeh; "Hydrogen production from a PV/PEM electrolyser system using a neural-network-based MPPT algorithm", International Journal of numerical modelling, vol. 24, issue 3, pp. 282-297, Wiley, InterScience,2010.

[8]. K. Rajeshwar, R. McConnell, S. Licht, "Solar hydrogen generation: Toward a renewable energy future," ISBN 978-0-387-72809-4, Springer, 2008

[9]. T. L. Gibson, A. Nelson; "Predicting efficiency of solar powered hydrogen generation using photovoltaic-electrolysis", International Journal of Hydrogen Energy 35, pp. 900-911, 2010.

Performance Analysis of a Solar Driven Single Stage LiBr/H_2O Absorption Refrigeration system

Islam Kamel Shahboun[1], Salem Omran Adeilla[2]

[1]Department of Mechanical Engineering, College of Engineering, University of Gharyan, Libya
[2]Department of Mechanical Engineering, Higher Institute For Sciences and Technology, Libya

DOI: https://doi.org/10.21467/proceedings.4.46
* Corresponding author email: kamel20122011@gmail.com

ABSTRACT

The solar-assisted combined ejector was configured with the basic cycle of solar absorption refrigeration system to evaluate the performance of this cycle which using LiBr/H_2O as a working fluid and operating under steady-state conditions. In this paper, the improvement of the system is achieved by utilizing the potential kinetic energy of the ejector to enhance refrigeration efficiency. However, the first and the second law of thermodynamics are used to analyze the performance of a single-stage water-lithium bromide absorption refrigeration system (ARS), whereas some working parameters are varied. Moreover, a mathematical model based on the exergy method is introduced to evaluate the system performance, exergy loss of each component and total exergy loss of all the system components. As well as, Parameters connected with performance of the cycle–circulation ratio (CR), coefficient of performance (COP), exergetic efficiency are calculated from the thermodynamic properties of the working fluids at various operating conditions. In addition, Minimum generator temperature that required to operate the system was evaluated. The results showed that, the evaporator, condenser loads and post-addition of the ejector are found to be permanently higher than that in the basic cycle. As well as, The COP of the modified cycle is improved by up to 60 % compared with that in the basic cycle at the given condition.

Keywords: LiBr-H2O, COP, Exergy, Optimization, Generator temperature, Combined ejector absorption cycle.

1 Introduction

Absorption refrigeration systems (ARSs) have been gaining popularity because, firstly, they operate on environment friendly refrigerants. Secondly, they harness cheap alternative energy sources, such as geothermal, biomass, solar energy or a waste by product heat source. Therefore, in recent years, research has been devoted to the improvement of ARSs. The main way of improving efficiency is through thermodynamic analysis and optimization [1–4].

 ISBN: 978-81-936820-6-7

The basis of thermodynamics is stated in the first and second laws. The first law describes the conservation of energy, while the second law is used to describe the quality of energy and material. The first law optimization should result in maximizing the coefficient of performance (COP), thus providing maximum heat removal for minimum power input, while the second law optimization should result in maximizing the exergetic efficiency and minimizing entropy generation within the system, hence providing maximum cooling for the smallest destruction of available energy (exergy).

The exergy method, known as the second law analysis, calculates the exergy loss caused by irreversibility, which is an important thermodynamic property that measures the useful work that can be produced by a substance or the amount of work needed to complete a process [5]. The exergy analysis is a powerful tool for thermodynamic analysis of energy-conversion systems. The concept of exergy is extensively discussed in the literature by Kotas [6], Szargut et al. [7] and Bejan [8]. Aphornratana and Eames [9] reported that the heat operated absorption refrigeration systems are attracting increasing interest, as they can be driven by low-temperature heat sources and employ environment friendly working fluids. Furthermore, they estimated the specific entropy field for temperatures ranging from 10 to 200 1C and concentrations ranging from 20% to 70%. Furthermore, some of the papers include economic analysis [10,11].

Many researches are recently interested in applications of solar-assisted absorption cooling/refrigeration systems and the improvement of their corresponding performance as it saves energy and is environmentally friendly. Solar energy is available in most areas and regarded as a good source of thermal energy. For many solar absorption cooling systems, LiBr/ Water and Ammonia/Water is a major working fluid pair in the context of these systems. The absorption performance of a cooling system is critically dependent on the chemical and thermodynamic properties of the working fluid[3]. In solar applications, the LiBr–H_2O system is superior to the NH_3–H_2O system, due to its simpler design and operation and low cost. Moreover, it is functional under low generator temperature and perform better than that of NH_3–H_2O, due to its simpler design and operation and low cost. Moreover, it is functional under low generator temperature and perform better than that of NH_3–H_2O The LiBr/water system has been widely used for many years and their properties are well established. Many types of absorption cycles have been developed, however, the system's complexities increased over a conventional single- effect absorption system. The double-effect absorption systems using lithium bromide/water seem to be a high performance system, which is available commercially. The (single-effect) cooling system using LiBr/H_2O as its working fluid system can provide COP as high as a double-effect system at minimal increase of system complexity. Thus, research has focused on improving these absorption cooling systems by enhancing the coefficient of performance (COP) of these systems with respect to both heating and cooling applications [5,6]. Ventas et al. [7] numerically studied single-effect

absorption cycles and utilized ammonia-lithium nitrate solution as its working pair to determine the effect of mass flow rate recirculating through the absorber, as well as system performance. Numerous works also aim to optimize the operating parameters to enhance performance and minimize energy consumption in ARS

This work conceptualizes and analyse the single effect absorption refrigeration system combined with the ejector and an upgraded system that considerably lower the energy footprint. This paper aims to improve the system's performance by using the potential kinetic energy from the primary streamlines to drive the low pressure secondary streamlines to produce a quieter flow with more thrust and lower temperature. The proposed cycle will be evaluated via the entrainment ratio and the effect of the operation temperature on the thermal loads and the system's performance. A general description of the proposed system will be presented, and further analysis on its performance is conducted based on a corresponding mathematical model.

2 Description of Absorption Cycle

There are many types of absorption cycles, single and multiple effect absorption cycles, the most commonly one is a single effect absorption cycle.

2.1 Description of Solar Single effect Absorption Cycle:

The basic cycle consists of generator, absorber, a condenser, an evaporator, solution heat exchanger, circulating pumps, and a solar collector. The cycle works between two pressure levels: low pressure at the evaporator-absorber, and high pressure at condenser-generator. The emitted vapours in the generator consist of pure water, while LiBr sal remained in the solution.

2.2 Description of Modified Single Effect Combined Ejector Absorption Refrigeration system:

The main part of the single effect absorption cooling system is shown schematically in Figure. 1.a The solution heat exchanger is advantageous, because it cools down the solution coming from the generator, which then heats up the solution entering the generator . An ejector was added between the generator and the condenser. The primary high-pressure water vapour from the generator enters the ejector, then from the secondary inlet of the ejector, the entrainment low pressure water vapor from the evaporator is mixed with the primary flow at the mixing chamber, passing the diffuser, then entering the condenser. In this new design, the lithium bromide mixture leaves the absorber (state 1) in the form of a saturated solution at low pressure. It is pumped to the system at high pressure (state 3). The generator operates from a high temperature source to separate the binary solution of water and Lithium bromide (strong solution comes from absorber). This two-phase mixture is separated, and the weak liquid flows through SHE (state 4 to state 5) than throttled to the low pressure system and sprayed into the absorber (state 6). On the ejector, the secondary flow (water vapour from evaporator (state

ISBN: 978-81-936820-6-7

Series: AIJR Proceedings
Proceedings DOI: 10.21467/proceedings.4

10A)) and the primary flow of water vapour from the generator are mixed and passed to the condenser (state 7).

3 Simulation and Analysis of Proposed Cycle

For the purpose of simulation and analysis, the following assumptions are made:

- The system operates under a steady state condition.
- The refrigerant leaving the condenser and evaporator is saturated (state points 8 and 10).
- LiBr/H_2O solution in the generator, solution heat exchanger, and absorber are assumed to be in the equilibrium state at their respective pressure and temperature and assumed saturated state.
- The frictional pressure drop in the cycle is neglected except through the expansion device.
- The flow inside the ejector is steady and one-dimensional. The ejector walls are adiabatic.
- The primary flow and the secondary flow are saturated and their velocities are negligible before entering the ejector (states 7 and 10B in Figure. 1a respectively). The velocity of the mixed flow leaving the ejector (at state 7′) is also neglected.

In order to calculate the heat and mass balance for the proposed cycle, the thermodynamic properties (pressure, temperature, concentration, enthalpy and density) are necessary for the simulation. The binary mixture of LiBr/H_2O and pure H_2O are used in the proposed system. The detailed thermodynamic property equations of LiBr/H_2O are found by Engineering Equation Software.

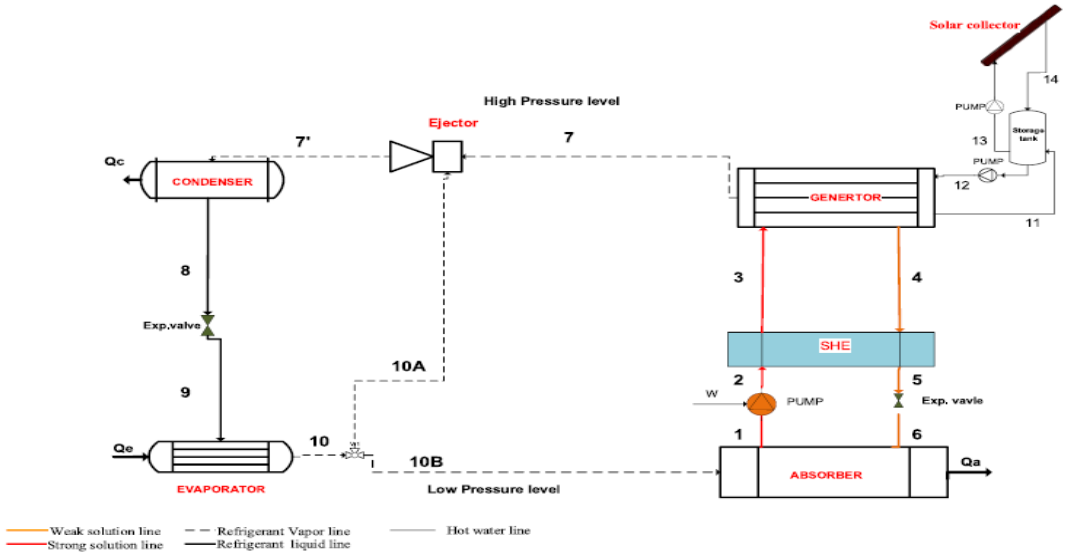

(a)

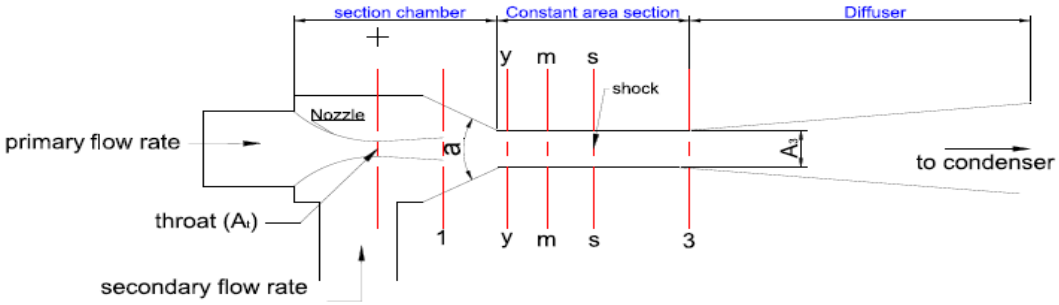

(b)

Figure 1: *(a)System schematic of single effect combined absorption–ejector cooling system, (b) schematic diagram of the ejector*

3.1 Thermodynamic Analysis

The thermodynamic analysis mainly aimed at assessing the thermodynamic imperfections and suggested possible ways of improving these imperfections. Here the system is analysed based on mass, energy and exergy balance. Each component of system can be assumed as control volume having inlet and outlet flow, work interactions and heat transfer. For analysing vapour absorption system circulation ratio is one of the most important parameter, it is defined as ratio of strong solution flow rate to refrigerant flow rate,

$$CR = \frac{\dot{m}_{ss}}{\dot{m}_r} = \frac{X_{SS}}{X_{SS} - X_{WS}} \quad (1)$$

The coefficient of performance (COP) is used to measure the system performance:

$$COP = \frac{Q_{eva}}{Q_{gen} + W_{pump}} \quad (2)$$

In order to use previous equation, mass and energy conservation should be determined at each component.

3.1.1 For the Generator – SHE – Absorber Loop:

The mass and energy balances around the generator

$$\dot{m}_3 = \dot{m}_4 + \dot{m}_7 \quad \rightarrow \quad \dot{m}_3 x_3 = \dot{m}_4 x_4 + \dot{m}_7 x_7 \quad (3)$$

$Where: \quad x_3 = x_1, \quad x_4 = x_6$

$$Q_{gen} = \dot{m}_4 h_4 + \dot{m}_7 h_7 - \dot{m}_3 h_3 \quad (4)$$

The fluid properties in this loop can be derived and developed as:
The liquid weak solution at state (4):
$T_4 = T_{gen} \quad , \quad P_4 = P_{gen}$
Exergy balance formulation for generator can be written as:

$$\Delta E_G = \dot{m}_{ws}(h_3 - T_0 s_3) + \dot{m}_{ss}(h_4 - T_0 s_4) - \dot{m}_r(h_7 - T_0 s_7) + \dot{m}_G(h_{11} - T_0 s_{11}) - \dot{m}_G(h_{12} - T_0 s_{12}) \quad (5)$$

ISBN: 978-81-936820-6-7
Proceedings DOI: 10.21467/proceedings.4

3.1.2 Heat Exchanger:

SHE performance is expressed in terms of effectiveness ϵ_{she}.
The solution and refrigerant heat exchanger performance, expressed in terms of an effectiveness ϵ_{she}

$$\epsilon_{she} = \frac{T_4 - T_5}{T_4 - T_2} \tag{6}$$

$$C_{hot} = \dot{m}_4 \left(\frac{h_4 - h_5}{T_4 - T_5} \right) \quad , \quad C_{cold} = \dot{m}_2 \left(\frac{h_3 - h_2}{T_3 - T_2} \right) \tag{7}$$

$$Q_{hx} = \dot{m}_2 (h_3 - h_2) \quad , \quad Q_{hx} = \dot{m}_4 (h_4 - h_5) \tag{8}$$

where,

$\dot{m}_1 = \dot{m}_2 = 0.05 \frac{kg}{s}$, $T_1 = T_{abs} = T_2$

Exergy balance formulation for solution heat exchanger can be written as:

$$\Delta E_{SHX} = \dot{m}_{ws}(h_2 - T_0 s_2) - \dot{m}_{ws}(h_3 - T_0 s_3) + \frac{Q_{SHX}}{T_b} \tag{9}$$

3.1.3 Solution Expansion Valve Model:

$h_5 = h_6$, $\dot{m}_5 = \dot{m}_6$, $x_5 = x_6$

Exergy balance formulation for expansion valve can be written as:

$$\Delta E_{REXP} = \dot{m}_{ss}(h_5 - T_0 s_5) - \dot{m}_{ss}(h_6 - T_0 s_6) \tag{10}$$

$$\Delta E_{SEXP} = \dot{m}_{ss}(h_8 - T_0 s_8) - \dot{m}_{ss}(h_9 - T_0 s_9) \tag{11}$$

3.1.4 Pump Calculation:

$$h_2 = h_1 + \frac{W_{pump}}{\dot{m}_1} \tag{12}$$

$$W_{pump} = \dot{m}_5 v_1 \frac{P_{hight} - P_{low}}{1000} \tag{13}$$

Exergy balance formulation for pump can be written as:

$$\Delta E_{pump} = \dot{m}_{ws}(h_1 - T_0 s_1) - \dot{m}_{ws}(h_2 - T_0 s_2) + \dot{W}_P \tag{14}$$

3.1.5 Absorber:

$$Q_{abs} = \dot{m}_{10} h_{10} + \dot{m}_6 h_6 - \dot{m}_1 h_1 \tag{15}$$

Exergy balance formulation for absorber can be written as:

$$\Delta E_{abs} = \dot{m}_r(h_{10} - T_0 s_{10}) + \dot{m}_{ss}(h_6 - T_0 s_6) - \dot{m}_{ws}(h_1 - T_0 s_1) + \frac{Q_{abs}}{T_b} \quad (16)$$

3.1.6 Condenser:

$$Q_{cond} = \dot{m}_7(h_7 - h_8) \quad (17)$$

Exergy balance formulation for condenser can be written as:

$$\Delta E_{cond} = \dot{m}_r(h_7 - T_0 s_7) - \dot{m}_r(h_8 - T_0 s_8) + \frac{Q_{cond}}{T_b} \quad (18)$$

3.1.7 Refrigerant Valve:

$$h_8 = h_9 \quad , \quad x_8 = x_9$$

3.1.8 Evaporator:

$$Q_{eva} = \dot{m}_9(h_{10} - h_9) \quad (19)$$

Exergy balance formulation for evaporator can be written as:

$$\Delta E_{eva} = \dot{m}_r(h_9 - T_0 s_9) - \dot{m}_r(h_{10} - T_0 s_{10}) + \frac{Q_{eva}}{T_b} \quad (20)$$

The total rate of exergy destruction of absorption system is the sum of exergy destruction in each component and can be written as:

$$\Delta E_{Sys} = \Delta E_G + \Delta E_{abs} + \Delta E_{eva} + \Delta E_{cond} + \Delta E_{SHX} + \Delta E_{REXP} + \Delta E_{SEXP} + \Delta E_P \quad (21)$$

3.2 Nozzle Equations

For a given pressure $P_{gen} = P_7$, tempertature $T_{gen} = T_7$and $\dot{m}_p = \dot{m}_7$ the nozzle throat area required for choking condition follows the gas dynamic equation:

$$A_t = \frac{\dot{m}_p\sqrt{T_{gen}}}{P_{gen}\sqrt{\eta_P}\sqrt{\frac{k}{R}\left[\frac{2}{K+1}\right]^{\frac{K+1}{K-1}}}} \quad (22)$$

where η_p is a coefficient relating to the isentropic efficiency of the compressible flow in the nozzle. The relations between the Mach number at the exit of nozzle Mp1 and the exit cross section area AP1 and pressure Pp1 are, using isentropic relations as showing in the following equations:

$$\frac{A_{p1}}{A_t} = \frac{1}{M_{p1}}\left[\frac{2}{k+1}\left(1 + \frac{k-1}{2}M_{p1^2}\right)\right]^{\frac{K+1}{K-1}} \quad (23)$$

ISBN: 978-81-936820-6-7
Proceedings DOI: 10.21467/proceedings.4

Series: AIJR Proceedings

4 Results and Discussions

Table 1 shows that the highest heat load occurs in the generator (approximately 13kW) and the heat transfer rate of the refrigerant heat exchanger is lower than that of the solution heat exchanger due to mass flow rate and temperature difference between the fluids.

Table 1 : Heat transfer rates of components and performance parameters of the system

Components	Heat transfer rates (KW)
Generator	12.985
Condenser	10.483
Evaporator	10.000
Absorber	12.502
Pump	0.00012
Solution heat exchanger	2.254
Refrigerant heat exchanger	0.165

Table 2 shows the simulation results of the second law analysis of the ARS. The generator has the highest exergy loss rate (approximately 2 kW), and the next largest exergy loss rate occurred in the absorber (approximately 1.5kW). Since exergy loss rates in the pump and expansion valves are very small, their effects on the total exergy loss rate are inconsiderable. The exergy losses of the generator and absorber are important fractions of the total exergy loss in the system.

Table 2 : Exergy loss rates of the components

Component	Exergy loss rate (KW)
Generator	2.002
Condenser	0.048
Evaporator	0.685
Absorber	1.533
Pump	0.00015
Solution expansion valve	-----
Refrigerant expansion valve	0.013
Solution heat exchanger	0.093
Refrigerant heat exchanger	0.008
Total	4.383

4.1 Comparison Between the Basic and the Modified Cycle:

Figure. 2(a–d) depicts the COP of basic cycle and the modified absorption cycle under various operating temperatures. Comparison of COP values vs. generator temperature for (basic and modified cycles) are shown in Figure. 2(a). It is noticed that for the two absorption cycle, there is an optimum value of COP. This value of COP increases with generator temperature until it reaches the optimum value. This value depends on the type of the cycle. Moreover, there is a low generator temperature limit, where the cycle cannot operate at a generator lower than this. This is an important point for the utilization solar energy, since the fluid temperature for solar collector are generally below 100 °C. Therefore, the simulation exhibited in this figure reveals that modified cycle has a higher COP value than the basic cycle. The effect of evaporator

temperature on the COP of the cycles is shown in Figure. 2(b). It is evident that the COP value of two cycles increases as the evaporation temperature increases, as shown in Figure. 2(b). It also can be seen that the highest value of the COP is obtained from the modified cycle. Figure. 2(c and d). illustrate the comparison of COP value vs. condenser and absorber temperature for two cycles. Increase condenser and absorber temperature causes a decrease in COP for each cycle. For modified cycle operation under choked conditions, the cycle is independent of condenser pressure when the condenser pressure is less than a certain critical value; however, the cycle falls to similar values to the basic cycle when the condenser pressure is greater than this critical value, as shown in Figure. 2(c). It is observed that the absorber temperature of 44 °C and above the performance of the system tend to lean towards zero. This is due to the fact that the concentration of the liquid leaving the absorber has dropped to the same concentration as the liquid coming back from the generator. From this figure, it could be determined that the COP of the modified cycle is higher than that of the conventional cycles at all simulated working conditions. This is due to the fact that the performance of a refrigeration system is influenced by adding an ejector to the basic cycle.

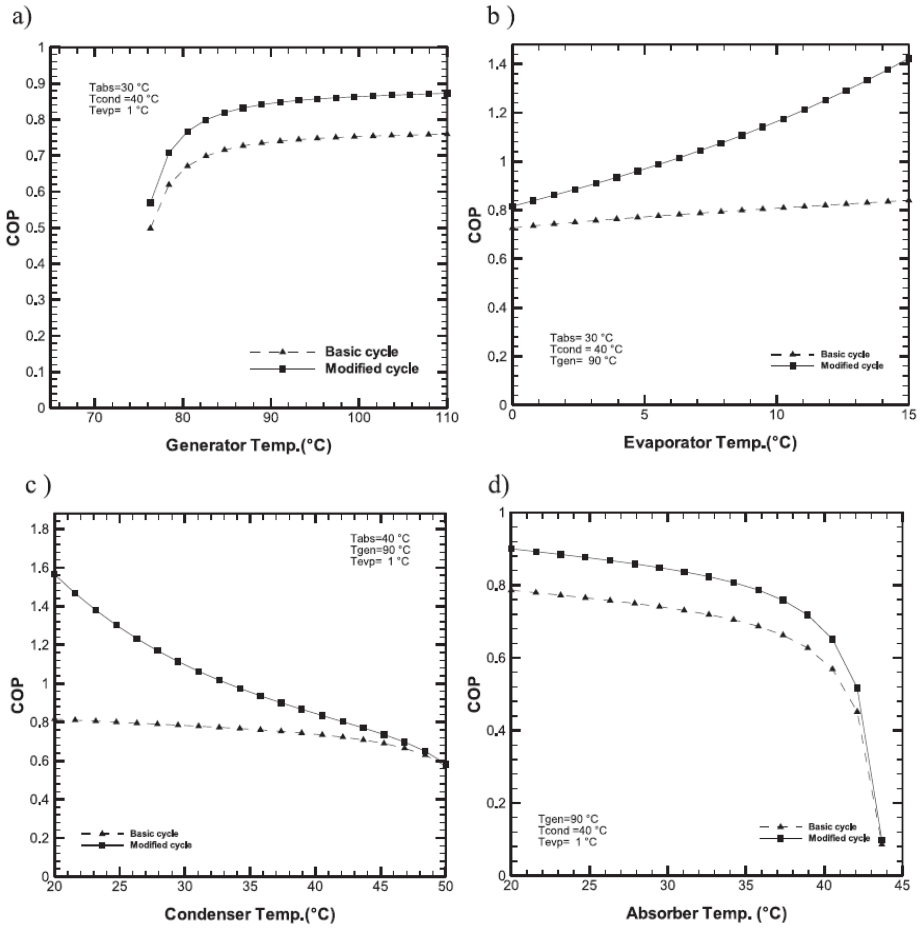

Figure 2: *(a–d) Comparison of influence of operation temperature on the COP values for basic and modified cycle*

ISBN: 978-81-936820-6-7
Proceedings DOI: 10.21467/proceedings.4

Series: AIJR Proceedings

4.2 Effect of Generator Temperature:

Variation of COP and total exergy destruction rate of system with generator temperature is depicted in Figure.3.a. It is observed that COP of system increase with generator temperature up to certain value and then after very negligible variation is observed. With increasing generator temperature, strong solution concentration increases hence mass flow rate of weak and strong solution decreases while refrigerant mass flow rate remains unchanged. Enthalpy of superheated refrigerant stream marginally increases with generator temperature while enthalpy of weak and strong solution increases rapidly hence lowering generator heat load. Therefore, COP of system increases with generator temperature.

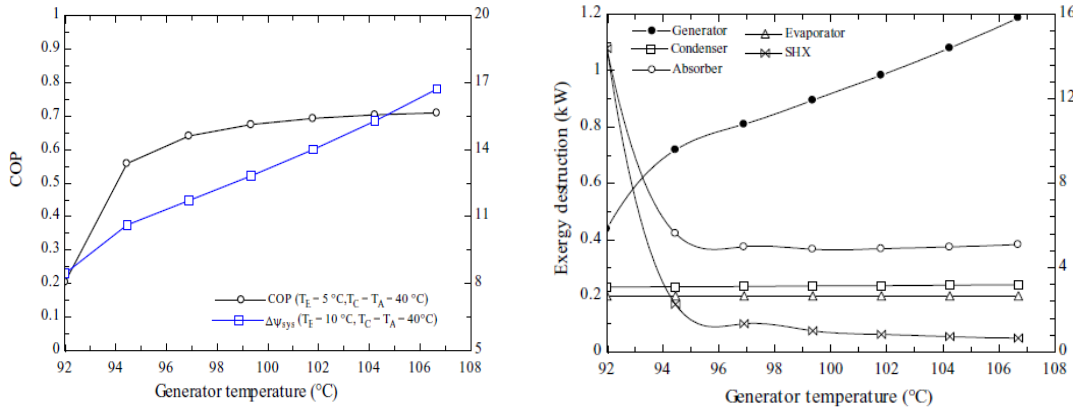

(a) (b)

Figure 3: a) Variation of COP and total exergy destruction of system with generator temperature**, b)** Variation of exergy destruction of various component system with generator temperature

From Figure.3.a. it is found that with increasing generator temperature, total exergy destruction of system increases. This can be understood by Figure.3.b. It is observed that exergy destruction in condenser and generator increases with increasing generator temperature while in SHX and absorber it decreases. It is clear that with increasing generator temperature total exergy destruction of system increases rapidly so it is necessary to optimize the generator temperature for minimization of exergy destruction of system. From Figure.3.a it is observed that optimum generator temperature corresponding to minimization of exergy destruction rate found lower than that for maximization of COP.

5 Conclusion

The results show that COP of the cycle increases with increasing generator and evaporator temperatures but decreases with increasing condenser and absorber temperatures. Moreover, exergy losses in the expansion valves, pump and heat exchangers, especially in refrigerant heat exchanger, are very small fractions of the total exergy loss in the ARS. Three components that obtained the highest exergy loss are the generator, the absorber and the evaporator.

In the parametric analysis of the system, it is shown that a low condenser temperature yields a higher cooling COP and higher exergetic efficiency. The system operating with relatively high evaporator temperatures has better cooling COP and experiences smaller exergetic efficiency than the one having low evaporator temperatures. Increasing the generator temperature can improve the cooling COP of the absorption system, but as the heat source temperature further increases, the COP of the system levels off. This negative effect of increasing the heat source temperature is more dominant on the exergetic efficiency of the system. Consequently, this negative result on the exergetic efficiency and the COP removes the beneficial effect of a high heat source temperature.

In this study, an improved system of the single-stage absorption cycle operated with LiBr/H_2O as its working fluid was conducted. Thermodynamic analysis of ejector–absorption refrigeration system has been carried out, and the theoretical performance of the cycles were compared. The results show that the modified combined absorption cycle is superior to the basic cycle over a wide range of operating conditions. The results also show that the thermal load of the condenser and the evaporator increase as the generator and evaporator temperature increases, while it decreases as the condenser temperature increases. The results in dicated that the overall COPs increments of the modified cycle was 8–60 % at a condenser temperature of 25–45 °C, and by 30–85% at evaporator temperature of 0–10 °C over the basic cycle.

References

[1] Misra RD, Sahoo PK, Gupta A. Thermoeconomic evaluation and optimization of an aqua-ammonia vapour-absorption refrigeration system. Int J Refrig 2006;29(1):47–59.
[2] So¨ zen A. Effect of heat exchangers on performance of absorption refrigeration systems. Energy Convers Manage 2001;42(14): 1699–716.
[3] Saravanan R, Maiya MP. Thermodynamic comparison of waterbased working fluid combinations for a vapor absorption refrigeration system. Appl Therm Eng 1998;18(7):553–68.
[4] Sun DW. Comparison of the performance of NH3–H2O, NH3–LiNO3 and NH3–NaSCN absorption refrigeration systems. Energy Convers 1998;39(5/6):357–68.
[5] Talbi MM, Agnew B. Exergy analysis: an absorption refrigerator using lithium bromide and water as the working fluids. Appl Therm Eng 2000;20(7):619–30.
[6] Kotas TJ. The exergy method of thermal plant analysis. Florida: Krieger Publishing Company; 1995.
[7] Szargut J, Morris DR, Steward FR. Exergy analysis of thermal, chemical, and metallurgical processes. New York: Hemisphere Publishing Corporation; 1988.
[8] Bejan A. Advanced engineering thermodynamics. New York: Wiley; 1988.
[9] M.M. Talbi, B. Agnew. Exergy analysis: an absorption refrigerator using lithium bromide and water as the working fluids. Applied Thermal Engineering 2000;20: 619-30.
[10] G. Gutiérrez-Urueta, A. Huicochea, P. Rodríguez-Aumente, W. Rivera. Energy and Exergy Analysis of Water-LiBr Absorption Systems with Adiabatic Absorbers for Heating and Cooling. Energy Procedia 2014;57: 2676-85.
[11] A. Arora, S.C. Kaushik. Theoretical analysis of LiBr/H2O absorption refrigeration systems. International Journal of Energy Research 2009;33: 1321-40.
[12] R. Gomri. Second law comparison of single effect and double effect vapour absorption refrigeration systems. Energy Conversion and Management 2009;50: 1279-87.
[13] J.D. Marcos, M. Izquierdo, E. Palacios. New method for COP optimization in water-and air-cooled single and double effect LiBr–water absorption machines, International journal of Refrigeration 2011;34: 1348-59.
[14] R. Saravanan, M.P. Maiya. Thermodynamic comparison of water-based working fluid combinations for a vapour absorption refrigeration system, Applied Thermal Engineering 1998;18: 553-68.
[15] Y.A. Cengel, M.A. Boles, M. Kanoglu. Thermodynamics: an engineering approach. Eight ed., McGraw-Hill, New York, 2015.
[16] R. Palacios-Bereche, R. Gonzales, S.A. Nebra. Exergy calculation of lithium bromide-water solution and its application in the exergetic evaluation of absorption refrigeration systems LiBr-H2O, International Journal of Energy Research 2012;36: 166-81.
[17] S.A. Klein, F.L. Alvarado. Engineering equation solver, F-Chart Software, Madison. WI 2002: 1.

ISBN: 978-81-936820-6-7

Series: AIJR Proceedings
Proceedings DOI: 10.21467/proceedings.4

Preserving. Architectural Heritage within the International Covenants and its Reflection in the Libyan Case

Husein AL derawe[1*], Ashraf Laswad[1] , Latefa Wafa[2]

[1] Department of Architecture, College of Engineering, Elmergib University, Libya
[2] Department of Architecture, College of Engineering, Tripoli University, Libya

DOI: https://doi.org/10.21467/proceedings.4.47
* Corresponding author email: architect.of.libya@gmail.com

ABSTRACT

The architectural and archeological heritage are exposed to many damage factors that differ in terms of origin; act of nature, others because of the human works and the most serious infringements represented in the wrong and not well studied restoration process. In the case of Libya; despite the historical and artistic diversity of its architectural heritage the preservation of which remains outside the priorities of legislators, which has led to cause various damage factors. In particular, the erroneous and misguided restoration processes, to distort many important architectural monuments which stood witness to many historical periods.

The purpose of this research is to emphasize that the international conventions of conservation are generate constitution of achieving their preservation and the importance of issuing a Libyan Charter that regulates the processes of architectural heritage in Libya according to the specificity of each case . This will be done through of a previous restoration study carried out on a single building at Leptis-magna for ensuring its valuation within parameters of international conventions. Furthermore, the same situation should highlight on the distortion due to the miss-performed conservation processes.

To sum up, the study tried to ensure the priority of the conservation operations that were done according to the international conventions, and highlighted the failure of other operations that were done neither scientifically nor well-prepared. Therefore, this problematic issue was reflected negatively on the origins and value of the undertaken case study. In addition, the study highly recommended that the Libyan local authority should establish its own Libyan charter to deal with every individual restoration case with its specialty. The study also insisted that Libyan authority should establish a specific law(s) and penalties that should deal to stop later similar operations.

Keywords: Restoration, preservation**,** charters .

1 Introduction

Architectural heritage is of great historical value as a living conveyor of history as well as its artistic value. it has become a major source of income in many countries of the world. But this

heritage is like any ancient monuments are exposed to many factors that lead to deterioration and distortion, but the archaeological holdings can be saved in museums that limit of its damage, unlike the archaeological buildings that are difficult to protect.

Accordingly , the specialists and who are interested in the fields related to antiquities on the world level with different opinions and directions to support their efforts to develop laws and regulations to control the processes for the restoration of architectural heritage to give it sustainability, and emerged the international conventions and treaties related to the preservation of the material human heritage as the fruit of their efforts.

2 International Conventions Related to the Preservation and Restoration of Monuments:

Improper and unthought restoration is one of the most serious aspects of damage to any archaeological building, therefore, before any restoration work, it was necessary to study carefully to the legislation items concerning the preservation and restoration of archaeological buildings to get it out of it a summary that enable us to develop a sound and legal methodology to carry out a successful restoration process for the purpose of preserving the original character of archaeological buildings. Likewise, the development of appropriate solutions to treat what can be cured of the previous faulty operations and damages to the archaeological buildings.

The beginning of these covenants began with the beginning of the 20th century, after the destruction of large architectural monuments as a result of the nineteenth centuries.

There have been numerous national efforts to deal with architectural and urban heritage during the 18th and 19th centuries. However, they were aimed at serving local objectives . There were fundamental difference between the approaches to dealing with architectural and urban heritage during the 19th century, which ranged from the rejection of any form of restoration to the preservation of the inherited reality, and interfering with it in the same contemporary thought which it was designed for it to confirm its continuity.

There was also the need to protect the fixed and moveable heritage of destruction due to the different wars in Europe during 18th and 19th century. Perhaps the first ideas developed in this direction are "the law of states " developed by the Swiss judge "Emanerich de Vattel" 1758 , who decided that ,if any country is destroyed for any reason, care must be taken to preserve those objects that glorify human society and do not add to the enemy's strength, such as temples Cemeteries and public buildings. It was followed by the draft international declaration of laws and customs of war adopted by the conference called by the Russian Emperor “Alexander II after the Russo-French war the main idea of these efforts was that the antique is a general human property, not just the surrounding community, and that it must be protected even during wars and armed conflicts so that the invading forces became responsible for its protection [1].

ISBN: 978-81-936820-6-7
Proceedings DOI: 10.21467/proceedings.4

Series: AIJR Proceedings

The second half of the 19th century witnessed a national effort to preserve the urban heritage in different parts of Europe with different concepts between the reconstruction in France, the preservation of whole areas with the permission of new facilities as in taly and the preservation of heritage in its historical state as in England. And there was a need for on international understanding on how to deal with unban and architectural heritage.

The most important of these efforts was the conference in "The Hague city " in 1899,1907, however these conferences did not place a specific collective responsibility on the international community that their application come be continued [1].

But that was not enough to lay the bases for limiting abuses that often occur unintentionally. The emergence of international conventions appeared in the decisions of the sixth international conference of Architects, held in Madrid in 1904. This was followed by the international scientific efforts in several conferences, which led to the issuance of a large number of charters. Where the charter of Athens was issued in 1931, which is the beginning of the existence of international conventions and recommendations agreed upon by experts and specialists in dealing with the heritage and the real beginning of the development of the thought of preserving the architectural and urban heritage, because of the great shortness of Athens document and the lack of defaited methodology through which to deal with the heritage and ted to the need for more effort as the charters followed and associations and organization were established that have been concerned with the protection of human heritage of all kinds where the "International center for the study of the preservation and the restoration of cultural property " ICCROM" was established in 1956.

Efforts of UNESCO have continued through its General Assembly and the recommendations emanating from the seminars it calls for the establishment of the "International council on monuments and Archeological sites" ICOMS in 1964, while who shared in the conference considered that many of the problems encountered by the restorer were not addressed in the Athens charter. It was therefore necessary to review the principles of the Athens charter with a view to deepening them and expanding their powers in a new document to solve these problems therefore, the second conference of architects and technicians specialized in archeological sites was held in VENICE 1964 under the auspices of UNESCO and came out with 13 documents most notably the first charter Known as the International document for the restoration and reservation of monuments and historical sites, which constituted a qualitative and important leap forward in establishing clear and specific foundations and rules for any restoration work. Also, it becomes the most important documents related to the preservation of historical and archaeological sites and areas. Also, it becomes the main reference for the restoration and maintenance operations and the basis on which many international conferences and conventions were built, which have woven a clear scientific and technical approach to the restoration process [1].

3 The Most Important Issues Covered by International Conventions on the Restoration of the Historic Building

The international conventions provided a set of specific laws which organize the restoration processes of archeological buildings in order to avoid any damage that may result from faulty and unplanned restoration operations :

a. The architectural heritage represents a wealth that is a common property of the people, and these peoples must protect it from the dangers that threaten it [7].
b. Historical sequence must be respected [4].
c. The role and priority of sciences and techniques for studying and rescuing the antique monuments [5].
d. Conservation and restoration must only be limited to authorized and specialized architects [3].
e. Local authority should establish a general policy for the conservation and restoration of cultural and natural heritage [6].
f. Documentation and proven methods [5].
g. The decision of what must or must not be removed should not be a single decision, Venice [5].
h. The selection of proper materials and techniques for later replacement and/or modification restoration operations [8].
i. The restoration must be carried out strictly according to precise analytical study. In another words, restoration must be carried out away from assumptions and probabilities [5].

From the above mentioned, we conclude that the international conventions have confirmed the importance of heritage and set the specific criteria and control of the conservation process within the stages and priorities of the restoration process in all its aspects, so as to result in a process of preservation as successful as possible with emphasis on the specificity of each case. However, the application of these covenants remains a non-binding literary responsibility, particularly terms of faulty repair operations. This will be evident in the case of study.

4 Articles of the Libyan law Regarding Archaeological Restoration Operations:

The last updated Law on the Protection of Monuments, Museums, Old Cities and Historical Buildings in Libya is Law No. (3) of the year 1993 AD, which confirmed some of the articles issued in the previous laws. It contains six articles concerning the restoration of ancient cities and historical buildings. nevertheless, these articles are considered gelatinous and insignificant without the existence of technical determinants and criteria that determine and assess restoration processes according to the specificity of each restoration case. The fourth chapter of the same law is related to penalties. Accordingly, the mentioned penalties were not deterrent, and without exaggeration they're not encouraging, since the maximum penalty is

ISBN: 978-81-936820-6-7
Proceedings DOI: 10.21467/proceedings.4

Series: AIJR Proceedings

not more than twenty thousand dinars, and the maximum sentence of imprisonment not exceeding one year.

5 The Case Study :

The selection was done of an important historical monument from the archaeological city of Libya as a campaign of restorations were carried out at different periods of time and the result were clearly different, and it was chosen to examine the scope of the commitment to what it contained in international conventions to maintain and reflect on the results of restoration operations.

In summary, all international legislations combine with the need to protect cultural property and lay the foundations and legal principles for implementing this.

The executive authorities should therefore put in their programs hew to activate this legislation and enact laws and implement them in cooperation with the security and judicial services.

As a field study, The Augustical theater was chosen from the ancient city of Leptis which mainly support the above mentioned criteria of the case study. Therefore, a number of the restoration operations has been done on different periods of time and the results were clearly different. Accordingly, these restoration operations were chosen to examine the scope of the commitment to what is contained in international convention to maintain and reflect on the results of restoration operations.

5.1 The Augustical theater historical background:

it was built by one wealthy man from city of Leptis named "Hanbal Rufus " between 1-2 , and presented as a gift to Emperor Auguat. The theater in the imperial era is only a listening room to hear the music, but was using a little for playing drama, (figure 1).

5.2 Its architectural and historical importance:

The importance of the historical theater is built one of the wealty Libyans of the time , which confirms that Leptis is not purely Roman city , but Libyans have a great role in its construction. And concerning its architectural importance is the creativity in the architectural configuration of the building in addition to being one of the largest buildings in the city of Leptis and performing its function until today.

Figure1*: general view of the Augusti theater(Authors,2018)*

5.3 Factors of damaged suffered and resulting deterioration:

the Augusti Theater is considered to be one of the building close to the sea, which has been exposed to many destructive factors such as erosion caused by winds and weathering, growing of vegetation and shrubs, as well as seawater filtration, which lead to deterioration of the building and damage its basic structure.

All these factors make it necessary to pay attention to its restoration and maintain it periodically and continuously, making it susceptible to wrong and unskilled restoration.

5.4 The restoration works that were carried out on the monument:

The stages of restoration can be divided according as its history to three historical stages starting from 1937 – 2001.

Note: (the most we can talk about in this regard, that there not monitoring … these monuments for the area of Leptis and the ministry of reports or documents of the restoration operations that have been conducted on the monument whether old or modern and these is only one book in the scientific library in Italian Language detailing the exploration & restoration carried out from 1937 – 1951. As for the modern restoration it has no documents except for some photographs).

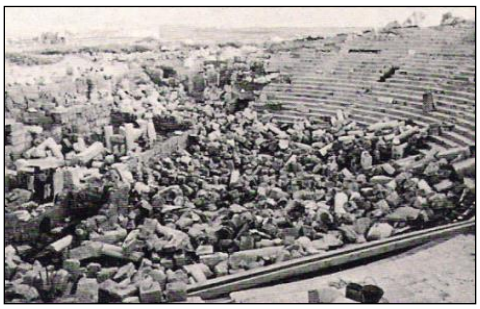

Figure 2*: The part found from the theater during the excavation and exploration [5].*

The first restoration process: began with excavation in 1937 the theater works continued for 14 years until 1951, in which the general shape of the building was substituted according to the materials found. The excavation of the building, which was prepared by the Italian team was commissioned to prepare preliminary studies of the restoration process. This is because most of the building materials disappeared & were destroyed as a result of the damage factors and thefts that the city exposed to it during different ages (figure 2), which forced these who are responsible for restoration process to make the decision to using building materials from the residential and service buildings in the city. As for the materials found it has Lost large parts of its features and therefore the team specialized in restoration and maintenance of the stones has paid effort to repair them and trying to restore their original form to be returned to their place [2], (figure 3).

ISBN: 978-81-936820-6-7
Proceedings DOI: 10.21467/proceedings.4

Series: AIJR Proceedings

***Figure 3**:restoration of the building stores found in the excavations[5].*

Despite the preparation of preliminary studies and perception of the architectural form of the theatre, it was not delivered from some of the violations to the restoration although a few in total and do not violate international conventions. The use of cement was warned only in the Venice convention in 1964. We note the use of cement mortars in the rear entrances and their negative effect on the finishing layers and building stones. The chemical reactions that occur in the cement mix change the colors of the building materials and the finish formed over time as well as the erosion of the stones and the deterioration of the stones, (Figures 4).

***Figure 4**:Effect of using cement mortar on building blocks[5].*

As well as the restoration of the vaults and the collapsed arches. The parts that found materials were rebuilt and the materials lost were replaced with good materials that fit in shape with the original materials. Materials of the same building were used, and white cement with sand was used, therefore these processors still exit so far after more than fifty years (Figure 5, 6).

After the reconstruction of the theater on the situation in (Figure 7), although some of the distortion of the area under the upper columns restored in a way that acquired a modern appearance, work processes were stopped at this point because the building materials are no longer available and continue to work to get the building to the situation as it was put into the study, which will somehow lead to the production of a building that may be a monster for the

original building. This is stated in Article 9 of the Venice charter of 1972, which stipulates that "the repair should stop when the guesswork begins".

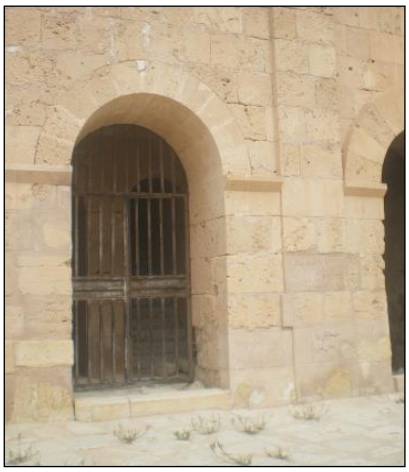

***Figure 5**:Treatment of arcs using materials of the same original building material [5].*

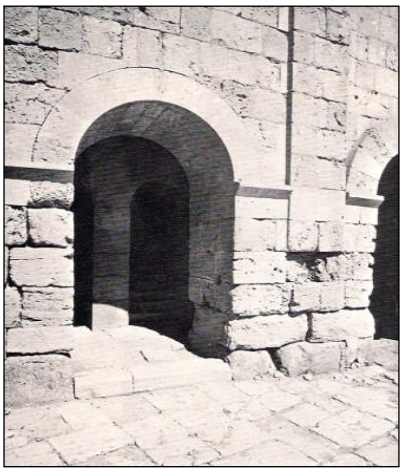

***Figure 6**:The current appearance of the arc with same old treatment,(Author-2018).*

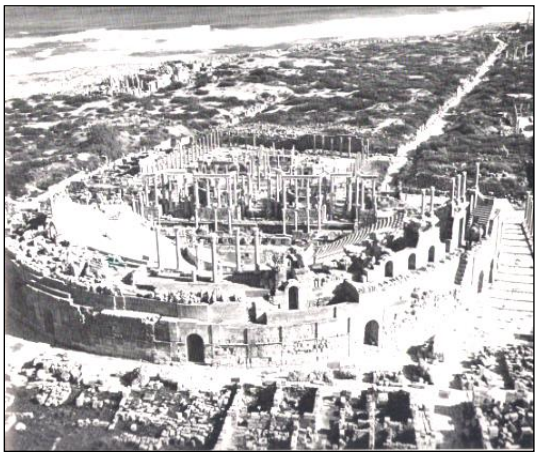

***Figure 7**:The The situation in which the first restoration process has stopped[5].*

The second restoration process: after the completion of the initial restoration, did not occur any important restoration operations, but were cases of treatment to the existing situation as a result of the factors of degradation that did not stop to this monument. We do not exaggerate if we said that it is sabotage rather than restoration, as it was not in the hands of specialists, no appropriate materials was used and was not documented, mostly using mortars and cement concrete, where many of the walls and stones that suffered from sludge and crumbled were restored by using black cement, which in turn led to worse situation by occurring holes in these stones. This was because of destroying and dispersing the remaining finishing layers over time. The worst was the distortion of the architectural character of the monument by the color of the materials used in the restoration, which appear to be irregular to the building, (Figures 8,9).

ISBN: 978-81-936820-6-7
Proceedings DOI: 10.21467/proceedings.4

Series: AIJR Proceedings

***Figure 8**: Using concrete in the floors and surfaces,(Authors,2012)*

***Figure 9**: The use of black cement and paint it with a contemporary paint,(Authors,2012)*

The third restoration process: it was the last restoration operations carried out on the theatre and it was in 2001. It was decided by the tourism sector, and the administration decision was not subject to any of the scientific and technical conditions. No preparatory studies were done, and it was carried out by non-specialists or trained stuff where the roof of the eastern entrance of the theatre and the vault leading to the orchestra area was restored using concrete block and reinforcing steel, (Figures10,11).

After restoration of the eastern entrance to the theater, there was a great controversy by the interested and specialists in the field of archeology to the extent of submitting complaints to UNESCO, but the process of restoration did not stop, and the restoration of the western entrance continued by using the limestone block and cement mortar as a bond and then poured concrete above it as a different treatment from was carried out on the eastern entrance, but these treatments were the implantation of cancerous tumor within the body of the building, even the attempt to replace it will lead to collapses and smash in the structure of the building, (Figure12), *[10]*.

***Figure 10**:Using the cement block in the theater[10].*

***Figure 11:** Using concrete and reinforcement steel in the roof of the eastern entrance of the theatre[10].*

***Figure 12:** Using the limestone bricks to roof the western entrance of the theatre [10].*

The wall of the external walls of the theater were reconstructed with cement blocks and was covered with black cement mortar and was decorated with random lines without taking in consideration the old lines of stones and treatments as a kind of an attempt to dive the

impression that it was a building of stones and then painted with colors compared to the stone color and then the crystallized salts appearing on the wall surfaces and the building turned into a monster that had nothing to do with the original form, (Figures 13,14,15 and 16).

Figure 13: *The outer well of the theater before its restoration[10].*

Figure 14: *The outer wall of the theater after its restoration (Authors, 2012)*

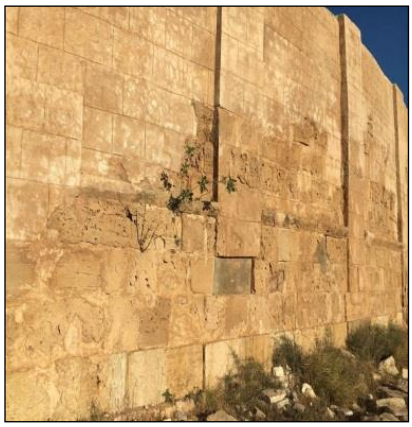

Figure 15: *Using the cement blocks in the restoration of outer wall (Authors, 2018)*

Figure 16: *That produced by using cement material (Authors, 2018)*

6 Summary of the case study

Through the previous presentation regarding the restoration process of the Augusti theater in the archaeological city of Leptis, the evidence that the first restoration of the monument after the completion of excavation and exploration, which although it was in an advanced time in 1937 where did not appear except some of the conventions and agreements, but it was according to a scientific approach based on steps and stages predetermined for all aspects that would affect the process of restoration. But later there were no major restoration, where most of the operation that are taking place were restoration for the purpose of prevention, and it was more destructive than restoration and has not been subjected to any scientific and technical basis, although it was at a later period after the emergence of the most international conventions to preserve the relics. The last major restoration operations that the monument

ISBN: 978-81-936820-6-7
Proceedings DOI: 10.21467/proceedings.4

Series: AIJR Proceedings

subjected to was in 2001, which was not based on any scientific or technical study, but was a decision by the tourism sector which was performed by one of the construction contractors.

7 Conclusions

All international legislation agreed to the need to protect cultural properties. Also, it emphasized the importance of the heritage and set criterion to evaluate it.

In addition to establishing the principles and technical bases to protect and preserved it in the form of international charters in order to control the preservation process within the stages and priorities of the restoration process in all its aspects with emphasis of each case. However, the Libyan Antiquities Law, despite the obvious infringements of the architectural monuments due to the erroneous and unthought restoration processes, which has distorted and lost some of its features, is still limited to the development of legal texts that impose deterrent penalties to limit these infringements. International covenants remain a literary responsibility and not mandatory to apply, especially with regard to faulty repair operations. Moreover, the articles of the law relating to antiquities remain loose unless the competent technical authorities referred to in the articles o the Libyan antiquities law in its articles regarding the restoration operations set clean technical parameters and standard which can be invoked according to the specificity of each case.

References

[1] Jukka Jokilehto, "A History Of Architectural Conservation," D.Phil. University of York, England, pp. 283-284, 1986.

[2] Giacomo Caputo, " Mnongrafie Di Archeologia Libica," *L`erma Di Bretschneider - Roma*, vol. III, pp. 5,11,22,133, 1987.

[3] International Congress Of Architects ,Madrid, Article 5, 1904.

[4] The Athens Charter, "for the Restoration of Historic Monuments", Article 2, 1931.

[5] The Venice Charter, "International Charter for the Conservation & Restoration of Monuments & Sites," Article 2,9,11,16, 1964.

[6] Paris Charter, "International Convention for the Protection of the World Cultural and Natural Heritage," Article 5, 1972.

[7] Europian Charter, "the Architectural Heritage, declaration of Amsterdam" Article 3, 1975.

[8] Appleton Charter, ", for the Protection & Enhancement of the Built Environment" Article 4, 1983.

[9] Libyan Law (No. 3), "For the Protection of the monuments, museums, ancient cities and historic buildings" Article 14,18,23,36,39,49, Libya, 1994.

[10] Antiquities monitoring of Leptis, "Reports of restoration works of the Augustic theater", 2001.

Measuring urban clarity of the built environment

Fawzi Mohamed Agael

Department of Architecture and urban planning, College of Engineering, Elmergib University, Libya

Corresponding author email: fawzi6664@gmail.com

ABSTRACT

since a very short time, how to measure urban spaces was an undefined issue in the scientific debate. Most of them have relied on theories that their results often selective; they based on complex variables that are rarely available simultaneously in the built environment and the human element. This paper aims to explain the "intelligibility" indicator of Urban Spaces, Built Environment and the relationship between Global Integration measurement and Connectivity measurement of spaces through the Axial Line Analysis from the point of view of Space Syntax theory.

This indicator helps to understand the surrounding Built Environment, which is critical to urban navigation and helps to understand the urban spatial restructuring of the Built Environment and facilitate its understanding of the observatory.

Key words: Urban clarity, Intelligibility, Urban spaces, Integration, Connectivity, Axial Analysis, Urban navigation.

Acknowledgment:

I wish to thank my supervisor Dr. Ozlem Ozer because this paper is a part of my Ph.D. thesis in Architecture and urban planning , Okan University, Istanbul, Turkey.

 ISBN: 978-81-936820-6-7

Track 6

Engineering Management

 ISBN: 978-81-936820-6-7

Key Performance Indicators in Libyan Oil and Gas Projects

Mahmoud Matoug[1*], Abdulbaset Frefer[2], Haleema Omer[3]

[1, 2] Mechanical and Industrial Engineering Department, University of Tripoli
[3] Engineering Management Department, University of Tripoli

DOI: https://doi.org/10.21467/proceedings.4.48

* Corresponding author email: mmmatoug54@ymail.com

ABSTRACT

Nowadays, the management system based on key performance indicators (KPIs) is one of the most effective systems from a project management perspective. Unfortunately, common key performance indicators do not exist for the assessment of the performance and success of Libyan oil and gas projects (LOGPs). A project's success or failure no longer depends solely on whether or not it meets traditional key performance indicators (cost, time and quality), instead, the assessment of a project's success is required from the beginning until the end of the project and product lifecycle. The purpose of this study is to advance understanding of KPIs and to develop the most common key performance indicators (KPIs) for the Libyan oil and gas projects. By reviewing the existing research and literature, 11 (eleven) most important KPIs were identified. Questionnaire surveys and semi-structured interviews were administered to gauge the opinions of project practitioners representing clients, consultants and contractors on the KPIs most relevant to the local oil and gas industry. The findings indicate that the traditional KPIs are no longer applicable in measuring performance and success of oil and gas projects in Libya. Other key performance indicators such as Health, Safety and Environment (HSE), Efficiency of use resource, Profitability, Experience gain from the project, Shareholder Satisfaction, Sustainability, Maintainability and Reliability are increasingly becoming more important. Key performance indicators for the assessment of Libyan oil and gas projects are far more complex than simply meeting cost, time and quality.

Keywords: Key Performance Indicators (KPIs), Libyan Oil and Gas Projects (LOGPs), Project Management, Project Success, Management Tools.

1 Introduction

Oil and gas projects with high level of uncertainty and risks have proven to be one of the most complex in business with high level challenges that are faced by the petroleum companies these days. These projects are executed at different stages of the oil and gas industry value chain and almost always involve multiple stakeholders, multiple nationalities and large number of staff [1]. The size and complexity of these projects require special attention in the project management process. Bodicha [2] argue that despite the globalization and much acquired knowledge for organizations to engage in project management, the use of project management

 ISBN: 978-81-936820-6-7

tools and techniques does not automatically guarantee project success. A project performance and success can be measured traditionally by three indicators: namely; cost, time and quality. Many researchers suggest that success can't be accessed only through these three key performance indicators, since project success is more complex. They advocate the expansion of success measurement towards project management success and product success [3]. Libya exports about 80% of its crude oil and earns about 96% of its revenue from oil and gas exports [4]. Unfortunately, common KPIs do not exist for the assessment of the performance and success of Libyan oil and gas projects. The purpose of this research paper is to advance understanding of KPIs and to develop a set of the most common KPIs for Libyan oil and gas projects.

2 Performance Measurement

Performance measurement is the first step in any performance improvement program. It helps to identify gaps in performance, opportunities for improving performance and to develop programs for continuous improvement. According to Fleming, et al. [5], the heart of effective project management is the establishment of performance measurement baseline and performance reporting. Salaheldin [6] stated that performance measurement is a critical factor for effective management since without measuring something; it is difficult to improve it.

Ofori-Kuragu [7] reported that there isn't distinction between measures and indicators. In fact, measurement alone is not enough to improve performance. The indicators are important within projects since they assess what should be measured and the control limits within which the performance should be. Also, the level of performance that project reaches is based on the efficiency and effectiveness of the actions taken. According to Alarcon, et al. [8], the result of a project is the product of various processes and decisions that interact during its execution. Along the same line, Libyan oil and gas industry represented by the National Oil Corporation (NOC) and its subsidiaries, most of which are focusing on traditional key performance indicators (cost, time and quality). Although KPIs have long been used to evaluate and judge the performance and success of projects; many researchers suggest that success can't be accessed only through those traditional KPIs, since project success is more complex, and these indicators do not provide an adequate vision of the potential for improvement [9]. In a recent study conducted to determine the strength of the relationship between different elements of project management performance indicators and project success, the results showed that the project management performance indicators have positive association with the project success [10]. Many studies that were carried out to determine KPIs to evaluate the performance and success of projects did not distinguish between "indicators and criteria", describing both as measures used to measure the performance and success [1]. In this research paper, "indicators" and "criteria" are both used as means to measure the performance and success, and hence used interchangeably.

In order to cover key performance indicators in greater depth, it is important to consider the various studies conducted on the construction industry. Although the oil and gas projects have unique characteristics, they have similarities with construction projects. Some of the construction projects in the oil and gas industry include the construction of oil refineries, of petrochemical plants or of gas treatment plants. Table 1 shows summary of key performance indicators in any project from the fifteen literature reviews discussed in this research paper [3,7,11-23]. The broad categories of stakeholders have been identified by many researchers, such as clients, contractors, consultants and material suppliers as the internal project stakeholders; where, the external stakeholders were identified as local communities and the government. Stakeholder participation in project evaluation is essential since it keeps the projects on track and often ensures early detection of problems that can reduce the likelihood of having major cost overruns or time delays and non-conformity to project specification [14]. Many researchers identified clients, contractors and consultants as the major internal stakeholders in projects, and their participation is essential in the evaluation of any project. The clients are considered as the financiers interested in how much had been spent and its corresponding progress. Whereas the contractors and the professional consultants were integral to the project implementation and the success or failure of the project depends on their performance [15]. In this research paper the authors consider stakeholders as clients, contractors and consultants.

Table 1: Summary of KPIs in Project from the Literature Review.

Sources / KPI	Al Hammadi [11]	Ahmed [12]	Sylvester et al. [13]	Bahia [14]	Olaku et al. [15]	Khosravi [16]	Toor et al. [3]	Al-Tmeemy et al. [17]	Ofori-Kuragu et al. [7]	KPI Working Group [18]	Lim et al [19]	Yeung et al. [20]	Ling et al. [21]	Ali et al. [22]	Cross et al. [23]	Frequency %
Cost	√	√	√	√	√	√	√	√	√	√	√	√	√		√	93.3%
Time	√	√	√	√	√	√	√	√	√	√	√	√	√		√	93.3%
Quality	√		√	√	√	√	√	√	√	√	√	√	√	√	√	93.3%
Customer Satisfaction	√			√	√	√		√	√	√			√	√	√	66.7%
Health, Safety and Environment	√			√		√	√		√	√	√			√		53.3%
Scope		√	√	√												20%
Efficiency of use resources					√		√						√			20%
Effectiveness					√		√						√			20%
Productivity									√						√	13.3%
Business performance									√	√						13.3%
Profitability													√	√		13.3%

ISBN: 978-81-936820-6-7
Proceedings DOI: 10.21467/proceedings.4

Series: AIJR Proceedings

3 Data Collection

This research paper was conducted based on intensive literature reviews to identify key performance indicators for oil and gas projects and to develop a survey questionnaire. Based on these literature reviews eleven (11) key performance indicators were identified in Libyan oil and gas sector. Table 1 presents the proposed key performance indicators of oil and gas projects success. The questionnaire consists of two sections. The first elicits information on the respondents' background as shown in Table 2, where the second consists of questions related to key performance indicators. The questionnaire survey was carried out in Libya in the beginning of 2017. Internal consistency of the data reliability analysis was achieved by employing Cronbach's Alpha coefficient. Cronbach's Alpha reliability coefficient ranges from 0 to1. The closer the coefficient value to 1, the greater is the internal consistency of the data [13,24,25]. Cronbach's Alpha coefficient for each field of the questionnaire is 0.843, this is considered high; the result is ensuring the reliability of each field of the questionnaire.

One hundred and twenty (120) questionnaires were administered to project practitioners, including clients, consultants and contractors who have experience in oil and gas projects that were recommended by the NOC, as part of the most important companies which have great experience in oil and gas projects in Libya. Out of the 120 distributed by hand, eighty-eight (88) were received back. Therefore, the questionnaires returned have a response rate of 73.33%. The respondents were requested to indicate their views on the importance of each key performance indicator. They were asked to use five-point Likert Scale ranging from 1 to 5, where 1 represents strongly disagree and 5 strongly agree. This scale was introduced by Likert in 1932 [26-27].

Table 2: Summary of Respondents' Profile.

Companies	%
Client	48.86
Consultant	23.86
Contractor	27.27

Qualification	%
HND	4.55
BSC	53.41
MSC	39.77
PHD	2.27
Other	0

Experience (years)	%
1-5	13.95
6-10	29.07
11-15	16.28
16-20	13.95
Above 20	26.74

4 Results and Discussion

4.1 Data Analysis

The data collected were analyzed with the aid of Statistical Package for Social Sciences (SPSS). Descriptive statistics were used to analyze the respondents' profiles using SPSS. The Relative Importance Index (RII) method [22,28-30] was used to rank the key performance indicators.

This method provides a score calculated upon the weight given to i^{th} response (Wi), (i=1,2,3,4,5); frequency of the i^{th} response (Xi); maximal weight (A) (5 in this research paper); and total number of respondents (N). RII refers to a value within [0–1] interval. The higher the RII, the more important the KPI. The RII for each KPI is calculated using the formula below [22]:

$$RII = \frac{\sum_{i=1}^{5} Wi\ Xi}{A * N}$$

4.2 RII and KPIs Used to Assess Performance and Success of LOGPs

From the perspective of the clients, consultants and contractors, all the eleven key performance indicators identified in the literature review were significant in the Libyan oil and gas industry, since all had RII score values above 0.7. The different categories of respondents seem to have a few different views about the most important KPIs. Table 3 shows the full details of RII scores of all key performance indicators.

Table 3: Shows the full details of RII scores of all key performance indicators.

Key Performance Indicators	RII (Client)	Rank	RII (Consultant)	Rank	RII (Contractor)	Rank	Overall RII	Overall Rank
Quality	0.9395	2	0.9333	1	0.9333	1	0.9364	1
Time	0.9442	1	0.9238	2	0.9250	2	0.9341	2
Cost	0.9395	2	0.8952	3	0.9167	3	0.9227	3
Health, Safety and Environment	0.9023	3	0.8571	5	0.8500	7	0.8773	4
Scope	0.8791	4	0.8476	6	0.8500	7	0.8636	5
Customer satisfaction	0.8279	5	0.8857	4	0.8833	5	0.8568	6
Efficiency of use of resources	0.8093	6	0.8476	6	0.9000	4	0.8432	7
Effectiveness	0.8047	7	0.8476	6	0.8417	8	0.8250	8
Productivity	0.7953	8	0.8476	6	0.8250	9	0.8159	9
Profitability	0.7814	9	0.8190	7	0.8667	6	0.8136	10
Business performance	0.7395	10	0.7429	8	0.7667	10	0.7477	11

The overall rankings of the most important key performance indicators are; Quality with an overall RII of 0.9364, followed by Time with 0.9341, then Cost with 0.9227, and finally Health, Safety and Environment (HSE) with 0.8773. RII scores equal or less than 0.8 were omitted.

The results from this research paper indicate that quality has been ranked by the clients as the second most important indicator, while consultants and contractors ranked the quality as first indicator, this is an indication that quality is the most important indicator for consultants and contractors. Time has been ranked by the clients as the first, this is an indication that time is the most important indicator for clients because overrun of time shatters all subsequent planning. However, both consultants and contractors ranked time as the second most important indicator. Cost has been ranked by the clients as the second, while consultants and

ISBN: 978-81-936820-6-7
Proceedings DOI: 10.21467/proceedings.4

contractors ranked it as the third; indeed, most project managers must ensure that the implemented projects do not experience cost overruns.

In one hand, Health, Safety and Environment (HSE) indicator has been ranked by the clients as the third indicator. Many industries, especially the oil and gas sector need to give priority consideration to the HSE, this necessitates that companies must track the number of dangerous occurrences, occupational injuries and oil spills to avoid damaging their reputation and to maintain the competitive advantage. On the other hand, HSE has been ranked by the consultants as the fifth indicator and by the contractors as the seventh indicator. Scope indicator has been ranked by the clients, consultants and contractors the fourth, sixth, and seventh indicator, respectively. Projects in oil and gas are carried out with specific scope aiming to achieve specific deliverables [13].

While clients and contractors ranked the Customer' Satisfaction indicator as the fifth, consultants ranked it as the fourth. Customer satisfaction is considered as an important KPIs when evaluating a project's performance and the success of a project that meets the end-users' expectations [11]. Efficiency of use of resources has been ranked by both the clients and consultants as the sixth indicator; it was ranked as the fourth indicator by the contractors. Effectiveness has been ranked by the clients as the seventh indicator but it was ranked by consultants and contractors as the sixth and eight indicator, respectively.

Productivity has been ranked by the clients as the eight indicator. The consultants and contractors ranked productivity as the sixth and ninth, respectively. Profitability has been ranked by the clients and consultants as the ninth and seventh indicator, respectively. However, it has been ranked by the contractors as the sixth indicator. The fact that survival of companies in the long-term depends on their ability to be profitable, this indicator is used to assess project success in the mid-term and long-term [25]. Business performance has been ranked by the clients and contractors as the tenth indicator and ranked as the eight indicator by the consultants.

4.3 Interviews and New Key Performance Indicators

Following the analysis of the questionnaire survey results, interviews were conducted with experts in the Libyan oil and gas projects from oil and gas industry to validate the results of this research and add any absent key performance indicators in the initial questionnaire survey. Five semi-structured interviews were conducted based on the result of the initial survey.

Interviewees were asked to comment on the outcome of the questionnaire survey and make suggestions for the final list of KPIs for Libyan oil and gas projects. The questions sought to establish whether the interviewees agreed with the outcome of the questionnaire analysis. The interviewees agreed and added more five indicators; namely, Experience Gain from the Project, Shareholder Satisfaction, Achievement of Project's Objectives, Reliability, Maintainability and Sustainability as the KPIs for Libyan oil and gas projects.

5 Conclusions

One of the most important conclusions that were reached from the literature and confirmed in this research paper is that the key performance indicators in projects in the construction industry seem to have similarities with the key performance indicators in projects in the oil and gas industry. Although many researchers have proposed various key performance indicators to measure both oil and gas project and construction success, there is no general agreement. Other significant conclusions are; the oil and gas industry are slowly departing from the traditional quantitative performance measurement to a rather mix of both quantitative and qualitative performance measurement; the results indicate that the traditional (Iron Triangle) KPIs only, are no longer applicable in measuring the performance and success of oil and gas projects in Libya. This fact should serve as an encouragement in finding a commonly accepted set of KPIs that will be used for performance benchmarking of the oil and gas projects. From the results of this research paper, other key performance indicators, such as Health, Safety and Environment (HSE), Efficiency of use resource, Profitability, Experience Gain from the project, Shareholder Satisfaction, Sustainability, Maintainability and Reliability are increasingly becoming more important. Libyan oil and gas companies need to think in more depth about the key performance indicators that are currently used globally in evaluating their projects and serve towards further setting new indicators to meet short-term, mid-term and long-term objectives in future projects. Sustainability has been identified as one of the most key performance indicators of oil and gas projects in Libya, also through literature review, the sustainability is considered to be one of the future developments in project management. Therefore, the researchers recommend further study to find the relationship between project management and sustainability, and the ability of oil and gas companies to implement sustainability's principles in project management in Libya.

References

[1] H. Omer, "Assessment of Projects Using Key Performance Indicators in Oil and Gas Companies", *MSc Thesis*, University of Tripoli, 2017.

[2] H. Bodicha, "How to Measure the Effect of Project Risk Management Process on the Success of Construction Projects: A Critical Literature Review", *The International Journal of Business & Management*, vol 3, no. 12, 2015.

[3] S. Toor and O. Ogunlana, "Beyond the 'Iron Triangle': Stakeholder Perception of Key Performance Indicators (KPIs) for Large Scale Public Sector Development Projects", *International Journal of Project Management*, pp. 228–236, 2010.

[4] Independent Statistics & Analysis," Country Analysis Brief: Libya", U.S. *Energy Information Administration*, 2015.

[5] Q. Fleming and J. Koppleman, "Earned Value Project Management", 2nd ed., *Project Management Institute*, Newton Square, PA: PMI, 2000.

[6] S. Salaheldin, "Critical Success Factors for TQM Implementation and their Impact on Performance of SMEs", *International Journal of Productivity and Performance Management*, vol. 58, no. 3, pp. 215-237, 2009.

[7] J. Ofori-Kuragu, F. Edum-Fotwe and E.Badu, "Key Performance Indicators for Project Success in Ghanaian Contractors", *International Journal of Construction Engineering and Management*, vol. 5, no. 1, pp. 1-10, 2016.

[8] L. Alarcon, A. Grillo, J. Freire and S. Diethelm, "Learning from Collaborative Benchmarking in the Construction Industry", *9th Annual Conference of the International Group for Lean Construction (IGLC-9)*, Singapore, 2001.

[9] A. Inkpen and M. Mofett, "The Global Oil and Gas Industry: Management, Strategy, and Finance", *PennWell Corporation*, Tulsa, USA, 2011.

[10] H. Maylor, "Project Management", *Pearson Education Limited*, 4th ed., UK, 2010.

[11] N. Al-Hammadi, "KPIs for Assessing Project Performance in the Oil and Gas Industry of the United Arab Emirates", 6th Engaged Management Scholarship Conference, September 2016, *University Paris-Dauphine*, Paris, France.

ISBN: 978-81-936820-6-7

Series: AIJR Proceedings
Proceedings DOI: 10.21467/proceedings.4

[12] M. Ahmed, "Critical Factors for the Success of Projects in Oil and Gas Sector of Kuwait", *MSc Thesis*, Department of Management Sciences, Virtual University of Pakistan, Pakistan, 2011.
[13] D. Sylvester, N. Abdul Rani and J. Shaikh, "Comparison Between Oil and Gas Companies and Contractors Against Cost, Time, Quality and Scope for Project Success in Miri, Sarawak, Malaysia", *African Journal of Business Management*, vol. 5, no. 11, pp. 4337- 4354, 2001.
[14] F. Bahia, "Analysis of Success Criteria in Engineering, Procurement and Construction (EPC) Projects", *Revista Gestao e Projetos - GeP*, Sao Paulo, vol. 1, no. 2, pp. 49-67, 2010.
[15] A. Olaku, A. Abdulmumin, S. Ibrahim and T. John, "Evaluation of Perception of Stakeholders on Key Performance Indicators for U.B.E Building Projects, *Journal of Multidisciplinary Engineering Science and Technology (JMEST)*, vol. 2, no. 3, pp. 277- 285, 2015.
[16] S. Khosravi and H. Afshari, "A Success Measurement Model for Construction Projects", *International Conference on Financial Management and Economics*, vol. 11, pp. 186-190, 2011.
[17] S. Al-Tmeemy, H. Abdul-Rahman and Z. Harun, "Future Criteria for Success of Building Projects in Malaysia", *International Journal of Project Management*, vol. 29, no. 3, pp. 337-348, 2011.
[18] KPI Working Group, "The KPI Report for the Minister for Construction", *Department for Transport and Environment*, London, 2000.
[19] C. Lim and M. Mohamed, "Criteria of Project Success: An Exploratory Re-Examination", *International Journal of Project Management*, vol. 17, no. 4, pp. 243-248, 1999.
[20] F. Yeung, A. Chan and D. Chan, "A Computerized Model for Measuring and Benchmarking the Partnering Performance of Construction Projects", *Automation in Construction*, vol. 18, no, 8, pp. 1099-1113, 2009.
[21] F. Ling, S. Low, S.Wang and H. Lim, "Key Project Management Practices Affecting Singaporean Firms' Project Performance in China*", International Journal of Project Management*, 2009.
[22] H. Ali, I. Al-Sulaihi and K. Al-Gahtani, "Indicators for Measuring Performance of Building Construction Companies in Kingdom of Saudi Arabia", *Journal of King Saud University – Engineering Sciences*, vol. 5, pp125–134, 2013.
[23] K. Cross and R. Lynch, "The SMART Way to Define and Sustain Success", *National Productivity Review*, vol. 8, no. 1, pp. 23- 33, 1989.
[24] L. Cronback, "Coefficient Alpha and the Internal Structure of Tests", *Psychometrika*, vol. 16, no. 3, pp. 297-334, 1951.
[25] Y. Yang and S. Green, "Coefficient Alpha: A Reliability Coefficient for the 21st Century", *Journal of Psychoeducational Assessment*, vol. 29, pp. 377-392, 2011.
[26] P. Vonglao, "Application of Fuzzy Logic to Improve the Likert Scale to Measure Latent Variables", *Kasetsart Journal of Social Sciences*, vol. 38, no. 3, pp. 337-344, 2017.
[27] R. Likert, "A Technique for the Measurement of Attitudes", *Archives of Psychology*, vol 22, no 140, pp. 5-55, 1932.
[28] K. Al-Gahtani, I. Al-Sulaihi, R. Al Rashed and A. Batarfi, "Key Performance Indicators for Value Management in Saudi Construction Industry", *International Journal of Application or Innovation in Engineering & Management (IJAIEM)*, vol. 4, no. 11, pp. 54-62,2015
[29] M. Nourbakhsh, S. Mydin, R. Zin, S. Zolfagharian, J. Irizarry and M. Zahidi, "Relative Importance of Key Performance Indicators of Construction Projects Towards Buildability at Design Stage", *Advanced Materials Research Online*: vols. 446-449, pp. 340-344, 2012.
[30] V. Tam, C. Tam and W. Ng, "On Prefabrication Implementation for Different Project Types and Procurement Methods in Hong Kong", *Journal of Engineering, Design and Technology*, vol. 5, no. 1, pp. 68-80, 2007.

An Investigation of Corrosion Risks in the Oil and Gas Pipelines Using Analytical Hierarchy Process and Fuzzy Analytical Hierarchy Process

Abdulbaset A. Frefer[1], Mahmoud M. Matoug[2] , Fatma L. Haddada[3]
[1, 2] Mechanical and Industrial Engineering Department, University of Tripoli
[3] Engineering Management Department, University of Tripoli

DOI: https://doi.org/10.21467/proceedings.4.49
* Corresponding author email: drfrefer@hotmail.com

ABSTRACT

The products of crude oil and gas can be considered as the main backbone of the global economy. The oil and gas industry has faced many potential risks and problems when the oil and gas is pumped into the pipelines during the production, transportation, and processing. Although experts are solving these problems; some have been difficult to resolve and remained as a complex issue. Among these problems, were the issues of corrosion in the oil and gas pipelines. Risk assessment of the oil and the gas pipelines is considered as the core content of the integrated management of the entire pipelines. This paper aims to assess the risks of corrosion in the oil and gas pipelines in Sabratha platform and Wafaa field. First, the Analytical Hierarchy Process (AHP) is used to identify the risk rate of the different types of corrosion. Second, the technique of Fuzzy Analytic Hierarchy Process (F-AHP) is also used to identify the risk rate of the different types of corrosion. The comparison between the classical (AHP) and the (F-AHP) indicate that the results of both techniques were close.

Keywords: Analytical Hierarchy Process (AHP), Fuzzy Analytical Hierarchy Process (F-AHP), Oil and Gas, Pipelines Corrosion, Pipelines Risk Assessment (PRA), Risk Assessment (RA).

1. Introduction

There are many reasons for the reduced strength capacity and destruction of pipelines. One of these reasons is the appearance of defects during its manufacture, construction, and operation. According to [1], defects may be visible, hidden, as well as critical, significant and insignificant. Out of all defects of pipeline systems the corrosion defects are considered to be the most significant ones.

Corrosion and other defects in oil and gas pipelines have been serious risks facing operators, inspectors, and corrosion management experts concerned with the offshore/onshore fields; the effects of these risks may be fatal. Oil and gas pipelines risk assessment (PRA) is the core content of the integrated management of the entire pipelines. The PRA allows detecting the danger factors on the pipelines, to facilitate control and prevention of corrosion & other risks, and to guarantee safe operation of the pipelines [2].

 ISBN: 978-81-936820-6-7

Research studies have been conducted on various topics to ensure pipeline integrity, reliability, and safety, such as qualitative, semi-quantitative, and quantitative risk assessment techniques [1,3-20]. Examples of these techniques are; the risk assessment matrix, the fuzzy Bayesian Belief network, the Fuzzy Petri net model, Fuzzy logic, AHP, and F-AHP, and the combined Analytical Hierarchy Process - Fault Tree Analysis (AHP-FTA), Monte Carlo, and hazard and operability study (HAZOP). The quantitative and semi-quantitative techniques are considered more accurate and provide more details prioritization of risks than the outcome of qualitative risk assessments techniques that can be evaluated quickly to assess risks.

2. Statement About the Pipelines Understudy

This study carried out on five pipelines, which are used in transporting oil and gas at both offshore and onshore fields: namely; (i) 10″ condensate, (ii) 16″ oil [section A, B, C], (iii) 36″ dry gas.

The historical report of the company regarding the detection of these pipelines after pigging (cleaning and inspection) indicates that there are several types of corrosion and other defects in each part of these pipelines, which can be summarized as: (i) Internal Metal Loss, (ii) External Metal Loss, (iii) Gouge Metal Loss, (iv) Dent Metal Loss, (v) Pipe Mill Metal Loss. All types of pipelines defects have been defined and classified in [22] and many more references were cited in [21].

3. Risk Assessment Techniques Proposed for the Analysis of the Pipelines

Several techniques have been proposed in order to analyze the risks of the pipelines, identify their causes and limiting their impacts, such as the AHP and the FAHP.

3.1. The Classical Analytical Hierarchy Process (AHP)

The theory of AHP is based on the fact that the elements of the problem can be arranged within a separate group, each of which has a specific hierarchical level within the overall hierarchical structure, each level affects directly the above level; therefore, the bottom level is affected too.

3.1.1. Hierarchical Structuring of the Problem

The assessment is decomposed into a hierarchy consisted of the problem (goal), then the criteria, followed by sub-criteria and alternatives in lower levels. At the core of the hierarchy is the goal of the problem being studied and analysed. The leaf nodes are the alternatives to be compared.

3.1.2. Priority Analysis

The AHP calculates the priorities between the elements of the hierarchy and collecting the opinions, to obtain a set of the overall priorities, and to check the stability of these opinions to draw a final decision based on the results of this process.

3.1.3. Identification Priorities

Priority setting is represented by making binary comparisons between elements in the second level of the hierarchy with values ranging from (1 to 9) as shown in Table 1.

Table 1: *Saaty' Scale for Quantitative Comparison of Alternatives [5].*

P.L	E.S	E.T.M.S	M.S	M.T.S.S	S.S	S.T.V.S.S	V.S.S	V.S.T.E.S	E.S
N.V	1	2	3	4	5	6	7	8	9

Abbreviations in this table mean: P.L=Preference Level, N.V=Numerical Value, E.S=Equally Serious, E.T.M.S= Equally to Moderately Serious, M.S=Moderately Serious, M.T.S.S=Moderately to Strongly Serious, S.S=Strongly Serious, S.T.V.S.S=Strongly to Very Strongly Serious, V.S.S=Very Strongly Serious, V.S.T.E.S=Very Strongly to Extremely Serious, E.S=Extremely Serious.

3.1.4. Estimating Priorities

To estimate the priorities in an approximate way; (i) sum of the values in each column should be calculated; (ii) each value should be divided by the summation of the column that allows meaningful comparisons between elements; (iii) the mean of the rows should be calculated by summation of the values in each row and divided by the number of elements in that row [11-13, 23].

3.1.5. Consistency Verification

When the matrix is steady, the normalized summation for each row shows how much each element is dominated by the other relative elements [24-25]. If the rules are contradictory, this value known as (Consistency Ratio), will be greater than 10% [10,26].

3.1.6. Estimating the Consistency Ratio

The consistency ratio is calculated as shown in equation (1) and is required to be less than 0.1 for acceptable consistency [24].

$$CR = \frac{CI}{RI} \qquad (1)$$

5.1 Where: CR = Consistency Ratio; RI = Random Index, CI = Consistency Index

3.2. The Fuzzy Analytical Hierarchy Process

In F-AHP, the factors that affect the decision-making are hierarchically arranged from the overall goal to the criteria, sub-criteria, and alternatives in successive levels.

Triangular Fuzzy Numbers (TFNs)

Da-Yong [27] has used the extent analysis technique and the principle of (TFN) comparison to obtain the priorities of alternatives from pair-wise comparison. TFNs contain three levels of comparison values; minimum possible value (L), the most possible value (M), and the maximum possible value (U). These values follow the scale shown in Table 2. The technique of F-AHP can be applied by using the equation (2), the fuzzy synthetic extent value (Si) with respect to the (ith) criterion is defined as [14,28]:

$$S_i = \sum_{j=1}^{m} M_{gi}^{j} \times \left[\sum_{i=1}^{n} \sum_{j=1}^{m} M_{gi}^{j}\right]^{-1} \qquad (2)$$

ISBN: 978-81-936820-6-7
Proceedings DOI: 10.21467/proceedings.4

Series: AIJR Proceedings

For Si = (Li, Mi, Ui) and Sj = (Lj, Mj, Uj), the degree of possibility that Sj ≥ Si for a convex fuzzy number can be obtained from equation (3):

$$V(S_j \geq S_i) = \begin{cases} 1 & if\ m_j \geq m_i \\ 0 & if\ l_i \geq u_j \\ \frac{l_i - u_j}{(m_j - u_j) - (m_i - l_i)} & otherwise \end{cases}$$

(3)

To obtain estimates for sets of weight values under each criterion, one must consider a principle of comparison for fuzzy numbers, the degree of possibility of Si ≥ Sj = (1, 2, 3...n) should be estimated by using equation (4).

$$V(S_j \geq S_1, S_{2,}\ S_3 \ldots S_n) = \min V(S_i \geq S_{i=1,\ 2,\ 3 \ldots n}) \quad (4)$$

Then, the normalized weight W (Si) will be formed in terms of a weight vector as follows:

$$W = \left(w(S_1), w(S_2), \ldots, w(S_n)\right)^T \quad (5)$$

Table 2: *Linguistic Terms and the Corresponding Triangular Fuzzy Numbers [28].*

	FAHP								
L.S.F.I	E.I	I.1	M.I	I.2	I	I.3	V.I	I.4	A.I
T.F.N	1,1,1	1,2,3	2,3,4	3,4,5	4,5,6	5,6,7	6,7,8	7,8,9	9,9,9
T.F.R.N	1,1,1	1/3,1/2,1/1	1/4,1/3,1/2	1/5,1/4,1/3	1/6,1/5,1/4	1/7,1/6,1/5	1/8,1/7,1/6	1/9,1/8,1/7	1/9,1/9,1/9

Abbreviations in this table mean: L.S.F.I=Linguistic Scales for Importance, T.F.N=Triangular Fuzzy Numbers, T.F.R.N= Triangular Fuzzy Reciprocal Numbers, E.I=Equally Important, I.1=Intermediate 1, M.I=Moderately Important, I.2=Intermediate 2, I=Important, I.3=Intermediate 3, V.I=Very Important, I.4=Intermediate 4, A.I=Absolutely Important.

4. Results and Discussion

The pair-wise comparison for the basic consequences in AHP and F-AHP techniques are done between the three types of consequences listed in Table 3.

Table 3: *The Basic Consequences Definitions.*

Consequence Types	Symbol
Environmental Impact	EV-I
Economic Impacts	EC-I
Health-Safety Impacts	HS-I

Table 4 clearly shows that the results of both the classical AHP and F-AHP techniques were close enough to agree that health and safety impacts are more important than economic and environmental impacts. The quantitative values explain that the criterion "Health and Safety", would have a higher importance of being attentive than the other two.

Table 4: *The Normalized Pair- Wise Comparison Matrix.*

Criteria	EV-I	EC-I	HS-I
AHP	0.1637	0.2972	0.5389
F-AHP	0.0769	0.3563	0.5667

Table 5 shows that the main type of corrosion, which should receive all the attention is the internal metal loss. The obtained result of the F-AHP for (EC-N) has value of zero, which means that the corresponding criterion has no importance as was stated by Liyuan [28].

Table 5: *Corrosion Risk Rates of AHP VS. F-AHP for 10" Condensate Pipelines.*

	AHP	**FAHP**
IC-N	0.7851	1.0000
EC-N	0.2148	0.0000

Table 6 shows the risk rates of corrosion types for each section in 16" oil pipeline by using both techniques, risk rates in section (A) were very close. The other two types of risks in section (B) are both cancelled in F-AHP, whereas the (IC-B) in AHP is the most important (0.7591). In section C, the classical AHP indicates the (IC-C) is the most important (0.5971), and that the (EC-C) is the next most important (0.2507); whereas the result of F-AHP cancelled both (MD-C) and (DC-C) and left the (IC-C) as the most important, this can be an advantage for F-AHP, where the decision maker can focus on the more important risks as was also reported by Ozdagoglu, et al. [26].

Table 6: *Corrosion Risk Rates of AHP VS. F-AHP for 16" Oil Pipelines for Each Section.*

Section A			**Section B**			**Section C**		
	AHP	**F-AHP**		**AHP**	**F-AHP**		**AHP**	**F-AHP**
GC-A	0.4879	0.4809	**GC-B**	0.1132	0.0000	**MD-C**	0.0725	0.0000
MD-A	0.5120	0.5190	**IC-B**	0.7591	1.0000	**IC-C**	0.5971	0.8300
			DC-B	0.1276	0.00000	**EC-C**	0.2507	0.1700
						DC-C	0.0796	0.0000

In 36", dry gas pipeline, pair-wise comparison proofed that (MD-D) was less important than the (IC-D) in AHP. Relatively, this type of risk has no importance in F-AHP, but (IC-D) was rated with value of one as the most risky type of corrosion in this study as shown in Table 7.

Table 7: *Corrosion Risk Rates of AHP VS. F-AHP for 36" Dry Gas Pipelines.*

	AHP	**FAHP**
IC-D	0.8648	1.0000
MD-D	0.1351	0.0000

5. Conclusions

The analysis of the risk assessment results as was discussed elsewhere [3,29] indicates that there is a range from convergent to divergent. Results showed that these pipelines are subject to damage due to high-risk rates of some types of corrosion and other defects. In the 10" condensate pipeline and by using the classical AHP, the type of corrosion that should receive all the attention is the (IC-N) (0.7851). However; in the 16" oil pipeline section A, the defect of (MD-A) when using the classical AHP was the most important (0.5120) than the other (GC-A). These results were close enough to the results of the F-AHP. In section B, the (IC-B) in the classical AHP was the most important (0.7591) and the other two types of risks were both

ISBN: 978-81-936820-6-7

Series: AIJR Proceedings
Proceedings DOI: 10.21467/proceedings.4

cancelled in F-AHP. In section C, the classical AHP indicates the (IC-C) is the most important (0.5971), and the (EC-C) was the next most important (0.2507); whereas the result of F-AHP cancelled both (MD-C) and (DC-C) and left the (IC-C) as the most important. Decision maker may be able to focus on the most significant types of risks. In oil and gas pipelines, assessment techniques allow corrosion risks to be assessed after the inspection processes (in this study, Pigging was the process used to inspect the five (5) pipelines). This can help the inspectors focus on the types that have high influence on pipelines.

References

[1] GOST 15467, "Quality Management. Basic Concepts. Terms and Definitions, *IPK Izd-vo standartov*, Moscow, 2009.

[2] D. Hang, W. Lixin, and W. Qiannan, "A Study on Oil Pipeline Risk Assessment Technique Based on Fuzzy Analytic Hierarchy Process", *The Open Petroleum Engineering Journal*, pp. 125-129, 2014.

[3] F. Afaf, "Corrosion Risk Assessment Study Onshore Field", *M.Sc. Thesis*, College of Engineering, University of Tripoli, 2008.

[4] K. Golam, S. Rehan, and T. Solomon, "A Fuzzy Bayesian Belief Network for Safety Assessment of Oil and Gas Pipelines", *Structure and Infrastructure Engineering Journal*, vol. 12, no. 8, pp. 874-889, 2016.

[5] Z. Tan, J. Li, Z. Wu, J. Zheng, and W. He, "An Evaluation of Maintenance Strategy Using Risk Based Inspection", *Safety Science*, vol. 49, pp. 852-860, 2011.

[6] G. Yanbao, M. Xiaoli, W. Deguo, M. Tao, L. Shuhai, and H. Renyang, "Comprehensive Risk Evaluation of Long-Distance Oil and Gas Transportation Pipelines Using a Fuzzy Petri Net Model", *Journal of Natural Gas Science and Engineering*, vol. 33,
pp. 18-29, 2016.

[7] H. Abid, "Security of Cross-Country Oil and Gas Pipelines: A Risk-Based Model", *Journal of Pipeline Systems Engineering and Practice*, vol.7, no.3, pp. 1-8, 2016.

[8] S. Oleg and T. Solomon, "Internal Corrosion Hazard Assessment of Oil & Gas Pipelines Using Bayesian Belief Network Model", *Journal of Loss Prevention in the Process Industries*, vol. 40, pp. 479-495, 2016.

[9] Z. Qi, W. Wei, L. Dongpeng, L. Kaikai, and Q. Qiao, "Estimation of Corrosion Failure Likelihood of Oil and Gas Pipeline Based on Fuzzy Logic Approach", *Engineering Failure Analysis*, vol. 70, pp. 48-55, 2016.

[10] C. Briggs, "Risk Assessment in the Upstream Crude Oil Supply Chain: Leveraging Analytic Hierarchy Process", *Ph.D. Dissertation*, Transportation and Logistics, College of Graduate and Interdisciplinary Studies, North Dakota State University, April 2010.

[11] R. Izak, "Applying the Analytic Hierarchy Process to Oil Sands Environmental Compliance Risk Management". *Ph.D. Dissertation*, College of Management and Technology, Walden University, 2014.

[12] B. Abdul-Lateef, M. Abdul-Nasir, and M. Adekunle, "A Fuzzy Multi-Criteria Decision Support System for Evaluating Subsea Oil Pipeline Routing Criteria In East Malaysia", *Environmental Earth Sciences*, vol. 74, pp. 4875-4884, 2015.

[13] T. Solomon and S. Rehan, "Risk-Based Environmental Decision-Making Using Fuzzy Analytic Hierarchy Process (F-AHP)", *Stochastic Environmental Research and Risk Assessment*, vol. 21, pp. 35-50, 2006.

[14] K. Dey, "Analytic Hierarchy Process Analyzes Risk of Operating Cross-Country Petroleum Pipelines in India", *Natural Hazards Review*, vol. 4, no.4, pp. 213-221, 2003.

[15] B. Yongqiang, L. Lv, and W.Tong, "The Application of the Semi-Quantitative Risk Assessment Method to Urban Natural Gas Pipelines", *Journal of Engineering Science and Technology*, pp. 74-77, 2013.

[16] I. Bertuccio and M. Moraleda, "Risk Assessment of Corrosion in Oil and Gas Pipelines Using Fuzzy Logic", *Corrosion Engineering, Science and Technology*, vol.47, no.7, pp. 553-558, 2012.

[17] D. Prasanta, "Analytic Hierarchy Process Helps Evaluate Project in Indian Oil Pipelines Industry", *International Journal of Operations & Production Management*, vol. 24, no. 6, pp. 588-604, 2004.

[18] A. Dawotola, P. van Gelder, and J. Vrijling, "Risk Assessment of Petroleum Pipelines Using A Combined Analytical Hierarchy Process - Fault Tree Analysis (AHP-FTA)", *Proceedings of the Seventh International Probabilistic Workshop*, pp. 491-501, 2009.

[19] S. Mubin and G. Mubin, "Risk Analysis for Construction and Operation of Gas Pipeline Projects in Pakistan", *Pakistan Journal of Engineering & Applied Sciences*, vol. 2, pp. 22-37, 2008.

[20] J. Yadhushree, P. Shiva, and S. Keerthi, "Qualitative Risk Assessment and HAZOP Study of a Glass Manufacturing Industry". *International Journal of Advance Research, Ideas and Innovations in Technology*, vol. 3, pp. 776-787, 2017.

[21] M. Xie and Z. Tian, "Risk-Based Pipeline Re-Assessment Optimization Considering Corrosion Defects", *Sustainable Cities and Society*, vol. 38, 746-757, 2018.

[22] J. Roland, T. Susannah, and H. Phil, "Proposal for the Development of an International Recommended Practice in Pipeline Defect Assessment and Repair Selection", *International Conference on the Evaluation and Rehabilitation of Pipelines Prague*, pp. 1-27, 2008.

[23] R. Dejan, "A Tool for Risk Assessment", *Safety Engineering*, pp.121-122, 2013.

[24] J. Alonso and M. Lamata, "Consistency in the Analytic Hierarchy Process: A New Approach", *International Journal of Uncertainty*, pp. 445-459, 2006.

[25] M. Ayhan, "A Fuzzy AHP Approach for Supplier Selection Problem.", *International Journal of Managing Value and Supply Chains*, pp.11-23, 2013.

[26] A. Ozdagoglu and G. Ozdagoglu, "Comparison of AHP and Fuzzy AHP for the Multicriteria Decision Making Processes with Linguistic Evaluations", *Istanbul Ticaret University Fen Bilimleri Dergisi*, pp. 65-85, 2007.

[27] C. Da-Yong, "Applications of the Extent Analysis Method on Fuzzy AHP", *European Journal of Operational Research*, pp. 649-655, 1996.

[28] Z. Liyuan, "Comparison of Classical Analytic Hierarchy Process (AHP) Approach and Fuzzy AHP Approach in Multiple-Criteria Decision Making", *M.Sc. Thesis*, University of Nebraska-Lincoln, Nebraska, 2010.

[29] F. Haddada, "Assessment of Corrosion Risks in the Oil and Gas Pipelines in Libya's Onshore/offshore Field", *M.Sc. Thesis*, College of Engineering, University of Tripoli, 2017.

ISBN: 978-81-936820-6-7

Series: AIJR Proceedings
Proceedings DOI: 10.21467/proceedings.4

AIJR Proceedings Series

A scientific conference explores the developments of scientific research in the field of applied engineering sciences, technologies, material science, environmental and engineering management, in order to support inter-disciplinary work. CEST-2018 was organized by Faculty of Engineering Garaboulli, and Faculty of Engineering, Al-khoms, Libya.

First Conference for Engineering Sciences and Technology

Volume 2

ISBN 978-81-936820-6-7